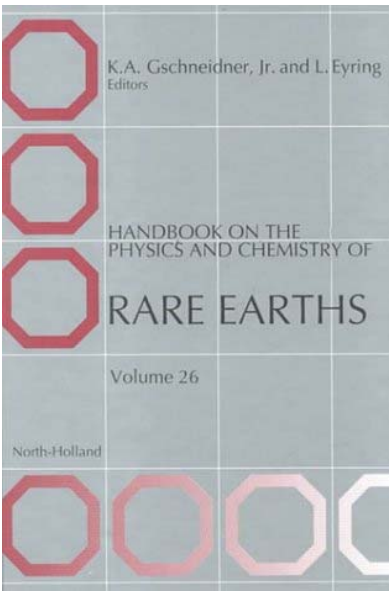

Handbook on the Physics and Chemistry of Rare Earths, volume 26

Elsevier, 1999

Edited by: Karl A. Gschneidner, Jr. and LeRoy Eyring
ISBN: 978-0-444-50185-1

Handbook on the Physics and Chemistry of Rare Earths
Vol. 26
edited by K.A. Gschneidner, Jr. and L. Eyring

PREFACE

Karl A. GSCHNEIDNER, Jr., and LeRoy EYRING

These elements perplex us in our rearches [sic], *baffle us in our speculations, and haunt us in our very dreams. They stretch like an unknown sea before us – mocking, mystifying, and murmuring strange revelations and possibilities.*

Sir William Crookes (February 16, 1887)

Three of the chapters in this volume deal with various aspects of the magnetic behaviors of the lanthanide metals and some of their compounds, while the fourth is concerned with the photoelectron spectroscopy of the anomalous f (heavy fermion) systems in cerium and uranium compounds.

For many years the only way to obtain information about the magnetic structures observed in lanthanide materials, many of which are quite elegant and exotic, was to use neutron diffraction. But that started to change about ten years ago when scientists began to exploit the unique features of X-rays from synchrotron sources, i.e. a high flux of photons which can be focussed into a small spot with a fairly wide tunable bandwidth. The information and results gleaned from X-ray scattering studies of the magnetic lanthanide metals, intra lanthanide alloys, a few intermetallic compounds, intra lanthanide superlayers and thin films are summarized in chapter 169 by McMorrow, Gibbs and Bohr.

The use of static pressure and alternating mechanical stresses to study the magnetic properties of the lanthanide metals, alloys and compounds is reviewed by Tishin, Spichkin and Bohr in chapter 170. The effects of these static and dynamic stresses on the magnetoelastic interactions is the main thrust. These interactions display themselves in the changing of the magnetic state under mechanical stress, causing a variation of the magnetic phase transition temperatures, magnetization and magnetic structures, and leads to anomalies in the elastic constants as well as the damping of sound oscillations.

Magnetic systems which are close to the critical conditions for the appearance of magnetic ordering are examined by Duc and Goto in chapter 171. The transition from a nonmagnetic or low-induced moment state to a ferromagnetic state under an applied magnetic field is known as itinerant electron metamagnetism. The first-order transition, which has been observed in several lanthanide–cobalt intermetallic compounds, can be affected by external parameters (i.e. temperature, pressure, magnetic fields) and

internal parameters, including the exchange field and stoichiometry. As noted by the authors itinerant electron metamagnetism was predicted over 35 years ago, but the major advances only occurred over the past decade.

The discovery of materials with extremely heavy electron masses (500 to 2000 times larger than that of copper metal) occurred about twenty five years ago, and these materials have become known as "heavy fermions." In the 1980s this was one of the hottest topics in condensed matter physics, only to be supplanted by high-temperature superconductors in the 1990s. Still a lot of work is being carried out on the heavy fermion materials, i.e. cerium- and uranium-based systems. As a matter of fact some of the most important studies were not made until this last decade. One of the prime research tools for understanding these 4f and 5f systems is photoelectron spectroscopy. Early work in this field was plagued by the lack of single crystals, the poor quality of polycrystalline samples, and inadequate theories to interpret photoelectron spectra. But that has changed in the last five to ten years. The new developments in the photoelectron spectroscopy (both experimental and theoretical) are reviewed in chapter 172 by Arko, Riseborough, Andrews, Joyce, Tahvildar-Zadeh and Jarrell.

The "unknown sea" as a metaphor, proposed 112 years ago by Sir William Crookes for the rare earth elements and quoted at the head of this preface, has been charted to a significant degree since then, including the contributions to this volume and the *Handbook* series. Nevertheless, they remain for us "mocking, mystifying and murmuring strange revelations and possibilities," and so shall remain beyond the distant horizon.

CONTENTS

CONTENTS OF VOLUMES 1–25

VOLUME 4: Non-metallic compounds – II

1979, 1st repr. 1984; ISBN 0-444-85216-6

VOLUME 5

1982, 1st repr. 1984; ISBN 0-444-86375-3

VOLUME 6

1984; ISBN 0-444-86592-6

VOLUME 7

1984; ISBN 0-444-86851-8

VOLUME 8

1986; ISBN 0-444-86971-9

VOLUME 9

1987; ISBN 0-444-87045-8

VOLUME 10: High energy spectroscopy

1988; ISBN 0-444-87063-6

VOLUME 11: Two-hundred-year impact of rare earths on science

1988; ISBN 0-444-87080-6

VOLUME 12

1989; ISBN 0-444-87105-5

VOLUME 13

1990; ISBN 0-444-88547-1

VOLUME 14

1991; ISBN 0-444-88743-1

VOLUME 15

1991; ISBN 0-444-88966-3

MASTER INDEX, Vols. 1–15
1993; ISBN 0-444-89965-0

VOLUME 16
1993; ISBN 0-444-89782-8

VOLUME 17: Lanthanides/Actinides: Physics – I
1993; ISBN 0-444-81502-3

VOLUME 18: Lanthanides/Actinides: Chemistry
1994; ISBN 0-444-81724-7

VOLUME 19: Lanthanides/Actinides: Physics – II

1994; ISBN 0-444-82015-9

VOLUME 20

1995; ISBN 0-444-82014-0

VOLUME 21

1995; ISBN 0-444-82178-3

VOLUME 22

1996; ISBN 0-444-82288-7

VOLUME 23

1996; ISBN 0-444-82507-X

VOLUME 24

1997; ISBN 0-444-82607-6

VOLUME 25

1998; ISBN 0-444-82871-0

Handbook on the Physics and Chemistry of Rare Earths
Vol. 26
edited by K.A. Gschneidner, Jr. and L. Eyring

Chapter 169

X-RAY SCATTERING STUDIES OF LANTHANIDE MAGNETISM

D.F. McMORROW
Condensed Matter Physics and Chemistry Department, Risø National Laboratory, DK-4000 Roskilde, Denmark

Doon GIBBS
Department of Physics, Brookhaven National Laboratory, Upton, NY 11973, USA

Jakob BOHR
Department of Physics, DTU, Lyngby, Denmark

Contents

List of symbols

$\vec{A}$	Vector potential of photon field	M	Atomic absorption edge
$\vec{A}''$	Spin polarization vector, non-resonant scattering	$\vec{P}$	Momentum of electron
$\vec{B}$	Orbital polarization vector, non-resonant scattering	$P(P')$	Degree of linear polarization of incident (scattered) beam
$\vec{E}$	Electric field	r_0	Classical electron radius
f	Total scattering atomic scattering amplitude	$\vec{S}(Q)$	Fourier transform of total atomic spin angular momentum
$f^{\text{non-res}}, f^{\text{magnetic}}$	Non resonant magnetic scattering amplitude	T_c	Superconducting critical temperature
f^{res}	Resonant magnetic scattering amplitude	T_C	Curie temperature
f'	Real part of dispersion correction	T_N	Néel temperature
f''	Imaginary part of dispersion correction	$\vec{q}$	Modulation wave vector
$\vec{H}$	Magnetic field	$\vec{Q}$	Wave-vector transfer of a photon
$\vec{k}$ ($\vec{k}'$)	Incident (final) photon wave vector	$\hat{z}$	Unit vector parallel to the total magnetic moment
K	Atomic absorption edge	$\hat{\varepsilon}$ ($\hat{\varepsilon}'$)	Incident (final) photon polarization vectors
L	Atomic absorption edge	μ	Electronic magnetic moment
$\vec{L}(Q)$	Fourier transform of total atomic orbital angular momentum	$\vec{\tau}_m$	Magnetic modulation wave vector

1. Introduction

Interest in the applications of X-ray synchrotron radiation has grown rapidly during the last decade. At the present time, intense, ultra-bright synchrotron radiation is available on a routine basis from third-generation sources located in Europe (ESRF), North America (APS) and Japan (Spring8). This burgeoning activity is driven both by advances in technology and a rapidly developing understanding of how to exploit the high-intensity beams from these sources. Widely diverse areas of science have benefited, including physics, chemistry, materials science, biology, medicine, geology, and others. With increasing frequency, cross-disciplinary efforts have led to the creation of entirely new fields, such as in the study of complex materials, surface science, and in applications of real space imaging. In synchrotron-based research generally, it is a time of enormous productivity and excitement that promises much for the future.

The study of magnetic materials by X-ray scattering techniques is among the fields that has benefited most from the routine availability of X-ray synchrotron radiation. While

virtually all of the knowledge we possess today concerning magnetic structures was gathered using the well-established technique of neutron diffraction, exploitation of the unique features of X-rays from synchrotron sources has led to qualitatively new kinds of experiments. All of these experiments have depended crucially on high flux: today more than 10^{12} photons s^{-1} can be focussed onto a 1 mm^2 spot within a 5 eV bandwidth. Another important factor in the development of this field has been the naturally high wave-vector resolution, that not only allows the determination of the magnetic modulation wave vectors to higher levels of accuracy than can be achieved with neutrons, but also allows magnetic correlation lengths to be explored on micron length scales. In addition, the well-defined polarization characteristics of synchrotron radiation and wavelength tuneability have been used to create new techniques involving, for example, resonance and interference studies of ferromagnets and antiferromagnets. New efforts are beginning in X-ray inelastic, high-energy (50–100 keV) and surface magnetic scattering. Other related techniques include spin-dependent Compton scattering, nuclear Bragg scattering, magnetization dependent absorption and dichroism, and experiments involving Faraday rotation. As might be expected for such recent endeavours, the basic properties of the cross-section are still of great interest, in addition to what may be learned about the magnetic and electronic structures of the samples under study.

In simple terms, an X-ray incident on an electron is scattered both by the electron's charge and by its magnetic moment. Charge scattering is the dominant mechanism and is the basis for crystallographic investigations of condensed matter. Although considerably weaker, the electric and magnetic fields of the incident X-ray also interact with the magnetic moment, and this gives rise to magnetic scattering. Generally speaking, the results of X-ray magnetic scattering experiments are considered within two regimes, determined by the incident photon energy. These are the non-resonant limit, when the incident X-ray energy is well separated from the excitation energy of any atomic absorption edge in the solid, and the resonant regime, where the incident X-ray energy lies near an absorption edge.

The amplitude for non-resonant X-ray magnetic scattering has the simple form $\vec{L} \cdot \vec{A}'' + \vec{S} \cdot \vec{B}$. Here, $\vec{L}$ and $\vec{S}$ refer to the Fourier transforms of the atomic orbital and spin magnetization densities respectively, and the vectors $\vec{A}''$ and $\vec{B}$ depend on the incident and scattered wave vectors, and on the incident and scattered photon polarization vectors. The polarization dependence of the magnetic cross-section provides a natural technique for quantitative determinations of magnetic structures. Beyond this, there are other novel possibilities that arise from the well-defined (and tunable) polarization characteristics of synchrotron radiation. For example, using the high degree of linear polarization of the incident beam, it has been possible to distinguish between charge peaks arising from lattice modulations and magnetic scattering. As a second example, because the vectors $\vec{A}''$ and $\vec{B}$ are distinct, the polarization dependence of the orbital contribution to the magnetic cross-section differs from that of the spin contribution. This leads to the possibility that the orbital- and spin-magnetization densities may be distinguished in X-ray scattering experiments by performing polarization analysis of the scattered beam. (The same separation is not directly possible by neutron diffraction techniques, where

the polarization dependence of the spin and orbital contributions are identical.) Early experiments of this sort carried out on lanthanides and actinides produced qualitative agreement with theoretical expectations (Gibbs et al. 1988, McWhan et al. 1990). More recently, similar experiments performed using the ESRF have begun to extract quantitative information (Sutter et al. 1999).

In the resonant regime, when the incident X-ray energy is tuned near an absorption edge, there are additional contributions to the X-ray scattering cross-section. Within a one-electron view of the scattering process, the incident photon promotes an inner shell electron to an unoccupied level above the Fermi energy E_F, which subsequently decays through the emission of an elastically scattered photon. The amplitude for resonant magnetic scattering then depends on the matrix elements which couple the ground and excited magnetic states allowed by the exclusion principle. In this way, the energy and polarization dependence of the magnetic scattering probes the fine structure of magnetic states. It follows that detailed modelling of the line shapes of the magnetic scattering may reveal the spectrum of allowed transitions near E_F, including perhaps the magnitude of the exchange splitting and induced polarization within metallic conduction bands. The largest resonant enhancements occur near the L and M absorption edges. As a consequence, experiments of this variety have been attempted in most of the lanthanides (for which the L absorption edges are easily accessible near 8 keV), in a variety of the actinides (for which the M absorption edges fall around 3.7 keV, allowing diffraction experiments to be performed), and in reflectivity measurements from transition elements using ultra-violet synchrotron radiation (near their L edges below 1 keV). Considerably smaller enhancements have also been observed at transition element K edges, for example in Ni (Namikawa et al. 1985) and NiO (Hill et al. 1997). In all of the studies performed so far, it has been found that the results are qualitatively consistent with atomic orbital descriptions of the electronic structure. Possible exceptions to this have been noted in determinations of the branching ratio in actinides (Tang et al. 1992a) and in the lanthanides (D. Watson et al. 1996), and in studies of the mixed valence compound TmSe (McWhan et al. 1993). It is also important to note that the polarization dependence of the resonant cross-section depends in a simple way on the directions of the local atomic moments (and which is distinct from the polarization dependence of the non-resonant cross-section). The existence of large resonant enhancements of the magnetic scattering then makes feasible the determination of magnetic structures in an even wider class of materials than was previously thought. Exciting possibilities include the extension of these techniques to alloys (Pengra et al. 1994, Stunault et al. 1995), to magnetic superlattices (Vettier et al. 1986, McMorrow et al. 1995), and to surfaces (Ferrer et al. 1996, G.M. Watson et al. 1996). In particular, in composite materials, the possibility of tuning the incident photon energy to the absorption edges of one or the other constituent will make possible species-specific determinations of the magnetic structure. A recent example is the observation of a small induced 5d moment at the site of non-magnetic Lu in Dy–Lu alloys (Everitt et al. 1995). With the development of beamlines specialized for coherent and inelastic scattering on the new sources, the future seems exciting, indeed.

The lanthanide metals have played a special role in these developments. The striking variety of modulated structures found in these elements has provided a testing ground for elucidating the basic features of the X-ray magnetic cross-section, for example, its polarization and energy dependence. At the same time, the application of these techniques to the lanthanides has provided a new understanding of their structural and magnetic properties. In this article, we review the progress made during the last ten years or so in X-ray scattering studies of lanthanide metals. We focus especially on the results of X-ray scattering experiments and their interpretation, avoiding a more general discussion of the basic properties of the lanthanide metals, as comprehensive reviews are provided in earlier volumes of this series, in the book edited by Elliott (1972), and most recently in the book by Jensen and Mackintosh (1991). As mentioned above, we also refrain from a more general discussion of related techniques such as spin-dependent Compton scattering, Faraday rotation, spin-dependent dichroism, and others (see Lovesey and Collins 1996 for a complete discussion of these subjects). By narrowing our perspective to this extent, we are able to present a somewhat more detailed discussion of X-ray scattering than would otherwise be possible in a review.

Before concluding this introduction it is appropriate to consider the historical background to this field. After the development of the Klein–Nishina equation in 1929, it was widely appreciated that X-ray photons interact with, and are scattered by, the magnetic moment of the electron. An interesting short paper on the classical interaction between a photon and a magnetic moment was written by Compton in the nineteen thirties (Compton 1936). Relevant discussions of magnetic scattering were made in the nineteen fifties, for example, by Gell-Mann and Goldberger (1954), and by Low (1954). Because of the weakness of the interaction (and, later, due to the enormous success of neutron magnetic diffraction), X-ray magnetic scattering was not considered a useful technique for the investigation of magnetism in solids. In 1970, a theoretical discussion of the cross-section for magnetic scattering of X-rays by bound electrons by Platzman and Tzoar (1970) led to the suggestion that magnetic diffraction could be observed using modern X-ray tubes. This suggestion was soon taken up by by de Bergevin and Brunel (1972), who in a *tour de force* experiment were able to see antiferromagnetic order in NiO. Later, de Bergevin, Brunel and coworkers conducted a series of experiments on both ferromagnets and antiferromagnets, and various aspects of the cross-section were quantitatively explored (de Bergevin and Brunel 1981, Brunel and de Bergevin 1981, Brunel et al. 1983).

In the last decade or so, the X-ray magnetic scattering cross-section has continued to attract interest, but it has also been exploited as a tool in the broader investigation of magnetism in solids. It is worthwhile mentioning in this context the early calculations of Blume (1985), who suggested that interesting effects might occur near an absorption edge, the original non-resonant experiments on Ho by Gibbs et al. (1985), the first resonant experiments by Namikawa et al. (1985) on Ni, the first X-ray magnetic studies of a superlattice by Vettier et al. (1986), the large enhancements of the magnetic scattering found in Ho by Gibbs et al. (1988), and the observation of even larger enhancements for the actinides by Isaacs et al. (1989). It is also worth noting the exhaustive and useful

X-ray scattering studies by Darnell (1963) on the temperature dependence of the lattice constants in the lanthanides, and a truly remarkable series of experiments performed by Keating in 1969 which revealed charge scattering at twice the magnetic wave vector in Ho and ascribed it to the aspherical charge distribution of the $^5I_8$ Hund's rule ground state.

The layout of this review is as follows. In sect. 2 we discuss the X-ray scattering cross-section, including both resonant and non-resonant cross-sections. We also develop the polarization dependence of the X-ray magnetic cross-section, and work through an example of the calculation of the scattering expected from a helix, as found in some of the heavy lanthanides, and discuss the principles behind the separation of spin and orbital contributions to the total moment. In sect. 3 we describe the results of X-ray scattering studies of the lanthanide metal Ho, while results from the rest of the lanthanide metals are considered in sect. 4. In sect. 5 a summary is given of work on random alloys, selected compounds, and artificial structures, including superlattices and thin films, with examples chosen to exemplify the benefits of X-ray magnetic scattering. The review closes with a summary in sect. 6.

2. The X-ray scattering cross-section

In this section we gather together the key ingredients that are required to describe the X-ray magnetic scattering cross-section. Although our understanding of this has to a large extent come from the results of experiments to be described in later sections, for the sake of clarity it is more useful to first present an overview of the current theoretical understanding.

2.1. *The non-resonant regime*

The classical approximation for the interaction of an X-ray with an electron is illustrated in fig. 1 (de Bergevin and Brunel 1981). In charge scattering (or Thomson scattering, fig. 1a) the electric field of the incident X-ray exerts a force on the electronic charge. The electron's subsequent acceleration leads to dipole re-radiation of the scattered field with the classical dependence on polarization of $\hat{\varepsilon} \cdot \hat{\varepsilon}'$. ($\hat{\varepsilon}$ and $\hat{\varepsilon}'$ are the incident and final photon polarization vectors respectively.) This term dominates and forms the basis for structural investigations by X-ray diffraction. Although considerably weaker, the electric and magnetic fields of the incident photon also interact with the magnetic moment in the solid and give rise to magnetic scattering. The possible scattering processes involving the magnetic moment are illustrated in fig. 1b–f, together with the forms of the emitted radiation. Quantum analogues to these classical interactions have been discussed by Gell-Mann and Goldberger (1954) and by Low (1954). For a free electron, the ratio of the magnetic dipole re-radiation to electric dipole re-radiation is $(\hbar\omega/m_e c^2)^2$, which is of order 10^{-4} for photons of energy $\hbar\omega = 10\,\text{keV}$.

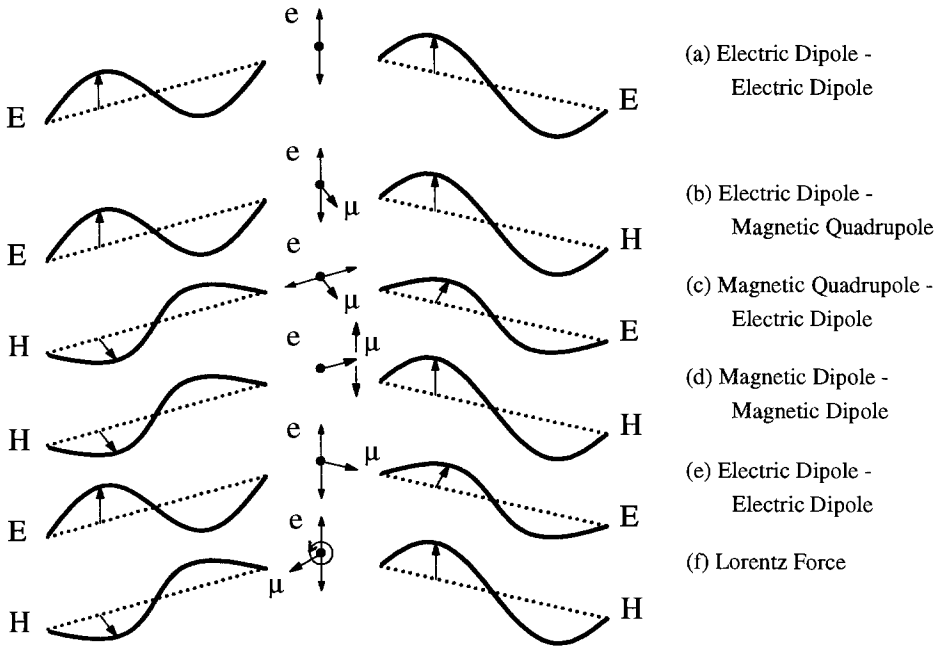

Fig. 1. A classical representation of the dominant scattering mechanisms of a plane-polarized X-ray by an electron. Here E and H are the electric and magnetic fields acting on an electron of charge e and magnetic moment μ. In (a) the X-ray is scattered from the electronic charge. All the other mechanisms involve the electronic magnetic moment. For each type of scattering the nature of the incident driving field and the scattered radiation are shown. (b)–(d) are pure spin scattering, whereas (e) and (f) are for a moving magnetic dipole with finite orbital angular momentum. (Adapted from de Bergevin and Brunel 1981 and Blume 1994.)

The cross-section for elastic scattering of X-rays from atomic electrons in a single crystal has the form

$$\left(\frac{\mathrm{d}\sigma}{\mathrm{d}\Omega}\right)_{k,\varepsilon\to k',\varepsilon'} = r_0^2 \left| \sum_n e^{i\vec{Q}\cdot\vec{r}_n} f_n(\vec{k},\vec{k}',\hbar\omega) \right|^2, \tag{1}$$

where $\vec{r}_n$ is the position of the nth atom in the crystal, $\hbar\omega$ is the incident photon energy, $\vec{Q} = \vec{k} - \vec{k}'$ is the wave-vector transfer of the photon, and r_0 is the classical electron radius. Using second-order perturbation theory Blume (1985, 1994) has shown that the scattering amplitude per atom f_n may be written as

$$f_n(\vec{k},\vec{k}',\hbar\omega) = f_n^{\text{charge}}(\vec{Q}) + f_n'(\vec{k},\vec{k}',\hbar\omega) + \mathrm{i}f_n''(\vec{k},\vec{k}',\hbar\omega) + f_n^{\text{spin}}(\vec{k},\vec{k}',\hbar\omega), \tag{2}$$

where f_n^{charge} is the usual Thompson contribution, f_n' and $\mathrm{i}f_n''$ are the contributions arising from the $\vec{A}\cdot\vec{P}$ term in the cross-section, and f_n^{spin} represents the amplitude for all scattering

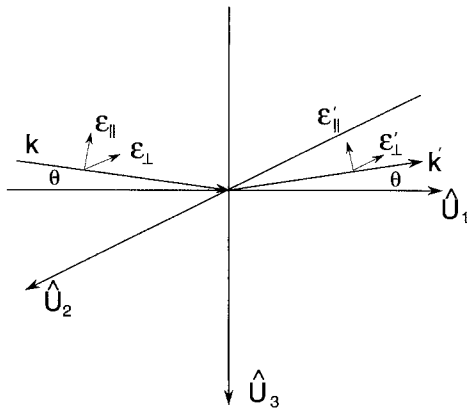

Fig. 2. The co-ordinate system ($\vec{U}_1, \vec{U}_2, \vec{U}_3$) used in this work for the incident and scattered photons. Here $\varepsilon_{\|}(\varepsilon_{\perp})$ refer to the components of the incident photon's polarization parallel (perpendicular) to the scattering plane, and k is its wave-vector: primed quantities refer to the scattered beam. (After Blume and Gibbs 1988.)

which explicitly contains the electron-spin operator. Sufficiently far from any absorption edge, the scattering amplitude f_n may be simplified:

$$f_n(\vec{k}, \vec{k}', \hbar\omega) = f_n^{\text{charge}}(\vec{Q}) + f_n^{\text{magnetic}}(\vec{Q}), \tag{3}$$

where

$$f_n^{\text{charge}}(\vec{Q}) = \rho_n(\vec{Q})(\hat{\varepsilon}'_\sigma \hat{\varepsilon}'_\pi) \cdot \begin{pmatrix} \hat{\varepsilon}_\sigma \\ \hat{\varepsilon}_\pi \end{pmatrix}$$

and

$$f_n^{\text{magnetic}}(\vec{Q}) = \mathrm{i} r_0 \left(\frac{\hbar\omega}{m_e c^2} \right) \left[\tfrac{1}{2} \vec{L}_n(\vec{Q}) \cdot \vec{A}'' + \vec{S}_n(\vec{Q}) \cdot \vec{B} \right]. \tag{4}$$

Here, f_n^{charge} and f_n^{magnetic} are the non-resonant amplitudes for pure charge and magnetic scattering, respectively, $\rho_n(\vec{Q})$ is the Fourier transform of the electronic charge density, and $\vec{L}_n(\vec{Q})$ and $\vec{S}_n(\vec{Q})$ are the respective Fourier transforms of the orbital- and spin-magnetization densities of the nth atom. The vectors $\vec{A}''$ and $\vec{B}$ depend on the initial and final photon polarization vectors and on the initial and final photon wave vectors. (Here we are following the notation of Blume and Gibbs (1988) and using double primes on the polarization vector $\vec{A}''$ to avoid confusion with $\vec{A}$, the vector potential of the photon field.) We choose the linear components of the photon polarization to be parallel or perpendicular to the diffraction plane (spanned by the vectors $\vec{k}$ and $\vec{k}'$). The σ-component of the polarization is defined to be perpendicular to the diffraction plane and the π-component to lie within the diffraction plane (see fig. 2). We note that in most synchrotron experiments performed to date, the incident polarization is predominantly linearly polarized within the median (horizontal) plane of the storage ring and elliptically polarized above and below the median plane. Thus, in experiments performed on the median plane and using a vertical diffraction geometry, the linear incident polarization is

predominantly σ-polarized, while in a horizontal scattering geometry it is predominantly π-polarized. With these conventions, the vectors $\vec{A}''$ and $\vec{B}$ may be written

$$\vec{A}'' = \frac{Q^2}{2k^2}(\hat{\varepsilon}'_\sigma \hat{\varepsilon}'_\pi) \begin{pmatrix} 0 & -(\hat{k}+\hat{k}') \\ (\hat{k}+\hat{k}') & 2(\hat{k}\times\hat{k}') \end{pmatrix} \begin{pmatrix} \hat{\varepsilon}_\sigma \\ \hat{\varepsilon}_\pi \end{pmatrix}$$

and

$$\vec{B} = (\hat{\varepsilon}'_\sigma \hat{\varepsilon}'_\pi) \begin{pmatrix} -\hat{k}'\times\hat{k} & -\hat{k}(1-\hat{k}'\cdot\hat{k}) \\ \hat{k}(1-\hat{k}'\cdot\hat{k}) & -\hat{k}'\times\hat{k} \end{pmatrix} \begin{pmatrix} \hat{\varepsilon}_\sigma \\ \hat{\varepsilon}_\pi \end{pmatrix}. \tag{5}$$

To re-cast this in a form that is useful for the interpretation of data, and following Blume and Gibbs (1988), we express all of the vectors appearing in eq. (5) in terms of the orthonormal basis vectors $\vec{U}_1$, $\vec{U}_2$, and $\vec{U}_3$ defined in fig. 2. Thus, the amplitude for pure non-resonant magnetic scattering may be written in matrix form as

$$f^{\text{magnetic}} = \mathrm{i}r_0 \left(\frac{\hbar\omega}{m_e c^2}\right) \times \begin{pmatrix} \sin 2\theta S_2 & -2\sin^2\theta\,[(L_1+S_1)\cos\theta - S_3\sin\theta] \\ 2\sin^2\theta\,[(L_1+S_1)\cos\theta + S_3\sin\theta] & \sin 2\theta[2\sin^2\theta L_2 + S_2] \end{pmatrix}, \tag{6}$$

where θ is the Bragg angle, and here and in what follows we are implicitly writing the scattering matrix using the polarization vectors as a basis. This equation contains all of the dependence on the components of the spin and orbital moments, and as we shall see in section 2, once the polarization characteristics of the beam are known, allows the scattering cross-section to be calculated.

The relative magnitudes of the pure magnetic scattering to the pure charge scattering, ignoring polarization factors, is given approximately by (Blume 1985)

$$\frac{\sigma_{\text{magnetic}}}{\sigma_{\text{charge}}} \simeq \left(\frac{\hbar\omega}{m_e c^2}\right)^2 \left(\frac{N_m}{N}\right)^2 \left(\frac{f_m}{f}\right)^2 \langle\mu^2\rangle, \tag{7}$$

where N_m and f_m are the number of magnetic electrons and the magnetic form factor, respectively; N and f are the total number of electrons and the charge form factor, respectively; and $\langle\mu\rangle$ is the average magnetic moment per magnetic electron. The prefactor is the amplitude for magnetic scattering from a free electron. For incident photon energies of 10 keV, its value is about 4×10^{-4}. Since each of the other ratios in this expression is typically of the order one, or smaller, the ratio of the magnetic scattering to the charge scattering in the non-resonant limit is always less than 10^{-5}.

It is clear from eq. (3) above that in addition to the pure charge scattering and the pure magnetic scattering, there is also in principal an interference term which couples the charge and the magnetic scattering. The interference term is reduced by only a single

factor ($\hbar\omega/m_e c^2$), and is therefore larger than the pure magnetic scattering. However, the interference term is non-negligible only for ferromagnets where the charge and magnetic scattering are coincident in reciprocal space, thus making it difficult to distinguish from the pure charge scattering. One method to overcome this limitation is to introduce a magnetic field and to measure the flipping ratio, thereby isolating the interference term in the cross-section (Brunel et al. 1983, Namikawa et al. 1985, Vettier et al. 1986). Our discussion of the interference term will be limited to ferromagnetic superlattices (see section 5). (The charge and magnetic scattering are of course $\pi/2$ out of phase and cannot interfere unless a phase shift is introduced, either by the use of circular polarization or by tuning to an absorption edge. See Lovesey and Collins (1996) for more details.)

2.2. *Resonant magnetic scattering*

When the incident X-ray energy is tuned near an absorption edge, there are additional resonant contributions to the X-ray magnetic scattering amplitude (Blume 1985, Namikawa et al. 1985, Gibbs et al. 1988, Hannon et al. 1988, Gibbs et al. 1991). In the following, only the resonant terms arising from the operator $\vec{A} \cdot \vec{P}$ in the Hamiltonian, which contribute directly to f' and f'' are considered, where $\vec{A}$ is the vector potential of the photon field, and $\vec{P}$ is the momentum of the electron in the presence of a field. Crystal-field effects are also neglected. An important consequence of such a simple description is that conventional electric multi-pole selection rules may be used to investigate which transitions are allowed. For the particular case of electric 2^L-pole (EL) transitions in a magnetic ion, the contribution to the coherent scattering amplitude from $\vec{A} \cdot \vec{P}$ may be written (Hannon et al. 1988)

$$f_{EL} = 4\pi\lambda \sum_{M=-L}^{L} \left[\hat{\varepsilon}'^{*} \cdot Y_{LM}\left(\hat{k}'\right) Y_{LM}^{*}\left(\hat{k}\right) \cdot \hat{\varepsilon} \right] F_{LM}(\omega), \tag{8}$$

where

$$F_{LM}(\omega) = \sum_{a,b} \frac{P_a P_{a(b)} \Gamma_x (aMb; EL)/\Gamma}{x(a,b) - \mathrm{i}}. \tag{9}$$

In this expression, the Y_{LM}'s are the vector spherical harmonics, λ is the photon wavelength, and a and b are the initial and excited ionic states with energy E_a and E_b, respectively. P_a gives the statistical probability for the initial state a, and $P_{a(b)}$ gives the probability that the excited state b is vacant for transitions from a. Summed over M, $\Gamma_x(aMb; LM)$ gives the partial width for EL radiative decay from the b to a, and Γ is the total width for b (determined from all radiative and non-radiative decay). In the denominator of eq. (9) $x(a,b) = 2(E_a - E_b - \hbar\omega)/\Gamma$. It is also clear from eq. (8) that the amplitude of the resonant scattering is determined by the detailed electronic structure through the F_{LM} factors. Specifically, the energy widths Γ_x and Γ depend directly on matrix elements of the initial and excited states. Provided that sufficient spin–orbit correlations exist among the

ground or excited states so that the sum over M is non-zero (Hannon et al. 1988, Hamrick 1994), it follows that the greater the overlap is of the wavefunctions, the greater the resonant magnetic intensity will be. For this reason, the L and M absorption edges of the lanthanides and actinides (for which the overlap is large) have been studied intensively in the 3–10 keV range convenient for most X-ray beamlines. It also follows from eq. (8) that the polarization dependence of the resonant scattering is determined independently of the F_{LM} terms through the dependence of the vector spherical harmonics on the direction of the local ionic moment $\hat{z}_n$. Further, as we shall see, the allowed diffraction harmonics ($m\vec{\tau}$, $m = 0, 1, 2$, etc., where $\vec{\tau}$ is the fundamental wave vector of the modulation) arises from the dependence of the Y_{LM} products on powers of $\hat{z}_n$. More recently, it has been shown that the energy-integrated resonant amplitudes may be written as a linear combination of the orbital and spin magnetization densities, plus higher order terms. For the heavy lanthanides, for which Russell–Saunders coupling is valid, this form is proportional to the magnetization provided that the higher-order terms are negligible (Luo et al. 1993).

For incident X-ray energies near the L_{III} absorption edges of the lanthanide metals, the dominant contributions to the resonant scattering (eq. 8) arise from (1) electric dipole transitions coupling $2p_{3/2}$ core and 5d-derived conduction-band states, and (2) electric quadrupole transitions coupling $2p_{3/2}$ and 4f states, as shown schematically in fig. 3.

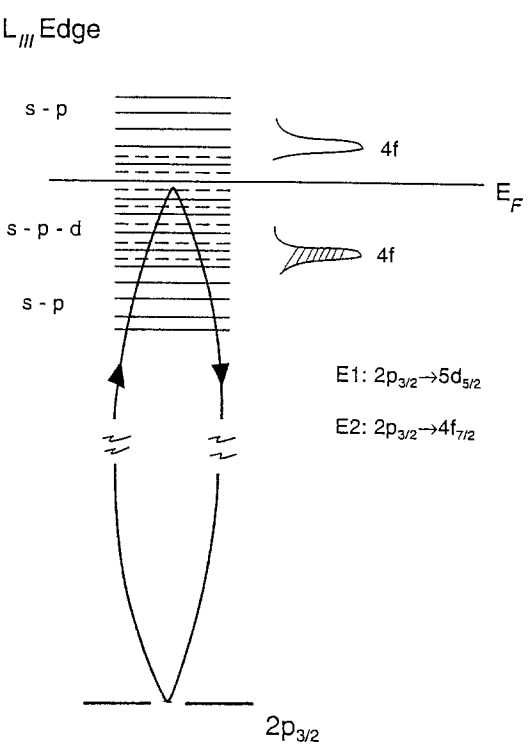

Fig. 3. Schematic, one-electron view of resonant magnetic scattering at the L_{III} absorption edge. The linearly polarised incident photon promotes a $2p_{3/2}$ core electron into an empty state above the Fermi level. In the lanthanides there are 5d states available in the dipole approximation, and unfilled 4f states available through a quadrupole transition. Magnetic scattering results when the virtually excited electron decays, thereby filling the core hole and coherently emitting an elastically scattered photon.

(Transitions involving 6s states are ignored by virtue of the assumed small induced s moment and the small overlap with the p states.) For core excitations involving typical X-ray energies between $\hbar\omega = 5$ and 10 keV, a reasonable first step is to assume that one-particle Hartree–Fock wave functions provide an adequate description of the electronic structure.

2.3. *Dipolar transitions (E1)*

The resonant cross-section is normally dominated by electric dipole processes for which $L = 1$ and $M = \pm 1$, such as the $2p_{3/2} \rightarrow 5d_{1/2}$ transition that occurs at the L_{III} edge in the lanthanides. For such a transition the scattering amplitude may be written as

$$f_{nE1}^{\mathrm{res}} = (\hat{\varepsilon}' \cdot \hat{\varepsilon})F^{(0)} - \mathrm{i}(\hat{\varepsilon}' \times \hat{\varepsilon}) \cdot \hat{z}_n F^{(1)} + (\hat{\varepsilon}' \cdot \hat{z}_n)(\hat{\varepsilon} \cdot \hat{z}_n)F^{(2)}, \tag{10}$$

where $F^{(0)}$ etc. are linear combinations of the F_{LM} factors given in eq. (9), and $\hat{z}_n$ is a unit vector parallel to the total magnetic moment (Hannon et al. 1988). Following the same procedure that allowed us to express the non-resonant amplitude as a 2×2 matrix, eq. (6), we can write the dipole contribution to the resonant scattering amplitude as

$$\begin{aligned} f_{E1}^{\mathrm{res}} = & F^{(0)} \begin{pmatrix} 1 & 0 \\ 0 & \cos 2\theta \end{pmatrix} - \mathrm{i}F^{(1)} \begin{pmatrix} 0 & z_1 \cos\theta + z_3 \sin\theta \\ z_3 \sin\theta - z_1 \cos\theta & -z_2 \sin 2\theta \end{pmatrix} \\ & + F^{(2)} \begin{pmatrix} z_2^2 & -z_2(z_1 \sin\theta - z_3 \cos\theta) \\ +z_2(z_1 \sin\theta + z_3 \cos\theta) & -\cos^2\theta(z_1^2 \tan^2\theta + z_3^2) \end{pmatrix}, \end{aligned} \tag{11}$$

where z_1 is the component parallel to $\vec{U}_1$, etc. (Pengra et al. 1994, Hill and McMorrow 1996). The first term in eq. (11) does not depend on the components of the moment and hence just contributes to the charge peaks, whereas the last two terms both contribute to the magnetic scattering. For example, in an incommensurate system the second term, which is linear in the components of the moment, produces scattering at the first harmonic, whereas the last term (quadratic in the components) gives rise to scattering at the second and zeroth harmonics.

2.3.1. *Quadrupolar transitions (E2)*

It has been established that at the L edges in the lanthanides there is a small but significant contribution to the resonant scattering amplitude from quadrupole transitions which is displaced by a few eV to lower energy than the dipole contribution. For example, at the L_{III} edge of Ho the cross-section for the $2p_{3/2} \rightarrow 4f$ processes at the first harmonic is approximately one quarter that of the dipole (Gibbs et al. 1988). One of the consequences of this contribution is that it produces up to four distinct high-order harmonics in the diffraction pattern. The scattering amplitude for quadrupole transition may be calculated following a similar procedure as outlined for the dipole term, but as it is much more involved than the dipole term and we do not reproduce it here (Hannon et al. 1988, Hill and McMorrow 1996).

2.4. *Scattering from a helix*

In this section we outline the derivation of the scattering cross-section for a simple helix, as found in Ho, Tb and Dy. For simplicity we start by assuming that the synchrotron radiation is perfectly plane polarized in the orbit plane, and consider contributions from the non-resonant and resonant dipole terms only. The contributions from the resonant quadrupolar terms are considered qualitatively at the end of this section, while a discussion of the consequences of having an imperfectly polarized beam are deferred until section 2, where we consider the principles behind the separation of the spin and orbital magnetization densities.

The elastic X-ray scattering cross-section may be generally written as

$$\frac{\mathrm{d}\sigma}{\mathrm{d}\Omega} = \sum_{\lambda\lambda'} P_\lambda \Big| \langle\lambda'|\langle M_\mathrm{c}\rangle|\lambda\rangle - \mathrm{i}\frac{\hbar\omega}{mc^2}\langle\lambda'|\langle M_\mathrm{m}\rangle|\lambda\rangle + \langle\lambda'|\langle M_{\mathrm{E1}}^{\mathrm{res}}\rangle|\lambda\rangle + \langle\lambda'|\langle M_{\mathrm{E2}}^{\mathrm{res}}\rangle|\lambda\rangle + \cdots\Big|^2, \tag{12}$$

where the terms on the right hand side in the sum represent the contributions from charge, non-resonant magnetic, resonant dipole and resonant quadrupole scattering, respectively. $|\lambda\rangle$ and $|\lambda'\rangle$ are the incident and final polarization states, and P_λ is the probability for incident polarization λ. The terms $\langle M_\mathrm{c}\rangle$, etc. are the respective expectation values of scattering operators evaluated in the initial and final states of the solid. For example, for non-resonant magnetic scattering $\langle M_\mathrm{m}\rangle = \left\langle a \middle| \sum_n \mathrm{e}^{\mathrm{i}\vec{Q}\cdot\vec{r}_n} f_n^{\mathrm{magnetic}} \middle| a \right\rangle$, where $|a\rangle$ is an eigen state of the solid. We now make the restrictive assumption that $P_\lambda = \delta_{\lambda\sigma}$, so that the only non-zero terms are $\sigma \to \sigma$ and $\sigma \to \pi$. From eq. (6) the non-resonant cross-section may then be written as

$$\frac{\mathrm{d}\sigma}{\mathrm{d}\Omega}^{\text{non-res}} = r_0^2\left(\frac{\hbar\omega}{m_\mathrm{e}c^2}\right)^2 \left[\left|\left\langle a \middle| \sum_n \mathrm{e}^{\mathrm{i}\vec{Q}\cdot\vec{r}_n} \sin 2\theta S_2 \middle| a \right\rangle\right|^2_{\sigma-\sigma} + \left|\left\langle a \middle| \sum_n \mathrm{e}^{\mathrm{i}\vec{Q}\cdot\vec{r}_n}(2\sin^2\theta[(L_1+S_1)\cos\theta + S_3\sin\theta]) \middle| a \right\rangle\right|^2_{\sigma-\pi}\right], \tag{13}$$

while the resonant dipole term assumes the form

$$\frac{\mathrm{d}\sigma}{\mathrm{d}\Omega}_{\mathrm{E1}}^{\mathrm{res}} = \left|\left\langle a \middle| \sum_n \mathrm{e}^{\mathrm{i}\vec{Q}\cdot\vec{r}_n} z_2^2 F^{(2)} \middle| a \right\rangle\right|^2_{\sigma-\sigma} + \left|\left\langle a \middle| \sum_n \mathrm{e}^{\mathrm{i}\vec{Q}\cdot\vec{r}_n}(\mathrm{i}F^{(1)}(z_1\cos\theta - z_3\sin\theta) + F^{(2)}z_2(z_1\sin\theta + z_3\cos\theta)) \middle| a \right\rangle\right|^2_{\sigma-\pi}. \tag{14}$$

It is important to note that in a typical experiment, *both* resonant and non-resonant contributions are present, and indeed their $\sigma \rightarrow \sigma$ and $\sigma \rightarrow \pi$ amplitudes interfere so that due considerations must be given to this when fitting the measured intensities.

For a basal-plane spiral described by a wave vector $\vec{\tau}$ the total angular momentum takes the form

$$\vec{J}_n = J(\cos(\vec{\tau} \cdot \vec{r}_n)\vec{U}_1 + \sin(\vec{\tau} \cdot \vec{r}_n)\vec{U}_2). \tag{15}$$

Writing this as a sum of complex exponentials and inserting it into eq. (13) yields for the non-resonant cross-section the result

$$\frac{\mathrm{d}\sigma}{\mathrm{d}\Omega}^{\text{non-res}} = r_0^2 \left(\frac{\hbar\omega}{m_e c^2}\right)^2 \left(\frac{J}{2}\right)^2 \sin^2 2\theta (|\phi_S|^2 + |\phi_L + \phi_S|^2 \sin^2\theta)\, \delta(\vec{Q} - \vec{G} \pm \vec{\tau}), \tag{16}$$

where $\vec{G}$ is a reciprocal lattice vector, and ϕ_L and ϕ_S are the normalized ionic form factors of the orbital- and spin-magnetization densities, respectively. (Equation 16 is only valid for wave-vector transfers along the $[00\ell]$ direction, and if both final polarization states are accepted equally.) Thus, first-order magnetic peaks will be observed a distance τ on either side of each charge Bragg peak. In this way the non-resonant X-ray magnetic scattering cross-section is similar to the neutron cross-section. Where it differs is that the unrotated ($\sigma \rightarrow \sigma$) channel contains contributions from the pure spin term ($|\phi_S|^2$), and the rotated ($\sigma \rightarrow \pi$) channel contains contributions from both orbital and spin ($|\phi_L + \phi_S|^2$). This important result offers the possibility to separate the spin and orbital form factors, and will be discussed more fully in the next section.

The resonant dipole cross-section for a basal-plane helix is also readily obtained by inserting eq. (15) into eq. (14), but in this case the magnitude of the moment does not enter the equation directly. The result is

$$\begin{aligned}\frac{\mathrm{d}\sigma}{\mathrm{d}\Omega}^{\text{res}}_{E1} &= \tfrac{1}{4}\left|F^{(2)}\right|^2 \delta(\vec{Q} - \vec{G}) + \tfrac{1}{4}\cos^2\theta \left|F^{(1)}\right|^2 \delta(\vec{Q} - \vec{G} \pm \vec{\tau}) \\ &\quad + \tfrac{1}{16}(1 + \sin^2\theta)\left|F^{(2)}\right|^2 \delta(\vec{Q} - \vec{G} \pm 2\vec{\tau}).\end{aligned} \tag{17}$$

Again this has been derived assuming that the rotated and unrotated components are collected with equal weight. It is apparent that even for a *pure* sinusoidal modulation, and in contrast to the non-resonant cross-section, magnetic scattering is produced at the second harmonic position for resonant dipole transitions. When the quadrupole terms are included, it is found that additional satellites appear at the third and fourth harmonic positions, each with its own characteristic polarization dependence. Hannon and coworkers (Hannon et al. 1988, Hamrick 1994) have computed the relative intensities expected for each of the harmonics from explicit calculations of the F_{LM} factors (eq. 9) using atomic wave functions of the lanthanide series. In addition, they have considered the corresponding intensities for the ($2p \rightarrow 5d$, $2p \rightarrow 4f$) and ($2s \rightarrow 6p$, $2s \rightarrow 5d$, $2s \rightarrow 4f$) transitions appropriate for the respective L_{II} and L_I absorption edges. A summary of the

Table 1
Allowed and forbidden $E1$ and $E2$ transitions at the L_{II} and L_{III} edges in a simple, magnetic spiral. A "1" indicates that the transition is allowed and "0" that it is forbidden

		Harmonics				
		Zeroth	First	Second	Third	Fourth
E1	$\sigma\sigma$	1	0	1		
E1	$\sigma\pi$	0	1	1		
E2	$\sigma\sigma$	1	1	1	1	1
E2	$\sigma\pi$	0	1	1	1	1

Table 2
Allowed and forbidden $E1$ and $E2$ transitions at the L_{II} and L_{III} edges in a pure c-axis modulated structure. A "1" indicates that the transition is allowed and "0" that it is forbidden

		Harmonics				
		Zeroth	First	Second	Third	Fourth
E1	$\sigma\sigma$	1	0	0		
E1	$\sigma\pi$	0	1	0		
E2	$\sigma\sigma$	1	0	1	0	0
E2	$\sigma\pi$	0	1	0	1	0

allowed and forbidden harmonics at the L_{II} and L_{III} edges calculated for the basal plane and c-axis structures are summarized in tables 1 and 2, respectively (Bohr et al. 1990). Finally, we note that the extension of calculations of the X-ray cross-section to terms other than $\vec{A} \cdot \vec{P}$ (leading to magnetic dipole and quadrupole contributions) and into the inelastic regime is ongoing (Luo et al. 1993, Blume 1994, Hamrick 1994, Carra et al. 1996).

2.5. *Separation of orbit and spin*

It is clear from eq. (13) that for non-resonant magnetic scattering the different polarization states of the scattered beam contains information on the spin- and orbital-magnetization densities. To develop this further, and to derive useful expressions that may allow us to separate these components experimentally, requires a description of the polarization characteristics of the incident and scattered beams. The detailed analysis required to do this has been developed elsewhere (see, for example, Blume and Gibbs (1988) and references therein), and here we make use of only those steps that are needed for our example of the scattering from a helix.

A general result is that the incident polarization may be expressed as a (2×2) density matrix

$$\rho = \sum_{\lambda} |\lambda\rangle p_{\lambda} \langle\lambda| ,$$

so that the elastic cross-section may be written as

$$\frac{d\sigma}{d\Omega} = r_0^2 \mathrm{Tr}(M\rho M^{\dagger}),$$

where M is one of the scattering matrices given in eq. (12). If we now assume that the incident beam is essentially plane polarized in the orbit plane of the synchrotron, then the density matrix simplifies to

$$\rho = \frac{1}{2}\begin{pmatrix} 1+P & 0 \\ 0 & 1-P \end{pmatrix}.$$

The degree of linear polarization is defined as $P = (I_\sigma - I_\pi)/(I_\sigma + I_\pi)$, where I_σ and I_π are the intensities of the linear components polarized perpendicular and parallel to the diffraction plane. Clearly, for perfectly σ polarized light $P = 1$, whereas for real sources it is typically $\geqslant 0.95$.

For the scattered beam a density matrix may also be defined with the degree of linear polarization given by

$$P' = \frac{I'_\sigma - I'_\pi}{I'_\sigma + I'_\pi}. \tag{18}$$

From eq. (13) it can be readily obtained that at the first diffraction harmonic of a helix the intensities in the two different linear polarization channels are

$$I'_\sigma \propto (1+P)\phi_S^2 + \sin^2\theta(1-P)(\phi_L + \phi_S)^2 \tag{19}$$

and

$$I'_\pi \propto \sin^2\theta(1+P)(\phi_L + \phi_S)^2 + (1-P)(2\sin^2\theta\,\phi_L + \phi_S)^2. \tag{20}$$

In the limit $P \rightarrow 1$, the σ-polarized component of the magnetic scattering from a helix depends only on the spin magnetization density, $I'_\sigma \propto \phi_S^2$, while the π-polarized component depends on the sum of the orbital and spin densities $I'_\pi \propto (\phi_L + \phi_S)^2$. Thus, it is in this sense that the spin and orbital contributions to the total moment may be separated. Semi-quantitative experiments to demonstrate these ideas in a helix have been performed on Ho (Gibbs et al. 1988, Gibbs et al. 1991). Both π- and σ-polarized scattered beams were observed. It was demonstrated that the π-component is dominant, consistent with the large orbital moment in Ho, and that the Q dependence of the orbital and spin form

factors was qualitatively in agreement with theoretical calculations. Further experiments at third generation synchrotron sources are ongoing (Sutter et al. 1999).

Finally, in this section we mention two technical developments that promise to further enhance the usefulness of X-ray scattering in the study of magnetism. Independent groups in France (Giles et al. 1995) and the USA (Yahnke et al. 1994, Lang and Srajer 1995) have produced efficient X-ray phase plates that allow the polarization of the incident beam to be varied continuously from linear to circular. An example of the great potential utility of such a device is the study of the magnetic spiral in Ho using both left and right polarized light by Sutter et al. (1997). By comparing the change in the intensities of the $+\tau$ and $-\tau$ satellites as the incident polarization was flipped from left to right Sutter et al. were able to estimate the relative domain population of right- to left-handed helices in their sample. The second important development concerns the use of high-energy X-rays. In the limit of $\hbar\omega \geqslant 100\,\text{keV}$, $\sin\theta \to 0$, and the non-resonant cross-section (eq. 6) simplifies considerably, such that it depends upon the spin magnetization density perpendicular to the diffraction plane only (Brückel et al. 1993). The main advantage, however, is that the increased penetration depth of the X-ray increases the total scattering volume, and hence the net signal. (This contrasts with the case for charge scattering, where the cross-section is much greater and the scattering comes from within an extinction length of the crystal surface.)

3. The magnetic structure of holmium

In this section we shall adopt a largely historical approach. We start with a summary of what was learned about the magnetic structure of Ho in the period from the mid-sixties up to the mid-eighties, when the first synchrotron based X-ray scattering experiments were performed.

3.1. *Early studies of holmium*

The magnetic structure of Ho was first solved using neutron diffraction by Koehler et al. (1966) shortly after single crystals became available. In their pioneering experiments they established the existence of two distinct ordered phases. Below a Néel temperature of ~133 K the moments in a given hexagonal basal plane order ferromagnetically, with successive planes along the c-axis rotated by a constant angle ψ. The structure can thus be described as a helix, with a modulation wave vector of magnitude $\tau_m = 2\pi(\frac{\psi}{2\pi})(\frac{2}{c})$, where ψ is in radians, and the extra factor of two in the numerator arises from the fact that there are two layers per unit chemical cell in the hcp structure of Ho. At the ordering temperature τ_m is incommensurable with a value close to $0.275c^*$. On cooling the wave vector reduces approximately linearly with temperature until around 20 K when it locks in to the commensurable value of $\frac{1}{6}c^*$. At or around the same temperature the moments lift out of the basal plane, so that the low temperature structure is actually a shallow cone. In addition to the main magnetic peak, it was noted in these first experiments that

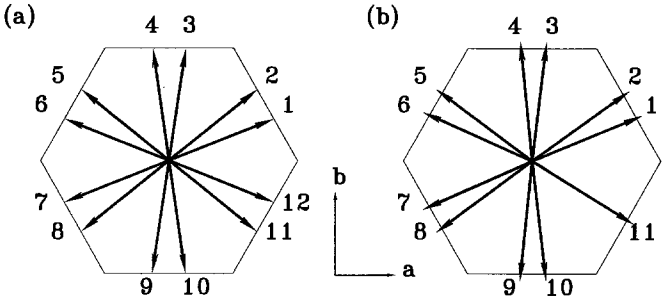

Fig. 4. A schematic of the magnetic structure of Ho. (a) Its low-temperature cone phase shown projected onto the hexagonal plane. The structure is modulated along the c-axis with a unit cell of twelve atomic planes, and has a small ferromagnetic component along the c-axis. (b) The one spin-slip phase. (From Simpson et al. 1995.)

at low temperatures there were fifth and seventh harmonics in the diffraction pattern, indicating that the moments were bunched around the nearest easy axis in the basal plane, as shown in fig. 4a. These and later neutron scattering studies by Felcher et al. (1976), and Pechan and Stassis (1984) established that there were additional features in the diffraction patterns that could not be explained by a simple bunched spiral, but a unified model capable of explaining all of the features was not forthcoming. Probably the most important X-ray scattering experiment in this period on Ho was performed by Keating (1969), who discovered additional charge scattering at $2\tau_m$, and attributed its origin to the asphericity of the 4f charge distribution.

Throughout this time is was appreciated that the helical structure of Ho, and indeed the rich diversity of complex structures that were discovered in the same period in many of the other lanthanides, resulted from a competition between the crystal-field and exchange interaction. It was first suggested by Vigren (1976) that this finely balanced competition could give rise to a structure with "spin discommensurations" or "spin slips", but it was not until the first X-ray magnetic scattering experiments were performed that the full importance of this proposal was realized.

3.2. *X-ray scattering studies of holmium*

The first X-ray synchrotron experiments on Ho were performed at the Stanford Synchrotron Radiation Laboratory (Gibbs et al. 1985). In fig. 5 we show a summary of the X-ray scattering observed in these studies around $(0, 0, 4)$, where the magnetic satellite is clearly visible and displaced from the charge peak by τ_m. (The energy of the X-rays in these measurements was 7500 eV, well away from any absorption edge which might lead to significant resonant contributions.) As the temperature is increased, the satellite shifts to larger wave-vector transfers and the intensity decreases, falling continuously to zero above T_N. In these scans, the peak counting rates were ~25 s^{-1} on large backgrounds of ~10 s^{-1}. The resolution full-width-half-maximum (FWHM) obtained at the $(0, 0, 2 + \tau_m)$ reflection was ~$0.001c^*$, where $c^* = (2\pi/c) \approx 1.11$ $Å^{-1}$ at 20 K. This width corresponds

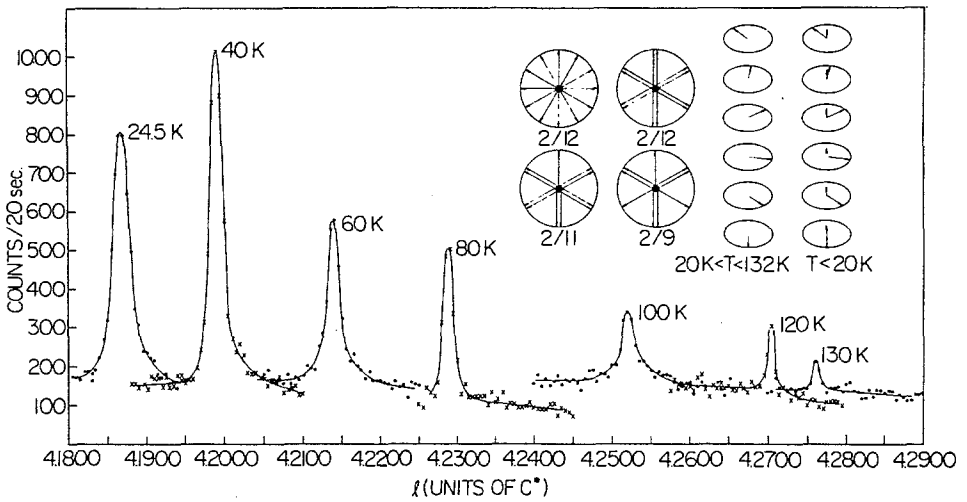

Fig. 5. The temperature dependence of the Ho $(0,0,4+\tau_m)$ magnetic satellite taken with non-resonant synchrotron radiation. (The temperature increases from right to left.) The lines are drawn to guide the eye. (From Gibbs et al. 1985.)

to correlation lengths of several thousand Å, or greater. More recent measurements made at the National Synchrotron Light Source on samples with larger surface areas and under better optimized conditions routinely give signals of several hundred counts s^{-1} at essentially the same energy on backgrounds of about $1\ s^{-1}$ (Gibbs et al. 1988). Although absolute measurements have not been made of the non-resonant signal rates for X-ray magnetic scattering, the signal rates in these experiments were reduced from the corresponding charge scattering by of order 1×10^6, which is consistent with a simple estimate of the non-resonant cross-section for Ho (eq. 7).

The temperature dependence of τ_m obtained in these early experiments by both X-ray (open circles) and neutron diffraction (solid circles) is shown in fig. 6. It is clear that in the temperature range above 20 K the wave vector τ_m determined by X-rays has preferred, commensurable values, whereas in the lower resolution neutron data there is a continuous variation of the wave vector with temperature. Other noteworthy features of the X-ray data include the appearance of an inflection point near $\tau_m = \frac{2}{9}$ at around 70 K, thermal hysteresis below 50 K, and coexistence among phases with differing wave vectors. At the lowest temperatures, there is a first-order transition between two commensurable wave vectors, namely, $\tau_m = \frac{2}{11}c^*$ and $\tau_m = \frac{1}{6}c^*$, and there is an indication of a lock-in transformation at $\frac{5}{27}c^*$. The inset in fig. 6 shows the variation of τ_m during several cycles of the temperature between 25 K and 13 K. The data suggest a clustering of the wave vectors around $\tau_m = \frac{2}{11}c^*$ and $\tau_m = \frac{5}{27}c^*$.

We now consider the apparent discrepancies in fig. 6 between the values of τ_m determined by X-ray and neutron scattering. This may be understood in part from the higher Q resolution of the former. Another factor is that the X-ray penetration depth in

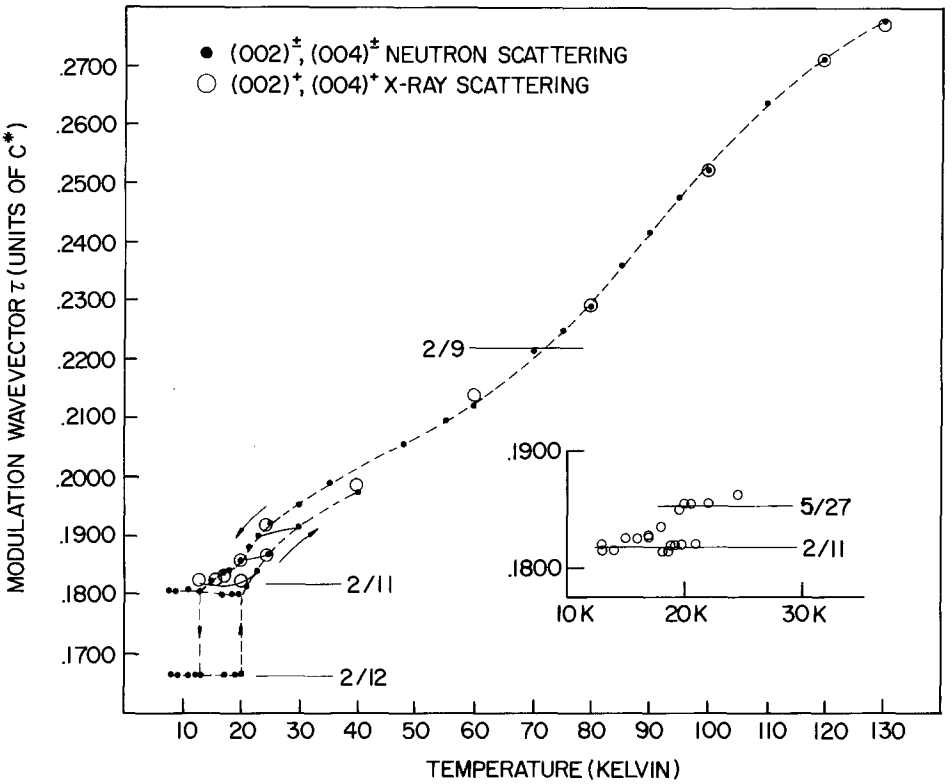

Fig. 6. Temperature dependence of the Ho modulation wave vector τ obtained with both synchrotron X-ray (open circles) and neutron (solid circles) scattering. The wave vectors obtained by neutron scattering in the coexistence region below 20 K are the result of fits to the first harmonic. The fine lines across the hysteresis loop indicate the results of cycles of the temperature below 50 K. Inset: Plot of the wave vectors obtained from several cycles of the temperature between 13 and 24.5 K, obtained with X-ray scattering. (From Gibbs et al. 1985.)

Ho at 8 keV is ~1 μm, whereas neutrons sample the bulk, and it has become clear in these and subsequent studies that the surface preparation can alter the magnetic structure within the first several μms. It was also found by Koehler et al. (1966) that not all bulk crystals displayed the same wave vectors, and this was ascribed to a variation in the impurity content between the different samples. In fig. 7 the temperature dependence of τ_m is shown for two different samples of Ho, and also for a thin film of Ho grown by molecular beam epitaxy. It is clear that large differences in τ_m can be observed depending in the case of bulk crystals on surface treatment, impurity content, etc., and in the case of thin films mainly on the strain resulting from the lattice mis-match between the film and substrate (the latter is discussed more fully in section 5).

In addition to the existence of preferred commensurable magnetic wave vectors in Ho, there was a second distinctive feature of the X-ray diffraction patterns that led

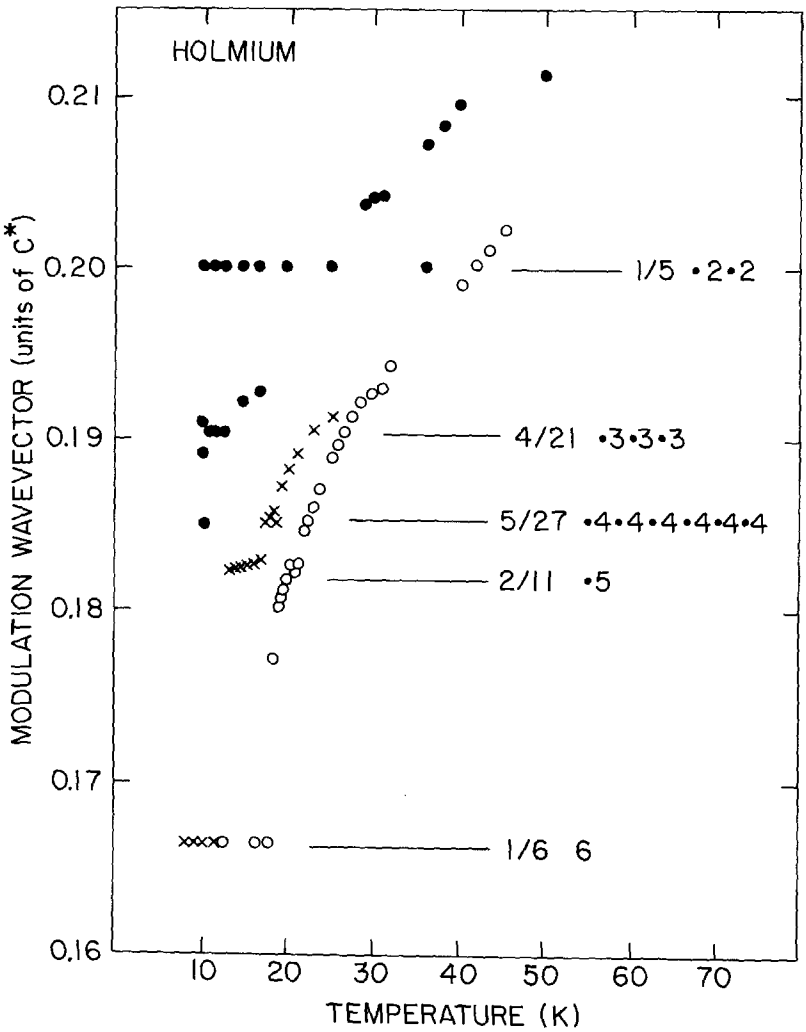

Fig. 7. Temperature dependence of the modulation wave vector τ_m for three different Ho samples: Ho(1) (crosses), Ho(2) (open circles), and thin film (solid circles). The spin-slip structure for the simply commensurate wave vectors are shown on the right. The data for $\tau_m = \frac{1}{6}$ in Ho(1) were obtained from neutron scattering. Note also the appearance of two new lock-in wave vectors at $\frac{1}{5}$ and $\frac{4}{21}$. (From Gibbs 1989.)

directly to a spin-slip description of the magnetic structure. Figure 8 shows the detailed evolution of the X-ray scattering as the temperature is lowered from around 25 K to 17 K. As the temperature is reduced a second, initially broad peak appears at larger wave-vector transfers. This peak arises from charge scattering, as discussed below. With decreasing temperature, both the magnetic peak and the charge peak shift to lower wave-vector transfers, although the charge scattering shifts considerably farther than the

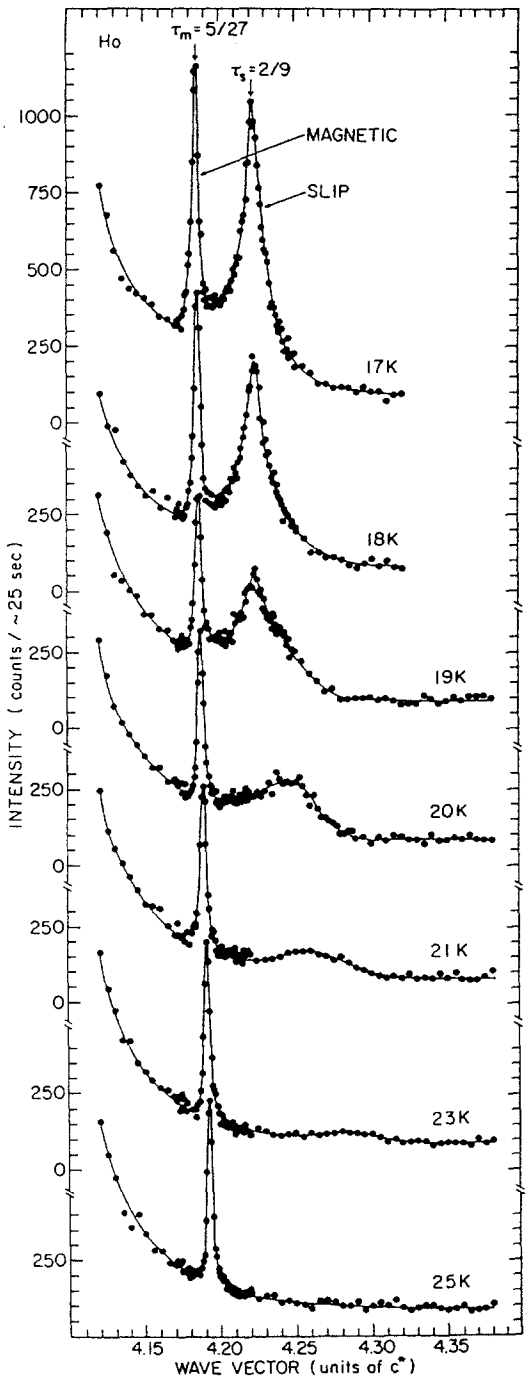

Fig. 8. Synchrotron X-ray diffraction patterns of the satellite above the (004) Bragg point of Ho, studied for decreasing temperature from $T = 25\,\mathrm{K}$ to $17\,\mathrm{K}$. Note that in addition to the sharp magnetic satellite, a second broad satellite appears at the slip position $\tau_s = 12\tau_m - 2$. When the temperature is lowered and τ_m approaches $\frac{5}{27}$ then the lattice modulation peak sharpens up and approaches $\tau_s = \frac{2}{9}c^*$. (From Bohr et al. 1986.)

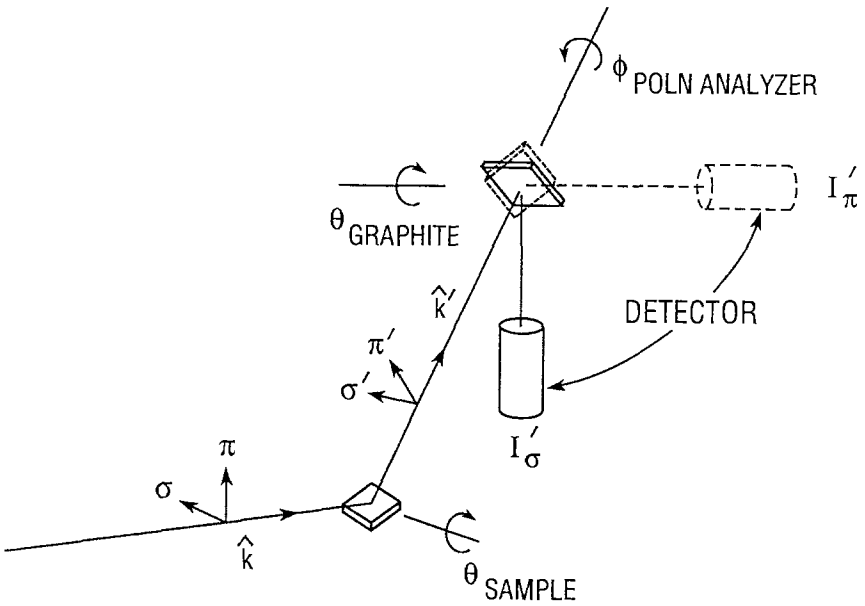

Fig. 9. A schematic of the X-ray diffractometer showing the polarization analyser. (From Gibbs et al. 1991.)

magnetic scattering for the same change in temperature. When the magnetic peak reaches $\tau_m = \frac{5}{27}c^*$, the radial width of the charge scattering narrows and grows in intensity. As the temperature is lowered still further, the charge peak broadens and disappears.

To establish that the second peak does indeed arise from charge scattering, polarization analysis was performed on both peaks. As may be seen from eq. (20), for linearly σ-polarized radiation incident upon a magnetic spiral, there is a rotated or π-polarized component of the magnetic scattering, which varies in the non-resonant limit as the sum of the orbital and spin magnetization densities. (There is also a rotated component in the resonant limit, however, in the present case, with an incident photon energy of 7500 eV, the cross-section may be safely analyzed in the non-resonant regime). In contrast, charge scattering does not rotate the linearly σ-polarized incident beam. Thus, it is possible to distinguish magnetic scattering from charge scattering in a spiral magnetic structure by the existence of a π-polarized component in the scattered beam. Polarization analysis was accomplished by placing a second crystal after the sample on the 2θ arm of the spectrometer, and scattering in the diffraction plane (see fig. 9). When the incident photon energy is appropriately tuned, the scattering angle for the second crystal is 90°. Consequently, one linear component of the beam scattered from the sample is reflected into the detector, while the other is suppressed. By rotating the second crystal by 90° around the axis of the scattered beam (ϕ_{poln} in fig. 9), the former is suppressed and the latter is reflected. In this way, the intensities of the linearly σ- and π-polarized components of the scattered beam may be measured independently. (For detailed discussions of the operation of the polarization analyser see Gibbs et al. (1991)).

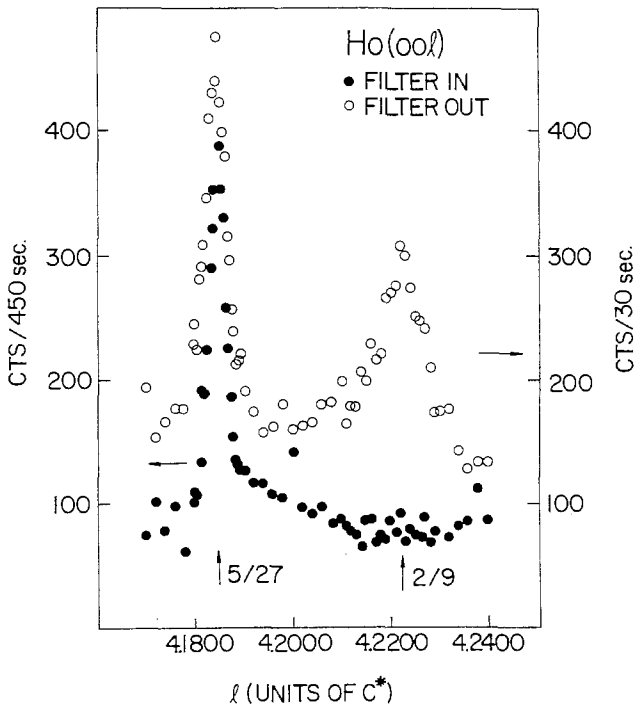

Fig. 10. X-ray scattering data from Ho. Open circles: scan of the Ho(004)$^+$ magnetic ($\tau_m = \frac{5}{27}c^*$) and ($\tau_s = \frac{2}{9}c^*$) satellites taken at 17 K. Solid circles: the same scan, but with the polarization analyses in place. (From Gibbs et al. 1985.)

Two radial scans taken through the magnetic and charge satellites of the (0, 0, 4) reflection at 17 K are shown in fig. 10. At this temperature the magnetic satellite is located at $\tau_m = \frac{5}{27}c^*$, while the charge peak is located at $\frac{2}{9}c^*$. The open circles show the scan performed without polarization analysis. The solid circles show the scan taken with the polarization analyzer in place and oriented to pass the π-polarized component of the scattering, but suppress the σ-polarized component. As may be seen in this figure, the peak at $\frac{5}{27}$ is passed while the peak at $\frac{2}{9}$ is suppressed entirely. This establishes that the peak at $\frac{2}{9}$ arises predominantly from charge scattering, while the peak at $\frac{5}{27}$ is magnetic in origin.

3.3. *The spin-slip model*

A unified model of the magnetic structure of Ho may be derived by making use of the concept of discommensurations, as originally proposed for structurally incommensurable materials by McMillan (1976) and discussed in the context of lanthanide metals by Vigren (1976), Greenough and Blackie (1981), and Bak (1982). During the last twenty years, investigations of a fascinating variety of incommensurable systems have revealed

inhomogeneous structures composed of commensurable regions separated by domain walls. Some prominent examples include charge-density wave materials, such as $TaSe_2$, various graphite intercalates, rare gas monolayers adsorbed on graphite surfaces, mercury chain compounds, clean Pt and Au surface layers, the magnetic structure of the lanthanide metals, and many others. An elegant discussion of the main ideas and models underlying these systems in one and two dimensions has been given by Bak (1982), to which the reader is referred. Our immediate aim in the following is to describe a simple spin-discommensuration, or spin-slip, model of the magnetic structure of Ho that applies to the commensurable magnetic wave vectors which were observed in the X-ray scattering study described above.

We imagine that the ferromagnetic basal planes of Ho are arranged in pairs or doublets along the c-axis, which are each associated with one of the six easy directions defined by the six-fold symmetric crystal field. It is not necessary to assume that the moments within a doublet are oriented parallel to one another, nor must all such pairs be identical. (Details of this sort are ultimately determined by comparing measured intensities with calculated structure factors, as discussed below). In the idealized $\frac{1}{6}$ magnetic phase of Ho, there are six pairs of planes in the magnetic unit cell, each associated with one easy direction, to form a spiral of doublets (see fig. 4a). The magnetic wave vector is inversely proportional to the number of layers in the magnetic unit cell, ie, $\tau_m = \frac{2}{12} = \frac{1}{6}c^*$. The factor two enters because the hcp lattice has two atomic planes for each chemical unit cell. This structure is, of course, identical to that first proposed for the $\frac{1}{6}$ phase of Ho by Koehler et al. (1966) to explain the observed fifth and seventh harmonics; it results from the basal-plane anisotropy that increases rapidly at low temperatures.

The fundamental building block of the spin-slip model for Ho is the $\frac{1}{6}$ magnetic unit cell. A spin slip is created by associating only a single atomic plane, instead of two, to a particular easy direction. For example, a single spin slip in the $\frac{1}{6}$ unit cell gives a new structure with one slip for every five doublets (see fig. 4b). The resulting magnetic wave vector is $\tau_m = \frac{2}{11}c^*$. A simple notation for this structure is (122222) where the "1" represents a spin slip and the "2" a doublet. More generally, commensurable spin-slip structures may be created by introducing s slips for every n full (2π) rotations of the moments about the c-axis. The wave vector for such a structure is the ratio of the number of 2π rotations of the moments to the number of layers in the magnetic unit cell, namely,

$$\tau_m = \frac{2n}{12n - s}, \tag{21}$$

where τ_m is in reciprocal lattice units. In this way, it is possible to construct spin-slip structures for any rational wave vector between $\frac{1}{6}$ and $\frac{1}{3}$. The simplest commensurable spin-slip structures are those with an integer ratio of doublets and slips: (222222), (122222), (12222)×6, (1222)×3, (122122), (121212), etc. The corresponding wave vectors for these structures are $\frac{1}{6}$, $\frac{2}{11}$, $\frac{5}{27}$, $\frac{4}{21}$, $\frac{1}{5}$ and $\frac{2}{9}$. These are precisely the wave vectors to which the wave vector in Ho shown in figs. 6 and 7 tends to lock. From this perspective, the decrease of the magnetic wavevector with temperature proceeds via the

Table 3
Summary of the spin-slip phases and the associated wave vectors of the peaks observed in the non-resonant x-ray scattering experiments in Er (after Gibbs et al. 1986)

Temperature (K)	Structure	τ_m [a]	τ_s [b]	$2\tau_m - \tau_s$ [c]	$2\tau_m$ [d]
52	2(43)	2/7	2/7	2/7	4/7
40	2(443)	3/11	2/11	4/11	6/11
34	2(4443)	4/15	2/15	6/15	8/15
29	2(44443)	5/19	2/19	8/19	10/19
25	2(444443)	6/23	2/23	10/23	12/23
20	(44)	1/4		1/2	1/2

[a] τ_m, fundamental magnetic.
[b] τ_s, triplet.
[c] $2\tau_m - \tau_s$, quartet.
[d] $2\tau_m$, magneto-elastic distortion.

decrease of the spin-slip density until $\tau_m = \frac{1}{6}$. A similar trend is observed also in the temperature dependence of the magnetic wavevector of Er (see table 3).

The next step in developing the spin-slip model is to recognize that the additional charge scattering peaks which appear in the diffraction pattern of Ho may be explained as lattice modulations accompanying magnetic ordering. To establish this, we make the plausible assumption that the magnetoelastic coupling varies at the spin-slip positions. For example, it might be imagined that the exchange interaction between neighbouring doublets differs from than that between a neighbouring doublet and a slip. If so, then we would expect inter-planar distortions of the lattice to occur with the frequency of the spin slips. To take a specific case, in the $\frac{5}{27}$ magnetic phase there is one spin slip, on-average, for every nine atomic planes. The spin-slip wave vector characterizing the lattice distortion for this phase is then $\frac{2}{9}c^*$. Referring to fig. 8, it may be seen that when the magnetic wave vector is located at $\frac{5}{27}c^*$, there is a second peak in the diffraction pattern, originating in charge scattering, which is located at precisely $\frac{2}{9}c^*$. We thus interpret this second peak as arising from the distortions of the lattice due to the spin-slips.

More generally, we may calculate the spin-slip wave vector τ_s for any commensurable phase as

$$\tau_s = \frac{2s}{12n - s}. \tag{22}$$

Rewriting this equation in terms of (s/n) and substituting in eq. (21) for τ_m, we can express the spin-slip wave vector τ_s in terms of the magnetic wave vector τ_m for a magnetic spiral:

$$\tau_s = 12\tau_m - 2. \tag{23}$$

This expression has been found to account accurately for the positions of the magnetic and spin-slip charge peaks in Ho as a function of temperature, as illustrated for two different

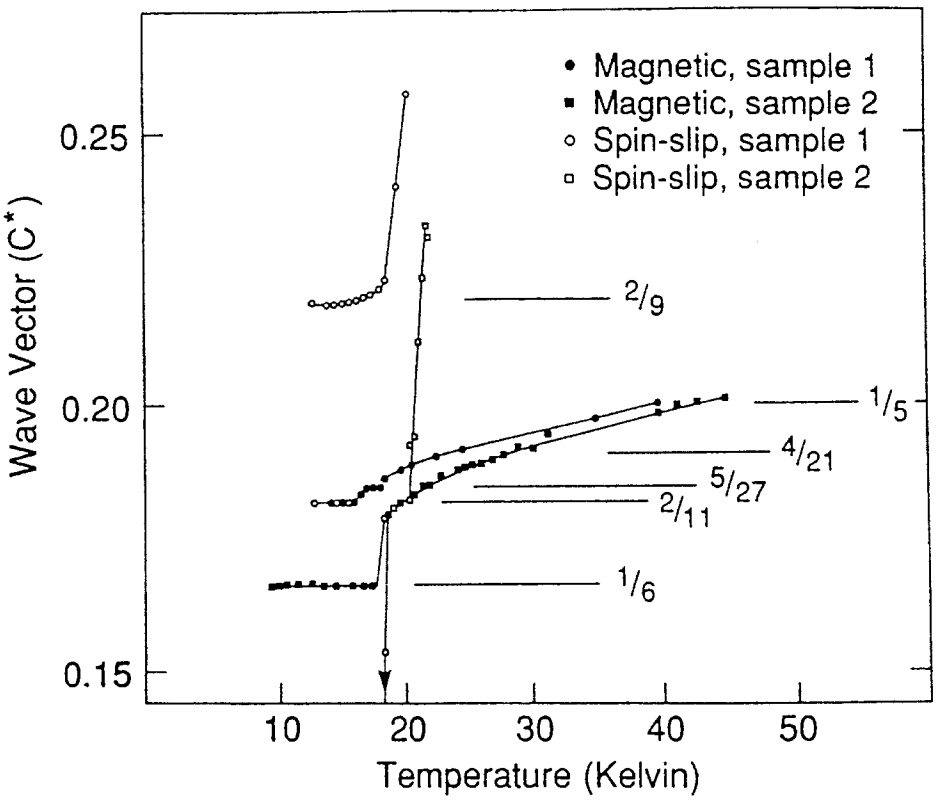

Fig. 11. Temperature dependence of the magnetic (solid symbols) and spin-slip (open symbols) wave vectors for two different bulk samples studied by X-ray diffraction. The wave vectors of the spin slips broadens considerably and moves to zero when the magnetic wave vector locks to $\frac{1}{6}$, as indicated by the arrow. (From Helgesen et al. 1994.)

samples in fig. 11. Note that when τ_m locks to $\frac{1}{6}c^*$, then from the above $\tau_s = 0$, and thus the disappearance of the slip scattering in the $\frac{1}{6}$ phase is explained.

Referring now to fig. 8, it may also be seen that when $\tau_m = \frac{5}{27}c^*$, then the radial width of the spin-slip scattering at $\frac{2}{9}c^*$ is at its narrowest. This is a recurring property of the simple commensurable phases of the lanthanides, namely, that the correlations among the spin-slips extend over the greatest distances in these phases. Moreover, it is only the simple commensurable phases that are observed to lock in zero field. Higher-order commensurable phases, involving non-integral ratios of doublets and slips (and, therefore, two or more spin-slip periods), have not to our knowledge been observed in bulk samples, although they have been observed in the presence of an applied magnetic field (Cowley et al. 1991), and in thin films (Helgesen et al. 1994). We conclude that the additional charge scattering observed in the diffraction patterns arises from magnetoelastic

modulations of the lattice accompanying magnetic ordering, and that the positions, intensities, and widths of these peaks reflect the correlations among the spin slips.

So far we have developed these arguments for the case of Ho only. General expressions for the relationship between τ_m and τ_s have been derived by Bohr et al. (1986), to which the reader is referred for more details.

3.3.1. *Lattice modulations*

The presence of spin slips in the magnetic structures leads through the magneto-elastic coupling to an induced modulation of the lattice. Magnetostriction is known to be significant in the lanthanides as expressed, for example, by their anomalous lattice distortions below the Néel point.

Three possible mechanisms that may produce a lattice modulation are shown in fig. 12. In fig. 12a a distance-dependent exchange interaction is sketched. At spin slip positions the turn angle differs from turn angles in the rest of the structure. A distance-dependent exchange interaction will therefore lead to lattices modulations which arise from spin slips. In fig. 12b the effect of quadrupoles in a crystal field is considered. The different orientations of the magnetic moments relative to the crystal field give rise to local differences in the magnetostriction. The third proposed mechanism (fig. 12c) is a quadrupole–quadrupole interaction. This mechanism would also give rise to a second harmonic of the magnetic satellite. The so-modified structure of the magnetic spiral will in addition to the magnetoelastically induced lattice modulation, give rise to weak magnetic satellites at $\tau_m \pm \tau_s$.

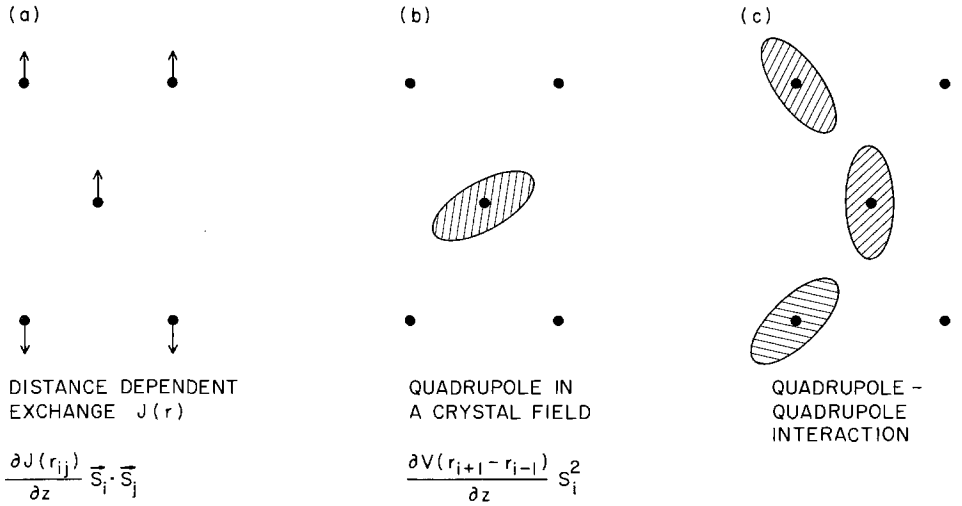

Fig. 12. Schematic of three mechanisms which can lead to lattice modulations: (a) distance dependent exchange, (b) quadrupole in a crystal field, and (c) quadrupole–quadrupole interaction. (From Bohr et al. 1989.)

3.3.2. *Neutron scattering*

The fact that the existence of spin slips in Ho was first revealed by X-ray magnetic scattering can be viewed as a major coup for this technique. Inevitably, it was not very long before a new series of neutron scattering experiments were undertaken (Cowley and Bates 1988). Instead of adopting the same approach used in the X-ray study of Gibbs et al. (1985), who concentrated on the first-order τ_m satellite, Cowley and Bates (1988) focussed on making a detailed study of the higher-order peaks. Two data sets from their work are shown in fig. 13, where it can be seen that in addition to the first, fifth and seventh harmonics reported in earlier neutron scattering studies, there are many additional peaks. An important aspect of their work, however, is that they developed a spin-slip model for the structure that was able not only to account for the positions of all the observed peaks, but also their intensities over nearly decades of intensity variation. In their notation, the position in $\vec{Q}$ of the spin-slip peaks is given by

$$\vec{Q}_{\text{mag}} = \pm[\vec{q}_0 + \frac{1}{b}(\vec{q}_0 + I\vec{c}^*)], \tag{24}$$

where $\vec{q}_0 = \frac{1}{6}\vec{c}^*$ for Ho, I is an integer, and b is the number of lattice planes between spin slips on different sub-lattices, so that b is necessarily odd. For example, for the $\frac{5}{27}$ phase shown in fig. 13a we have that $b = 9$, and all of the peaks in this figure can be indexed using eq. (24). In order to account for the intensities of the magnetic peaks Cowley and Bates found it necessary to introduce a few extra ingredients into the original spin-slip model. The most significant of these modifications was the inclusion of a Debye–Waller factor to allow both for the fact that the position of the slips was not sharply defined, but was instead represented by a distribution with a width of a few lattice planes, and that there was a distribution in the bunching angles. With these modifications it was found that a good fit to the peak intensities could be achieved for both the $[00\ell]$ and $[10\ell]$ data as shown in fig. 14. (It is worth noting that the higher-order magnetic satellites have so far eluded attempts to observe them by X-ray scattering techniques.)

Support for the results of the detailed modelling of the spin-slip structures by Cowley and Bates (1988) was produced by self-consistent mean-field calculations (Jensen and Mackintosh 1991). The Hamiltonian used in these calculations was essentially the same as developed to explain the magnetic excitations in Ho and its alloys (Larsen et al. 1987), with the exchange parameters adjusted to produce the correct τ_m at a given temperature. As shown in fig. 15 for the $\frac{1}{6}$ and $\frac{2}{11}$ phases the mean-field calculations were able to confirm the salient features of the spin-slip structures. This modelling was later extended to calculate the magnetic excitations in the $\frac{2}{11}$, or one-spin-slip phase as it is referred to. This showed that the effect of the spin-slips on the excitations is to open up a characteristic gap near $\frac{5}{11}$. The presence of this gap was subsequently confirmed by high-resolution neutron scattering (McMorrow et al. 1991).

The spin-slip model has also found application in the interpretation of neutron diffraction data obtained from Ho in a magnetic field. In 1986, Bohr and coworkers noted that the $\frac{2}{11}$ phase of Ho possesses a ferrimagnetic component in the basal plane (due to

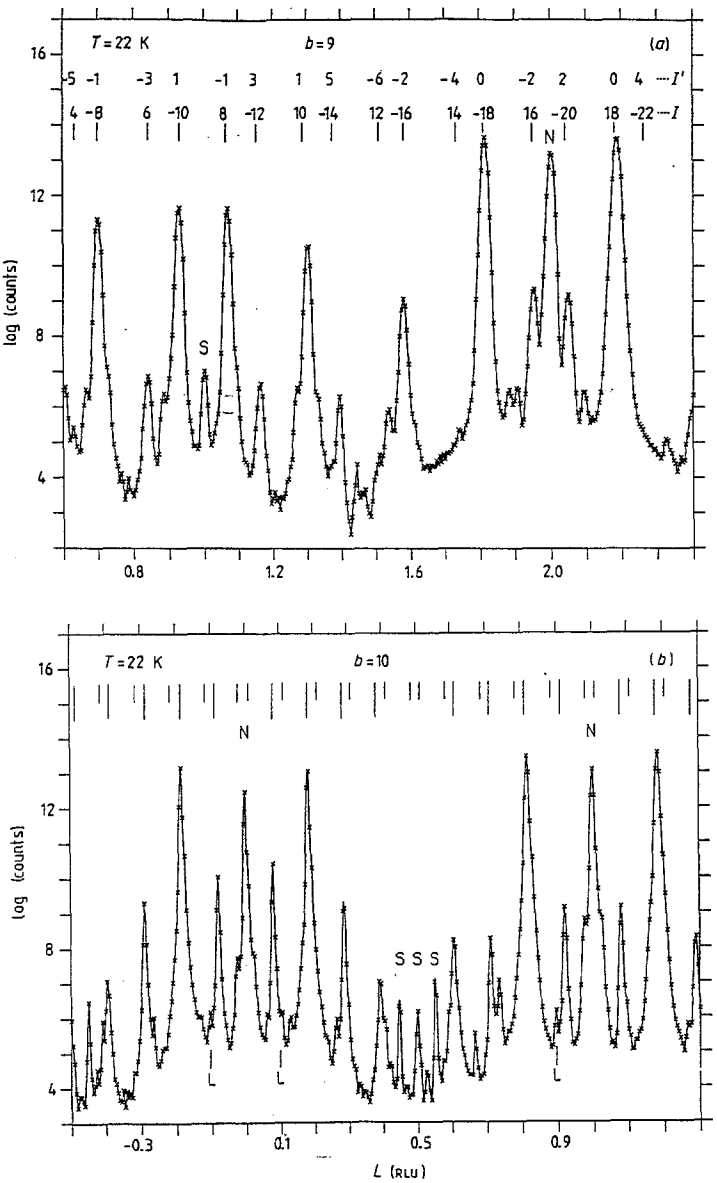

Fig. 13. The scattered neutron intensity from Ho in 50 seconds, plotted on a logarithmic (natural) intensity scale for scans of the wave-vector transfer along (a) [00ℓ] and (b) [10ℓ]. The scans were performed at two different temperatures and correspond closely to structures with integer b values as indicated. The bars at the top of the figure show the predicted wave vectors of the peaks (large to strong, or small to weak). For the [10ℓ] scan the indices of the peaks are indicated above the bars in two notations. The lower notation indexes the peaks from the origin, while the upper notation labels them from the nearest main Bragg peak. Key: N, nuclear reflections; S, second-order contamination; L, possible longitudinal spin modulation. (From Cowley and Bates 1988.)

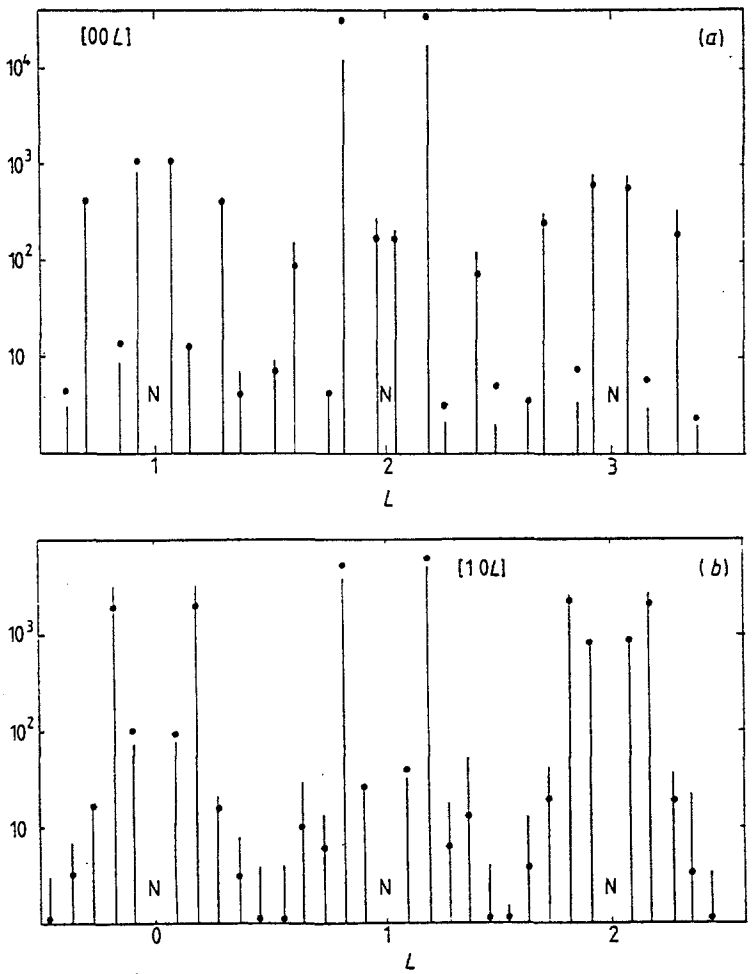

Fig. 14. A comparison between the measured neutron peak intensities (solid circles) and those calculated (lines) from the spin-slip model of Ho: (a) $[00\ell]$ scan for the $b = 9$ structure, and (b) $[10\ell]$ scan for the $b = 11$ structure. (From Cowley and Bates 1988.)

the uncompensated singlet), and suggested that this might explain the stability of the $\frac{2}{11}$ phase observed by Koehler et al. (1967), who performed the first diffraction study of the magnetic phase diagram of Ho in a field. (Although Koehler et al. noted the unusual stability of a structure with $\tau_m \approx 0.182c^*$ they did not realize that it was in fact a simple commensurable structure.) More recently, Cowley et al. (1991) have studied the neutron diffraction pattern exhibited by Ho when a magnetic field is applied along the c-axis. The field has the effect of suppressing the onset of the commensurable cone phase found at low temperatures in zero-field, and instead produces a sequence of lock-in transformations to

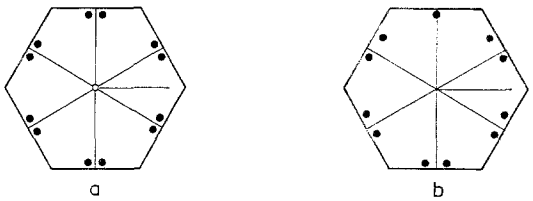

Fig. 15. The self-consistent periodic structures in Ho, calculated at different temperatures. Each circle represents the magnitude and direction of the ordered moment in a specific plane, relative to the size of the moment at absolute zero (10 μ_B), indicated by the length of the horizontal lines. The orientation of moments in adjacent planes is depicted by the positions of neighbouring circles. (a) The 12-layer zero-spin-slip structure at 4 K. The open circle in the centre indicates the ferromagnetic component in the cone structure. (b) The 11-layer one-spin-slip structure at 25 K. The bunched pairs of moments are disposed unsymmetrically with respect to the easy axis in the vicinity of the spin slip (Jensen and Mackintosh 1991).

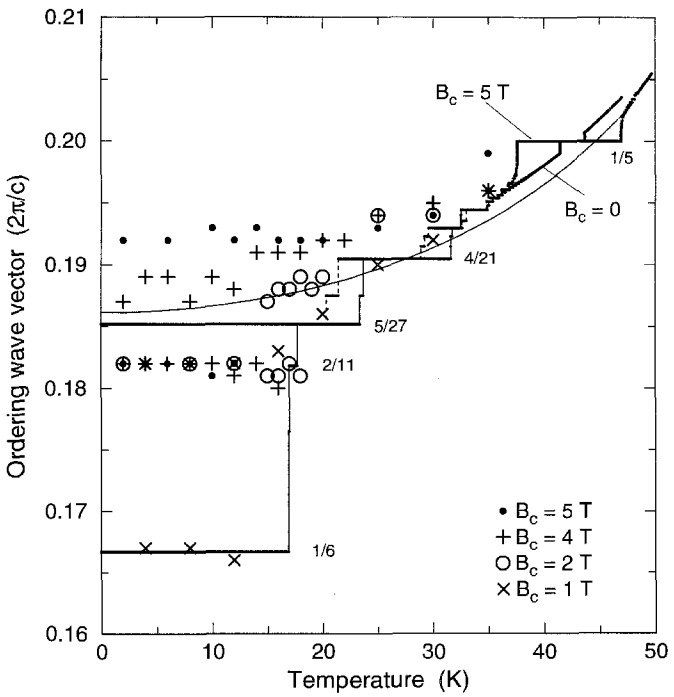

Fig. 16. The ordering wave vector in Ho as a function of temperature below 50 K. The calculated results are shown by the horizontal solid lines, which are connected with vertical thin solid or thin dashed lines corresponding respectively to the results obtained at zero field, or at a field of 10 kOe applied along the c-axis. The symbols show the neutron scattering results of Cowley et al. (1991) at various values of the c-axis field as defined in the figure. The thick dashed line, between 35 and 48 K, indicates the variation of τ derived by Tindall et al. (1993) from the position of the primary magnetic peak in a c-axis filed of 30 kOe. The smooth curve shown by the thin solid line is the temperature dependent position of the maximum in $J(q)$. (From Jensen 1996.)

spin-slip structures with increasing field. In contrast to the zero-field neutron diffraction experiments (Cowley and Bates 1988), where a continuous variation of the magnetic wave vector with temperature was observed, it was found that below 15 K, the magnetic wave vector is always commensurable and forms a Devil's Staircase with increasing field. This is illustrated in fig. 16, which shows the temperature dependence of τ_m measured in four different magnetic fields. Although some of the spin-slip structures observed in a field are similar to those found in zero-field (for example, $\frac{1}{6}$, $\frac{2}{11}$, and $\frac{4}{21}$), there are additional phases which have not been observed previously in Ho (for example, $\frac{3}{16}$ and $\frac{5}{26}$). The phase diagram of Ho in a basal-plane field has also been studied (Jehan et al. 1992), where the field again had the effect of stabilizing the $\frac{2}{11}$ phase, and other simple commensurable structures. Other studies include the work of Tindall et al. (1993), who have reported the observation of lock-in transitions in Ho to the wave vectors $\frac{5}{18}$ at 130 K, $\frac{1}{4}$ at 98 K, and $\frac{1}{5}$ at 42 K in a magnetic field. The same mean-field techniques that were used to model the zero-field spin-slip structures have been recently extended to the case of an applied field. As shown in fig. 16, Jensen (1996) was able to obtain remarkably good agreement with the data from Cowley et al. (1991), but found that terms of trigonal symmetry had to be included in the Hamiltonian, in agreement with an earlier zero-field study (Simpson et al. 1995). Clearly, elucidating the phase diagrams of the lanthanide metals when subjected to a magnetic field still remains a challenging problem nearly three decades after the original experiments by Koehler et al. (1967).

3.3.3. *Ancillary measurements*

Further support for the spin-slip model of Ho has come from the observation of anomalies in the temperature dependence of its elastic constants and its transport properties. In 1988, Bates and coworkers reported the results of ultra-sound measurements of the C_{11}, C_{33}, C_{44}, and C_{66} elastic constants in which anomalies were found near 98, 40, 24, and 20 K. An example of the temperature dependence of the elastic constant C_{44} is shown in fig. 17 for shear waves polarized parallel to the c-axis, where clear anomalies are seen for temperatures near 18, 24, 98, and 130 K. (The behaviour at the Néel point near 130 K is associated with magnetic ordering. Similarly, there is a rise at 18 K, associated with the conical transition.) Bates et al. (1988) also performed complementary neutron scattering studies of the temperature dependence of the magnetic structure in the same sample, and were able to correlate the anomalies in the elastic constants with the appearance of commensurable wave vectors: at 98 K, $\tau_m = \frac{1}{4}c^*$; at 40 K, $\tau_m = \frac{1}{5}c^*$; at 24 K, $\tau_m = \frac{3}{16}c^*$; and at 20 K $\tau_m = \frac{2}{11}c^*$. In a calculation of the elastic constants, Bates et al. showed that the broken symmetry associated with all of these "special" super-commensurable structures leads to the anomalies observed in the ultra-sound, and suggested that other properties might similarly be affected. (Similar effects have been reported by Venter et al. (1992) at 98 K.) Subsequently, anomalies in several other properties of Ho have been observed at precisely these temperatures, including resistivity by Willis and Ali (1992) and magnetization by Steinitz et al. (1989). It is interesting to note that studies pre-dating the emergence of the spin-slip model had suggested that anomalies in thermal expansion

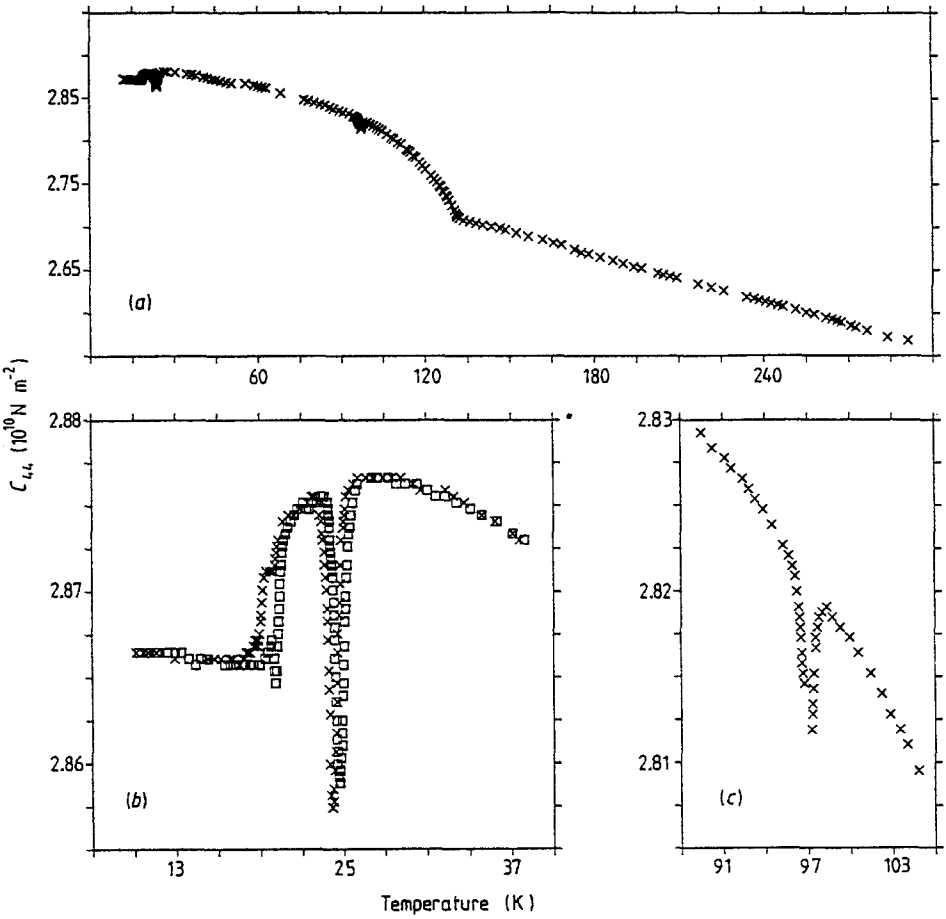

Fig. 17. The temperature dependence of the elastic constant C_{44} (shear waves polarized parallel to c). Key: cross, cooling; open square, warming. (a) 4.2–300 K; (b) 7–40 K; (c) 88–106 K. (From Bates et al. 1988.)

measurements of Tb–Ho (Greenough 1979), and in magnetization measurements of Ho–Tb, and Gd–Y (Hettiarachchi and Greenough 1982) alloys, arose from the formation of high-order commensurable structures.

3.4. *Separation of orbit and spin in holmium*

We now briefly present the results of early attempts to separate the spin- and orbital-magnetization densities in Ho (Gibbs et al. 1988, 1991). As discussed in sect. 2, the σ- and π-polarized components of the scattered beam are sensitive to different combinations of the spin- and orbital-magnetization densities. Specifically, if $P = 1$, the intensity in the σ channel is sensitive to the spin components only, whereas the π channel is sensitive

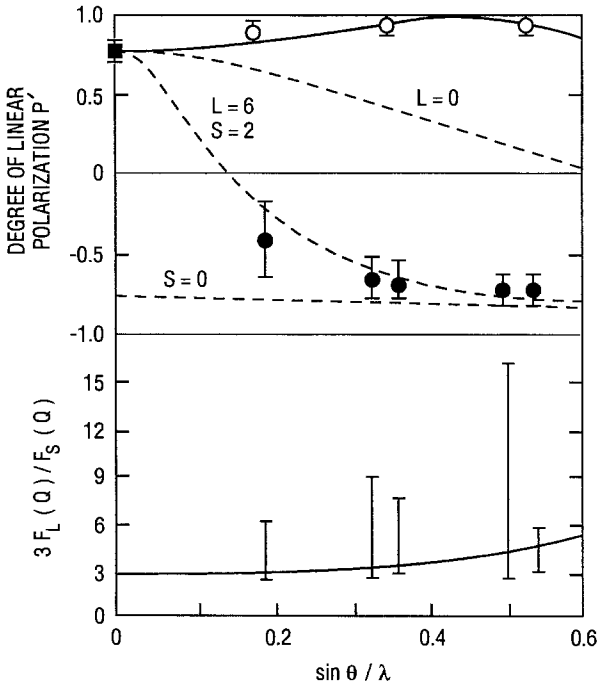

Fig. 18. Non-resonant X-ray scattering from Ho. Top: the solid square at $\theta = 0$ corresponds to the degree of linear polarization of the incident beam. The open circles show the degree of linear polarization measured for the charge scattering and plotted verses wave-vector transfer for the (0,0,2), (0,0,4) and (0,0,6) chemical reflections. The solid line is the degree of linear polarization for the charge scattering. The solid circles show the degree of linear polarization measured for the magnetic scattering at $(0,0,2+\tau)$, $(0,0,4\pm\tau)$, and $(0,0,6\pm\tau)$. The dashed lines show the degree of linear polarization calculated from eq. (18) for the non-resonant magnetic cross-section under different assumptions: $L=6$, $S=$arbitrary; $L=6$, $S=2$; $L=$arbitrary, $S=0$. Bottom: the brackets indicate the corresponding ratio of the orbital and spin form factors, $g(Q)$, while the solid line gives the calculated value. (From Gibbs et al. 1991.)

to both spin and orbital moments (eqs. 19 and 20). In fig. 18 we show the results of measurements of the degree of linear polarization of the charge and magnetic scattering P'_c and P'_m, respectively, in Ho for predominantly σ-polarized incident radiation. The respective degrees of linear polarization are plotted versus $\sin(\theta)/\lambda$. The solid square at $Q = 0$ represents the incident degree of linear polarization P, which in these experiments was about 0.77. The open circles show the degree of linear polarization P'_c of the charge scattering for the (002), (004), and (006) chemical reflections. The solid circles in fig. 18 represent the average degree of linear polarization P'_m measured for the positive and negative magnetic satellites at $(0,0,2+\tau)$, $(0,0,4\pm\tau)$, and $(0,0,6\pm\tau)$. The dashed line labelled ($L = 6$, $S = 2$) shows the degree of linear polarization P'_m calculated from eq. (18) for a spiral assuming $L = 6$ and $S = 2$ and using calculated form factors for the Q dependence of the orbital and spin magnetization densities (Blume et al. 1962). The remaining dashed lines show P'_m assuming first ($L = 0$ and S arbitrary), and then

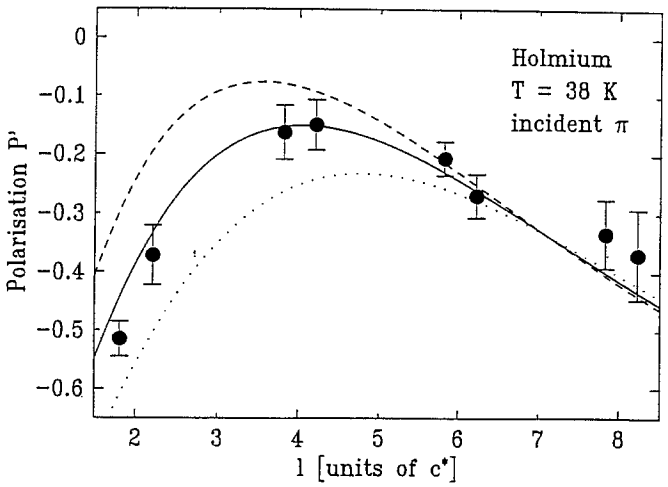

Fig. 19. The measured polarization of the scattered beam from Ho at 38 K. The solid line has been calculated by assuming that $R = |(L \cdot J)/(S \cdot J)| = 3$, as appropriate to the $^5I_8$ Hund's rule ground state of Ho. (The dashed and dotted lines have been calculated assuming that $R = 4$ and 2, respectively.) At small Q this provides an adequate description of the data, but at high Q there is a significant deviation from the expected form. Note: the experiments were performed with an incident π geometry, so that the expressions developed in section 2 are not applicable (see Sutter et al. 1999 for details).

(L arbitrary and $S = 0$). It is clear from the figure that the predominantly σ-polarized character of the incident beam is preserved upon charge scattering ($P'_c > 0$), but that the incident linear polarization is rotated upon magnetic scattering ($P'_m < 0$). To within experimental error, this is consistent with the non-resonant cross-sections for both the charge and magnetic scattering. In terms of the non-resonant cross-section for magnetic scattering, this behaviour reflects the fact that the orbital-magnetization density in Ho is large relative to the spin magnetization density, and that the π-polarized component of the intensity follows a sin-squared dependence on θ (see eq. 20).

The measured and calculated ratio of the orbital to spin form factor, $g(Q)$, are compared in the lower panel of fig. 18, where the calculations were based on non-relativistic Hartree–Fock wave functions. At $Q = 0$, the calculated ratio (solid line) equals 3.0. At higher Q, the ratio increases, reflecting the rapid fall-off of the form factor for spin in Ho. As may be seen, however, the experimental error bars are too large to draw any firm conclusions, other than that the orbital contribution is large compared to the spin contribution. The limiting factor in determining a more accurate estimate of $g(Q)$ is the low signal-to-noise ratio in the experiments. More recently Sutter et al. (1999) have performed an experiment at the ESRF where the much higher counting rates enabled them to show that $g(Q)$ has a form consistent with a ratio of 3.0 at small Q, as expected for the $^5I_8$ Hund's rule ground state of Ho (fig. 19). Interestingly, $g(Q)$ apparently deviates from simple predictions at high Q, suggesting that the orbital magnetization may be more extended in real space than previously believed.

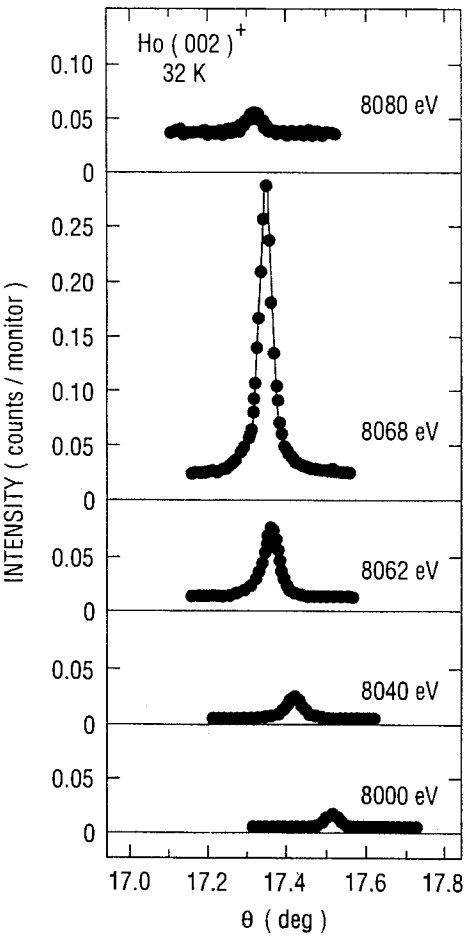

Fig. 20. Rocking curves of the X-ray magnetic scattering for Ho at the (0,0,2+τ) reflection plotted as the incident X-ray energy is tuned through the L_{III} absorption edge at $\hbar\omega$ = 8067 eV. The sample temperature was fixed at 32 K, at which temperature Ho exhibits a simple spiral magnetic phase with $\tau_m = 0.189c^*$. (From Gibbs et al. 1991.)

3.5. *Resonant cross-section*

The effect on the magnetic scattering of tuning the incident X-ray energy through the L_{III} edge of Ho is illustrated in fig. 20, where a series of rocking curves through the (0,0,2+τ) peak are shown (Gibbs et al. 1991). Well below the edge at 8000 eV, typical count rates in the magnetic peak were about 1000 s^{-1} (on backgrounds of about 1 s^{-1}). As the incident photon energy is increased the peak intensity increases, until $\hbar\omega$ = 8070 eV, where the magnetic intensity reaches a maximum. At this energy the measured count rate in the magnetic peak is about 45 000 s^{-1} on a background of about 2000 s^{-1}. Above $\hbar\omega$ = 8070 eV, the magnetic intensity decreases. Thus, the measured peak intensity increases by nearly a factor of fifty when the energy is tuned to the L_{III} absorption edge. Relative to the intensity of the charge scattering at (0,0,2), the resonant scattering at the

$(0, 0, 2 + \tau)$ reflection is reduced by a factor of order 10^4. The increased background above the edge originates in the Ho L_{III} fluorescence.

In addition to the resonant enhancement observed for the magnetic scattering at $(0, 0, \ell = 2 + \tau)$, resonant harmonics of the magnetic scattering at $\ell = 2 + 2\tau$, $2 + 3\tau$, and $2 + 4\tau$ have also been observed. The origin of the resonant harmonics has been discussed in sect. 2. For each of these harmonics the integrated intensity of un-rotated (σ channel) and rotated (π channel) components was determined separately as a function of the incident energy, and the results are summarized in fig. 21. The top panel of the figure shows the measured absorption coefficient plotted as the incident X-ray energy is tuned through the L_{III} absorption edge. The solid vertical line indicates the inflection point of the abrupt change of the absorption located at $\hbar\omega = 8067\,\text{eV}$. In the lower panels, the open circles indicate the results obtained for the π-polarized components of the scattered beam, while the solid circles indicate the results obtained for the σ-polarized component. Referring to the second panel from the top of the figure, it is clear that the σ- and π-polarized components of the magnetic scattering have significantly different line shapes. In particular, the π-polarized component of the intensity takes a maximum about 3 eV above the inflection point of the absorption, while the σ-polarized component peaks about 3 eV below. Furthermore, the π-polarized component of the scattering appears asymmetric, with a long tail to lower energy. In contrast to this behaviour at τ, the π-polarized component of the scattering at 2τ, shown in the third panel, takes a maximum below the inflection point of the absorption and the σ-polarized component reaches a maximum above. At 2τ, neither line shape appears asymmetric to within the available statistics. For the scattering at 3τ, both components peak below the inflection point and no scattering is observed above.

The data presented in fig. 21 is most simply explained by supposing that the energy dependence of the diffraction pattern is derived from two excitations, split below and above the inflection point of the absorption. In the excitation channel corresponding to X-ray energies below the inflection point, resonant scattering exists at four harmonics (τ, 2τ, 3τ, and 4τ), while in the channel corresponding to X-ray energies above the inflection point, resonant scattering exists at only two harmonics (τ and 2τ). This aspect of the data finds a natural explanation in the theory of resonant magnetic scattering, as summarized in sect. 2 (Hannon et al. 1988, Hamrick 1994). According to this theory, both resonant and non-resonant contributions to the X-ray cross-section may exist for incident X-ray energies near the L_{III} absorption edge. The non-resonant contributions depend on the atomic orbital- and spin-magnetization densities, as has been discussed in sect. 2. The resonant contributions arise from electric multi-pole contributions to the X-ray scattering cross-section. In application to Ho, it has been shown that the dipole-allowed transitions, coupling 2p core electrons with 5d-derived conduction-band states, lead to only two harmonics: at τ and 2τ. Similarly, the quadrupole-allowed transitions, coupling 2p core electrons to 4f-derived states, lead to four harmonics at τ, 2τ, 3τ, and 4τ. It is then natural to associate the scattering observed above the inflection point of the absorption in fig. 21 with the $2p \rightarrow 5d$ transitions and, similarly, to associate the scattering below the inflection point with $2p \rightarrow 4f$ transitions. Importantly, the observed polarization dependence of

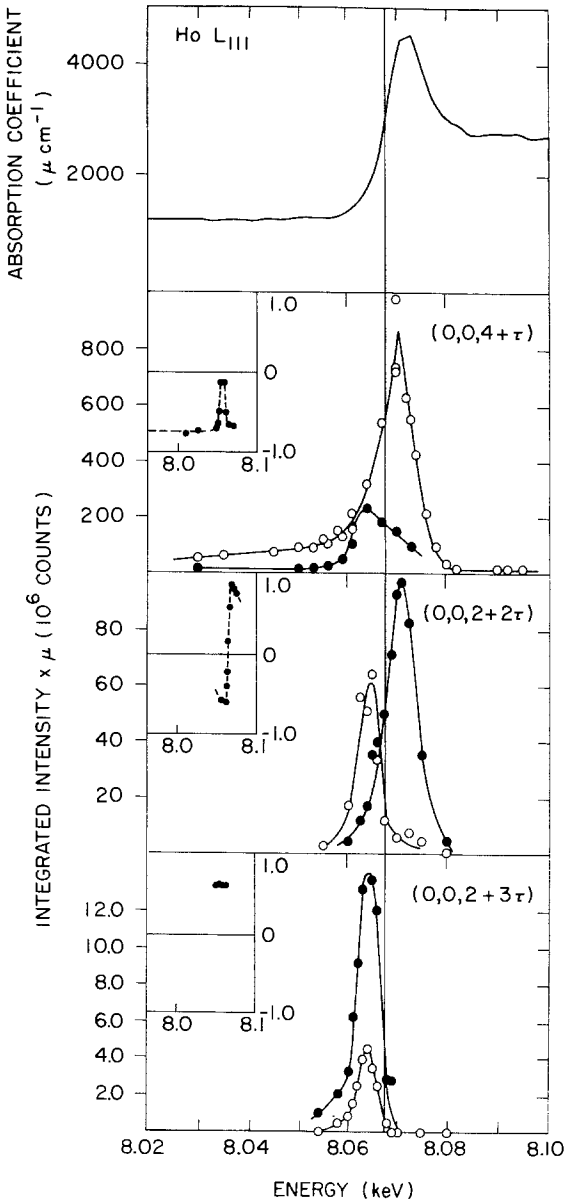

Fig. 21. Resonant X-ray scattering from Ho. Top: measured absorption coefficient plotted vs incident X-ray energy for the L_{III} edge of Ho. Lower: integrated intensities plotted vs energy for the linear components scattered parallel and perpendicular (solid circles) to the diffraction plane at τ, 2τ and 3τ. Lines are drawn only to guide the eye. Polarization analysis was performed at the (0,0,4+τ) below 20 K, where $\tau = \frac{1}{6}c^*$, and at the (0,0,2+2τ) and (0,0,2+3τ) at 25 K, where $\tau = (0.186)c^*$. At the (0,0,2+4τ) resonant scattering was observed only below the edge. Insets, lower: corresponding degree of linear polarization plotted vs energy. Vertical line indicates the energy of L_{III} edge. Solid lines are the results of fits, which are discussed in the text. (From Gibbs et al. 1988.)

the resonant scattering is consistent with the polarization dependence calculated for a magnetic spiral in table 1. On this basis, the main features of the energy and polarization dependence of the resonant magnetic scattering observed in Ho may be explained.

To investigate the line shapes of these resonances, and in particular to understand their dependence on the induced polarization and exchange splitting within the d band, and on the non-resonant magnetic scattering, systematic studies were made of the integrated magnetic intensity as a function of Q. In summary, it was found by Gibbs et al. (1991) that the data were qualitatively consistent with one-electron predictions for the electronic structure of Ho. The discrepancies between the values of the fitted parameters and those derived from calculations suggest that more sophisticated calculations of the electronic structure may be required before a quantitative comparison is possible. In the calculation, for example, the influence of the core-hole on the wave functions of the excited state has been ignored. Therefore, while the present results are consistent with an orbital model of the electronic structure which includes exchange splitting of the d band, these fits are not unique. It also seems clear that in order to achieve further progress beyond being able to comment on the qualitative features of the line shapes, the higher fluxes available from next generation synchrotron sources will be required. The one exception to these conclusions found to date concerns the discrepancy found in the L_{III}/L_{II} branching ratio, which is discussed in more detail in sect. 5.

3.6. *Critical scattering*

We shall close this section with two examples of how the resonantly enhanced cross-section has allowed new aspects of the critical region near the Néel temperature to be explored. Studies performed in this region require the use of resonant techniques to enhance the intensity, as the critical scattering is very weak relative to that obtained well inside the ordered phase. Even at resonance the measured intensity is proportional to the magnetization squared, at least at the first harmonic (Hill and McMorrow 1996), and so results taken at resonace may be compared directly to data from neutron scattering experiments. The motivation for these experiments is that although the magnetic properties of the Ho (and the other lanthanides) are reasonably well understood in the ordered phase, where the magnetic structures have been modelled successfully using mean-field theory, the state of affairs in the critical regime remains controversial.

As is well known, for an antiferromagnet the development of static long-range magnetic order below T_N is reflected by the appearance of a new Bragg peak, in the case of Ho positioned at τ_m. The intensity I of this Bragg peak grows as a power law in the reduced temperature, such that $I \propto [(T_N - T)/T_N]^{2\beta}$, where β is the order-parameter critical exponent and has a value that depends on the universality class to which the transition belongs. For Ho the value of β has been determined by neutron scattering (Eckert and Shirane 1976). It is, however, difficult in such measurements to ascertain to what extent the derived value of β is affected by extinction. By contrast, the relative weakness of the X-ray magnetic scattering signal, even at resonance, ensures that the value of β obtained is extinction-free. A second, more interesting possibility offered by resonant X-ray scattering is that the order parameters characterizing the higher-order satellites at two, three and possibly four times τ_m may be determined. This is of particular interest as predictions have been made of what may be termed higher-order critical phenomena, with only a few experimental tests (Brock et al. 1986, Aharony et al. 1986, Zinkin et al. 1996).

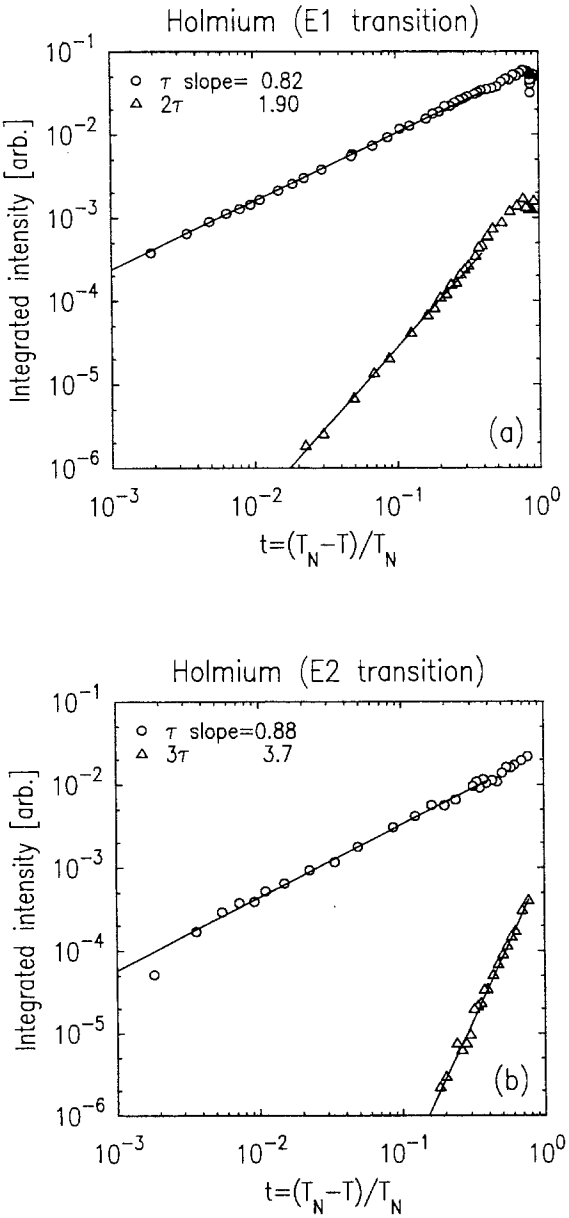

Fig. 22. Integrated intensity data from Ho plotted as a function of the reduced temperature t. The solid lines are fits to power-law behaviour. (a) First- and second-order peaks at the dipole transition ($\hbar\omega$ = 8072 eV). (b) First- and third-order peaks at the quadrupole transition ($\hbar\omega$ = 8064 eV). (From Helgesen et al. 1994.)

The temperature dependence of the integrated intensity of the first three harmonics of Ho in the vicinity of T_N is shown in fig. 22 (Helgesen et al. 1994). The value of β_1 at the first harmonic is 0.39 ± 0.04, and does not depend on whether the scattering is

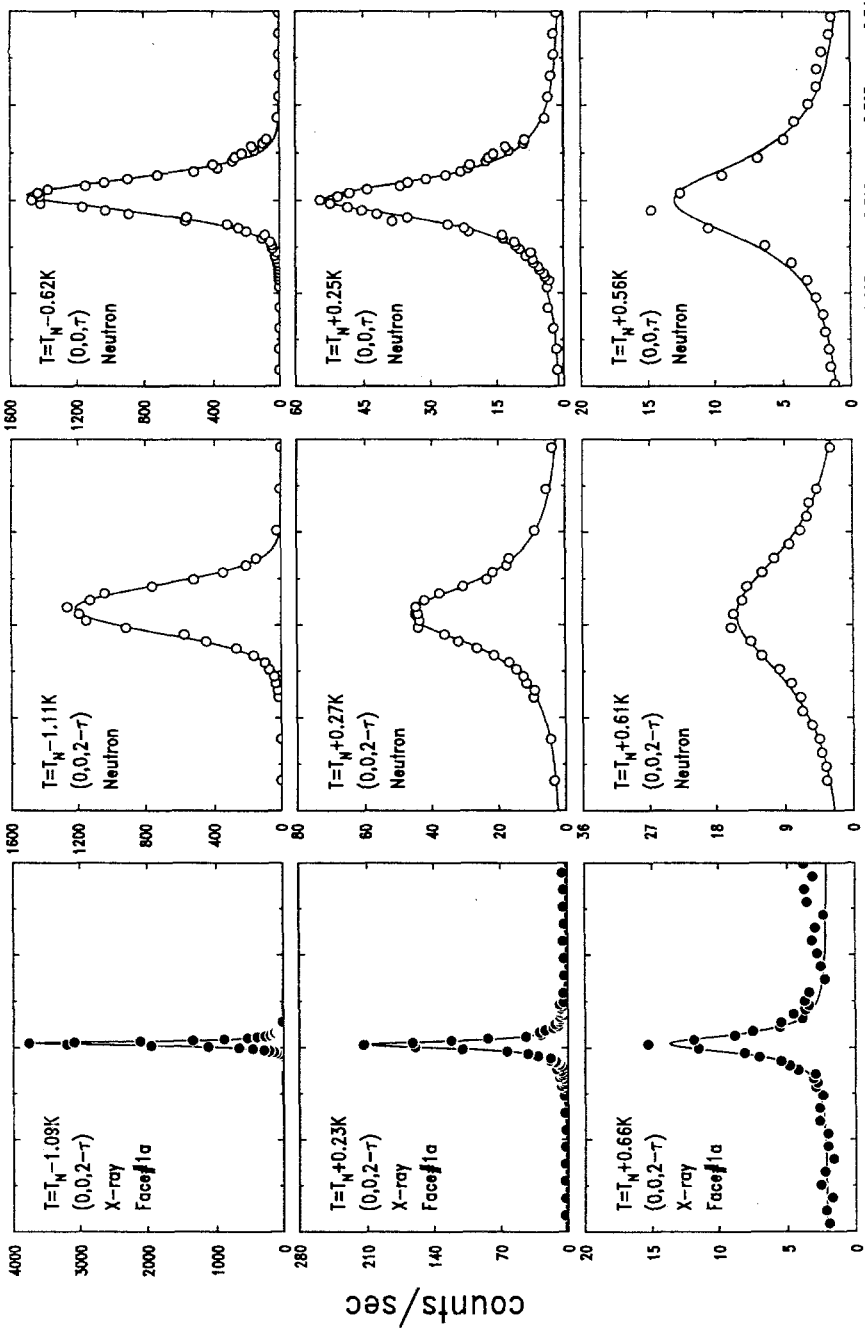

Fig. 23. Transverse X-ray and neutron scattering scans from Ho taken at the $(0,0,2-\tau)$ and $(0,0,\tau)$ magnetic peak positions. The scans in the top row of the figure were taken at temperatures below the transition, and represent the effective resolution of the different experimental configurations. The centre and bottom rows show critical scattering observed at temperatures above the transition. The solid lines represent fits to the Lorentzian plus Lorentzian squared line shape discussed in the text. (From Thurston et al. 1993.)

measured in the E1 dipole or E2 quadrupole channels. Moreover, its value is consistent with that derived from neutron scattering (Eckert and Shirane 1976), and tends to support the assignment of the phase transition in Ho to the $O(4)$ model ($\beta_1 = 0.39$) as proposed by Bak and Mukamel (1976), rather than to the Chiral model ($\beta = 0.25$, Kawamura 1988). The higher harmonics also display power-law behaviour with exponents of $\beta_2 = 0.85 \pm 0.1$ and $\beta_3 = 1.85 \pm 0.1$ which do not agree with the results expected for simple mean-field scaling, where for the nth harmonic $\beta_n = n \times \beta_1$. These results have been further discussed by Helgesen et al. (1994) in the context of recent work on the XY universality class (Brock et al. 1986, Aharony et al. 1986). The values of β determined for the other lanthanides using X-ray techniques are considered in sect. 4.

In the first experiment of its type, the critical scattering for $T \geqslant T_N$ was investigated by Thurston et al. (1993) using resonant X-ray techniques. The unique aspect of these experiments is that because of the inherently high wave-vector resolution the critical fluctuations can be studied on much longer length scales than is routinely achievable with neutron scattering. Hence in principle, X-ray techniques allow the critical region to be probed in more detail. A summary of their X-ray data for Ho is shown in fig. 23, where they are compared with conventional neutron scattering data from the same sample, and with neutron scattering data taken in a high-resolution mode. The striking aspect of this figure is that at a given temperature the X-ray data shows a single sharp component, whereas the high-resolution neutron data has an additional broad component, and the low-resolution neutron data is dominated by the broad component only. The latter corresponds to the normal critical fluctuations, so that the existence of the sharp component was not expected. The temperature dependence of the correlation lengths of these two components is shown in fig. 24, (overleaf) where the widths of the peaks have been extracted by fitting a model scattering function comprising a sum of a Lorentzian and Lorentzian-squared to represent the broad and sharp components respectively. It is clear from this figure that the extra sharp component represents true critical fluctuations on a length scale that is over an order of magnitude larger than those associated with the normal component. As it transpired, a similar second component had been observed already in the critical fluctuations associated with structural phase transitions in a number of perovskite systems (see McMorrow et al. 1990 and references therein). Although a consensus has yet to emerge on the detailed origin of the second component, it seems to be agreed that it is predominantly located in a surface skin, some 1–10 μm thick, and is probably related to the presence of structural defects of an unknown nature (see Zinkin et al. 1996 and references therein).

4. The lanthanide elements

4.1. *The heavy lanthanides*

With the exception of non-magnetic Yb, X-ray magnetic scattering has now been observed from all of the heavy lanthanide elements. In the case of ferromagnetic Gd, experiments

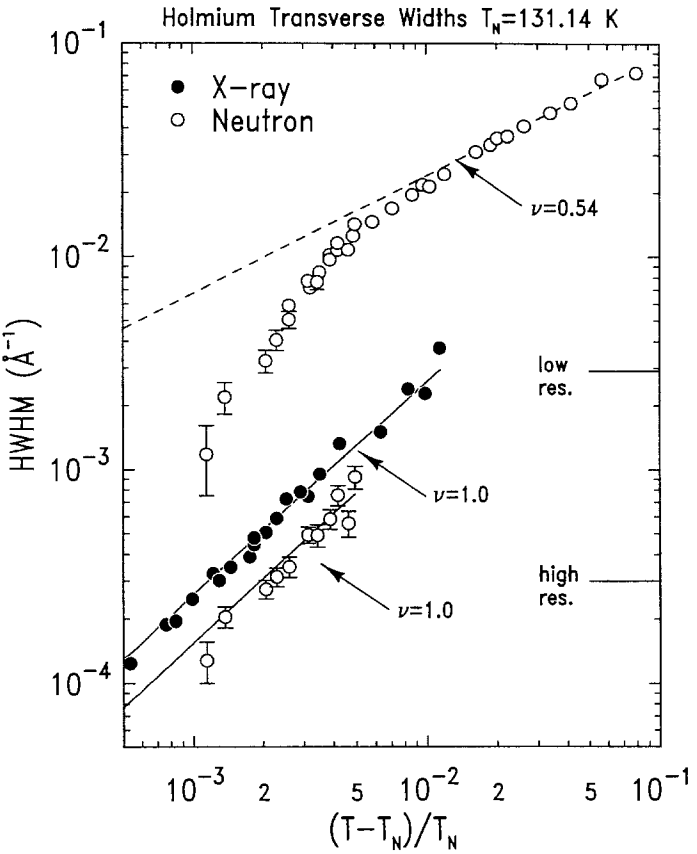

Fig. 24. Half-width at half maxima (HWHM) of the broad and narrow components for scans taken within the basal plane. The solid lines through the data represent fits to a power law HWHM$=\kappa_0[(T - T_C)/T_C]^{\nu}$. The resolution limits for the various configurations are shown to the right of the data. The low resolution neutron scattering limit is identified by "low res", while the X-ray and high-resolution neutron scattering limits are identified by "high res". (From Thurston et al. 1993.)

are more difficult to perform as the magnetic scattering falls on top of the much stronger charge contribution. (For a preliminary account of progress that has been made in studying Gd see Namikawa 1992.)

4.1.1. *Erbium*

Er probably displays the most complex magnetic phases of any of the heavy lanthanides, and the gradual way in which the model of its magnetic structure has been refined over the years is typical of the steady progress that has been made in our understanding of all the lanthanide metals. The basic magnetic structures that exist in Er were determined by Cable et al. (1965) using neutron diffraction. This work, combined with the later study by Habenschuss et al. (1974), established that the magnetic phase diagram has three distinct

regions. (1) Just below $T_N \approx 87$ K the moments lie along the c axis, and have a sinusoidal modulation of their magnitudes described by a wave vector $\tau_m \approx \frac{2}{7}$. As the temperature is decreased the structure begins to "square up" as the magnitudes of the moments on each site tend to the same value. (2) At $T_N' \approx 52$ K a second phase transition occurs and the moments tilt away from the c axis and develop a basal-plane component. (3) At $T_C \approx 18$ K the basal-plane components of the moments align along the c axis producing a cone phase; the basal-plane moments form a helix, and there is a large net ferromagnetic moment along c. In the cone phase $\tau_m = \frac{5}{21}$.

The precise nature of the magnetic structure between T_N' and T_C proved difficult to pin down for some years, as the neutron scattering data were consistent with two conflicting models. The structure could either be a basal-plane helix with an alternating c-axis moment, or a cycloidal structure, where the moments form an ellipse in the a–c plane with the major axis of the ellipse along the c axis. It was originally believed by Cable et al. (1965) that the six-fold basal-plane anisotropy was insufficient to confine the basal-plane components to an a axis, and so they argued that the cycloid was probably not stable. This was subsequently questioned by Jensen (1976), who used a mean-field calculation to show that the cycloid was in fact energetically favoured, even in the absence of hexagonal anisotropy.

The main contribution of X-ray magnetic scattering to the study of Er has been to shed further light on the phases in the intermediate temperature interval between T_N' and T_C, and more recently to characterize the temperature dependence of the magnetic order parameter near T_N. X-ray magnetic scattering has revealed a great wealth of new information on these intermediate phases that fits most easily with the cycloidal model.

4.1.1.1. *Non-resonant scattering.* The first synchrotron based X-ray scattering study of Er was by Gibbs et al. (1986), and followed shortly after their work on Ho. These experiments were performed well away from the L edges of Er at incident photon wavelengths of either 1.58 or 1.70 Å. As was the case for Ho, the X-ray diffraction revealed a complex pattern of peaks arising from magnetic and charge scattering. In fig. 25 a summary of the temperature dependence of the wave vector of all of the additional peaks is given. The most striking feature of this figure is the existence of preferred commensurable values of the wave vectors over certain temperature intervals. This result is strongly reminiscent of what was found in Ho, and indeed it was established by Gibbs et al. (1986) that the commensurable wave vectors in Er are an expression of an underlying simple spin-slip structure. Before describing this in detail, we first consider several other features of fig. 25.

In the intermediate phase below 52 K, satellite peaks appear at τ_m with τ_m slightly greater than $\frac{2}{7}$. On cooling the wave vector decreases and locks to the series of commensurable values $\frac{2}{7}$, $\frac{4}{15}$, $\frac{5}{19}$, $\frac{6}{23}$, $\frac{1}{4}$ and $\frac{5}{21}$. In addition to the scattering at τ_m, there are three other peaks which also display lock-ins to commensurable values, and are labelled $2\tau_m$, $2\tau_m - \tau_s$ and τ_s in fig. 25. Polarization analysis of the various peaks shows that these latter three all arise from charge scattering, while the peak at τ_m has contributions from both magnetic and charge scattering.

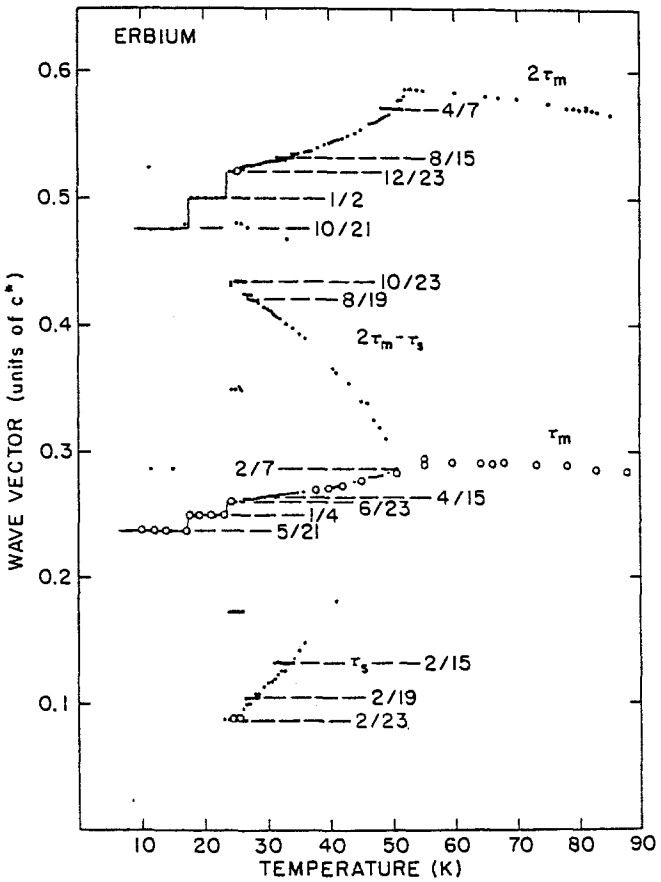

Fig. 25. Combined X-ray (solid circles) and neutron (open circles) scattering results from Er for the fundamental wave vector τ_m and for the additional scattering from lattice modulations at $2\tau_m$, τ_s and $2\tau_m - \tau_s$. The peak observed at τ_m in the c-axis modulated phase above 52 K is the principle magnetic satellite of the (110) reflection, obtained by neutron scattering. All remaining data are satellites of the Bragg (002) and (004) reflections. The X-ray results at $2\tau_m - \tau_s = \frac{6}{15}$ were partially obscured by higher-order contamination. (From Gibbs et al. 1986.)

A full explanation for the origin of these peaks is given by a modified version of the spin-slip model already described for Ho. Here, we shall first consider the peak at τ_m. The generating structure has $\tau_m = \frac{1}{4}$, which is formed from one block of four planes of moments that point along the c axis, followed by a second quartet of moments that points antiparallel. Other phases are generated by introducing a spin slip into the structure, which is equivalent to removing one of the moments in a quartet to form a triplet. For example, the phase with $\tau_m = \frac{2}{7}$ is composed of a quartet and a triplet which we can write as (43). In table 3 we summarize the observed commensurable wave vectors and the spin-slip structures which they reflect. Following similar arguments to those already

given for Ho (see eq. 21) the wave vector of the fundamental magnetic satellite in Er is given by

$$\tau_m = \frac{2n}{8n - s}, \tag{25}$$

where there are s slips for every n full (2π) rotations of the moments along the c axis.

The position of the charge satellites may also be explained readily using this model. First, the peak at $2\tau_m$ may be understood by assuming that magneto-elastic distortions occur with a frequency of half the magnetic unit cell. Second, the peaks at $2\tau_m - \tau_s$ and τ_s can be shown to arise from correlations among the triplet and quartet distributions. These correlations produce peaks at $2\tau_m - \tau_s = 2 - 6\tau_s$ and $\tau_s = 8\tau_m - 2$, respectively, in agreement with the data shown in fig. 25.

As well as allowing the identification of the commensurable phases, the high wave-vector resolution also makes it possible to study changes in the magnetic coherence length. In fig. 26 the X-ray scattering near $2\tau_m$ is shown for temperatures between 55 and 47.5 K. At 52 K, the basal plane component of the magnetic structure orders and regions of the crystal lock to the commensurate wave vector $2\tau_m = 0.571c^* = \frac{4}{7}c^*$. The single peak observed at 55 K in fig. 26 splits into three, all of which appear broader than the resolution. At these temperatures there is coexistence among a distribution of magnetic phases (with differing wave vectors). It seems likely that the scattering at higher momentum-transfer is associated with a pure c-axis modulated structure, while the scattering at smaller momentum-transfer corresponds to magnetic structures which also support a basal plane modulation. As the temperature is lowered further, the scattering at $2\tau_m = \frac{4}{7}c^*$ grows in intensity and narrows in width until, at 50.5 K, it dominates the diffraction pattern. By 49.5 K a second, broader peak becomes visible at lower momentum transfer. At still lower temperatures, this second peak grows in intensity and shifts to smaller momentum transfer until by 48 K the scattering at the commensurate wave vector $2\tau_m = \frac{4}{7}c^*$ has disappeared entirely. In summary, it is seen that the lock-in transformation of the magnetic structure to $\tau_m = \frac{2}{7}c^*$ ($2\tau_m = \frac{4}{7}c^*$) involves the coexistence of a broad, distribution of incommensurate magnetic phases and an ordered, commensurate magnetic phase. The average wave vector of the incommensurate component decreases continuously with temperature. Its radial width is approximately constant, however, and corresponds to a correlation length of only several hundred Å. In contrast, the radial width of the commensurate peaks are often resolution limited, corresponding to a correlation length of several thousand Å or greater.

One other notable feature of the data shown in fig. 25 is that in the non-resonant scattering experiments no scattering was observed at the primary satellite position τ_m in the purely c-axis modulated phase that exists above 52 K, where the cross-section varies as $\sin^6\theta$ and is weak. This observation had to wait for resonant scattering techniques to be applied to the problem.

4.1.1.2. *Resonant scattering.* The resonant X-ray magnetic scattering from Er was studied in some detail by Sanyal et al. (1994) for X-ray energies in the vicinity of

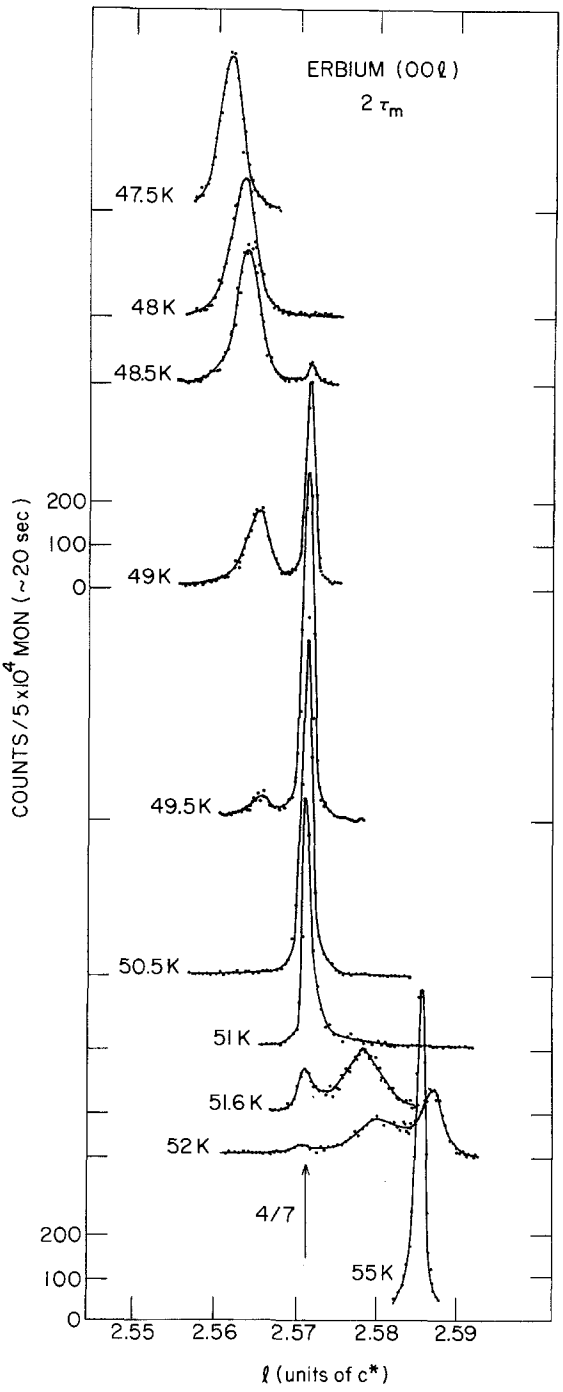

Fig. 26. Temperature dependence of the scattering at $2\tau_m$ near the $\tau_m = \frac{2}{7}$ transition in Er. The peak at $2\tau_m = \frac{4}{7}$ is resolution limited. The solid lines are drawn to guide the eye. (From Gibbs et al. 1986.)

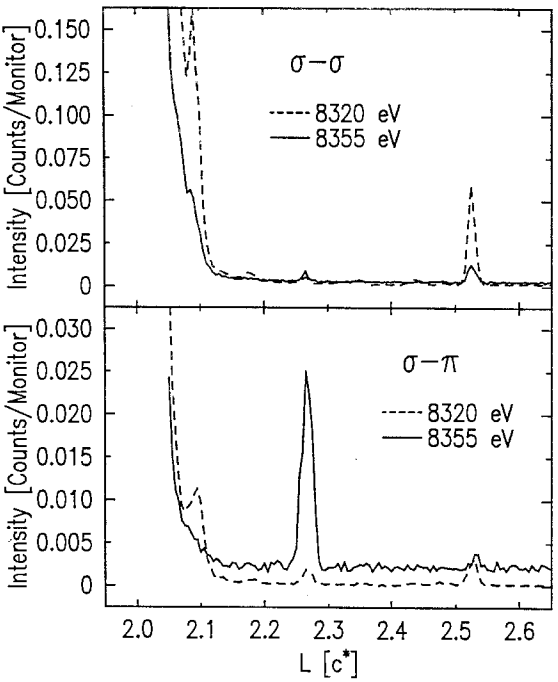

Fig. 27. Scans of the σ-polarized (top) and π-polarized (bottom) components of the scattered beam from Er taken along the $[00\ell]$ direction at 40 K for two energies near and below the L_{III} absorption edge (8358 eV) of Er. (From Sanyal et al. 1994.)

the L_{III} (8358 eV) absorption edge. For temperatures above T_C, it was found that the energy and polarization characteristics of the scattering at τ_m were consistent with a dipolar $E1$ transition. In fig. 27 the scattering from the intermediate phase at 40 K is shown for energies both on and off resonance. In this figure there are three satellites: $(2 + \tau_s) = 2.105 \approx (2 + \frac{2}{15})$, $(2 + \tau_m) = 2.267 \approx (2 + \frac{4}{15})$, and $(2 + 2\tau_m) = 2.534$ (all in units of c^*). As can be seen, the peaks at $2\tau_m$ and τ_s in the $\sigma - \sigma$ channel both decrease in intensity as the energy is tuned to the absorption edge, as is expected for charge scattering processes. It is also evident that the magnetic scattering at τ_m occurs mainly in the $\sigma \rightarrow \pi$ channel, as expected for an $E1$ transition (see tables 1 and 2). Because of the existence of the charge scattering peak at $2\tau_m$ discussed above it was not possible to test the selection rules for resonant scattering at the positions of the higher harmonics.

In addition to clarifying the form of the resonant cross-section, the study of Sanyal et al. (1994) also produced some intriguing results. For example, the data taken for temperatures below 18 K in the cone phase of Er do not fit into any simple picture of the resonant scattering process. A scan of the energy at the $(0,0,2+\tau_m)$ peak in the cone phase is shown in fig. 28. Instead of observing a sharp resonance at the L_{III} edge as found at higher temperatures in the intermediate phase, the spectrum displays several peaks well away from the edge, with no discernible resonance at the edge at all. Presently it is not known whether the effect is intrinsic, related to the change of symmetry that occurs at the

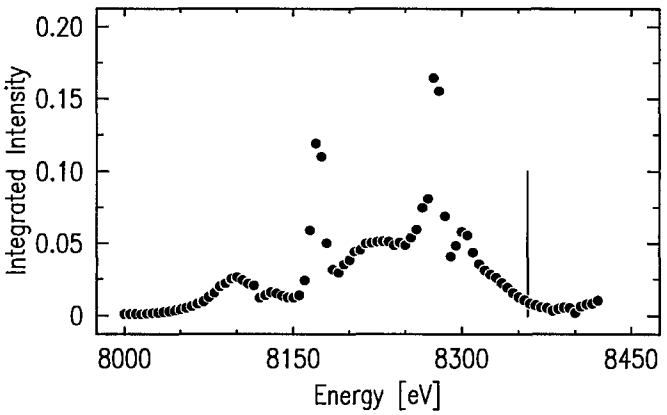

Fig. 28. The measured integrated intensity from Er (arbitrary units) for the (0,0,2+τ_m) reflection at 12 K as a function of the incident photon energy. The vertical solid line indicates the position of the L_{III} absorption edge. (From Sanyal et al. 1994.)

transition to the cone phase, or whether it is an artifact of the experiment, such as multiple scattering. It was also shown by Sanyal et al. (1994) that the cone phase is disordered with c-axis magnetic correlation lengths reaching only ~100 Å.

4.1.1.3. *Neutron scattering and ancillary measurements.* Following on from the discovery of the spin-slip structures in the intermediate phase of Er by Gibbs et al. (1986), several neutron scattering experiments were undertaken. The most comprehensive of these is the study by Cowley and Jensen (1992), who used a combination of neutron scattering and mean-field modelling to derive a detailed description of the spin-slip phases. One of the interesting features of this work is that the scattering could not be explained unless a two-ion coupling of trigonal symmetry was included in the Hamiltonian. The effect of this coupling is to break the symmetry between the otherwise equivalent two sites in the hexagonal unit cell, and causes the cycloid to "wobble" as shown in fig. 29. Other neutron scattering studies have mainly focussed on the phase diagram in the presence of an applied field (Lin et al. 1992, McMorrow et al. 1992, Jehan et al. 1994). A common feature of these studies is that the spin-slip phases with a ferrimagnetic moment are found to be exceptionally stable. This is illustrated in fig. 30 for the case of field applied in the basal plane. The phases with $\tau_m = \frac{2}{7}$, $\frac{4}{15}$ and $\frac{6}{23}$ are seen to dominant, and all of these phases have a net ferrimagnetic moment along c with an odd ratio of quartets and triplets (see table 3).

In addition to these scattering studies, anomalies associated with the spin-slip phases have now been identified in magnetization, AC susceptibility, thermal expansivity, and electrical resistance measurements (Ali and Willis 1990, B. Watson and Ali 1995, 1996a,b, Eccleston and Palmer 1992). For example, in fig. 31 we show the temperature dependence of the resistivity for the c and b axes of single crystal Er.

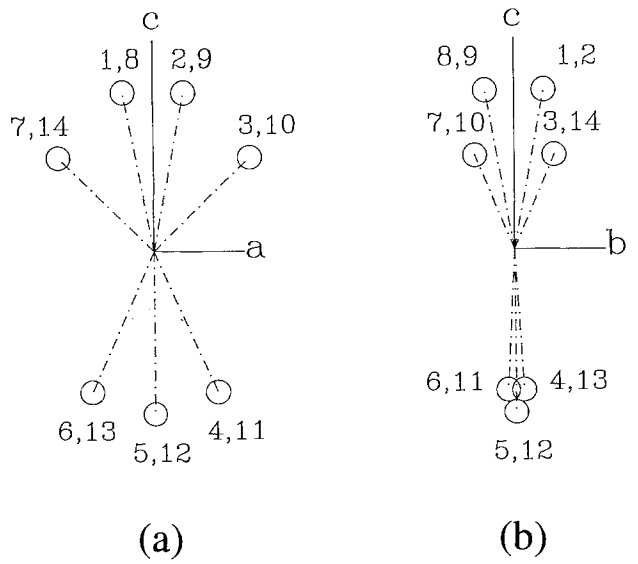

Fig. 29. The calculated arrangement of moments in the $\tau_m = \frac{2}{7}$ cycloidal structure of Er in zero field: (i) in the $a-c$ plane and (ii) in the $b-c$ plane. The figure is drawn to emphasize the fact that the moments are not confined to the $a-c$ plane, but instead "wobble" about this plane. Scaling: a to c 1:1, and b to c 10:1. The numerical labels refer to moments in successive planes along the c axis. (From Jehan et al. 1994.)

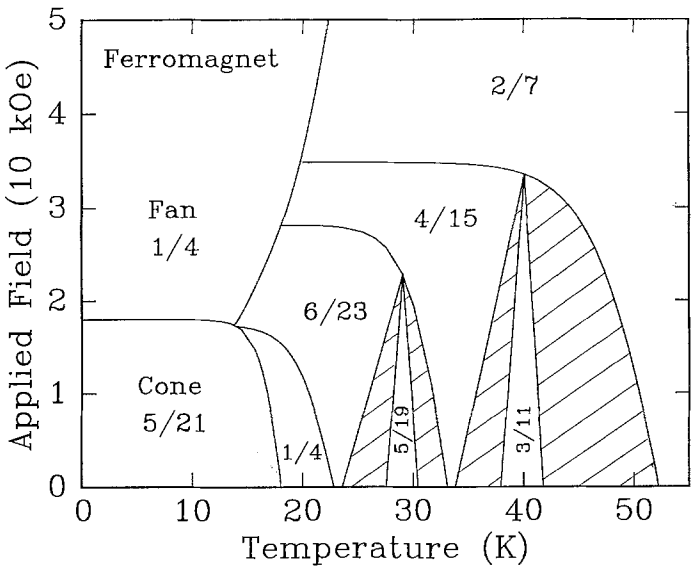

Fig. 30. Schematic phase diagram of Er in a basal-plane field determined from neutron diffraction. The shaded regions represent incommensurable values of the modulation wave vector. (From Jehan et al. 1994.)

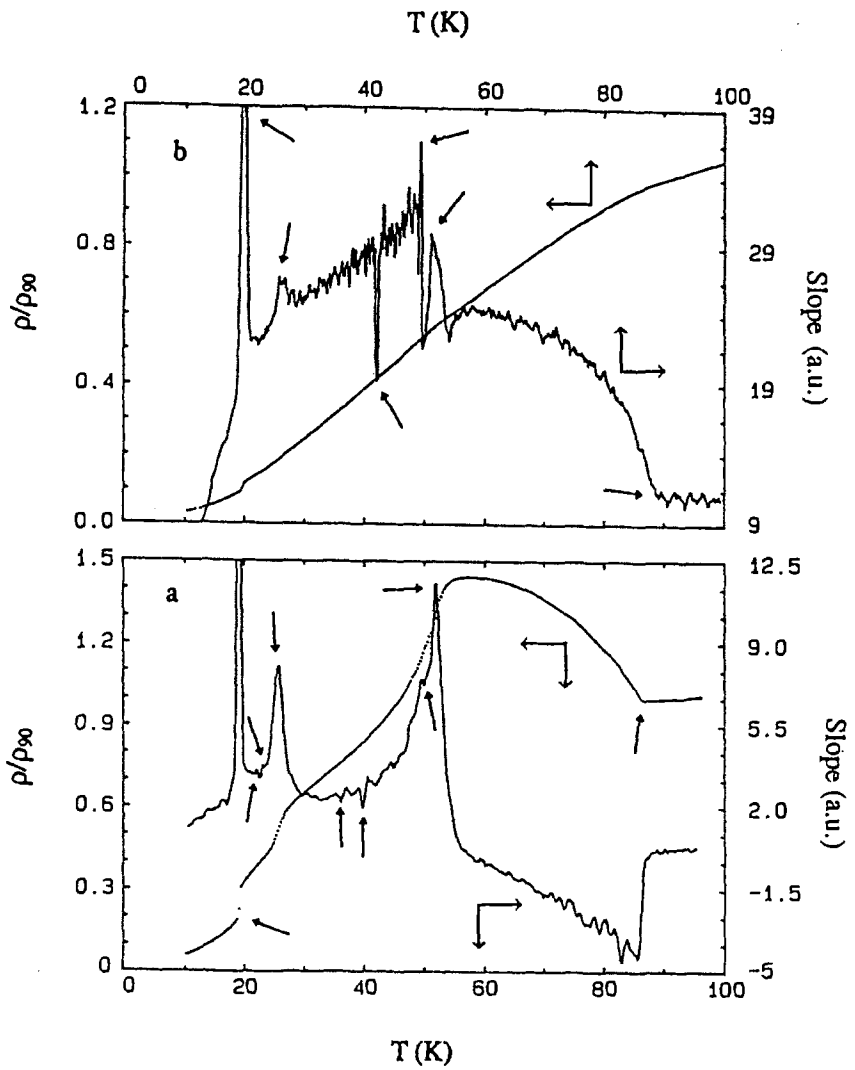

Fig. 31. (a) Resistivity (ρ) relative to the resistivity at 90 K (ρ_{90}) versus temperature for the c axis of single-crystal Er in the temperature range from 10 K to 100 K. The derivative of the c axis resistivity versus temperature is also included. (b) Resistivity (ρ) relative to the resistivity at 90 K (ρ_{90}) versus temperature for the b axis of single-crystal Er in the temperature range from 10 K to 100 K. The derivative of the b axis resistivity versus temperature plot is also included. (From B. Watson and Ali 1995.)

In the same figure the derivative of the resistivity is also plotted, where many anomalies (indicated by arrows) related to transitions between spin-slip phases are apparent.

4.1.2. *Thulium*

Next to Er, Tm is the only other heavy lanthanide element that orders with a longitudinal modulation of the moments along the c axis. In contrast to Er, the c-axis anisotropy in Tm is so large that the ordering of the basal-plane components is completely suppressed at all temperatures below T_N of ≈ 56 K. From neutron diffraction it was established that the wave vector describing the modulation is weakly temperature dependent below T_N, and at $T_C \approx 30$ K locks in to a value of $\frac{2}{7}$ (Koehler et al. 1962, Brun et al. 1970). The magnetic structure in this phase is similar to that observed in Er just below T_N', with a quartet of moments along the positive c axis followed by a triplet of negative moments, which can be be written in the spin-slip notation as (43). The main difference is that in Tm the modulation is almost completely square-wave at low temperature, as attested to by the presence of odd-order harmonics in the neutron diffraction patterns.

The X-ray scattering from Tm has been investigated by Bohr et al. (1990) and by Helgesen et al. (1995) for energies both off resonance and in the vicinity of the L_{III} edge (8648 eV). For the non-resonant experiments, charge peaks were observed along the $[00\ell]$ direction at 2 and 4 times the fundamental wave vector τ_m, and were associated with a magneto-elastic distortion of the lattice. In the resonant regime, the scattering at $(0,0,2\text{-}\tau_m)$ was found to come from the rotated $\sigma \rightarrow \pi$ component only. This contrasts with the case of Ho, where both rotated and unrotated components are present at the first harmonic, but is in accordance with the selection rules for multipole scattering summarized in tables 1 and 2.

4.1.3. *Dysprosium and terbium*

In this section we consider the results of X-ray scattering experiments on the two remaining heavy lanthanide metals not yet considered, Dy and Tb, both of which order as basal-plane helices below their respective Néel temperatures.

The helical order in Tb is only stable over a very narrow range of temperature, from $T_N = 232$ K to about 220 K when the moments undergo a first order transition to form a basal-plane ferromagnet (Koehler 1965). The X-ray magnetic scattering from Tb has been studied by Gehring et al. (1992) and by Tang et al. (1992b), who both observed a weak resonance in the magnetic scattering at the L_{III} edge (7514 eV). The lower limit of the enhancement at resonance was estimated to be 20. The main features of the magnetism were in accord with an earlier neutron scattering study (Koehler 1965). Two notable new features uncovered are: the magnitude of the wave vector increases initially just below T_N, before decreasing monotonically (see fig. 32); the magnetic correlation length in the helical phase decreases with decreasing temperature, similar to what had already been observed in Tm, Er and Ho.

In the case of Dy, helical order persists over a wider temperature range, from its Néel temperature of 176 K down to 83 K, when a transition to a basal-plane ferromagnet occurs. X-ray magnetic scattering from Dy has been reported by Isaacs et al. (1989) and by Helgesen et al. (1995) for energies in the vicinity of the L_{III} edge (7796 eV). Their results for the energy and polarization characteristics of the scattering at the first harmonic τ_m

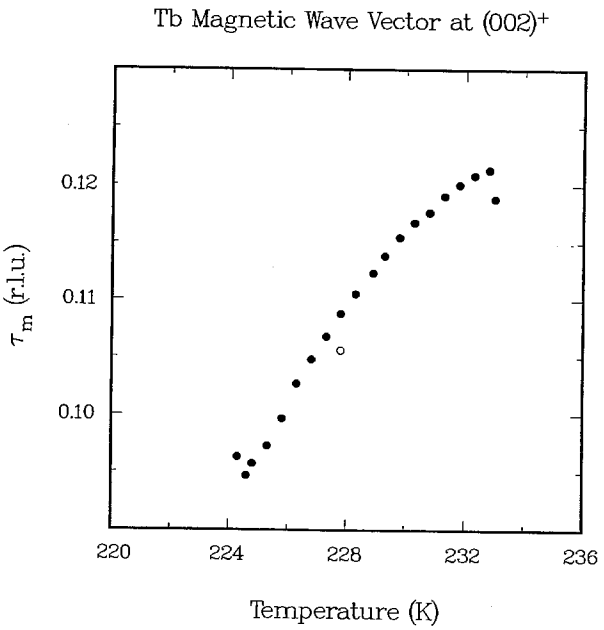

Fig. 32. Temperature dependence of the magnetic modulation wave vector τ_m in Tb. The open circle indicates the change in τ_m after quenching the sample from well into the paramagnetic state. Here 1 r.l.u. = 1.1036 Å^{-1}. (From Gehring et al. 1992.)

were in agreement with those from Ho, and the selection rules for dipole and quadrupole radiation summarized in table 1 (Hannon et al. 1988). Helgesen et al. (1995) found that the observed magnetic correlation lengths in Dy were shorter than the corresponding lattice correlation lengths at all temperatures below T_N, and increased dramatically on approaching T_C (see fig. 33).

4.1.4. *Magnetic correlation lengths and lattice constants*

A good example of the utility of high-Q resolution X-ray studies is illustrated in figs. 33 and 34 where the temperature dependence of the inverse magnetic correlation lengths, *c*-axis lattice parameters, and magnetic wave vectors of the heavy lanthanides are compared (Helgesen et al. 1995). The temperature scale in each case is normalized by the respective Néel temperatures. It is interesting that each of the peaks in the temperature dependence of the correlation length (fig. 33) corresponds to a transition to a commensurable ferri- or ferro-magnetic state. All of these transitions are first order and, with the exception of Tm, they are accompanied by significant changes in the *c*-axis lattice parameters. It seems clear that the loss of long-range magnetic order is produced by alterations in the magneto-elastic coupling on passing through the various transitions. However, a detailed explanation is lacking.

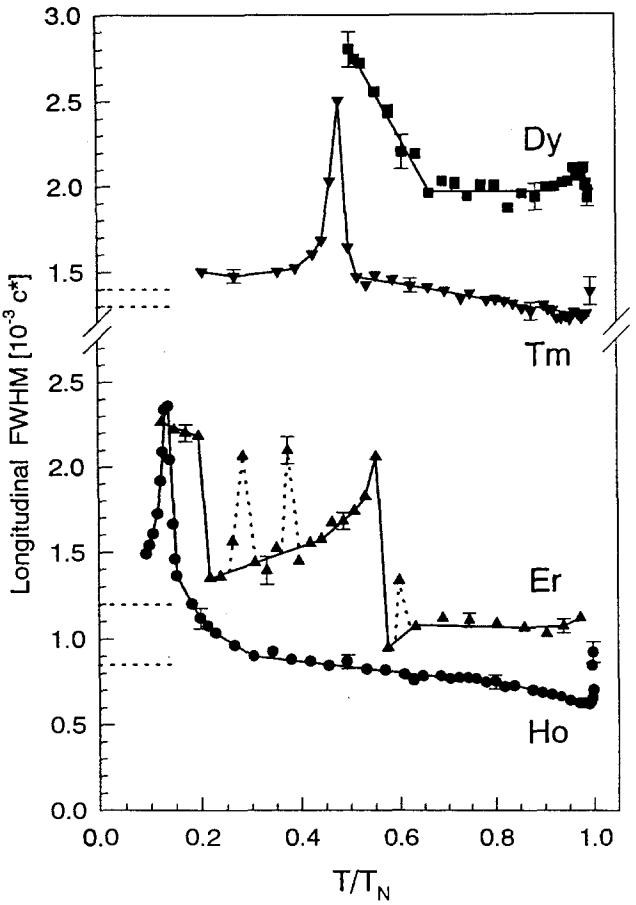

Fig. 33. Longitudinal FWHM vs temperature for the (0,0,2−τ) magnetic peaks of Dy, Ho, and Tm and the (0,0,2+τ) peak of Er. (Note the break in the y axis between the Er and Tm curves.) The solid lines are guides to the eye. The horizontal, dotted lines at the left axis show the widths of the (0,0,2) charge peak for Tm, Dy, Er and Ho (top to bottom). (From Helgesen et al. 1995.)

4.1.5. *Critical scattering from the heavy lanthanides*

It is clear from what has already been covered in this section, and in the preceding section on Ho, that X-ray magnetic scattering has helped refine our understanding of the magnetic structures found in the heavy lanthanides. Apart from these structural studies, it has also been outlined how X-ray magnetic scattering can be used to study profitably the phase transition at T_N. We will end this section on the heavy lanthanide elements by considering the work of Helgesen et al. (1995), who made a comparative study of the behaviour of the order parameters in Dy, Ho, Er and Tm, measured both at the fundamental wave vector τ_m and at the higher order harmonics.

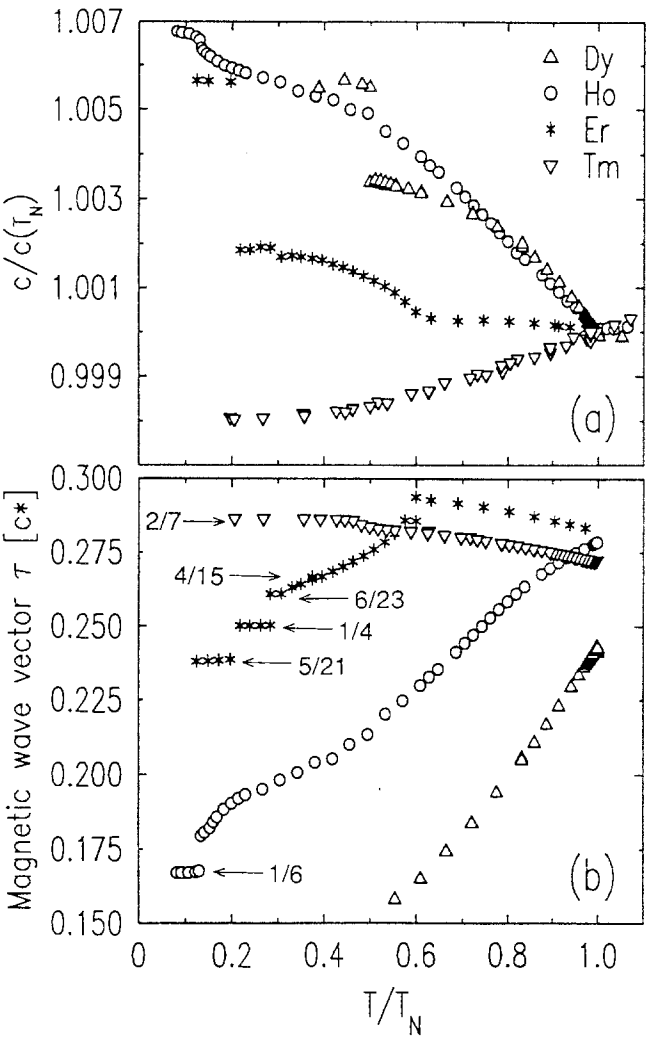

Fig. 34. (a) Lattice constant c vs temperature T for Dy, Ho, Er amd Tm. T and c are normalized by the Néel temperature T_N and the lattice constants at T_N, $c(T_N)$, respectively. (b) Magnetic wave vector τ (in units of c^*) vs temperature. (From Helgesen et al. 1995.)

Although the critical behaviour of the heavy lanthanides has been the subject of numerous theoretical and experimental studies, a consensus has yet to emerge on an appropriate description (see Helgesen et al. 1995, and references therein). As both Ho and Dy form helices in their ordered phase, they should in principal belong to the same universality class. But whether the correct assignment is to the symmetric $O(n)$ model with $n = 4$, proposed by Bak and Mukamel (1976), to the chiral model proposed by Kawamura (1988), or to some other model entirely is still unclear. Similarly, for the

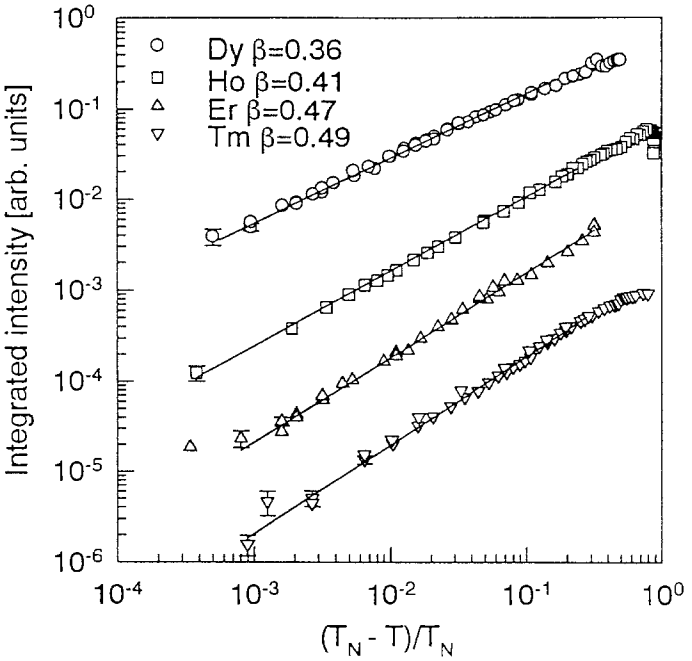

Fig. 35. Integrated intensity of the $(0,0,2-\tau_m)$ magnetic satellite of Dy, Ho, Tm and Er on log–log plots as a function of the reduced temperature. The best fits to the power law behaviour are shown as solid lines. (From Helgesen et al. 1995.)

c-axis modulated systems, Er and Tm, it is still uncertain whether the transition at T_N is described by the $3DXY$ or mean-field models.

The critical behaviours of higher order satellites near a continuous phase transition are of particular interest, as they provide the opportunity to study the crossover exponents of the respective symmetry breaking perturbations in the spin Hamiltonian. Each order of satellite has an associated order parameter critical exponent given by $\beta_n = 2 - \alpha - \phi_n$, where α is the specific heat exponent, and ϕ_n is a crossover exponent. As an example, if the transition is described by the $3DXY$ model, then the exponent ϕ_2 measures the crossover caused by a perturbation of uniaxial symmetry. For this model, theory predicts that $\beta_n = \sigma_n \beta$, with

$$\sigma_n = n + \lambda n(n-1), \tag{26}$$

where n is the order of the harmonic and λ is a temperature-independent parameter and equal to ≈ 0.3 for the $3DXY$ model. For mean-field scaling, $\beta_n = n\beta$ so that $\lambda = 0$ (Aharony et al. 1986).

In fig. 35 a summary is given of the order parameters measured at the first harmonic of Dy, Ho, Er and Tm (Helgesen et al. 1995). Within error (here $\approx \pm 0.05$) the derived exponents for Dy and Ho are the same and equal to values reported earlier from neutron

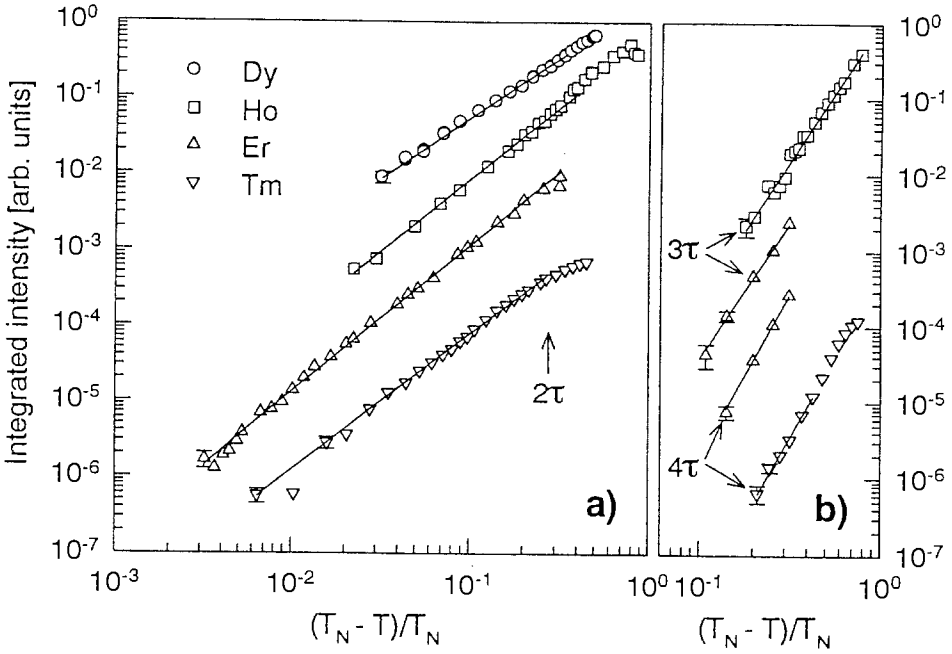

Fig. 36. Integrated intensity vs temperature of the higher harmonic satellites. The solid lines show the best fits to power-law behaviour $I_{n\tau} \propto (T_N - T)^{2\beta_n}$. (a) Second harmonics with exponents $\beta_2 = 0.80$, 0.95, 0.97, and 0.90 for Dy, Ho, Er, and Tm, respectively. (b) The curves (from top to bottom) show the third harmonic of Ho, the third and fourth harmonics of Er, and the fourth harmonic of Tm. Their exponents are $\beta_3(\text{Ho}) = 1.85$, $\beta_3(\text{Er}) = 1.80$, $\beta_4(\text{Er}) = 2.2$, and $\beta_4(\text{Tm}) = 2.1$. (From Helgesen et al. 1995.)

scattering studies. Also, the exponents for Er and Tm are the same, and are close to the mean-field value of $\frac{1}{2}$.

The temperature dependence of the higher order satellites is shown in fig. 36, where it can be seen that at least for Er and Tm it was possible to measure up to the fourth order satellite. An analysis of the data from Ho in terms of eq. (26) shows that $\lambda = 0.22(8)$. While the data from Dy is consistent with this value of λ, it was not possible to exclude the possibility of mean-field scaling. On the other hand, for both Er and Tm the higher order satellites are found to obey mean-field scaling.

4.2. *The light lanthanides*

To date only two of the light lanthanides, Nd and Sm, have been studied in their elemental form using X-ray magnetic scattering. This is due to the fact that the other light lanthanides are either difficult to prepare as single crystals (Ce, Eu and Pm), or have a very low ordering temperature (Pr). Compared to the heavy lanthanides, the light lanthanides are more chemically reactive, exhibit more complex chemical structures, and two of the series (Pr and Nd) exhibit multi-q magnetic structures. All of these factors

combine to make the study of the light lanthanides a challenging field for X-ray scattering investigations.

4.2.1. *Neodymium*

Nd has a double hexagonal crystal (dhcp) structure, with two inequivalent lattice sites of approximately cubic and hexagonal symmetries. In addition, the fact that the magnetic order in Nd is multi-q at low temperatures means that the magnetic structure of Nd is probably the most complex of any of the lanthanides, and explains why a complete understanding of its magnetic structure has emerged only in recent times.

Just below $T_N \approx 19.9\,K$, the moments on the hexagonal sites in Nd are sinusoidally modulated along {100} type directions in the hexagonal basal planes (Moon et al. 1964). This single-q phase persists for approximately 1 K below T_N. At lower temperatures the moments rotate in the basal plane away from the high symmetry directions, and a sequence of phase transitions occur to magnetic structures described by an increasing number of modulation wave vectors (Moon et al. 1964, Forgan et al. 1989, 1992, McEwen et al. 1985, Zochowski et al. 1991). Thus, at the lowest temperatures the magnetic structure is 4q. Order on the cubic sites occurs only for temperatures below 8.2 K.

One of the problems that occurs in systems with multi-q ordering is that the interpretation of the data is often complicated by the presence of more than one magnetic domain. This is illustrated in fig. 37 for the 2q phase of Nd. In order to overcome these difficulties attempts are usually made to prepare the system in a single domain state, for example by applying a magnetic field or a uniaxial stress, but these attempts are not always successful. In their X-ray scattering study of Nd, D. Watson et al. (1996) found a single double-q magnetic domain in zero applied magnetic field. This remarkable result is summarized in fig. 38, where from the inset in the lower panel it is apparent that the sample exhibits only a single double-q domain. Currently it is not known whether this single-domain state is a near-surface effect or a characteristic of the particular crystal used in their study. (It is known from studies on other systems that the domain population in the near surface of a crystal can be significantly different from that of the bulk; Hill et al. 1995b, McMorrow

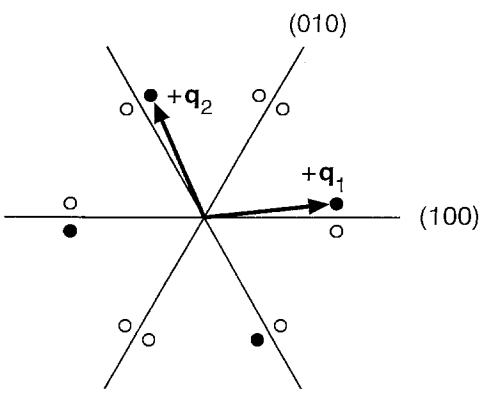

Fig. 37. Pattern of magnetic satellites seen around a reciprocal lattice point in the 2q phase of Nd. When all three antiferromagnetic domains are present there are 12 satellites, shown as the solid and open circles. A single-domain sample will produce only four satellites, for example, those represented by the solid circles. Also shown are the coupled **q** vectors that give rise to these four satellites. (From D. Watson et al. 1996.)

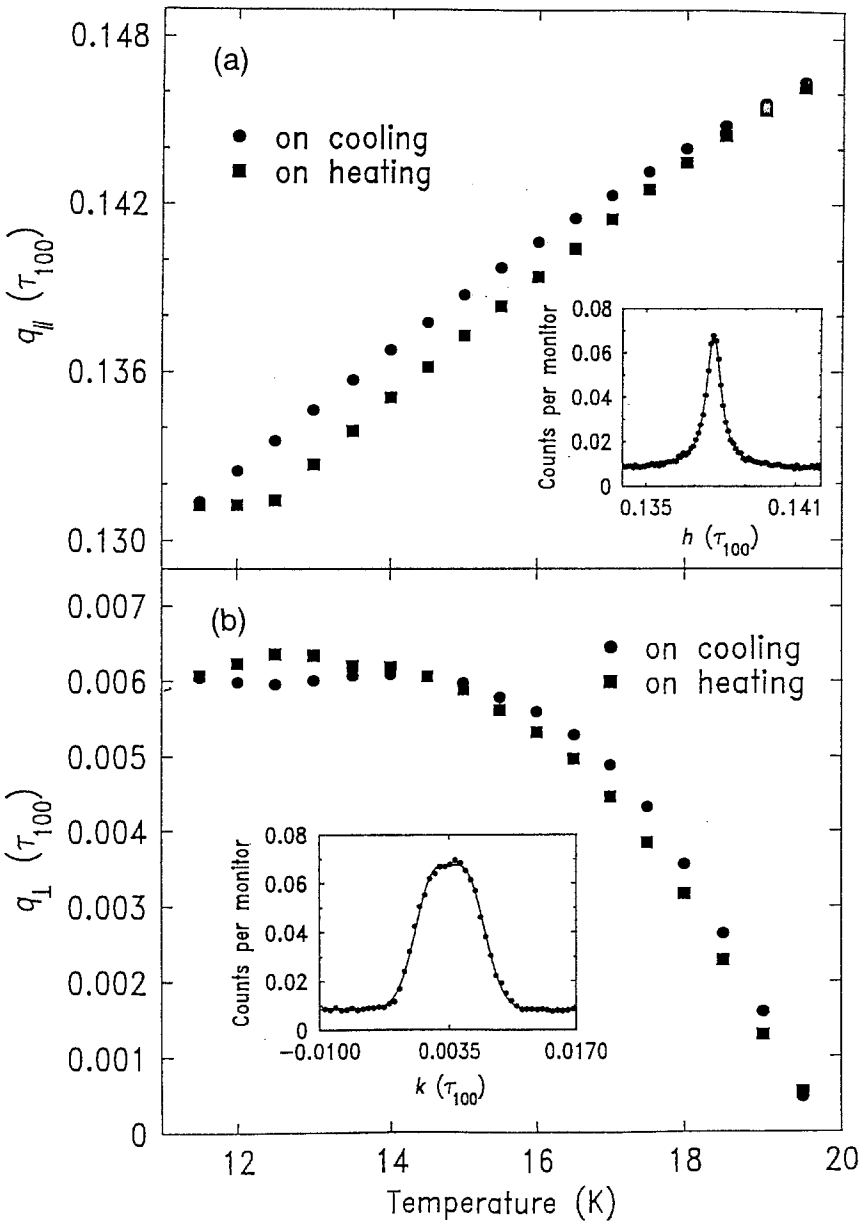

Fig. 38. Temperature variation of the components of $\boldsymbol{q}_1$ in Nd (a) parallel and (b) perpendicular to the (100) direction. (A temperature calibration shift of 1.5 K has been applied to obtain the correct T_N of 19.9 K.) The inset shows data taken at 15.5 K on cooling. In (a) is a (100) scan through the $\boldsymbol{q}_1$ satellite of (005) fitted with a variable-width Lorentzian, and in (b) is a (120) scan through the same satellite; this was fitted with a flat-topped line shape to represent the angular acceptance of the detector. This inset also shows no satellite centred at $k \approx -0.007$ (r.l.u.) (the position labelled $\boldsymbol{q}'$ in fig. 37), which would arise from a different domain to the single one observed. The data shown in this figure were taken at the L_{II} edge of Nd (6722 eV). (From D. Watson et al. 1996.)

et al. 1997.) In the context of the study of Nd, the significance of the work of Watson et al. is that it establishes directly the multi-q nature of the ordering in zero field.

Another noteworthy aspect of the work of D. Watson et al. (1996), and in contrast to the results from the heavy lanthanides, the resonant signal at the L_{II} edge was greater than at L_{III}. In fact, the ratio of the enhancement in intensity at the two edges, the branching ratio, was measured to be $I(L_{II})/I(L_{III}) \approx 6$. This differs from the predictions for the resonant cross-section considered in its simplest form, for which the L_{II} and L_{III} intensities are approximately equal (Hannon et al. 1988).

4.2.2. *Samarium*

The crystal structure of Sm is unique amongst the lanthanides. The unit cell comprises nine close packed planes in the sequence ABABCBCAC along the c axis. As with the dhcp structure, there are sites of approximately cubic (C) and hexagonal (H) symmetries, so that the stacking sequence may be written *CHHCHHCHH*. From neutron scattering measurements on an isotopically enriched sample (Sm has a high absorption cross-section for neutrons), Koehler and Moon (1972) determined that below 106 K the moments on the H sites order along the c-axis in a ferrimagnetic structure that may be written as $C++C--C++$, where a +(−) indicates order on a hexagonal site with a moment parallel(anti-parallel) to the c axis.

The X-ray resonant magnetic scattering from Sm has been investigated for energies in the vicinity of the L_{II} and L_{III} edges by Lee et al. (1993), and by D. Watson et al. (1995). In both cases the results are qualitatively in agreement with the known magnetic structure of Sm. The branching ratio for the scattering at the two edges, $I(L_{II})/I(L_{III})$, was found to be approximately one half, as shown in fig. 39, (overleaf) in contrast to the results described above for Nd.

5. Alloys, compounds and superlattices

Up to this point we have concerned ourselves solely with X-ray scattering from the lanthanide elements. In this section we shall review key results that have been gathered on composite systems containing lanthanides including alloys, compounds and artificial structures, such as superlattices and thin films. The aim here is not to give an exhaustive list, but rather to choose examples that illustrate how the unique characteristics of the X-ray scattering cross-section can be exploited to illuminate particular features of the system under investigation. As we shall see, the chosen examples encompass many disparate fields, and this reflects the wide ranging applicability of the technique.

5.1. *Lanthanide alloys*

In a general context, the study of random alloys has helped to advance our understanding of the magnetic interactions in the lanthanides (Jensen and Mackintosh 1991). From an X-ray scattering point of view the appeal in studying these systems is to apply resonant

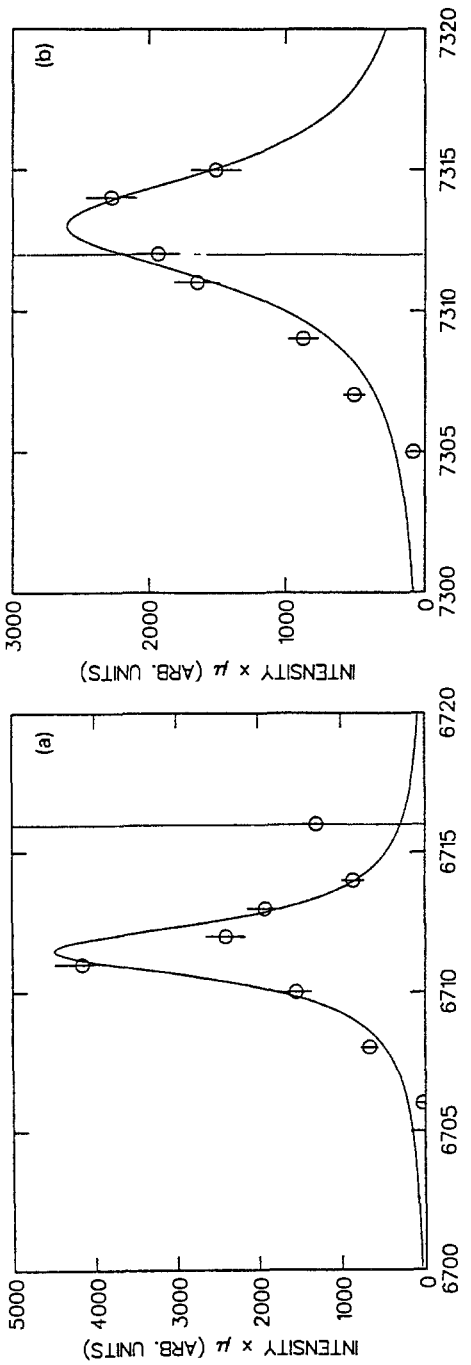

Fig. 39. (a) Magnetic resonant scattering from Sm at the (0,0,16.5) satellite near the L_{III} absorption edge (6716 eV). In this and (b), the solid line represents a calculation using the dipolar model of Hannon et al. (1988), with parameters chosen to give an approximate description of the data. (b) Magnetic resonant scattering observed at the (0,0,16.5) satellite near the L_{II} absorption edge (7312 eV). (From Lee et al. 1993.)

scattering techniques. By tuning the X-ray energy to the L edge of one the constituents it is possible to selectively enhance its contribution to the total magnetic scattering. This species-sensitive magnetic diffraction is a unique feature of X-ray resonant scattering, and several experiments have now been performed to exploit it in a variety of ways.

5.1.1. *Ho–Er*

As has been outlined in previous sections, Ho and Er each exhibit spin-slip structures at low temperatures, and the expectation is that alloys of these two elements should also display some interesting and related features. Indeed a neutron scattering study of a $Ho_{0.5}Er_{0.5}$ alloy by Howard and Bohr (1991) revealed three distinct temperature intervals. (1) $47.5\,K \leqslant T \leqslant 104\,K$. The alloy orders at a temperature close to the weighted average of the bulk transition temperatures, but unusually the moments form a c-axis modulated spiral in which the Ho and Er moments adopt different tilt angles with respect to the basal plane. (2) $35\,K \leqslant T \leqslant 47.5\,K$. The Ho and Er moments collapse into the basal plane to form a flat helix. (3) $T \leqslant 35\,K$. The Ho and Er moments lift out of the basal plane to form a cone.

Pengra et al. (1994) studied a single crystal of $Ho_{0.5}Er_{0.5}$ using resonant scattering. In fig. 40 a comparison is given between the modulation wave vector $\boldsymbol{q}$ determined both

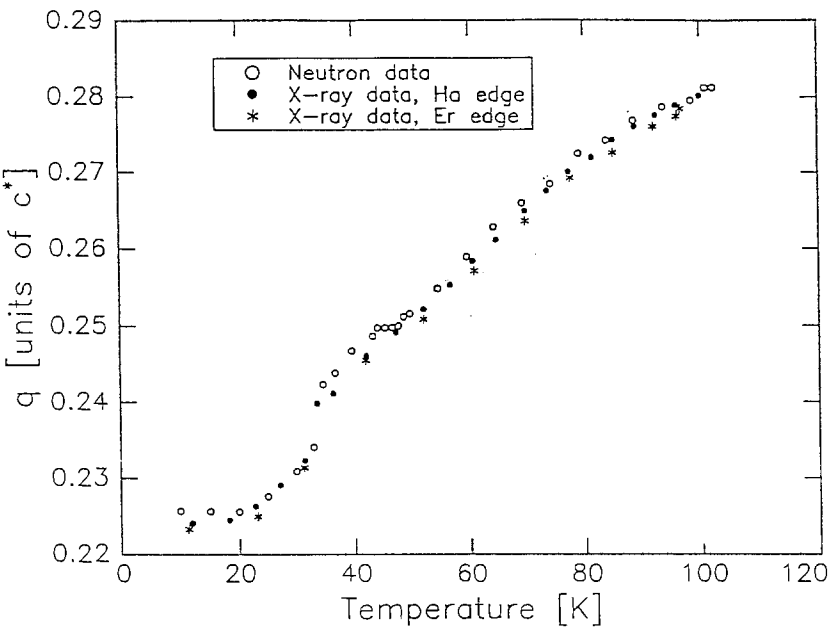

Fig. 40. The temperature dependence of the modulation wave vector $\boldsymbol{q}$ in a $Ho_{0.5}Er_{0.5}$ alloy. The X-ray data were taken at the (0,0,4+q) satellite at the Ho L_{III} resonance (solid circle, 8069 eV) and at the Er L_{III} resonance (*, 8358 eV). Also shown are neutron measurements (open circles) taken at the (0,0,2–q) satellite. (From Pengra et al. 1994.)

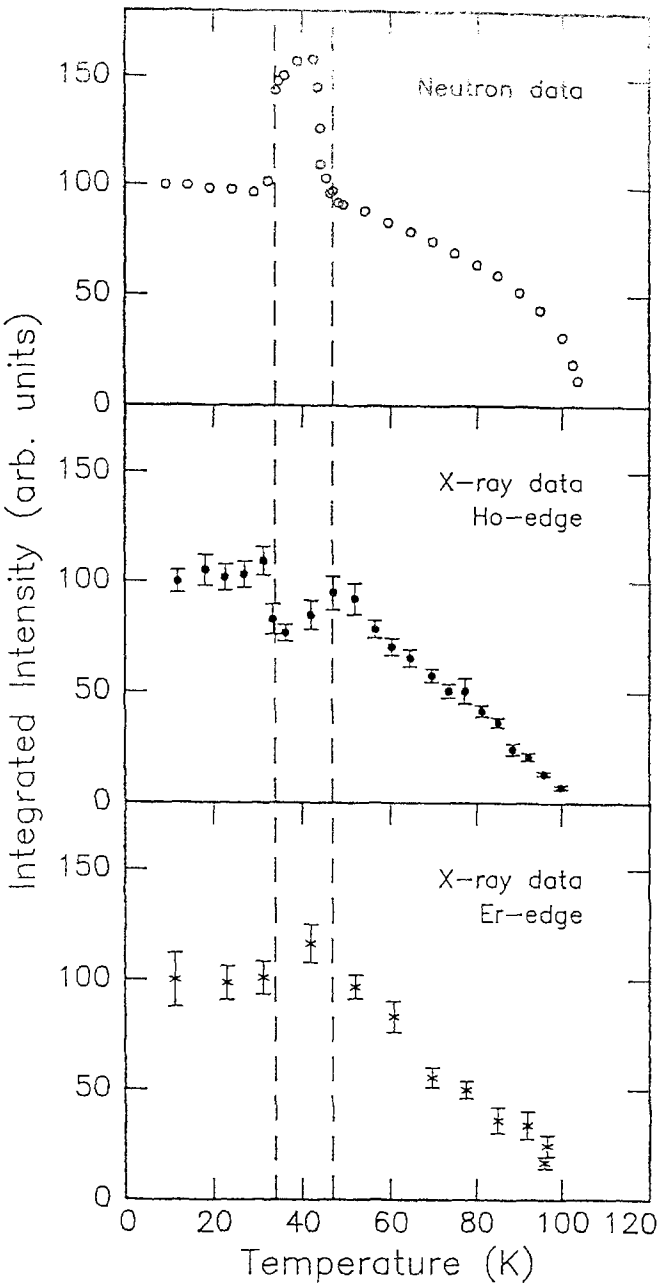

Fig. 41. $Ho_{0.5}Er_{0.5}$ alloy. Integrated intensity of the resonant satellites from the same data series as in fig. 40: Ho edge X-ray data (solid circles), Er edge data (*), and neutron data (open circles). The vertical lines mark the boundaries of the three magnetic phases. (From Pengra et al. 1994.)

from neutron and X-ray scattering experiments, where the X-ray data were obtained with the energy tuned to the L_{III} edges of Ho and Er. These results establish that in the alloy the individual Ho and Er moments order with the same wave vector, so as to produce a structure described by a single wave vector. A similar comparison for the temperature dependence of the intensity of the magnetic scattering is given in fig. 41. Here it can be seen that whereas the neutron data has an increase in intensity in the intermediate phase, the X-ray data has a dip. This was shown by Pengra et al. to arise from differences in the geometric selection rules for neutron and X-ray resonant magnetic scattering. The former is sensitive to the component of the moment perpendicular to Q, while for dipolar transitions the latter is most sensitive to the component of the moment along the scattered wave vector (Hill and McMorrow 1996). Thus, for Q along $[00\ell]$, as the moments collapse into a basal plane spiral the former increases and the latter decreases. The study by Pengra et al. also highlights how X-ray and neutron scattering can be combined to good effect to tackle a complex structural problem.

5.1.2. *Dy–Lu*

Everitt et al. (1995) also exploited the species-sensitivity of the resonant cross-section in their study of Dy alloyed with non-magnetic Lu. (Lu is the last element in the lanthanide series, and as such has a full complement of fourteen 4f electrons and no net 4f moment.) The novel aspect of this experiment was that the X-ray scattering displayed a resonant peak not only at the Dy L_{III} edge, but also a much weaker peak at the L_{III} edge of Lu (fig. 42). From the selection rules governing the polarization dependence of magnetic scattering, it was shown that the latter peak was magnetic in origin. As expected, it was found that the Lu scattering peaked at the same wave-vector in reciprocal space, and

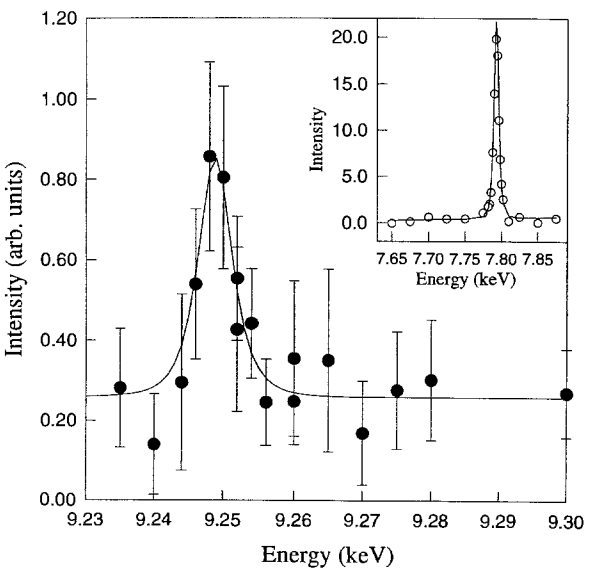

Fig. 42. Q-integrated intensity of the $(0,0,2+\tau_m)$ magnetic peak vs energy through the Lu L_{III} edge in a $Dy_{0.6}Lu_{0.4}$ alloy. The residual intensity is attributed to the non-resonant scattering from the Dy moments. Inset: The same, measured through the Dy L_{III} edge. An MgO (420) analyzer was used for both measurements. Lorentzian-squared curves with a FWHM of 7 eV have been fitted to both data sets. (From Everitt et al. 1995.)

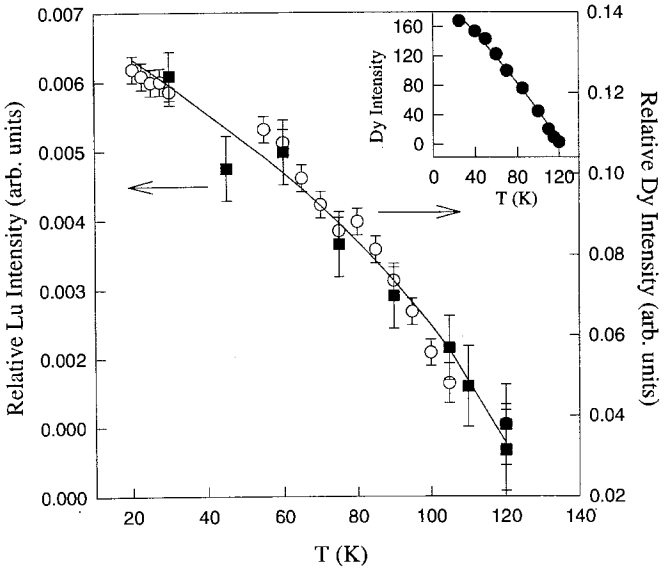

Fig. 43. $Dy_{0.6}Lu_{0.4}$ alloy. Temperature dependence of the $(0,0,2+\tau_m)$ magnetic peak. Squares, Lu-edge data taken in the $\sigma - \pi$ geometry; circles, Dy-edge data taken in high-resolution mode. Inset: neutron diffraction data for the same sample. (From Everitt et al. 1995.)

followed the same temperature dependence (see fig. 43), as the scattering at the L_{III} edge of Dy. If we recall that a dipole transition at the L_{III} edge of the lanthanides couples a $2p_{3/2}$ core state to a 5d level, and that in the lanthanides the 5d electrons form part of the conduction band, then it is apparent that the scattering at the Lu L_{III} edge is sensitive to the magnetization of the 5d band induced at the Lu sites. By comparing the intensity of the scattering at the two L_{III} edges, the amplitude of the 5d polarization was estimated to be about $0.2\mu_B$ per atom, within a factor of two of its mean-field value.

5.1.3. *Ho–Pr*

A recent related study to the work on Ho–Er involves a combined X-ray and neutron scattering characterization of the structure and magnetism of a series of Ho–Pr alloys (Goff et al. 1998, Vigliante et al. 1998). In contrast to Ho, Pr has a dhcp chemical lattice and a non-magnetic singlet ground state which does not exhibit magnetic ordering above $T = 0.05$ K. The combined results show that the alloys exhibit three distinct lattice and magnetic structures versus Pr concentration, c. In the Pr-rich phase (c(Pr) > 60%), the alloy chemical lattice has dhcp symmetry and does not exhibit magnetic ordering down to 0.1 K, just as in bulk. For Pr concentrations between 40 and 60%, the alloys have a Sm lattice and magnetic structure. In the Ho-rich phase (c(Pr) < 40%), the chemical lattice has hcp symmetry and supports a spiral magnetic structure, as in bulk Ho. Each of the magnetic alloys exhibited a concentration-dependent Néel temperature and lock-in transitions to simply commensurate wave vectors at low temperatures (see fig. 44).

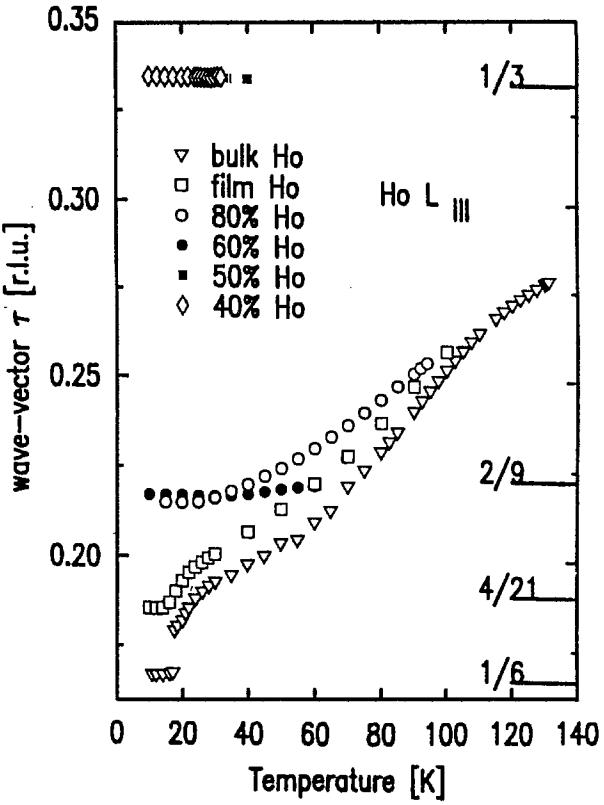

Fig. 44. Summary of the temperature dependence of the wave vector for a series of Ho–Pr alloys. (From Vigliante et al. 1998.)

In the Sm-like phase, the magnetic wave vectors remained locked to $\tau_m = \frac{1}{3}$ at all temperatures, while in the spiral phase they locked to $\tau_m = \frac{2}{9}$, the latter is reminiscent of Ho thin films. X-ray resonant magnetic scattering was also used to show that a small static spin-density-wave is induced in the alloy 5d bands, propagating at both Ho and Pr sites of the spiral and Sm-like magnetic structures. To within the available statistics, it was found that the induced Pr 5d moment/atom was independent of concentration. Among the most intriguing results of these studies was the observation of asymmetric L_{III}/L_{II} branching ratios, just as previously observed in the pure elements (Gibbs et al. 1991, Hill et al. 1995a, D. Watson et al. 1995). Specifically, it was found that L_{III}/L_{II} (Ho) ≈ 10 and L_{III}/L_{II} (Pr) ≈ 0.1. In the simplest theories (Hannon et al. 1988), these branching ratios are predicted to be of order unity. Resolving these discrepancies will be required before induced moment amplitudes can be reliably extracted from the resonant intensities. Moreover, their existence in both the heavy and light elements implies that

the standard picture of the lanthanide electronic structure used in the calculations of the resonant cross-section is not adequate (van Veenendaal et al. 1997).

5.2. *Compounds*

5.2.1. *Magnetism and superconductivity in RNi_2B_2C*

The RNi_2B_2C (R = lanthanide) family of compounds are of interest because the ground state may either be superconducting or magnetic, or even both at the same time. The study of the interaction between these two ground states has benefited greatly from the use of X-ray magnetic scattering techniques, with perhaps the study of $HoNi_2B_2C$ being the prime example (Hill et al. 1996).

$HoNi_2B_2C$ adopts a tetragonal crystal structure (space group *I4/mmm*) and is a type-II superconductor for temperatures below $T_C = 8\,K$. Approximately 1 K lower the Ho 4f moments order with an incommensurable modulation, and at the same temperature there is a large reduction in the upper critical field H_{c2}. (Currently, a clear picture of the role of the smaller Ni moments is not available.) Below 5 K, the 4f moments are confined to the *a–b* plane and are antiferromagnetically coupled along the *c* axis. The main contributions of X-ray scattering experiments in the study of this material has been to show that the magnetic structure of the incommensurable phase is more elaborate than had been deduced from neutron diffraction. These latter measurements had indicated that the incommensurable phase was characterized by two wave vectors, $\boldsymbol{q}_c = 0.915\boldsymbol{c}^*$ and $\boldsymbol{q}_a = 0.585\boldsymbol{a}^*$. Utilising the higher Q resolution of X-ray scattering and the resonant enhancement of the magnetic scattering at the L_{III} edge of Ho, Hill et al. (1996) were able to show that the *c*-axis modulation was in fact comprised of two components with wave vectors of $\boldsymbol{q}_1 = 0.906\boldsymbol{c}^*$ and $\boldsymbol{q}_2 = 0.919\boldsymbol{c}^*$, as shown in fig. 45. At the lowest temperatures studied in the antiferromagnetic phase a scan along the $[00\ell]$ direction revealed a sharp peak at the (0,0,3) position, confirming the simple antiferromagnetic stacking of the moments. For temperatures above 5 K this peak broadened and decreased rapidly in intensity, and two new peaks appeared near (0,0,2.906) and (0,0,2.919). The interaction between complex incommensurate order and the superconducting ground state revealed in this study has yet to be explained and, as Hill et al. (1996) point out, it provides a good test case for theories of antiferromagnetic superconductors.

Although not a superconductor, the X-ray study of $GdNi_2B_2C$ by Detlefs et al. (1996) is also worth mentioning in this section, as it represents the first attempt to solve a magnetic structure by combining resonant and non-resonant techniques. Due to the very large neutron absorption cross-section of naturally occurring Gd, $GdNi_2B_2C$ is unsuitable for study with neutron diffraction, and so prior to the study of Detlefs et al. (1996) all that was known about its magnetic structure had been gleaned from bulk probes, such as magnetization experiments. These had established that the Gd 4f moments order below $T_N = 20\,K$, and indicated the existence of a possible spin reorientation below $T_R = 14\,K$.

The X-ray scattering experiments of Detlefs et al. (1996) were performed with the sample mounted in the $(h0\ell)$ zone, and with the *a* axis bisecting the incident and

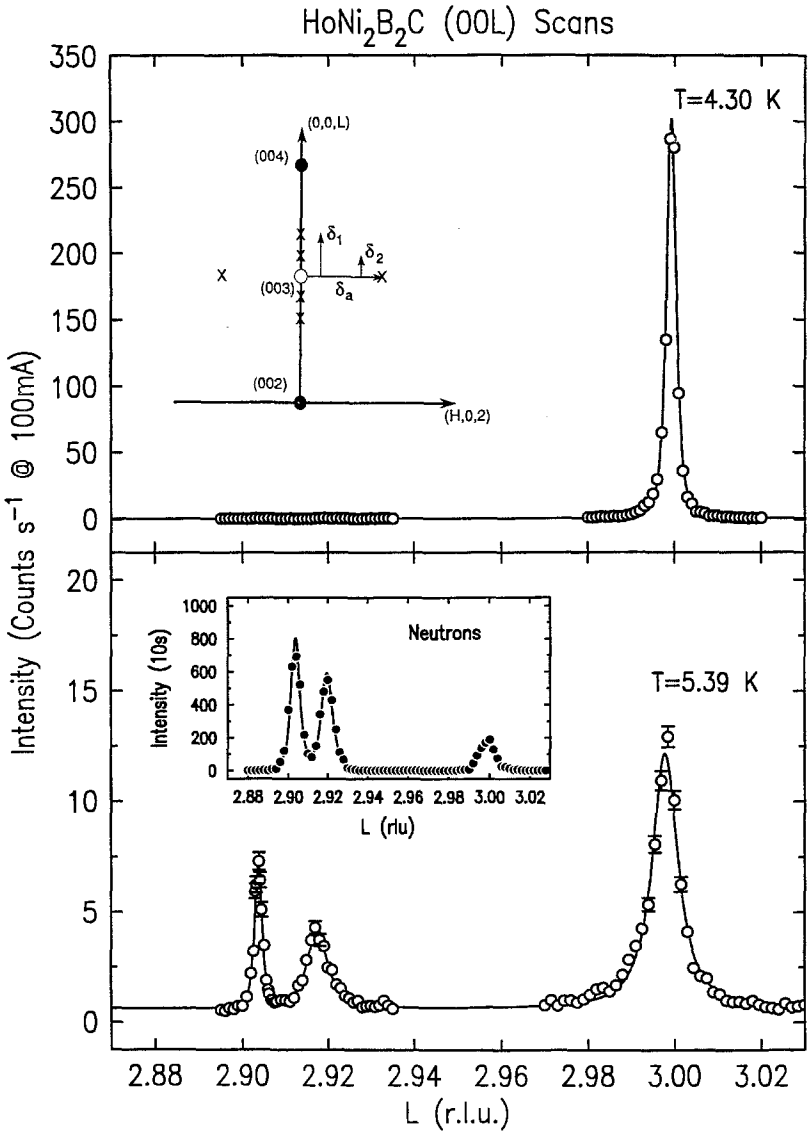

Fig. 45. Longitudinal X-ray scans from $HoNi_2B_2C$ in the vicinity of the (003) antiferromagnetic reciprocal-lattice point. These data were taken with the incident photon energy tuned to the Ho L_{III} edge. Top: $T = 4.3$ K. Only the commensurate peak is present. Inset: Schematic of reciprocal space. Solid (open) circles represent charge (antiferromagnetic) Bragg peaks. The crosses correspond to the incommensurate satellites present for temperatures above 5.2 K. Higher-order incommensurate peaks are not shown. Bottom: data taken at $T = 5.39$ K, in the incommensurate (IC) phase. The IC peak is comprised of two satellites at $(0,0,2+q_1)$ and $(0,0,2+q_2)$. The (003) commensurate peak is still present but significantly reduced and broadened. Inset: high-resolution neutron-scattering data taken at an equivalent temperature confirming that the splitting of the IC satellite is a bulk effect. (From Hill et al. 1996.)

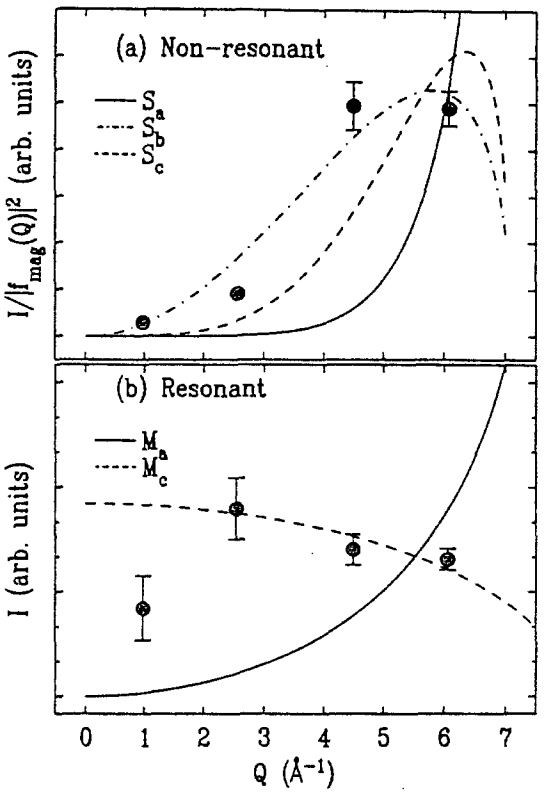

Fig. 46. The $\boldsymbol{Q}$ dependence of the integrated intensity of magnetic satellites in $GdNi_2B_2C$ along the [h,0,0] direction at 3.6 K, obtained off resonance (a) and on resonance (b). The solid lines show the $\boldsymbol{Q}$ dependence of the integrated intensity expected from eqs. (27) and (28) for ordered components of the Gd 5d magnetic moment M and the Gd 4f spin S along the a (solid line), b (dot-dashed line), and c axis (dashed line) respectively. (From Detlefs et al. 1996.)

scattered beams. A standard vertical scattering geometry was used, so that the non-resonant magnetic cross-section is (eq. 6)

$$I_{\text{non-res}} \propto S_b^2 \sin^2 2\theta + 4 \sin^4 \theta \, [S_a \sin\theta + (L_c + S_c)\cos\theta]. \tag{27}$$

Here $S_{a,b,c}$ and $L_{a,b,c}$ are the components of the spin and orbital angular momenta along the crystal axes. In writing down eq. 27 only the terms in the cross-section that depend on the direction of the spin have been given. For the case of Gd, L is essentially zero, and hence it is apparent that at small scattering angles the non-resonant scattering is most sensitive to the b component of the spin. At higher scattering angles all three components contribute to the measured intensity. In the dipole approximation the resonant scattering at the L edges assumes a particularly simple form for the configuration used in the experiment, *viz.*,

$$I_{\text{res}} \propto (M_a \sin\theta - M_c \cos\theta)^2, \tag{28}$$

where M_a and M_c are the components of the magnetic moment along the a and c axes, respectively (see eq. 11). It is evident that the resonant cross-section is insensitive to

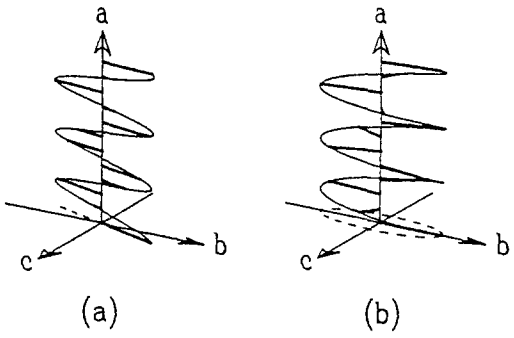

Fig. 47. The two components of the ordered magnetic moment along the b and c axes in $GdNi_2B_2C$ feature the same modulation wave vector $q_a \approx 0.55\ a^*$. However, the measurements did not yield any information on the relative phase shift $\Delta\phi$ between the two oscillations. Two possible structures with $\Delta\phi = \pi$ (spiral like, a) and $\Delta\phi = 0$ (transverse wave, b) are displayed. (From Detlefs et al. 1996.)

the b component of the moment. Thus, by comparing how the intensity of the non-resonant and resonant cross-sections vary as a function of the scattering angle it is possible to obtain the three components of the magnetic moments from one orientation of the crystal.

From the non-resonant scattering, the phase transition at 20 K was shown to be into an incommensurably modulated phase described by a single wave vector $\boldsymbol{q} \approx 0.55\boldsymbol{a}^*$. While the intensity of the non-resonant scattering increased smoothly with decreasing temperature, the resonant intensity increased abruptly below 13.6 K. From the above, it is immediately clear that moments in the temperature interval $13.6\,\mathrm{K} \leqslant T \leqslant 20\,\mathrm{K}$ align along b, transverse to the modulation direction, and that for temperatures below 13.6 K, the moments develop a component either along the a or c axes. In order to distinguish between these possibilities, the variation of the integrated intensity of the satellites along [h,0,0] was compared with the above expressions (see fig. 46). It was concluded that in the low temperature phase the moments in fact develop a component along the c axis. However, this information was not enough to uniquely solve the structure, as the relative phase between the b and c axis components could not be determined, so that the data are consistent with either of the models shown in fig. 47.

5.2.2. *Valence fluctuations in TmSe*

TmSe has a mixed valence ground state where the Tm ions fluctuate between a $4f^{12}$ (Tm^{3+}) and a $4f^{13}$ (Tm^{2+}) configuration. What distinguishes TmSe from other mixed-valent systems is that both configurations are magnetic with anti-ferromagnetic order being established below $T_N = 3.2\,\mathrm{K}$ (Bjerrum Møller et al. 1977). The two possible configurations have a slightly different binding energy, and this manifests itself in the X-ray absorption spectrum at the L edges, where two resonant "white lines" are observed with a separation of ~7 eV. This separation is greater than the energy resolution that is routinely achievable with standard diffraction techniques at a synchrotron, and the possibility therefore exists to use resonant X-ray magnetic scattering to probe selectively the magnetic correlations of the Tm^{2+} and Tm^{3+} valence states. Such an experiment has in fact been performed by McWhan et al. (1993), and the key results of their work are given in fig. 48.

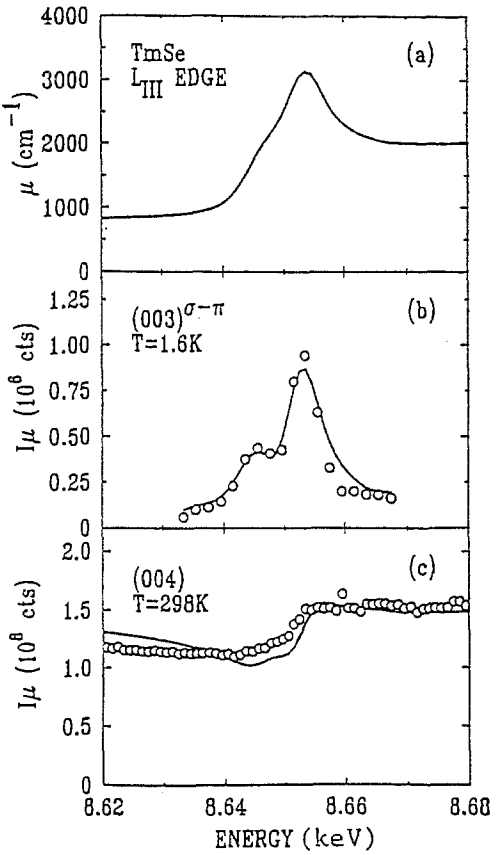

Fig. 48. (a) Measured absorption coefficient, (b) X-ray resonant scattering and (c) charge scattering of TmSe as a function of energy through the L_{III} absorption edge of Tm. The solid curves in (b) and (c) are calculated as described in the text. (From McWhan et al. 1993.)

In the top panel of fig. 48 the energy dependence of the absorption coefficient calculated from fluorescence measurements is shown for energies in the vicinity of the L_{III} edge of Tm (8648 eV). In addition to the main peak, the spectrum also has a distinct bulge ≈ 8 eV lower in energy. This extra feature is even more evident in diffraction as shown in the middle panel of fig. 48, where the data were taken with the instrument set for for the (003) antiferromagnetic peak, and where a polarization analyser was used to select the magnetic signal in the $\sigma - \pi$ channel. The fact that two resolved peaks are seen at energies corresponding to the Tm^{2+} and Tm^{3+} valence states in a diffraction geometry immediately establishes that both valence states exhibit long-range magnetic order. McWhan et al. (1993) went on to show that a good description of the data was obtained using an Anderson impurity model, where the Tm ions spend approximately equal amounts of time in the two possible configurations.

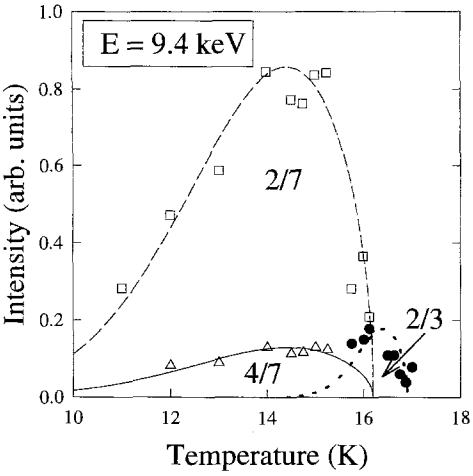

Fig. 49. The temperature dependence of the satellite peak intensities in CeSb observed at an X-ray energy of 9.4 keV. (From McMorrow et al. 1997.)

5.2.3. *Interplay of structure and magnetism in CeSb*

CeSb has continued to attract interest over the years as it has the most complex phase diagram of any of the lanthanide monopnictides, and arguably of any binary compound, added to which is the fact that it has several other anomalous properties. (For a recent review, see Vogt and Mattenberger 1993.) Although many different techniques have been applied to unravelling the phase diagram, almost all that we know about the details of the magnetic structures come from a series of neutron diffraction studies. Recently, the results of an X-ray scattering study have been reported by McMorrow et al. (1997), who performed experiments for X-ray energies both in the vicinity and well away from the L edges of Ce.

In the non-resonant regime at 9.4 keV, peaks were observed with commensurable wave vectors below T_N, as summarized in fig. 49. From their polarization and wave-vector dependence, these were deduced to arise mainly from a periodic lattice distortion. It transpired that the relationship, between the position of these peaks and the magnetic peaks seen with neutrons could be explained in terms of a modified version of the spin-slip model developed for Ho. (The structural peaks had not been reported in earlier neutron scattering studies, and indeed are probably not observable with this technique as they would be masked by more intense high-order harmonics from the magnetic structure.) In the resonant regime, weak resonantly enhanced scattering was found at the L_{II} edge of Ce. Thus, it has been established that X-ray scattering is a useful probe of the magnetism in compounds of Ce, and as these often display various anomalous properties (heavy fermion, intermediate valence, etc.) it can be anticipated that more studies of this type will be forthcoming in the near future.

5.3. *Superlattices and thin films*

One of the developments that has helped rejuvenate interest in the lanthanides in the last decade is the production of artificial structures, such as superlattices and thin films, using molecular beam epitaxy (MBE). This technique offers the possibility to combine lanthanide elements in novel structures with a control of the growth process down to the atomic level. A wide variety of systems has now been fabricated and many interesting results have been reported, as reviewed by Majkrzak et al. (1991), Rhyne et al. (1994) and Cowley et al. (1995). At first glance, X-rays appear to be an ideal probe for this type of system as their thickness (typically 1 μm) is better matched to the penetration depth of an 8 keV photon, than it is to that of a thermal neutron. This has been borne out in studies of thin films of the lanthanides and their alloys (Helgesen et al. 1994, Gehring et al. 1996, Helgesen et al. 1997, Vigliante et al. 1998, Everitt et al. 1995). To date, however, there have been relatively few studies of lanthanide superlattices using X-ray magnetic scattering. One of the reasons for this is that the chemical superlattice structure produces harmonics which may overlap with the magnetic scattering and be of similar or much greater intensity. (In the case of neutron scattering the magnetic scattering from lanthanide superlattices is often much stronger than the scattering from the chemical satellites.) In addition, the specular reflectivity from a series of ideally terminated interfaces leads to charge scattering along the growth direction of an intensity comparable to the magnetic signal itself. As will be illustrated below, these limitations can be partly overcome by employing polarization analysis. We expect that as it becomes easier to manipulate the polarization of the X-ray beam, using for example quarter wave plates, etc., more studies will be attempted on these and related systems.

5.3.1. *Gd/Y superlattices*

The study of interfacial magnetism in Gd/Y superlattices by Vettier et al. (1986) was one of the early successes of X-ray magnetic scattering. The sample studied had the composition $[Gd_{21}/Y_{21}]_{40}$, where there were 21 planes of Gd and 21 planes of Y in a superlattice period, which was repeated 40 times. One of the challenges offered by this system is that the Gd moments couple ferromagnetically both within the Gd blocks and across the non-magnetic Y blocks. The charge and magnetic Bragg peaks thus fall at the same positions in reciprocal space. (This is in contrast to all of the examples we have so far considered, where the charge and magnetic scattering occurred at different points in the Brillouin zone.) The positions of the Bragg peaks perpendicular to the layers can then be written as $Q(l, m) = 2\pi(l/c + m/\Lambda)$, where c is the average lattice constant, Λ is the superlattice period and l and m are integers. In the case of ferromagnetic order the charge and magnetic scattering can be separated by the use of the polarization dependence of the magnetic cross-section.

To understand the way in which this is achieved we first recall from eq. 2 that the X-ray scattering amplitude may be written as

$$f = f_0 + f' + \mathrm{i}f'' + f^{\mathrm{magnetic}}. \tag{29}$$

We then assume that the incident beam is perfectly plane polarized (σ), and that the magnetic ion has $L = 0$ which is a good approximation for Gd^{3+}. If a large enough magnetic field is now applied so that the moments align perpendicular to the scattering plane, then from eq. 6 the magnetic contribution assumes the simple form

$$f^{\text{magnetic}} = \mathrm{i} r_0 \left(\frac{\hbar\omega}{m_e c^2} \right) \sin(2\theta) S_2, \tag{30}$$

where S_2 is the component of the spin perpendicular to the scattering plane and all of the response is in the $\sigma - \sigma$ channel.

In the experiment the field is flipped with a concomitant change in the sign of f^{magnetic}. The change in intensity is then recorded, with the measurement cycle repeated a number of times to improve the statistics. From the above two equations it can readily be seen that the relative change in intensity on reversing the field is dominated by the interference between f'' and the magnetic contribution, and may be written as

$$\frac{\Delta I}{I} \propto \frac{f'' \sin(2\theta) S_2}{(f_0 + f')^2 + f''^2}. \tag{31}$$

The change of intensity on field reversal was measured for superlattice satellites around the (002), (004) and (006) Bragg peaks. The results are summarized in fig. 50. The measurements were then compared with different models for the magnetic structure in the interface region, as also shown in fig. 50. The best description of the data was found to be one in which the Gd moment is fully saturated at the centre of each Gd block, with a smooth reduction in the size of the moment through the interface region as shown in the top panel.

5.3.2. *Ho/Er superlattices*

Ho and Er may be viewed as having competing anisotropies, in the sense that in its ordered phase the magnetic moments in Ho are predominantly confined to the basal plane, whereas the moments in Er are mainly polarized along the c axis. In this way Ho/Er superlattices offer the opportunity to study the effects of competing anisotropies at magnetic interfaces. Prior to the X-ray experiments, neutron diffraction experiments had revealed some unexpected features. For temperatures in the interval $T_N(\text{Er}) \leqslant T \leqslant T_N(\text{Ho})$ the Ho moments form a basal-plane spiral which propagates coherently through the paramagnetic Er. Below $T_N(\text{Er})$ the coherence length of the basal-plane magnetic order decreases on cooling, and the longitudinal (i.e. c axis) component of the Er moment fails to develop long-range order at all. We thus have the unusual situation that the basal plane order of the Ho ions propagates coherently through the Er, but the longitudinal order of the Er ions is confined to a single Er block.

In an attempt to gain further insight into the magnetic correlations in this system, resonant X-ray magnetic scattering experiments were performed on a $[Ho_{20}/Er_{20}]_{80}$ superlattice (Simpson et al. 1996). The experiments were performed with the energy tuned

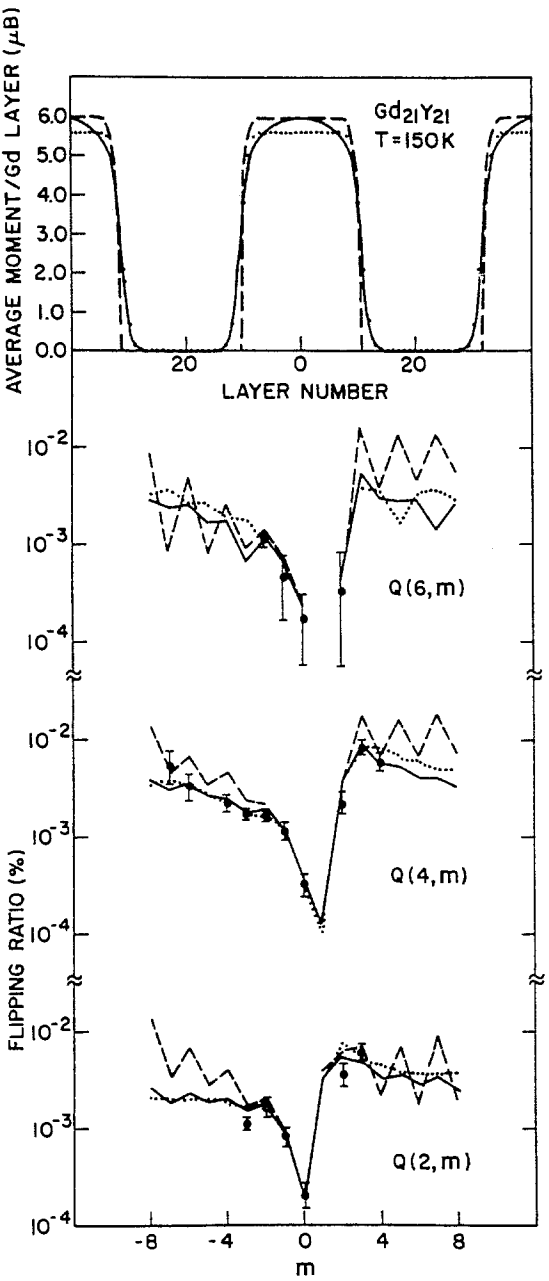

Fig. 50. Summary of the X-ray scattering from a Gd/Y superlattice. Top: three models for the magnetic-moment modulation. Bottom: the calculated flipping ratio corresponding to no magnetic contribution from the two interfacial layers (dashed curve), a smooth decrease in the moment (solid curve), and a uniform reduction in moment (i.e., a moment modulation that comes from the composition modulation) (dotted curve), compared with the values measured at 8.04 keV. Key: the satellite peaks are labelled as $Q(l, m)$, so that the (002) Bragg peak in this notation is written as $Q(2, 0)$, and its first-order superlattice peaks $Q(2, 1)$, etc. (From Vettier et al. 1986.)

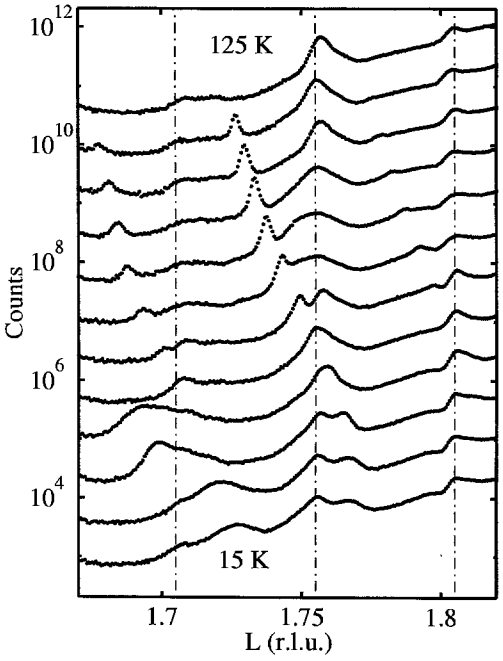

Fig. 51. The temperature dependence of the X-ray scattering from Ho_{20}/Er_{20} for scans of the wave-vector transfer along $[00\ell]$. The energy of the photons was equal to the L_{III} edge of Ho (8075 eV). The scans were performed in warming from 15 K at intervals of 10 K. The vertical lines represent the positions of the superlattice charge peaks. (From McMorrow et al. 1995.)

to either the L_{III}(Ho) or L_{III}(Er) edge, but magnetic scattering was only found at the former. The temperature dependence of the X-ray scattering is shown in fig. 51 with the energy tuned to the L_{III}(Ho) edge. As the sample is cooled below its Néel temperature of 123(1) K, a peak appears at $l \approx 1.72$, corresponding to a wave vector of $\boldsymbol{q} = 0.28c^*$. On further cooling the peak moves to higher l, increases in intensity and broadens rapidly below 70 K. The fact that a scan of the incident energy through this feature revealed a sharp (~10 eV, FWHM) resonance at the L_{III}(Ho) edge shows that this peak is magnetic in origin, and arises predominantly from the Ho. At least for temperatures above 55 K, weak magnetic superlattice peaks are evident flanking the main peak with a separation of 0.05 r.l.u., the same spacing as the chemical satellites. (The origin of the broad feature that appears below 60 K around $l = 1.68$ is unknown.) The temperature dependence of the Ho magnetic correlation length is shown in detail in fig. 52. From these results, it is clear that the X-ray results are qualitative in agreement with the neutron data (Simpson et al. 1994), and reflect the effects of competing crystal-field interactions between the Ho and Er: specifically that above T_N(Er) the Ho moments order into a structure with a long coherence length, and that this coherence is reduced markedly when Er moments attempt to order. Figure 51 also serves to illustrate some of the problems in applying X-ray magnetic scattering to study superlattices, as it is evident that the satellite charge peaks are of a similar magnitude as the main magnetic peak, and that the two sets can overlap in certain temperature intervals.

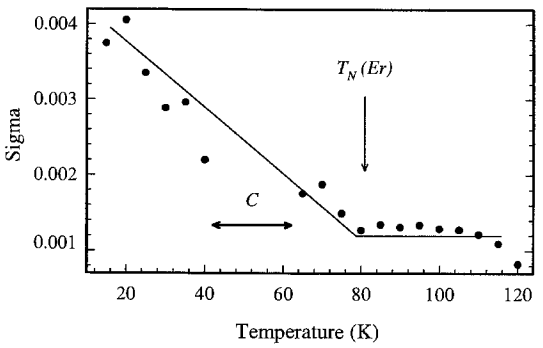

Fig. 52. The temperature dependence of the Gaussian width of the principal magnetic peak from a Ho_{20}/Er_{20} superlattice. For $T \geqslant T_N(Er)$ the width is constant, and decreases rapidly below this temperature. In the temperature interval marked by a C the position of the magnetic peak coincided with that of a charge peak, so that its width could not be determined. (From Simpson et al. 1996.)

5.3.3. *Erbium thin films*

Recently a series of Er thin films have been studied by X-ray resonant magnetic scattering (Helgesen et al. 1997). As in earlier studies of Ho thin films, a central issue involves the modification of the magnetic phase diagram as a result of the strain arising from the lattice mismatch between the thin film and the substrate. Figure 53 shows a comparison of the temperature dependence of the magnetic wave vectors of two Er films with the bulk behaviour. One of the Er films was grown on a Y substrate (leading to an in-plane expansion and an out-of-plane compression of the film), while the other was grown on a Lu substrate (leading to an in-plane compression and an out-of-plane expansion). It is apparent from the figure that the main differences between the films and the bulk include multi-phase coexistence, marked hysteresis and the suppression of the $\frac{5}{21}$ cone structure at low temperature. Moreover, while in the thin films the lattice retains its hcp symmetry, the structural and magnetic coherence lengths are reduced, reflecting a high degree of disorder. These kinds of effects are typical of lanthanide thin films when compared to the best bulk crystals and generally reflect the strain imposed by the substrate. Interestingly, in Er/Lu below 20 K, two new magnetic wave vectors ($\frac{12}{49}$ and $\frac{6}{25}$) falling between $\frac{5}{21}$ and $\frac{1}{4}$ appear. These probably correspond to conical phases, like the $\frac{5}{21}$ phase of the bulk, but that remains to be verified experimentally.

5.4. *Resonant branching ratios*

When performing resonant scattering experiments, of the type described in this and earlier sections, it is important to understand what factors determine the intensity of the observed signal. What is of most interest is to be able to relate the magnitude of the resonance at any one absorption edge to details of the resonant process, including whatever effects the electronic and magnetic structure may produce. For the lanthanides one of the factors that has attracted some interest is the relative intensity of the resonant enhancement at the L_{II} and L_{III} edges. Here we remind the reader that the former arises predominantly from $2p_{1/2} \rightarrow 5d$ and the latter from $2p_{3/2} \rightarrow 5d$ dipole transitions, and that within a simple one-electron view of the resonance process the ratio of intensities measured at these two edges is expected to be of order unity. In table 4 we summarize the

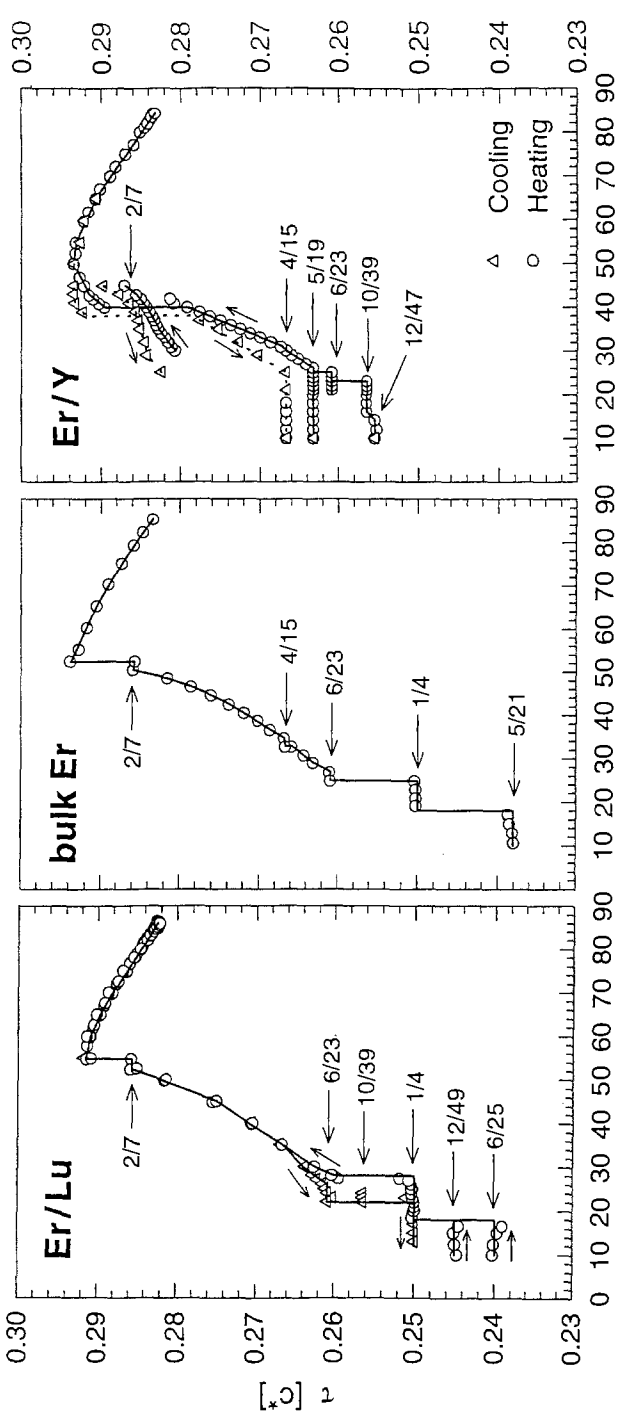

Fig. 53. The magnetic wave vector τ of Er as a function of temperature for an Er film on Lu substrate (left), for bulk Er (middle), and for an Er film on a Y substrate (right). Small arrows are used to indicate the hysteresis found between measurements done on heating and cooling of the sample. (From Helgesen et al. 1997.)

Table 4
A summary of materials that have been studied using resonant x-ray magnetic scattering techniques where estimates of the intensity branching ratio $I(L_{II}/L_{III})$ have been given (after D. Watson et al. 1996)

Element	Branching ratio $I(L_{II}/L_{III})$	Sample	Reference
La			
Ce	$\gg 1$	CeSb	McMorrow et al. (1997)
Pr	~10	Ho–Pr alloy	Vigliante et al. (1998)
Nd	~6	Nd	D. Watson et al. (1996)
	~100	Nd_2CuO_4	Hill et al. (1995a)
	$\gg 1$	$NdNi_2B_2C$	Detlefs et al. (1997)
	~50	Nd_2BaNiO_5	Zheludev et al. (1996)
Pm			
Sm	~0.5	Sm	D. Watson et al. (1995)
	~10	$SmNi_2B_2C$	Detlefs et al. (1997)
Eu	~0.5	$EuAs_3$	Chattopadhay et al. (1992)
Gd	~1	GdSe	Costa et al. (1996)
	~1	$GdNi_2B_2C$	Detlefs et al. (1996)
Tb	~1	Tb	Perry et al. (1998)
Dy			
Ho	~0.1	Ho	Gibbs et al. (1991)
		$HoNi_2B_2C$	Hill et al. (1996)
Er	$\prec 0.1$	Er	Sanyal et al. (1994)
Tm	$\ll 1$	Tm	Bohr et al. (1990)
Yb			
Lu			

materials where the $I(L_{II}/L_{III})$ ratio has been reported. It is clear that this ratio deviates from unity for many of the lanthanide ions, and that it does so in a systematic way. In the middle of the series (Eu, Gd, Tb) the ratio is close to unity, whereas for the light lanthanides (Ce, Pr, Nd) it tends to be greater than one, and in the heavy lanthanides (Ho, Er, Tm) it is much less than one. A similar trend has been noted in X-ray magnetic circular dichroism experiments on various ferromagnetic lanthanide compounds (see van Veenendaal et al. 1997, and references therein). (The resonant scattering cross-section is essentially proportional to the modulus squared of the dichroic signal.) This variation has been explained by van Veenendaal et al. as arising from a contraction of the final-state 5d radial wave functions due to orbit–orbit exchange interactions mainly with the 4f shell. This interaction causes the 5d wave function to either contract or expand ("breathe") depending on whether the 5d and 4f moments are parallel or anti-parallel. As the resonant amplitude depends on the radial matrix elements, a contraction of the 5d band produces a larger resonant enhancement. When the details are worked through (van Veenendaal et al. 1997) it is found that the systematic variation of the dichroic branching ratio across the

lanthanide series seems well accounted for. The same arguments apply to the variation of the branching ratio seen in resonant scattering experiments. One interesting possibility that may follow from these ideas is that the different values for the branching ratios obtained for compounds containing the same lanthanide (such as the different ratio found in metallic Sm and $SmNi_2B_2C$, or the values reported for pure Nd and its compounds) reveal important information concerning the band structure.

6. Summary

Starting with the first experiments performed by de Bergevin and Brunel on NiO in 1972, remarkable progress has been made in the study of magnetism using X-rays. Progress was at first steady, but has accelerated rapidly within the last decade as more and better sources of synchrotron radiation have come on line, and a greater understanding of how to exploit them has been won. X-ray studies of the lanthanides in particular have produced a great wealth of information. This includes, on the one hand, a deeper insight into the specific magnetic properties of these elements, while on the other, it has allowed general principles of the X-ray scattering cross-section to be both explored and developed. On the theoretical front the salient features of the non-resonant and the resonant cross-sections are now well understood. Probably the main challenge here is to establish a framework for the resonant cross-section that is capable of explaining the discrepancies from the one-electron view of the resonant process, such as the asymmetry in the branching ratios (L-edges) for the light and heavy lanthanides, and to push into the inelastic regime. Presently, the pace of innovation in experimental techniques shows no sign of slowing, with recent examples including the observation of surface magnetic scattering (Ferrer et al. 1996, G.M. Watson et al. 1996), and the application of high-energy X-rays to the study of magnetic phase transitions in transition metal compounds (Brückel et al. 1993). It is certain that more extensive use will be made of the polarization dependence of the X-ray cross-section, most immediately by exploiting $\frac{1}{4}$-wave plates on undulator sources (Sutter et al. 1997). In this regard it is worth making the point that polarization analysis is in many ways easier to perform for X-rays than neutrons, and this gives even greater incentive to develop fully these techniques.

Acknowledgements

We would like to express our deep gratitude to all of our colleagues who have contributed to the work described in this review. In particular we would like to thank to John Hill for his careful reading of the manuscript. The work at Brookhaven is supported under a grant by the US DOE under contract No. DE-ACH02-276CH00016.

References

Aharony, A., R.J. Birgeneau, J.D. Brock and J.D. Lister, 1986, Phys. Rev. Lett. **57**, 1012.

Ali, N., and F. Willis, 1990, Phys. Rev. B **42**, 6820.

Bak, P., 1982, Rep. Prog. Phys. **45**, 587.

Bak, P., and D. Mukamel, 1976, Phys. Rev. B **13**, 5086.

Bates, S., C. Patterson, G.J. MacIntyre, S.B. Palmer, A. Mayer, R.A. Cowley and R. Melville, 1988, J. Phys. C **21**, 4125.

Bjerrum Møller, H., S.M. Shapiro and R.J. Birgeneau, 1977, Phys. Rev. Lett. **39**, 1921.

Blume, M., 1985, J. Appl. Phys. **57**, 3615.

Blume, M., 1994, in: Resonant Anomalous X-ray Scattering – Theory and Practice, eds G. Materlik, C.J. Sparks and K. Fischer (Elsevier Science) p. 495.

Blume, M., and D. Gibbs, 1988, Phys. Rev. B **37**, 1779.

Blume, M., A.J. Freeman and R.E. Watson, 1962, J. Chem. Phys. **37**, 1245.

Bohr, J., D. Gibbs, D.E. Moncton and K.L. D'Amico, 1986, Physica **140A**, 349.

Bohr, J., D. Gibbs, J.D. Axe, D.E. Moncton, K.L. D'Amico, C.F. Majkrzak, J. Kwo, M. Hong, C.L. Chen and J. Jensen, 1989, Physica B **159**, 93.

Bohr, J., D. Gibbs and Kegang Huang, 1990, Phys. Rev. B **42**, 4322.

Brock, J.D., A. Aharony, R.J. Birgeneau, K.W. Evans-Lutterrodt, J.D. Lister, P.M. Horn, G.B. Stephenson and A.R. Tajbakhsh, 1986, Phys. Rev. Lett. **57**, 98.

Brückel, T., M. Lippert, R. Bouchard, T. Schmidt, J.R. Schneider and W. Jauch, 1993, Acta Crystallogr. A **49**, 679.

Brun, T.O., S.K. Sinha, N. Wakabayashi, G.H. Lander, L.R. Edwards and F.H. Spedding, 1970, Phys. Rev. B **1**, 1251.

Brunel, M., and F. de Bergevin, 1981, Acta Crystallogr. A **37**, 324.

Brunel, M., G. Patraff, F. de Bergevin, F. Rousseau and M. Lemonnier, 1983, Acta Crystallogr. A **39**, 84.

Cable, J.W., E.O. Wollan, W.C. Koehler and M.K. Wilkinson, 1965, Phys. Rev. **140**, 1896.

Carra, P., M. Fabrizio, G. Santoro and B.T. Thole, 1996, Phys. Rev. B **53**, R5994.

Chattopadhay, T., G. Grübel, J.D. Axe and D. Gibbs, 1992, J. Magn. Magn. Mater. **104–107**, 1213.

Compton, A.H., 1936, Phys. Rev. **50**, 878.

Costa, M.M.R., M.J.M. de Almeida, W.J. Nutall, W.G. Stirling, C.C. Tang, J.B. Forsyth and M.J. Cooper, 1996, J. Phys. Condens. Matter **8**, 2425.

Cowley, R.A., and S. Bates, 1988, J. Phys. C **21**, 4113.

Cowley, R.A., and J. Jensen, 1992, J. Phys. Condens. Matter **4**, 9673.

Cowley, R.A., D.A. Jehan, D.F. McMorrow and G.J. McIntyre, 1991, Phys. Rev. Lett. **66**, 1521.

Cowley, R.A., D.F. McMorrow, P.P. Swaddling, R.C.C. Ward and M.R. Wells, 1995, Ind. J. Pure Appl. Phys. **33**, 509.

Darnell, F.J., 1963, Phys. Rev. **130**, 1825.

de Bergevin, F., and M. Brunel, 1972, Phys. Lett. A **39**, 141.

de Bergevin, F., and M. Brunel, 1981, Acta Crystallogr. A **37**, 314.

Detlefs, C., A.I. Goldman, C. Stassis, P.C. Canfield, B.K. Cho, J.P. Hill and D. Gibbs, 1996, Phys. Rev. B **53**, 6355.

Detlefs, C., A.H.M.Z. Islam, A.I. Goldman, C. Stassis, P.C. Canfield, J.P. Hill and D. Gibbs, 1997, Phys. Rev. B **55**, R680.

Eccleston, R.S., and S.B. Palmer, 1992, J. Phys. Condens. Matter **4**, 10037.

Eckert, J., and G. Shirane, 1976, Solid State Commun. **19**, 911.

Elliott, R.J., 1972, Magnetic Properties of Rare Earth Metals (Plenum Press, London).

Everitt, B.A., M.B. Salamon, B.J. Park, C.P. Flynn, T. Thurston and D. Gibbs, 1995, Phys. Rev. Lett. **75**, 3182.

Felcher, G.P., G.H. Lander, T. Arai, S.K. Sinha and F.H. Spedding, 1976, Phys. Rev. B **13**, 3034.

Ferrer, S., P. Fajardo, F. de Bergevin, J. Alvarez, X. Torrelles, H.A. van der Vegt and V.H. Etgens, 1996, Phys. Rev. Lett. **77**, 747.

Forgan, E.M., E.P. Gibbons, K.A. McEwen and D. Fort, 1989, Phys. Rev. Lett. **62**, 470.

Forgan, E.M., S.L. Lee, W.G. Marshall and D. Fort, 1992, J. Magn. Magn. Mater. **104–107**, 913.

Gehring, P.M., L. Rebelsky, D. Gibbs and G. Shirane, 1992, Phys. Rev. B **45**, 243.

Gehring, P.M., A. Vigliante, D.F. McMorrow, D. Gibbs, C.F. Majkrzak, G. Helgesen, R.A. Cowley, R.C.C. Ward and M.R. Wells, 1996, Physica B **221**, 398.

Gell-Mann, M., and M.J. Goldberger, 1954, Phys. Rev. **96**, 1433.

Gibbs, D., 1989, J. Less-Common Met. **148**, 109.
Gibbs, D., D.E. Moncton, K.L. D'Amico, J. Bohr and B.H. Grier, 1985, Phys. Rev. Lett. **55**, 234.
Gibbs, D., J. Bohr, J.D. Axe, D.E. Moncton and K.L. D'Amico, 1986, Phys. Rev. B **34**, 8182.
Gibbs, D., D.R. Harshman, E.D. Isaacs, D.B. McWhan, D. Mills and C. Vettier, 1988, Phys. Rev. Lett. **61**, 1241.
Gibbs, D., G. Grübel, D.R. Harshman, E.D. Isaacs, D.B. McWhan, D. Mills and C. Vettier, 1991, Phys. Rev. B **43**, 5663.
Giles, C., C. Malgrange, J. Goulon, F. de Bergevin, C. Vettier, A. Fontaine, E. Dartyge, S. Pizzini, F. Baudelet and A. Freund, 1995, Rev. Sci. Inst. **66**, 1549.
Goff, J.P., C. Bryn-Jacobsen, D.F. McMorrow, G.J. McIntyre, J.A. Simpson, R.C.C. Ward and M.R. Wells, 1998, Phys. Rev. B **57**, 5933.
Greenough, R.D., 1979, J. Phys. C **12**, 1113.
Greenough, R.D., and G.N. Blackie, 1981, J. Phys. Chem. Solids **42**, 533.
Habenschuss, M., C. Stassis, S.K. Sinha, H.W. Deckman and F.H. Spedding, 1974, Phys. Rev. B **10**, 1020.
Hamrick, M., 1994, Ph.D. Thesis (Rice University, USA).
Hannon, J.P., G.T. Tramell, M. Blume and D. Gibbs, 1988, Phys. Rev. Lett. **61**, 1245.
Helgesen, G., J.P. Hill, T.R. Thurston, D. Gibbs, J. Kwo and M. Hong, 1994, Phys. Rev. B **50**, 2990.
Helgesen, G., J.P. Hill, T.R. Thurston and D. Gibbs, 1995, Phys. Rev. B **52**, 9446.
Helgesen, G., Y. Tanaka, J.P. Hill, P. Wochner, D. Gibbs, C.P. Flynn and M.B. Salamon, 1997, Phys. Rev. B **56**, 2635.
Hettiarachchi, N.F., and R.D. Greenough, 1982, J. Phys. C **15**, 4573.
Hill, J.P., and D.F. McMorrow, 1996, Acta Crystallogr. A **52**, 236.
Hill, J.P., A. Vigliante, D. Gibbs, J.L. Peng and R.L. Greene, 1995a, Phys. Rev. B **52**, 6575.
Hill, J.P., G. Helgesen and D. Gibbs, 1995b, Phys. Rev. B **51**, 10336.
Hill, J.P., B.J. Sternlieb, D. Gibbs, C. Detlefs, A.I. Goldman, C. Stassis, P.C. Canfield and B.K. Cho, 1996, Phys. Rev. B **53**, 3487.
Hill, J.P., C.-C. Kao and D.F. McMorrow, 1997, Phys. Rev. B **55**, R8662.
Howard, B.K., and J. Bohr, 1991, Phys. Scripta T **39**, 96.
Isaacs, E.D., D.B. McWhan, D.P. Siddons, J.B. Hastings and D. Gibbs, 1989, Phys. Rev. B **40**, 9336.
Jehan, D.A., D.F. McMorrow, R.A. Cowley and G.J. McIntyre, 1992, Europhys. Lett. **17**, 553.
Jehan, D.A., D.F. McMorrow, J.A. Simpson, R.A. Cowley, P.P. Swaddling and K.N. Clausen, 1994, Phys. Rev. B **50**, 3085.
Jensen, J., 1976, J. Phys. F **6**, 1145.
Jensen, J., 1996, Phys. Rev. B **54**, 4021.
Jensen, J., and A.R. Mackintosh, 1991, Rare Earth Magnetism: Structure and Excitations (Oxford University Press, Oxford).
Kawamura, H., 1988, J. Appl. Phys. **63**, 3086.
Keating, D.T., 1969, Phys. Rev. **178**, 732.
Koehler, W., J.W. Cable, M.K. Wilkinson and E.O. Wollan, 1966, Phys. Rev. **151**, 414.
Koehler, W., J.W. Cable, H.R. Child, M.K. Wilkinson and E.O. Wollan, 1967, Phys. Rev. **158**, 450.
Koehler, W.C., 1965, J. Appl. Phys. **36**, 1078.
Koehler, W.C., and R.M. Moon, 1972, Phys. Rev. Lett. **29**, 1468.
Koehler, W.C., J.W. Cable, E.O. Wollan and M.K. Wilkinson, 1962, Phys. Rev. **126**, 1672.
Lang, J.C., and G. Srajer, 1995, Rev. Sci. Instrum. **66**, 1540.
Larsen, C.C., J. Jensen and A.R. Mackintosh, 1987, Phys. Rev. Lett. **59**, 712.
Lee, S.L., E.M. Forgan, S.J. Shaikh, C.C. Tang, W.G. Stirling, S. Langridge, A.J. Rollason, M.M.R. Costa, M.J. Cooper, E. Zukowski, J.B. Forsyth and D. Fort, 1993, J. Magn. Magn. Mater. **127**, 145.
Lin, H., M.F. Collins, T.M. Holden and W. Wei, 1992, Phys. Rev. B **45**, 12873.
Lovesey, S.W., and S.P. Collins, 1996, X-ray Scattering and Absorption by Magnetic Materials (Oxford University Press, Oxford).
Low, F.E., 1954, Phys. Rev. **96**, 1428.
Luo, J., G.T. Trammell and J.P. Hannon, 1993, Phys. Rev. Lett. **71**, 287.
Majkrzak, C.F., J. Kwo, M. Hong, Y. Yafet, D. Gibbs, C.L. Chen and J. Bohr, 1991, Adv. Phys. **40**, 99.
McEwen, K.A., E.M. Forgan, H.B. Stanely, J. Bouillot and D. Fort, 1985, Physica B **130**, 360.
McMillan, W.L., 1976, Phys. Rev. B **14**, 1496.
McMorrow, D.F., Y. Fujii, N. Hamaya, S. Shimomura, S. Kishimoto and H. Iwasaki, 1990, Solid State Commun. **76**, 443.
McMorrow, D.F., C. Patterson, H. Godfrin and D.A. Jehan, 1991, Europhys. Lett. **15**, 541.

McMorrow, D.F., D.A. Jehan, R.A. Cowley, R. Eccleston and G.J. McIntyre, 1992, J. Phys. Condens. Matter **4**, 8599.

McMorrow, D.F., J.A. Simpson, R.A. Colwey, D.A. Jehan, R.C.C. Ward, M.R. Wells, T.R. Thurston and D. Gibbs, 1995, J. Magn. Magn. Mater. **140–144**, 779.

McMorrow, D.F., J.-G. Lussier, B. Lebech, S.Aa. Sørensen and M.J. Christensen, 1997, J. Phys. Condens. Matter **9**, 1133.

McWhan, D.B., C. Vettier, E.D. Isaacs, G.E. Ice, D.P. Siddons, J.B. Hastings, C. Peters and O. Vogt, 1990, Phys. Rev. B **42**, 6007.

McWhan, D.B., E.D. Isaacs, P. Carra, S.M. Shapiro, B.T. Thole and S. Hoshino, 1993, Phys. Rev. B **47**, 8630.

Moon, R.M., J.W. Cable and W.C. Koehler, 1964, J. Appl. Phys. **35**, 1041.

Namikawa, K., 1992, KEK Monthly Report, National Laboratory for High-Energy Physics **21** No. 5, p. 6.

Namikawa, K., M. Ando, T. Nakajima and H. Kawata, 1985, J. Phys. Soc. Jpn. **54**, 4099.

Pechan, M.J., and C. Stassis, 1984, J. Appl. Phys. **55**, 1900.

Pengra, D.B., N.B. Thoft, M. Wulff, R. Feidenhans'l and J. Bohr, 1994, J. Phys. Condens. Matter **6**, 2409.

Perry, S.C., M.M.R. Costa, W.G. Stirling, M.J. Longford, D. Mannix and T. Brückel, 1998, J. Phys.: Condens. Matter **10**, 1451.

Platzman, P.M., and N. Tzoar, 1970, Phys. Rev. **2**, 3556.

Rhyne, J.J., M.B. Salamon, C.P. Flynn, R.W. Erwin and J.A. Borchers, 1994, J. Magn. Magn. Mater. **129**, 39.

Sanyal, M.K., D. Gibbs, J. Bohr and M. Wulff, 1994, Phys. Rev. B **49**, 1079.

Simpson, J.A., D.F. McMorrow, D.A. Jehan, R.A. Cowley, M.R. Wells, R.C.C. Ward and K.N. Clausen, 1994, Phys. Rev. Lett. **73**, 1162.

Simpson, J.A., D.F. McMorrow, D.A. Jehan and R.A. Cowley, 1995, Phys. Rev. B **51**, 16073.

Simpson, J.A., R.A. Cowley, D.A. Jehan, R.C.C. Ward, M.R. Wells, D.F. McMorrow, K.N. Clausen, T.R. Thurston and D. Gibbs, 1996, Z. Phys. B **101**, 35.

Steinitz, M.O., M. Kahrizi, D.A. Tindall and N. Ali, 1989, Phys. Rev. B **40**, 763.

Stunault, A., C. Vettier, F. de Bergevin, F. Maier, G. Grübel, R.M. Gelera and S.B. Palmer, 1995, J. Magn. Magn. Mater. **140–144**, 753.

Sutter, C., G. Grübel, C. Vettier, F. de Bergevin, A. Stunault, D. Gibbs and D. Giles, 1997, Phys. Rev. B **55** 954.

Sutter, C., G. Grübel, D. Gibbs, C. Vettier, F. de Bergevin and A. Stunault, 1999, to be published.

Tang, C.C., W.G. Stirling, G.H. Lander, D. Gibbs, W. Herzog, P. Carra, B.T. Thole, K. Mattenberger and O. Vogt, 1992a, Phys. Rev. B **46**, 5287.

Tang, C.C., W.G. Stirling, D.L. Jones, P.W. Haycock, A.J. Rollason, A.H. Thomas and D. Fort, 1992b, J. Magn. Magn. Mater. **103**, 86.

Thurston, T.R., G. Helgesen, D. Gibbs, J.P. Hill, B.D. Gaulin and G. Shirane, 1993, Phys. Rev. B **70**, 3151.

Tindall, D.A., M.O. Steinitz and M.T. Holden, 1993, J. Appl. Phys. **73**, 6543.

van Veenendaal, M., J.B. Goedkoop and B.T. Thole, 1997, Phys. Rev. Lett. **78**, 1162.

Venter, A.M., P. de V. du Plessis and E. Fawcett, 1992, Physica B **180–181**, 290.

Vettier, C., D.B. McWhan, E.M. Gyorgy, J. Kwo, B.M. Buntschuh and B.W. Batterman, 1986, Phys. Rev. Lett. **56**, 757.

Vigliante, A., M.J. Christensen, J.P. Hill, G. Helgesen, S.A. Sorensen, D.F. McMorrow, D. Gibbs, R.C.C. Ward and M.R. Wells, 1998, Phys. Rev. B **57**, 5941.

Vigren, D.T., 1976, Solid State Commun. **18**, 1599.

Vogt, O., and K. Mattenberger, 1993, in: Handbook on the Physics and Chemistry of the Rare Earths, Vol. 17, eds K.A. Gschneidner Jr. and L. Eyring (North-Holland, Amsterdam) ch. 114.

Watson, B., and N. Ali, 1995, J. Phys. Condens. Matter **7**, 4713.

Watson, B., and N. Ali, 1996a, J. Phys. Condens. Matter **8**, 361.

Watson, B., and N. Ali, 1996b, J. Phys. Condens. Matter **8**, 1797.

Watson, D., E.M. Forgan, W.G. Stirling, W.J. Nutall, S.C. Perry, M.M.R. Costa and D. Fort, 1995, J. Magn. Magn. Mater. **140–144**, 743.

Watson, D., E.M. Forgan, W.J. Nutall, W.G. Stirling and D. Fort, 1996, Phys. Rev. B **53**, 726.

Watson, G.M., D. Gibbs, G.H. Lander, B.D. Gaulin, L.E. Berman, H. Matzke and W. Ellis, 1996, Phys. Rev. Lett. **77**, 751.

Willis, F., and N. Ali, 1992, J. Alloys and Compounds **181**, 287.

Yahnke, C.J., G. Srajer, D.R. Haeffner and L. Mills, 1994, Nuc. Inst. Meth. A **347**, 128.

Zheludev, A., J.P. Hill and D.J. Buttrey, 1996, Phys. Rev. B **54** 7216.

Zinkin, M.P., D.F. McMorrow, J.P. Hill, R.A. Cowley, J.-G. Lussier, A. Gibaud, G. Grübel and C. Sutter, 1996, Phys. Rev. B **54**, 3115.

Zochowski, S.W., K.A. McEwen and E. Fawcett, 1991, J. Phys. Condens. Matter **3**, 8079.

Handbook on the Physics and Chemistry of Rare Earths
Vol. 26
edited by K.A. Gschneidner, Jr. and L. Eyring

Chapter 170

STATIC AND DYNAMIC STRESSES

A.M. TISHIN and Yu.I. SPICHKIN
Faculty of Physics, M.V. Lomonosov Moscow State University, Moscow, 119899, Russia

J. BOHR
Department of Physics, Technical University of Denmark, Building 307, DK-2800 Lyngby, Denmark

Contents

List of symbols

a	a-axis lattice constant
a_i	lattice constant
A	amplitude of sound wave
b	b-axis lattice constant
$b_{\vec{k}}$, $b^+_{\vec{k}}$	annihilation and creation phonon operators
B^{α}_{12}, B^{α}_{22}, B^{γ}, B^{τ}	single-ion magnetoelastic coupling constants
c	c-axis lattice constant
$\vec{c}^*$	c-axis basis vector of reciprocal unit cell
C_S	Curie constant of the lanthanide ions
C_{d}	d-electron Curie constant
c_{ij}	elastic constants
Δc_{ij}	change in elastic constant
e	electronic charge
$\vec{e}_k$	polarization vector of a sound wave
E	Young's modulus
ΔE	change in Young's modulus
$\mathcal{E}_{\mathrm{F}}$	Fermi energy
$\mathcal{E}_{\mathrm{me}}$	magnetoelastic energy
$\mathcal{E}_{\mathrm{an}}$	anisotropic energy
F	free energy
$\mathcal{G}$	de Gennes factor = $(g_J - 1)^2 J(J+1)$
g_J	Landé factor
H	magnetic field
$\mathcal{H}$	Hamiltonian
H_{cr}	critical magnetic field
$H_{\mathrm{cr}}^{\max}$	maximum value of critical magnetic field
$\hbar$	Planck's constant divided by 2π
I_{ij}, I_i	exchange interaction integrals
I_{eff}	effective exchange interaction integral between itinerant electrons
$I(0)$	paramagnetic indirect exchange integral
$I(\vec{Q})$	Fourier transformation of exchange integral
J	total angular magnetic moment quantum number
K	kinetic coefficient
K_i, K_i^j	magnetocrystalline anisotropy constants
k_{B}	Boltzmann's constant
$\vec{k}$	wave vector
k_{F}	conduction electron wave vector at the Fermi surface
m^*	effective mass of the conduction electron
$M_{ij,kl}$	first-order magnetoelastic interaction tensor
n_{RR}, n_{RM}	molecular field constants
N	number of lanthanide ions per unit volume
$N(\mathcal{E})$	density of states per unit volume
p, p_i	uniaxial mechanical stress
P	pressure
$\vec{Q}$	magnetic spin structure wave vector
Q^{-1}	internal friction
$\vec{Q}_S$	spin-slip magnetic structure wave vector
$\vec{q}$	reciprocal space vector
R	distance between ions
$\vec{R}_i$	atom position vector
$\vec{R}$	interatomic distance vector
$\vec{r}$	conduction electron position vector
$R_{ij,klno}$	second-order magnetoelastic interaction tensor
s_{ij}	elastic compliance constants
S	spin momentum quantum number
$\vec{S}$	spin angular moment
T	absolute temperature
T_{C}	Curie temperature
T_{N}	Néel temperature
T_{p}	paramagnetic Curie temperature
ΔT_{NC}	interval where helical structure exists
T_{sr}	spin-reorientation transition temperature
T_{d}	Curie temperature of the d-electron system
T_{CY}	transition temperature to cycloidal structure
T_{D}	Debye's temperature
T_{ij}	components of the mechanical stress tensor
$\vec{u}$	lattice displacement vector
V	volume
V_{a}	atomic volume
υ_{l}, υ_{t}	longitudinal and shear sound velocities
x	concentration
W	bandwidth
z	coordination number
Z	ionic charge
$\alpha, \beta, \gamma, \varepsilon$	thermodynamic coefficients in free energy expansion
α_{T}	linear coefficient of thermal expansion

α_M	molecular field constant for collective d-electrons	σ_0	saturation magnetization at $T = 0\,K$
		σ_i	component of magnetization vector
$\alpha_l, \alpha_t, \alpha_{ij}$	sound attenuation coefficients	σ_s	saturation magnetization
$\Gamma(\vec{q}), \Gamma_0$	s–f exchange interaction integrals	τ	relaxation time
Δ_{E_i}	degree of relaxation of Young's modulus	ϕ	angle between the magnetic moment and c-axis
$\delta(r)$	Dirac's function		
ϵ_{ij}	mechanical strain tensor components	φ	helical turn angle
κ	volume compressibility	χ_d	magnetic susceptibility of collective d-electrons
λ	linear magnetostriction		
μ_B	Bohr magneton	χ_s	magnetic susceptibility of lanthanide spin system
μ_s	saturation magnetic moment		
μ_{eff}	effective magnetic moment	χ_{d0}	magnetic susceptibility of noninteracting collective d-electrons
ν	critical exponent of the attenuation coefficient	χ_{hf}	high field magnetic susceptibility
ρ	density	$\chi(\vec{q})$	generalized conduction electron magnetic susceptibility
ρ_m	magnetic contribution to resistivity		
σ	magnetization	ω	frequency

Abbreviations

FM	ferromagnetic phase	R	lanthanide (rare earth) metals
HAFM	helicoidal antiferromagnetic structure	TM	transition metal
LSW	longitudinal spin wave	RKKY	Ruderman–Kittel–Kasuya–Yosida

1. Introduction

In this chapter we shall consider the properties of lanthanide metals, their alloys and compounds which can be studied using static and alternating mechanical stresses. The main attention will be paid to the effects related to magnetoelastic interactions. These interactions in magnetic materials can display themselves in static magnetostriction deformations (this effect is not considered here) and in the changing of the magnetic state under mechanical stress. The latter causes variation of the magnetic phase transition temperatures, magnetization and magnetic structures, and leads to the appearance of anomalies in elastic constants, as well as to additional damping of sound oscillations in the lanthanide materials. The importance of understanding the nature of magnetoelastic interactions and related effects arises from the scientific desire to gather a better knowledge of magnetism, as well as from possible technological applications.

The elastic and magnetic properties of the lanthanide metals under pressure were reviewed in the late 1970s – see Scott (1978) and Jayaraman (1978). In this chapter we are concerned with various theoretical models and their consequences, and with the experimental results obtained in the past 20 years as well as some important topics which were not reviewed before.

In sections 2–5 we consider the influence of hydrostatic and uniaxial pressure on the transition temperatures of magnetic phase transformations, magnetization, magnetic phase diagrams and spin structures in the lanthanide metals and their alloys, and compounds with 3d transition metals (TM) and nonmagnetic elements. Pressures causing elastic strains without nonreversible deformations are considered here.

Sections 6–7 are concerned with values measured with the help of dynamic elastic stresses. Section 6 deals with the sound attenuation and internal friction in lanthanide metals arising from the existence of magnetic order. The anomalies of the elastic constants and moduli in these metals and their alloys and compounds with Fe and Co and their origin are discussed in sect. 7. Special attention is paid to the influence of commensurate magnetic structures on elastic properties and sound attenuation in lanthanide metals. Section 7.8 is devoted to the higher-order elastic constants which characterize the anharmonic properties of crystal lattices and explain the dependence on pressure of elastic constants. The magnetic phase diagrams obtained from magnetization and elastic properties measurements are discussed.

2. Effect of static pressure on the phase transition to a magnetically ordered state

2.1. *Systems with localized magnetic moments*

2.1.1. *General considerations*

The magnetic properties of the rare earth metals systems with localized magnetic moments, can be described by means of the molecular field theory. In the frame of this model the Curie temperature T_C and the paramagnetic transition temperature T_p may be expressed as (Smart 1966)

$$T_C = T_p = \frac{2(J+1)S^2}{3Jk_B} zI_{ij}, \tag{1}$$

where z is the coordination number of the system, J and S are the quantum numbers of the total angular and spin momentums of magnetic ion, k_B is the Boltzmann constant, and I_{ij} the integral of exchange interaction between the magnetic ions i and j, which has the Heisenberg form:

$$\mathcal{H}_{ij} = -2I_{ij}\vec{S}_i\vec{S}_j, \tag{2}$$

$\vec{S}$ is the spin angular momentum. It is supposed in eq. (1) that exchange interaction for every pair of nearest neighbors has the same value I_{ij}.

By differentiating eq. (1) on pressure one can derive the expression for the pressure shift of the Curie temperature:

$$\frac{dT_C}{dP} = \frac{dT_p}{dP} = \frac{2(J+1)S^2}{3Jk_B} z \frac{dI_{ij}}{dP}, \tag{3}$$

or, by using Hooke's law in the form of $dV/V = -\kappa\, dP$, we obtain

$$\frac{d\ln T_C}{d\ln V} = \frac{d\ln T_p}{d\ln V} = \frac{d\ln I_{ij}}{d\ln V}, \tag{4}$$

where V is the volume, and κ the volume compressibility (it is assumed that the quantum numbers of the ion are not affected by the pressure).

In the lanthanide metals where the magnetic 4f-electrons are strongly localized the exchange interaction is indirectly mediated via conduction electrons and has an oscillatory character. The exchange integral of this interaction can be expressed as (Liu 1978, Ruderman and Kittel 1954)

$$I_{ij}(R) = \sum_{\vec{q}} \Gamma^2(\vec{q})\chi(\vec{q}) \exp\left[i\vec{q}\left(\vec{R}_i - \vec{R}_j\right)\right], \tag{5}$$

where R is the distance between the atoms with position vectors $\vec{R}_i$ and $\vec{R}_j$, $R = |\vec{R}_i - \vec{R}_j|$; $\Gamma(\vec{q})$ is the coupling constant between the spin of a 4f-electron and a conduction electron (s–f interaction integral), and its value is determined by the wave functions of the conduction and 4f-electrons, $\vec{q}$ is the reciprocal space vector and $\chi(\vec{q})$ is the generalized conduction electron magnetic susceptibility. In the Ruderman–Kittel–Kasuya–Yosida (RKKY) model of indirect exchange interaction (Ruderman and Kittel 1954, Kasuya 1956, Yosida 1957) the supposition that the exchange interaction between conduction electrons and 4f-electrons had a point character was used, i.e.,

$$\Gamma\left(\vec{r} - \vec{R}\right) = \Gamma_0 \delta\left(\vec{r} - \vec{R}\right), \quad \text{i.e.} \quad \Gamma(\vec{q}) = \Gamma_0 = \text{const}, \tag{6}$$

(where $\vec{r}$ is the conduction electron position vector, and $\delta(\vec{r} - \vec{R})$ is the Dirac function) and the conduction electrons are regarded as the system of free electrons with spherical Fermi surface. In the framework of this approach the exchange integral (5) can be expressed in the following form:

$$I_{ij}(R) = \frac{9\pi Z^2 \Gamma_0^2}{2V_a^2 \mathcal{E}_F} \phi(2k_F R), \tag{7}$$

where Z is the lanthanide ionic charge, V_a is the atomic volume, k_F is the value of conduction electron wave vector on the Fermi surface, $\mathcal{E}_F$ is the Fermi energy, and

$\phi(x) = (\sin x - \cos x)/x^4$. Equation (7) can be rewritten through the density of states at the Fermi energy $N(\mathcal{E}_F)$:

$$I_{ij}(R) = \frac{3\pi Z}{4N} \Gamma_0^2 N(\mathcal{E}_F) \phi(2k_F R), \tag{8}$$

where N is the number of lanthanide ions per unit volume. Using the molecular field model one can write down the Curie temperature in the RKKY approximation (De Gennes 1962, Taylor and Darby 1972) as

$$T_C = T_p = \frac{2}{3} \frac{\mathcal{G}}{k_B} I(0) = \frac{3\pi Z^2 \Gamma_0^2 \mathcal{G}}{k_B V_a^2 \mathcal{E}_F} \sum_R \phi(2k_F R), \tag{9}$$

where $I(0)$ is the paramagnetic indirect exchange integral; $\mathcal{G} = (g_J - 1)^2 J(J+1)$, the de Gennes factor; and g_J, the Landé factor.

Liu (1962) showed that for the free conduction electrons model the sum in eq. (9) should not depend on the pressure, then using for $I(\vec{R})$ eq. (8) one can derive

$$\frac{d \ln T_C}{d \ln V} = \frac{d \ln T_p}{d \ln V} = \frac{d \ln I(0)}{d \ln V} = \frac{d \ln N(\mathcal{E}_F)}{d \ln V} + \frac{2 d \ln \Gamma_0}{d \ln V}. \tag{10}$$

In the framework of the approximation of the point character of the s–f interaction made in RKKY model, the coupling constant Γ should not depend on the interatomic distance, and consequently on pressure. If one assumes that in the general case Γ is determined by wave functions of the s- and f-electrons, then its volume dependence can be explained by the change of amplitude of the conduction electron wave functions caused by the change of lattice elementary cell dimensions (Liu 1962). So the variation of the volume effects on the energy spectrum of the conduction electrons can cause a change of the s–f coupling constant and the conduction electron susceptibility $\chi(\vec{q})$, which in turn causes a change of exchange integral I_{ij}.

Robinson et al. (1971) proposed the modified RKKY model in which the space extent of the 4f wave function was taken into account, and $\Gamma(\vec{q})$, in contrast to eq. (6), was written in the form

$$\Gamma(q) = \Gamma_0 \exp(-\Delta|q - q_0|), \tag{11}$$

where parameters Δ and q_0 are related to width and shape of the 4f function, respectively. This model gives a distance dependent s–f interaction and the complex expression for I_{ij}

$$I_{ij} = \frac{m^* \Gamma_0^2}{2^6 \pi^3} \frac{4\Delta \cos q_0 R}{R(R^2 + 4\Delta^2)} \left(q_0^2 - 4k_F^2\right) + \cdots, \tag{12}$$

where m^* is the conduction electron effective mass. Here for simplicity only the first term of the expression for $I_{ij}(\vec{R})$ is shown. When $\Delta \to 0$, I_{ij} transforms to the usual form with

the oscillatory Ruderman–Kittel function $\phi(2k_F R)$ (see eq. 7), and if $\Delta \to \infty$, $I_{ij} \to 0$. The paramagnetic Curie temperature was expressed as

$$T_p = \frac{m^* \Gamma_0^2}{96 k_B \pi^3} \left(q_0^2 - 4k_F^2\right) \sum_R \frac{\cos q_0 R}{R\Delta \left(1 + \left(\frac{R}{2\Delta}\right)^2\right)}. \tag{13}$$

The magnitude of I_{ij} and T_p and their dependence on interatomic distance are determined by the values of Δ, q_0 and Γ_0 which were regarded by Robinson et al. (1971) as adjusting parameters.

For the transition temperature from paramagnetic to noncollinear magnetically ordered phase, T_N, the contribution from the magnetocrystalline anisotropy T_A should be taken into account (Fujiwara et al. 1977):

$$T_N = \frac{2}{3} \frac{\mathcal{G}}{k_B} I(\vec{Q}) + T_A, \tag{14}$$

where

$$T_A = \tfrac{2}{5} K_1 \left(J - \tfrac{1}{2}\right) \left(J + \tfrac{3}{2}\right) \tag{15}$$

for the helical antiferromagnetic (HAFM) spin structure, and

$$T_A = -\tfrac{4}{5} K_1 \left(J - \tfrac{1}{2}\right) \left(J + \tfrac{3}{2}\right) \tag{16}$$

for structures with a spin component along the hexagonal c-axis, K_1 is the unique axis anisotropy constant, $\vec{Q}$ is the wave vector of magnetic spin structure, and $I(\vec{Q})$ is the Fourier transform of the exchange interaction $I_{ij}(R)$:

$$I\left(\vec{Q}\right) = \sum_{\vec{R}} I_{ij}(R) \exp\left(i\vec{Q}\vec{R}\right). \tag{17}$$

For alloys the average values of the de Gennes factor $\mathcal{G}$ and the anisotropy constant K_1 should be used.

For the shift of T_N under pressure one has

$$\frac{dT_N}{dP} = \frac{2}{3} \frac{\mathcal{G}}{k_B} \frac{dI(\vec{Q})}{dP} + \frac{dT_A}{dP}, \tag{18}$$

The value of dT_A/dP can be estimated with the help of eqs. (15) and (16), the elastic constant data, and the expression for dK_1/dP

$$\frac{dK_1}{dP} = \frac{\partial K_1}{\partial \ln a} \frac{d \ln a}{dP} + \frac{\partial K_1}{\partial \ln b} \frac{d \ln b}{dP} + \frac{\partial K_1}{\partial \ln c} \frac{d \ln c}{dP}, \tag{19}$$

where a, b and c are the lattice parameters along the a-, b- and c-axes in the hexagonal crystal structure. The values of $\partial K_1/\partial \ln a_i$ can be derived from the experimental

measurements of magnetostriction (Nikitin et al. 1976a, Nikitin 1989) or calculated theoretically on the basis of the single-ion anisotropy theory relating K_1 with the lattice parameters (Kasuya 1966). The calculations show that dT_A/dP in heavy lanthanide metals and their alloys is about two orders of magnitude smaller than the measured values of dT_N/dP (Nikitin 1989).

2.1.2. *Lanthanide metals and their alloys*

Many authors have contributed to the study of the shift of magnetic phase transition temperatures under pressure in the heavy lanthanides and their alloys – see tables 1–3

Table 1
Magnetic phase transition temperatures and their pressure dependence in gadolinium

Ref.	T_C (K)	T_p (K)	T_{sr} (K)	$\frac{dT_C}{dP}$ (K/kbar)	$\frac{dT_p}{dP}$ (K/kbar)	$\frac{dT_{sr}}{dP}$ (K/kbar)
1	292 [a,c]		223 [a,c]	−1.35 [a,c]		−6.7 [a,c]
	291 [a,b]		227 [a,b]	−1.2 [a,b]		−2.9 [a,b]
2	293			−1.41±0.02 [a,b]		
				−1.39±0.02 [a,b]		
				−1.48±0.02		
3	291					
4	290.1		231	−1.63±0.02		−4.3±0.2 [a]
5	292.6	304		−1.56	−1.46	
6,7			250			−6 [a]
8				−1.56		
9				−1.48		
10				−1.50		
11				−1.2		
12				−1.60		
13				−1.34		
14				−1.40		
15	294±1					
16	293					

[a] Measurements on single crystals. [b] $H \parallel b$. [c] $H \parallel c$.

References

(1) Nikitin et al. (1991a, 1992)
(2) Bartholin and Bloch (1968a)
(3) Klimker and Rosen (1973)
(4) McWhan and Stevens (1967)
(5) Fujiwara et al. (1977)
(6) Mihai and Franse (1976)
(7) Franse and Mihai (1977)
(8) Austin and Mishra (1967)
(9) Bartholin and Bloch (1968b)
(10) Vinokurova et al. (1972)
(11) Patrick (1954)
(12) Robinson et al. (1964)
(13) Lifshitz and Genshaft (1965)
(14) Iwata et al. (1968)
(15) Dan'kov et al. (1996, 1998)
(16) Tishin (1990)

Table 2
Magnetic phase transition temperatures and their pressure dependence in several lanthanide metals

R	T_C (K)	$\frac{dT_C}{dP}$ (K/kbar)	T_N (K)	$\frac{dT_N}{dP}$ (K/kbar)	T_p (K)	$\frac{dT_p}{dP}$ (K/kbar)
Eu			90[l]	−0.45[o]		−0.6[p]
Tb	210[a], 220[*,b], 220.6[*,c], 219.3[d], 225[*,e]	−1.1[d], −1.17[*,c], −1.33[*,b], −1.24[h,i], −1.28[*,e]	230[a,f], 230[*,b,c], 228[m], 221.7[d], 231[*,e]	−0.8[*,e], −0.86[f], −1.08[m], −0.85[*,b], −1.0[a], −0.84[h], −1.1[k], −1.05[h], −0.82[e]	230[f,d], 236[*,b]	−0.75[f], −0.76[d], −1.04[*,b]
Dy	87.6[f], 86[*,b], 85[*,g]	−1.28[f], −1.24[j], −1.4[*,b], −1.27[h], −0.8[a], −1.50[*,k], −1.3[*,g]	178[f], 178.3[d], 179[m], 180[*,g], 181[*,b], 177[a]	−0.44[f,i,k], −0.62[m], −0.39[*,b], −0.4[a,p], −0.6[*,g], −0.41[h], −0.64[*,k]	148[f,d]	−0.17[f,d]
Ho	20[*,s]	-0.10[*,s]	125[f], 133[n], 134[b], 131[*,s]	−0.40[f], −0.48[n], −0.5[p], −0.48[*,b], −0.45[q], −0.47[*,s]	87[f]	−0.39[f]
Er	52[*,r] (T_{CY})	−0.43[*,r] (dT_{CY}/dP)	82[f], 85[j], 88[*,b], 84[*,r]	−0.24[f], −0.26[j], −0.24[*,b], −0.14[*,r]	39[f]	−0.53[f]

[*] Measurements on single crystals.

References

(a) Robinson et al. (1966)
(b) Nikitin et al. (1991a)
(c) Nikitin et al. (1991d)
(d) Tatsumoto et al. (1968)
(e) Kawano et al. (1992)
(f) Fujiwara et al. (1977)
(g) Nikitin and Leontiev (1987)
(h) Bartholin and Bloch (1968a)
(i) Wazzan et al. (1967)
(j) Milton and Scott (1967)
(k) Vinokurova et al. (1972)
(l) Nerensen et al. (1964)
(m) McWhan and Stevens (1967)
(n) McWhan and Stevens (1965)
(o) Menyuk et al. (1971)
(p) Kawai et al. (1967)
(q) Bloch and Pauthenet (1964)
(r) Kawano et al. (1995)
(s) Kurisu et al. (1996).

and also the review of Jayaraman (1978). Measurements were made on poly- and single-crystal samples and a lowering of the transition temperatures was observed which corresponded in the RKKY model to the increase of the indirect exchange integral when the interatomic distance increased. McWhan and Stevens (1967) determined from experimental $I(R)$ curves obtained for heavy lanthanide that $I(\vec{Q})/dR = 42 \pm 6$ K/Å. The variation of dT_N/dP values in heavy lanthanide metals was related to the variation of the de Gennes factor $\mathcal{G}$ (dT_N/dP is almost directly proportional to $\mathcal{G}$). However, Fujiwara et al. (1977) found that $dI(\vec{Q})/dR$ and $dI(0)/dR$ display a nonmonotonic dependence on the average number of 4f-electrons (see figs. 1 and 2). Bartholin and Bloch (1968a) considered the variation of the indirect exchange integral in Gd, Tb and Dy under pressure in the framework of the model proposed by Herpin and Meriel (1961) and Enz (1960)

Table 3
Magnetic phase transition temperatures and their pressure dependence in intra lanthanide (rare earth) alloys

Alloy	T_C (K)	T_N (K)	T_p (K)	$\frac{dT_C}{dP}$ (K/kbar)	$\frac{dT_N}{dP}$ (K/kbar)	$\frac{dT_p}{dP}$ (K/kbar)
$Gd_{0.9}Tb_{0.1}$				−1.3 [*,a]		
$Gd_{0.8}Tb_{0.2}$	278 [*,b]			−1.35 [*,a]		
$Gd_{0.5}Tb_{0.5}$	262.4 [c]		270 [c]	−1.30 [c]		
$Gd_{0.95}Dy_{0.05}$	287 [*,d]			−1.4 [*,d]		
$Gd_{0.80}Dy_{0.20}$	275 [*,d]			−1.4 [*,d]		
$Gd_{0.75}Dy_{0.25}$	265 [c]		274 [c]	−1.05 [c]		
$Gd_{0.60}Dy_{0.40}$	253 [*,d]			−1.3 [*,d]		
$Gd_{0.50}Dy_{0.50}$	233 [c]		240 [c]	−1.0 [c]		
$Gd_{0.30}Dy_{0.70}$		215 [*,d]			−0.9 [*,d]	
$Gd_{0.25}Dy_{0.75}$		155.2 [c]	203 [c]	−1.06 [c]	−0.66 [c]	−0.51 [c]
$Gd_{0.75}Ho_{0.25}$	253.8 [c]		265 [c]	−1.2 [c]		
$Gd_{0.50}Ho_{0.50}$	172 [c]	206.7 [c]	213 [c]	−0.84 [c]	−0.76 [c]	−0.83 [c]
$Gd_{0.25}Ho_{0.75}$	168.6 [c]	158 [c]		−0.54 [c]	−0.40 [c]	
$Gd_{0.75}Er_{0.25}$	247.3 [c]		255 [c]	−1.05 [c]		
$Gd_{0.50}Er_{0.50}$	171 [c]	184.8 [c]	200 [c]	−0.48 [c]	−0.66 [c]	−0.68 [c]
$Gd_{0.25}Er_{0.75}$		131.8 [c]	111 [c]		−0.46 [c]	−0.72 [c]
$Gd_{0.45}Y_{0.55}$	161 [e]			−0.59 [e]		
$Gd_{0.45}Lu_{0.55}$	147 [e]			−0.5 [e]		
$Tb_{0.50}Dy_{0.50}$	150.8 [c]	204.4 [c]	201 [c]	−0.96 [c]	−0.61 [c]	−0.46 [c]
	146 [*,f]	201.5 [*,f]	204.9 [*,f]	−1.08 [*,f]	−0.59 [*,f]	−112 [*,c]
$Tb_{0.91}Y_{0.09}$	179 [*,g]	217 [*,g]		−1.4 [*,g]	−0.7 [*,g]	
$Tb_{0.85}Y_{0.15}$		211 [e]			−0.77 [e]	
$Tb_{0.835}Y_{0.165}$	135 [*,g]	210 [*,g]		−1.2 [*,g]	−1.0 [*,g]	
$Tb_{0.70}Y_{0.30}$		196 [e]			−0.63 [e]	
$Tb_{0.57}Y_{0.43}$		181 [e]			−0.6 [e]	
$Tb_{0.50}Y_{0.50}$		149 [e]			−0.32 [e]	
$Tb_{0.40}Y_{0.60}$		129 [e]			−0.32 [e]	
$Tb_{0.30}Y_{0.70}$		111 [e]			−0.28 [e]	
$Tb_{0.675}Lu_{0.325}$		175 [e]			−0.51 [e]	
$Dy_{0.75}Ho_{0.25}$		166 [c]	143 [c]		−0.42 [c]	−0.09 [c]
$Dy_{0.50}Ho_{0.50}$		154.7 [c]	126 [c]		−0.40 [c]	−0.12 [c]
$Dy_{0.25}Ho_{0.75}$		141.5 [c]	108 [c]		−0.40 [c]	−0.26 [c]
$Dy_{0.75}Er_{0.25}$		156.5 [c]	126 [c]		−0.41 [c]	−0.20 [c]
$Dy_{0.50}Er_{0.50}$		132.2 [c]	94 [c]		−0.38 [c]	−0.32 [c]
$Dy_{0.25}Er_{0.75}$		103.4 [c]	63 [c]		−0.30 [c]	−0.48 [c]

continued on next page

Table 3, *continued*

Alloy	T_C (K)	T_N (K)	T_p (K)	$\frac{dT_C}{dP}$ (K/kbar)	$\frac{dT_N}{dP}$ (K/kbar)	$\frac{dT_p}{dP}$ (K/kbar)
$Ho_{0.75}Er_{0.25}$		113.5[c]	73[c]		−0.35[c]	−0.46[c]
$Ho_{0.50}Er_{0.50}$		98.6[c]	54[c]		−0.34[c]	−0.56[c]
$Ho_{0.25}Er_{0.75}$		84.6[c]	42[c]		−0.28[c]	−0.55[c]

[*] Measurements on single crystals.

References

(a) Bezdushnyi (1988)
(b) Nikitin (1989)
(c) Fujiwara et al. (1977)
(d) Leontiev (1988)
(e) Austin and Mishra (1967)
(f) Bykhover et al. (1990)
(g) Nikitin and Bezdushnyi (1991)

for antiferromagnets with helical spin structure. According to the model $I(\vec{Q})$ can be expressed as

$$I\left(\vec{Q}\right) = I_0 + 2I_1 \cos\varphi + 2I_2 \cos 2\varphi, \tag{20}$$

where φ is the helical turn angle, i.e., the angle between the magnetic moments lying in successive basal planes ($|\vec{Q}| = 2\varphi/c$), I_0, I_1 and I_2 are the exchange integrals characterizing the interactions in the basal plane, between the nearest neighbor basal planes and between

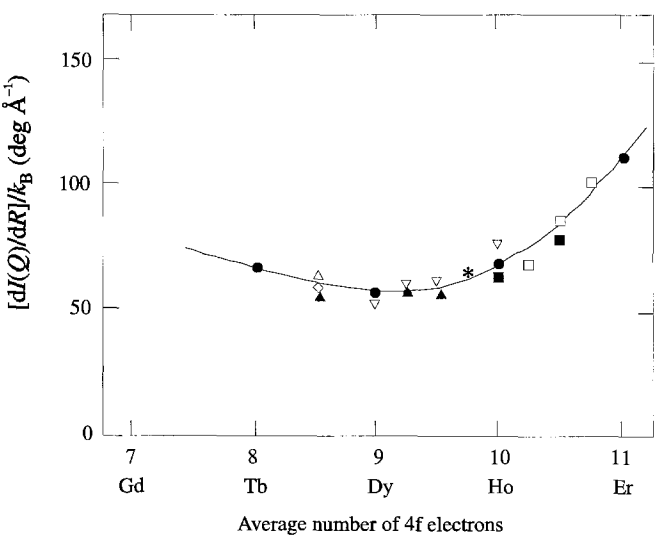

Fig. 1. Dependence of $dI(Q)/dR$ on the average number of 4f-electrons for the lanthanide metals and their alloys (Fujiwara et al. 1977). Symbols: solid circle, elements; open diamond, Gd–Dy; solid triangle, Gd–Ho; open inverted triangle, Gd–Er; open triangle, Tb–Dy; star, Dy–Ho; solid square, Dy–Er; open square, Ho–Er.

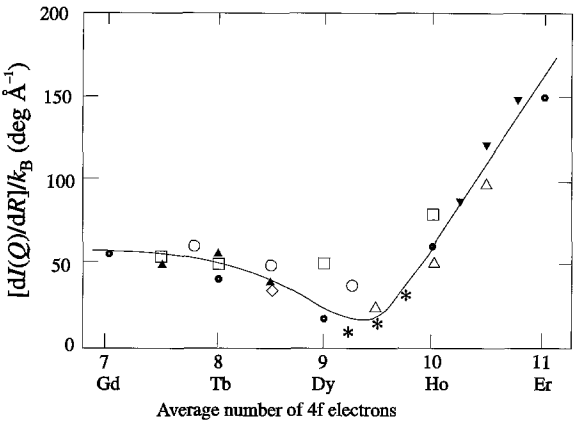

Fig. 2. Dependence of $dI(0)/dR$ on the average number of 4f-electrons for the lanthanide metals and their alloys (Fujiwara et al. 1977). Symbols: solid circle, elements; solid triangle, Gd–Dy; open circle, Gd–Ho; open square, Gd–Er; open diamond, Tb–Dy; star, Dy–Ho; open triangle, Dy–Er; solid inverted triangle, Ho–Er.

the second nearest neighbor planes, respectively (I_0, $I_1 > 0$, $I_2 < 0$). It was suggested that T_N depended on pressure via I_1 and I_2 which are functions of c. To calculate the $\partial I_i/\partial \ln c$ the following expression was used:

$$\frac{I\left(\vec{Q}\right)}{dP} = \frac{\partial I_1}{\partial \ln c}\frac{d\ln c}{dP}\cos\varphi + \frac{\partial I_2}{\partial \ln c}\frac{d\ln c}{dP}\cos 2\varphi. \tag{21}$$

Using the experimental elastic constant data, the helical turn angle and dT_N/dP the values of $\partial I_1/\partial \ln c = 75$ K and $\partial I_2/\partial \ln c = 0$ were determined by Bartholin and Bloch (1968a).

Liu (1962) and Fleming and Liu (1970) regarded the effect of pressure on the magnetic ordering temperature from the band structure point of view. The band structure and generalized conduction electron susceptibility $\chi(\vec{q})$ were calculated for atmospheric pressure and 20 kbar. The shifts of magnetic ordering temperature in Gd ($dT_C/dP = -2.3$ K/kbar), Tb ($dT_N/dP = -1$ K/kbar) and Dy ($dT_N/dP = -0.4$ K/kbar) were determined by means of the calculated variation of $\chi(\vec{q})$. These values are consistent with experimental data. Liu (1962) considered the variation of the Curie temperature in the framework of the RKKY model by means of eq. (10). It was suggested that $d\ln I_0/d\ln V$ lies in the interval

$$-1 < \frac{d\ln I_0}{d\ln V} < 0. \tag{22}$$

The low limit corresponds to the decrease of the Bloch function amplitude of the conduction electrons under increasing volume and the high limit to their independence of the volume. From the experimental value of $d\ln T_C/d\ln V = 1.6$ for Gd Liu (1962) showed that $d\ln N(\mathcal{E}_F)/d\ln V$ lies in the interval $-1.6 < d\ln N(\mathcal{E}_F)/d\ln V < 3.6$. This is consistent with the experimental measurements of $d\ln N(\mathcal{E}_F)/d\ln V$ for some metals, e.g., tantalum, mercury.

The pressure derivatives of the s–f coupling constant I_0 and the conduction electron effective mass m^* can be determined from electrical resistivity measurements in

Table 4
The volume variation of s–f coupling constant Γ_0 and the conduction electron effective mass m^* in Gd, Tb and Dy

Element	$\frac{d \ln \Gamma_0}{d \ln V}$	$\frac{d \ln m^*}{d \ln V}$	Reference
Gd	~2	~ –1	Nikitin et al. (1976a)
Tb	~0.6	–1.8	Nikitin and Bezdushnyi (1984)
Dy	~1.2	~ –0.5	Nikitin et al. (1976a)

paramagnetic state under pressure. According to the RKKY model the resistivity ρ_m which is not dependent on the temperature and is related to disorder in the magnetic spin system has the form (De Gennes 1962, Kasuya 1966, Dekker 1965)

$$\rho_m = \frac{3\pi \Gamma_0^2 m^* \mathcal{G}}{8\hbar e^2 V \mathcal{E}_F}, \tag{23}$$

where e is the electronic charge. By means of eqs. (3), (7) and (23), and taking into account the spherical form of the Fermi surface, one can get the equations for $d \ln T_C / d \ln V$ and $d \ln \rho_m / d \ln V$ (Jayaraman 1978):

$$\frac{d \ln T_C}{d \ln V} = -\frac{4}{3} + 2\left(\frac{d \ln \Gamma_0}{d \ln V}\right)_{H,T} + \left(\frac{d \ln m^*}{d \ln V}\right)_{H,T}, \tag{24}$$

$$\frac{d \ln \rho_m}{d \ln V} = -\frac{1}{3} + 2\left(\frac{d \ln \Gamma_0}{d \ln V}\right)_{H,T} + 2\left(\frac{d \ln m^*}{d \ln V}\right)_{H,T}, \tag{25}$$

From eqs. (24) and (25) the derivatives $d \ln \Gamma_0 / d \ln V$ and $d \ln m^* / d \ln V$ can be determined. Such studies were made on the lanthanide metals and their alloys by Austin and Mishra (1967), Nikitin and Bezdushnyi (1984), Nikitin et al. (1976b). Some of their data are presented in table 4 (see also the review of Jayaraman (1978)). As one can see the experimental values of $d \ln \Gamma_0 / d \ln V$ are inconsistent with the interval proposed by Liu (1962) (see eq. 22). For Dy_xGd_{1-x} alloys it was found that $d \ln \Gamma_0 / d \ln V$ is negative and increases in the absolute value with increasing Gd concentration (Nikitin et al. 1976b). In Tb_xY_{1-x} $d \ln \Gamma_0 / d \ln V$ has a general tendency to decrease in the absolute value with increasing yttrium concentration and reaches a maximum at $x \approx 0.5$ (Nikitin and Bezdushnyi 1984). The observed concentration dependence of $d \ln \Gamma_0 / d \ln V$ and $d \ln m^* / d \ln V$ was related to changes in the electron band structure and to an increase of the amount of 4d- and 5d-electrons after addition of yttrium.

The anisotropy of $\partial I / \partial \ln a_i$ (with I the indirect exchange integral ($I(0)$ or $I(\vec{Q})$, and a_i the a-, b- or c-axis) and the effect of unique axis stresses on the magnetic phase transition temperatures were studied by Bartholin et al. (1971), Landry (1970), Bartholin

Table 5
The dependence of the transition temperature from the paramagnetic to the magnetically ordered state and the indirect exchange integral on the uniaxial mechanical stress and on the lattice parameters in Gd, Tb, Dy and $Tb_{0.5}Gd_{0.5}$

R, alloy	$\frac{\partial T_N}{\partial p_i}; \frac{\partial T_C}{\partial p_i}$ (K/kbar)			$\frac{\partial T_N}{\partial \ln a_i}$ (K)			$\frac{\partial I}{\partial \ln a_i}$ (K)	
	a	*b*	*c*	*a*	*b*	*c*	*a*, *b*	*c*
Gd	0 ± 0.05[a]	0 ± 0.05[a]	-1.55 ± 0.05[a]				12[b], 25[a], 0.5[c]	52[b], 103[a], 59[c]
Tb	0.33[d]	−0.50[d]	−1.22[d]	172[d]	544[d]	965[d]	−12[b], −6.2[c]	100[b], 108[c]
Dy				−22[5]	−22[e]	550[e]	−29[b], 67[c]	115[b], 270[c]
$Tb_{0.5}Gd_{0.5}$	0.34[d]	−0.06[d]	−1.8[d]	188[d]	370[d]	1300[d]		

References
(a) Bartholin and Bloch (1969)
(b) Bartholin et al. (1971)
(c) Nikitin (1989)
(d) Nikitin et al. (1978)
(e) Landry (1970)

and Bloch (1969), Nikitin et al. (1978). The results are shown in table 5. The values of $\partial T_C/\partial p_i$, $\partial T_N/\partial p_i$ and $\partial I/\partial \ln a_i$ were obtained from direct measurements of the unique axis stress effect on the magnetic ordering temperature (Bartholin et al. 1971, Landry 1970, Bartholin and Bloch 1969), and indirectly from the data of the forced magnetostriction and thermal expansion (Nikitin 1989, Nikitin et al. 1978). One can see from table 5 that $\partial T_C/\partial p_i$, $\partial T_N/p_i$ and $\partial I/\partial a_i$ are characterized by sufficient anisotropy and have maximum values for measurements along the *c*-axis. As was shown by Tonegawa (1964) and Chapman and March (1986) such anisotropy can be related to the complex structure of the Fermi surface. Tonegawa (1964) by means of the RKKY model with spherical Fermi surface calculated $\partial I/\partial \ln c = 62\,\mathrm{K}$ and $\partial I/\partial \ln a = 71\,\mathrm{K}$ for gadolinium. The calculated value for $\partial I/\partial \ln a$ is inconsistent with the experimentally measured value (see table 5) and cannot explain the sufficient anisotropy of the forced magnetostriction in Gd measured along the *c*-axis and in the basal plane. To improve the situation Tonegawa used the supposition about the asphericity of the Fermi surface which allowed him to decrease $\partial I/\partial \ln a$ and increase $\partial I/\partial \ln c$ and thus he obtained a better agreement with experimental magnetostriction results. It was also shown that $\partial I/\partial \ln a_i$ strongly depends on the position of the Fermi surface relative to the Brillouin zone boundaries. The discrepancy of the supposition about the sphericity of the Fermi surface with the experimental data on the Curie temperature shift in Gd under pressure was also shown by Chapman and March (1986).

Since a considerable number of studies of the lanthanide metals under pressure is devoted to gadolinium (see table 1) it should be considered more thoroughly. It is known that below T_C gadolinium orders ferromagnetically with magnetic moments aligned along the *c*-axis. Further cooling causes a spin-reorientation transition at temperature T_{sr}, where the magnetic moments rotate from the *c*-axis to the basal plane (Mihai and Franse 1976, Franse and Mihai 1977, Feron and Pauthenet 1969, Corner et al. 1962, Cable and Wollan 1968). The experimental data on T_{sr}, dT_{sr}/dP, the deviation angle ϕ (from the *c*-axis)

and its temperature dependence, obtained by various authors are essentially different. The mechanism of the T_C shift under pressure in Gd was regarded in the framework of the RKKY model and explained by the change of the conduction electron energy spectrum (Liu 1962, Fleming and Liu 1970).

The anisotropy energy in gadolinium can be written as

$$\mathcal{E}_{an} = K_1 \sin^2 \phi + K_2 \sin^4 \phi + \cdots, \tag{26}$$

where ϕ is the angle between the magnetic moment and the c-axis; K_1 and K_2 are the anisotropy constants. The spin-reorientation transition arises when K_1 changes its sign from positive to negative (K_2 is positive over the whole temperature range). Klimker and Rosen (1973) explained the observed linear decrease of T_{sr} under pressure by the change of K_1 via magnetoelastic interaction. The value of $\partial K_1/\partial P$ was calculated by means of a magnetostriction model proposed by Callen and Callen (1965) and Callen (1968) and the experimental magnetostriction data. It was found that $\partial K_1/\partial P$ was positive. The pressure shift of T_{sr} was determined from the expression

$$\frac{dT_{sr}}{dP} = -\frac{\partial K_1/\partial P}{(\partial K_1/\partial T)_{T_{sr}}}. \tag{27}$$

The calculated value $dT_{sr}/dP = -4.9$ K/kbar is in accordance with the measured one. The pressure effect on the anisotropy constants was studied by Mihai and Franse (1976), Franse and Mihai (1977) and Toyama et al. (1969). The experiments showed that $\partial K_1/\partial P > 0$. Franse and Mihai determined the direction of the magnetic easy axis with the help of a torque magnetometer. It was shown that below T_{sr} the magnetic moment lies in the basal plane. At temperature $T'_{sr} = 100$ K the angle ϕ begins to decrease reaching the value of ~ 45° at $T = 0$ K. The temperature interval $\Delta T_{sr} = T'_{sr} - T_{sr}$ expands under pressure and $dT'_{sr}/dP = -1.0$ K/kbar. The observed magnetic behavior of Gd is explained by the complex dependence of K_1 and K_2 on temperature and pressure.

The ac susceptibility of gadolinium single crystals under pressure was measured by Nikitin et al. (1991a, 1992) along the c- and b-axes. A considerable anisotropy of dT_{sr}/dP was found (see table 1). At 140 K an additional anomaly was observed which was shifted by pressure to the low temperature region. It can be related to the deviation of magnetic moments from the basal plane which happens near this temperature (Mihai and Franse 1976, Franse and Mihai 1977).

2.1.3. *Lanthanide nonmagnetic element compounds*

The model of localized magnetic moments with a RKKY exchange interaction is also used for the alloys and compounds of the lanthanide metals with nonmagnetic elements. The distinctive feature of such systems is the increase of the magnetic ordering temperature under pressure in most materials (see table 6).

The cubic Laves phase compounds RAl_2 (R = Gd, Tb, Dy, Ho, Er and Tm), which are ferromagnets, were studied under pressure by Jaakkola and Hannien (1980), Jaakkola (1974), Sato et al. (1988, 1990) and Kratzer et al. (1986). Jaakkola and Hannien (1980)

Table 6
Magnetic phase transition temperatures and their pressure dependence for lanthanide–nonmagnetic element alloys and compounds

Compound	T_C (K)	T_N (K)	$\frac{dT_C}{dP}$, $\frac{dT_N}{dP}$ (K/kbar)
$GdAl_2$	170[a]		0.71[b,c], 0.50[d]
$TbAl_2$	114[a]		0.60[b,c], 0.55[e]
$DyAl_2$	58[a], 61[f]		0.39[b], 0.35[f]
$HoAl_2$	27[a]		0.21[b]
$ErAl_2$	14.5[a]		0.09[b]
$TmAl_2$			0.00[b]
$Gd(Al_{0.95}Co_{0.05})_2$			0.38[d]
$Gd(Al_{0.90}Co_{0.10})_2$			0.25[d]
$Gd(Al_{0.80}Co_{0.20})_2$			0.0[d]
Gd_3Al_2	280[e], 279[f], 279.2[k]		0.36[e], 0.26[f,k]
TbCu		116[a]	0.06[g]
GdCu		140[a], 144[h]	0.27[g], 0.03[h]
TbAg		106[a]	0.38[h]
GdAg		160[a], 140[h]	1.1[g], 0.43[h]
Gd_5Si_4	338[e]		0.29[e]
Dy_5Si_4	136[e]		0.30[e]
Ho_5Si_4	75[e]		0.18[e]
Gd_3In	190[e]		0.98[e]
Dy_3In	121[e]		0.29[e]
Nd_3In	105[e]	0.14[e]	
Gd_2In			0.4±0.2[i]
Tb_2In			0.6±0.2[i]
Dy_2In			0.1±0.3[i]
Ho_2In			0.7±0.2[i]
$GdCu_2$	41[a]		−0.2±0.1[j]
$TbCu_2$	54[a]		−0.1±0.1[j]

References

(a) Taylor and Darby (1972)
(b) Jaakkola and Hannien (1980)
(c) Jaakkola (1974)
(d) Sato et al. (1988)
(e) Sato et al. (1990)
(f) Kratzer et al. (1986)
(g) Yoshida et al. (1987)
(h) Sekizawa et al. (1970)
(i) Szytula and Zach (1988)
(j) Luong and Franse (1981)
(k) Nikitin et al. (1989)

found that they were characterized by a decrease of the ratio $T_p/\mathcal{G}$ and the s–f coupling constant Γ with increasing lattice parameter. This is consistent with the T_C increase under pressure. The dependence of Γ on the interatomic distance was considered in the framework of the modified RKKY model proposed by Robinson et al. (1971). At the same time in $Gd(Al_{1-x}Co_x)_2$ ($x \leqslant 0.2$) compounds T_C decreases with increasing lattice parameter, but dT_C/dP is positive (Sato et al. 1988). The calculation of the

oscillating Ruderman–Kittel function $\phi(2k_F R)$ made by Sato et al. (1988) on the basis of the $LaAl_2$ band structure showed that the nearest neighbor interatomic distance provided the positive exchange and the T_C increase under compression. However the restrictions of the RKKY model and the possible change of the band structure under pressure should be taken into account. Sato et al. (1990) studied the compounds $Tb(Al_{1-x}\ Co_x)_2$ ($x \leqslant 0.1$). The derivatives dT_C/dP are positive for all compounds, but the dependence of dT_C/dP on cobalt concentration has a nonmonotonic character displaying a minimum at $x \approx 0.05$. Sato et al. (1990) related such a different behavior of the $Gd(Al_{1-x}\ Co_x)_2$ and $Tb(Al_{1-x}\ Co_x)_2$ systems to the different crystal field effect of terbium and gadolinium on the conduction electron energy spectrum. The compounds Gd_3Al_2 and Dy_3Al_2 which are also ferromagnetic below T_C were studied under pressure by Sato et al. (1990), Kratzer et al. (1986) and Nikitin et al. (1989). Sato et al. (1990) explained the T_C variation under pressure by a change of the s–f coupling constant (a possible variation of the density of states $N(\mathcal{E}_F)$ was not taken into account).

The compounds RCu, RAg and RAu (R = Tb, Gd) which are antiferromagnetic were investigated under pressure by Yoshida et al. (1987) and Sekizawa et al. (1970). The dependence of T_N on the lattice parameter in the set RCu, RAu, RAg is nonmonotonic and has a minimum for the RAu alloy. This is not consistent with the increase of T_N under pressure observed in RAg and RAu (R = Tb, Gd).

The positive derivatives of the magnetic transition point are observed also in the compounds with indium and silicon: R_3In, R_2In and R_5Si_4 (Sato et al. 1990, Szytula and Zach 1988).

In contrast to the above compounds, RCu_2 (R = Gd, Tb) the magnetic transition temperature decreases under pressure (Luong and Franse 1981). The authors explained this behavior by the decrease of the density of states at the Fermi level caused by the expansion of the conduction electron band under compression. The exchange integral variation was not taken into account.

2.2. *Lanthanide 3d transition metal systems*

2.2.1. *General considerations for the R–Fe, R–Co and R–Ni compounds*

Let us consider the hydrostatic pressure effect on the magnetic ordering temperature of the lanthanide 3d transition metal (TM) compounds which in the case of light lanthanides are ferromagnets and in the case of heavy lanthanides are ferrimagnets (Buschow 1977, Kirchmayer and Poldy 1978). Experimental values of dT_C/dP and $d \ln T_C/d \ln V$ for some compounds were adduced in the review of Jayaraman (1978) and additional data are given in table 7 and figs. 3–5. As one can see from figs. 3–5, in the R–Co and R–Fe compounds dT_C/dP tends to decrease with increasing T_C. However, this tendency is not observed for all R–Ni compounds.

Originally the formula obtained for purely itinerant electron ferromagnets was used to explain the dependence of dT_C/dP on T_C in the lanthanide–3dTM compounds:

$$\frac{dT_C}{dP} = \frac{5}{3}\kappa T_C - \frac{C_\Theta}{T_C}, \tag{28}$$

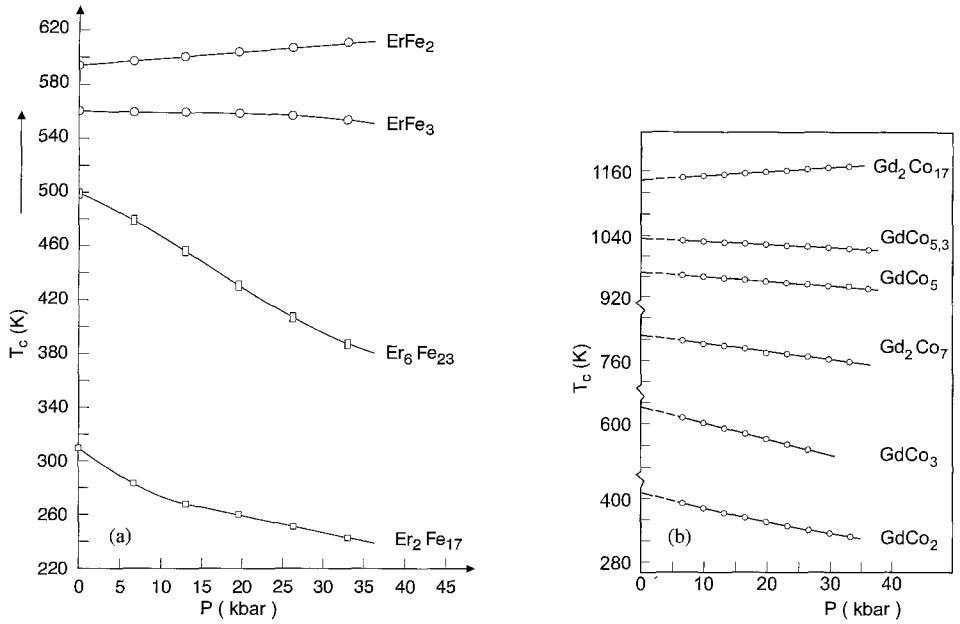

Fig. 3. Pressure dependence of the Curie temperature in Er–Fe (a) and Gd–Co (b) compounds (Brouha and Buschow 1973, Buschow et al. 1977).

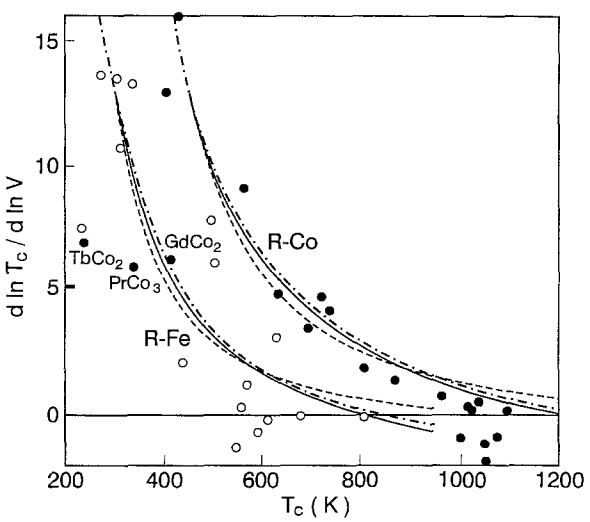

Fig. 4. Dependencies of d ln T_C/d ln V on T_C calculated for R–Fe and R–Co compounds by using eq. (29) (dot-dashed curve), eq. (44) (solid curve), and eq. (45) (dashed curve). Experimental values are shown as solid circles for R–Co and as open circles for R–Fe (Inoue and Shimizu 1984).

or

$$\frac{\mathrm{d}\ln T_C}{\mathrm{d}\ln V} = -\frac{5}{3} + \frac{C'_\Theta}{T_C^2}, \tag{29}$$

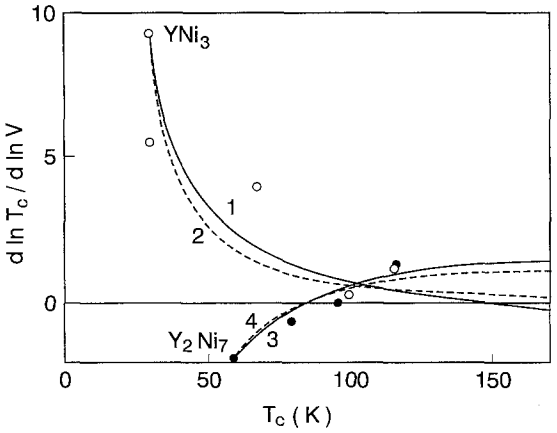

Fig. 5. Dependencies of $d \ln T_C / d \ln V$ on T_C calculated for RNi_3 and R_2Ni_7 by using eq. (44) (solid curves 1 and 3) and eq. (45) (dashed curves 2 and 4), respectively. Experimental values are shown as open circles for RNi_3 and as solid circles for R_2Ni_7 (Inoue and Shimizu 1984).

where $C'_\Theta = C_\Theta / \kappa$,

$$C_\Theta = \frac{5}{6} \kappa \frac{I_{\text{eff}}}{I_b} T_F^2, \tag{30}$$

where

$$T_F = \frac{\sqrt{6}}{\pi k_B} \left[\left(\frac{N_1(\mathcal{E}_F)}{N(\mathcal{E}_F)} \right)^2 - \frac{N_2(\mathcal{E}_F)}{N(\mathcal{E}_F)} \right]^{-1/2}, \tag{31}$$

$N(\mathcal{E}_F)$ is the density of states at the Fermi energy: $N_i(\mathcal{E}) = \partial^i N(\mathcal{E}) / \partial \mathcal{E}^i$, I_{eff} is the interaction between the itinerant electrons after correction for many-body correlation effects, and I_b is the bare interaction. The effect of pressure on the Curie temperature in itinerant electron ferromagnets was calculated by Wohlfarth (1969, 1981), Lang and Ehrenreich (1968), Wagner and Wohlfarth (1981), Shiga (1969), Shimizu (1977, 1978, 1980, 1981) and Kanamori (1963). Shiga (1969) derived eq. (28) with the help of the molecular field theory in which the pressure derivative of T_C was calculated by considering the pressure induced shift of the pole in the static spin susceptibility. The following main assumptions were made. Firstly, when the crystal is compressed the 3d magnetic band widens uniformly so that the dependence of $N(\mathcal{E}_F)$ on the bandwidth W has the form

$$N(\mathcal{E}_F) = N(\mathcal{E}_F, W) = \frac{N_W(\mathcal{E}_F, W)}{W}, \tag{32}$$

where $N_W(\mathcal{E}_F, W)$ does not depend on W if the number of magnetic electrons does not change. The second proposition is that the bandwidth volume dependence is given by Heine's (1967) formula

$$W \approx V^{-5/3}. \tag{33}$$

Table 7
The Curie temperatures and their pressure dependence for some lanthanide–3dTM compounds

Compound	T_C (K)	$\frac{dT_C}{dP}$ (K/kbar)	$\frac{d \ln T_C}{d \ln V}$
Y_6Fe_{23}	495[a]	−4[a], 0.1[b]	
Dy_2Fe_{17}	371[c]	−6.0[c]	20.2[c]
Y_2Fe_{17}	320[j]	−4.7[j]	
YFe_2	545[a]	5[a]	−0.1[d]
$Gd_{0.9}Y_{0.1}Co_2$		−2[h]	
$Gd_{0.8}Y_{0.2}Co_2$	350[c]	−2.3[e]	
$Gd_{0.6}Y_{0.4}Co_2$		−2.1[e]	
$Gd_{0.4}Y_{0.6}Co_2$		−2[e]	
Gd_4Co_3	225[f]	−0.7[f]	2.2[f]
$DyCo_2$	135[i]	−2.1[i]	
$GdNi_5$	32[f]	−0.03[f]	1.4[f]
Y_2Ni_7	59[f], 58[g]	0.08[f], −0.46[g]	−1.9[f]
Gd_2Ni_7	116[f]	−0.11[f]	1.3[f]
Tb_2Ni_7	98[f]	0.00[f]	0[f]
Dy_2Ni_7	80[f]	0.03[f]	−0.6[f]
Nd_2Ni_7	93[f]	0.08[f]	−1.2[f]
$GdNi_3$	115[f]	−0.10[f]	1.2[f]
$TbNi_3$	100[f]	−0.02[f]	0.3[f]
$DyNi_3$	67[f]	−0.20[f]	4.0[f]
YNi_3	30[g]	−0.25[g]	
$GdNi_2$	85[f]		0[f]
GdNi	71[6]	−0.19[f]	2.2[f]
Y_2Ni_{17}	149[g]	−0.45[g]	
$GdMn_2$	107[i] (T_N)	−5.0[i]	

References

(a) Brouha and Buschow (1973)
(b) Bloch and Chaisse (1972)
(c) Radwanski et al. (1985)
(d) Buschow et al. (1977)
(e) Yoshida et al. (1988)
(f) Jaakkola et al. (1983)
(g) Beille et al. (1983)
(h) Murata et al. (1995)
(i) Kamarad et al. (1995)
(j) Nikitin et al. (1991c).

The third assumption is that the dependence of I_{eff} on W is described by Kanamori's (1963) formula

$$I_{eff} = \frac{I_b}{1 + \frac{\gamma_k I_b}{W}}, \tag{34}$$

where I_b and the constant γ_k do not depend on the volume.

The curves obtained by fitting eq. (29) to experimental data on the lanthanide–3dTM compounds are shown in fig. 4 by dot-dashed lines. The constant C'_Θ is equal

to $2.9 \times 10^6\,K^2$ for R–Co and $1.25 \times 10^6\,K^2$ for R–Fe compounds (Brouha et al. 1974). As one can see from fig. 5 for the R–Ni compounds eqs. (28) and (29) do not hold.

Subsequently for the lanthanide–3dTM compounds the so-called s–d model was used in which the coexistence of localized spin and collective electrons was assumed. It was proposed by Takahashi and Shimizu (1965) for dilute Pt–Fe, Pt–Co, Pd–Fe and Pd–Co alloys and by Bloch and Lemaire (1970) for the RCo_2 compounds. According to this model the lanthanide ions have a localized magnetic moment and the transition metal is an exchange-enhanced paramagnet. The molecular field acting on the collective electron system from the lanthanide ions induced in it the magnetic moment. The s–d model adequately explains the magnetic ordering temperatures of RCo_2, R_4Co_3, RNi_2 and RNi_5 which become paramagnetic over the whole temperature range if the lanthanide metal is substituted by the nonmagnetic element yttrium (Wohlfarth 1979, Jaakkola et al. 1983).

The transition temperature to the magnetically ordered state can be written as (Bloch and Lemaire 1970)

$$T_C = \mathcal{G}\frac{N\mu_B}{3k_B}[2I_{RR} + I_{RM}^2\chi_d(T_C)], \tag{35}$$

where μ_B is the Bohr magneton; χ_d, the susceptibility of collective d-electrons; and I_{RR} and I_{RM} are the exchange interaction integrals between lanthanide ions, and between lanthanide and TM ions, respectively (M = 3dTM). Voiron et al. (1973) derived the equation for $d \ln T_C / d \ln V$ by differentiation of eq. (35) with respect to the volume:

$$\frac{d \ln T_C}{d \ln V} = \frac{I_{RM}^2\chi_d(T_C)}{2I_{RR} + I_{RM}^2\chi_d(T_C)} \frac{d \ln \chi_d(T_C)}{d \ln V}. \tag{36}$$

It was assumed that I_{RM} and I_{MM} did not change under pressure and the pressure shift of T_C is related to the variation of the susceptibility χ_d. Using eq. (36) gave good results for dT_C/dP in $GdCo_2$ and $TbCo_2$ ($d \ln \chi_d / d \ln V$ was equal to 14 ± 2 (Voiron et al. 1973)) and the concentration dependence of dT_C/dP in the $Gd_{1-x}Y_xCo_2$ and $Gd(Co_{1-x}Ni_x)_2$ compounds (Yoshida et al. 1988).

Shimizu (1977, 1978, 1980, 1981) regarded the magnetovolume effects in the framework of a thermodynamic approach with the help of mean field and band models. He expanded the free energy in a power series of magnetization and relative volume change $\Delta V/V$. The Curie temperature shift under compression was determined from the position of the spin susceptibility pole $\chi^{-1}(T, P) = 0$. From this condition the formula for calculating dT_C/dP was derived (Inoue and Shimizu 1985):

$$\frac{dT_C}{dP} = -\left(\frac{\partial\chi^{-1}/\partial P}{\partial\chi^{-1}/\partial T}\right)_{T_C}. \tag{37}$$

Inoue and Shimizu (1980) wrote down the spin susceptibility $\chi(T, V)$ in the form

$$\chi(T, V) = \frac{\chi_d + \chi_s + 2n_{RM}\chi_d\chi_s}{1 - n_{RM}^2\chi_d\chi_s}, \tag{38}$$

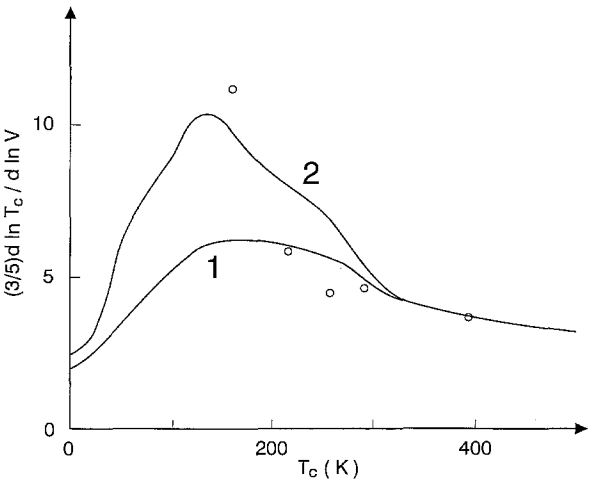

Fig. 6. Dependencies of $\frac{3}{5}\mathrm{d}\ln T_C/\mathrm{d}\ln V$ on T_C for (R–Y)Co_2 alloys. Solid curves are calculated by eq. (41). Curve 1: $\xi = -1$; $\xi_1 = 1.4$; $L = 52$. Curve 2: $\xi = -1$; $\xi_1 = -2.3$; $L = 0$. Experimental values of (Gd–Y)Co_2 are shown by open circles (Inoue and Shimizu 1980, Brouha et al. 1974, Leontiev et al. 1992).

where χ_s is the susceptibility of the lanthanide spin system,

$$\chi_s^{-1} = \frac{T - n_{RR}C_S}{C_S}, \tag{39}$$

C_S is the Curie constant of the lanthanide ions, $C_S = Ng_J\mu_B J(J+1)/3k_B$,

$$\chi_d = \frac{\chi_{d0}(T)}{1 - \alpha_M\chi_{d0}(T)}, \tag{40}$$

where $n_{RM} = 2I_{RM}/g_J^2\mu_B^2$ and $n_{RR} = 2I_{RR}/g_J^2\mu_B^2$ are the molecular field constants of the R–TM and R–R interactions, α_M is the molecular field constant in the d-electron system (it is proportional to I_{eff}), and $\chi_{d0}(T)$ is the magnetic susceptibility of d-electrons without exchange interactions.

Using eqs. (37) and (38) and the models proposed by Lang and Ehrenreich (1968), Kanamori (1963), Heine (1967), the equation for the pressure derivative of the Curie temperature in the s–d model was derived (Inoue and Shimizu 1980)

$$\frac{\mathrm{d}\ln T_C}{\mathrm{d}\ln V} = -\frac{5}{3} + \frac{5}{3}\frac{(I_{eff}/I_b)\alpha_M\chi_d(T_C) + L(\xi+1)\chi_d^{-1}(T_C) + 2(\xi_1+1)}{T_C\chi_d(T_C)\frac{\partial}{\partial T}\chi_d^{-1}(T_C) + L\chi_d^{-1}(T_C) + 1}, \tag{41}$$

where $L = 2I_{RR}/I_{RM}^2$, $\xi = \frac{3}{5}\partial\ln I_{RR}/\partial\ln V$ and $\xi_1 = \frac{3}{5}\partial\ln I_{RM}/\partial\ln V$.

In eq. (41) the variation of all three exchange parameters α_M, I_{RR} and I_{RM} is taken into account. In the absence of localized magnetic moments eq. (41) turns into eq. (29) for an itinerant ferromagnet. If $T_C \to \infty$ then eq. (41) and eq. (29) give $\mathrm{d}\ln T_C/\mathrm{d}\ln V = -5/3$. However for $T_C \to 0$ it follows from eq. (29) that $\mathrm{d}\ln T_C/\mathrm{d}\ln V = \infty$. At the same time eq. (41) leads to a finite value at $T_C \to 0$. The latter means that $\mathrm{d}T_C/\mathrm{d}P$ is proportional to T_C or $-T_C$ at $T_C \to 0$.

The results of calculations using eq. (41) for the (Gd–Y)Co_2 compounds are shown in fig. 6 (Inoue and Shimizu 1980). The parameters L and α_M used in the calculations

were determined from experimental data of $\chi_d(T)$ for YCo_2 and $\chi(T)$ for $GdCo_2$. The low temperature maximum is due to the maximum of the experimental dependence of $\chi_d(T)$ for YCo_2. In fig. 6 the experimental points for compounds $(Gd_xY_{1-x})Co_2$ are also shown (Brouha et al. 1974, Leontiev et al. 1992). As one can see, the character of the calculated dependence of $d \ln T_C / d \ln V$ on T_C is confirmed by experiment, which was also observed for the dilute alloys PdFe, PdCo, PdNi, PtFe and PtCo (Inoue and Shimizu 1980).

Originally, Inoue and Shimizu (1980) regarded the alloys with paramagnetic collective d-electrons over the whole temperature range. Subsequently this model was used also for lanthanide–3dTM alloys with ferromagnetic order in the collective electron system (Inoue and Shimizu 1984, 1986). The following two types of d-electron susceptibility temperature dependences were used:

$$\chi_d(T) = \frac{C_d}{(T - T_d)}, \tag{42}$$

$$\chi_d(T) = [\chi_{d0}^{-1}(0)(1 + A_T T^2) - \alpha_M]^{-1}, \tag{43}$$

where C_d is the Curie constant, T_d is the Curie temperature of the d-electron system, and A_T is a constant. The R–R interaction was not taken into account because of its small value compared with R–M and M–M interactions. The following two equations were derived for $d \ln T_C / d \ln V$

$$\frac{d \ln T_C}{d \ln V} = \frac{\frac{d \ln T_d}{d \ln V} + \frac{10}{3}\xi_1 \left(\frac{T_C}{T_d} - 1\right)}{2\frac{T_C}{T_d} - 1}, \tag{44}$$

$$\frac{d \ln T_C}{d \ln V} = \frac{2\frac{d \ln T_d}{d \ln V} + \frac{5}{3}(2\xi_1 - 1)\left(\left(\frac{T_C}{T_d}\right)^2 - 1\right)}{3\left(\frac{T_C}{T_d}\right)^2 - 1}, \tag{45}$$

where $d \ln T_d / d \ln V$ is the relative change of the d-electron system Curie temperature with the relative volume change, which could be calculated by using eq. (29). In figs. 4 and 5 the results of the calculations of $d \ln T_C / d \ln V$ on T_C for various compounds R–Co, R–Fe, R_2Ni_7 and RNi_3 using eqs. (44) and (45) are shown. For R–Ni compounds the experimental values of T_d and $d \ln T_d / d \ln V$ for Y_2Ni_7 and YNi_3 were used (Jaakkola et al. 1983, Beille et al. 1983). For R–Co and R–Fe T_d were chosen to be 450 and 300 K, and $d \ln T_d / d \ln V$ was calculated by eq. (29) with experimental values of C'_Θ from Brouha et al. (1974). The value of $\partial \ln I_{RM} / \partial \ln V$ which was regarded as an adjustable parameter for R–Co and R–Fe was equal to –3.5 for calculations by eq. (44) and zero using eq. (45). For RNi_3 and R_2Ni_7 compounds $\partial \ln I_{RM} / \partial \ln V$ are 1 and 2.5, respectively, for calculations by eq. (44); and 1 and 3, respectively, when eq. (45) is used. Figures 4 and 5 show that eqs. (44) and (45) describe the experimental data of $d \ln T_C / d \ln V$ for R–Co

and R–Fe compounds reasonably well with the itinerant and s–d models giving practically equal results. Indeed, $d \ln T_C / d \ln V$ in eq. (29) depends only on T_C which is sufficiently affected by the lanthanide subsystem. However, the dependence of $d \ln T_C / d \ln V$ on T_C for R_2Ni_7 alloys can be explained only by the s–d model.

The compound Y_2Ni_7 exhibits an interesting behavior. Between two magnetic transition temperatures T_S (= 6 K) and T_C (= 58 K) it is a ferromagnet and outside this interval a paramagnet (Beille et al. 1983). Such a behavior was related to the negative coefficient of the fourth-order term in the expansion of the free energy in a power series of magnetization (Shimizu 1981). Under pressure the ferromagnetic temperature range gets narrow since dT_C/dP is negative (see table 7) and dT_S/dP is positive (= 0.52 K/kbar). The decrease of T_C and the increase of T_S was explained by Inoue and Shimizu (1985) in the framework of an itinerant magnetism model taking into account thermal spin fluctuations.

Leontiev et al. (1988) used the s–d model to explain the observed nonmonotonic dependence of $d \ln T_C / d \ln V$ on the composition in the $Dy(Co_{1-x}Al_x)_2$ and $Tb(Co_{1-x}Al_x)_2$ compounds. It was shown that the observed maximum could be related to the Fermi level passing through a local maximum on the density of state curve $N(\mathcal{E})$ when cobalt was substituted by aluminum.

2.2.2. *First-order transitions in RCo_2*

It is known that in RCo_2 alloys for R = Gd and Tb the phase transition to the magnetically ordered state is of the second-order and for R = Dy, Ho and Er a first-order transition is observed (Buschow 1977, Kirchmayer and Poldy 1978). The first-order transition in RCo_2 was explained by Bloch et al. (1975) by using the s–d model and the expansion of the free energy in a power series on d-electron magnetization. The negative sign of the fourth-order term coefficient in the free energy expansion was regarded as an indication of the first-order transition. An analogous approach was used by Shimizu (1981) for itinerant ferromagnets. Inoue and Shimizu (1982b) expanded the free energy in a power series of the total magnetization which is more correct than the expansion in a power series of just the d-electron magnetization

$$F = \tfrac{1}{2}C_1(T)\sigma^2 + \tfrac{1}{4}C_3(T)\sigma^4 + \tfrac{1}{6}C_5(T)\sigma^6 + \cdots, \tag{46}$$

where $C_1(T)$ is equal to the inverse magnetic susceptibility,

$$C_3 = [b_3(T)(\chi_d^{-1}(T) + n_{RM})^4 + a_3(T)(\chi_S^{-1}(T) + n_{RM})^4]/B; \tag{47}$$

$$C_5 = [b_5(T)(\chi_d^{-1}(T) + n_{RM})^6 + a_5(T)(\chi_S^{-1}(T) + n_{RM})^6]/B^6 - [3b_3(T)(\chi_d^{-1}(T) + n_{RM}) + a_3(T)(\chi_S^{-1}(T) + n_{RM})^3]^2/B^7; \tag{48}$$

$$B = \chi_d^{-1}(T) + \chi_S^{-1}(T) + 2n_{RM}; \tag{49}$$

where a_3 and a_5, and b_3 and b_5 are the coefficients in the expansion of the free energy in a power series of 3d-electrons and R-subsystem magnetization, respectively, and σ is

the magnetization. The coefficients $a_3(T)$ and $a_5(T)$ are determined by the band structure parameters, and $b_3(T)$ and $b_5(T)$ by the mechanical momentum of R ions. The temperature of the second-order transition T_C is determined from the condition $C_1(T_C) = 0$ and that of the first-order transition T_C' from the equation (Inoue and Shimizu 1982b)

$$16C_5(T_C')C_1(T_C')/3C_3^2(T_C') = 1, \tag{50}$$

where $C_1(T_C') > 0$, $C_3(T_C') < 0$ and $C_5(T_C') > 0$ for all temperatures. By means of eq. (50) and some simplifications the volume change of T_C' is obtained as

$$\frac{\mathrm{d}\ln T_C'}{\mathrm{d}\ln V} = -\frac{\frac{\mathrm{d}\ln T_C}{\mathrm{d}\ln V} + \left(2\frac{\partial \ln|C_3(T_C')|}{\partial \ln V} - \frac{\partial \ln C_5(T_C')}{\partial \ln V}\right)\left(\frac{T_C'}{T_C} - 1\right)}{\left(2\frac{\partial \ln|C_3(T_C')|}{\partial \ln T} - \frac{\partial \ln C_5(T_C')}{\partial \ln T}\right)\left(\frac{T_C'}{T_C} - 1\right) - 1}, \tag{51}$$

where $\mathrm{d}\ln T_C/\mathrm{d}\ln V$ was obtained for the second-order magnetic phase transition from the s–d model (see eq. 36). On the basis of eq. (51) Inoue and Shimizu (1982b) showed that the value of $\mathrm{d}\ln T_C'/\mathrm{d}\ln V$ should be larger than that of $\mathrm{d}\ln T_C/\mathrm{d}\ln V$. This is confirmed by experiment, since the values of $\mathrm{d}\ln T_C/\mathrm{d}\ln V$ calculated by eq. (36) and the experimental data ($\mathrm{d}\ln T_C/\mathrm{d}\ln V$ is 4.8, 5.9 and 3.7 for $DyCo_2$, $HoCo_2$ and $ErCo_2$, respectively) are less than the experimentally observed values of $\mathrm{d}\ln T_C'/\mathrm{d}\ln V$ (6, 9, 13 for $DyCo_2$, $HoCo_2$ and $ErCo_2$, respectively) (Inoue and Shimizu 1982b).

Inoue and Shimizu (1988), in the framework of the model described above, calculated the volume dependence of the transition temperature to the magnetically ordered state at the boundary between the first- and second-order transition, see fig. 7. Thus, pressure can alter the order of the magnetic phase transition. Such a behavior can be explained by the decrease of the molecular field acting on the 3d-electron subsystem which causes the reduction of the Co moment (Inoue and Shimizu 1988).

According to fig. 7, $ErCo_2$ with $T_C = 33$ K (Bloch et al. 1971) lies on the boundary between the first and the second-order transition and therefore should reveal the transition order change at low pressure. On the basis of the experimental data on the pressure dependence and compressibility of $HoCo_2$ (at ambient pressure $T_C \approx 77$ K) (Voiron and Bloch 1971) one can estimate from fig. 7 that the change of the magnetic transition order in this compound should occur at ~ 18 kbar.

Kamarad et al. (1995) measured the temperature dependence of the relative volume change in $DyCo_2$ and $GdMn_2$. The volume jump at the transition temperature to the magnetically ordered state at atmospheric pressure (in $DyCo_2$ $\Delta V/V \approx 2.2\times10^{-3}$ at $T_C = 135$ K), which is characteristic of the first-order transition, was transformed under a pressure of 10 kbar to a smooth increase with a much smaller value of $\Delta V/V$. This can point to the change of the transition order from first to second. However, the experimental point corresponding to the Curie temperature of $DyCo_2$ under 10 kbar lies inside the region of the first-order transition (see fig. 7) as was calculated by Inoue and Shimizu (1988).

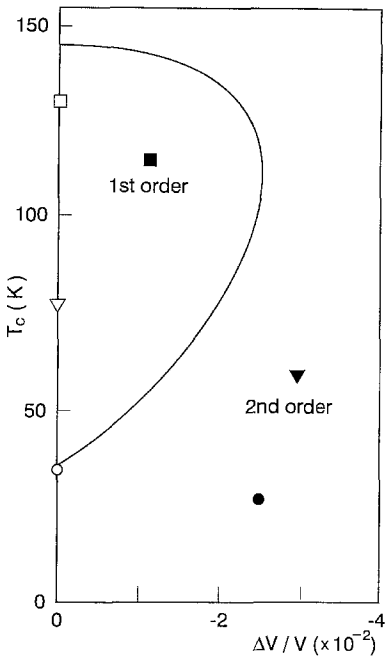

Fig. 7. Volume dependence of the magnetic transition temperature on the boundary between the first- and second-order transitions (Inoue and Shimizu 1988). The points correspond to the experimental values of T_C at atmospheric (open symbols) and high hydrostatic pressure (solid symbols): open, solid circles, $ErCo_2$ (P = 25 kbar); open, solid inverted triangles, $HoCo_2$ ($P \approx$ 30 kbar) (Voiron and Bloch 1971); open, solid squares, $DyCo_2$ (P = 10 kbar) (Kamarad et al. 1995).

2.2.3. *R_2Fe_{17} compounds*

Although in the R–Fe compounds the general tendency to a change of the sign of dT_C/dP from negative to positive with increasing T_C as predicted by eq. (28) is observed (see fig. 3), for the R_2Fe_{17} compounds this dependence is in poor agreement with experiment. The model of localized magnetic moments and the mean field approximation give good results for the description of the magnetic properties of the R–Fe compounds (Belorizky et al. 1987, Pszczola and Krop 1986, Radwanski 1986) due to the localization of the Fe magnetic moments. The R_2Fe_{17} compounds are characterized essentially by magnetovolume effects which are manifested in large values of the volume magnetostriction and dT_C/dP (Brouha and Buschow 1973, Gignoux et al. 1979, Radwanski et al. 1988, Radwanski and Krop 1983, Radwanski 1985). This was related to the properties of the Fe subsystem and the Fe–Fe exchange interactions which mainly determine the magnetic behavior and the Curie temperature. The value of $dI_{Fe-Fe}/d \ln V$ obtained by Radwanski et al. (1985) from the variation of T_C with unit cell volume in R_2Fe_{17} was 7×10^{-4} erg (the integral of the Fe–Fe exchange interaction I_{Fe-Fe} is 3.1×10^{-15} erg in Lu_2Fe_{17} and 5.3×10^{-15} erg in Gd_2Fe_{17}). Radwanski et al. (1988) proposed that the local environment of the Fe atoms in R_2Fe_{17} resembles that in γ-Fe.

The existence of a noncollinear antiferromagnetic helical structure in Lu_2Fe_{17} which has the smallest unit cell volume in the R_2Fe_{17} set of compounds was explained by the negative Fe–Fe exchange interactions (Gignoux et al. 1979, Givord and Lemaire 1974). According to the work of Givord and Lemaire (1974) negative and positive interactions

between Fe ions in R_2Fe_{17} can exist depending on the ion position in the crystal lattice and the interatomic distance. The magnetic properties of such systems should be very sensitive to the volume variation.

Nikitin et al. (1991c) studied the influence of pressure on the magnetization and ac susceptibility of Y_2Fe_{17}. It was shown that the magnetic behavior of the compound under pressure indicated the appearance of a helical type noncollinear spin structure. A thermodynamic approach with the thermodynamic potential in the form of the Ginzburg–Landau functional was used to describe the origin of the noncollinear magnetic structure and the magnetic temperature–pressure phase diagram. Beuerle and Fähnle (1992) calculated $\mathrm{d}\ln T_C/\mathrm{d}P = -1.27\times10^{-2}\,\mathrm{kbar}^{-1}$ for Y_2Fe_{17} by means of the linear muffin-tin orbital theory in atomic sphere approximation. This value is consistent with the experimental value $-1.47\times10^{-2}\,\mathrm{kbar}^{-1}$ (Nikitin et al. 1991c), $-1.5\times10^{-2}\,\mathrm{kbar}^{-1}$ (Buschow et al. 1977).

3. Influence of static pressure on the magnetic phase diagrams and magnetic order–order phase transitions

At low temperatures in heavy lanthanides magnetic order–order phase transitions occur. In particular, in Tb, Dy and Ho at T_C a transition from a helical antiferromagnetic phase to a ferromagnetic state (FM) is observed. According to the models of Miwa and Yosida (1961), Cooper (1969), Elliott (1961) and Evenson and Liu (1969) the exchange interaction between neighboring spin layers stabilizes the helical structure and the transition to the ferromagnetic phase is caused by the basal plane anisotropy and the magnetoelastic energy increase upon cooling. All these values are affected by the interatomic distance variation. In the model of Herpin and Meriel (1961) and Enz (1960) the exchange interaction which favors a ferromagnetic alignment of spins in the nearest neighbor basal planes competes with the antiferromagnetic exchange interaction between the next-nearest planes (anisotropy and magnetoelastic energies are not taken into account). This leads to the appearance of a helical spin structure whose stability is determined by the relation

$$\frac{I_1}{|I_2|} \leqslant 4. \tag{52}$$

The values of $\partial I_1/\partial \ln c$ and $\partial I_2/\partial \ln c$ obtained experimentally by Bartholin and Bloch (1968a) allow one to make the conclusion that $I_1/|I_2|$ decreases under pressure. This should stabilize the antiferromagnetic phase and move the temperature T_C toward low temperatures which is consistent with the sign of the experimentally measured value of $\mathrm{d}T_C/\mathrm{d}P$ in the heavy lanthanides and their alloys (see tables 1–3). So one may propose that the increase of the anisotropy and the magnetoelastic energies on cooling is compensated under pressure by the variation of the exchange interaction.

The stabilization of the helical structure is displayed as an increase under pressure of the maximum value of the critical field H_{cr}^{max} necessary to destroy the helical structure and

in the expansion of the temperature interval $\Delta T_{NC} = T_N - T_C$ corresponding to the range of existence of this structure. Bykhover et al. (1990), Nikitin and Bezdushnyi (1991), Nikitin et al. (1991d,e) and Nikitin and Leontiev (1987) studied the influence of pressure on the magnetic phase diagrams of Tb, Dy and their alloys $Tb_{0.5}Dy_{0.5}$, $Tb_{0.91}Dy_{0.09}$ and $Tb_{0.835}Y_{0.165}$. The magnetic phase diagram under pressure preserves its form by shifting to the low temperature region.

Among the studied lanthanide metals the maximum effect of the pressure on H_{cr}^{max}, T_C and T_N occurs in terbium, where $d\Delta T_{NC}/dP = 0.38$ K/kbar (according to neutron diffraction data $d\Delta T_{NC}/dP = 0.3$ K/kbar (Umebayashi et al. 1968) and 0.52 K/kbar (Kawano et al. 1992)) and H_{cr}^{max} increases from 180 Oe at atmospheric pressure to 380 Oe at 10 kbar (Bykhover et al. 1990). The increase of H_{cr}^{max} under pressure was also observed in $Tb_{0.91}Y_{0.09}$ and $Tb_{0.835}Y_{0.165}$ by Nikitin and Bezdushnyi (1991). In Dy the pressure practically does not affect H_{cr}^{max} and only increases the value of ΔT_{NC}. According to Herpin and Meriel (1961), the value of H_{cr} is determined by the formula

$$H_{cr} = -7.76\mu_s I_2 \sin^4(\varphi/2), \tag{53}$$

where μ_s is the saturation magnetic moment of the lanthanide ion. Differentiation of eq. (53) on pressure gives

$$\frac{\partial \ln H_{cr}}{\partial P} = \frac{\partial \ln I_2}{\partial P} + 2\frac{\partial \varphi}{\partial P}\cot(\varphi/2). \tag{54}$$

Experiments show that in heavy lanthanide metals $\partial \ln I_2/\partial P = 0$ and $\partial\varphi/\partial P > 0$ (Bartholin and Bloch 1968a, Umebayashi et al. 1968), which is consistent with the observed increase of H_{cr} under pressure in Tb and Tb–Y, Tb–Dy alloys. It follows from eq. (54) that the sensitivity of H_{cr} to the change of the interatomic distances should increase for the lanthanides with a large period to the helical structure. This agrees with the experimentally observed value of $\partial H_{cr}^{max}/\partial P$ in terbium which has the minimum $\varphi(\sim 20°)$ near T_N in the heavy lanthanide metals set (in Dy $\varphi \approx 40°$) (Taylor and Darby 1972). Dilution of terbium by yttrium leads to an increase of the value of φ (Child et al. 1965) and, as was shown by Nikitin and Bezdushnyi (1991), to a decrease of $\partial H_{cr}^{max}/\partial P$.

The anomaly that was observed in the magnetic phase diagram of Tb at 223 K was related to the commensurate magnetic structure existing at this temperature (Nikitin et al. 1991d). The helical turn angle here is equal to 18° (Drillat et al. 1984) which corresponds to the coincidence of the basal plane magnetic moment with easy magnetization axis every 10 layers (5 lattice constants along the c-axis). At 10 kbar no peculiarities caused by commensurability were observed.

Elliott and Wedgewood (1964), Jackson and Doniach (1969) and Dzialoshinski (1964a,b) explained the existence of a phase transition from the helical to the ferromagnetic state by the change of the energy spectrum of the conduction electrons as a result of their interaction with the spins of magnetic ions. Kaino and Kasuya (1981) point to the nonlinear s–f exchange interaction as a possible mechanism of the helicoidal antiferromagnet–ferromagnet (HAFM–FM) transition. Pressure can affect the

Fermi surface structure, the energy spectrum of the conduction electrons and the s–f exchange interaction parameter which in turn will affect T_C and the characteristics of the helical structure (φ, H_{cr}). A more thorough discussion of this question will be presented in the next section.

4. The effect of static pressure on the spin structures of the lanthanide metals

Neutron diffraction measurements under hydrostatic pressure were made on Tb, Ho and Er by Umebayashi et al. (1968), Kawano et al. (1992, 1993, 1995) and Achiwa et al. (1988). The results on the temperature dependence of the helical turn angle φ and wave vector $\vec{Q}$ of the magnetic structure at various pressures are shown in figs. 8–10. As one can see, φ increases in Tb and Ho under pressure: in accordance with the data of Umebayashi et al. (1968) $\partial \ln \varphi/\partial P$ is equal to $2.3 \times 10^{-3}\,\text{kbar}^{-1}$ at $T = T_N - 36.5\,\text{K}$ in Ho and to $2\times10^{-2}\,\text{kbar}^{-1}$ at $T = T_N - 4\,\text{K}$ in Tb, and according to Kawano et al. (1992) $\partial \ln \varphi/\partial P = 1.2\times10^{-2}\,\text{kbar}^{-1}$ at the same temperature for Tb. In Tb an increase of the temperature range of the existence of the helical spin structure $\Delta T_{NC} = T_N - T_C$ is observed with $\mathrm{d}\Delta T_{NC}/\mathrm{d}P = 0.52\,\text{K/kbar}$ (Kawano et al. 1992).

Lee (1964) and Landry (1967) considered the pressure influence on the turn angle φ of the helical antiferromagnetic spin structure in the framework of the model proposed by Herpin and Meriel (1961) and Enz (1960). The free energy of the crystal was assumed to be:

$$F = -\left[\left(I_1 + \frac{\partial I_1}{\partial \ln c}\epsilon_{33}\right)\cos\varphi + \left(I_2 + \frac{\partial I_2}{\partial \ln c}\epsilon_{33}\right)\cos 2\varphi\right]\sigma^2 + \frac{E_c\epsilon_{33}^2}{2} + p_c\epsilon_{33}, \tag{55}$$

where the first term expresses the exchange energy, the second term is the axial strain energy, the third term the external axial stress energy; E_c, the Young's modulus along the c-axis; and ϵ_{33} and p_c are the strain and stress, respectively, along the c-axis. Minimization

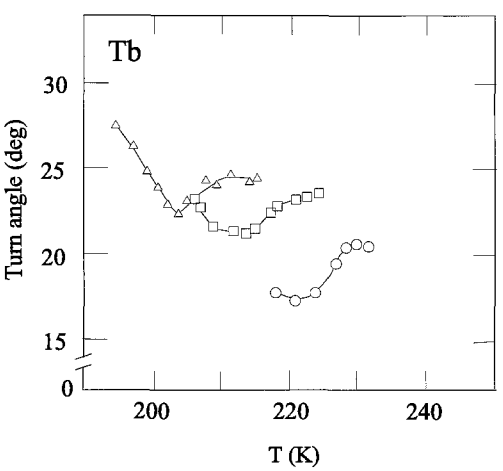

Fig. 8. Temperature dependence of the helical turn angle in terbium. Open circles, ambient pressure; open squares, 10.3 kbar; open triangles, 19.3 kbar (Kawano et al. 1992).

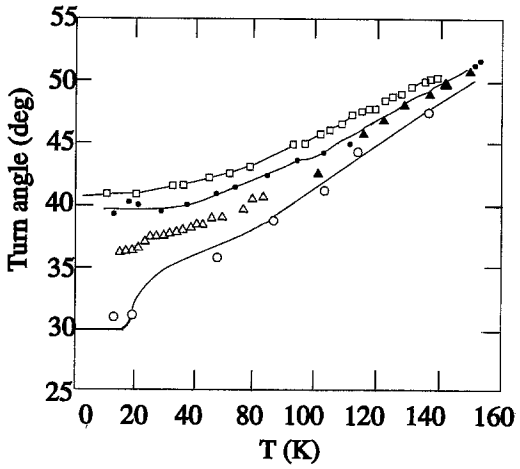

Fig. 9. Temperature dependence of the helical turn angle in holmium. Open circles, ambient pressure; solid triangles, 6 kbar; open triangles, 7 kbar; solid circles, 16 kbar; open squares, 21 kbar. The data at ambient pressure (open circles) are from Koehler et al. (1966) and 6 kbar (solid triangles) from Umebayashi et al. (1968). The figure is taken from Achiwa et al. (1988).

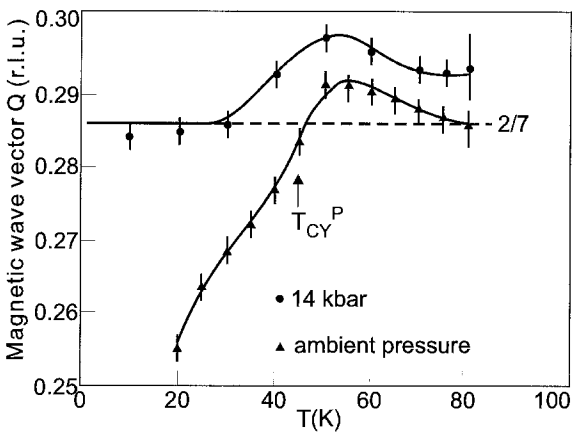

Fig. 10. Temperature dependence of the magnetic wave vector $\vec{Q}$ in erbium (in units of c^*). Solid triangles, ambient pressure; solid circles, 14 kbar (Kawano et al. 1995).

of eq. (55) gives the following expression, which allows one to calculate the variation of the helical turn angle caused by the c-axis strain

$$\cos\varphi = -\frac{I_1 + \frac{\partial I_1}{\partial \ln c}\epsilon_{33}}{4\left(I_2 + \frac{\partial I_2}{\partial \ln c}\epsilon_{33}\right)}. \tag{56}$$

It was assumed that the variation of φ with temperature was due to the magnetostriction deformations. From the experimental dependence $\varphi(T)$ the $\partial I_1/\partial \ln c \approx 1500\,\mathrm{K}$ and $\partial I_2/\partial \ln c \approx 340\,\mathrm{K}$ were determined (Landry 1967). These values differ considerably from the values of $\partial I_1/\partial \ln c = 75\,\mathrm{K}$ and $\partial I_2/\partial \ln c = 0$ obtained by Bartholin and Bloch

(1968a) from the dT_C/dP data. From eq. (56) one can obtain the expression for $d\varphi/dP$ as

$$\frac{d\varphi}{dP} = -(2s_{13}+s_{33})\frac{I_2\frac{\partial I_1}{\partial \ln c} - I_1\frac{\partial I_2}{\partial \ln c}}{4\left(I_2+\frac{\partial I_2}{\partial \ln c}\epsilon_{33}\right)^2 \sin\varphi}, \tag{57}$$

where s_{ij} are the elastic compliance constants. For Dy calculations of $d\ln\varphi/dP$ by means of eq. (57) and experimental data on φ and s_{ij} near T_N give two different values of $d\ln\varphi/dP$ ($\sim 10^{-3}$ and 4×10^{-5}) for two different experimental values of $\partial I_i/\partial \ln c$ obtained by Landry (1967) and Bartholin and Bloch (1968a), respectively.

De Gennes and Saint James (1963) explained the temperature variation of the spin periodicity in the HAFM structure near T_N by the effects of conduction electrons scattering by the 4f spin disorder. Elliott and Wedgewood (1964) considered the influence of superzone boundaries introduced by the helical structure into the energy spectrum of the conduction free electrons. They showed that with an increase of the 4f spin order the value of $\vec{Q}$ should decrease and the first-order HAFM–FM transition should occur. Miwa (1965) in his model took into account both these factors. On the base of Miwa's model Umebayashi et al. (1968) obtained the following expression for the pressure dependence of φ

$$\frac{\partial \ln\varphi}{\partial P} = -\frac{\kappa f}{\varphi \partial f/\partial\varphi}\left(\frac{2}{3}+\frac{\partial \ln m^* \Gamma_0}{\partial \ln V}\right), \tag{58}$$

where

$$f(\varphi, S, \bar{S}) = \Gamma/\mathcal{E}_F \approx m^* V^{2/3}\Gamma_0, \tag{59}$$

and $\bar{S}$ is the thermal average value of the spin quantum number at temperature T. The value in brackets in eq. (58) was obtained from electrical resistivity measurements (see eqs. 24 and 25) and $f(\varphi, S, \bar{S})$ was chosen so as to give the best fit for the experimental dependence of $\varphi(T)$. The $\partial\ln\varphi/\partial P$ values of $1.9\times10^{-2}\,\text{kbar}^{-1}$ for Tb and $0.9\times10^{-3}\,\text{kbar}^{-1}$ for Ho calculated by Umebayashi et al. (1968) are in good agreement with experimental data.

Kaino and Kasuya (1981) proposed the model of nonlinear s–f exchange interaction for the explanation of the temperature spin structure changes in the heavy lanthanides. The nonlinear s–f exchange interaction is realized for the conduction electrons from the flat sheets of webbing between two arms near the L point at the Fermi surface which are responsible for helicoidal ordering of the 4f spin. As was shown the increase of the s–f exchange constant and the decrease of the flat surface size lead to the stabilization of the cone (or fan) and then to the collinear ferromagnetic structure. The decrease of the s–f exchange constant should cause an increase of the helical wave vector and turn angle. Earlier Keeton and Loucks (1968) made band calculations for the heavy lanthanide metals and showed that the thickness of the webbing on the Fermi surface correlated with the value of the helical wave vector which was increasing from Gd to Y.

The results of the calculation of the $\varphi(T)$ dependence made by Kaino and Kasuya (1981) are in fairly good agreement with experiment. The authors related the observed increase of φ near T_C in Tb (see fig. 8) with the existence of the fan structure. As one can see from fig. 8 this tendency increases under pressure. This may imply a reduction of the size of the flat sheets under pressure.

Achiwa et al. (1988) on the basis of experimental data on the pressure dependence of φ in Ho in the framework of Miwa's model found that the s–f exchange constant reduces under pressure at the relative rate of $\sim -0.2\,\text{kbar}^{-1}$.

Vinokurova et al. (1981) with the help of experimental data of the de Haas–Van Alphen effect and model calculations studied the pressure influence on the Fermi surface of yttrium (heavy lanthanide metals have analogous Fermi surfaces). They found a decrease of the webbing thickness under pressure.

Theoretical calculations of $\mathrm{d}\varphi/\mathrm{d}P$ in Tb and Dy were made by Fleming and Liu (1970). On the basis of the band structure computed by the relativistic augmented plane wave method they calculated the generalized conduction electron susceptibility $\chi(\vec{q})$ along the c-axis at atmospheric pressure and at 20 kbar. From the position of the maximum of $\chi(\vec{q})$ it was found that the decrease of the helical turn angle under pressure was $\partial \ln \varphi/\partial P = -0.36\,\text{kbar}^{-1}$ for Tb and $-0.38\,\text{kbar}^{-1}$ for Dy. This value is not consistent with the experimental results for Tb (the data for Dy are lacking). At the same time the values of $\mathrm{d}T_C/\mathrm{d}P$ and $\mathrm{d}T_N/\mathrm{d}P$ obtained by Fleming and Liu (for Gd: –2.3 K/kbar, Tb: –1 K/kbar and Dy: –0.4 K/kbar) are in fairly good agreement with experiment (see tables 1 and 2).

Below 20 K the temperature dependence of the helical turn angle in Ho shows features corresponding to the lock-in behavior, when the wave vector $\vec{Q}$ characterizing the magnetic structure takes on a constant value over a finite temperature interval (see fig. 9). Achiwa et al. (1988) observed lock-in features of $\varphi = 36°$ at 7 kbar, 40° at 16 kbar and 41° at 21 kbar. X-ray scattering studies made on Ho by Gibbs et al. (1985) at atmospheric pressure revealed the presence of spin-slips in the lock-in phase. The spin-slip structures will be discussed in sect. 7 since they have a strong influence on the elastic properties.

The effect of pressure on the magnetic spin structure of Er was studied by means of neutron diffraction by Kawano et al. (1993, 1995). Erbium has a complex magnetic structure: according to neutron diffraction measurements by Cable et al. (1965), Habenschuss et al. (1974) and Atoji (1974) in the temperature range between $T_N = 85$ K and $T_{CY} = 53$ K there is a longitudinal spin wave along the c-axis (LSW phase), below T_{CY} the structure changes to a cycloid in which the LSW is superimposed on the basal plane spiral, and below $T_C = 18$ K the c-axis component orders ferromagnetically and the basal planes retain a spiral ordering forming the ferromagnetic cone structure (conical phase). Kawano et al. (1995) found that pressure decreases T_N and T_{CY}: at atmospheric pressure $T_N = 84$ K and $T_{CY} = 53$ K and at 14 kbar $T_N = 82 \pm 1$ K and $T_{CY} = 46 \pm 1$ K. The spin structure wave vector increases under pressure and below 30 K locks into the commensurate value $\frac{2}{17}\vec{c}$ (see fig. 10). It was concluded that the conical structure observed at atmospheric pressure below T_{CY} was suppressed by the pressure and a cycloidal structure existed down to 4.5 K (Kawano et al. 1993, 1995).

5. Influence of static pressure on the magnetization

Kornetzki (1935) and Kouvel and Wilson (1961) derived the formula for the saturation magnetization σ_s derivative with respect to pressure under the assumption that σ_s was a function of the reduced temperature T/T_C:

$$\frac{1}{\sigma_s}\frac{\partial \sigma_s}{\partial P} = \frac{\sigma_0^{-1}\frac{\partial \sigma_0}{\partial P} - \frac{T}{\sigma_s}\frac{\partial \sigma_s}{\partial T}T_C^{-1}\frac{\partial T_C}{\partial P}}{1+3\frac{\alpha_T T}{\kappa}T_C^{-1}\frac{\partial T_C}{\partial P}}, \tag{60}$$

where σ_0 is the saturation magnetization at $T = 0\,\mathrm{K}$; α_T, the linear thermal expansion coefficient. Since $3(\alpha_T/\kappa)T_C^{-1}(\partial T_C/\partial P) \approx 0$, then eq. (60) can be rewritten in the form

$$\frac{1}{\sigma_s}\frac{\partial \sigma_s}{\partial P} = \frac{1}{\sigma_0}\frac{\partial \sigma_0}{\partial P} - \frac{1}{\sigma_s}\frac{\partial \sigma_s}{\partial P}\frac{T}{T_C}\frac{\partial T_C}{\partial P}, \tag{61}$$

where the first term is due to the change of the saturation magnetization at 0 K, and the second term is the contribution from the variation of the exchange interaction under pressure. Equations (60) and (61) were used for the description of the pressure effect on the saturation magnetization and the paraprocess in the system with localized magnetic moments which can be attributed to the lanthanide metal. By a paraprocess we refer to the magnetization when the field acts against heat agitation, and the process of turning of the magnetization vector is completed.

There is a considerable amount of experimental data on the effect of pressure on the magnetization (the so-called $\Delta\sigma$ effect) in the lanthanide metals and their alloys. Vinokurova and Kondorskii (1964a,b) studied the $\Delta\sigma$ effect in heavy lanthanides. It was assumed that at magnetic fields corresponding to the initial magnetization the $\Delta\sigma$ effect was connected with the anisotropy constant variation, and in the fields of the paraprocess it was due to the change of the exchange interaction. The measurements were made on polycrystals and these two contributions were not separated.

The $\Delta\sigma$ effect in heavy lanthanide single crystals was studied by Nikitin and Leontiev (1987), Nikitin and Bezdushnyi (1987–1989). The maxima of the $\Delta\sigma$ effects were found to be near the magnetic phase spin-reorientation transition temperatures, and for the field dependencies of the $\Delta\sigma$ effect they were found at $H = H_{cr}$. In high fields the $\Delta\sigma$ effect in heavy lanthanides is negative and has large absolute values (for example in Tb at $H = 13\,\mathrm{kOe}$ $\partial\sigma/\partial P \approx -10\,\mathrm{emu/g\,kbar}$ near T_N Nikitin et al. 1991e). Nikitin and Bezdushnyi (1988) using the $\Delta\sigma$ effect data determined the relative variation of the basal plane anisotropy constant K_6^6 in terbium with pressure, i.e. $\partial \ln K_6^6/\partial P = -10^{-2}\,\mathrm{kbar}^{-1}$ at 80 K which is consistent with crystal field model calculations.

For polycrystalline heavy lanthanide metals the effect of pressure on σ_0 was studied by Bloch and Pauthenet (1964), Vinokurova and Kondorskii (1964a,b, 1965) and Bartholin and Bloch (1967). It was found that $\partial \ln \sigma_0/\partial P$ lies in the interval from -10^{-4} (Dy) to $-1.17\times10^{-4}\,\mathrm{kbar}^{-1}$ (Er). For terbium the magnetization measurements

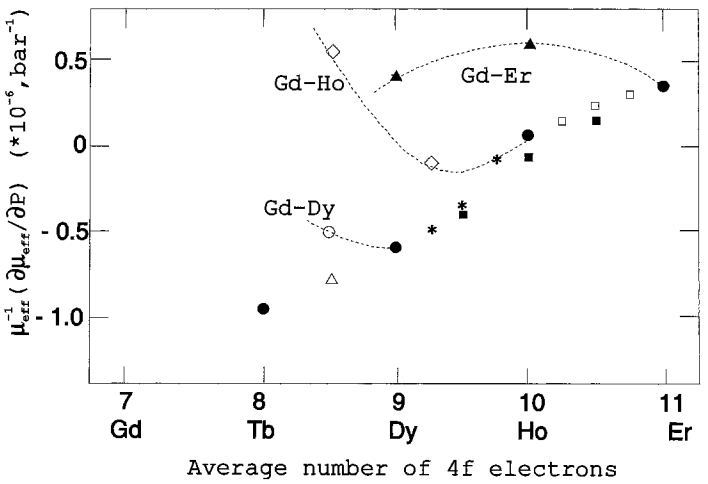

Fig. 11. Dependence of $\partial \ln \mu_{eff}/\partial P$ on the average number of 4f-electrons for heavy lanthanide metals and their alloys (Fujiwara et al. 1977). Solid circles, elements; open cicles, Gd–Dy; open diamonds, Gd–Ho; solid triangles, Gd–Er; open triangles, Tb–Dy; solid squares, Dy–Er; asterisks, Dy–Ho; open squares, Ho–Er.

gave $\partial \ln \sigma_0/\partial P = -7.3\times10^{-3}\,\mathrm{kbar}^{-1}$ (Vinokurova and Kondorskii 1965). However, the hyperfine field measurements of a terbium single crystal reveal a considerably smaller value of $\partial \ln \sigma_0/\partial P = -5\times10^{-5}\,\mathrm{kbar}^{-1}$ (Lindgren and Meyer 1990). Fujiwara et al. (1977) from the magnetic susceptibility measurements obtained the relative change of the atomic effective magnetic moment $\partial \ln \mu_{eff}/\partial P$ and found a complex dependence of this value on the average number of 4f-electrons in the heavy lanthanide metals and their alloys (see fig. 11).

Fujiwara et al. (1977) and Lindgren and Meyer (1990) assumed that the pressure effect on σ_0 and μ_{eff} in the heavy lanthanides is due to the change of the conduction electron magnetization. The deviation of experimental points for alloys with Gd from the general curve (see fig. 11) was thought to be related to the conduction electron polarization in Gd (Fujiwara et al. 1977).

Mulder et al. (1997) calculated the pressure effect on the magnetic moment of Gd by means of the augmented spherical wave method employing the atomic sphere approximation. It was shown that the main valence electron contribution to the total atomic magnetic moment of Gd and its decrease under pressure results from 5d-electrons. The calculated values are: $\partial \ln \mu_t/\partial P \approx -1\times10^{-4}\,\mathrm{kbar}^{-1}$, $\partial \ln \mu_s/\partial P \approx 9\times10^{-3}\,\mathrm{kbar}^{-1}$, $\partial \ln \mu_p/\partial P \approx -3\times10^{-3}\,\mathrm{kbar}^{-1}$ and $\partial \ln \mu_d/\partial P \approx -8\times10^{-4}\,\mathrm{kbar}^{-1}$, where μ_t is the total magnetic moment of the Gd atom and μ_s, μ_p and μ_d are the partial contributions to the total magnetic moment arising from 6s-, 6p- and 5d-electrons, respectively. According to Mulder et al. (1997) the decrease of the magnetic moment of the 5d-electrons is due to the widening of the 5d band under pressure. The character of the magnetic moment pressure dependence in Gd was confirmed by the experimental measurements of the hyperfine field at 4.2 K by means of the Mössbauer effect, although the calculated values of the hyperfine

Table 8
Influence of pressure on the saturation magnetization at 0 K for some compounds with Fe and Ni

Compound	$\partial \ln \sigma_0/\partial P$ (kbar^{-1})	Compound	$\partial \ln \sigma_0/\partial P$ (kbar^{-1})
Y_6Fe_{23}	-1.85[a]	$CeFe_2$	-2.7 ± 0.5[b]
Y_2Fe_{17}	0 ± 0.5[b]	YNi_3	0.5[c]
YFe_3	-1.4[a]	Y_2Ni_7	0 ± 0.5[b], -4.16[a]
YFe_2	1 ± 0.5[b], -0.84[a]		

References
(a) Armitage et al. (1989) (b) Buschow et al. (1977) (c) Beille et al. (1983).

field pressure effect was about a factor of 2 smaller than that obtained in experiments (Mulder et al. 1997).

Altshuller et al. (1981) showed by means of band calculations that compression did not lead to a change of the 4f energy level occupation in the heavy lanthanides but induced (s, p)–d transitions. A different situation takes place in metals where the f level lies close to the Fermi level. In this case the transition of the f-electrons to the conduction band is possible under pressure. Such a behavior was observed in Ce which was characterized by a substantial decrease of the magnetization (MacPherson et al. 1971).

For the lanthanide–3dTM compounds the $\Delta\sigma$ effect has hardly been studied. In the literature there are data on Y–Ni and Y–Fe alloys (Buschow et al. 1977), R(Co–Al_2) (Leontiev et al. 1988) and Y_2Fe_{17} and Er_2Fe_{17} (Nikitin et al. 1991b). For an interpretation of the experimental results some authors used the formula obtained for weak itinerant ferromagnets (Wagner and Wohlfarth 1981, Inoue and Shimizu 1982a, Tange et al. 1981)

$$\frac{\partial \ln T_C}{\partial P} = \frac{\partial \ln \sigma_0}{\partial P} + \frac{5}{3}\kappa. \tag{62}$$

However, the essential differences between the experimental data on $\partial \ln \sigma_0/\partial P$ obtained by the various authors makes the analysis of the relation between $\partial \ln \sigma_0/\partial P$ and $\partial \ln T_C/\partial P$ difficult.

From the band model point of view one can expect an essential variation of σ_0 under pressure in ferromagnets where 3d subbands of opposite spin directions are not full (Buschow et al. 1977). Such a situation is realized in R–Fe compounds where large values of $\partial \ln \sigma_0/\partial P$ are observed experimentally for Y_6Fe_{23}, YFe_3, YFe_2 and $CeFe_2$ with exclusion of Y_2Fe_{17} (see table 8). On the contrary in R–Co compounds the 3d band of one spin direction is full and this should correspond to the small variation of σ_0. Unfortunately, experimental data on $\partial \ln \sigma_0/\partial P$ in R–Co compounds are not available.

Mulder et al. (1997) calculated the pressure dependence of the magnetic moment of the Co atoms in the intermetallic compound $GdCo_5$. Near ambient pressure the pressure dependence of Co atom moment is relatively weak since $GdCo_5$ is a strong ferromagnet in which the majority spin 3d subband is fully occupied. Upon application of pressure the 3d bands broaden and $GdCo_5$ becomes a weak ferromagnet with high pressure dependence

of the Co atom moments. The calculations of Mulder et al. (1997) show that the decrease of the Co magnetic moment related to this process occurs at a pressure of about 80 kbar and has a discontinuous character.

6. Sound attenuation and internal friction

6.1. *Introduction*

One of the important characteristics of a material which can be studied by means of dynamic mechanical stresses is the damping of sound vibrations. The damping in magnetic metals can be divided into two parts: one of them is due to the crystal lattice, and the other is due to the interaction of the magnetic system with the lattice. The first type of damping is caused by various crystal lattice relaxation processes such as thermoelastic damping, the relaxation of internal stresses, the motion of various crystal lattice defects (dislocations, vacancies) and impurity atoms in the stress field of an acoustic wave, slip on the grain boundaries in polycrystals. The question about hydrogen impurities relaxation in rare earth metals was studied by Vajda (see Vajda 1995). We will not consider here the sound damping related to the crystal lattice, and we will focus our attention on the damping caused by the magnetic system, such as the domain structure and the variation of the magnetic order caused by elastic strains.

6.2. *Paramagnetic phase*

6.2.1. *Ultrasound attenuation*

In the region of the transition from the paramagnetic to the magnetically ordered state the contribution to the ultrasonic attenuation caused by the variation of magnetic order by elastic strains has special importance.

One of the models regarding the attenuation in a magnetic insulator with localized magnetic moments is presented in the work of Tani and Mori (1968). According to the model the spin–lattice coupling has a volume magnetostriction character. The longitudinal acoustic wave propagating through the crystal induces an oscillation of the interatomic distances R which distort the exchange integral I_{ij} by the amount $\delta R \partial I/\partial R$. This distortion results in an interaction of the sound wave with the spins resulting in a sound wave perturbation by the thermal spin fluctuations. Since the spin fluctuations increase anomalously as the critical temperature is approached, the sound attenuation should have an anomaly at this temperature. The Hamiltonian of the spin–lattice interaction for the longitudinal acoustic wave $\vec{u} \approx A\vec{e_k} \exp(i\vec{k}\vec{R})$ has the following form in the long wave length limit (Tani and Mori 1968, Lüthi and Pollina 1968, Lüthi et al. 1970)

$$\mathcal{H}_{\text{s-ph}} = \sum_{i,\vec{R}} \frac{\partial I}{\partial \vec{R}} \delta\vec{R}\, \vec{S}_i \vec{S}_{i+R} = \sum_{i,\vec{R}} A \frac{\partial I}{\partial \vec{R}} \vec{e}_k (\vec{R}\vec{k}) \mathrm{e}^{i\vec{k}\vec{R}} \vec{S}_i \vec{S}_{i+R}, \tag{63}$$

where $\delta\vec{R} = \vec{u}_{i+R} - \vec{u}_R$ with $\vec{u}$ the lattice displacement vector, $\vec{e}_k$ is the polarization vector of the sound wave, A is the amplitude of the sound wave, and $\vec{k}$ is the sound wave vector. When the lattice displacement is expressed by the phonon operators, the interaction Hamiltonian takes the form

$$\mathcal{H}_{\text{s-ph}} = \sum_{i,R} \sqrt{\frac{\hbar}{2\rho V\omega}} \frac{1}{R} \frac{\partial I}{\partial \vec{R}} (\vec{k}\vec{R})(\vec{R}\vec{e}_k) \left(b_{\vec{k}} e^{i\vec{k}\vec{R}_i} - b_{\vec{k}}^{+} e^{-i\vec{k}\vec{R}_i} \right) \vec{S}_i \vec{S}_{i+R}, \tag{64}$$

where ω is the sound wave frequency, $b_{\vec{k}}$ and $b_{\vec{k}}^{+}$ are the annihilation and creation phonon operators and ρ is the density of the crystal. The full Hamiltonian of the system consists of the noninteracting phonons energy, the exchange energy in the Heisenberg form and the spin–phonon energy in the form of eq. (64). By means of this Hamiltonian the longitudinal sound attenuation coefficient $\alpha_\parallel$ (the sound wave amplitude varies in the crystal as $\exp(-\alpha_\parallel R)$) was calculated as the difference between the phonons with wave vector $\vec{k}$ absorbed and those emitted:

$$\alpha_\parallel = \sum B(R, R', \vec{k}) \int_0^\infty dt\, e^{i\omega t} e^{i\vec{k}(\vec{R}_i - \vec{R}_j)} \langle \vec{S}_i \vec{S}_{i+R} \vec{S}_j(t) \vec{S}_{j+R}(t) \rangle, \tag{65}$$

where

$$B(R, R', \vec{k}) = \left(\frac{1}{R} \frac{\partial I}{\partial \vec{R}}\right)^2 (\vec{R}\vec{e}_k)(\vec{R}'\vec{e}_k)(\vec{R}\vec{k})(\vec{R}'\vec{k})(1 - e^{\hbar\omega/k_B T})(2\rho V\hbar\omega)^{-1}. \tag{66}$$

The coefficient $B(R, R', \vec{k})$ defines the attenuation dependence on the propagation direction and the polarization vector of the sound wave. Here $\langle\rangle$ denotes statistical averaging of the equilibrium ensemble. The integral in eq. (65) is the space-time Fourier transform of a four-spin correlation function. The existing theories of sound attenuation differ mainly in the treatment of the four-spin correlation function. In the models of Papoular (1964), Tani and Mori (1968), Bennett and Pytte (1967), Okamoto (1967), Kawasaki (1968b) and Laramore and Kadanoff (1969) the factorization procedure in breaking the four-spin correlation function into two-spin correlation functions was used. Calculations of the attenuation coefficient based on the Hamiltonian represented by eq. (64) which is squared on spins and linear in the phonon variables give the second-order dependence of $\alpha_\parallel$ on sound frequency in the paramagnetic region of the form

$$\alpha_\parallel \approx \omega^2 (T - \Theta)^{-\nu}, \tag{67}$$

where Θ is the magnetic ordering temperature (critical temperature) and critical exponent ν, calculated by various models, is presented in table 9. The calculations were made for the isotropic and unique axis anisotropy cases. Taking into account in Hamiltonian (64) the term squared in phonon variables ~ $\partial^2 I/\partial R^2 \delta R^2$ should lead to a

Table 9
Theoretical critical exponent ν for ferro- and antiferromagnets

Ferromagnet		Antiferromagnet		Refs.
Isotropic	Anisotropic	Isotropic	Anisotropic	
	1		1	1,2
7/3	5/2	3/2	3/2	3,4
	5/2		3/2	5
2.2	5/2	1.6	3/2	6
5/3			1	7
		4/3	4/3	8,9

References
1 Tani and Mori (1966)
2 Tani and Mori (1968)
3 Bennett and Pytte (1967)
4 Pytte and Bennett (1967)
5 Okamoto (1967)
6 Kawasaki (1968a)
7 Kawasaki (1968b)
8 Kadanoff (1969)
9 Laramore and Kadanoff (1969)

frequency dependence of α_1 which differs from ω^2. Such a consideration was made by Papoular (1964) who found $\alpha_1 \approx \omega^3(T - \Theta)^{-1/2}$ for ferromagnets.

The papers which describe the attenuation mechanism in the lanthanide metals with the participation of the conduction electrons are discussed next. Maekawa and Tachiki (1977) considered the microscopic mechanism of sound wave interaction with the conduction electrons in itinerant ferromagnets and the lanthanide metals. This interaction causes the variation of the indirect exchange between 4f magnetic moments leading to their coupling with sound wave and attenuation. The derived results were analogous to that determined from the model of the exchange modulation in magnetic insulators. Vigren (1977) proposed a mechanism of phonon scattering by the polarized conduction electron density. The ordered 4f spins split the conduction electron subzones via the s–f exchange interaction and cause an electron repopulation with the appearance of the electron density polarization. Thermal fluctuations of the 4f spin via the s–f exchange can carry the conduction electron charge density fluctuations. The sound attenuation occurs by phonon interaction with these charge fluctuations by means of the electron–phonon coupling. Maekawa and Tachiki (1978) showed that Vigren's model is equivalent to the exchange modulation model. It should be noted that according to Tachiki et al. (1968) the direct conduction electron–phonon attenuation in the lanthanide metals is negligible since the relaxation time of the conduction electron system ($\sim 10^{-11}$–10^{-14} s) is much less than the period of the sound waves and the stable configuration of the conduction electrons follows the strain adiabatically.

The model of the spin–phonon interaction via the exchange modulation discussed above was used for the interpretation of the results of the ultrasound (10–200 MHz) attenuation in Gd, Tb, Dy, Ho, Er (Lüthi and Pollina 1968, Pollina and Lüthi 1969, Lüthi et al. 1969, 1970, du Plessis and Elbaum 1977). It was found that longitudinal sound wave propagating along the c-axis (and also along the a-axis in Gd) displays an attenuation maximum in the vicinity of the temperature corresponding to the magnetic ordering

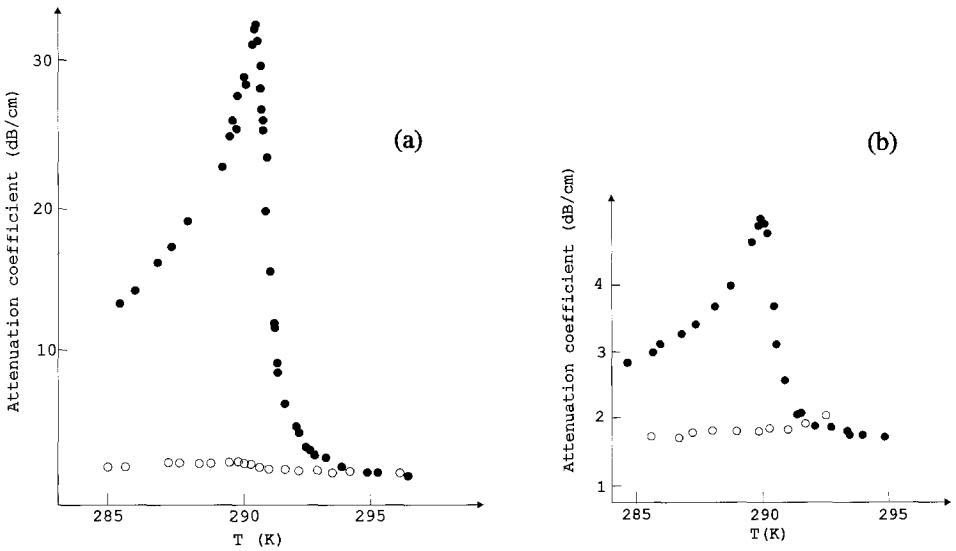

Fig. 12. Temperature dependence of the sound attenuation coefficient in single-crystal Gd for longitudinal (solid circles) and shear (open circles) waves. (a) Propagation along the c-axis; (b) propagation along the a-axis (polarization vector in the hexagonal plane). The sound frequency was 50 MHz (Lüthi and Pollina 1968).

transition (see fig. 12, where attenuation temperature dependencies for Gd are shown). At the same time there are no anomalies for the temperature dependence of the shear wave attenuation coefficient α_t, except for Dy where a small maximum near T_N was observed.

A longitudinal wave propagating through the sample produces a change in the interatomic distances and its attenuation can be explained by the volume magnetostriction mechanism described by the Hamiltonian (64). The difference in the attenuation values for the wave propagating along the a- and the c-axis observed in Gd can be attributed to essentially the difference in the $\partial I/\partial \ln a$ and $\partial I/\partial \ln c$ values (see table 5).

The change of the interatomic distance caused by a shear sound wave is of the second order compared with a longitudinal wave. The main contribution to the attenuation arises in this case from the single-ion magnetoelastic interaction. The Hamiltonian of this interaction can be expressed in the form proposed by Callen and Callen (1965) and is linear in strain and squared in spin variables:

$$\begin{aligned} H_{\mathrm{me}}(f) = &- B_{12}^{\alpha}\epsilon^{\alpha,1}\frac{\sqrt{3}}{2}\left[(S_f^z)^2 - \tfrac{1}{3}S(S+1)\right] - B_{22}^{\alpha}\epsilon^{\alpha,2}\left[(S_f^z)^2 - \tfrac{1}{3}S(S+1)\right] \\ &- B^{\gamma}\left\{\tfrac{1}{2}\epsilon_1^{\gamma}\left[(S_f^x)^2 - (S_f^y)^2\right] + \tfrac{1}{2}\epsilon_2^{\gamma}\left[S_f^x S_f^y + S_f^y S_f^x\right]\right\} \\ &- B^{\epsilon}\left\{\tfrac{1}{2}\epsilon_1^{\epsilon}\left[(S_f^y S_f^z + S_f^z S_f^y\right] + \tfrac{1}{2}\epsilon_2^{\epsilon}\left[(S_f^x S_f^z + S_f^z S_f^x\right]\right\}, \end{aligned} \tag{68}$$

where symmetry strains are used which are related to Cartesian strain ϵ_{ij} by the relations

$$\epsilon^{\alpha,1} = \epsilon_{xx} + \epsilon_{yy} + \epsilon_{zz}; \qquad \epsilon^{\alpha,2} = \frac{\sqrt{3}}{2}(\epsilon_{zz} - \tfrac{1}{3}\epsilon^{\alpha,1}); \tag{69}$$

$$\epsilon^{\gamma,1} = \tfrac{1}{2}(\epsilon_{xx} - \epsilon_{yy}); \qquad \epsilon_2^{\gamma} = \epsilon_{xy}; \qquad \epsilon_1^{\epsilon} = \epsilon_{yz}; \qquad \epsilon_2^{\epsilon} = \epsilon_{xz}, \tag{70}$$

where B_{12}^{α}, B_{22}^{α}, B^{γ} and B^{ϵ} are the single-ion magnetoelastic coupling constants. The last two terms in eq. (68) are responsible for the single-ion magnetoelastic interaction with the shear wave.

Pollina and Lüthi (1969) estimated the value of single-ion magnetoelastic coupling constants B^{γ} and B^{ϵ} with the help of linear magnetostriction data. They showed that in Tb, Dy and Ho the constants had the same order of magnitude as the volume magnetostrictive coupling constant which is proportional to $\mathrm{d}I/\mathrm{d}\ln c$ (in Gd they were smaller by two orders of magnitude) with the maximum value in Dy. According to Pollina and Lüthi (1969) the weak critical attenuation of shear sound waves observed in Tb, Dy and Ho cannot be explained by the small value of single-ion magnetoelastic coupling constants.

The explanation of the observed experimental results on shear sound attenuation along the c-axis in the strongly anisotropic heavy lanthanide metals was proposed by Tachiki et al. (1975). According to this model the strong magnetocrystalline anisotropy in Tb, Dy and Ho suppresses the spin fluctuations along the c-axis. Near the temperature of transition to the magnetically ordered state the spin fluctuations become extremely anisotropic: the fluctuations along the c-axis remain finite, but at the same time the fluctuations in the basal plane diverge. For the calculation of the attenuation coefficient the spin–phonon interaction for a shear wave was expressed by means of a two-ion magnetoelastic Hamiltonian in the form proposed by Callen and Callen (1965). It was shown that the attenuation coefficient of the shear acoustic wave is proportional to the correlation function of the spin components along the sound wave vector and along the polarization vector of sound. When the shear wave propagates along the c-axis the attenuation coefficient does not reveal any critical anomaly because it is proportional to the spin component along the c-axis which does not diverge. On the other hand as was shown by Tachiki and Maekawa (1974) the longitudinal wave attenuation coefficient was proportional to the square of the correlation function of the basal plane spin components and thus had a critical anomaly near T_{N}. So, according to the described mechanism, the critical attenuation of shear acoustic waves is possible only if their propagation and polarization vectors lie in the basal plane. Such a behavior was observed experimentally on Tb and Ho by Tachiki et al. (1975).

Experiments show that in the paramagnetic region near the critical temperature a dependence of α_{l} and α_{t} on ω and T in the form of eq. (67) is observed. The experimental values of the critical exponent ν and the critical temperatures for heavy lanthanide metals are presented in table 10. Just above the critical temperature ($T - \Theta < 1\,\mathrm{K}$) a deviation from the dependence given by eq. (67) was observed by Lüthi et al. (1970) in connection with impurities in the sample. Experimental values of ν for lanthanide metals lie in the interval 1–1.6 which is consistent with the models of Kawasaki (1968b), Laramore and Kadanoff (1969) and Kadanoff (1969). Tb, Dy and Er with ν close to 4/3 are characterized by high uniaxial anisotropy. The observed value of ν for the isotropic ferromagnet Gd is close to theoretical value 5/3. Holmium can be regarded as a boundary case between an isotropic and an anisotropic antiferromagnet ($\nu = 1$). Lüthi et al. (1969) explained the

Table 10
Experimental critical exponent ν and critical temperatures for the heavy lanthanide metals; the sound attenuation was measured for a sound wave propagating along the c-axis

R	T_C, T_N (K)	Longitudinal wave	Shear wave	Refs.
Gd	290.4	1.2 ± 0.1		1
Gd	290.1	1.63 ± 0.1		2
Tb	227.6	1.24 ± 0.1		2,3
Dy	177.3	1.37 ± 0.1	0.8	2,3
Ho	132.1	1.0 ± 0.1		2,3
Er	84.84	1.26 ± 0.04		4

References
(1) Lüthi and Pollina (1968)
(2) Lüthi et al. (1970)
(3) Pollina and Lüthi (1969)
(4) du Plessis and Elbaum (1977)

observed critical exponent ($\nu = 0.8$) for the shear wave attenuation in Dy in the framework of Kawasaki's (1968a) model taking into account in the spin–phonon Hamiltonian terms linear in strain but having a fourth power dependence in the spin variables.

The influence of a magnetic field on the attenuation of the longitudinal acoustic wave propagating along the c-axis in the lanthanide metals in the paramagnetic phase was studied in Ho (Tachiki et al. 1972), Tb (Maekawa et al. 1976), Dy (Treder and Levy 1977), and Er (Treder et al. 1979). It was shown that in Tb and Ho near the magnetic ordering temperature in a low magnetic field aligned parallel to the basal plane a rapid increase of the attenuation occurred. In terbium the attenuation passes through a maximum and then rapidly decreases in high field. Such a behavior is not a confirmation of the spin fluctuation attenuation mechanism (Tani and Mori 1968) since fluctuations should be suppressed by the magnetic field. In Dy there is a more complex behavior of α_l in the paramagnetic phase: for temperatures $T/T_N > 1.01$ α_l exhibits an increase with H, but for $1 < T/T_N < 1.01$ α_l first shows a decrease followed by a minimum and an eventual increase. Erbium was investigated for two directions of the magnetic field – parallel and perpendicular to the crystallographic c-axis and quite different behaviors of the attenuation were observed. When H is parallel to the c-axis α_l reveals a field dependence on H with a minimum (analogous to that observed in Dy for $1 < T/T_N < 1.01$) and a weak increase at high fields. When H was perpendicular to the c-axis a rapid increase of α_l was observed. In all cases the increase of α_l was quadratic in the applied field strength. To explain the observed field dependence of α_l the model proposed by Tachiki and Maekawa (1974) and Maekawa et al. (1976) was used. The Hamiltonian contained the contribution from the exchange energy for the undistorted lattice, the energy due to the applied magnetic field, the magnetocrystalline anisotropy energy, the uniform elastic and magnetoelastic (single-ion and two-ion) energy contributions in the form given by Callen and Callen (1965), and the energy of noninteracting phonons and the spin–phonon interaction energy arising from the modulation of two- and single-ion interactions by the propagating acoustic wave. The last contributions were taken only to first order in

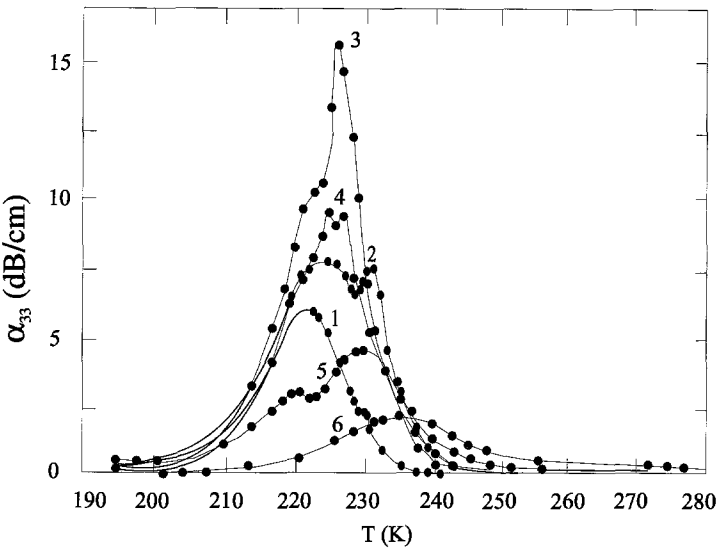

Fig. 13. Constant field attenuation coefficient α_{33} (longitudinal sound wave propagating along the c-axis) for terbium: (1) H = 0 kOe; (2) 1.25 kOe; (3) 2.5 kOe; (4) 4 kOe; (5) 6 kOe; (6) 11 kOe. The sound frequency is 15 MHz (Maekawa et al. 1976).

the phonon variables. Using this Hamiltonian the attenuation coefficient was calculated by means of a general procedure given by Tani and Mori (1968) as a sum over four-spin time correlation functions which were broken into products of two-spin correlation functions and then expressed in terms of so-called staggered susceptibilities which were dependent on corresponding spin fluctuations. The resultant expression for $\alpha_\parallel$ can be reduced to (Treder et al. 1979)

$$\alpha_\parallel = C_1(T)[\sigma_H \chi_H(\vec{k})]^2 + C_2(T) \sum_{\vec{K}} \{[\chi_x(\vec{K})]^3 + [\chi_y(\vec{K})]^3 + [\chi_z(\vec{K})]^3\}, \tag{71}$$

where $\vec{K}$ is the reciprocal lattice vector, σ_H and χ_H are the components of magnetization and the staggered susceptibility in the direction of the applied field H, χ_i are the components of staggered susceptibility, and C_1(T) and C_2(T) are the temperature dependent coefficients. When the temperature approaches the critical temperature some components of the staggered susceptibility in the absence of a magnetic field can diverge due to spin fluctuations and thus cause the attenuation maxima. In the presence of a magnetic field there are two competing effects. One of them increases the first term in eq. (71) and is due to the spin polarization induced by the applied magnetic field. The other one is caused by the suppression of spin fluctuations in the field and tends to decrease $\alpha_\parallel$. Under assumption that in low fields σ has a linear dependence on the magnetic field, Treder et al. (1979) obtained the attenuation coefficient $\alpha_\parallel$ of the form

$$\alpha_\parallel \approx [C_1(T) - C_2(T)]H^2. \tag{72}$$

Which of the two contributions dominates depends on the relative size of $C_1(T)$ and $C_2(T)$ which can change with temperature. Numerical calculations on the basis of this model allowed Maekawa et al. (1976) and Treder and Levy (1977) to explain the experimentally observed $\alpha_1(H)$ in the heavy lanthanides in the paramagnetic region.

For the temperature dependencies of α_1 in Tb, Dy and Er field induced shifts of the maxima corresponding to magnetic phase transitions were observed. This allowed Maekawa et al. (1976) to construct the magnetic phase diagram of terbium which is consistent with the one obtained from magnetization measurements. An interesting feature is the appearance of an additional attenuation maximum which occurs above the critical peak; in terbium it shifts toward high temperatures with increasing field strength (see fig. 13). According to the theory considered above such a behavior is associated with the first term in eq. (71) – when $H \neq 0$ it exhibits a maximum due to the maximum in $\chi_H(\vec{k})$. This attenuation anomaly is field dependent and lies above the temperature of the transition to the magnetically ordered state. This is due to the spin fluctuations associated with short range ferromagnetic ordering induced by the field.

6.2.2. *Internal friction*

Anomalous sound attenuation at the transition temperature to the magnetically ordered state can be also explained thermodynamically by the fluctuation mechanism proposed by Landau and Khalatnikov (1954) for second-order phase transitions. For ferromagnets this type of model was regarded by Belov et al. (1960) and Papoular (1965).

The mechanical stress impressed on a ferromagnet causes the deviation of the spin system from the equilibrium state. The process of equilibrium reduction is described by the kinetic equation

$$\frac{\partial \sigma}{\partial t} = -K \frac{\partial F}{\partial \sigma}, \tag{73}$$

where F is the free energy of ferromagnet, and K, the kinetic coefficient. The relaxation time is determined by the equation

$$\tau = K^{-1} \left(\frac{\partial^2 F}{\partial \sigma^2} \right)_T^{-1}, \tag{74}$$

and depends on the character of the magnetic phase transition. For second-order phase transitions the free energy of a ferromagnet can be expanded in a power series of magnetization

$$F = F_0 + \tfrac{1}{2}\alpha\sigma^2 + \tfrac{1}{4}\beta\sigma^4 + \cdots, \tag{75}$$

where α and β are thermodynamic coefficients [near T_C one has $\alpha = \alpha_\Theta(T - T_C)$]. The minimization of F with respect to σ gives $\sigma^2 = \alpha/2\beta$. Then τ depends on the temperature in the following way

$$\tau = -\frac{1}{2\beta K \sigma^2} = \frac{1}{K\alpha_\Theta (T - T_C)}, \tag{76}$$

i.e., for second-order phase transitions τ diverges on approaching the Curie point, which is related to an intensive development of spin fluctuations near T_C. For a first-order magnetic

phase transition τ has a maximum at the transition temperature. Since the velocity of approaching the equilibrium magnetic state can be expressed as

$$\frac{\partial \sigma}{\partial t} = -\frac{\sigma - \sigma_{eq}}{\tau}, \tag{77}$$

(here σ_{eq} is the equilibrium value of the magnetization) then a sharp increase of τ at T_C means the appearance of "magnetic viscosity" due to the paraprocess. Sound attenuation arises from the phase lag between the impressed stress and induced strain and has a maximum in the vicinity of the Curie temperature. Since in the framework of this model above T_C $\sigma = 0$ in both equilibrium and nonequilibrium states, in the paramagnetic region the sound attenuation should not be observed in contrast to the models discussed above.

By means of this thermodynamic model the internal friction Q^{-1} for an isotropic ferromagnet near T_C was calculated by Belov et al. (1960) and Papoular (1965). The internal friction characterizes the damping of the sample's sound vibrations with time and is defined as a ratio of the mechanical energy dissipated over a period of time to the full mechanical energy of the sample. It is related to the sound attenuation coefficient as

$$Q^{-1} = 2\alpha_l \upsilon/\omega, \tag{78}$$

were υ is the sound velocity. When calculating the internal friction, the energy of the magnetic field, $-\sigma H$, and the magnetoelastic coupling in the form of $\gamma p \sigma^2$ (p is the mechanical stress and γ the thermodynamic coefficient) were taken into account in the free energy, and the following expression was derived

$$Q^{-1} = K\gamma E^0 \sigma^2 \frac{\omega\tau^2}{1+\omega^2\tau^2}, \tag{79}$$

where E^0 is the Young's modulus due to lattice effects only and

$$\tau = \frac{\sigma}{K(H + 2\beta\sigma^3)}. \tag{80}$$

The thermodynamic model stated above gives the following internal friction behavior for second-order magnetic phase transitions:

(a) the internal friction maximum occurs at the temperature T_m below the Curie point T_C;

(b) with increasing frequency T_m shifts to lower temperatures:

$$T_C - T_m = \frac{\omega}{2K\alpha_\Theta}; \tag{81}$$

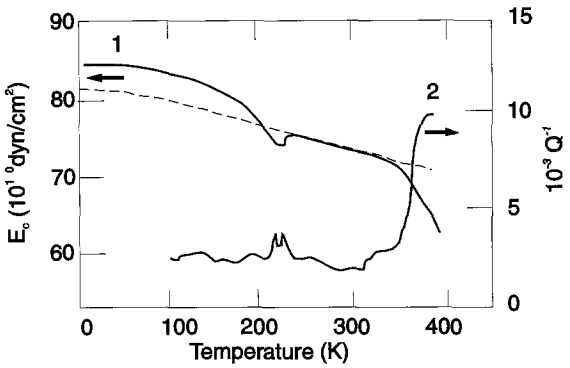

Fig. 14. Temperature dependence of E_c, Young's modulus (curve 1) and internal friction Q^{-1} (curve 2) of terbium measured along the crystallographic c-axis. The dashed line is the calculated lattice part of E_c. The frequency of measurement was ~1.5 kHz (Spichkin et al. 1996a).

(c) at high magnetic field strength Q^{-1} decreases as $H^{-2/3}$.

Although a lot of experimental work has been devoted to internal friction measurements in the lanthanide metals and their alloys for acoustic frequencies of 1–2 kHz, near the magnetic transition temperature only a limited number of studies of Q^{-1} have been carried out. The internal friction maximum in the vicinity of the critical temperature was observed in poly- and single crystals of the lanthanide metals and their alloys: Gd (Bodriakov et al. 1991, 1992), Tb (Spichkin et al. 1996a, Shubin et al. 1985) (see fig. 14), Dy (Tishin and Shipilov 1992, Kataev et al. 1985, 1989a, Kataev and Shubin 1979, Tishin and Spichkin 1996) (see fig. 15), $Tb_{0.125}Dy_{0.875}$ (Kataev and Sattarov 1989), Gd–Dy system

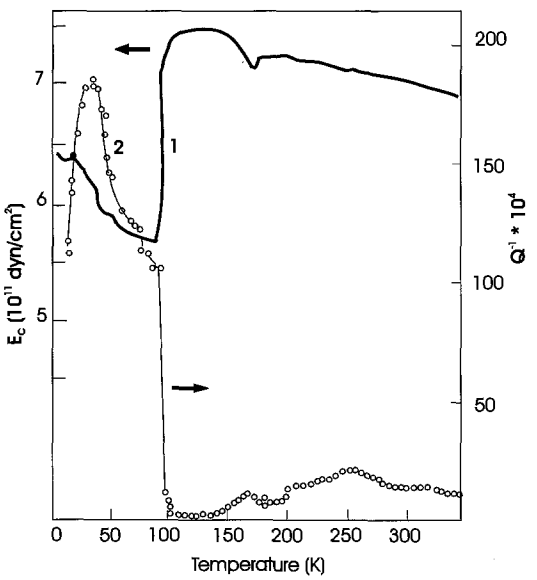

Fig. 15. Temperature dependence of Young's modulus E_c (curve 1) and internal friction Q^{-1} (curve 2) of dysprosium measured along the crystallographic c-axis. The frequency of measurement was ~2 kHz (Tishin and Spichkin 1996).

(Tishin and Shipilov 1993), $Er_{0.25}Tb_{0.75}$ (Kataev and Shubin 1979). In polycrystalline Dy, $Tb_{0.125}Dy_{0.875}$ and single-crystal $Tb_{0.5}Dy_{0.5}$ at temperatures between 280 and 300 K, which is high above T_N, internal friction maxima were observed by Kataev and Shubin (1979), Kataev et al. (1989a), Kataev and Sattarov (1989) which according to the authors were of magnetic origin and were related to the disappearance of short-range magnetic order (antiferromagnetic clusters). The temperatures of the maxima correspond to the disappearance of hysteresis of the Young's modulus temperature dependencies and the maxima's height is affected by the magnetic field. At the same time, Burhanov et al. (1993) showed by $Q^{-1}(T)$ dependencies measurements at various frequencies that the observed high temperature internal friction maxima were caused by relaxation processes in the crystal lattice and had a dislocation nature. In addition, the internal friction investigations of the nonmagnetic metals Y and La by Bodriakov et al. (1993, 1994) and Tishin et al. (1995) reveal similar maxima at ~ 300 K which indirectly points to the nonmagnetic character of these high temperature maxima in the magnetic lanthanide metals. Another, more plausible, reason for this anomaly is the relaxation of gas impurities or crystalline lattice defects (see Vajda 1995).

6.3. *Magnetically ordered state*

6.3.1. *Ultrasound attenuation*

The ultrasonic attenuation in the magnetically ordered state of the lanthanide metals was investigated experimentally in Tb, Dy, Ho and Er, and in the Tb–Ho, Gd–Y alloys. Longitudinal sound waves propagating along the *c*-axis reveal attenuation maxima at the temperatures of magnetic phase transitions in the absence of a magnetic field. A maximum was observed at the temperature of the transition from a helicoidal to a ferromagnetic state (T_N) in terbium by Maekawa et al. (1976) and Jiles et al. (1981) on cooling and warming (see fig. 13) and in holmium by Levy and Lee (1970), Lee and Levy (1973) on cooling (see fig. 16). It should be noted that conditions of measurement (cooling or warming circle) strongly affect the attenuation results below T_N. In Dy no anomaly was observed at T_C on cooling but on warming a large maximum was found near T_C by Palmer (1975) and Blackie and Palmer (1980), see fig. 17. A similar behavior was observed in alloys with the helical spin structure – Tb–Ho and Gd–Y (Palmer 1975, Blackie and Palmer 1982, Braga et al. 1982, Sousa et al. 1982). In some papers the direction of the temperature change was not indicated and this could lead to confusion. A wide maximum was observed also in Ho (see fig. 16) at ~ 95 K which was suppressed by an increase of frequency or magnetic field strength.

Erbium was investigated by du Plessis and Elbaum (1977) and Treder et al. (1979). There are longitudinal sound attenuation maxima at the temperatures of the magnetic phase transition $T_N \approx 85$ K, $T_{CY} \approx 53$ K and $T_C \approx 20$ K. At a temperature slightly higher than T_C (22 K on cooling and 26 K on warming) an additional small peak occurs. Hysteresis of the attenuation coefficient was also observed near T_C in Er and Tb which is characteristic of a first-order transition.

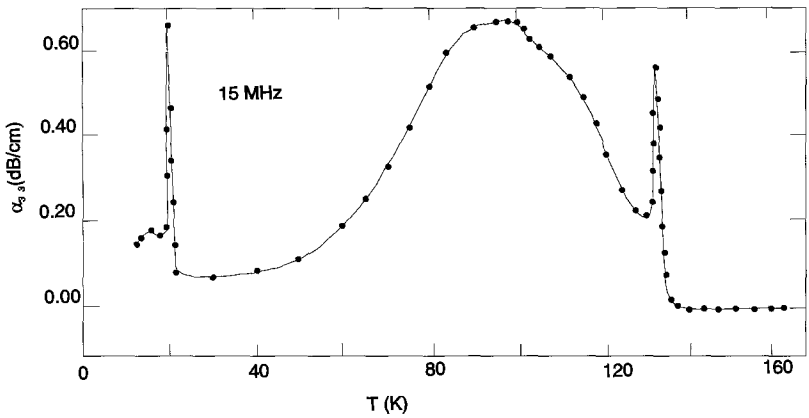

Fig. 16. Temperature dependence of the attenuation coefficient α_{33} in holmium. The sound frequency is 15 MHz (Lee and Levy 1973).

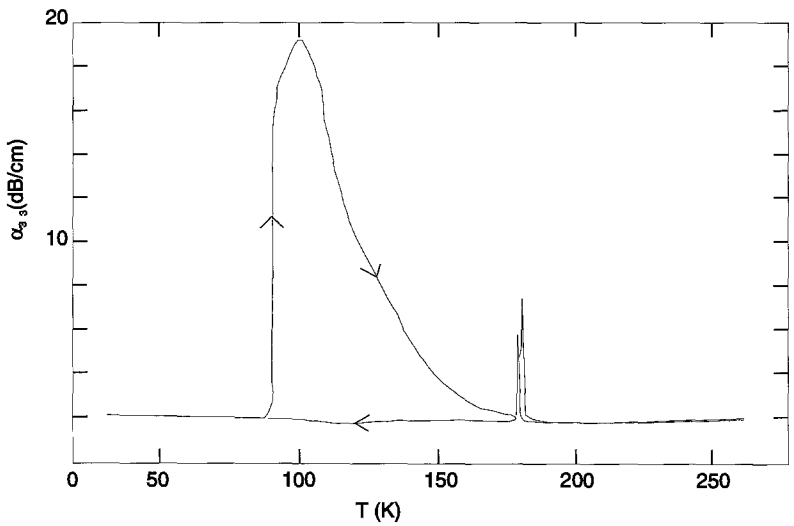

Fig. 17. Temperature dependence of the attenuation coefficient α_{33} in dysprosium. The sound frequency is 15 MHz (Blackie and Palmer 1980).

The attenuation of the acoustic shear waves propagating along the hexagonal axis in holmium was measured by Tachiki et al. (1974) and Lee et al. (1975) and reveals two maxima, at 24 and 95.5 K.

Mechanisms of longitudinal and shear sound wave attenuation in the spiral spin state were proposed by Tachiki et al. (1968), Lee and Levy (1973), Vigren (1976) and Palmer (1975). According to the model of Tachiki et al. (1968) the longitudinal acoustic wave propagating through the sample along the c-axis perturbs the conduction electron system thus leading to a variation of the exchange energy. The variation causes a distortion of

the helical wave vector $\vec{Q}$ due to the rotation of 4f spins around the c-axis. The spins will try to relax to their equilibrium state providing an absorption of acoustic energy. The attenuation due to this spin–lattice relaxation process can be written for a longitudinal acoustic wave as

$$\alpha_l = \frac{N\bar{S}^2}{\rho v_l} \frac{(\partial^2 I/\partial Q \partial \epsilon_{33})^2}{\partial^2 I/\partial Q^2} \frac{\tau\omega^2}{1+\omega^2\tau^2}, \tag{82}$$

where v_l is the longitudinal acoustic velocity; τ, the relaxation time of the spin system; and $\bar{S}$, the thermal average of the spin. Since according to the experimental data of Umebayashi et al. (1968) the mechanical stress essentially affects the helical turn angle in the lanthanide metals one may expect a considerable contribution to α_l from this mechanism. The mechanism is characteristic for the helical spin structure and does not work for collinear ferro- and antiferromagnets because $\partial^2 I/\partial Q \partial \epsilon_{33} = 0$. For the attenuation coefficient of shear waves the following expression was derived:

$$\alpha_t = \frac{N\bar{S}^2 \mathcal{E}_t}{2\rho^2 v_t^2} \frac{(\partial^3 I/\partial Q \partial^2 \epsilon_{31})^2}{\partial^2 I/\partial Q^2} \frac{\tau\omega^2}{1+4\omega^2\tau^2}, \tag{83}$$

where $\mathcal{E}_t$ is the acoustic wave energy density and v_t is the shear sound velocity. The value of the shear attenuation coefficient is much less than the longitudinal one because $\vec{Q}$ is coupled to the shear strain only to second order. An important feature of the model is that the attenuation can exist over the whole temperature range corresponding to the helical spin phase.

It follows from eqs. (82) and (83) that the attenuation coefficient should have a maximum when the condition $\omega\tau = 1$ is satisfied. Lee and Levy (1973) explained the maximum of the longitudinal sound attenuation observed in Ho (fig. 16) in the helical phase at ~ 97 K by the competition of the temperature dependent values in eq. (82). They also found that in the temperature region from 50 K to T_N the expression for τ may be given as $\tau \approx (2.16\times10^{-2}\,\mathrm{s\,K^3})T^{-3}$. The observed magnetic field suppression of the maximum at 97 K was explained by Levy and Lee (1970) as a restriction of the spin motion resulting in a decrease of the spin–phonon interaction. It should be noted that in other lanthanide systems with a helical phase (Dy, Ho–Tb, Gd–Y) no pronounced maximum of the spiral phase was observed upon cooling.

Another possible reason of sound attenuation in the magnetically ordered state is interaction of the acoustic wave with the domain structure, namely with domain walls. Such a sound–wall interaction is realized via exchange energy modulation. This modulation acts on the walls as an effective pressure and drives them harmonically with the frequency of sound in the potential walls at their pinning site. The pinning occurs at the various impurities and imperfections of the crystal structure. The sound absorption arises from the intrinsic effects (spin–lattice interaction) and from eddy currents associated with local fluctuations of magnetization caused by the wall motion.

Palmer (1975) proposed that there are two possible types of spiral spin domains in the helical antiferromagnetic state of the lanthanide metals with an unique anisotropy axis –

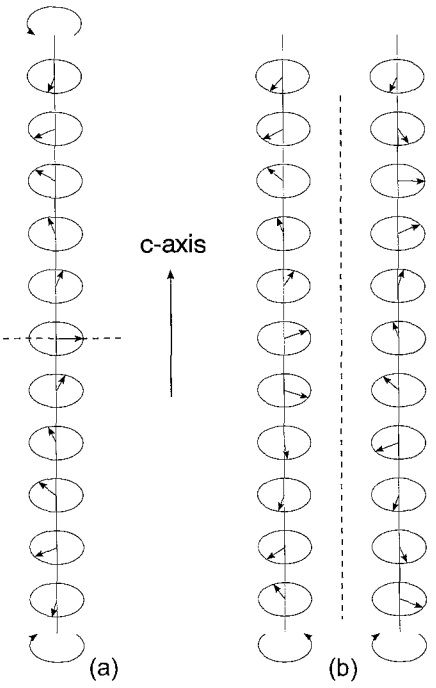

Fig. 18. Domain walls in the helical phase (shown by dashed lines). (a) Type one; (b) type two (Palmer 1975).

these are depicted schematically in fig. 18. The first type of domains have the form of parallel sided plates with walls perpendicular to the c-axis and spins rotating clockwise or counter-clockwise along the c-axis in the neighboring domains. The second type domains have walls lying parallel to the c-axis and a complex structure due to the meshing of the two spirals. The domains of the first type will interact with the longitudinal sound wave propagating along the c-axis through the exchange modulation mechanism. The domains of the second type will have the most intensive interaction with the longitudinal waves propagating in the basal plane since the compressive nature of these waves affects the meshing of domain walls. The shear waves have very little influence on the spiral domains because of the second-order coupling with the spins.

Palmer (1975) discussed the process of domain formation on cooling and heating in the lanthanide metals with the following transitions: paramagnetism–HAFM–FM phase. It was shown that the second type spiral domains should exist in the helical phase in equal amounts independent of the magnetic and thermal history of the sample. On the contrary the domains of the first type will be much more numerous when the sample is heated from the ferromagnetic phase than those present when the sample is cooled down from the paramagnetic state. This is caused by the mechanism of domain formations on warming from the FM phase – they arise from the 180° Bloch domain walls, which are themselves short lengths of spirals and are numerous in the ferromagnetic state. Since the attenuation of the acoustic wave propagating along the hexagonal axis is

directly proportional to the number of first type domains, it should increase under heating from the ferromagnetic region. Such a behavior was observed experimentally in the elements and alloys with helical structure: in Dy single crystal (see fig. 17) and $Tb_{0.5}Ho_{0.5}$ (Palmer 1975, Blackie and Palmer, 1980), $Gd_{0.689}Y_{0.311}$ (Blackie and Palmer 1982, Braga et al. 1982), $Gd_{0.654}Y_{0.346}$ (Sousa et al. 1982), $Gd_{0.6}Y_{0.4}$ (Palmer 1975), $Gd_{0.7}Y_{0.2}Lu_{0.1}$ (Takeuchi et al. 1990b) and Tb (Jiles et al. 1981). The described attenuation mechanism was confirmed by the field measurements on a $Tb_{0.5}Dy_{0.5}$ single crystal (Palmer 1975): on the isothermal cycles of $\alpha_{33}(H)$ at the temperatures corresponding to the helical phase a sufficient increase of attenuation is observed when the field is decreased from values higher than the critical field H_{cr} of the transition to the ferromagnetic state (the field is applied in the basal plane). In the ferromagnetic phase such a behavior was not observed.

Greenough and Blackie (1981) considered the energy of the spiral spin structure by means of the model of Enz (1960) and Herpin and Meriel (1961). It was shown that when the spiral periodicity was commensurate with the crystal lattice the energy was greater than for a noncommensurate spiral. The main energy maximum takes place at a helicoid turn angle of ~ 30°, which corresponds to the attenuation maximum observed in Dy on warming (see fig. 17). Greenough and Blackie related this anomaly to the instability of the magnetic spin structure caused by commensurability. However, in this case it is not clear why this anomaly appears only for warming from the ferromagnetic phase.

Gadolinium alloys with nonmagnetic elements Y, Sc and Lu display different magnetic behavior depending on the composition. According to the magnetization measurements in alloys with high gadolinium concentration ferromagnetic order is observed and when the gadolinium concentration is reduced the alloys reveal an antiferromagnetic helical structure. The attenuation and velocity of the longitudinal ultrasonic wave propagating along the *c*-axis in the alloys near the critical composition where ferromagnetic and antiferromagnetic phases meet were investigated by Takeuchi et al. (1985, 1990a,b, 1991). The $Gd_{0.75}Sc_{0.25}$ alloy is characterized by "double ferromagnetism" (Legvold et al. 1980, Ito et al. 1981). Below the Curie temperature $T_C = 185$ K the alloy orders in a phase with a net magnetization along the *c*-axis but the basal plane component of the magnetic moment is paramagnetic. The latter orders at the temperature $T_C^l = 77$ K. Both transitions manifest themselves in maxima of the temperature dependence of the attenuation coefficient: at T_C a sharp λ-type peak was observed in the cooling down process and at T_C^l there was a small maximum. Near T_C temperature hysteresis of α_{33} in cooling and warming processes was observed (upon warming the attenuation coefficient was lower than under cooling conditions). The hysteresis was attributed to the antiphase ferrimagnetic domain structure, which arises just below T_C in a narrow temperature interval (Ito et al. 1987). A similar temperature behavior of α_{33} was observed in $Gd_{0.75}Y_{0.175}Sc_{0.075}$ by Takeuchi et al. (1990b, 1991) (see fig. 19), where $T_C = 215$ K and $T_C^l = 188$ K. The $Gd_{0.7}Y_{0.2}Lu_{0.1}$ alloy, which has a helical antiferromagnetic structure below $T_N = 21$ K and a ferromagnetic one below $T_C = 180$ K, shows α_{33}(T) dependencies (fig. 19) similar to that observed in Dy by Palmer (1975). This behavior was explained by Takeuchi et al. (1985) by a domain mechanism analogous to that proposed by Palmer (1975). The $Gd_{0.3}Y_{0.7}$ alloy has a $\alpha_{33}(T)$ behavior which is characteristic of both $Gd_{0.75}Y_{0.175}Sc_{0.075}$ and $Gd_{0.7}Y_{0.2}Lu_{0.1}$ alloys (see fig. 19).

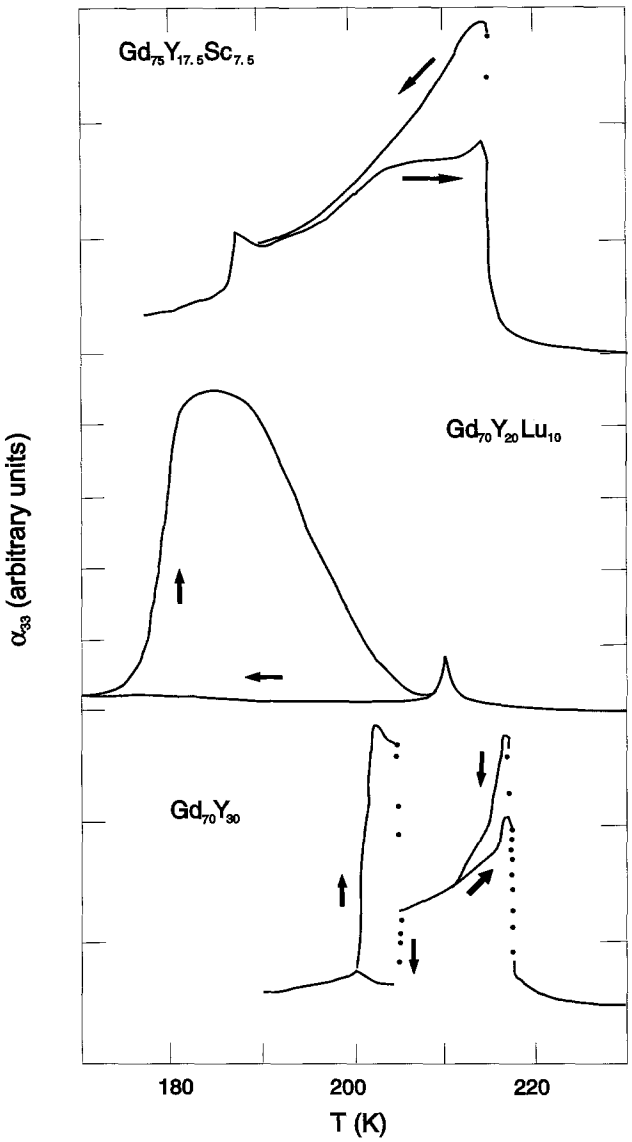

Fig. 19. Temperature dependencies of the attenuation coefficient α_{33} for $Gd_{0.75}Y_{0.175}Sc_{0.075}$ (sound frequency 110 MHz), $Gd_{0.7}Y_{0.2}Lu_{0.1}$ (65 MHz) and $Gd_{0.7}Y_{0.3}$ (75 MHz) (Takeuchi et al. 1990b).

This allows one to propose that it has three magnetic phases, double ferromagnetism below T_C = 217 K, a helical antiferromagnetic state T_N = 205 K and a ferromagnetic state below 200 K.

The domain mechanism was also used to explain the attenuation anomalies of the shear acoustic waves propagating along the c-axis in the helical phase in the heavy lanthanide metals. Narrow (~3 K) attenuation maxima were observed in Ho at 95 and 24 K by Tachiki et al. (1974) and Lee et al. (1975), at 95 K by Simpson et al. (1976), at 97.5 K by Venter et al. (1992a) and in Dy at 112 K by Greenough and Isci (1979). According to neutron diffraction studies (Koehler et al. 1966, Wilkinson et al. 1961) these temperatures correspond to the magnetic structures in which the spin periodicity becomes commensurate with the periodicity of the crystal lattice. Vigren (1976) showed that the interplanar exchange energy could be modulated by a shear acoustic wave via single-ion magnetoelastic coupling provided the helical spin structure was perturbed by basal plane anisotropy. The modulation can occur only for commensurate spin structures. It was also shown that at the commensurate temperature a mixed domain structure consisting of commensurate and incommensurate spiral domains was established. The sound attenuation arises from the domain wall motion caused by the propagating acoustic wave by means of the mechanism described above. Vigren used his model for the interpretation of the shear attenuation anomaly in Ho at 24 K. As follows from this model, the magnetic field impressed on the basal plane should move the attenuation peak at 24 K in Ho to higher temperatures. Such a behavior was observed experimentally.

Later the shear sound attenuation anomaly in Ho at 97.5 K was interpreted by Venter et al. (1992a) in terms of a spin-slip model (Gibbs et al. 1985, Bohr et al. 1986, Bohr 1991, Bates et al. 1988). A more thorough discussion of this question will be presented in sect. 7.

The magnetic field dependence of the attenuation coefficient of the longitudinal acoustic waves propagating along the c-axis (H aligned in the basal plane) was studied for the helical state of Dy by Isci and Palmer (1978). According to the authors the observed series of attenuation peaks were related to the transitions between various intermediate magnetic phases arising during the transition from helical antiferromagnetic to ferromagnetic.

6.3.2. *Internal friction*

The internal friction in the magnetically ordered state of Gd, Tb, Dy, Er and the Gd–Dy, Tb–Dy, Er–Tb, Ho–Er alloys was measured at acoustic frequencies. The temperature dependence of Q^{-1} for a gadolinium single crystal measured along the c-axis exhibits a maximum not only at the Curie temperature, but also in the region of spin-reorientation, where a considerable temperature hysteresis of Q^{-1} is observed (Bodriakov et al. 1992). The internal friction maxima were observed at T_C and T_N in a terbium single crystal (Spichkin et al. 1996a, Shubin et al. 1985) – see fig. 14. Some hysteresis was found in the helical phase of Tb with a higher internal friction value on warming compared with that observed on cooling (Shubin et al. 1985). Such a hysteresis was also observed in polycrystalline Dy and $Tb_{0.125}Dy_{0.875}$ by Kataev et al. (1989a) and Kataev and Sattarov (1989) where it was much less pronounced than in the case of ultrasound wave

attenuation in Dy and Gd–Y discussed above, and furthermore, it was observed only in the vicinity of the first-order transition at T_C. This may imply that the spiral spin domain contribution to the internal friction does not play a sufficient role at acoustic frequencies.

The low temperature dependence of the internal friction of a Dy single crystal on warming was measured by Tishin and Spichkin (1996) (see fig. 15). At T_C a sharp decrease of the internal friction was observed with a relatively low value of Q^{-1} for the helical phase. At low temperatures in the ferromagnetic region a large maximum occurred at ~ 40 K. Such a maximum was also found at the same temperature in Gd–Dy polycrystalline alloys by Tishin and Shipilov (1993) and in an Er single crystal by Nikitin et al. (1993). The nature of the maximum was discussed by Tishin and Makhro (1994) and Bohr et al. (1995). According to the suggested model the observed maximum in the ferromagnetic region may be connected with an additional energy loss due to the movement of the narrow 180° Bloch domain walls inside the crystal. The walls are pinned in the potential pits of the intrinsic coercivity. At a certain temperature the interaction of the walls and the thermal magnons is sufficient to overcome the potential barriers of the pinning sites. In this case the wall can be moved through the crystal even by a weak magnetoelastic field caused by sample vibrations, which causes the damping to increase.

An interesting behavior of internal friction was observed in an erbium single crystal by Nikitin et al. (1993). Although the peculiarities of the Q^{-1} temperature dependence measured along the c-axis were rather weakly pronounced at the temperatures of the magnetic phase transitions, there was a large maximum in the low temperature region where the internal friction value was about two orders of magnitude larger than outside of this region. As was mentioned above this anomaly could be attributed to the thermally activated domain wall relaxation process. Studies along the crystallographic a- and b-axes revealed analogous anomalies. Besides that, additional peculiarities were observed for $Q^{-1}(T)$ at 27, 35 and 41.5 K, where Young's modulus also display anomalies. Nikitin et al. (1993) explained the observed anomalies by commensurate effects – namely the transition between spin-slip structures which, in accordance with the neutron and X-ray diffraction data took place near these temperatures (see sect. 7).

The internal friction in a $Ho_{0.5}Er_{0.5}$ single crystal was measured in the basal plane by Spichkin et al. (1996b) (see fig. 20). According to the neutron diffraction and X-ray studies this alloy has a complex magnetic structure (Howard and Bohr 1991, Pengra et al. 1994). Below T_N = 104 K a binary phase, which can be described as a c-axis modulated spiral with different tilt angles for Ho and Er, exists. At 47.5 K this phase is transformed to a basal plane antiferromagnetic spiral and below T_C = 35 K the transition to a conical ferromagnetic spiral occurs. The internal friction, which, while it has a small value in the low temperature region, displays weak anomalies near the temperatures of these transitions: an increase near T_C and inflection points near 50 K and T_N. The observed increase of Q^{-1} at high temperatures in the paramagnetic region was related to the relaxation processes in the crystal lattice.

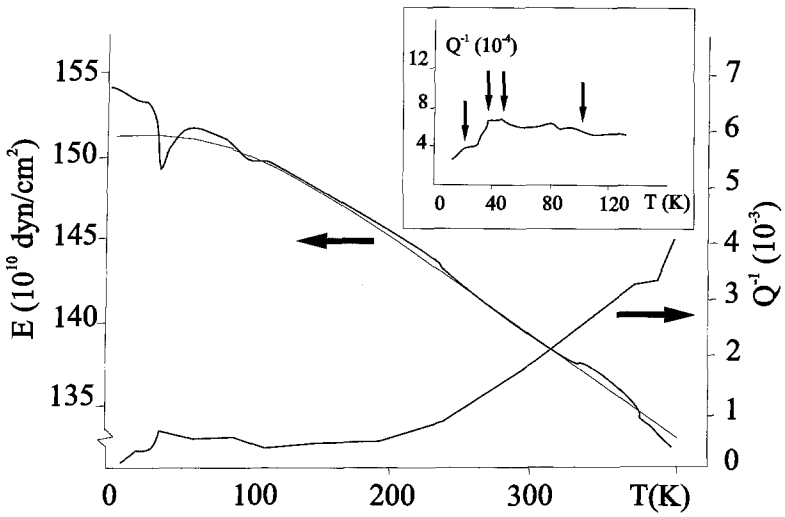

Fig. 20. Temperature dependence of Young's modulus and internal friction of $Ho_{0.5}Er_{0.5}$ single crystals measured in the basal plane. The thin solid line is the calculated lattice part of the Young's modulus. The frequency is ~3 kHz (Spichkin et al. 1996b).

7. Elastic properties

7.1. *Introduction*

The magnetic structure has a strong influence on the elastic properties causing the appearance of various anomalies at magnetic transition points, and a strong magnetic field dependence in the magnetically ordered states. A large amount of the experimental data on the temperature dependence of the elastic constants of the rare earth metals can be found in the review of Scott (1978). Here the main attention will be paid to the models describing the behavior of the elastic constants related to the existence of magnetic order and to results that were not reviewed earlier.

7.2. *Anomalies near magnetic transitions*

7.2.1. *Thermodynamic consideration*

In a single-domain ferromagnet the Young's modulus anomaly at the Curie temperature arises from an additional magnetostriction deformation of the sample caused by the change of spontaneous magnetization under the influence of a mechanical stress acting on the sample during measurement. This is called the "mechanostriction of the paraprocess". The expression for such an anomaly was obtained by Von Döring (1938) on the base of a thermodynamic approach

$$\frac{\Delta E}{EE^0} = -\frac{(\partial\lambda/\partial H)^2}{\chi_{hf}}, \tag{84}$$

where E is Young's modulus in magnetically ordered state, $\Delta E = E - E^0$ is the Young's modulus change due to the change of magnetic ordering, $\partial\lambda/\partial H$ is the forced linear magnetostriction of the paraprocess, and χ_{hf} is the high field susceptibility. The Young's modulus anomaly of this type is always negative.

In helical antiferromagnets an additional contribution to the Young's modulus anomaly is observed which is due to the influence of the stress on the spiral spin structure. It was considered by Lee (1964) and Landry (1967) in the framework of a model proposed by Herpin and Meriel (1961) and Enz (1960). It was assumed that the magnetoelastic interaction which caused the Young's modulus anomaly, was due to the variation of exchange integrals I_1 and I_2 under the variation of lattice constant c. The Young's modulus anomaly measured along the c-axis (ΔE_c) was obtained to be:

$$\frac{\Delta E_c}{E_c E_c^0} = -\frac{s_{33}^2}{2s_{13} + s_{33}} \left(\frac{\partial I_1}{\partial \ln c} \sin \varphi + 2 \frac{\partial I_2}{\partial \ln c} \sin 2\varphi \right) \frac{\mathrm{d}\varphi}{\mathrm{d}P}. \tag{85}$$

This anomaly is also negative in heavy lanthanide metals (according to experiment $\mathrm{d}\varphi/\mathrm{d}P > 0$, and $\partial I_i/\partial \ln c \gtrless 0$).

The negative anomaly of elastic constant c_{33} and Young's modulus E_c at the temperature of transition to a magnetically ordered state was observed experimentally in all heavy lanthanide metals (see for example Scott 1978, Spichkin et al. 1996a,b, Bodriakov et al. 1992). However, at further cooling in some of these metals an increase of c_{33} and E_c was observed in spite of the fact that ΔE should have a negative value in the magnetically ordered state due the mechanostriction. Belov et al. (1960) and Kataev (1961) used the thermodynamic theory of second-order phase transitions of Landau and Lifshitz (1958) to describe the Young's modulus anomaly at the Curie temperature in a single-domain isotropic ferromagnet. In the simplest case the magnetoelastic energy can be written as a power series of the mechanical stress p

$$\mathcal{E}_{me} = -(\gamma p \sigma^2 + \varepsilon p^2 \sigma^2 + \cdots), \tag{86}$$

where γ and ε are the thermodynamic coefficients.

Belov et al. (1960) took into account in the free energy of the system the first term in eq. (86), which is linear in mechanical stress. As a result the equation for the Young's modulus anomaly, which was derived for the static case in the absence of an external magnetic field, has the form

$$\frac{\Delta E}{E E^0} = -\frac{\gamma^2}{2\beta}, \tag{87}$$

where β is the thermodynamic coefficient (see eq. 75). Equation (87) is analogous to eq. (84) derived by Von Döring (1938).

The second term in expansion (86), squared in mechanical stress, was taken into account by Kataev (1961). For an isotropic ferromagnet the following formula was derived:

$$\frac{\Delta E}{EE^0} = -\frac{\gamma^2}{2\beta} + \varepsilon\sigma_S^2. \tag{88}$$

The second term in eq. (88) was related to the change of the bonding forces between the atoms in a crystalline lattice due to the magnetostriction deformations in the magnetically ordered state.

The Young's modulus anomaly arising at the transition from the paramagnetic to the helical phase in a single-domain spiral antiferromagnet, which belongs to the 6 mm (D_{6h}^4) Laue class, was considered by Spichkin and Tishin (1997).

The total thermodynamic potential of the system in a magnetic field H was written in the form

$$\begin{aligned} F = {} & \tfrac{1}{2}\alpha\sigma^2 + \tfrac{1}{4}\beta\sigma^4 - \sigma^2(n_1\cos\varphi + n_2\cos 2\varphi) \\ & - M_{ij,kl}\sigma_i\sigma_j T_{kl} - R_{ij,klno}\sigma_i\sigma_j T_{kl}T_{no} - \tfrac{1}{2}S_{ij,kl}T_{ij}T_{kl} - H_i\sigma_i. \end{aligned} \tag{89}$$

The first and second terms here represent the exchange contribution to the free energy. The third term is the energy of the helical spin structure written down in the form proposed by Herpin and Meriel (1961) and Enz (1960), where n_1 and n_2 are the exchange parameters related to the exchange integrals I_1 and I_2 by the expression

$$n_i = \frac{2(g_J - 1)^2}{g_J^2 N\mu_B^2} I_i. \tag{90}$$

The parameters n_1 and n_2 were assumed to depend on the crystal lattice parameter c in the same way as proposed by Lee (1964) and Landry (1967):

$$n_i = n_{i0} + \frac{\partial n_i}{\partial \ln c}\epsilon_{33}. \tag{91}$$

The fourth and fifth terms are the magnetoelastic contribution written down in the tensor form (Mason 1951). Here the terms, which are linear and squared on the mechanical stress tensor components T_{ij}, were taken into account. The Cartesian axes x, y and z coincide with crystallographic axes a, b and c, respectively. The nonzero components of the tensors $M_{ij,kl}$ and $R_{ij,klno}$ for a crystal with a 6 mm symmetry class were derived by Fumi (1952). The sixth term is the elastic energy.

The spontaneous magnetization σ_S, the magnetization σ in a magnetic field and the equilibrium value of the helical turn angle can be derived by minimizing the free energy F, which is considered to be a function of σ and φ. With the magnetization found one

Table 11
The values of coefficients B_ε and D_ε from eqs. (93) and (94) (Spichkin and Tishin 1997)

Measurement conditions	Measured value	B_ε	D_ε
H or σ_s aligned along crystallographic a-axis; $\sigma_1 = \sigma \neq 0; \sigma_2 = \sigma_3 = 0$	s_{11}; $\Delta E_a/E_a E_a^0$	$(\gamma_{11} + s_{13}\eta)^2$	ε_{111}
	s_{22}; $\Delta E_b/E_b E_b^0$	$(\gamma_{12} + s_{13}\eta)^2$	a_ε
	s_{33}; $\Delta E_c/E_c E_c^0$	$(\gamma_{13} + s_{33}\eta)^2$	ε_{133}
	s_{21}	$(\gamma_{11} + s_{13}\eta)(\gamma_{12} + s_{13}\eta)$	ε_{112}
	s_{31}	$(\gamma_{11} + s_{13}\eta)(\gamma_{13} + s_{33}\eta)$	ε_{113}
H or σ_s aligned along crystallographic b-axis; $\sigma_2 = \sigma \neq 0; \sigma_1 = \sigma_3 = 0$	s_{11}; $\Delta E_a/E_a E_a^0$	$(\gamma_{12} + s_{13}\eta)^2$	ε_{211}
	s_{22}; $\Delta E_b/E_b E_b^0$	$(\gamma_{11} + s_{13}\eta)^2$	ε_{222}
	s_{33}; $\Delta E_c/E_c E_c^0$	$(\gamma_{13} + s_{33}\eta)^2$	ε_{133}
	s_{21}	$(\gamma_{11} + s_{13}\eta)(\gamma_{12} + s_{13}\eta)$	a'_ε
	s_{31}	$(\gamma_{11} + s_{13}\eta)(\gamma_{13} + s_{33}\eta)$	ε_{123}
H or σ_s aligned along crystallographic c-axis; $\sigma_3 = \sigma \neq 0; \sigma_1 = \sigma_2 = 0$	s_{11}; $\Delta E_a/E_a E_a^0$	γ_{31}^2	ε_{311}
	s_{22}; $\Delta E_b/E_b E_b^0$	γ_{31}^2	ε_{311}
	s_{33}; $\Delta E_c/E_c E_c^0$	γ_{33}^2	ε_{333}
	s_{21}	γ_{31}^2	ε_{312}
	s_{31}	$\gamma_{31}\gamma_{33}$	ε_{313}

can calculate the energy of the magnetically ordered state and then by means of the thermodynamic relation

$$s_{ij} = -\frac{\partial^2 F}{\partial T_i \partial T_j}, \tag{92}$$

where the elastic compliances s_{ij} and Young's modulus E_i are for the magnetically ordered state. Here the two interchangeable indices are replaced by a single index according to the equations: $11 = 1$; $22 = 2$; $33 = 3$; $12 = 21 = 6$; $13 = 31 = 5$; $23 = 32 = 4$. The results obtained can be summarized in the following general formulas (Spichkin and Tishin 1997):

$$s_{ij} = s_{ij}^0 + \left(\frac{B_\varepsilon}{2\beta\sigma^2 + H/\sigma} - D_\varepsilon\right)\sigma^2, \tag{93}$$

$$\frac{\Delta E_i}{E_i E_i^0} = -\left(\frac{B_\varepsilon}{2\beta\sigma^2 + H/\sigma} - D_\varepsilon\right)\sigma^2, \tag{94}$$

where the coefficients B_ε and D_ε are given in table 11 for different cases of measurement. In table 11 the following notations are made

$$\begin{aligned} &\gamma_{ij} = 2M_{ij}; \qquad \varepsilon_{ijk} = 2R_{ijk}; \\ &a_\varepsilon = \varepsilon_{111} + \varepsilon_{211} - \varepsilon_{222}; \qquad a'_\varepsilon = \varepsilon_{111} + \varepsilon_{112} - \varepsilon_{222}. \end{aligned} \tag{95}$$

The parameter η characterizes the effect of the elastic stresses on the helical spin structure and has the form

$$\eta = \frac{2n_{10}n_{20}\frac{\partial n_1}{\partial \ln c} + 8(n_{20}^2 - n_{10}^2)\frac{\partial n_2}{\partial \ln c}}{4n_{20}^2}. \tag{96}$$

For measurements in a magnetic field high enough to destroy the helical structure, $\eta = 0$.

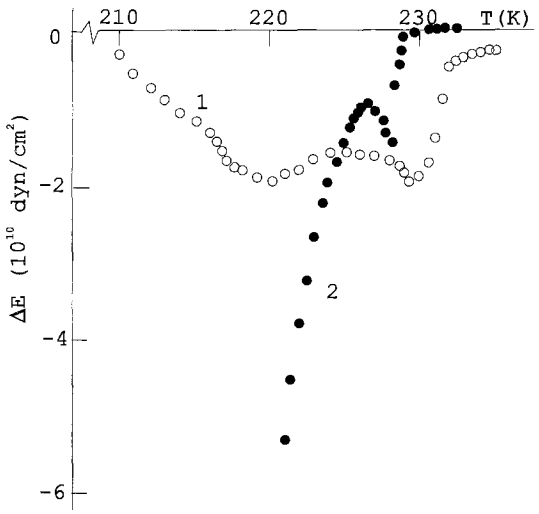

Fig. 21. Temperature dependence of ΔE_c (curve 1) and ΔE_b (curve 2) for terbium in the range of the magnetic phase transitions (Spichkin and Tishin 1997).

Near the Curie point according to the theory of second-order phase transitions the following field dependence of magnetization takes place:

$$\sigma = \beta^{-1/3} H^{1/3}, \tag{97}$$

which leads to a $H^{2/3}$ field dependence of E_i

$$\frac{\Delta E_i}{E_i E_i^0} = -\left(\frac{B_\varepsilon}{3\beta} - \frac{D_\varepsilon H^{2/3}}{\beta^{2/3}}\right). \tag{98}$$

Since the experimental measurements of the elastic properties are made in a dynamic regime, when the elastic waves are excited in the sample, it is necessary to take into account the relaxation effects. According to Belov et al. (1960) and Kataev (1961) this gives the following relaxation relations:

$$\frac{\Delta E_i}{E_i^0} = -\left(\frac{\Delta_{E_i}}{1+\omega^2\tau^2} - E_i D_\varepsilon \sigma^2\right), \tag{99}$$

$$s_{ij} = s_{ij}^0 + \frac{B_\varepsilon \sigma^2}{(2\beta\sigma^2 + H/\sigma)(1+\omega^2\tau^2)} - D_\varepsilon \sigma^2, \tag{100}$$

where Δ_{E_i} is the Young's modulus relaxation degree,

$$\Delta_{E_i} = \frac{E_i^0}{2\beta\sigma^2 + H/\sigma}, \tag{101}$$

ω is the frequency of sample oscillations, and τ is the relaxation time (see sect. 6.2.2).

Spichkin and Tishin (1997) and Spichkin et al. (1996a) studied the temperature and field dependencies of Young's modulus E_a and E_b in Tb at acoustic frequencies. Figure 21 shows $\Delta E_c(T)$ and $\Delta E_b(T)$ – the parts of Young's modulus due to the existence of a magnetic structure in the region near T_N and T_C. The pure lattice Young's

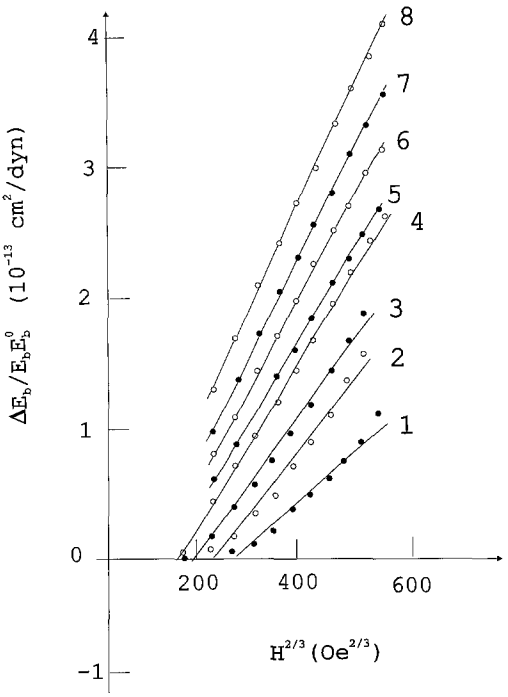

Fig. 22. $\Delta E_b/E_bE_b^0$ as a function of $H^{2/3}$ for terbium near T_N. (1) T = 246 K; (2) 240 K; (3) 235 K; (4) 232 K; (5) 229 K; (6) 226 K; (7) 220 K; (8) 210 K. The magnetic field was applied along the b-axis (Spichkin and Tishin 1997).

modulus $E^0(T)$ was calculated by means of the model proposed by Lakkad (1971) and experimentally tested by Tishin et al. (1995) on yttrium. The observed temperature dependencies of E_c and E_b are analogous to that of c_{33} and c_{11} obtained earlier by ultrasound methods (see Jiles et al. 1984, Scott 1978). Field measurements of E_b (H along the b-axis) revealed near T_N the linear dependence of $\Delta E_b/E_bE_b^0$ on $H^{2/3}$ in accordance with eq. (98) – see fig. 22. Far from T_N in the paramagnetic phase a deviation from this dependence was observed. The experimental values of γ_{11} (obtained from $\Delta E_b(H)$ curves), β (obtained from magnetization measurements), s_{ij} from the work of Salama et al. (1972) and $\partial I_i/\partial \ln c$ data of Bartholin and Bloch (1968a) allowed one to calculate $\Delta E_b/E_bE_b^0 = -1.5\times10^{-10}$ cm^2/dyn at T_N using eq. (94); this is consistent with the experimental value of -0.7×10^{-10} cm^2/dyn. If the coefficients ε_{133} and ε_{222} ($\varepsilon_{222} \approx 4.5\times10^{-19}$ G^{-4} as obtained from experiment) are positive then the magnetic anomalies ΔE_c and ΔE_b below T_N should decrease in absolute value upon cooling because of the spontaneous magnetization. Such a behavior was observed experimentally near T_N (see fig. 21).

7.2.2. *Microscopic models*

Southern and Goodings (1973) and Goodings (1977) used the theory developed by Brown (1965) and Melcher (1972) for the description of elastic constant anomalies and their field dependence in the ferromagnetic state and near the transition from the paramagnetic

to the magnetically ordered state in the lanthanide metals with a hexagonal structure. This theory is based on the finite deformations approach and imposes the requirement that the Hamiltonian of the system should be invariant under rigid rotation of magnetic and lattice subsystems. The Hamiltonian included the Heisenberg exchange term (in molecular field approximation), crystal field, magnetoelastic, elastic energy terms and the magnetic energy due to the external magnetic field. For the paramagnetic state the magnetoelastic energy in terms of the first and second order in small strains originating in either the single-ion or two-ion interactions was taken into account, and complex formulas of the field changes for the elastic constants c_{11} and c_{33} were obtained (the case of the ferromagnetic state will be discussed later). The main consequence from these formulas is that Δc_{ii} (here Δc_{ii} is the change of c_{ii} in magnetic field, $\Delta c_{ii} = c_{ii}(H) - c_{ii}(H = 0)$) should be directly proportional to the second order of the magnetization. Since magnetization is supposed to be $\sigma = \chi(T)H$ (where susceptibility χ is not dependent on H) this leads to a H^2 dependence of Δc_{ii}. Such a dependence in the paramagnetic region was observed experimentally in Gd, Tb, Dy and Ho by Moran and Lüthi (1970) and Jiles and Palmer (1980), in Dy by Isci and Palmer (1978), in Tb by Salama et al. (1974) for temperatures far from T_N. Near T_N deviation from the H^2 dependence of Δc_{ii} was observed. This may be related to the field dependence of the magnetic susceptibility. The nonlinear dependence of σ on H following from the theory of second-order magnetic phase transitions leads to a $H^{2/3}$ dependence of ΔE (see eq. 98) and was observed experimentally in Tb for ΔE_b and H applied along the b-axis (see fig. 22).

Vasconcelos (1982) by means of the model of Southern and Goodings (1973) considered the $c_{33}(T)$ behavior near T_N in erbium. Good agreement of the calculated $c_{33}(T)$ dependence with the experimentally observed drop in c_{33} near T_N was found.

7.3. *Magnetically ordered state of the heavy lanthanide metals and their alloys*

7.3.1. *Helical phase*

The behavior of the elastic constants c_{11} and c_{33}, and Young's moduli E_a and E_b of the lanthanide metals in the helical antiferromagnetic phase has been studied most. The temperature dependencies of these values reveal peculiarities not only at the transition to the magnetically ordered state, T_N, but also at the temperature of the transition to the phase with the ferromagnetic component, T_C (see Scott 1978).

The temperature hysteresis of c_{33} in the helical state was observed in Dy, $Tb_{0.5}Ho_{0.5}$ and $Gd_{0.6}Y_{0.4}$ alloys by Palmer (1975) and Blackie and Palmer (1980). Figure 23 shows the result of thermal cycling near T_C in Dy. First the sample was cooled below T_C into the ferromagnetic state and then warmed into the helical phase. Under this condition a drop in c_{33} (compare with the value obtained under cooling conditions) was observed. This effect was explained by Palmer (1975) to be due to the existence of spiral domains and domain walls between them as discussed in sect. 6. Compressive and expansive stresses parallel to the c-axis produced by the sound wave causes the rotation of the magnetization in the walls, changing their thickness and the dimension of the domains. This leads to the development of additional magnetostrictive strains reducing the elastic

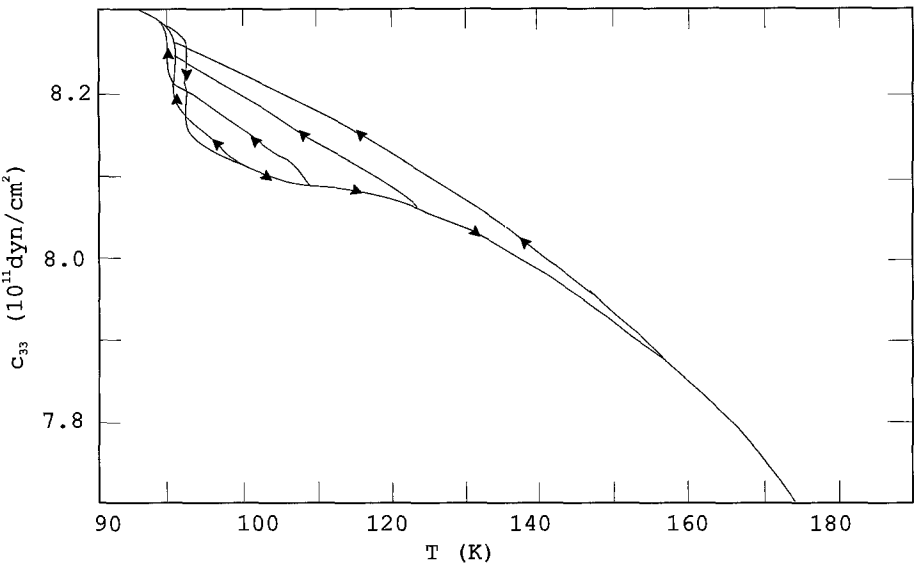

Fig. 23. Temperature dependence of the elastic constant c_{33} in Dy near T_C (Blackie and Palmer 1980).

constants (i.e., this is the mechanostriction mechanism discussed above). The difference in the value of c_{33} observed on cooling from the paramagnetic state and warming from the ferromagnetic state is connected with the difference in the number of spiral domains in the two cases. The maximum number of spiral domains exists near T_C and it decreases as T_N is approached. Blackie and Palmer (1980) measured $c_{33}(T)$ when the sample was cooled from various temperatures in the helical phase (see fig. 23). In this case the number of spiral domains remains approximately constant and all $c_{33}(T)$ curves were nearly parallel down to T_C.

Hysteresis was observed also in other rare earth alloys with the helical phase – $Gd_{0.6}Y_{0.4}$ (see fig. 24), $Gd_{0.654}Y_{0.346}$ and $Gd_{0.689}Y_{0.311}$ by Palmer et al. (1977), Sousa et al. (1982) and Blackie and Palmer (1982), respectively. At the same time the elastic constant in the basal plane c_{11} and shear elastic constant c_{44} do not reveal any hysteresis of this type. According to the model proposed by Palmer (1975) the number of spiral domains interacting with the longitudinal sound wave propagating in the basal plane is the same on cooling from the paramagnetic phase and warming from the ferromagnetic state as was discussed in sect. 6. The shear sound wave is coupled with spins only in second order and its interaction with spiral domain walls is small. In the ferromagnetic alloy $Gd_{0.703}Y_{0.297}$ no hysteresis was observed (Blackie and Palmer 1982).

Later, Palmer et al. (1986) investigated the influence of the sample purity on domain patterns and the hysteresis in the helical phase in Tb and Ho. The domain patterns were observed by polarized neutron diffraction topography. It was found that the size of the spiral domains in the helical state was very sensitive to the sample purity. For the low purity material the size of the domains was below the resolution limit of the method, and

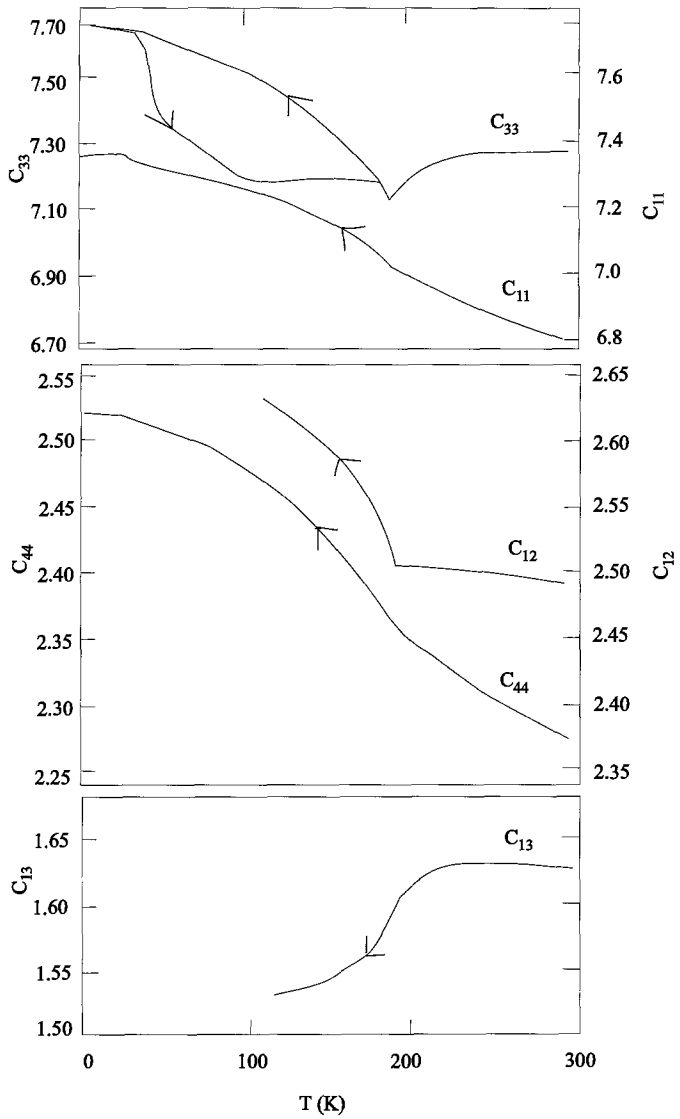

Fig. 24. Temperature dependence of the elastic constant c_{12}, c_{13}, c_{33}, c_{11} and c_{44} for the $Gd_{0.6}Y_{0.4}$ alloy for increasing and decreasing temperature. c_{ij} in units of 10^{11} dyn/cm^2 (Palmer et al. 1977).

for high purity Tb (resistivity ratio $R_{300}/R_{4.2} > 150$) domains ranging from 0.15 mm to several mm were observed. The c_{33} temperature dependence measurements in high purity Tb did not reveal the hysteresis on warming from the ferromagnetic state. Palmer et al. (1986) explained this by the small number of domain walls which exist in the high purity sample. They noted that in Ho the situation is quite different since even below T_C the spin

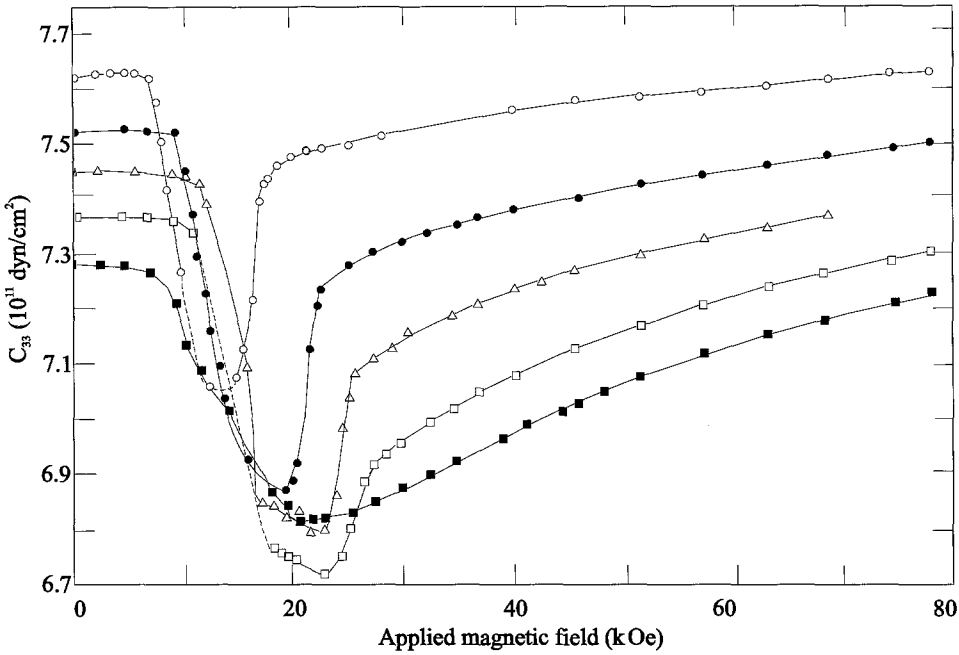

Fig. 25. Magnetic field dependence of the elastic constant c_{33} at various temperatures in Dy (field along the a-axis). Open circles, 135 K; solid circles, 150 K; open triangles, 160 K; open squares, 168 K; solid squares, 175 K (Isci and Palmer 1978).

structure has a spiral character. So the domain pattern should not change when warming from the phase below T_C. This can explain the absence of hysteresis in Ho observed experimentally.

The field dependencies of the elastic constant c_{33} in the helical phase were measured in $Gd_{0.6}Y_{0.4}$ and $Ho_{0.5}Tb_{0.5}$ alloys, and in Tb and Dy by Palmer et al. (1977), Isci and Palmer (1977, 1978), Jiles et al. (1984). We will consider the results obtained for Dy by Isci and Palmer (1978) because the features of the $c_{33}(H)$ curves in the helical state are characteristic for all lanthanide metals with a spiral antiferromagnetic structure (see fig. 25). Just above T_C in the helical state a shallow minimum was observed which was attributed to the helical antiferromagnetic to the ferromagnetic transition. Above 125 K there is a sudden drop in c_{33} at what was assumed to be the HAFM–fan structure transition followed by a rapid increase at the fan–FM state transition. The interval of the fan structure existence is governed by the basal plane anisotropy which brings H_f (the field corresponding to the transition from fan to FM structure) down to the same value as H_{cr} at low temperatures leading to one minimum at $c_{33}(H)$. With increasing temperature the plane anisotropy decreases and two separate transitions are observed at the $c_{33}(H)$ curves. The results of sound attenuation measurements show that the transition HAFM–FM phases are realized through intermediate phases. Above H_f the constant c_{33} still has

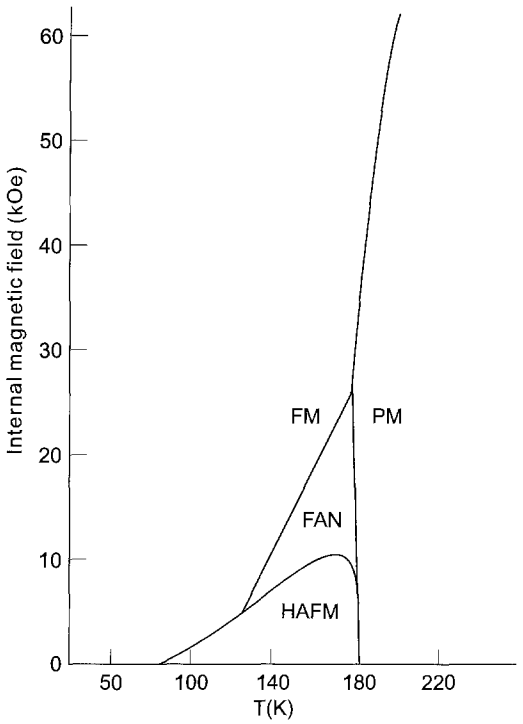

Fig. 26. Magnetic phase diagram of dysprosium obtained from elastic constant c_{33} measurements in a magnetic field (Isci and Palmer 1978). Ferromagnetic (FM), paramagnetic (PM), helical antiferromagnetic (HAFM) and fan phases are shown.

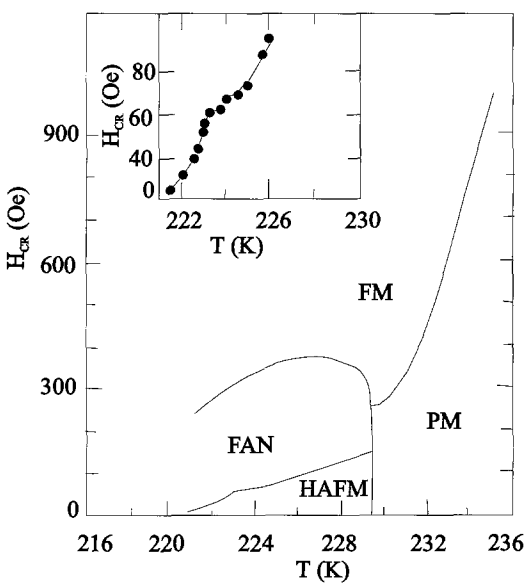

Fig. 27. Magnetic phase diagram of terbium obtained from the field measurements of Young's modulus E_b (Kataev et al. 1989b). The insert shows the behavior of H_{cr} near 223.5 K.

a significant magnetic field dependence. On the base of these $c_{33}(H)$ measurements a simplified magnetic phase diagram of Dy was constructed by Isci and Palmer (1978) which is shown in fig. 26.

Jiles et al. (1984) studied the isotherms $c_{33}(H)$ and isofields $c_{33}(T)$ of high purity terbium and constructed its magnetic phase diagram. Kataev et al. (1989b) investigated Young's modulus E_b in high purity Tb ($R_{300}/R_{4.2} \approx 100$) in fields up to 2.5 kOe. The phase diagram obtained in this work is shown in fig. 27. The anomalous behavior of H_{cr} observed near 223.5 K was associated with the commensurate effect by the authors.

The field dependencies of E_a and E_b were measured for a $Tb_{0.5}Dy_{0.5}$ single crystal by Kataev et al. (1989c). Like Tb and Dy this alloy is a helical antiferromagnet with an easy basal plane (Bykhover et al. 1990). The field behavior of E_b and E_a in the HAFM phase is analogous to that observed for c_{33} in Dy and Tb by Isci and Palmer (1978) and Jiles et al. (1984) (see fig. 28). The magnetic phase diagram $H_{cr}(T)$ of $Tb_{0.5}Dy_{0.5}$ constructed

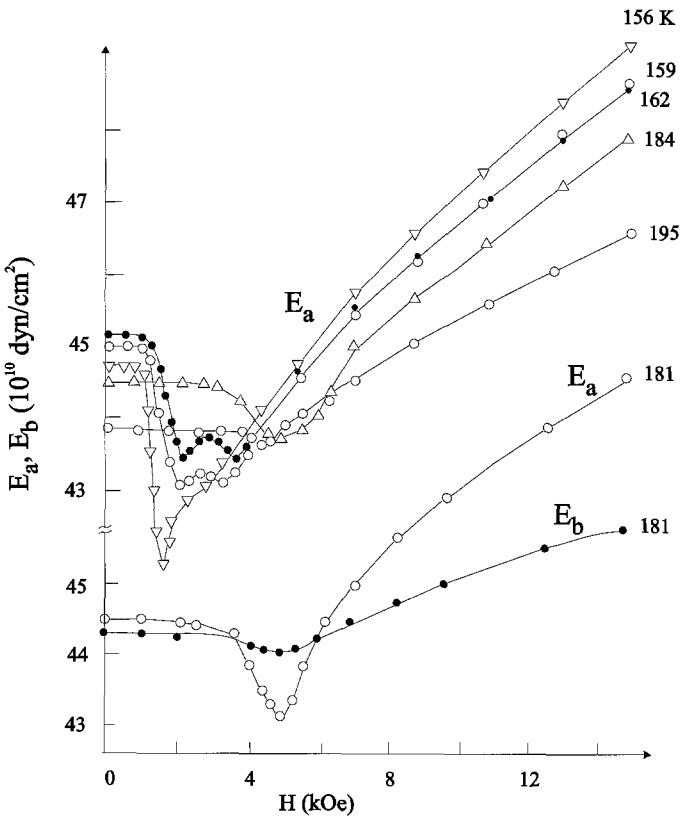

Fig. 28. The isothermal magnetic field dependencies of Young's moduli E_a and E_b measured for the $Tb_{0.5}Dy_{0.5}$ alloy (field directed along the a- and the b-axis, respectively). E_b: solid circles, 181 K. E_a: open inverted triangles, 156 K; open circles, 159 K; solid circles, 162 K; open circles, 181 K; open triangles, 184 K; open circles, 195 K (Kataev et al. 1989c).

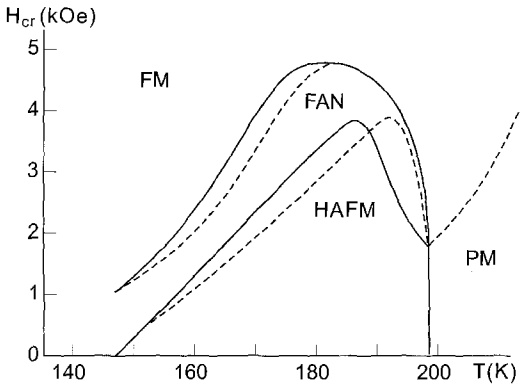

Fig. 29. Magnetic phase diagram of $Tb_{0.5}Dy_{0.5}$ obtained from field measurements of Young's moduli E_a (dashed lines) and E_b (solid lines) (Kataev et al. 1989c).

on the base of the data on $E_b(H)$ and $E_a(H)$ is shown in fig. 29. As for Tb and Dy three magnetically ordered phases were distinguished: HAFM, fan and FM. In spite of some anisotropy in the field behavior of E_a and E_b (see fig. 28, the curve for 181 K), the phase diagrams obtained from $E_a(H)$ and $E_b(H)$ curves are quite similar. The magnetic phase diagrams of Tb, Dy and $Tb_{0.5}Dy_{0.5}$, which were constructed on the base of the data on elastic constants and moduli, are consistent with those obtained by means of magnetization measurements.

7.3.2. *Ferromagnetic phase*

Southern and Goodings (1973) considered theoretically the field dependence of the elastic constants c_{ij} in the ferromagnetic state in the lanthanide metals with a hexagonal crystal structure. It was found that for H applied parallel to the c-axis c_{11}, c_{33} and c_{66}, and for H aligned along the a- or b-axis in the basal plane c_{11} and c_{33} were not affected by the magnetic field. For the c_{44} and c_{66} field dependencies complex expressions were obtained. In the case of a magnetic field aligned parallel to the c-axis the change of the c_{44} elastic constant has the form

$$\Delta c_{44} = c_{44}(H) - c_{44}(H_0) = \frac{\sigma(h - h_0)(b^{\epsilon}\sigma^3 \pm f_1)}{4(f_1 + \sigma h_0)(f_1 + \sigma h)} \tag{102}$$

where

$$f_1 = -3k_1 - 10k_2\sigma^{10} - 21k_6^6\sigma^{21}. \tag{103}$$

Here b^{ϵ} is the magnetoelastic coupling constant connected with the constant B^{ϵ} from eq. (68); the constants k_1, k_2 and k_6^6 describe the uniaxial and basal plane magnetocrystalline anisotropy, respectively; σ, the reduced magnetization; H_0, the magnetic field large enough to overcome the magnetocrystalline anisotropy and to ensure really complete alignment of domains; and $h = Ng_J\mu_B HJ$, the reduced magnetic field. The sign in the last term of the numerator in eq. (102) depends on the direction of propagation

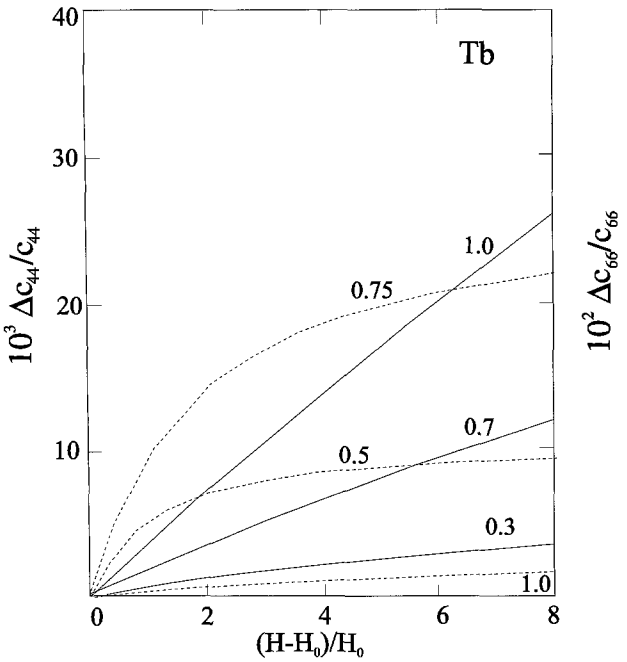

Fig. 30. $\Delta c_{66}/c_{66}$ and $\Delta c_{44}/c_{44}$ as a function of $(H - H_0)/H_0$ calculated for terbium by Southern and Goodings (1973) (magnetic field along the *b*-axis). The values near the curves are the reduced magnetization. Solid curves: $\Delta c_{44}/c_{44}$ for sound wave propagation along the *c*-axis; dashed curves, $\Delta c_{66}/c_{66}$ for propagation along the *b*-axis.

and polarization of the sound wave: the plus refers to the wave propagating along the *c*-axis and polarized along the *a*- or *b*-axis, and the minus is for the opposite situation. For the case of a ferromagnetic phase two-ion magnetoelastic interactions were not taken into account. The calculations made by Southern and Goodings (1973) for Gd, Tb, Dy and Er, which were based on experimental data of the anisotropy and magnetoelastic coupling constants, showed a nonlinear increase of c_{44} and c_{66} with the field aligned in the basal plane. Field saturation of Δc_{66} was observed for $H \approx 9H_0$ ($H_0 = 10\,\text{kOe}$) for Gd, Dy and Ho. The dependencies $c_{44}(H)$ do not reveal saturation in Tb and Dy. The maximum saturated value of $\Delta c_{66}/c_{66}$ was calculated to be about 10^{-2}–10^{-1} for $H = 9H_0$ for Tb, Dy and Ho (for $\sigma = 0.5$) and the minimum ($\sim 10^{-4}$) for Gd. Figure 30 shows the calculated $\Delta c_{44}/c_{44}$ and $\Delta c_{66}/c_{66}$ as functions of the field directed along the *b*-axis for Tb. Experimental measurements of c_{33} in Dy and the $Ho_{0.5}Tb_{0.5}$ alloy made by Isci and Palmer (1977, 1978) reveal a significant field dependence in high fields which is not consistent with results of Southern and Goodings (1973). Isci and Palmer attributed this effect to the incomplete alignment of spins or to the existence of ferromagnetic and fan domains even in such high fields above H_f.

Jensen and Palmer (1979) studied the behavior of c_{66} in the ferromagnetic phase of Tb under magnetization along the hard *a*-axis in the basal plane. Application of a

magnetic field of sufficient magnitude (~ 32 kOe) leads to the alignment of moments in this direction. Below this critical field value the moments make some angle with the a-axis. The transition between the two phases is of the second order and the transverse differential magnetic susceptibility diverges. Under these conditions the action of elastic stresses will give rise to a strong variation of the magnetic structure leading to a large softening of the elastic constants. It was shown with the help of the random-phase theory of a coupled spin–lattice system (Jensen 1971, Liu 1972, Chow and Keffer 1973) that at the field corresponding to the above described transition, c_{66} should go to zero if the shear wave propagates along the hard a-axis and it should display a deep minimum if it propagates along the easy axis. Experimental results obtained by Jensen and Palmer (1979) confirm the theoretical predictions.

Kataev et al. (1985) measured the field dependencies of Young's modulus along the easy b- and hard a-axis in the ferromagnetic alloy $Tb_{0.4}Gd_{0.6}$ for H directed along the b-axis. In the low field region (~ 2 kOe) a negative ΔE effect ($\Delta E = E(H) - E(H = 0)$) and hysteresis of the $\Delta E/E(0)$ curves were found. For an explanation of this behavior the domain model was used. Two utmost cases were considered: (a) the domain walls are displaced by the field and applied mechanical stresses and spin rotations are absent; (b) the same factors alter the equilibrium spin direction in the domains and the domain walls are fixed. It was shown that both mechanisms can cause the negative ΔE effect and the minimum on $E_b(H)$, but the main role is played by the rotation of the spins. It happens in fields where the domain structure is in a nonequilibrium state, and the abrupt reorientation of the non-180° domains to the easy basal plane axis closest to the field direction takes place. This can lead to a considerable softening of E, and its field hysteresis. A further increase of Young's modulus in high fields can be related to the process of domain moments alignment.

The temperature and field dependencies of the elastic constants of Er were studied by du Plessis (1976), Jiles and Palmer (1981) and Eccleston and Palmer (1992). The transitions at T_N, T_{CY} and T_C manifest themselves in anomalies of the temperature dependencies of c_{11}, c_{33} and c_{44} (see fig. 31). A magnetic field applied along the c-axis softens c_{33} and c_{44} in the longitudinal spin wave (LSW) and cycloidal phases, and restiffens c_{11} and c_{66} from the values in zero magnetic field. Jiles and Palmer (1981) studied the field dependencies of c_{11} and c_{33}. For the $c_{33}(H)$ curves measured below T_C for H aligned along the b-axis a lowering of c_{33} at ~ 17 kOe was observed, and in the temperature range 30–50 K for a c-axis field a rapid increase in c_{11} occurred between 5 and 12 kOe depending on temperature. The authors thought this behavior was related to the changes in spin structure: the destruction of the basal plane spiral in the first case and with a collapse of cycloidal structure into a cone in the second case. Above T_{CY} and in the paramagnetic phase the field had little influence on c_{33}. The zero field measurements of c_{33}, c_{11}, c_{44}, and c_{66} made by Jiles and Palmer (1981) and Eccleston and Palmer (1992) confirmed the general form of the $c_{ij}(T)$ curves obtained by du Plessis. In the cycloidal phase these authors observed various inflection points and changes in the slope of the $c_{ij}(T)$ dependencies at 27, 33, 41 and 48 K. These peculiarities were related to commensurate effects in this temperature interval, and these are discussed below.

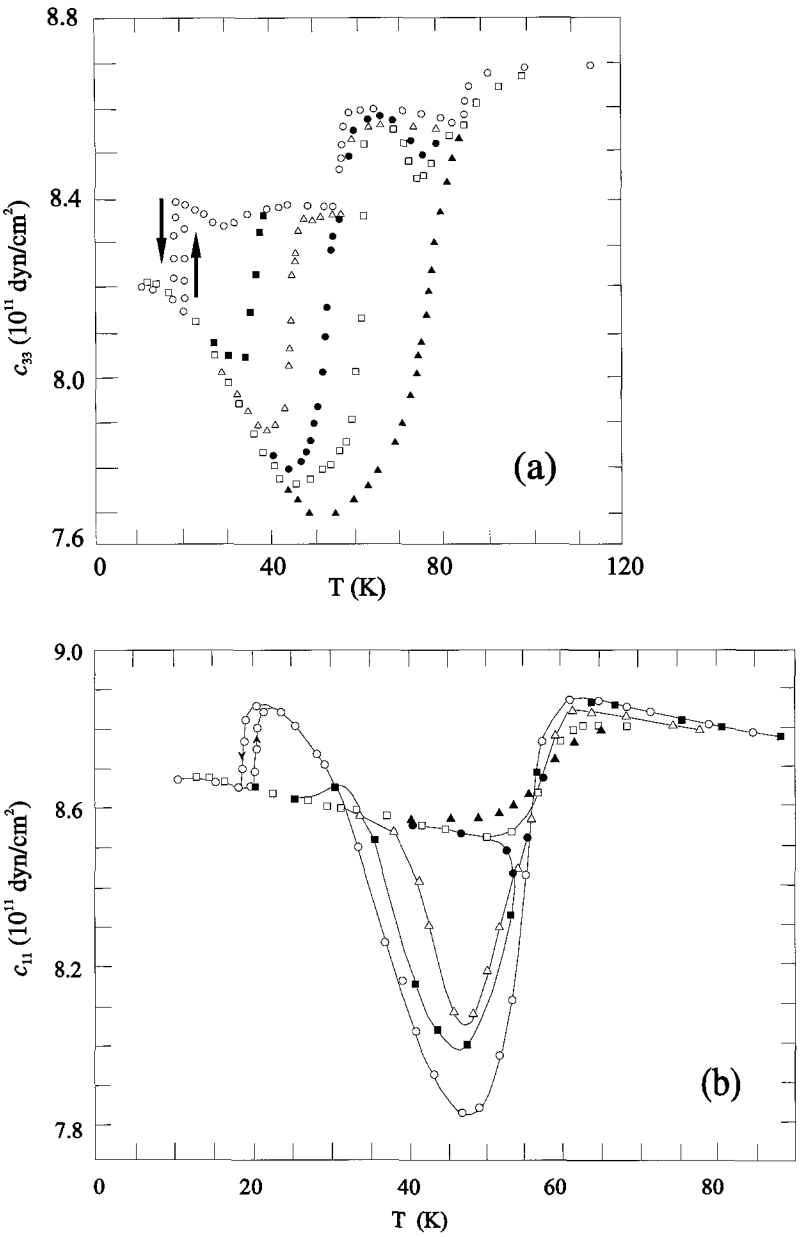

Fig. 31. Temperature dependencies of elastic constants c_{33} (a) and c_{11} (b) of erbium for various values of the magnetic field applied along the c-axis. Open circles, zero field; solid squares, 10 kOe; open triangles, 15 kOe; solid circles, 20 kOe; open squares, 24 kOe; solid triangles, 39 kOe (du Plessis 1976).

7.4. *Gadolinium*

Since the gadolinium was investigated the most thoroughly of all of the lanthanide metals it will be considered separately. All investigators observed anomalies in the elastic constants of gadolinium in the vicinity of the Curie temperature (see Scott 1978). The temperature dependence of the elastic constant c_{33} reveals two dips: at the Curie temperature T_C and at the spin-reorientation transition temperature T_{sr} (see fig. 32).

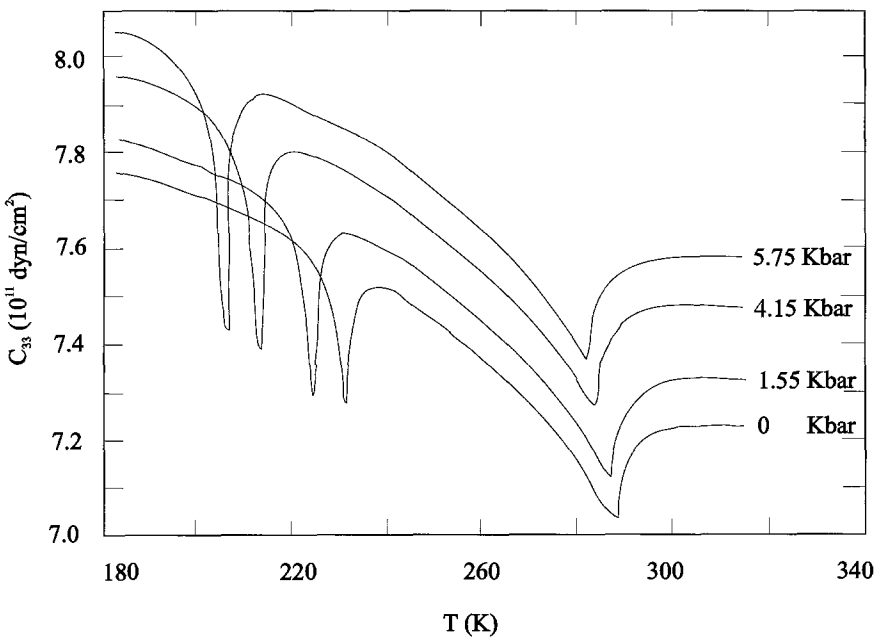

Fig. 32. Temperature dependencies of the elastic constant c_{33} of gadolinium at various hydrostatic pressures (Klimker and Rosen 1973).

The origin and field dependence of the anomaly at T_{sr} were considered by Levinson and Shtrikman (1971), Freyne (1972) and Klimker and Rosen (1973). The mechanostriction mechanism was assumed to cause the anomaly. The application of strain along the c-axis induces a spin rotation back towards the c-axis which changes the magnetization and causes additional magnetostrictive deformations leading to the drop in c_{33}. Using a system Hamiltonian consisting of the isotropic energy term, the elastic energy associated with homogeneous strains, the energy of the magnetocrystalline anisotropy, and the energy of single-ion and two-ion magnetoelastic coupling squared in spin components and linear in

strain, Klimker and Rosen (1973) derived the following expressions for the c_{ij} change at T_{sr}:

$$\begin{aligned} c_{11} &= c_{11}(0) - \frac{(b_{11}(\phi))^2}{2K_2}, \qquad c_{12} = c_{12}(0) - \frac{(b_{11}(\phi))^2}{2K_2}, \\ c_{33} &= c_{33}(0) - \frac{(b_{33}(\phi))^2}{2K_2}, \qquad c_{13} = c_{13}(0) - \frac{b_{33}(\phi)b_{11}(\phi)}{2K_2}, \\ c_{44} &= c_{44}(0), \qquad c_{66} = c_{66}(0), \end{aligned} \tag{104}$$

where $c_{ij}(0)$ are the elastic constants for $\phi = 0$; $b_{ij}(\phi)$ are the constants of magnetoelastic coupling which depend on the angle ϕ and are connected with the constants B_{11}^{α} and B_{22}^{α} from Callen and Callen (1965). The constants $b_{ij}(\phi)$ were calculated with the help of the available magnetostriction and elastic constant data and it was shown that near T_{sr} $| b_{11}(\phi) | \ll | b_{33}(\phi) |$. This means that the noticeable c_{ij} anomaly at T_{sr} in gadolinium should take place only for c_{33}. The experimental measurements of c_{11} and c_{44} made by Palmer et al. (1974) and Savage and Palmer (1977) confirm the validity of this conclusion.

The hydrostatic pressure dependence of c_{33} was also studied by Klimker and Rosen (1973) (see fig. 32). The increase of c_{33} under pressure is ascribed to the variation of $c_{33}(0)$ due to the higher-order elastic constants. The observed increase of the spin-reorientation anomaly dip under pressure was explained by the pressure dependence of magnetoelastic coupling parameters and changes in magnetic ordering due to the shifts of T_C and T_{sr}.

Freyne (1972) used the same method and took into account the energy of the external magnetic field, $H_i\sigma_i$, in the total Hamiltonian of the system. According to Freyne's result the anomaly at T_{sr} should become shallower with increasing field and the position of the dip should shift to lower temperatures for a field applied in the basal plane. Experimental measurements of the field behavior of c_{33} in the region of spin-reorientation were carried out by Long et al. (1969) (see fig. 33), and are in qualitative agreement with Freyne's theory. However, a quantitative estimate of the field where the anomaly in c_{33} should vanish in the framework of Freyne's theory gives a value of about 100 Oe (Levinson and Shtrikman 1971), which is inconsistent with the experimental results of Long et al. (1969). To overcome this discrepancy Levinson and Shtrikman included in the total Hamiltonian of the system the self-magnetostatic energy contribution and took into account the corresponding domain structure. According to their model in a weak magnetic field the sample consists of the domains whose magnetization lies closest to the applied field direction, i.e. "plus domains", and the domains with magnetization largely opposed to the field (the "minus domains"). In such a domain structure the spin rotation induced by the strains will not alter the magnetostatic energy since the magnetization component in the field direction will remain unchanged. However, for sufficiently large magnetic fields the sample consists only of "plus" domains and the strain induced rotation will strongly change the magnetostatic energy. This will effectively restrict the ability of the magnetic moments to rotate under application of strain and consequently, to lower c_{33}. Since Long et al. (1969) used a cylindrical specimen with a large demagnetizing factor,

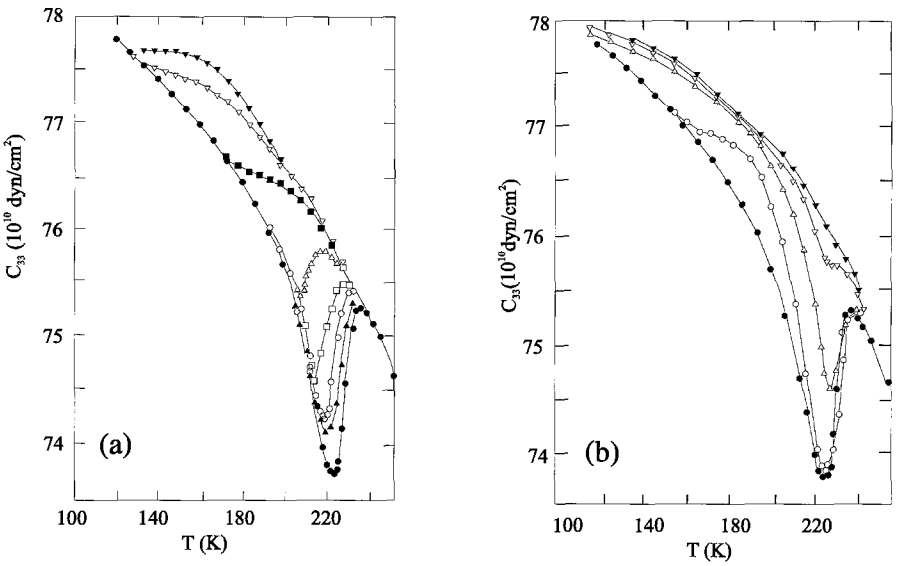

Fig. 33. Temperature dependencies of the elastic constant c_{33} of gadolinium in various magnetic fields. (a) Field in the basal plane; (b) field along the c-axis. Solid circles, zero field; solid triangles, 1 kOe; open circles, 2 kOe; open squares, 3 kOe; open triangles, 4 kOe; solid squares, 5 kOe; open inverted triangles, 6 kOe; solid inverted triangles, 8 kOe (Long et al. 1969).

then the spin-reorientation anomaly vanished in strong enough fields (see fig. 33). The results of the modified calculations made by Levinson and Shtrikman agree well with the experimental field measurements of c_{33} in the spin-reorientation temperature range.

The details of the domain structure and domain rearrangement process strongly depends on the sample purity, internal stresses in the sample, and on the orientation of the applied field with respect to the crystallographic axes. All these factors will affect the magnitude of the spin-reorientation anomaly on c_{33} in gadolinium. Savage and Palmer (1977) did $c_{33}(T)$ measurements on a high purity Gd single crystal and found a much shallower spin-reorientation anomaly than other investigators. Evidently the difference in the spin-reorientation anomaly value obtained by various authors (see Jiles and Palmer 1980, Savage and Palmer 1977, Klimker and Rosen 1973) can be explained by different sample purities and the existence of internal stresses in the samples.

The position of the dip in c_{33} at the Curie temperature was found by Jiles and Palmer (1980) to be weakly dependent on magnetic field and became broad and indistinct in strong magnetic fields. In the paramagnetic phase the decrease of c_{33} was found to be proportional to H^2 which is consistent with the theory of Southern and Goodings (1973).

7.5. *The effect of commensurate magnetic structures on the elastic properties*

As was noted in sect. 6 the maxima in the temperature dependence of the shear attenuation coefficient α_{44} observed in Ho and Dy by Tachiki et al. (1974), Lee et al. (1975) and

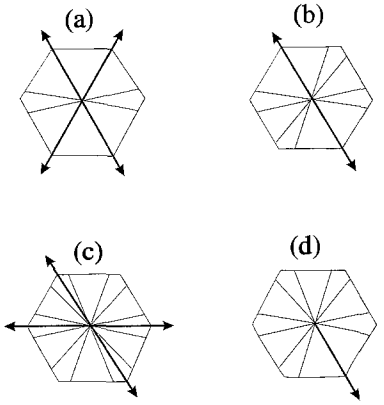

Fig. 34. Spin-slip structures in Ho: (a) $s = 2$; (b) $s = 5$; (c) $s = 8$; (d) $s = 11$. The arrows show the singlets and the thin lines the doublets.

Greenough and Isci (1979) was interpreted by means of incommensurate–commensurate domain effects. Greenough et al. (1981) explained the changes of $\partial c_{44}/\partial T$ observed in Dy in the temperature range T_C to T_N by the effects of the commensurability of magnetic and crystal structures. Kataev et al. (1989b) constructed the magnetic phase diagram of Tb (see fig. 27) on the basis of E_b measurements in a magnetic field. The anomaly at 223.5 K in this phase diagram was connected with the commensurate value of the helical turn angle at this temperature.

Later the influence of commensurate effects on the elastic properties of Ho was intensively studied by Bates et al. (1988), Venter et al. (1992a,b) and Venter and du Plessis (1995). For an explanation of the observed results they used the spin-slip structure model proposed by Gibbs et al. (1985) which was based on X-ray scattering results on holmium. According to this model the periodic magnetic structure, such as observed in the helical phase of Ho, can be regarded as made up of sequential blocks of m or $m - 1$ atomic layers; the spins of the atomic layer in each block being associated with the same easy direction (Bohr 1991, Bohr et al. 1986). A block of length $m - 1$ introduces the discommensuration in the structure and is called a spin-slip. The shorthand notation of the magnetic structure consists of integers and dots ($\bullet d$), where the integer d gives the number of blocks of length m and a dot represents a block of length m in the sequence. For holmium $m = 2$, so the helical spiral of holmium consists of doublets and singlets. The sequence of doublets and singlets is a unique property of magnetic wave vector $\vec{Q}$ characterizing the magnetic structure. Thus, in such structures the regions of commensurate spin structure are separated by spin-slips. If spin-slips occur at regular intervals then we get a supercommensurate structure which is characterized by a unique number (s) of interplanar distances between two successive spin-slips and by the wave vector $\vec{Q}_s$. Some of the supercommensurate spin-slip structures which may arise in holmium are shown schematically in fig. 34. At the spin-slip the helical turn angle experiences an additional change as if there is an extra atomic layer in the structure. This causes a magnetoelastically induced lattice modulation and a change of the hexagonal symmetry. There are three possible mechanisms of such a modulation: (a) distance

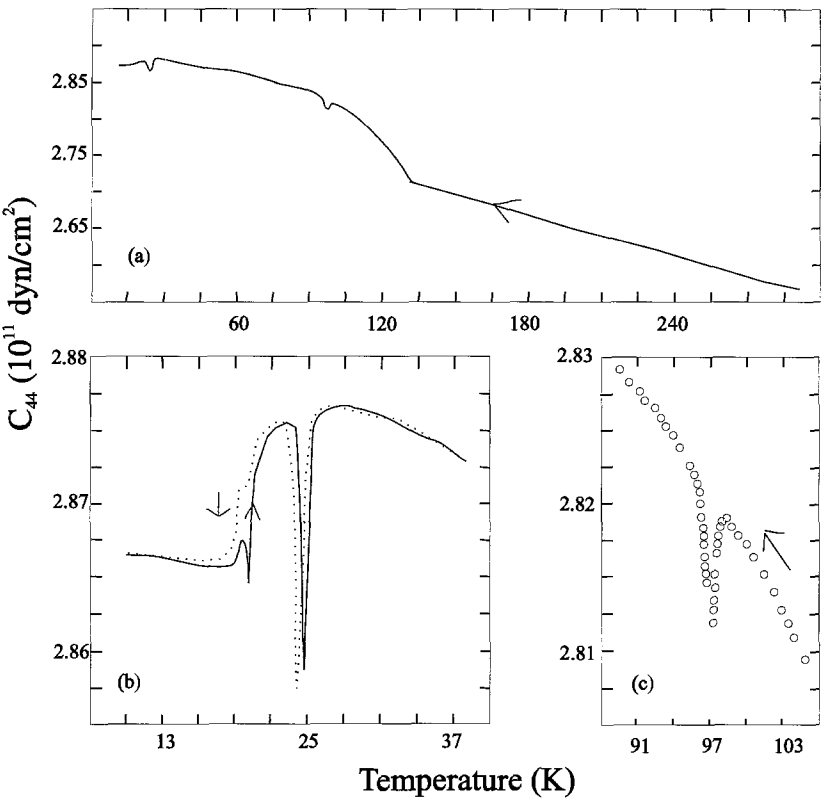

Fig. 35. Temperature dependence of the elastic constant c_{44} of holmium: (a) 4.2–300 K; (b) 7–40 K; (c) 88–106 K (Bates et al. 1988).

dependent exchange interaction (it is connected with the abrupt change in the helical turn angle at the spin-slip); (b) the effect of quadrupoles in a crystal field; and (c) quadrupole–quadrupole interactions. Such lattice modulation displays itself in the X-ray diffraction patterns by an additional nonmagnetic peak near the magnetic satellite corresponding to the wave vector of the magnetic structure and it should have an influence on the elastic properties of the metal.

Bates et al. (1988) studied the temperature dependencies of the elastic constants c_{11}, c_{33}, c_{44} and c_{66} of holmium. Besides the usual anomalies at $T_N \approx 133$–133.4 K and $T_C = 17.8$ K a number of additional anomalies were found. When $c_{33}(T)$ was measured on cooling a sharp dip centered at 19.8 K was observed. On warming from the phase with a ferromagnetic component along the c-axis it was less pronounced and some hysteresis took place. The temperature dependence of c_{44} reveals anomalies at 97.4, 24.5 and 19.8 K (see fig. 35). Earlier the shear sound velocity and attenuation peculiarities in Ho were reported near 95 and 24 K by Simpson et al. (1976), Lee et al. (1975) and Tachiki et al. (1974). Anomalies at 40.5 K (broad dip ~10 K wide), 24 and 20 K were observed in

the temperature dependence of c_{66} and at 23.8 and 20.1 K for $c_{11}(T)$. According to the neutron diffraction measurements by Bates et al. (1988) and Cowley and Bates (1988) the temperatures of these anomalies correspond to the spin-slip supercommensurate structures with $s = 2$ (anomaly at 97.4 K), $s = 5$ (40.5 K), $s = 8$ (24.5 K) and $s = 11$ (19.8 K).

Bates et al. (1988) explained the appearance of the anomalies at c_{ij} by a change of the effective magnetic symmetry caused by supercommensurate spin-slip structures which break the underlying hexagonal crystal symmetry. The anomalous elastic constant change at the spin-slip transition was expressed as

$$\Delta c_{ij} = -\sum_{klmn} B_{ikl} T_{klmn} B_{jmn}. \tag{105}$$

Here B_{ikl} is the magnetoelastic coupling tensor (its elements are determined by crystal symmetry and are connected with magnetoelastic coupling constants), and T_{klmn} is the magnetic tensor whose elements are governed by magnetic symmetry alone. The existence and magnitude of the elastic constant anomaly is determined by the relationship between the magnetic and crystal symmetry, and the values of the tensor elements. As one can see from fig. 34, spin-slip structures with s is 2, 5, 8 and 11 change the hexagonal crystal lattice symmetry. The crystal symmetry breaking also results in the formation of magnetic domains which contribute to the elastic constant anomaly via a domain relaxation process. The domain dependent contribution was taken into account by a summation over the magnetic tensor components for the possible magnetic domains in a given spin-slip structure. The results of calculations confirm the spin-slip nature of the observed c_{ij} anomalies.

The influence of the magnetic field on c_{44} and α_{44} temperature dependencies in Ho near 97.5 K, which corresponds to the spin-slip structure with $s = 2$, was investigated by Venter et al. (1992a,b). A marked hysteresis near the c_{44} dip at 97.5 K was found for cooling and warming runs for zero and nonzero magnetic fields. The field impressed in the basal plane shifted the anomaly to a higher temperature region and the field applied along the c-axis practically had no influence on the temperature of the anomaly. According to neutron diffraction measurements by Venter et al. (1992b), the temperature corresponding to the spin-slip structure had the same field dependence. The measurements in a magnetic field aligned along the b-axis indicate a lock-in behavior near 98 K (in this case $\vec{Q} = 1/4\vec{c}^*$, where $\vec{c}^*$ is the c-axis basis vector of the reciprocal unit cell).

The lock-in at $\vec{Q} = \frac{5}{18}\vec{c}^*$ in a magnetic field of 30 kOe in Ho was found between 126 K and T_N by Tindall et al. (1993). This peculiarity shows itself in the $c_{33}(T)$ and $\alpha_{33}(T)$ dependencies measured in a magnetic field (~ 10 kOe) directed along the b-axis (Venter and du Plessis 1995). Instead of one marked step observed at $T_N = 132.9$ K at zero field, the c_{33} temperature dependence for $H = 10$ kOe exhibited a plateau and a second step at a lower temperature. Two α_{33} peaks coincide with the step at T_N and the second step.

Eccleston and Palmer (1992) studied the temperature dependencies of c_{11} and c_{33} in erbium below 53 K. In this temperature range a number of successive locks at the values

of $\vec{Q} = \frac{2}{7}\vec{c}^*$, $\frac{4}{15}\vec{c}^*$, $\frac{6}{23}\vec{c}^*$, $\frac{1}{4}\vec{c}^*$ and $\frac{5}{21}\vec{c}^*$ was observed in the temperature dependence of the magnetic wave vector (Gibbs et al. 1986, Bohr 1991). The supercommensurate spin-slip structures with $\vec{Q}_s = \frac{2}{7}\vec{c}^*$; $\frac{2}{15}\vec{c}^*$ and $\frac{2}{23}\vec{c}^*$ occur for $\vec{Q} = \frac{2}{7}\vec{c}^*$, $\frac{4}{15}\vec{c}^*$ and $\frac{6}{23}\vec{c}^*$ having short hand notations •1, •3 and •5. In erbium the fundamental building blocks of the magnetic structures consist of four (quartet) and three (triplet) atomic layers in which spins are oriented either parallel or antiparallel to the c-axis. The spin-slip structures with odd ratio of quartets and doublets posses a net ferrimagnetic moment parallel to the c-axis. This moment breaks the symmetry of the crystal structure and according to the model of Bates et al. (1988) should lead to the anomalies in c_{ij}. Eccleston and Palmer (1992) point out that this mechanism accounts for the anomalies observed in the $c_{33}(T)$ and $c_{11}(T)$ curves at 48, 33 and 28 K, where the spin-slip structures were observed by X-ray diffraction measurements. Earlier the anomalies in c_{11}, c_{33}, and c_{66} elastic constants near these temperatures were found in the work of Jiles and Palmer (1981). As was noted in sect. 6, the internal friction peculiarities near the temperatures corresponding to spin-slip structures were observed in Er by Nikitin et al. (1993).

7.6. *Young's moduli of the metals and their alloys*

Young's moduli of the lanthanide metals and their alloys were studied at acoustic frequencies in the temperature range 4.2–400 K.

The temperature dependence of Young's modulus measured along the c-axis in Gd resembles that of the elastic constant c_{33}, i.e., there are two minima at T_C and T_{sr} (Spichkin et al. 1998).

In the case of Dy there is a small minimum near T_N and an abrupt decrease (~ 20%) near T_C in $E_c(T)$ (see fig. 15), which was observed for both cooling and warming processes. A small amount of hysteresis was found in $E(T)$ near T_C and in the HAFM state which is characteristic for a first-order transition (Kataev and Sattarov 1989). This behavior essentially differs from that observed for $c_{33}(T)$ measured at ultrasound frequencies (see fig. 23). A substantial decrease of Young's moduli measured on poly- and single crystals at the HAFM to FM phase transition was also observed in Tb–Dy, Gd–Dy and Er–Tb alloys (Tishin and Shipilov 1993, Kataev et al. 1989c, Shubin et al. 1985, Kataev and Shubin 1979).

In terbium the $E_c(T)$ and $E_b(T)$ curves reveal a quite different behavior (see fig. 21). For $E_c(T)$ there are two minima, at T_C and T_N, while for $E_b(T)$ there is a small peculiarity at T_N and in the region of T_C a rapid decrease of about 45% compared with the value just above T_N. According to the data of Salama et al. (1972) the decrease of c_{11} at T_C is about 8.5%, and according to the measurements made by Rosen (1968) on polycrystalline Tb the change at T_C is about –2%. The general behavior of $E_c(T)$ and $E_b(T)$ is analogous to $c_{33}(T)$ and $c_{11}(T)$ (see Salama et al. 1972, Scott 1978).

Young's modulus of a $Ho_{0.5}Er_{0.5}$ single crystal alloy was measured in the basal plane by Spichkin et al. (1996b). At the transition temperature to the magnetically ordered state (T_N = 104 K) only a small minimum was observed. In the region of T_C = 35 K where the transition from basal plane antiferromagnetic spiral to conical ferromagnetic spiral occurs

a significant hysteresis was found (the hysteresis in T_C was ~ 10 K). This indicates that the transition at T_C is a first-order phase transition. Earlier a crystal lattice distortion reducing its symmetry was found at this temperature by Pengra et al. (1994).

Young's moduli of the nonmagnetic metals La and Y display a monotonous increase with decreasing temperature approaching the absolute zero temperature with a zero slope (Tishin et al. 1995, Bodriakov et al. 1994). The experimental temperature dependence of Young's modulus of yttrium was fitted with the help of a theoretical phenomenological model considering the crystal lattice as a quantum ensemble of inharmonic oscillators, which was proposed by Lakkad (1971). This model was consequently used to separate the contributions to Young's modulus from lattice effects and the magnetic structure.

Some of the experimentally obtained Young's moduli values are shown in table 12.

7.7. *Elastic properties of R–Fe and R–Co intermetallic compounds*

Young's and shear moduli of RFe_2 (R = Ce, Sm, Gd, Tb, Dy, Ho, Er and Y), (Ho, Er)Fe_2 and (Ho, Tb)Fe_2 polycrystalline compounds were studied from 4.2 to 300 K by an ultrasonic method at a frequency of 10 MHz by Rosen et al. (1973, 1976) and Klimker et al. (1974, 1985). These cubic Laves phase compounds (type $MgCu_2$) have Curie temperatures well above room temperature (with the exception of $CeFe_2$, where $T_C = 227$ K), and some of them exhibit a spin-reorientation transition at low temperatures. The values of Young's and shear moduli, the Debye temperature (which are calculated from the elastic moduli), the relative change of Young's modulus in a magnetic field of 25 kOe ($\Delta E(H)/E$) and the relative change of Young's modulus under pressure of 10 kbar ($\Delta E(P)/E$) are given in table 13.

The temperature dependencies of E and G for YFe_2, $GdFe_2$ and $DyFe_2$ show a monotonic increase (of about 8%) upon cooling from 300 to 4.2 K. $TbFe_2$ and $CeFe_2$ have relatively small values of E and G compared with other investigated RFe_2 compounds. $TbFe_2$ exhibits a small increase of the elastic moduli at low temperatures and $ErFe_2$ a rapid increase near 120 K. In $CeFe_2$ a shallow minimum at T_C was observed.

$HoFe_2$ has a deep minimum (~ 8% decrease at ~ 14 K) in its elastic moduli. According to Mössbauer effect measurements in this temperature region there is a first-order spin-reorientation transition with a change of the easy axis direction from [001] to [uuw] (Klimker et al. 1974).

The minima of the $E(T)$ and $G(T)$ dependencies which are connected with spin-reorientation transitions were also observed in ternary systems $Ho_xTb_{1-x}Fe_2$ and $Ho_xEr_{1-x}Fe_2$ (Rosen et al. 1973, 1976). The depth of the spin-reorientation minimum in the $E(T)$ and $G(T)$ curves in the $Ho_xTb_{1-x}Fe_2$ system increases under substitution of terbium for holmium (Rosen et al. 1973). The temperature dependencies of Young's moduli for $Ho_xEr_{1-x}Fe_2$ compounds with x = 0.4–0.7 reveal two distinct minima in the low temperature region corresponding to a rotation of the easy magnetization direction upon cooling from [100] to [110] and then to the [111] direction. Compounds with x = 0.1, 0.8 and 0.9 exhibit only one transition. On the basis of Young's modulus measurements

Table 12
Young's modulus measured in various rare earth metals and their alloys at acoustic frequencies

R, alloy	T (K)	E[a] (10^{11} dyn/cm^2)	E_a (10^{11} dyn/cm^2)	E_b (10^{11} dyn/cm^2)	E_c (10^{11} dyn/cm^2)	Refs.
Gd	300	5.5				1
	4.2	6.2				
Tb	300			5.3	7.4	2
	4.2			3.8	8.45	
Dy	300	7			7	3,12
	4.2				6.4	
	300	6.9				4
	4.2	5.4				
Er	4.2		10.98	10.36	6.43	5
La	300	3.68				6
	4.2	4.16				
Y	300	5.63	12.09[b]		4.54	7
	4.2	6.09	13.4[b]		5.1	
$Gd_{0.6}Tb_{0.4}$	300		5.2	5.2	11	8
	4.2				12.5	
$Gd_{0.25}Dy_{0.75}$	300	6.8				1
	4.2	6.7				
$Gd_{0.5}Dy_{0.5}$	300	6.3				1
	4.2	6.4				
$Gd_{0.7}Dy_{0.3}$	300	6.1				1
	4.2	6.6				
$Tb_{0.5}Dy_{0.5}$	300		4.14	4.14		9
$Tb_{0.125}Dy_{0.875}$	300	7.0				10
$Er_{0.25}Tb_{0.75}$	300	8.4				8
	4.2	8.65				
$Ho_{0.5}Er_{0.5}$	300		13.9[b]			11
	4.2		15.4[b]			

[a] Measurements on polycrystals.

[b] Measurements in basal plane.

References

1 Tishin and Shipilov (1993)
2 Spichkin et al. (1996a)
3 Tishin and Spichkin (1996)
4 Burhanov et al. (1993)
5 Nikitin et al. (1993)
6 Bodriakov et al. (1994)
7 Tishin et al. (1995)
8 Kataev and Shubin (1979)
9 Kataev et al. (1989c)
10 Shubin et al. (1985)
11 Spichkin et al. (1996b)
12 Kataev and Sattarov (1989)

the spin-orientation temperature–concentration phase diagram for the $Ho_xEr_{1-x}Fe_2$ system was constructed by Rosen et al. (1976).

A magnetic field and hydrostatic pressure increased Young's modulus (see table 13), and the maximum effect was observed for the $TbFe_2$ and $SmFe_2$ compounds. Substitution

Table 13
Young's and shear moduli, Debye temperature T_D, and relative change of Young's modulus in a magnetic field and under hydrostatic pressure measured on polycrystalline RFe_2 intermetallic compounds at ultrasound frequencies

Compound	T (K)	E (10^{11} dyn/cm^2)	G (10^{11} dyn/cm^2)	T_D (K)	$\frac{\Delta E(H)}{E}$ (%)	$\frac{\Delta E(P)}{E}$ (%)	Refs.
$CeFe_2$	300	5.9	2.2	208			1
	4.2	5.9	2.15	208	1.02		
$SmFe_2$	300	4.25	1.59		66.7	17.0	4
$GdFe_2$	300	10.6	4.08	280	1.02	2.8	1,4
	4.2	11.7	4.53	293			
$TbFe_2$	300	7.7	2.8	232	56.0	22.4	1,4
	4.2	8.3	3.1	242	44.5		
$DyFe_2$	300	11	4.32	282	1.8	2.7	1,4
	4.2	12.6	4.95	303			
$HoFe_2$	300	11.5	4.4	283	0.85	2.4	1,4
	4.2	11.7	4.3	283	2.65		
$ErFe_2$	300	10.6	4	268	5.95	3.1	1,4
	4.2	11.9	4.4	288	5.80		
YFe_2	300	11.2	4.35	330			1
	4.2	11.7	4.7	347			
$Ho_{0.3}Er_{0.7}Fe_2$	300	10.7			4.8		2
	4.2	11.7					
$Ho_{0.6}Er_{0.4}Fe_2$	300	11.3			0.5		2
	4.2	12.1					
$Ho_{0.8}Er_{0.2}Fe_2$	300	11.4			0.3		2
	4.2	12.2					
$Ho_{0.3}Tb_{0.7}Fe_2$	300				25		3
	4.2	7.2	7				
$Ho_{0.6}Tb_{0.4}Fe_2$	300	8.3	8.6		15		3
	4.2		126				
$Ho_{0.8}Tb_{0.2}Fe_2$	300	10.1	9.7		10		3
	4.2						

References

1 Klimker et al. (1974)
2 Rosen et al. (1976)
3 Rosen et al. (1973)
4 Klimker et al. (1985)

of Tb and Er in $HoFe_2$ reinforced the magnetic field influence of Young's modulus. Rosen et al. (1973, 1976) related the influence of pressure and field on the elastic moduli of $TbFe_2$ and $SmFe_2$ with approximately equal magnitudes of the magnetoelastic and the magnetocrystalline anisotropy energies (they have the maximum magnetostriction

Table 14
Elastic constants c_{ij}, Debye temperature T_D, Young's moduli of poly- and single-crystal R–Co intermetallic compounds, measured at ultrasound frequencies

Compound	T (K)	Elastic constants[a]					T_D (K)	$E^{a,b}$	$E_{a,b}$[a]	E_c[a]	Refs.
		c_{11}	c_{33}	c_{44}	c_{66}	c_{13}					
YCo_5	300	20.0	24.15	5.39	5.12	9.6			14	17.96	1
	4.2	25.76	24.88	5.50	5.14	10.15	374		16.86	19.88	
$CeCo_5$	4.2	18.28	22.90	4.95	3.74	9.37	322		11.1	16.9	1
$NdCo_5$	300	17.39	21.56	4.69	3.93	9.47			11.05	14.9	1,2
	4.2	18.21	23.02	4.67	4.09	10.06	320		11.5	15.6	
$GdCo_5$	300	19.5	23.5	5.4	4.82	9.9			10.77	16.82	1
	4.2	20.17	24.68	5.57	4.92	10.35	327		13.6	17.7	
$TbCo_5$	300	19.8	24.3	5.4	4.7	10.3			13.08	17.27	1,3
	4.2	21.2	25.5	5.68	5.28	10.92	344		14.4	18	
$DyCo_5$	300	20.9	24.9	5.6	5.45	10.8			14.47	17.35	1,3
	4.2	22.16	26.42	5.84	5.69	11.60	348		15.2	18.3	
$HoCo_2$	300							9			4
	4.2							8.75			
$Ho_{0.8}Tb_{0.2}Co_2$	300							8.7			4
	4.2							9			
$Ho_{0.6}Tb_{0.4}Co_2$	300							9			4
	4.2							9			
$Ho_{0.4}Tb_{0.6}Co_2$	300							8.3			4
	4.2							8			
$TbCo_2$	300							8.1			4
	4.2							7.8			

[a] In 10^{11} dyn/cm^2.

[b] Measurements on polycrystals.

References

(1) Kvashnin and Kvashnina (1991)
(2) Deriagin et al. (1984)
(3) Deriagin et al. (1985)
(4) Klimker et al. (1980)

constant among the RFe_2 compounds). In this case one can expect an important variation of the elastic moduli.

Young's modulus measurements on the cubic Laves phase (type $MgCu_2$) polycrystalline $Ho_xTb_{1-x}Co_2$ alloys were done by Klimker et al. (1980). The Curie temperatures in this system lie in the interval between 237.5 K ($TbCo_2$) and 86.8 K ($HoCo_2$) (Buschow 1977). Below T_C there is a drastic drop of the $E(T)$ curves with a smooth minimum spreading over about 50 K below T_C in the compounds with $x \leqslant 0.6$. As the holmium content increased a narrowing of the minimum at T_C and a decrease of its depth was observed. In the low temperature region in the compounds containing Ho a sharp minimum connected with the spin-reorientation process was observed.

The elastic constants c_{ij} in RCo_5 (R = Y, Ce, Nd, Gd, Tb, Dy) single-crystal compounds with hexagonal crystal structure of the $CaCu_5$ type were measured in the temperature interval 4.2–300 K at a frequency of 20 MHz by Deriagin et al. (1984, 1985) and Kvashnin and Kvashnina (1991). According to the review of Buschow (1977) the Curie temperatures of the investigated RCo_5 compounds exceed 900 K, and $TbCo_5$ and $DyCo_5$ have compensation points at 110 and 123 K, respectively. However, no anomalies were observed at these temperatures in the c_{ij} temperature dependencies (Deriagin et al. 1985). On cooling the elastic constants of the RCo_5 (R = Ce, Nd, Tb, Dy) compounds have a general tendency to increase.

Theory and experimental results show (Irhin and Rosenfeld 1974, Ohkoshi et al. 1977, Tsushima et al. 1978, Kelarev et al. 1983) that in RCo_5 compounds for R = Nd, Tb, Dy, Ho a second-order spin-reorientation transition "basal plane–hexagonal c-axis" occurs in the temperature interval T_{sr}^1–T_{sr}^2. Between the start T_{sr}^1 and the finish T_{sr}^2 temperature an intermediate phase exists. Anomalies at T_{sr}^1 and T_{sr}^2 in the $c_{ij}(T)$ curves of RCo_5 (R = Nd, Tb, Dy) were observed by Deriagin et al. (1984, 1985). The values of T_{sr}^1 and T_{sr}^2 determined from the anomaly boundaries (245 and 285 K for $NdCo_5$, 410 and 418 K for $TbCo_5$, 326 and 368 K for $DyCo_5$, respectively) are in good agreement with those obtained from heat capacity and magnetic moment orientation angle measurements (Tsushima et al. 1978, Kelarev et al. 1983).

The elastic constants c_{ij} of YCo_5 and $GdCo_5$ increase monotonously with decreasing temperature with exception of c_{33} and c_{66} in YCo_5 and c_{33}, c_{44} in $GdCo_5$ for which a small decrease was observed at low temperatures.

The numerical values of c_{ij} at 300 and 4.2 K and the values of the basal plane $E_{a,b} = 1/s_{11}$ and c-axis $E_c = 1/s_{33}$ Young's moduli calculated from the elastic constants data are shown in table 14.

7.8. *Higher-order elastic constants of the metals*

The anharmonicity of the crystal lattice exhibits itself in hydrostatic pressure dependence of the elastic constants, moduli, lattice parameters, thermal expansion, temperature variation of the volume compressibility and in the existence of phonon–phonon interactions. The anharmonic properties of the crystal can be characterized by higher-order elastic constants.

In the general case the dependence of the internal energy U of the crystal upon strain may be expressed as a power series of strain tensor components (Hearmon 1953)

$$U = \tfrac{1}{2}c_{ijkl}\epsilon_{ij}\epsilon_{kl} + \tfrac{1}{6}c_{ijklmn}\epsilon_{ij}\epsilon_{kl}\epsilon_{mn} + \tfrac{1}{24}c_{ijklmnpq}\epsilon_{ij}\epsilon_{kl}\epsilon_{mn}\epsilon_{pq} + \cdots, \tag{106}$$

where c_{ijkl} are the second-order adiabatic elastic constants (SOEC),

$$c_{ijkl} = \left.\frac{\partial^2 U}{\partial\epsilon_{ij}\partial\epsilon_{kl}}\right|_{\epsilon\to 0}, \tag{107}$$

Table 15
Third-order elastic constants of some rare earth metals (in 10^{11} dyn/cm^2)

R	Elastic contants										Ref.
	c_{111}	c_{112}	c_{113}	c_{123}	c_{133}	c_{144}	c_{155}	c_{222}	c_{333}	c_{344}	
Sc	−91.185	−30.779	−0.49	−10.994	−21.721	−7.923	−3.561	−112.02	−82.207	−21.721	1
Y	−74.19	−24.353	5.295	−14.738	−17.472	−7.897	−1.546	−92.449	−64.691	−17.472	2
Pr	−58.18	−20.11	2.28	−9.84	−15.12	−3.66	−3.90	−70.86	−60.48	15.12	3
Nd	−65.54	−22.57	1.43	−9.93	−17.01	−4.00	−4.51	−79.74	−68.03	−17.01	3
Gd	−50.3	13.3	0.4	−6.3	−9.7	−3.9	−2.0	−55.1	−76.2	−9.7	4
Tb	−48.0	−16.2	−1.1	−5.4	−11.1	−4.3	−2.2	−57.1	−73.7	−11.1	5
Dy	−53.2	−16.4	−0.8	−6.9	−12.4	−4.6	−3.1	−62.0	−73.5	−12.4	6
Ho	−60.9	−23.3	−2.3	−5.7	−15.5	−5.5	−2.6	−75.7	−70.3	−15.5	7
Er	−79.6	−18.7	−5.0	−7.0	−16.7	−5.4	−6.6	−87.8	−74.7	−16.7	8
Tm	−99.41	−35.45	−1.91	−10.35	−22.91	−7.97	−4.29	−121.72	−85.67	−22.91	9

References

1 Ramji Rao and Rajput (1979a)
2 Ramji Rao and Rajput (1979b)
3 Ramji Rao and Narayanamurthy (1979)
4 Ramji Rao and Menon (1974)
5 Ramji Rao and Ramanand (1977a)
6 Ramji Rao and Menon (1973a)
7 Ramji Rao and Ramanand (1977b)
8 Ramji Rao and Menon (1973b)
9 Ramji Rao and Rajput (1979c)

c_{ijklmn} are the third-order adiabatic elastic constants (TOEC),

$$c_{ijklmn} = \left.\frac{\partial^3 U}{\partial\epsilon_{ij}\partial\epsilon_{kl}\partial\epsilon_{mn}}\right|_{\epsilon\to 0}, \tag{108}$$

and $c_{ijklmnpq}$ are the fourth-order adiabatic elastic constants (FOEC),

$$c_{ijklmnpq} = \left.\frac{\partial^4 U}{\partial\epsilon_{ij}\partial\epsilon_{kl}\partial\epsilon_{mn}\partial\epsilon_{pq}}\right|_{\epsilon\to 0}. \tag{109}$$

The constants c_{ijklmn} and $c_{ijklmnpq}$ (c_{ijk} and c_{ijkl} in matrix notation which will be used further) are related to the anharmonic properties of the crystal.

Some work has been devoted to the calculation of TOEC in the rare earth metals (see Ramji Rao and Ramanand (1980, 1984) and the references in tables 15 and 16). Various theoretical models used for the calculation of TOEC were reviewed by Ramji Rao and Ramanand (1980, 1984). TOEC of Gd, Dy and Er were determined on the basis of experimental data on hydrostatic pressure derivatives of SOEC (c_{ij}) measured by Fisher et al. (1973) at pressures up to 5 kbar. For Tb and Ho the dc_{ij}/dP were obtained from interpolation of the experimental data for Gd, Dy and Er. For Y, Sc, Nd, Pr and Tm TOEC were calculated on the basis of experimental data on the volume compression under pressure. The results of TOEC calculations (the room temperature values) are listed in table 15.

Table 16
Pressure derivatives of second-order elastic constants of some rare earth metals; experimental values were measured at room temperature

R	$\frac{dc_{11}}{dP}$	$\frac{dc_{12}}{dP}$	$\frac{dc_{13}}{dP}$	$\frac{dc_{33}}{dP}$	$\frac{dc_{44}}{dP}$	$\frac{dc_{66}}{dP}$	Refs.
Sc	4.40	2.75	1.82	4.79	0.83		1
Y	4.57	3.39	2.08	5.52	1.05		2
Pr	6.19	4.06	2.47	7.86	1.48		3
Nd	6.41	4.03	2.54	8.14	1.55		3
Gd	3.018±0.02	2.26±0.02	3.53±0.05	5.726±0.05	0.185±0.012	0.377±0.002	4
Tb	2.48±0.66[a]			3.31±0.22[a]	0.25±0.03[a]	0.27±0.03[a]	5
	8.3±1.8[b]			6.0±0.4[b]	1.7±0.2[b]	3.0±0.7[b]	
Dy	3.092±0.006	2.277±0.006	3.32±0.1	5.331±0.008	0.434±0.001	0.408±0.002	4
	2.50±0.30[a]			3.58±0.01[a]	0.49±0.04[a]	0.245±0.01[a]	5
	6.8±1.0[b]			6.5±1.2[b]	2.6±0.3[b]	2.5±0.05[b]	
Er	4.768±0.02	3.062±0.044	2.16±0.04	5.448±0.018	0.949±0.005	0.853±0.012	4
	3.31±0.05[a]			3.20±0.28[a]	0.72±0.04[a]	0.67±0.09[a]	5
	11.5±0.9[b]			12.1±1.8[b]	4.4±0.2[b]	3.1±0.6[b]	
Tm	6.92	3.98	2.46	7.08	1.43		6

[a] Measurements up to 5 kbar.

[b] Measurements up to 45 kbar.

References

(1) Ramji Rao and Rajput (1979a)
(2) Ramji Rao and Rajput (1979b)
(3) Ramji Rao and Narayanamurthy (1979)
(4) Fisher et al. (1973)
(5) Jiles and Palmer (1981)
(6) Ramji Rao and Rajput (1979c)

Ramji Rao and Srinivasan (1969) used the finite strain theory of Murnaghan (1951) to derive the relations between SOEC, TOEC and dc_{ij}/dP for a hexagonal crystal. The dc_{ij}/dP values for Sc, Y, Pr, Nd and Tm are shown in table 16. The values of dc_{ij}/dP for Gd, Tb, Dy and Er, presented in table 16, were measured experimentally.

The dc_{ij}/dP data and the theoretically derived TOEC were used for calculations of thermal expansion coefficients, temperature dependence of the volume compressibility and the pressure variation of lattice constants, and the agreement with experiment was quite good. For more detail about these calculations see Ramji Rao and Ramanand (1980, 1984) and references given in tables 15 and 16.

As one can see from table 16, pressure increases SOEC. This effect together with magnetoelastic interaction can be responsible for the increase of c_{33} and the elastic moduli under pressure observed in Gd and the RFe_2 compounds (Klimker and Rosen 1973, Klimker et al. 1985) in the magnetically ordered state. Jiles and Palmer (1981) measured the SOEC variation in Tb, Dy and Er at pressures up to 45 kbar. They showed that dc_{ij}/dP strongly decreases with increasing pressure (see table 16). This was related to significant fourth-order elastic effects due to nonzero and negative FOEC.

According to Ramji Rao and Ramanand (1984) with the help of FOEC one can calculate the temperature dependence of SOEC. However, the data for the FOEC of the lanthanide metals in literature are absent. However, in the case of yttrium Tishin et al. (1995) calculated the temperature dependence of the Young's modulus using the model of Lakkad (1971), which provided a good fit for the experimentally measured data.

8. Conclusion

This chapter is devoted to the influence of dynamic and static stresses on the magnetic and elastic properties of metals, alloys and intermetallic compounds studied during the last twenty years. The aim was to provide a comprehensive survey of the experimental and theoretical results which have been published. The available theoretical models describing the effect of hydrostatic pressure on the magnetic transition temperature and the nature of the elastic constants anomalies at the magnetic transition points are discussed. The results for magnets with localized moments, itinerant moments and combined systems are compared. Special attention is paid to the thermodynamic background of these effects. The extensive experimental data on the influence of the hydrostatic pressure on the magnetic phase transition temperatures, magnetic phase diagrams and magnetization are systematically reviewed and discussed. The origin of the magnetic anomalies of the elastic properties (mainly pure metals) are considered. The magnetic phase diagrams for metals and alloys obtained by means of the elastic constants measurements are reviewed.

Acknowledgments

The authors wish to thank to M.E. Koukouli and D.P. Pavlichenko for technical assistance.

References

Achiwa, N., S. Kawano, A. Onodera and Y. Nakai, 1988, J. Phys. (France) **49**, C8-349.

Altshuller, L.V., A.I. Voropinov, G.M. Gandelman, N.A. Dmitriev and G.V. Podvalni, 1981, Fiz. Met. Metalloved **51**, 76.

Armitage, J.G.M., T. Dumelow, P.C. Riedi and J.S. Abell, 1989, J. Phys.: Condens. Matter **1**, 3987.

Atoji, M., 1974, Solid State Commun. **14**, 1074.

Austin, A.G., and P.K. Mishra, 1967, Philos. Mag. **15**, 529.

Bartholin, H., and D. Bloch, 1967, C.R. Acad. Sci. Ser. A+B **264**, 1135.

Bartholin, H., and D. Bloch, 1968a, J. Phys. Chem. Solids **29**, 1063.

Bartholin, H., and D. Bloch, 1968b, J. Appl. Phys. **39**, 889.

Bartholin, H., and D. Bloch, 1969, Phys. Rev. **188**, 845.

Bartholin, H., J. Beille, D. Bloch, P. Boutron and J. Feron, 1971, J. Appl. Phys. **42**, 1679.

Bates, S., C. Patterson, G.J. McIntyre, S.B. Palmer, A. Mayer, R.A. Cowley and R. Melville, 1988, J. Phys. C **21**, 4125.

Beille, J., D. Gignoux, R. Lemaire, M. Shimizu and J. Voiron, 1983, Physica B **119**, 133.

Belorizky, E., M.A. Fremy, G.P. Gavigan, D. Givord and M.S. Li, 1987, J. Appl. Phys. **61**, 3971.

Belov, K.P., G.I. Kataev and R.Z. Levitin, 1960, Sov. Phys. JETP **37**, 670.
Bennett, S., and E. Pytte, 1967, Phys. Rev. **155**, 553.
Beuerle, T., and M. Fähnle, 1992, J. Magn. Magn. Mater. **110**, L29.
Bezdushnyi, R.V., 1988, Ph.D. Thesis (Moscow State University, Moscow).
Blackie, G.N., and S.B. Palmer, 1980, Portugal. Phys. **11**, 23.
Blackie, G.N., and S.B. Palmer, 1982, J. Phys. C **15**, L4883.
Bloch, D., and F. Chaisse, 1972, C.R. Acad. Sci. B **274**, 221.
Bloch, D., and R. Lemaire, 1970, Phys. Rev. B **2**, 2648.
Bloch, D., and R. Pauthenet, 1964, in: Proc. Int. Conf. on Magnetism, Proc. Vol. 255 (Institute of Physics/ Physical Society, London).
Bloch, D., F. Chaisse, F. Givord and J. Voiron, 1971, J. Phys. (France) **32**, 659.
Bloch, D., D.M. Edwards, M. Shimizu and J. Voiron, 1975, J. Phys. F **5**, 1217.
Bodriakov, V.Y., S.A. Nikitin and A.M. Tishin, 1991, Fiz. Tverd. Tela **33**, 2233.
Bodriakov, V.Y., S.A. Nikitin and A.M. Tishin, 1992, J. Appl. Phys. **72**, 4247.
Bodriakov, V.Y., G.S. Burhanov, S.A. Nikitin, A.M. Tishin, O.D. Chistiakov and N.N. Panov, 1993, Visokochist. Veshestva **4**, 12.
Bodriakov, V.Y., G.S. Burhanov, S.A. Nikitin, N.N. Panov, A.M. Tishin and O.D. Chistiakov, 1994, Visokochist. Veshestva **3**, 96.
Bohr, J., 1991, Surface Structures, Magnetic Structures, and Small Inclusions, as Studied by X-ray Diffraction, Report Riso-R-585, 69pp.
Bohr, J., D. Gibbs, D.E. Moncton and L.L. D'Amico, 1986, Physica A **140**, 349.
Bohr, J., V.V. Makhro and A.M. Tishin, 1995, Phys. Lett. A **202**, 230.
Braga, M.E., R.P. Pinto, J.B. Sousa, G.N. Blackie, D.J. Hemsley and S.B. Palmer, 1982, J. Magn. Magn. Mater, **29**, 203.
Brouha, M., and K.H.J. Buschow, 1973, J. Appl. Phys. **44**, 1813.
Brouha, M., K.H.J. Buschow and A.R. Miedema, 1974, IEEE Trans. Magn. **MAG-10**, 182.
Brown Jr, W.F., 1965, J. Appl. Phys. **36**, 994.
Burhanov, G.S., S.A. Nikitin, A.M. Tishin, O.D. Chistiakov and O.A. Shipilov, 1993, Vestn. Mosk. Univ. Ser. 3 **34**, 46.
Buschow, K.H.J., 1977, Rep. Progr. Phys. **40**, 1179.
Buschow, K.H.J., M. Brouha, J.W.M. Biesterbos and A.G. Dirks, 1977, Physica B **91**, 261.
Bykhover, S.E., S.A. Nikitin, Y.I. Spichkin, A.M. Tishin and Z.S. Umhaeva, 1990, Sov. Phys. JETP **70**, 1114.
Cable, J.W., and E.O. Wollan, 1968, Phys. Rev. **165**, 733.
Cable, J.W., E.O. Wollan, W.C. Koehler and M.K. Wilkinson, 1965, Phys. Rev. **140**, 1896.
Callen, E., 1968, J. Appl. Phys. **39**, 519.
Callen, E., and H.B. Callen, 1965, Phys. Rev. **139**, 455.
Chapman, R.G., and N.H. March, 1986, J. Magn. Magn. Mater. **61**, 81.
Child, H.R., W.C. Koehler, E.O. Wollan and J.W. Cable, 1965, Phys. Rev. A **138**, 1655.
Chow, H., and F. Keffer, 1973, Phys. Rev. B **7**, 2028.
Cooper, B.R., 1969, Solid State Phys. **21**, 393.
Corner, W.D., W.C. Roe and K.N.R. Taylor, 1962, Proc. R. Soc. **80**, 927.
Cowley, R.A., and S. Bates, 1988, J. Phys. C **21**, 4113.
Dan'kov, S.Yu., Yu.I. Spichkin and A.M. Tishin, 1996, J. Magn. Magn. Mater. **152**, 208.
Dan'kov, S.Yu., A.M. Tishin, V.K. Pecharsky and K.A. Gschneidner Jr, 1998, Phys. Rev. B **57**, 3478.
De Gennes, P.G., 1962, J. Phys. Rad. **23**, 630.
De Gennes, P.G., and D. Saint James, 1963, Solid State Commun. **1**, 62.
Dekker, A., 1965, J. Appl. Phys. **36**, 906.
Deriagin, A.V., G.M. Kvashnin and A.M. Kapitonov, 1984, Fiz. Met. Metalloved. **57**, 686.
Deriagin, A.V., G.M. Kvashnin and A.M. Kapitonov, 1985, Fiz. Tverd. Tela **27**, 255.
Drillat, A., J. Baruchel, S. Bates and S.B. Palmer, 1984, J. Magn. Magn. Mater. **44**, 232.
du Plessis, P. de V., 1976, J. Phys. F **6**, 873.
du Plessis, P. de V., and C. Elbaum, 1977, J. Phys. F **7**, 273.
Dzialoshinski, I.E., 1964a, Zh. Eksp. Teor. Fiz. **46**, 1420.
Dzialoshinski, I.E., 1964b, Zh. Eksp. Teor. Fiz. **46**, 1420.
Eccleston, R.S., and S.B. Palmer, 1992, J. Magn. Magn. Mater. **104-107**, 1529.
Elliott, R.J., 1961, Phys. Rev. **124**, 346.
Elliott, R.J., and F.A. Wedgewood, 1964, Proc. Phys. Soc. **84**, 63.
Enz, U., 1960, Physica **26**, 698.
Evenson, W.E., and S.H. Liu, 1969, Phys. Rev. **178**, 783.

Feron, J.L., and R. Pauthenet, 1969, C.R. Acad. Sci. Paris, Ser. B **269**, 549.
Fisher, E.S., M.H. Manghnani and R. Kikuta, 1973, J. Phys. Chem. Solids **34**, 687.
Fleming, G.S., and S.H. Liu, 1970, Phys. Rev. B **2**, 164.
Franse, J.J.M., and V. Mihai, 1977, Physica B **86–88**, 49.
Freyne, F., 1972, Phys. Rev. B **5**, 1327.
Fujiwara, H., H. Fujii, Y. Hidaka, T. Ito, Y. Hashimoto and T. Okamoto, 1977, J. Phys. Soc. Japan **42**, 1194.
Fumi, F.G., 1952, Nuovo Cimento **9**, 739.
Gibbs, D., D.E. Moncton, K.L. D'Amico, J. Bohr and B.H. Grier, 1985, Phys. Rev. Lett. **55**, 234.
Gibbs, D., J. Bohr, J.D. Axe, D.E. Moncton and K.L. D'Amico, 1986, Phys. Rev. B **34**, 8182.
Gignoux, D., D. Givord, F. Givord and R. Lemaire, 1979, J. Magn. Magn. Mater. **10**, 288.
Givord, G., and R. Lemaire, 1974, IEEE Trans. Magn. **MAG-10**, 109.
Goodings, D.A., 1977, Z. Phys. B **26**, 37.
Greenough, R.D., and G.N. Blackie, 1981, J. Phys. Chem. Solids **42**, 533.
Greenough, R.D., and C. Isci, 1979, J. Phys. Chem. Solids **40**, 209.
Greenough, R.D., G.N. Blackie and S.B. Palmer, 1981, J. Phys. C **14**, 9.
Habenschuss, M., C. Stassis, S.K. Sinha, H.W. Deckman and F.H. Spedding, 1974, Phys. Rev. B **10**, 1020.
Hearmon, R.F.S., 1953, Acta Crystallogr. **6**, 331.
Heine, V., 1967, Phys. Rev. **153**, 673.
Herpin, A., and P. Meriel, 1961, J. Phys. Rad. **22**, 337.
Howard, B.K., and J. Bohr, 1991, Phys. Scripta **39**, 96.
Inoue, J., and M. Shimizu, 1980, J. Phys. F **10**, 721.
Inoue, J., and M. Shimizu, 1982a, Phys. Lett. A **90**, 85.
Inoue, J., and M. Shimizu, 1982b, J. Phys. F **12**, 1811.
Inoue, J., and M. Shimizu, 1984, Phys. Lett. A **104**, 166.
Inoue, J., and M. Shimizu, 1985, Phys. Lett. A **112**, 81.
Inoue, J., and M. Shimizu, 1986, J. Magn. Magn. Mater. **54-57**, 991.
Inoue, J., and M. Shimizu, 1988, J. Phys. (France) **49**, C8-299.
Irhin, Y.P., and E.V. Rosenfeld, 1974, Fiz. Tverd. Tela **16**, 485.
Isci, C., and S.B. Palmer, 1977, J. Phys. Chem. Solids **38**, 1253.
Isci, C., and S.B. Palmer, 1978, J. Phys. F **8**, 247.
Ito, T., S. Legvold and B.J. Beaudry, 1981, Phys. Rev. **23**, 3409.
Ito, T., J. Takeuchi, K. Mizumo, K. Ito, M. Oka and B.J. Beaudry, 1987, Jpn. J. Appl. Phys. **26**, L1868.
Iwata, N., T. Okamoto and A. Tatsumoto, 1968, J. Phys. Soc. Japan **24**, 948.
Jaakkola, S., 1974, Phys. Lett. A **50**, 35.
Jaakkola, S., S. Parviainen and S. Pentilla, 1983, J. Phys. F **13**, 491.
Jaakkola, S.M., and M.K. Hannien, 1980, Solid State Commun. **36**, 275.
Jackson, C., and S. Doniach, 1969, Phys. Lett. A **30**, 328.
Jayaraman, A., 1978, High Pressure Studies: Metals, Alloys and Compounds, in: Handbook on the Physics and Chemistry of Rare Earths, Vol. 1, eds K.A. Gschneidner Jr and L. Eyring (North- Holland, Amsterdam) ch. 9.
Jensen, J., 1971, Int. J. Magn. **1**, 271.
Jensen, J., and S.B. Palmer, 1979, J. Phys. C **12**, 4573.
Jiles, D.C., and S.B. Palmer, 1980, J. Phys. F **10**, 2857.
Jiles, D.C., and S.B. Palmer, 1981, Philos. Mag. A **44**, 447.
Jiles, D.C., G.N. Blackie and S.B. Palmer, 1981, J. Magn. Magn. Mater. **24**, 75.
Jiles, D.C., S.B. Palmer, D.W. Jones, S.P. Farrant and K.A. Gschneidner Jr, 1984, J. Phys. F **14**, 3061.
Kadanoff, L.P., 1969, Phys. Rev. **187**, 619.
Kaino, K., and T. Kasuya, 1981, J. Phys. F **11**, 883.
Kamarad, J., Z. Arnold and M.R. Ibarra, 1995, J. Magn. Magn. Mater. **140–144**, Pt. 2, 837.
Kanamori, J., 1963, Progr. Theor. Phys. **30**, 275.
Kasuya, T., 1956, Progr. Theor. Phys. **16**, 45.
Kasuya, T., 1966, S–d and s–f Interaction in Rare Earth Metal, in: Magnetism, Vol. VIIB, eds G. Rado and H. Suhl (Academic Press, New York) pp. 215–294.
Kataev, G.I., 1961, Fiz. Met. Metalloved **11**, 375.
Kataev, G.I., and M.R. Sattarov, 1989, Fiz. Met. Metalloved **68**, 1200.
Kataev, G.I., and V.V. Shubin, 1979, Fiz. Met. Metalloved. **48**, 188.
Kataev, G.I., A.F. Popkov, V.G. Shavrov and V.V. Shubin, 1985, Sov. Phys. JETP **64**, 820.
Kataev, G.I., M.R. Sattarov and V.V. Shubin, 1989a, Vestn. Mosk. Univ., Ser. 3 **30**, 97.
Kataev, G.I., M.R. Sattarov and A.M. Tishin, 1989b, Phys. Status Solidi (a) **114**, K79.

Kataev, G.I., M.R. Sattarov and A.M. Tishin, 1989c, Vestn. Mosk. Univ. Ser. 3 **30**, 84.

Kawai, N., M. Sakakihara, A. Morizumi and A. Sawaoka, 1967, J. Phys. Soc. Japan **23**, 475.

Kawano, S., N. Achiwa, A. Onodera and Y. Nakai, 1992, Physica B **180–181**, 46.

Kawano, S., B. Lebech and N. Achiwa, 1993, J. Phys.: Condens. Matter **5**, 1535.

Kawano, S., S.A. Sorensen, B. Lebech and N. Achiwa, 1995, J. Magn. Magn. Mater. **140–144**, 763.

Kawasaki, K., 1968a, Solid State Commun. **6**, 57.

Kawasaki, K., 1968b, Phys. Lett. A **26**, 543.

Keeton, S.C., and T.L. Loucks, 1968, Phys. Rev. **168**, 672.

Kelarev, V.V., V.V. Chuev, A.N. Pirogov and S.K. Sidorov, 1983, Phys. Status Solidi (a) **79**, 57.

Kirchmayer, H.R., and C.A. Poldy, 1978, J. Magn. Magn. Mater. **8**, 1.

Klimker, H., and M. Rosen, 1973, Phys. Rev. B 7, 2054.

Klimker, H., M. Rosen, M.P. Dariel and U. Atzmony, 1974, Phys. Rev. B **10**, 2968.

Klimker, H., M.P. Dariel and M. Rosen, 1980, J. Phys. Chem. Solids **41**, 215.

Klimker, H., Y. Green and M. Rosen, 1985, J. Phys. Chem. Solids **46**, 157.

Koehler, W.C., J.W. Cable, M.K. Wilkinson and E.O. Wollan, 1966, Phys. Rev. **151**, 414.

Kornetzki, M., 1935, Z. Physik **98**, 289.

Kouvel, J.S., and R.H. Wilson, 1961, J. Appl. Phys. **32**, 435.

Kratzer, A., V. Potzel, J. Moser, F.J. Litterst, W. Potzel and G.M. Kalvins, 1986, J. Magn. Magn. Mater. **54–57**, 489.

Kurisu, N., Y. Nakano, K. Yamamoto, Y. Andoh and S. Kawano, 1996, J. Phys. Soc. Japan **65**(suppl. B), 162.

Kvashnin, G.M., and O.P. Kvashnina, 1991, Fiz. Tverd. Tela **33**, 613.

Lakkad, S.C., 1971, J. Appl. Phys. **42**, 4277.

Landau, L.D., and I.M. Khalatnikov, 1954, Dokl. Akad. Nauk SSSR **96**, 984.

Landau, L.D., and E.M. Lifshitz, 1958, Statistical Physics, 2nd Ed. (Pergamon Press, New York).

Landry, P.C., 1967, Phys. Rev. **156**, 578.

Landry, P.C., 1970, Colloq. Int. CNRS **188**, 319.

Lang, N.D., and H. Ehrenreich, 1968, Phys. Rev. **168**, 605.

Laramore, G., and L.P. Kadanoff, 1969, Phys. Rev. **187**, 619.

Lee, E.W., 1964, Proc. Phys. Soc. **84**, 693.

Lee, M.C., and M. Levy, 1973, J. Phys. Chem. Solids **34**, 995.

Lee, M.C., R.A. Treder and M. Levy, 1975, J. Phys. Chem. Solids **36**, 1281.

Legvold, S., T. Ito and B.J. Beaudry, 1980, Phys. Rev. Lett. **45**, 1275.

Leontiev, P.I., 1988, Ph.D. Thesis (Moscow State University, Moscow).

Leontiev, P.I., A.S. Markosian, S.A. Nikitin and V.V. Snegirev, 1988, Fiz. Tverd. Tela **30**, 3700.

Leontiev, P.I., S.A. Nikitin, A.F. Ostrovski, Y.I. Spichkin and A.M. Tishin, 1992, Fiz. Tverd. Tela **34**, 2196.

Levinson, L.M., and S. Shtrikman, 1971, J. Phys. Chem. Solids **32**, 981.

Levy, M., and M.C. Lee, 1970, Phys. Lett. A **32**, 294.

Lifshitz, L.D., and Y.S. Genshaft, 1965, Zh. Eksp. Teor. Fiz. **48**, 1050.

Lindgren, B., and A. Meyer, 1990, J. Magn. Magn. Mater. **84**, 115.

Liu, S.H., 1962, Phys. Rev. **127**, 1889.

Liu, S.H., 1972, Int. J. Magn. **3**, 327.

Liu, S.H., 1978, Electronic Structure of Rare Earth Metals, in: Handbook on the Physics and Chemistry of Rare Earths, Vol. 1, eds K.A. Gschneidner Jr and L. Eyring (North-Holland, Amsterdam) ch. 3, p. 233.

Long Jr, M., A.R. Wazzan and R. Stern, 1969, Phys. Rev. **178**, 775.

Luong, N.H., and J.J.M. Franse, 1981, Phys. Status Solidi (a) **66**, 399.

Lüthi, B., and R.J. Pollina, 1968, Phys. Rev. **167**, 488.

Lüthi, B., P. Papon and R.J. Pollina, 1969, J. Appl. Phys. **40**, 1029.

Lüthi, B., T.J. Moran and R.J. Pollina, 1970, J. Phys. Chem. Solids **31**, 1741.

MacPherson, M.R., C.E. Everett, D. Wohlleben and M.B. Maple, 1971, Phys. Rev. Lett. **26**, 20.

Maekawa, S., and M. Tachiki, 1977, Progr. Theor. Phys. **58**, 787.

Maekawa, S., and M. Tachiki, 1978, Phys. Rev. B **18**, 3736.

Maekawa, S., R.A. Treder, M. Tachiki, M.C. Lee and M. Levy, 1976, Phys. Rev. B **13**, 1284.

Mason, W.P., 1951, Phys. Rev. **82**, 715.

McWhan, D.B., and A. Stevens, 1965, Phys. Rev. **139**, 682.

McWhan, D.B., and A. Stevens, 1967, Phys. Rev. **154**, 438.

Melcher, R.L., 1972, Phys. Rev. Lett **28**, 165.

Menyuk, N., K. Dwight and J.A. Kafalas, 1971, J. Appl. Phys. **42**, 1301.
Mihai, V., and J.J.M. Franse, 1976, Rev. Roum. Phys. **21**, 1041.
Milton, J.E., and T.A. Scott, 1967, Phys. Rev. **160**, 387.
Miwa, H., 1965, Proc. Phys. Soc. **85**, 1197.
Miwa, H., and K. Yosida, 1961, Progr. Theor. Phys. (Kyoto) **26**, 693.
Moran, T.J., and B. Lüthi, 1970, J. Phys. Chem. Solids **31**, 1735.
Mulder, F.M., R. Koehoorn, R.C. Thiel and K.H.J. Buschow, 1997, Phys. Rev. B **56**, 5786.
Murata, K., K. Fukamichi, Y. Fujinaga, Y. Syono and T. Goto, 1995, J. Magn. Magn. Mater. **140–144**, Pt. 2, 833.
Murnaghan, F.D., 1951, Finite Deformation of an Elastic Solid (Wiley, New York).
Nerensen, N., C. Olsen and G. Arnold, 1964, Phys. Rev. A **135**, 176.
Nikitin, S.A., 1989, Magnetic Properties of Rare Earth Metals and their Alloys (MSU, Moscow). In Russian.
Nikitin, S.A., and R.V. Bezdushnyi, 1984, Fiz. Met. Metalloved **58**, 463.
Nikitin, S.A., and R.V. Bezdushnyi, 1987, Sov. Phys. JETP **65**, 1058.
Nikitin, S.A., and R.V. Bezdushnyi, 1988, Vestn. Mosk. Univ. Ser. 3 **29**, 68.
Nikitin, S.A., and R.V. Bezdushnyi, 1989, Fiz. Tverd. Tela **31**, 306.
Nikitin, S.A., and R.V. Bezdushnyi, 1991, Phys. Status Solidi (a) **124**, 327.
Nikitin, S.A., and P.I. Leontiev, 1987, Fiz. Tverd. Tela **29**, 2147.
Nikitin, S.A., D. Kim and O.D. Chistiakov, 1976a, Zh. Eksp. Teor. Fiz. **71**, 1610.
Nikitin, S.A., S.S. Slobodchikov and O.D. Chistiakov, 1976b, Zh. Eksp. Teor. Fiz. **70**, 104.
Nikitin, S.A., S.M. Nakvi and D. Kim, 1978, Vestn. Mosk. Univ. Ser. Fiz. Astr. **19**, 29.
Nikitin, S.A., Y.I. Spichkin and A.M. Tishin, 1989, Fiz. Tverd. Tela **31**, 250.
Nikitin, S.A., Y.I. Spichkin, A.M. Tishin and O.D. Chistiakov, 1991a, Moscow Univ. Phys. Bull. **46**, 90.
Nikitin, S.A., A.M. Tishin, Y.I. Spichkin, P.I. Leontiev and A.F. Ostrovski, 1991b, Fiz. Tverd. Tela **33**, 984.
Nikitin, S.A., A.M. Tishin, M.D. Kuzmin and Y.I. Spichkin, 1991c, Phys. Lett. A **153**, 155.
Nikitin, S.A., A.M. Tishin, R.V. Bezdushnyi, Y.I. Spichkin and S.V. Redko, 1991d, J. Magn. Magn. Mater. **92**, 397.
Nikitin, S.A., A.M. Tishin and P.I. Leontiev, 1991e, J. Magn. Magn. Mater. **92**, 405.
Nikitin, S.A., Y.I. Spichkin and A.M. Tishin, 1992, Vestn. Mosk. Univ. Ser. 3 **33**, 88.
Nikitin, S.A., A.M. Tishin, S.K. Godovikov, V.Y. Bodriakov and I.A. Avenarius, 1993, J. Magn. Magn. Mater. **125**, 190.
Ohkoshi, M., H. Kobayashi and T. Katayama, 1977, IEEE Trans. Magn. **MAG-13**, 1158.
Okamoto, H., 1967, Progr. Theor. Phys. **37**, 1348.
Palmer, S.B., 1975, J. Phys. F **5**, 2370.
Palmer, S.B., E.W. Lee and M.N. Islam, 1974, Proc. R. Soc. A **338**, 341.
Palmer, S.B., D. Hukin and C. Isci, 1977, J. Phys. F **7**, 2381.
Palmer, S.B., V. Baruchel, A. Drillat, C. Patterson and D. Fort, 1986, J. Magn. Magn. Mater. **54–57**, 1626.
Papoular, M., 1964, C.R. Acad. Sci. **258**, 4446.
Papoular, M., 1965, Phys. Lett. **16**, 259.
Patrick, L., 1954, Phys. Rev. **93**, 384.
Pengra, D.B., N.B. Thoft, M. Wulff, R. Feidenhans'l and J. Bohr, 1994, J. Phys. C **6**, 2409.
Pollina, R.J., and B. Lüthi, 1969, Phys. Rev. **177**, 841.
Pszczola, J., and K. Krop, 1986, J. Magn. Magn. Mater. **59**, 95.
Pytte, E., and H.S. Bennett, 1967, Phys. Rev. **164**, 712.
Radwanski, R.J., 1985, J. Phys. F **15**, 459.
Radwanski, R.J., 1986, Z. Phys. B **65**, 65.
Radwanski, R.J., and K. Krop, 1983, Physica B **119**, 180.
Radwanski, R.J., J.J.M. Franse and K. Krop, 1985, Acta Phys. Pol. A **68**, 373.
Radwanski, R.J., J.J.M. Franse and K. Krop, 1988, Physica B **149**, 306.
Ramji Rao, R., and C.S. Menon, 1973a, J. Phys. Chem. Solids **34**, 1879.
Ramji Rao, R., and C.S. Menon, 1973b, J. Appl. Phys. **44**, 3892.
Ramji Rao, R., and C.S. Menon, 1974, J. Phys. Chem. Solids **35**, 425.
Ramji Rao, R., and J.V.S.S. Narayanamurthy, 1979, Physica B **96**, 194.
Ramji Rao, R., and A. Rajput, 1979a, Can. J. Phys. **57**, 983.
Ramji Rao, R., and A. Rajput, 1979b, Can. J. Phys. **57**, 120.

Ramji Rao, R., and A. Rajput, 1979c, Z. Naturf. A **34**, 200.
Ramji Rao, R., and A. Ramanand, 1977a, J. Phys. Chem. Solids **38**, 1035.
Ramji Rao, R., and A. Ramanand, 1977b, Phys. Status Solidi (a) **42**, 247.
Ramji Rao, R., and A. Ramanand, 1980, Phys. Status Solidi (a) **58**, 11.
Ramji Rao, R., and A. Ramanand, 1984, Phys. Status Solidi (b) **122**, 11.
Ramji Rao, R., and R. Srinivasan, 1969, Phys. Status Solidi **31**, K39.
Robinson, L.B., F. Milstein and A. Jayaraman, 1964, Phys. Rev. A. **134**, 187.
Robinson, L.B., Swie-In Tan and K.F. Sterrett, 1966, Phys. Rev. **141**, 548.
Robinson, L.B., L.N. Ferguson Jr and F. Milstein, 1971, Phys. Rev. B **3**, 1025.
Rosen, M., 1968, Phys. Rev. **174**, 504.
Rosen, M., H. Klimker, U. Atzmony and M.P. Dariel, 1973, Phys. Rev. **8**, 2336.
Rosen, M., H. Klimker, U. Atzmony and M.P. Dariel, 1976, J. Phys. Chem. Solids **37**, 513.
Ruderman, M.A., and C. Kittel, 1954, Phys. Rev. **96**, 99.
Salama, K., F.R. Brotzen and P.L. Donoho, 1972, J. Appl. Phys. **13**, 3254.
Salama, K., C.L. Melcher and P.L. Donoho, 1974, IEEE Trans. Sonics Ultrasonics **SU-21**, 73.
Sato, K., I. Umehara, Y. Isikawa, K. Mori, H. Yoshida, T. Kaneko and K. Kamigaki, 1988, J. Phys. (France) **49**, 453.
Sato, K., K. Nishimura, Y. Isikawa, K. Kamigaki, H. Yoshida and T. Kaneko, 1990, J. Appl. Phys. **67**, 5298.
Savage, S.J., and S.B. Palmer, 1977, Phys. Lett. A **60**, 358.
Scott, T.E., 1978, Elastic and Mechanical Properties, in: Handbook on the Physics and Chemistry of Rare Earths, Vol. 1, eds K.A. Gschneidner Jr and L. Eyring (North-Holland, Amsterdam) ch. 8.
Sekizawa, K., H. Sekizawa and C.T. Tomizuka, 1970, J. Phys. Chem. Solids **31**, 215.
Shiga, M., 1969, Solid State Commun. **7**, 559.
Shimizu, M., 1977, Physica B **86-88**, 315.
Shimizu, M., 1978, J. Phys. Soc. Japan **44**, 792.
Shimizu, M., 1980, J. Magn. Magn. Mater. **20**, 47.
Shimizu, M., 1981, Rep. Progr. Phys. **44**, 329.
Shubin, V.V., G.I. Kataev and T.I. Ivanova, 1985, Fiz. Met. Metalloved **59**, 746.
Simpson, A.M., M.H. Jericho and M.C. Jain, 1976, Can. J. Phys. **54**, 1172.
Smart, J.S., 1966, Effective Field Theories of Magnetism (W.B. Saunders Company, Philadelphia/ London).
Sousa, J.B., R.P. Pinto, M.F. Pinheiro, M.E. Braga, J.M. Moreira, G.N. Blacke, S.B. Palmer and D. Hukin, 1982, J. Magn. Magn. Mater. **28**, 175.
Southern, B.W., and D.A. Goodings, 1973, Phys. Rev. B **7**, 534.
Spichkin, Y.I., and A.M. Tishin, 1997, Phys. Rev. B. **56**, 63.
Spichkin, Y.I., J. Bohr and A.M. Tishin, 1996a, Phys. Rev. B **54**, 6019.
Spichkin, Y.I., J. Bohr and A.M. Tishin, 1996b, J. Magn. Magn. Mater. **161**, 265.
Spichkin, Y.I., A.M. Tishin and K.A. Gschneidner Jr, 1998, to be published.
Szytula, A., and R. Zach, 1988, J. Less-Common Met. **141**, L5.
Tachiki, M., and S. Maekawa, 1974, Progr. Theor. Phys. **5**, 1.
Tachiki, M., M. Levy, R. Kagivada and M. Levy, 1968, Phys. Rev. Lett. **21**, 1193.
Tachiki, M., M.C. Lee and M. Levy, 1972, Phys. Rev. Lett. **29**, 488.
Tachiki, M., M.C. Lee, R.A. Treder and M. Levy, 1974, Solid State Commun. **15**, 1071.
Tachiki, M., S. Maekawa, R.A. Treder and M. Levy, 1975, Phys. Rev. Lett. **34**, 1579.
Takahashi, T., and M. Shimizu, 1965, J. Phys. Soc. Japan **20**, 26.
Takeuchi, J., T. Ito and M. Oka, 1985, J. Phys. Soc. Japan **54**, 3076.
Takeuchi, J., A. Hikata, M.J. McKenna, C. Elbaum and T. Ito, 1990a, Jpn. J. Appl. Phys. **29**, 2778.
Takeuchi, J., I. Hiromitsu and T. Ito, 1990b, J. Magn. Magn. Mater. **90-91**, 541.
Takeuchi, J., A. Hikata, M.J. McKenna, C. Elbaum and T. Ito, 1991, J. Phys. Soc. Japan **60**, 931.
Tange, H., T. Yonei and M. Goto, 1981, J. Phys. Soc. Japan **50**, 454.
Tani, K., and H. Mori, 1966, Phys. Lett. **19**, 627.
Tani, K., and H. Mori, 1968, Progr. Theor. Phys. **39**, 876.
Tatsumoto, E., H. Fujiwara, H. Fujii, N. Iwata and T. Okamoto, 1968, J. Appl. Phys. **39**, 894.
Taylor, K.N.R., and M.I. Darby, 1972, Physics of Rare Earth Solids (Chapman and Hall, London).
Tindall, D.A., M.O. Steinitz and T.M. Holden, 1993, J. Appl. Phys. **73**, 6543.

Tishin, A.M., 1990, Sov. Tech. Phys. Lett. **16**, 47.
Tishin, A.M., and V.V. Makhro, 1994, Phys. Lett. A **189**, 331.
Tishin, A.M., and O.A. Shipilov, 1992, Fiz. Tverd. Tela **34**, 3554.
Tishin, A.M., and O.A. Shipilov, 1993, Vest. Mosk. Univ. Ser. 3 **34**, 80.
Tishin, A.M., and Y.I. Spichkin, 1996, unpublished.
Tishin, A.M., S.A. Nikitin and V.Y. Bodriakov, 1995, J. Phys. (France) I **5**, 525.
Tonegawa, T., 1964, J. Phys. Soc. Japan **19**, 1168.
Toyama, K., K. Tajima, S. Chikazumi and A. Sawaoka, 1969, J. Phys. Soc. Japan **27**, 1070.
Treder, R., M. Tachiki and M. Levy, 1979, J. Magn. Magn. Mater. **12**, 167.
Treder, R.A., and M. Levy, 1977, J. Magn. Magn. Mater. **5**, 9.
Tsushima, T., M. Okhoshi, M. Hirano and T. Katayama, 1978, Bull. Electrotech. Lab. (Japan) **42**, 41.
Umebayashi, H., G. Shirane, B.C. Frazer and W.B. Daniels, 1968, Phys. Rev. **165**, 688.
Vajda, P., 1995, Hydrogen in Rare-Earth Metals, including RH_{2+x} Phases, in: Handbook on the Physics and Chemistry of Rare Earths, Vol. 20, eds K.A. Gschneidner Jr and L. Eyring (North-Holland, Amsterdam) ch. 137.
Vasconcelos, J., 1982, Phys. Rev. **26**, 1403.
Venter, A.M., and P. de V. du Plessis, 1995, J. Magn. Magn. Mater. **140-144**, 757.
Venter, A.M., P. de V. du Plessis and E. Fawcett, 1992a, J. Magn. Magn. Mater. **104–107**, 1517.
Venter, A.M., P. de V. du Plessis and E. Fawcett, 1992b, Physica B **180-181**, 290.
Vigren, D.T., 1976, Solid State Commun. **18**, 1599.
Vigren, D.T., 1977, Phys. Rev. Lett. **38**, 1155.
Vinokurova, L.I., and E.I. Kondorskii, 1964a, Izv. AN SSSR **28**, 537.
Vinokurova, L.I., and E.I. Kondorskii, 1964b, Zh. Eksp. Teor. Fiz. **46**, 1149.
Vinokurova, L.I., and E.I. Kondorskii, 1965, Zh. Eksp. Teor. Fiz. **48**, 429.
Vinokurova, L.I., E.I. Kondorskii, H. Rahimova and V.Y. Ivanov, 1972, Fiz. Tverd. Tela **14**, 720.
Vinokurova, L.I., A.G. Gapotchenko, E.S. Iskevich and E.T. Kulatov, 1981, Pis'ma Zh. Eksp. Teor. Fiz. **34**, 590.
Voiron, J., and B. Bloch, 1971, J. Phys. (France) **32**, 949.
Voiron, J., J. Beille, D. Bloch and C. Vettier, 1973, Solid State Commun. **13**, 201.
Von Döring, W., 1938, Ann. Physik **32**, 465.
Wagner, D., and E.P. Wohlfarth, 1981, J. Phys. F **11**, 2417.
Wazzan, A.R., R.S. Vitt and L.B. Robinson, 1967, Phys. Rev. **159**, 400.
Wilkinson, M.K., W.C. Koehler, E.O. Wollan and J.W. Cable, 1961, J. Appl. Phys. **32**(Suppl), 48.
Wohlfarth, E.P., 1969, Phys. Lett. A **28**, 569.
Wohlfarth, E.P., 1979, J. Phys. F **9**, L123.
Wohlfarth, E.P., 1981, Metallic Magnetism under High Pressure, in: Physics of Solids under High Pressure, eds J.S. Schilling and R.N. Shelton (North-Holland, Amsterdam) p. 175.
Yoshida, H., T. Komatsu, T. Kaneko, S. Abe and K. Kamigaki, 1988, J. Phys. (France) **49**, 275.
Yoshida, K., S. Abe, T. Kaneko and K. Kamigaki, 1987, J. Magn. Magn. Mater. **70**, 275.
Yosida, K., 1957, Phys. Rev. **106**, 893.

Handbook on the Physics and Chemistry of Rare Earths
Vol. 26
edited by K.A. Gschneidner, Jr. and L. Eyring

Chapter 171

ITINERANT ELECTRON METAMAGNETISM OF Co SUBLATTICE IN THE LANTHANIDE–COBALT INTERMETALLICS

Nguyen Huu DUC
Cryogenic Laboratory, Faculty of Physics, National University of Hanoi, 334 Nguyen Trai, Thanh Xuan, Hanoi, Vietnam

Tsuneaki GOTO
Institute for Solid State Physics, University of Tokyo, Minato-ku, Tokyo 106, Japan

Contents

Abbreviations

AF	antiferromagnetic
DOS	density of states
CEF	crystalline electric field
CSF	complete saturated ferromagnetic
F	ferromagnetic
f.u.	formula unit
FOT	first-order transition
IEM	itinerant electron metamagnetism
ISF	intermediate saturated ferromagnetic
LMTO	linear muffin tin orbital
MT	metamagnetic transition
NMR	nuclear magnetic resonance
R	lanthanide
HR	heavy lanthanide
LR	light lanthanide
RPA	random phase approximation
SF	strongly ferromagnetic
SOT	second-order transition
T	transition metal
WF	weakly ferromagnetic
WRS	Wohlfarth–Rhodes–Shimizu

List of symbols

a	lattice parameter
a_n	coefficients in the Landau expansion of the free energy of the d subsystem
A_n	coefficients in the Landau expansion of the free energy of the d subsystem, taking into account effects of spin fluctuations
A_{ij}	spin–spin coupling parameter
A_{RR}	spin–spin coupling parameter between R spins
A_{RT}	spin–spin coupling parameter between R and T spins
A_{TT}	spin–spin coupling parameter between T spins
b_n	coefficients in the Landau expansion of the free energy of the 4f subsystem
B	magnetic induction ($\mu_0 H$)
B_c	critical magnetic field of the metamagnetic transition
B^R_{mol}	effective molecular field acting on R moment in R–T compounds
B^T_{mol}	effective molecular field acting on T moment in R–T compounds
$B^T_{mol,RT}$	molecular field acting on T moment due to intersublattice (R–T) interactions
$B^T_{ex,TT}$	molecular field acting on T moment due to intrasublattice (T–T) interactions
C	coefficient of the first term in the development of elastic energy
c_n	coefficients in the Landau expansion of the free energy of the system containing both 4f-spin and itinerant electrons
D	determinant

D	exchange stiffness constant
F	free energy
g_J	Landé factor
I	effective interaction energy between the d electrons
J_R	the total angular momentum for the 4f ions
J	quantum number of the total angular momentum J_R for the 4f ions
K	contribution to the elastic constant due to all terms other than band contribution
k_B	Boltzmann constant
m_i	magnetic moment per ion
m_R	magnetic moment per R ion
m_T	magnetic moment per T ion
M_i	sublattice magnetization
M_f	magnetization of the R sublattice
M_d	magnetization of the d subsystem
M_s	spontaneous magnetization
$N(\varepsilon_F)$	density of states at the Fermi level
N_R	number of R atoms per mole
N_T	number of T atoms per mole
n	total number of d electrons
$n_\pm$	number of electrons with spin-up and spin-down
n_{ij}	molecular-field coefficient
n_{RR}	intrasublattice molecular-field coefficient
n_{RT}	intersublattice molecular-field coefficient
n_{TT}	intrasublattice molecular-field coefficient
p	pressure
p_{eff}	effective paramagnetic d-moment
R	resistance
S	Stoner enhancement factor
S_R	spin of the 4f ion
S_T	spin of the 3d ion
T	temperature
T	tesla
T_N	Néel temperature
T_C	Curie temperature
T_F	Fermi temperature
T_{max}	temperature at which paramagnetic susceptibility shows maximum
T^*	temperature above which magnetic susceptibility obeys the Curie–Weiss law
T_{sf}	spin fluctuation temperature
W	bandwidth
χ_d	paramagnetic susceptibility of d subsystem
$\Delta\varepsilon$	exchange splitting
ε	conduction-electron energy
ε_F	Fermi level
$\varepsilon^\pm$	chemical potential in the subbands
γ	electronic specific heat constant
Γ	exchange integral
λ	molecular field coefficient representing electron–electron interactions
$\lambda_\parallel$	longitudinal magnetostriction
$\lambda_\perp$	transverse magnetostriction
μ_B	Bohr magneton
ν_n	derivatives of density of states
Θ_p	paramagnetic Curie temperature
ρ	resistivity
ω	volume magnetostriction
Ω	normalized volume
$\xi(T)^2$	square of the fluctuating magnetic moment

1. Introduction

This chapter is devoted to one of the specific manifestations of magnetic systems which are close to the critical conditions for the appearance of magnetism. That is, the first-order transition (FOT) which has been observed in several lanthanide–cobalt (R–Co) intermetallics under the effect of varying external parameters (such as magnetic field, pressure or temperature) and internal parameters (exchange field, stoichiometry, and so on). This transition occurs between a nonmagnetic or low-induced moment state and a ferromagnetic state. This phenomenon is called itinerant electron metamagnetism (IEM).

IEM has its origin in peculiar band-structures near the Fermi level (ε_F). Since Wohlfarth and Rhodes (1962) predicted this phenomenon, many theoretical and experimental studies

have been made to elucidate it. In the last 20 years, band-structure calculations have been performed by different methods. They can account quantitatively for the magnetic and electronic properties of the d-systems (Cyrot and Lavagna 1979, Yamada et al. 1984, Yamada and Shimizu 1985, Brooks and Johansson 1993). Significant progress has been achieved with development of methods for calculating effects owing to fluctuations of spin density (Yamada 1991, 1993). However, progress has been made in the experimental research of IEM thanks to the availability of ultrahigh magnetic fields. In magnetic fields of megagauss, IEM has been systematically studied for various RCo_2, RCo_3 and RCo_5-based compounds (Goto et al. 1991, 1992, Katori et al. 1994a,b, Bartashevich et al. 1996).

The magnetic instability causes not only IEM, but many other striking properties such as enhanced magnetic susceptibility, a huge electronic specific heat constant, fluctuations of the spin density, and a volume anomaly. IEM thus is interesting not only in itself but, in addition, by studying this phenomenon it is possible to understand more deeply other aspects of the itinerant theory of metamagnetism and open up the possibilities incorporated in this theory for describing other unusual effects observed in experiments. Among the R–Co compounds, in which the Co sublattice shows metamagnetic behaviour, there are only the RCo_2 Laves phase compounds, for which the exhibition of various aspects mentioned above have been studied intensively (Duc et al. 1992a and refs. therein, Goto et al. 1994). For this system, the subject becomes more interesting (and more complicated) for the magnetic lanthanide compounds in which the local moments and itinerant electrons coexist (Duc et al. 1992a). In order to explain the metamagnetic character of such a system, many developments of the s–d model have been carried out (Inoue and Shimizu 1982, Brommer 1989, Duc et al. 1993a). For the two-sublattice ferrimagnets an external magnetic field can induce phase transitions from the ferrimagnetic collinear phase to the ferromagnetic one through a noncollinear phase. Field-induced magnetic phase transitions in a ferrimagnet with one unstable magnetic subsystem is thus of special interest. In practice, the multi-metamagnetic transition connected demagnetizing and re-entrant magnetizing of the d-sublattice have been observed in the $(Tm,Y)(Co,Al)_2$ compound. In a survey concentrated on the RCo_2 Laves phase compounds, in particular, a wealth of information concerning IEM and effects of spin fluctuations has been presented by Duc and Brommer (1999). In this chapter, the focus is on the IEM of the Co sublattice in different R–Co systems. The published experimental information on the electronic and magnetic properties of the RCo_2 compounds is also reviewed. However, the anomalies observed in the physical parameters at the MT are presented, but not discussed.

The chapter is organized as follows. Section 2 deals with the various models that have been proposed to describe IEM. At the beginning, the basic concepts of the band theory of metamagnetism describing the magnetically uniform states are presented. Then, the role of volume effects and spin fluctuation effects on the metamagnetic behaviour are also briefly introduced. The magnetic properties of the systems consisting of both itinerant electrons and localized spins are formulated on the basis of the s–d model. Section 3 is an experimental overview of IEM. This section consists of three major parts.

The first part deals with the nearly ferromagnets RCo_2 and $R(Co,M)_2$ (R = Y, Lu, Sc and M = Fe, Ni, Al, Cu, Si, Ga, Sn, ...); this major part is then continued with the 4f–3d exchange interactions and their effects on the induced Co-metamagnetic behaviour in the magnetic rare-earth–Co_2 compounds. In this subsection, the role of the magnetic R-atom as well as the influence of the 3d electrons affecting the character of the magnetic phase transitions and the spin fluctuation scattering are discussed. High-field magnetization in the RCo_2 with one unstable magnetic sublattice is also discussed. IEM in the RCo_3- and RCo_5-based compounds is presented in the second and third parts of sect. 3, respectively. Finally, sect. 4 discusses steps toward a complete understanding of metamagnetism in R–Co compounds.

We wish to emphasize that this chapter is primarily intended as a survey of experimental data for the RCo_2 compounds. The theory is summarized for the benefit of the reader and is therefore incomplete.

2. Theoretical approaches to itinerant electron metamagnetism (IEM)

2.1. *Itinerant electron system*

2.1.1. *Magnetically uniform state*

2.1.1.1. *The Stoner model.* The itinerant electron model of magnetism in metals is based on the simple assumption that the magnetic electrons collectively obey the Fermi–Dirac statistics. In addition, the essential electron–electron interactions are included by the use of the molecular field hypothesis. With these assumptions, it is possible to write down the total energy per atom of an itinerant ferromagnet as the sum of two terms. The first term is the total molecular field energy (F_m) which may be expressed as

$$F_m = -\tfrac{1}{2}\lambda M^2, \tag{1}$$

where M is the magnetization and λ is the coefficient of the molecular field related to the effective exchange energy between the electrons, I, given by $I = 2\mu_B^2\lambda$.

Introducing the standard notation $N(\varepsilon)$, $n_\pm$ and $\varepsilon^\pm$ for the density of the states at a given energy ε, the number of + and − spins per atom and the chemical potential in the subbands, respectively, the magnetization can be written as

$$M = \mu_B(n_+ - n_-), \tag{2}$$

where

$$n_\pm = \int_0^{\varepsilon\pm} N(\varepsilon)\,\mathrm{d}\varepsilon. \tag{3}$$

Letting ε_F be the Fermi energy for an itinerant paramagnet, then the total one-electron (kinetic) energy per atom at 0 K is given by

$$F_e = \int_{\varepsilon_F}^{\varepsilon_+} \varepsilon N(\varepsilon)\,\mathrm{d}\varepsilon - \int_{\varepsilon_F}^{\varepsilon_-} \varepsilon N(\varepsilon)\,\mathrm{d}\varepsilon. \tag{4}$$

The total energy is given by the sum of F_m and F_e which, when minimized, gives

$$\varepsilon^+ - \varepsilon^- = \frac{IM}{\mu_B} = \Delta\varepsilon, \tag{5}$$

where $\Delta\varepsilon$ is the so-called exchange splitting. The second derivative $\partial^2 F/\partial M^2 < 0$ leads to the following condition for the appearance of ferromagnetism (Stoner criterion):

$$\bar{I} = IN(\varepsilon_F) > 1. \tag{6}$$

At 0 K, the corresponding equilibrium value of the relative magnetization μ $(=M/n\mu_B)$ is given by

(i) $\mu = 0$ if $IN(\varepsilon_F) < 1$,

(ii) $0 < \mu < 1$ if $IN(\varepsilon_F) > 1$ but $N(\varepsilon_F)$ is not very small,

(iii) $\mu = 1$ if $IN(\varepsilon_F) > 1$ and $N(\varepsilon_F)$ is very small.

Correspondingly, there exist (i) paramagnetic, (ii) weakly itinerant ferromagnetic, and (iii) strongly itinerant ferromagnetic materials.

2.1.1.2. *Wohlfarth–Rhodes–Shimizu (WRS) model for IEM.* Using a Landau-type expression of the free energy of the d-electrons, Wohlfarth and Rhodes (1962) have pointed out that IEM occurs in a paramagnet if there exists a maximum in the temperature dependence of its magnetic susceptibility. Shimizu (1982), however, has obtained a more detailed condition for the appearance of IEM. We refer to their works together as the Wohlfarth–Rhodes–Shimizu (WRS) theory and briefly review it as follows.

The behaviour of an itinerant paramagnet in an applied magnetic field depends on the form of $N(\varepsilon)$ near the Fermi level. For a paramagnetic system, where the Stoner condition is close to being satisfied, magnetic ordering can appear if it is possible to have a situation that an applied magnetic field increases the density of states at the Fermi level. Figure 1 illustrates schematically sections of $N(\varepsilon)$ near $\varepsilon = \varepsilon_F$ for some characteristic cases where $N(\varepsilon_F)$ decreases (case a) or increases (cases b–d) when spin subbands are split in the magnetic field (B). As one can see from this figure, the condition

$$[N(\varepsilon_F) = N_+(\varepsilon_F) + N_-(\varepsilon_F)]_{B=0} < [N(\varepsilon_F) = N_+(\varepsilon_F) + N_-(\varepsilon_F)]_{B>0} \tag{7}$$

holds when the function $N(\varepsilon)$ has a positive curvature near ε_F, i.e., $N''(\varepsilon_F) > 0$. As we will discuss below, this is also the condition of the MT for an itinerant electron system.

In the case when the resulting splitting of the subbands is much smaller than their bandwidth, the band-splitting $\Delta\varepsilon$, and therefore the magnetization, are small parameters. The free energy F(M) can be expanded in powers of M as

$$F(M) = \tfrac{1}{2}(a_1 - \lambda)M^2 + \tfrac{1}{4}a_3M^4 + \tfrac{1}{6}a_5M^6 - BM, \tag{8}$$

where the last term is the magnetostatic energy in the presence of the external magnetic field. The Landau expansion coefficients a_1, a_3 and a_5 are determined by the behaviour

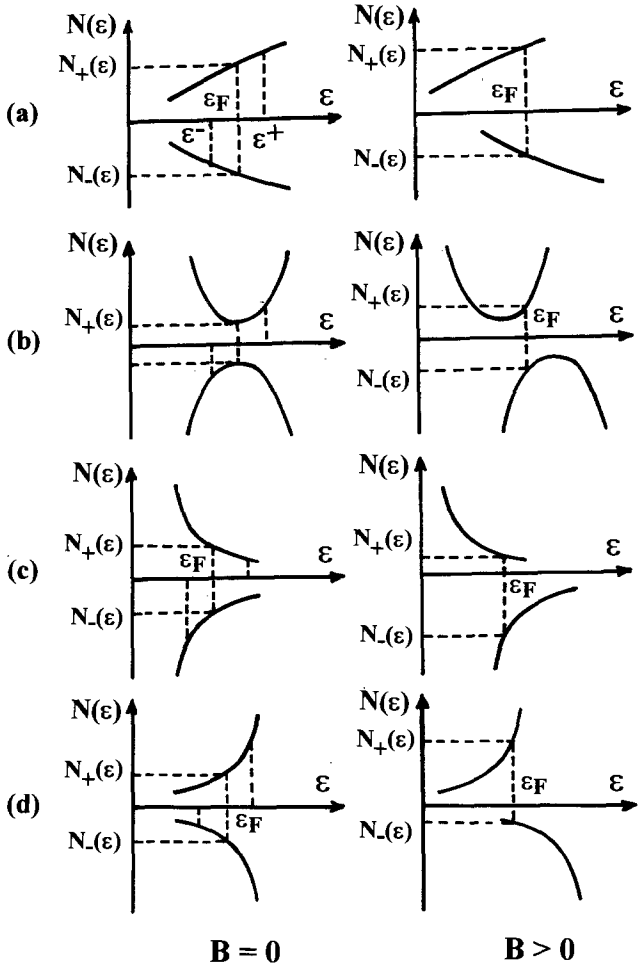

Fig. 1. Schematic diagrams of the dependence of the density of states on the energy $N(\varepsilon)$ near $\varepsilon = \varepsilon_F$ for cases of (a) negative curvature and (b–d) positive curvature of $N(\varepsilon)$ for (left) $B = 0$ and (right) $B > 0$. (After Levitin and Markosyan 1988.)

of the $N(\varepsilon)$ curve near $\varepsilon = \varepsilon_F$ and, indeed, can be represented as series in even powers of the temperature (Wohlfarth and Rhodes 1962, Edwards and Wohlfarth 1968, de Châtel and de Boer 1970 and Bloch et al. 1975):

$$a_1(T) = \frac{1}{2\mu_B^2 N(\varepsilon_F)}(1 + \alpha T^2 + \beta T^4), \tag{9.a}$$

$$a_1'(T) = a_1(T) - \lambda = \frac{1}{2\mu_B^2 N(\varepsilon_F)}(1 - \bar{I} + \alpha T^2 + \beta T^4), \tag{9.b}$$

$$a_3(T) = \frac{1}{2\mu_B^2 N(\varepsilon_F)}(\gamma + \delta T^2), \tag{10}$$

$$a_5(T) = \frac{1}{2\mu_B^2 N(\varepsilon_F)}\eta, \tag{11}$$

where α, β, γ, δ and η depend only on the second and fourth derivatives of $N(\varepsilon)$ and are given by

$$\alpha = -\frac{\pi^2 k_B^2}{6}\nu_2, \tag{12}$$

$$\beta = \frac{\pi^4 k_B^4}{360}(10\nu_2^2 - 7\nu_4), \tag{13}$$

$$\gamma = -\frac{1}{24\mu_B^2 N(\varepsilon_F)^2}\nu_2, \tag{14}$$

$$\delta = \frac{\pi^2 k_B^2}{144\mu_B^2 N(\varepsilon_F)^2}(4\nu_2^2 - \nu_4), \tag{15}$$

$$\eta = \frac{1}{1920\mu_B^4 N(\varepsilon_F)^4}(10\nu_2^2 - \nu_4), \tag{16}$$

where

$$\nu_n = \frac{N^{(n)}(\varepsilon_F)}{N(\varepsilon_F)}. \tag{17}$$

As $\chi(T) = 1/a_1'(T)$, the temperature dependence of the paramagnetic susceptibility is given as (see eq. 9.b):

$$\chi(T) = \frac{2\mu_B^2 N(\varepsilon_F)}{1 - \bar{I} + \alpha T^2 + \beta T^4}. \tag{18}$$

At 0 K,

$$\chi(0) = \frac{2\mu_B^2 N(\varepsilon_F)}{1 - IN(\varepsilon_F)} \tag{19a}$$

is the Pauli susceptibility ($\chi_0 = 2\mu_B^2 N(\varepsilon_F)$), which is enhanced by the Stoner enhancement factor $S = [1 - IN(\varepsilon_F)]^{-1}$:

$$\chi(0) = S\chi_0. \tag{19b}$$

At low temperatures, $\chi(T)$ can be written as

$$\chi(T) = S\chi_0[1 - \alpha \mathrm{S} T^2]. \tag{19c}$$

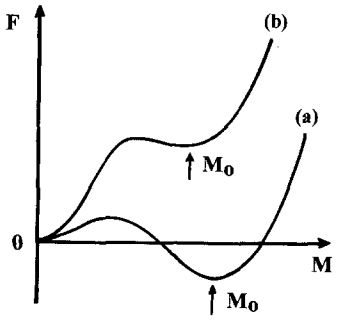

Fig. 2. Magnetic part of the free energy as a function of magnetization: the curves corresponding to (a) $a_1a_5/a_3^2 < \frac{3}{16}$ and (b) $\frac{3}{16} < a_1a_5/a_3^2 < \frac{1}{4}$. (After Yamada 1993.)

The equation of state can be determined from the condition for the minimum of the free energy (8):

$$B = a_1'(T)M + a_3(T)M^3 + a_5(T)M^5. \tag{20}$$

According to eq. (20), the field dependences of the magnetization and susceptibility of an itinerant paramagnet can be represented, respectively, as

$$\begin{aligned} M(T,B) &= \frac{1}{a_1'(T)}B - \frac{a_3(T)}{a_1'(T)^4}B^3 + \cdots \\ &= \chi(T,0)B - a_3(T)\chi(T,0)^4B^3 + \cdots, \end{aligned} \tag{21}$$

$$\chi(T,B) = \chi(T,0)[1 - a_3(T)\chi(T,0)^3B^2] + \cdots. \tag{22}$$

The character of these field dependences is determined by the sign of the $a_3(T)$ coefficient. One can see from here that the susceptibility of the itinerant paramagnet can increase as the field intensifies. In this case $a_3(T)$ must be negative. This corresponds to the condition of $\nu_2 > 0$ (see eqs. 10 and 14), i.e., corresponds to the case of the positive curvature of the DOS near ε_F as already mentioned at the beginning of this section. In this case, as can be seen from eqs. (12), (13) and (18), $\chi(T)$ will also show a maximum. Thus, the experimental observation of a susceptibility maximum was usually regarded as an indication of the possibility of the MT in the itinerant paramagnet (Wohlfarth and Rhodes 1962). However, as discussed below, the appearance of the MT still depends strictly on the values of the coefficients a_1', a_3 and a_5 (Shimizu 1982).

In the case of $a_1' > 0$, $a_3 < 0$, $a_5 > 0$ and $a_1'a_5/a_3^2 < \frac{1}{4}$, it can be seen from eq. (8) that the free energy $F(M)$ has two minima at $M = 0$ and at a finite value of M $(= M_0)$, and a maximum between the two (see fig. 2). When $a_1'a_5/a_3^2 < \frac{3}{16}$, $F(M_0)$ is negative as shown by curve (a). Then, the ferromagnetic state at $M = M_0$ is most stable without the external field. When $\frac{1}{14} > a_1'a_5/a_3^2 > \frac{3}{16}$, $F(M_0)$ is positive as shown by curve (b) and the state at $M = M_0$ is metastable. However, this metastable state can be stabilized by the external magnetic field and the MT from the paramagnetic to the ferromagnetic state occurs at a critical field B_c. To see this fact more clearly we discuss the magnetization curve $M(B)$ as follows.

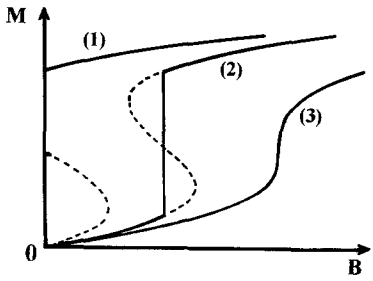

Fig. 3. Schematic curves of $M(B)$ for the (1) ferromagnetic, (2) metamagnetic and (3) paramagnetic states.

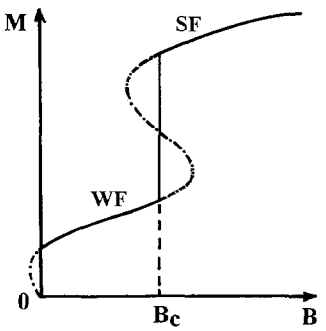

Fig. 4. Schematic magnetization curve for a weakly ferromagnetic (WF) system undergoing a MT into the strongly ferromagnetic (SF) state in an external magnetic field.

The magnetization curves obtained from eq. (21) are presented in fig. 3. In the case of $a_1' > 0$, $a_3 < 0$, $a_5 > 0$ and $a_1' a_5 / a_3^2 > \frac{9}{20}$, $M(B)$ increases monotonically with increasing B (curve 3). On the other hand, when $\frac{9}{20} > a_1' a_5 / a_3^2 > \frac{3}{16}$, $M(H)$ is S-shaped (curve 2). That is a metamagnetic first-order transition from the paramagnetic into the ferromagnetic state with hysteresis in the magnetization curve. Then the complete condition for the appearance of the MT is given as

$$a_1' > 0, \quad a_3 < 0, \quad a_5 > 0, \quad \frac{9}{20} > \frac{a_1' a_5}{a_3^2} > \frac{3}{16}. \tag{23}$$

When $a_1' a_5 / a_3^2 < \frac{3}{16}$, the system becomes ferromagnetic even at $B = 0$, as shown by curve (1) in fig. 3.

The MT discussed above has been described for an itinerant electron paramagnet with $a_1' > 0$. It should be noted that in the model under consideration, the FOT induced by an applied magnetic field can also arise when the starting state is magnetically ordered, i.e., in the case of $a_1' < 0$. This is the field-induced transition from a weakly ferromagnetic (WF) into strongly ferromagnetic (SF) state. Shimizu (1982) has described such a transition by including the term of $\frac{1}{8} a_7 M^8$ in the expression of the free energy (8). Then, if $a_3 > 0$, $a_5 < 0$ and $a_7 > 0$ for a definite ratio of the magnitude of these coefficients, this transition will be a FOT. The behaviour of the magnetization of such a weakly ferromagnetic system is shown systematically in fig. 4. This is the case for the $Y(Co,Al)_2$ and $Lu(Co,Al)_2$ compounds which will be discussed in sect. 3.1.1.2.

2.1.1.3. *A new approach to itinerant electron metamagnetism (Duc et al. 1992b).* In the well-known approach for IEM, volume effects are not considered. However, large volume increases ($\Delta V/V \approx 5\%$) are systematically observed to occur at the transition towards ferromagnetism (Givord and Shah 1972, Wada et al. 1988), indicating that the contribution from the elastic-energy term may be important. This has been confirmed by band structure calculations on YCo_2 (Schwarz and Mohn 1984), showing that YCo_2 is a Pauli paramagnet at the equilibrium volume but at a slightly larger volume, ferromagnetism is stable. Subsequently, Hathaway and Cullen (1991) have incorporated the effect of volume variations to discuss the magnetic properties of the RCo_2 compounds. A new approach to IEM in which the mechanism for the FOT is connected with the volume discontinuity at this transition has been proposed by Duc et al. (1992b). In this approach, the MT results simply from the interplay between the magnetic energy and the elastic energy.

2.1.1.3.1. *Description of the model.* A simple band structure cannot describe the intermetallic compounds, but it has the advantage of giving IEM without considering the structure of the DOS. Here, an elliptic density of states whose curvature is always negative is chosen:

$$N(\varepsilon) = \frac{10}{\pi W^2}\sqrt{W^2 - \varepsilon^2},$$

where $2W$ is the bandwidth.

In the Stoner model at 0 K the total energy in the presence of a magnetic field is written as a summation of the electronic (F_{el}) and elastic (F_{lat}) parts. The electronic energy can be given as:

$$F_{el} = \int_{-W}^{\varepsilon_+} \varepsilon N(\varepsilon)\,d\varepsilon + \int_{-W}^{\varepsilon_-} \varepsilon N(\varepsilon)\,d\varepsilon - \frac{IM^2}{4} - MB. \tag{24}$$

The total number of electrons, n, and the magnetization, M, are obtained by solving two self-consistent equations.

The lattice energy can be written as (Ohkawa 1989, Duc et al. 1992b)

$$F_{lat} = C\Omega + K\Omega^2, \tag{25}$$

where $\Omega = (V - V_0)/V_0$, and C and K are the expansion coefficients. K is the contribution to the elastic constant due to all terms other than the band contribution. Here, the reference volume V_0 was chosen in order to get a minimum of the total energy at this volume in the paramagnetic state. C is determined by minimizing eq. (25) at $\Omega = 0$, which gives

$$\left.\frac{\partial F_{el}}{\partial \Omega}\right|_{\Omega=0} + C = 0. \tag{26}$$

The elastic constant $\overline{K}$ of the system in the paramagnetic state is then given by

$$\overline{K} = K + \frac{1}{2}\left.\frac{\partial^2 F_{el}}{\partial^2 \Omega}\right|_{\Omega=0}, \tag{27}$$

which is smaller than K.

If the d-electrons are treated in the tight-binding approximation, the volume dependence of the bandwidth is given by $W = W_0 \exp(-q\Omega)$, where q is of the order of 1 to $\frac{5}{3}$ for 3d electrons (Slater and Koster 1954). In this approximation, the energy of the paramagnetic state also varies exponentially with volume. From eq. (26), the value of C is deduced as

$$C = qF_{el}(\Omega = 0, M = 0).$$

In the following sections, different aspects of IEM are discussed.

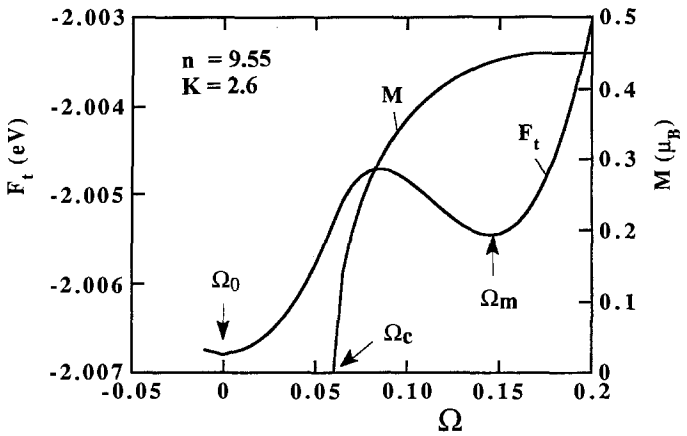

Fig. 5. Variation of the total energy and magnetic moment as a function of volume for the electrons in the elliptic band with $n = 9.55$, $K = 2.6$ eV, $I = 2.5$ eV and $W_0 = 5$ eV (see text). (After Duc et al. 1992b.)

2.1.1.3.2. *Magnetic state at $B = 0$.* For $B = 0$, as mentioned above, a magnetic state is obtained if the inverse of the Stoner parameter, $S^{-1} = 1 - IN(\varepsilon)$, is negative at $\Omega = 0$. With regard to the IEM, we restrict our consideration to the case $S^{-1}(\Omega = 0) > 0$. By increasing Ω, the bandwidth decreases and $S^{-1}(\Omega)$ may become negative at $\Omega > \Omega_c$. For small values of the Stoner parameter, Ω_c is given by

$$\Omega_c = -\frac{1}{q}\ln\left(1 - \frac{1}{S(\Omega = 0)}\right) \approx \frac{1}{S(\Omega = 0)q}.$$

If K is not too large, the competition between the elastic energy which increases with volume and the magnetic energy which decreases when the volume increases will give the total energy $F_{tot}(\Omega, M)$ a second minimum at $\Omega = \Omega_M$ ($> \Omega_c$), with $M \neq 0$ as shown in fig. 5. However, in the present case the magnetic state is not a stable one, since $F_{tot}(\Omega_0) < F_{tot}(\Omega_M)$: the stable state is paramagnetic but a MT can be induced by an applied magnetic field or a negative pressure.

2.1.1.3.3. *The induced-field metamagnetic transition.* The total energy in different magnetic fields is presented in fig. 6a for the electron system described above (see also

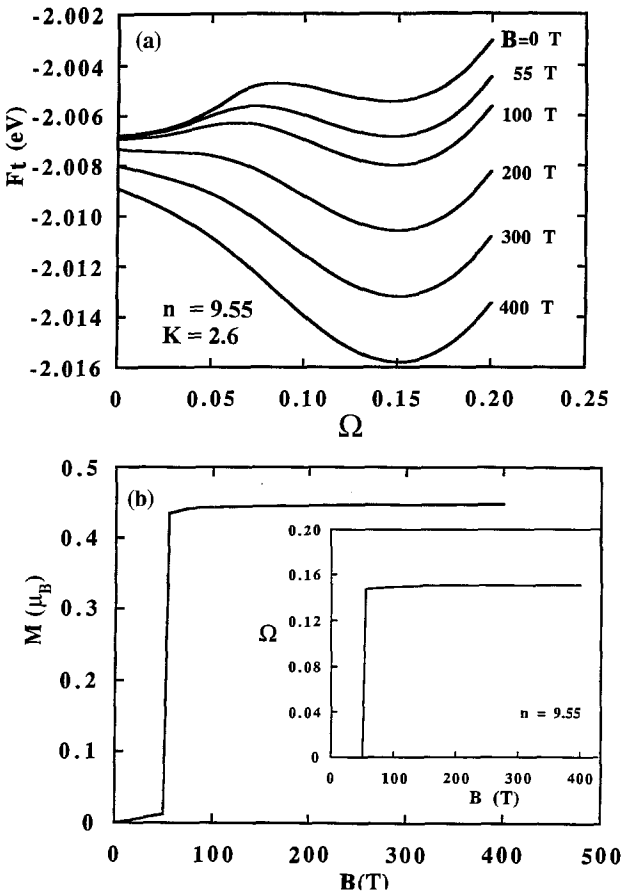

Fig. 6. (a) Total energy for the same parameters as in fig. 5 in the presence of a magnetic field. (b) The corresponding magnetization and magnetostriction curves. (After Duc et al. 1992b.)

fig. 5). As the metastable state for $\Omega = \Omega_M$ is magnetic, the decrease in energy due to magnetic fields is larger for this state than the paramagnetic state at $\Omega = 0$. For this case, i.e., when $F_{tot}(\Omega_0, B) = F_{tot}(\Omega_M, B)$, a metamagnetic transition occurs at a field of $B_c = 55$ T, and a large volume discontinuity ($\Omega = 0.15$) is found (see fig. 6b). Such an order of magnitude of the critical field of metamagnetism was found for the YCo_2 and $LuCo_2$ compounds.

2.1.1.3.4. *Metamagnetic transition induced by pressure.* The effect of pressure on IEM can be discussed by introducing a contribution $p\Omega$ to the total energy. Starting from the non-magnetic state, an IEM is obtained for negative values of p. For $|p| < p_c$, the volume increases as $\Omega = -p/K$. But for $|p| > p_c$ ferromagnetism appears, with a volume anomaly (see fig. 7a,b).

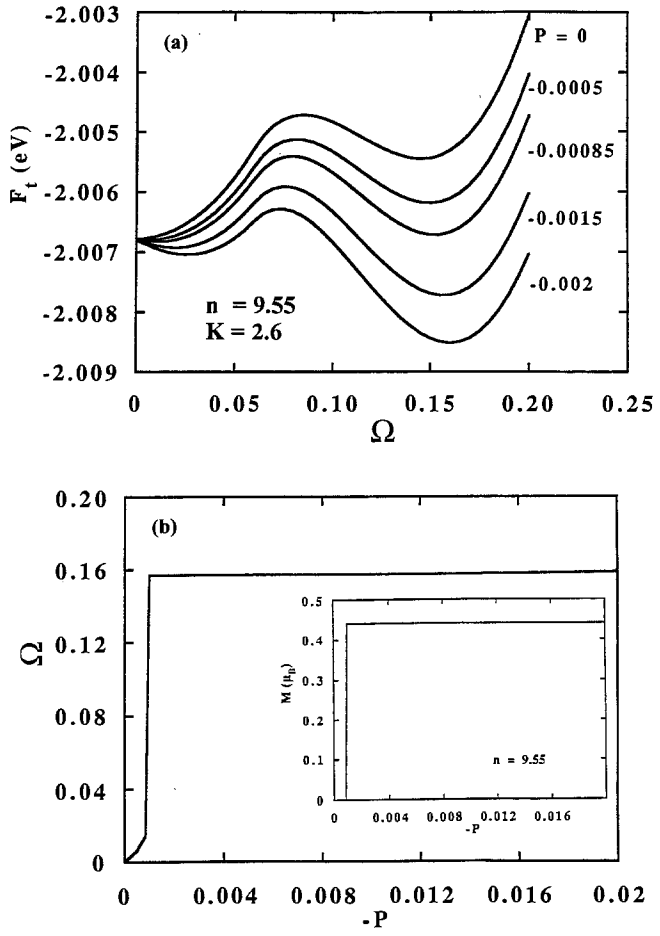

Fig. 7. (a) Total energy for the same parameters as in fig. 5 in the presence of a negative pressure. (b) The corresponding magnetization and magnetostriction curves.

From an experimental point of view, a negative chemical pressure may be obtained by alloying. This is the case in the compounds $Y(Co_{1-x}Al_x)_2$ (Yoshimura and Nakamura 1985), where the volume increases linearly with Al concentration. A transition from Pauli paramagnetism to ferromagnetism occurs at a critical concentration $x \approx 0.12$. On the other hand, starting from a ferromagnetic state, an application of external pressure leads to a paramagnetic state at a critical pressure (Armitage et al. 1990, Duc et al. 1993a, Goto et al. 1994).

A combination of the magnetic field and the (negative) pressure on the appearance of ferromagnetism is illustrated in fig. 8a. Within this mechanism, a decrease in the critical magnetic field B_c for the MT with increasing volume and the volume anomalies at the onset of ferromagnetism are pointed out (see figs. 8b,c). The model has been shown to

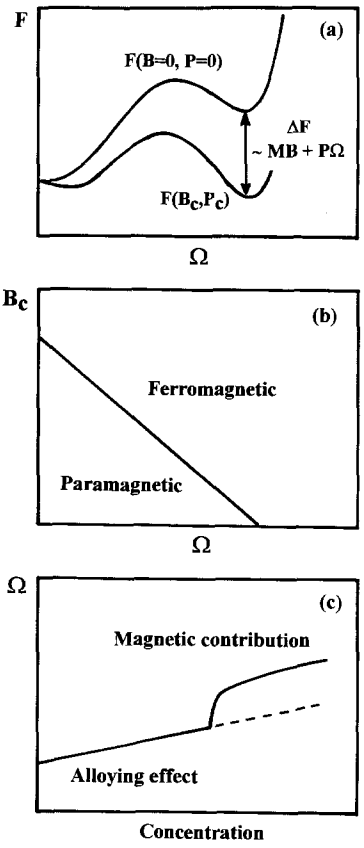

Fig. 8. Schematic diagrams of (a) total energy, (b) critical magnetic field, and (c) volume anomaly for IEM, predicted from Duc et al. (1992b).

be in qualitative agreement with several experimental observations in $Y(Co_{1-x}Al_x)_2$, see sect. 3.1.1.2.

2.1.1.3.5. *Influence of the elastic constant K.* We have discussed above that K should not be too small for IEM to be possible. However, there is also an upper value for K above which the system always stays paramagnetic. Metamagnetism can not be expected in materials with large K values because too large an increase in elastic energy is associated with any volume change. We will follow this discussion for the metamagnetic behaviour in the invariable d-electron concentration $Y(Co_xAl_yCu_z)_2$ compounds (Duc and Tai 1993) in sect. 3.1.1.4.

2.1.2. *Spin fluctuation effects (Yamada 1991, 1993)*

The band theory discussed above can only be considered as the first part of the theory of itinerant electron magnetism, where the magnetization can be regarded as uniform over the volume and time-independent. In the foregoing models, the effect of fluctuations of

the spin density on the properties of an itinerant paramagnet was ignored. The collective modes of spin fluctuations in the nearly ferromagnetic system play a crucial role in thermal properties such as specific heat and magnetic susceptibility. In this context, different itinerant-electron theories of magnetism have been developed. The first approach, using the random phase approximation (RPA), pointed out that paramagnons induce a logarithmic temperature dependence of the electron specific heat constant (Doniach 1967, Doniach and Engelsberg 1966, Berk and Schrieffer 1966) and lead to an enhancement of the coefficient of S^3T^2 in the magnetic susceptibility (Béal-Monod and Lawrence 1980). In a Fermi liquid description of IEM, Misawa (1988, 1995) has shown that the thermal variation of χ is proportional to $T^2 \ln T$ rather than T^2. The relation between susceptibility maximum and metamagnetism was also clarified. Using a self-consistent renormalization (SCR) theory of spin fluctuations, a unified picture has been proposed (Moriya 1985, 1991 and references therein). Among the results of this approach, one can quote the quantitative description of the nuclear spin relaxation rate and high temperarure susceptibility. The latter follows a Curie–Weiss law without localized moments. As regards IEM, we present below Yamada's theory.

When spin-fluctuation effects are taken into account, the state can no longer be regarded as magnetically uniform. Instead of the free energy mentioned in eq. (8) for an itinerant magnet, we must now study the free energy density per unit volume $\Delta f(r)$, which is given as (Shimizu 1981, Yamada 1991, 1993)

$$\begin{aligned}\Delta f(r) = {} & \tfrac{1}{2}a_1' \,|m(r)|^2 + \tfrac{1}{4}a_3 \,|m(r)|^4 + \tfrac{1}{6}a_5 \,|m(r)|^6 + \cdots \\ & + \tfrac{1}{2}D \,|\nabla \cdot m(r)|^2 + \cdots - m_z(r)\,B,\end{aligned} \tag{28}$$

where $m(r)$ is the magnetization density, a_i are the Landau coefficients, which can be given as a function of T in terms of the DOS curve as shown in eqs. (9)–(16), and D is the exchange stiffness constant.

The total free energy ΔF is obtained by

$$\Delta F = \frac{1}{V}\int_V \mathrm{d}r^3\, \Delta f(r), \tag{29}$$

where V is the volume.

Introducing the thermal average of the square of the fluctuating magnetic moment, $\xi(T)^2$, into eq. (29), one obtains the equation of state in the magnetic system with the bulk magnetization M and external field B at temperature T as

$$B = A_1(T)M + A_3(T)M^3 + A_5(T)M^5 + \cdots, \tag{30}$$

i.e., in this approximation the spin fluctuation correction reduces to renormalization of the expansion coefficients in the equation of state (8) with:

$$A_1(T) = a_1' + \tfrac{5}{3}a_3\xi(T)^2 + \tfrac{35}{9}a_5\xi(T)^4, \tag{31}$$

$$A_3(T) = a_3 + \tfrac{14}{3} a_5 \xi(T)^2, \tag{32}$$

$$A_5(T) = a_5, \tag{33}$$

and

$$\xi(T)^2 = 2k_B T^2 \sum \chi_q, \tag{34}$$

where χ_q is the wave number dependent susceptibility (see Moriya 1979, 1991).

2.1.2.1. *Paramagnetic susceptibility.* $\chi(T,B)$ at $B=0$ is equal to $1/A_1(T)$, where $A_1(T)$ is given by eq. (31). It is easily seen that the term due to spin fluctuations modifies the variation of the magnetic susceptibility. In the case of $a_1' > 0$, $a_3 < 0$ and $a_5 > 0$, at low temperatures $\chi(T)$ is mainly governed by the first term in eq. (31) and shows a T^2 dependence. $\xi(T)^2$ increases rapidly with increasing temperature and reaches an upper limit determined by the charge neutrality condition at a certain temperature T^*. At $T > T^*$ the system behaves as if having local moments, and the Curie–Weiss type of the magnetic susceptibility may be the only type possible at high temperature region.

The temperature T_{max}, where $\chi(T)^{-1}$ reaches a minimum, is given by $\partial A_1(T)/\partial \xi(T) = 0$, from which one gets (Yamada 1991, 1993)

$$\xi(T_{max})^2 = -\frac{3}{14}\frac{a_3}{a_5} \tag{35}$$

and

$$\chi(T_{max}) = \frac{1}{a_1' - \frac{5}{28}\frac{a_3^2}{a_5}}. \tag{36}$$

For $a_1' a_5 / a_3^2 < \frac{5}{28}$, $\chi(T_{max})$ becomes negative. Then, the condition for the appearance of the maximum in $\chi(T)$ must be

$$a_1' > 0, \quad a_3 < 0, \quad a_5 > 0, \quad \frac{a_1' a_5}{a_3^2} > \frac{5}{28}. \tag{37}$$

In addition, it is noted here that T_{max} given by eq. (35) is also the temperature at which $A_3(T) = 0$. This means that $A_3(T)$ changes sign from negative to positive at T_{max}.

2.1.2.2. *Metamagnetic transition.* The differential susceptibility $\chi(T,B)$ $(= dM/dB)$ can be obtained from the equation of state (30). Expanding it with respect to B, one gets, in the paramagnetic state,

$$\chi(T, B) = \frac{1}{A_1(T)} - \frac{A_3(T)}{A_1(T)^4} B^2 + \cdots. \tag{38}$$

In the case where the MT occurs, as shown in the preceding section, $A_3(T)$ is negative. This means that the coefficient of B^2 in eq. (38) is positive. Then, $\chi(T,B)$ increases with increasing B.

Upon replacing a_1', a_3 and a_5 in eq. (23) with $A_1(T)$, $A_3(T)$ and $A_5(T)$, the conditions for the appearance of the MT at finite temperature are given as

$$A_1(T) > 0, \quad A_3(T) < 0, \quad A_5(T) > 0, \tag{39}$$

and

$$\frac{9}{20} > \frac{A_1(T)A_5(T)}{A_3(T)^2} > \frac{3}{16}. \tag{40}$$

The MT disappears at a temperature T_0 when $A_1(T)A_5(T)/A_3(T)^2 = \frac{9}{20}$. Using eqs. (31)–(33), these conditions lead to

$$\xi(T_0)^2 = \frac{|a_3|}{a_5}\left\{\frac{3}{14} - \sqrt{\frac{45}{266}}\sqrt{\frac{a_1'a_5}{a_3^2} - \frac{5}{28}}\right\}, \tag{41}$$

which is positive when $a_1'a_5/a_3 < \frac{9}{20}$. As seen from eqs. (35)–(41), $\xi(T_0)^2$ is smaller than $\xi(T_{\max})^2$. T_0 is then always lower than $T_{\max}$, as $\xi(T)^2$ is a monotonically increasing function of T (see eq. 34).

The system becomes ferromagnetic at $B=0$ when $A_1(T)A_5(T)/A_3(T)^2 < \frac{3}{16}$, see also fig. 2. Similarly, the critical temperature, T_1, at which the ferromagnetic state becomes unstable and the FOT occurs, is given as

$$\xi(T_1)^2 = \frac{|a_3|}{a_5}\left\{\frac{3}{14} - \sqrt{\frac{36}{7}}\sqrt{\frac{a_1'a_5}{a_3^2} - \frac{5}{28}}\right\}. \tag{42}$$

Clearly, T_1 is lower than T_0 ($T_1 < T_0 < T_{\max}$).

Under the condition (37) for the appearance of a susceptibility maximum $\chi_{\max}$ at $T_{\max}$, the characteristics of the IEM, which is corrected by the effects of spin fluctuations, are summarized as follows:

(i) For $\frac{5}{28} < a_1a_5/a_3^2 < \frac{3}{16}$, the ferromagnetic state becomes stable below T_1, the MT occurs at $T_1 < T < T_0$.

(ii) For $\frac{3}{16} < a_1a_5/a_3^2 < \frac{9}{20}$, the system is paramagnetic at $H=0$ and the MT occurs at $0 < T < T_0$.

(iii) For $\frac{9}{20} < a_1a_5/a_3^2$, the susceptibility shows a maximum at $T_{\max}$, but the MT does not occur.

When the effects of spin fluctuations are taken into account, one cannot obtain an analytical expression for the temperature dependence of the critical field B_c. However, in

the limiting case of $a_1 a_5/a_3^2 = \frac{3}{16}$, where $B_c = 0$ at $T = 0$, one can get $B_c(T)$ in the lowest order of T as

$$B_c(T) = \tfrac{1}{2}\sqrt{\frac{|a_3|}{3a_5}}\left(a_1 - \frac{3}{16}\frac{a_3^2}{a_5}\right) + O(T^2). \tag{43}$$

As $O(T^2) > 0$, $B_c(T)$ is expected to increase with increasing T as T^2. Finally, from eqs. (35)–(36) and (49), $B_c(0)$ is given as

$$B_c(0) = \sqrt{\frac{7}{18}\frac{\xi(T_{max})}{\chi(T_{max})}}\left(\frac{20}{21} - \frac{1}{20}\frac{\chi(T_{max})}{\chi(0)}\right). \tag{44}$$

Since $\xi(T_{max})$ is proportional to T_{max}, when T_{max} is low, a linear relation between the values of $B_c(0)$ and T_{max} can be obtained (Yamada 1993). However, at present, it is not a universal constant for all materials. We will come back to this point in sect. 3.1.1.2.

2.2. *System consisting of localized moments interacting with itinerant electrons*

2.2.1. *The Inoue–Shimizu model*

The magnetic properties of a system consisting of localized magnetic moments interacting with itinerant electrons have been discussed in terms of the so-called s–d model (e.g. Takahashi and Shimizu 1965, 1966). On the basis of such a model, Bloch and Lemaire (1970) and Bloch et al. (1975) have explained the type of magnetic properties of the RCo_2 compounds. In these models, the presence of the localized 4f–moments is considered as an effective field acting on the itinerant d-electron subsystem. The free energy has thus been expanded in powers of M_d only (see also Jarlborg and Freeman 1981, Levitin and Markosyan 1988). Inoue and Shimizu (1982), however, have presented a version of the s–d model in which the free energy is expanded in the proper thermodynamic variable, i.e., the total magnetization of both the d electrons, M_d and the localized spin, M_f. In this case, the free energy can be considered as the sum of two separate contributions depending on the magnetization of the itinerant subsystem and that of the 4f moment, respectively, together with one coupling term proportional to the product of these magnetizations. The expression for the free energy is therefore written as

$$F = F_d + F_f - n_{RCo} M_d M_f, \tag{45}$$

where F_d is the free energy of the itinerant d-electron subsystem already described in eq. (8):

$$F_d = \tfrac{1}{2}a_1' M_d^2 + \tfrac{1}{4}a_3 M_d^4 + \tfrac{1}{6}a_5 M_d^6 - B M_d, \tag{46}$$

and F_f is the free energy of the localized spin system, which is given as (Shimizu 1981, Inoue and Shimizu 1982)

$$F_f = \tfrac{1}{2}b_1' M_f^2 + \tfrac{1}{4}b_3 M_f^4 + \tfrac{1}{6}b_5 M_f^6 - B M_f, \tag{47}$$

with

$$b_1'(T) = b_1(T) - n_{RR}, \qquad b_1(T) = \frac{3k_BT}{N_R J(J+1)(g\mu_B)^2}, \tag{48a,b}$$

$$b_3(T) = \tfrac{9}{20}k_BT\frac{(2J+1)^2+1}{N_R^3J^3(J+1)^3(g\mu_B)^4}, \tag{49}$$

$$b_5(T) = \tfrac{27}{2800}k_BT\frac{11(2J+1)^4+32[(2J+1)^2+11]}{N_R^5J^5(J+1)^5(g\mu_B)^6}. \tag{50}$$

Here, n_{RR} and n_{RCo} are the molecular field coefficients representing the interactions between 4f moments and the R–Co intersublattice interactions, respectively.

Because the thermodynamic variable of this system is neither M_f nor M_d, but $M\,(=M_d+M_f)$, F has been expanded in a power series of M. By minimizing F with respect to M_f or M_d with the condition that M is constant, one gets

$$F = \tfrac{1}{2}c_1M^2 + \tfrac{1}{4}c_3M^4 + \tfrac{1}{6}c_5M^6 + \cdots, \tag{51}$$

where

$$c_1 = \frac{a_1'(T)\,b_1'(T) - n_{RCo}^2}{Q}, \tag{52}$$

$$c_3(T) = \frac{b_3(T)[a_1'(T)+n_{RCo}]^4 + a_3(T)[b_1'(T)+n_{RCo}]^4}{Q^4}, \tag{53}$$

$$c_5(T) = \frac{b_5(T)[a_1'(T)+n_{RCo}]^6 + a_5(T)[b_1'(T)+n_{RCo}]^6}{Q^6} - 3\frac{\left(b_3(T)[a_1'(T)+n_{RCo}]^3 + a_3(T)[b_1'(T)+n_{RCo}]^3\right)^2}{Q^7}, \tag{54}$$

with

$$Q = a_1'(T) + b_1'(T) + 2n_{RCo}.$$

The FOT will occur if the condition $c_3(T_c) < 0$ is satisfied. (Hereafter, we use the notation T_c for the transition of both FOT and SOT). T_c is determined from $c_1(T_c) = \chi(T_c)^{-1} = 0$, which gives

$$T_c = C_R(n_{RR} + n_{RCo}^2\chi_{Co}). \tag{55}$$

Making use of this equation, one can write $c_3(T_c)$ as

$$c_3(T_c) = \frac{b_3(T_c) + a_3(T)[\chi_d(T_c)\,n_{RCo}]^4}{[1+\chi_d(T_c)\,n_{RCo}]^4}. \tag{56}$$

For a system of localized moments, where the free energy (47) is expanded only in powers of M_f, the signs of the b_n coefficients are always positive and the FOT

will not occur. For an itinerant-electron system, as the sign of the $a_3(T)$ term can be negative (see preceding section), the FOT is possible. Presently, in the s–d model, where localized spins and itinerant electrons coexist, $c_3(T_c)$ in eqs. (53) or (56) can be negative or positive depending on the contributions of the negative value of $a_3(T_c)$ and the positive value of $b_3(T_c)$. Thus both the FOT and the SOT can exist in the s–d model, even at low temperatures. As discussed in sect. 3.1.2, this model has been utilized to explain the type of the magnetic phase transitions not only in RCo_2 compounds but also in a number of more complicated compounds such as $(R_xY_{1-x})Co_2$, $R(Co,Cu)_2$ and $R(Co,Al)_2$, etc. (see Duc et al. 1992a). For compounds such as $Tb_xHo_{1-x}Co_2$ (Duc et al. 1991), however, the exchange field acting on a Tb moment differs from that acting on a Ho moment. Consequently, the total R magnetization cannot be used as a proper (internal) thermodynamic variable. In this case, the free energy should be considered as the sum of three coupled contributions and the Inoue–Shimizu model cannot be applied straightforwardly. A generalization of the Inoue–Shimizu model for an arbitrary number of interacting contributions has been made by Brommer (1989) (see also Duc et al. 1993a).

2.2.2. *A generalization of the Inoue–Shimizu model (Brommer 1989)*

The first attempt to generalize the Inoue–Shimizu model was to describe a system with a mixture of different kinds of R atoms, such as $(R_i,R_j)Co_2$ compounds. Such an attempt was carried out by Brommer (1989). In this version, however, the R–R interaction within the R sublattice was ignored and the R–Co coupling parameter A_{RCo} was assumed to be constant for all R elements. It is now generally accepted that the interaction between R moments is by no means small (Lee and Pourarian 1976, Duc et al. 1993b,c, 1995a). However, the basic interactions between R spins and (itinerant) Co spins appear to be enhanced when going from the heavy to the light rare-earth compounds. The same behaviour is true for the R–R interactions. Taking into account all of these factors, an elaborate version of the generalized Inoue–Shimizu model was presented by Duc et al. (1993b). The approach is given as follows:

The molecular free energy of a system of coupled magnetic subsystems is written as

$$F = \sum_j F_j(M_j) - \sum_j n_{ij} M_i M_j, \tag{57}$$

$$F_j = \tfrac{1}{2} a'_{1j} M_j^2 + \tfrac{1}{4} a_{3j} M_j^4 + \tfrac{1}{6} a_{5j} M_j^6, \tag{58}$$

where

$$a'_{1j} = a_{1j} - n_{jj},$$

with n_{jj} and n_{ij} the intra-sublattice and inter-sublattice molecular field coefficients, respectively.

Let Q_{ij} be the inverse of the matrix $(a'_{1j}\delta_{ij} - n_{ij})$. With the definitions $Q_i = \sum_j Q_{ij}$ and $Q_t = \sum_i Q_i$, one can write the expression of the free energy in terms of the (total) molar magnetization in the form

$$F = \tfrac{1}{2}c_1M^2 + \tfrac{1}{4}c_3M^4 + \tfrac{1}{6}c_5M^6, \tag{59}$$

with the Landau coefficients c_n given as (Brommer 1989)

$$c_1 = Q_t^{-1}, \tag{60}$$

$$c_3 = \sum_j a_{3j}\left(\frac{Q_j}{Q_t}\right)^4 \tag{61}$$

$$c_5 = \sum_j a_{5j}\left(\frac{Q_j}{Q_t}\right)^6 + \frac{3}{Q_t^7}\sum_j a_{3j}Q_i^3\left(Q_iQ_j - Q_tQ_{ij}\right)a_{3j}Q_j^3. \tag{62}$$

The transition temperature is determined by $c_1 = Q_t^{-1} = 0$, or rather by

$$D \equiv \det(a'_{1j}\delta_{ij} - n_{ij}) = 0. \tag{63}$$

The present approach can be applied to the case of three-coupled subsystems (three-sublattice model). We consider quasi-binary compounds $(R_1, R_2)Co_2$, where R_1 and R_2 are different lanthanide atoms with concentrations x_1 and x_2, respectively $(x_1 + x_2 = 1)$. In the expressions of the free energy we change the notation slightly: for the d-subsystem the coefficients are written as a_n and for the R_i subsystem, the coefficients are b_{ni}. With these notations, eq. (61) becomes

$$c_3 = a_3\left(\frac{Q_d}{Q_t}\right)^4 + \sum_j b_{3j}\left(\frac{Q_j}{Q_t}\right)^4. \tag{64}$$

Let M_1 be the magnetization (per mol f.u.) of R_1 atoms, M_2 that of R_2 atoms and M_d that of the itinerant d electrons. For this system of exchange-coupled magnetizations, placed in an external magnetic field B, the linearized equations can be written in the molecular field approximation as

$$\begin{aligned} a_dM_d - n_{1d}M_1 - n_{d2}M_2 &= B, \\ -n_{d1}M_d - b'_1M_1 - n_{12}M_2 &= B, \\ -n_{d2}M_d - n_{12}M_1 - b'_2M_2 &= B. \end{aligned}$$

Here, a_d is the inverse susceptibility of the d-subsystem, and $b'_j = b_{1j} - n_{jj}$ (see also eqs. 48a,b).

The set of linearized equations above is solved by calculating the inverse of the matrix of coefficients, with elements Q_{dd}, Q_{d1}, and so on. Since all elements diverge at $T = T_c$

(where the determinant D vanishes), we instead give the non-divergent products DQ_{dd}, DQ_{d1}, and so on. By assuming that $n_{11}n_{22} = n_{12}^2$, $n_{12}n_{d2} = n_{d1}n_{22}$, and so on, the expressions can be simplified and one obtains (Duc et al. 1993a):

$$D = b_1' b_2' \left(a_d - \sum_j \frac{n_{dj}^2 + a_d n_{jj}}{b_j'} \right), \tag{65}$$

$$DQ_{dd} = b_1' b_2' \left(1 - \sum_j \frac{n_{jj}}{b_j'} \right), \tag{66}$$

$$DQ_{d1} = b_1' b_2' \frac{n_{d1}}{b_1'}, \tag{67}$$

$$DQ_{11} = b_1' b_2' \left(\frac{a_d}{b_1'} - \frac{a_d n_{22} + n_{d1}^2}{b_1' b_2'} \right), \tag{68}$$

$$DQ_{12} = b_1' b_2' \left(\frac{a_d n_{12} + n_{d1} n_{d2}}{b_1' b_2'} \right), \tag{69}$$

$$DQ_d = b_1' b_2' \left(1 - \sum_j \frac{n_{dj} - n_{jj}}{b_j'} \right), \tag{70}$$

$$DQ_1 = b_1' b_2' \left(\frac{n_{d1} + a_d}{b_1'} + \frac{a_d(n_{12} - n_{22}) + n_{d1} n_{d2} - n_{d2}^2}{b_1' b_2'} \right), \tag{71}$$

$$DQ = b_1' b_2' \left(1 + \sum_j \frac{a_d + 2n_{dj} - n_{jj}}{b_j'} + \frac{a_d(n_{12} - n_{11} - n_{22}) + (n_{d1} - n_{d2})^2}{b_1' b_2'} \right). \tag{72}$$

The relative contributions Q_d/Q_t, Q_1/Q_t and Q_2/Q_t are actually calculated as DQ_d/DQ_t, DQ_1/DQ_t and DQ_2/DQ_t, and so on, and are used as input in the calculation of c_3 (see eq. 64). In the case where the interaction between the R moments is neglected, one arrives at the expression for c_3 presented by Brommer (1989):

$$c_3 = \frac{a_3 + \sum_j x_j b_{3j} (n_{dj}/b_{1j})^4}{q^4}, \tag{73}$$

where

$$q = 1 + \sum_j x_j \frac{n_{dj}}{b_{1j}}. \tag{74}$$

The generalized expressions and their simplifications can be used also in the case where one of the rare-earth ions is non-magnetic, in particular, for $R_xY_{1-x}Co_2$, where

R represents a magnetic lanthanide ion (say R_1) and Y (say R_2) the non-magnetic one. If we eliminate the explicit concentration dependence of q (eq. 74), i.e. of the denominator in eq. (73), by the substitution $xn_{d1}/b_1 = a_d/n_{d1}$ (at the critical temperature), the resulting expression for $c_3(T_c)$ is identical to that given by Inoue and Shimizu (1982), see eq. (56).

3. Experimental observation of metamagnetic transitions

3.1. *The RCo_2 Laves phase compounds*

3.1.1. *Nearly ferromagnetic RCo_2 compounds (R = Y, Lu, Sc and Hf)*

3.1.1.1. *The RCo_2 compounds.* The rare-earth–transition metal intermetallics can be considered to be formed by the association of a relatively narrow T 3d band with a wider (and higher in energy) R 5d (or Y 4d) band. These two bands are close to each other and lead to the 3d–5d (or 3d–4d) hybridization states. The Fermi level of the compounds often lies in this region. Thus, in general, alloying of the 3d elements with rare-earth metals, first leads to a decrease of the DOS at the Fermi level and then weakens the 3d magnetism. This effect is illustrated for yttrium compounds as shown in fig. 9 in a plot of magnetic moment per 3d atom as a function of Y concentration. The system reaches a critical concentration range at YCo_2, where the alloy is close to the conditions required for the onset of magnetism (Stoner criterion). The Y(Lu)Co_2 compounds, thus, do not order magnetically, but exhibit strongly enhanced paramagnetism. The susceptibility of the YCo_2 and $LuCo_2$ compounds increases with increasing temperature, passing through a broad maximum at 250 K and 370 K, respectively (Lemaire 1966, Givord and Lemaire 1971, Ikeda et al. 1984). The compound $ScCo_2$ shows a similar behaviour, indicating that it is an inherent property of the Co sublattice.

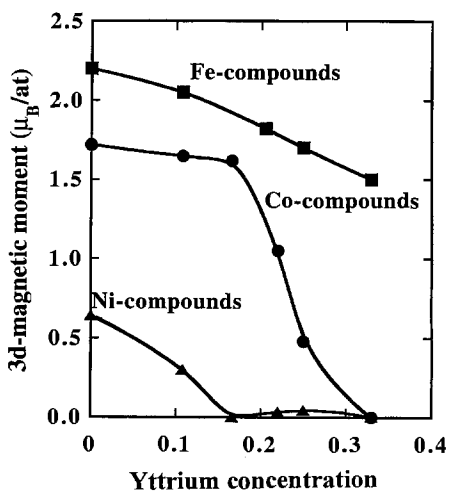

Fig. 9. 3d-magnetic moment as a function of yttrium concentration in Y–Ni, Y–Co and Y–Fe intermetallics.

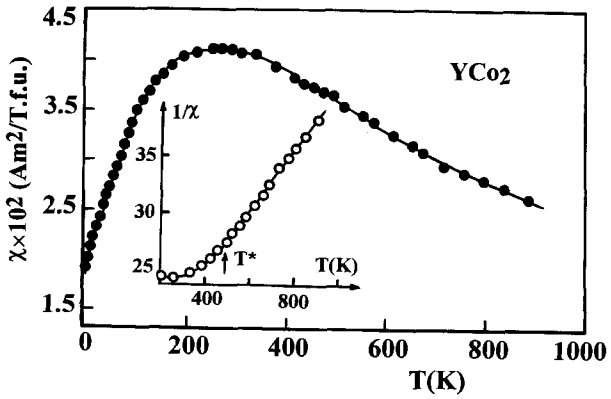

Fig. 10. Temperature dependence of the magnetic susceptibility for YCo_2. In the inset, the high temperature behaviour of the reciprocal susceptibility is shown. (After Burzo et al. 1994.)

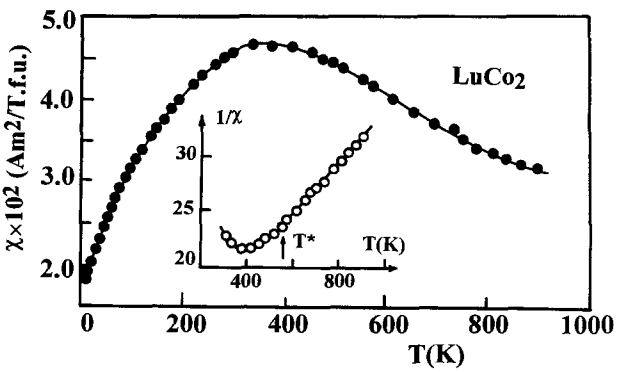

Fig. 11. Temperature dependence of the magnetic susceptibility for $LuCo_2$. The inset shows the high temperature behaviour of the reciprocal susceptibility. (After Burzo et al. 1994.)

A complete magnetic behaviour of RCo_2 (R = Y, Lu and Sc) has recently been described by Burzo et al. (1994) on the basis of the analysis of the susceptibility data measured up to 1100 K. In addition to the above mentioned maximum at T_{max}, the magnetic susceptibility shows a Curie–Weiss behaviour at $T > T^*$ ($> T_{max}$) (see figs. 10–12). In this high-temperature range, the values of the effective cobalt moments p_{eff}(Co) are 3.7 and 3.86 μ_B/at. for YCo_2 and $LuCo_2$, respectively. Note that a value of the effective Co^{2+} moments up to 4.6 μ_B/at. has experimentally been determined (Vonsovski 1971). Following the theory of spin fluctuations, it is possible that in RCo_2 compounds the local spin fluctuations $\xi(T)^2$ are saturated at $T > T^*$ and the charge neutrality condition gives the effective moments characteristic of the Co^{2+} ion as experimentally observed (Moriya 1979). Data obtained from the magnetic susceptibility measurements on YCo_2 and $LuCo_2$ are listed in table 1. Magnetic data for $ScCo_2$ and $HfCo_2$ is also included in this table. The effective Co-moments and the paramagnetic Curie temperature Θ_p seem to show

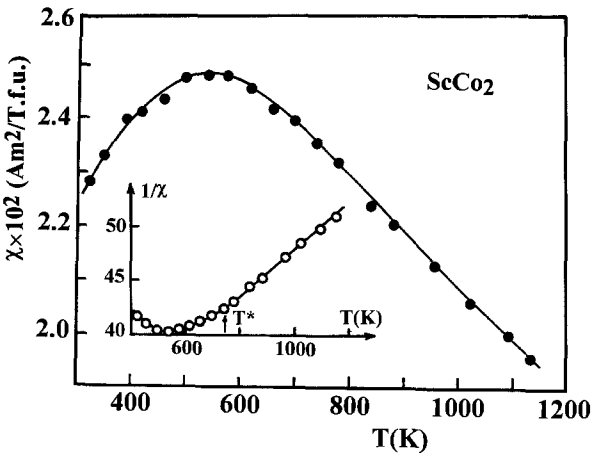

Fig. 12. Temperature dependence of the magnetic susceptibility for $ScCo_2$. The inset shows the high temperature behaviour of the reciprocal susceptibility. (After Burzo et al. 1994.)

Table 1
Lattice constant a, magnetic and electronic characteristics of the RCo_2 compounds[a]

Compound	a (Å)	T_{max} (K)	p_{eff}(Co) (μ_B/at)	Θ_p (K)	γ (mJ/K^2 mol)
YCo_2	7.215	260	3.7	−535	36.2[b]
					34.2[c]
$LuCo_2$	7.121	370	3.86	−326	26.6[d]
$ZrCo_2$	6.957	90	–	–	23.3[e]
$ScCo_2$	6.927	550	3.92	−1150	18.4[d]
$HfCo_2$	6.919	90	4.1	−2040	

[a] See text for explanation.
[b] Muraoka et al. (1977).
[c] Bloch et al. (1972).
[d] Ikeda et al. (1984).
[e] Muraoka et al. (1979).

a regular trend as a function of lattice constant. Note that the same trend also follows the electronic specific heat for YCo_2, $LuCo_2$ and $ScCo_2$. The temperature T_{max} results from a competition between the susceptibility increases at low temperatures due to spin fluctuations and susceptibility decreases in the local moment regime at high temperatures. However, it does not follow a regular behaviour. High-temperature susceptibility data of the magnetic RCo_2 compounds also allow the derivation of the effective Co moment. Its value steadily decreases from about $4\mu_B$/Co in YCo_2 and $LuCo_2$ to about $2.6\mu_B$/Co in $GdCo_2$ which has the largest T_c. The value of p_{eff}(Co) thus has been used as a measure of the effects of spin fluctuations in this series of compounds (Burzo and Lemaire 1992).

A detailed analysis shows that the magnetic susceptibilities of YCo_2 and $LuCo_2$ are linearly dependent on T^2 for $T < 15$ K (see fig. 13). This is almost the same thermal variation as in eq. (19c), but the coefficient of the T^2 term is proportional to S^3 instead of S^2. It is in agreement with Béal-Monod (1982), who showed that the paramagnon results –

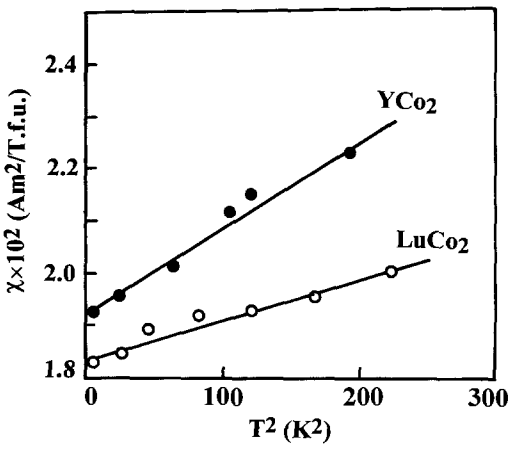

Fig. 13. Thermal variation of the susceptibility for YCo_2 and $LuCo_2$ at $T \leqslant 15$ K as a function of T^2. (After Burzo et al. 1994.)

for a general band structure – lead to a temperature dependence of the susceptibility of the form:

$$\chi(T) \sim S\chi_0[1 - \alpha S^2 T^2]. \tag{75}$$

Theoretical studies have also been devoted to the analysis of the magnetic behaviour of these systems. Yamada et al. (1984) and Yamada and Shimizu (1985) calculated the electronic structure of d-electrons in RCo_2 compounds by using the self-consistent tight binding approximation. Starting from the calculated DOS and taking into account the effects of spin fluctuations, the authors showed that the observed magnetic susceptibility may be explained by the shape of the DOS around the Fermi level. The different magnetic behaviour of RCo_2 (R = Y, Lu and Sc) is mainly attributed to the difference between atomic potentials of R and Co and thus to the different degree of the mixing of the d bands. This result is consistent with the above argument and suggests the importance of the effect of the volume on the 3d–5d(4d) hybridization.

As regards the metamagnetic behaviour of a paramagnet, for which the temperature dependence of the magnetic susceptibility shows a maximum, Bloch et al. (1975) have measured the magnetization of a polycrystalline YCo_2 sample. The magnetization data are shown in fig. 14 in a plot of $M(T)/B$ vs. B^2. At 4.2 K and 77 K, the slope of these curves indicates an increase of the susceptibility with increasing magnetic fields and/or a negative value of the coefficient a_3 in eqs. (8), (21) and (22). At 300 K, however, a_3 is positive. By fitting eq. (22) to the 4.2 K curve of fig. 14, they found $a_3(0) \approx a_3(4.2\,\text{K}) \approx -50T(\text{mol/Am}^2)^3$. The increase of the susceptibility at 4.2 K by about 20% between 0 and 35 T has also been observed by Schinkel (1978). Bloch et al. (1975) have also analyzed the temperature dependence of the susceptibility of YCo_2 in terms of

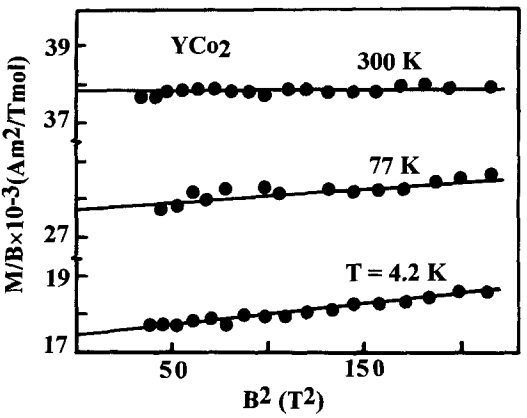

Fig. 14. Plots of M/B versus B^2 at 4.2 K, 77 K and 300 K for YCo_2. (After Bloch et al. 1975.)

eqs. (12), (13) and (18). They found that ν_2 is positive and obtained the thermal variation of $a_3(T)$ as

$$a_3(T) = a_3(0)\left[1 - \left(\frac{T}{T_3}\right)^2\right], \tag{76}$$

where $a_3(0) = -6.92\,\mathrm{T(mol/Am^2)^3}$ and $T_3 = 250\,\mathrm{K}$.

This result for $a_3(T)$ is smaller than that deduced from the field dependence of the susceptibility by a factor of 7. However, it is consistent with the change in sign of a_3 in the neighbourhood of 200 K and the possibility of a MT which may occur at a magnetic field higher than what was available in laboratories. Realistic band structure calculations show a value of around 80 T for the critical magnetic field of the MT in the compound YCo_2 (Cyrot and Lavagna 1979, Yamada and Shimizu 1985). A large effort to study metamagnetism in the RCo_2 Laves phase compounds, for more than two decades, has been carried out by utilizing the molecular field due to the magnetic rare earths (see sect. 3.1.2). In order to directly observe the MT in this system, an attempt was made to depress the critical field by substitution effects and in 1985 this was obtained by substituting for Co by a small amount of Al in YCo_2 (Aleksandryan et al. 1985) where the transition occurs below 40 T. Finally, the most dramatic event in this fascinating story occurred quite recently thanks to the availability of magnetic measurements in fields up to megagauss (Goto et al. 1989, 1990). As shown in fig. 15 the MT was directly observed in YCo_2 and $LuCo_2$ at 69 T and 74 T, respectively. In $ScCo_2$, however, no MT can be observed in fields up to 120 T.

The MT of YCo_2 is very sharp at low temperatures, but it broadens rapidly with increasing temperature. The MT is smeared and is not observed above $T \approx 100\,\mathrm{K}$ (see fig. 16). This temperature corresponds to the tricritical point above which the MT becomes a second-order phase transition. In addition, the critical field B_c increases quadratically with temperature (see fig. 17). This positive shift of $B_c(T)$ has been derived from the theory of spin fluctuations (Yamada 1993). It suggests a reduction of the

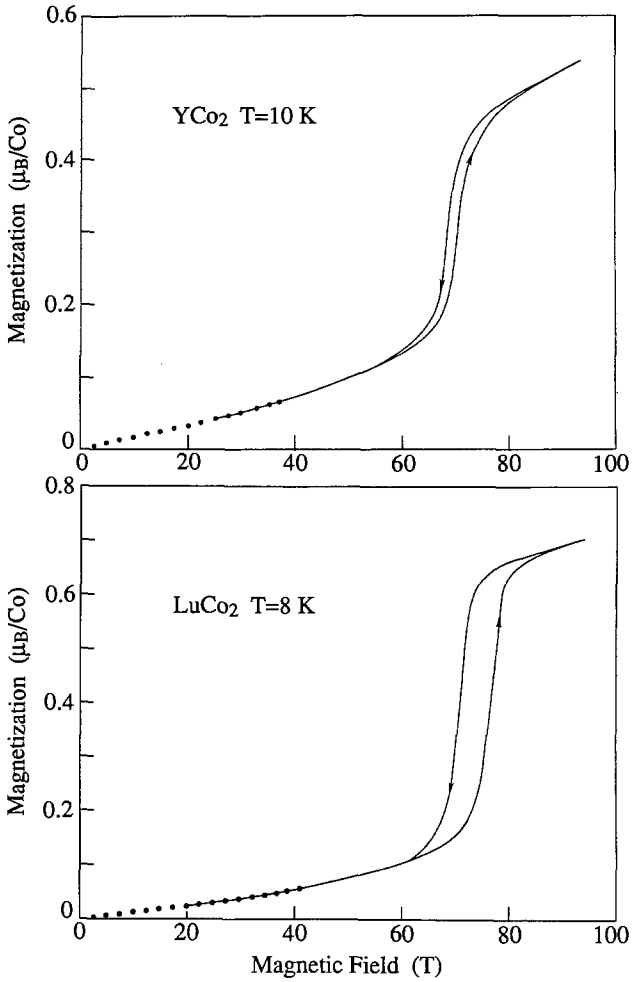

Fig. 15. High-field magnetization data for YCo_2 and $LuCo_2$. (After Goto et al. 1991.)

entropy of the d-electrons at the MT. The entropy reduction results from the quenching of spin fluctuations leading to a decrease of the electronic specific heat constant, γ. A thermodynamical consideration based on the Clausius–Clapeyron relation has estimated a decrease of γ for YCo_2, $\Delta\gamma = -11\,\mathrm{mJ/K^2\,mol}$ (Goto et al. 1994).

3.1.1.2. *The R(Co,M)$_2$ (M = Al, Ga, Sn) compounds.* In attempts to depress the critical magnetic field of the MT in RCo_2 Yoshimura and Nakamura (1985) discovered the onset of ferromagnetism in the dilute system $Y(Co_{1-x}Al_x)_2$. Al substitution in this system expands the lattice at the rate $da/dx = 5.44 \times 10^{-3}$ Å/at% and enhances the magnetic susceptibility (Yoshimura and Nakamura 1985, Aleksandryan et al. 1985). The appearance

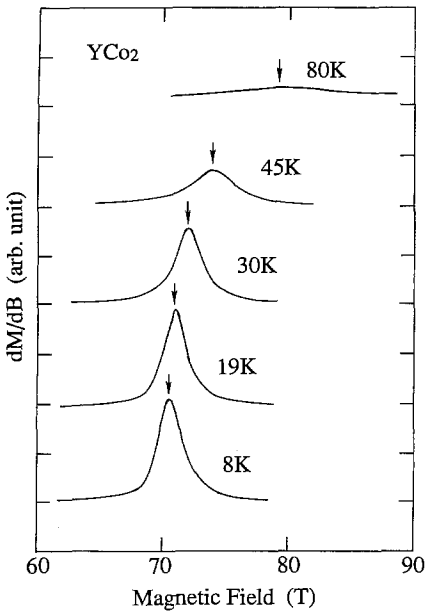

Fig. 16. Plots of dM/dB versus B at different temperatures for YCo_2. The arrows indicate the magnetic field at which dM/dB shows maximum. (After Goto et al. 1994.)

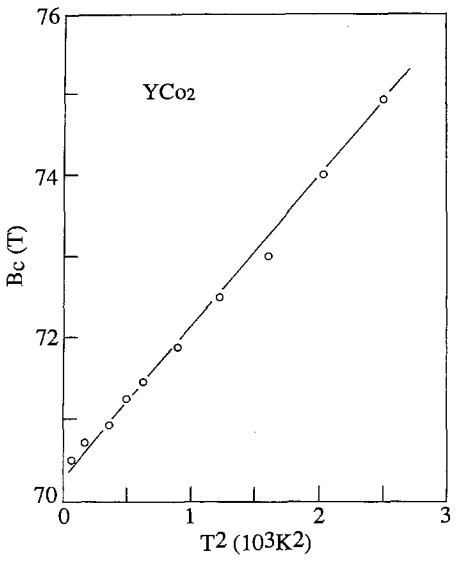

Fig. 17. Plot of the critical field B_c as a function of T^2 for YCo_2. (After Goto et al. 1994.)

of spontaneous magnetic order in $Y(Co_{1-x}Al_x)_2$ takes place at $x \sim 0.12$. The maximum values of the spontaneous magnetization and the Curie temperature are $0.14\mu_B$/Co at. and 26 K, respectively, at $x \approx 0.16$ (Armitage et al. 1990, Duc et al. 1993a). The appearance of weak ferromagnetism in these compounds was associated with the volume effect. However, it was suggested that partial substitution of Al, with an unfilled 3d band (the electronic configuration of $3d^0$), for Co will decrease the concentration of d-electrons and shift the Fermi level towards low energies with higher density of states. This leads to satisfaction of the Stoner criterion. Metamagnetism in these compounds was first studied in magnetic field of 42 T by Aleksandryan et al. (1985) and Sakakibara et al. (1986, 1987). These studies showed the similar results that the critical field B_c decreases with increasing Al content, and they roughly estimated B_c of YCo_2 to be about 66 T. A similar but less sharp MT was found in $Lu(Co_{1-x}Al_x)_2$ (Sakakibara et al. 1987, Gabelko et al. 1987, Endo et al. 1988) and $Sc(Co_{1-x}Al_x)_2$ (Ishiyama et al. 1987).

A complete study of IEM in the nearly ferromagnetic $Y(Co_{1-x}Al_x)_2$ compounds was performed by Sakakibara et al. (1989) in magnetic fields up to 100 T. The temperature dependence of the magnetic susceptibility and the field dependence of the magnetic moment are presented in figs. 18 and 19, respectively. For all compounds under consideration, both the temperature T_{max} where the susceptibility shows the maximum and the critical field B_c decrease with increasing Al concentration, see fig. 20. These results

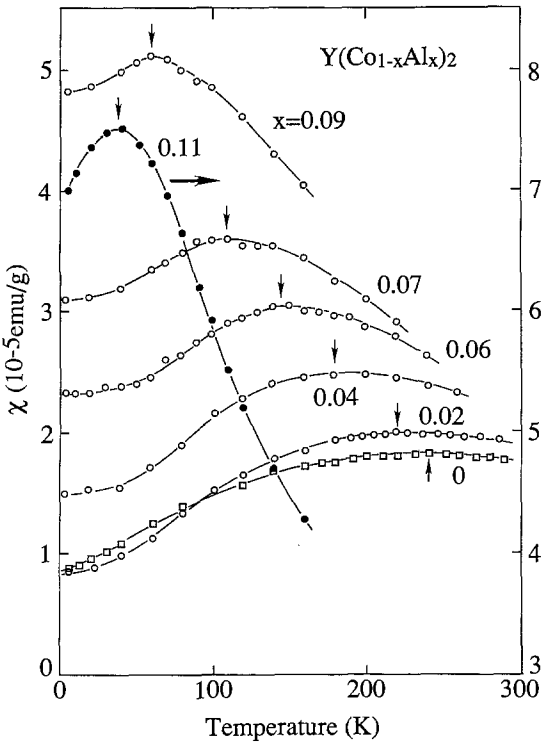

Fig. 18. Temperature dependence of the magnetic susceptibility for $Y(Co_{1-x}Al_x)_2$. The down and up arrows indicate the temperature at which the susceptibility shows a maximum. (After Sakakibara et al. 1989.)

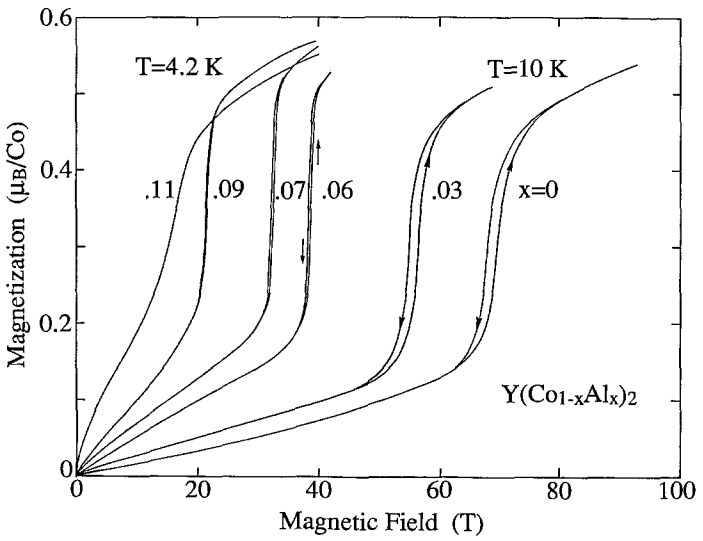

Fig. 19. 3d-magnetic moment as a function of B for $Y(Co_{1-x}Al_x)_2$. (After Sakakibara et al. 1989.)

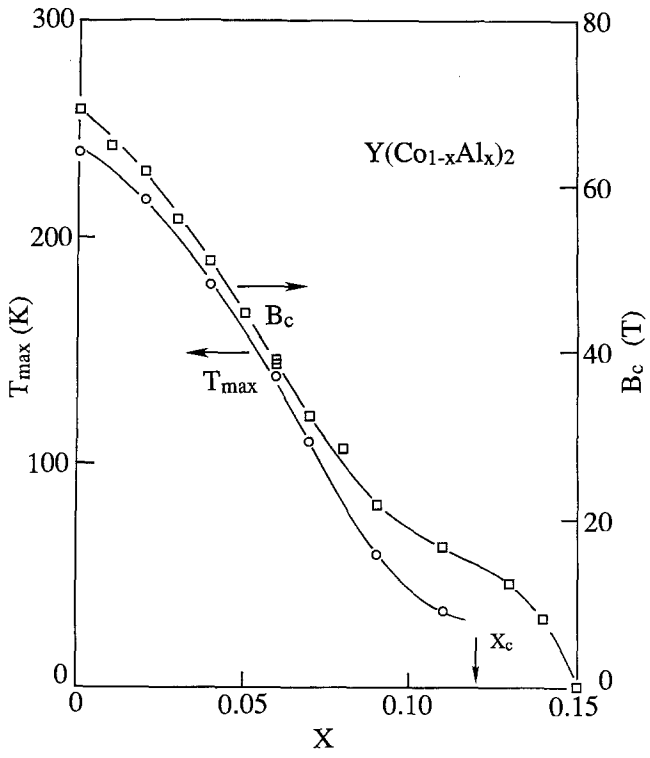

Fig. 20. Al-concentration dependence of B_c and T_{max} for $Y(Co_{1-x}Al_x)_2$. (After Goto et al. 1994.)

reveal a simple correlation between B_c and T_{max} (see fig. 21) that is, B_c/T_{max} = constant. This may suggest that T_{max} and B_c have the same band-structure origin. Indeed, this relation was derived from the theory of spin fluctuations (Yamada 1991, 1993) (see sect. 2.1.2). The above correlation between susceptibility maximum and metamagnetism is also evident in $Lu(Co_{1-x}Al_x)_2$ (Endo et al. 1988, Sakakibara et al. 1988) and other nearly ferromagnetic alloys such as $TiBe_2$ and Ni_3Ga (Acker et al. 1981, Schinkel et al. 1973), however with different values of B_c/T_{max}. The quadratic temperature increase of B_c also holds for these compounds.

A non-linear Arrott plot is a characteristic of all nearly ferromagnetic and weak ferromagnetic $Y(Co_{1-x}Al_x)_2$ compounds (Sakakibara et al. 1986 and Duc et al. 1993a; see fig. 22). This behaviour exists up to $T \approx 80$ K. At higher temperatures, the Arrott plots become almost linear. As already mentioned in sect. 2.1.1, in the case of the unusual Arrott plot, the description of the magnetization curves needs the higher power terms in the equation of state:

$$\frac{B}{M} = a_1 + a_3 M^2 + a_5 M^4 + a_7 M^6 + \cdots . \tag{77}$$

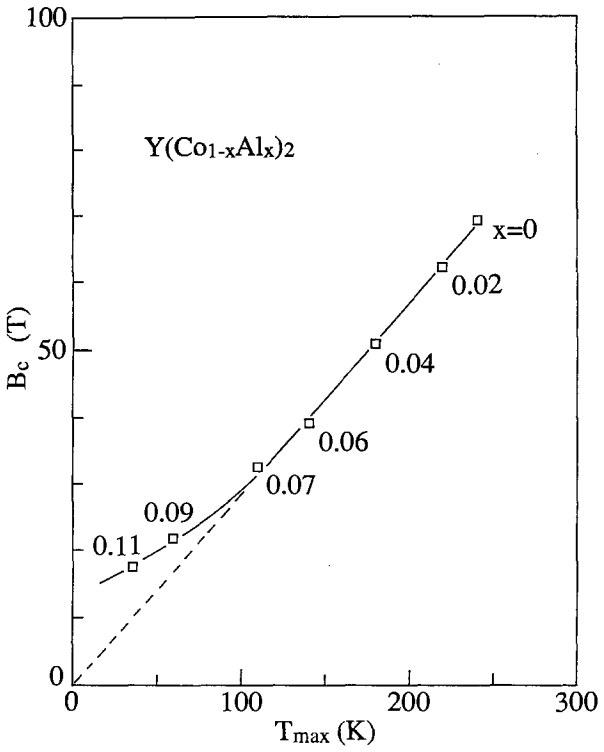

Fig. 21. Plot of B_c versus T_{max} for $Y(Co_{1-x}Al_x)_2$. (After Sakakibara et al. 1989.)

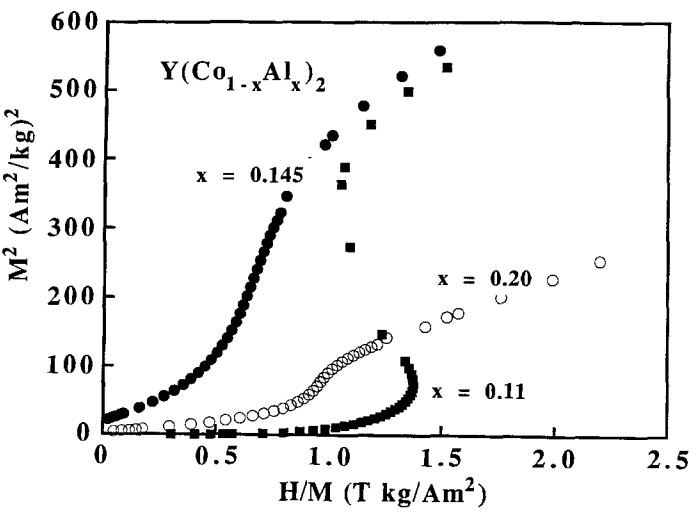

Fig. 22. Arrott plots at 4.2 K for $Y(Co_{1-x}Al_x)_2$. (After Duc et al. 1993a.)

Table 2
The value of the Landau coefficients a_1, a_3, a_5 and a_7 for $Y(Co_{1-x}Al_x)_2$ [a]. The values of the ratio a_1a_5/a_3^2 are also included

x	a_1 (Tmol/Am^2)	a_3 (T(mol/Am^2)^3)	a_5 (T(mol/Am^2)^5)	a_7 (T(mol/Am^2)^7)	a_1a_5/a_3^2
0.0	48.3	−2.84	0.055	–	0.33
0.03	39.4	−2.46	0.051	–	0.33
0.06	22.8	−1.22	0.02	–	0.31
0.07	15.6	−0.66	0.01	–	0.4
0.09	10.3	−0.47	0.009	–	0.43
0.11	3.76	−0.21	−0.016	0.038	–
0.145	−1.76	3.25	−0.625	0.066	–
0.20	−0.05	6.5	−2.820	0.042	–

[a] Data derived from the analysis of the magnetization data of Sakakibara et al. (1989).

The MT from the paramagnetic to ferromagnetic state is described with $a_1 > 0$, $a_3 < 0$ and $a_5 > 0$ ($a_7 = 0$). For the magnetic phase transitions from the weakly ferromagnetic to strongly ferromagnetic state, one has $a_1 < 0$, $a_3 > 0$, $a_5 > 0$ and $a_7 > 0$. We list the values of the Landau coefficients obtained from the fit of the high-field magnetization of $Y(Co_{1-x}Al_x)_2$ in table 2 (Duc, unpublished). Note that the ratio a_1a_5/a_3^2 ranges from 0.33 to 0.43, i.e., consistent with the condition of the MT predicted from WRS theory, $\frac{3}{16} < a_1a_5/a_3^2 < \frac{9}{20}$.

The volume change in the paramagnetic $Y(Co_{1-x}Al_x)_2$ compounds under metamagnetic transition was reported by Wada et al. (1988). The longitudinal magnetostriction curves are presented in fig. 23. A large magnetostriction jump has been found around the MT for $x = 0.095$. With increasing x, the magnetostriction rapidly decreases. The transverse magnetostriction shows a quantitative agreement with the longitudinal one indicating an isotropic expansion. This behaviour of the volume magnetostriction is attributed to the induced Co moments. For this purpose, the relation $\omega_s = (3\Delta l/l) = \kappa C M_{Co}^2$ has been considered. However, a large scattering in the value of κC was found. A similar behaviour was also observed for $Lu(Co,Al)_2$ compounds (Iijma et al. 1989). For the weakly ferromagnetic $Y(Co_{1-x}Al_x)_2$ compounds, the forced magnetostriction at 4.2 K also shows characteristics of the volume magnetostriction (Armitage et al. 1990, Duc et al. 1993a). Additionally, a spontaneous volume magnetostriction, ω_s, was observed below T_c for these compounds. The decrease of B_c with increasing Al content and the volume anomaly due to the formation of 3d magnetism in $Y(Co_{1-x}Al_x)_2$ can be described in terms of the model proposed by Duc et al. (1992b). It has already been summarized in fig. 8 (see sect. 2.1.1.3). This effect of volume on the IEM is strongly supported by the study on the $Lu(Co_{1-x}Sn_x)_2$ compounds (Murata et al. 1990, 1994a): at partial substitution of Co by Sn, initially the lattice parameter increases and critical field B_c decreases at $x < 0.04$. For $x > 0.06$, the lattice parameter almost saturates, then B_c remains

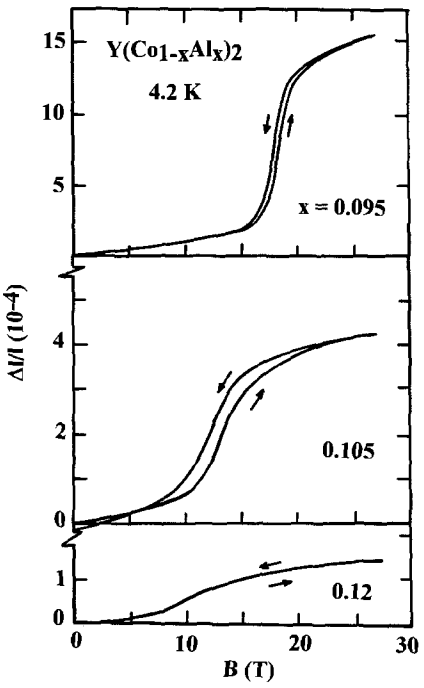

Fig. 23. $\Delta l/l$ vs. B for $Y(Co_{1-x}Al_x)_2$. (After Wada et al. 1988.)

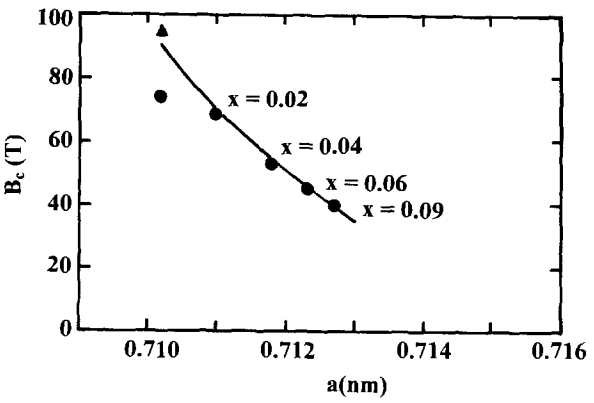

Fig. 24. Plot of B_c as a function of lattice parameter for $Lu(Co_{1-x}Sn_x)_2$: (•) experimental data; (▲) theory. (After Murata et al. 1990.)

constant at about 40 T. As can be seen in fig. 24, a linear relationship between B_c and a exists in this system.

Pressure effects on the metamagnetic behaviour were reported for $Lu(Co_{0.088}Ga_{0.12})_2$ by Goto et al. (1994). The pressure dependence of the magnetization process for this compound at 4.2 K is presented in fig. 25. This compound is a ferromagnet at 0 kbar. With increasing pressure the MT appears and the critical field increases linearly. Figure 26 shows the temperature dependence of susceptibility at different pressures. The application

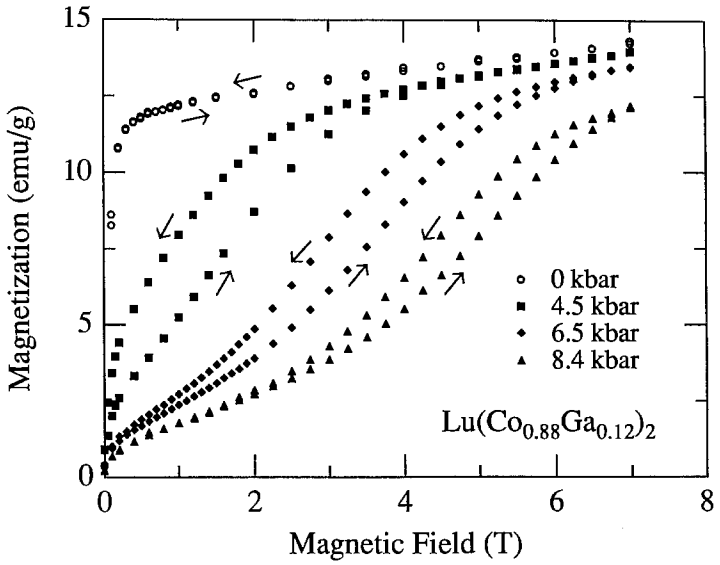

Fig. 25. Pressure effect on the magnetization process of $Lu(Co_{0.88}Ga_{0.12})_2$. (After Goto et al. 1994.)

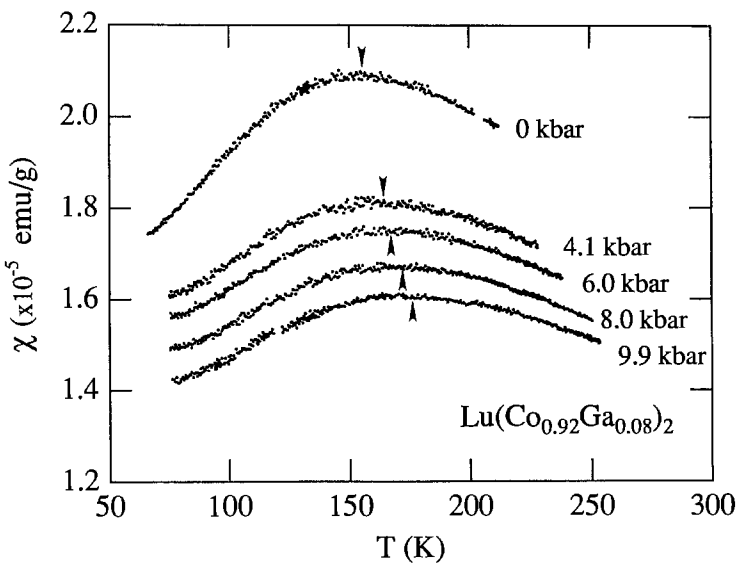

Fig. 26. Pressure effect on the susceptibility of $Lu(Co_{0.88}Ga_{0.12})_2$. The down and up arrows indicate the temperature at which the susceptibility has a maximum. (After Goto et al. 1994.)

of pressure decreases the magnetic susceptibility and increases T_{max}. The increase of B_c and decrease of $\chi(0)$ under pressure can be understood in terms of the volume dependence of the bandwidth. However, the shift of T_{max} towards higher temperature reflects the

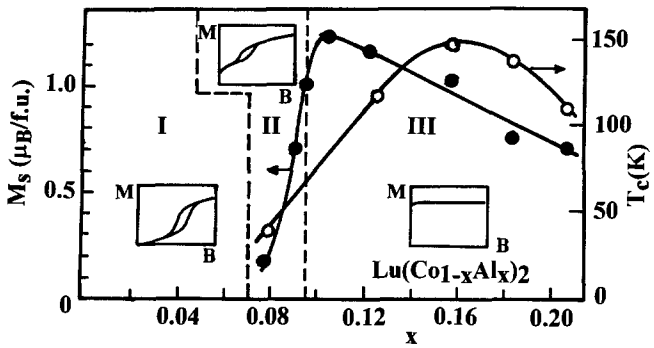

Fig. 27. Magnetic phase diagram of $Lu(Co_{1-x}Al_x)_2$. The insets show the schematic form of $M(B)$ in the (I) paramagnetic, (II) weakly ferromagnetic, and (III) strongly ferromagnetic phases. (After Levitin and Markosyan 1988.)

contribution of the effect of spin fluctuations. According to Yamada's theory (Yamada 1993) T_{max}^2 is proportional to the inverse of $\chi(0)$.

The appearance of itinerant metamagnetism in the system $Lu(Co_{1-x}Al_x)_2$ is in many ways reminiscent of the features observed in $Y(Co_{1-x}Al_x)_2$ compounds. One can see from fig. 27, which shows the magnetic phase diagram for the $Lu(Co_{1-x}Al_x)_2$ compounds, that the compounds are paramagnetic with the MT existing in the concentration range $0 \leqslant x \leqslant 0.07$. For compositions with $0.078 \leqslant x \leqslant 0.09$, a weak ferromagnetic order arises. A transition from weakly ferromagnetic to strongly ferromagnetic state occurs in applied magnetic fields at low temperature. The phase transition from the ferromagnetic state to the paramagnetic state, however, is diffused and it is difficult to accurately determine the ordering temperature. For compositions with $0.095 \leqslant x \leqslant 0.208$ the compounds are strongly ferromagnetic. The FOT from the paramagnetic state to the ferromagnetic state was evidenced by a jump in lattice parameter at around 150 K (Gabelko et al. 1987), however, the variation in magnetization and resistivity is gradual (Duc, unpublished).

The large differences in the magnetic behaviour between the $Y(Co_{1-x}Al_x)_2$ and $Lu(Co_{1-x}Al_x)_2$ systems are well explained in the recent study of Dubenko et al. (1994) on the $(Y_{1-t}Lu_t)(Co_{0.88}Al_{0.12})_2$ compounds. The concentration dependences of the spontaneous moment in this system at 4.2 K are shown in fig. 28. For $t > t_c$ (= 0.38) a strongly ferromagnetic state appears; the spontaneous moment is rather large and increases with increasing t. In contrast, for $t < t_c$ a weakly ferromagnetic state with magnetic moment of about $0.1\mu_B$ per formula unit appears and is independent of t. In this concentration range, there exists an MT from weakly ferromagnetic to strongly ferromagnetic state. By making use of the phenomenological Landau energy expanded up to the eighth power of magnetization (see eq. 77), it is explicitly shown that small changes in the Landau coefficients lead to the transition from a weakly to a strongly ferromagnetic state. The concentration dependences of the coefficients a_1/a_7, a_3/a_7 and a_5/a_7, and the calculated energy, are illustrated in figs. 29 and 30, respectively. The different origin of the

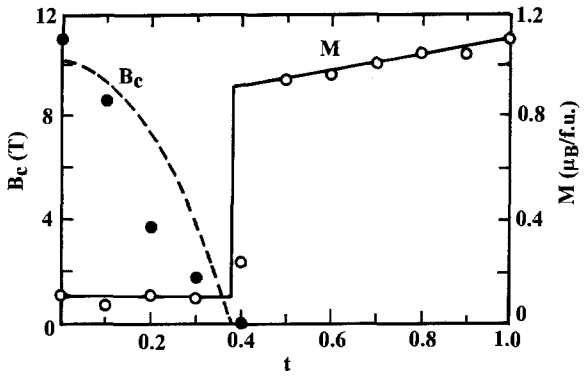

Fig. 28. Concentration dependences of the observed magnetization (open circles) and B_c of the MT (solid circles) for $(Y_{1-t}Lu_t)(Co_{0.88}Al_{0.12})_2$. (After Dubenko et al. 1994.)

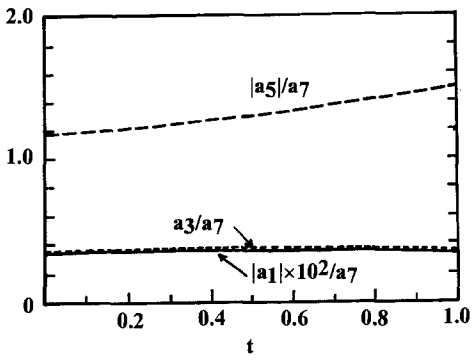

Fig. 29. Concentration dependences of the Landau coefficients a_1/a_7, a_3/a_7 and a_5/a_7 for $(Y_{1-t}Lu_t)$-$(Co_{0.88}Al_{0.12})_2$. (After Dubenko et al. 1994.)

magnetic behaviours in the $Y(Co_{1-x}Al_x)_2$ and $Lu(Co_{1-x}Al_x)_2$ systems has been confirmed by the temperature specific heat measurements (Wada et al. 1990, Pillmayr et al. 1990).

Magnetoresistance data for the $Y(Co_{1-x}Al_x)_2$ reported by Duc (1994) and Duc et al. (1995b) are presented in fig. 31. For the nearly ferromagnetic $Y(Co_{1-x}Al_x)_2$ compounds, a discontinuous reduction of $\Delta R/R(0)$ is observed at the MT. This discontinuity becomes less pronounced with increasing Al-content. The effect may be described by stating that the resistivity in the "low-spin state" (or "spin fluctuation state") is larger than that in the "high-spin state" (or "strongly ferromagnetic state"). In so far as this difference is ascribed to a suppression of spin fluctuations, the magnitude of the drop in resistivity at the MT can be regarded as a measure for the amplitude of the spin fluctuations.

As already discussed for YCo_2, the quenching of spin fluctuations at the MT, evidenced by the reduction of the electronic specific heat constant, has also been derived from thermodynamical analysis for several $Y(Co_{1-x}Al_x)_2$ (Sakakibara et al. 1992) and $Lu(Co_{1-x}Ga_x)_2$ (Murata et al. 1993a,b) compounds. In order to confirm directly the reduction of γ at the MT, the specific heat has been measured for $Lu(Co_{0.91}Ga_{0.09})_2$. The result is presented in fig. 32. This compound shows a low B_c value (about 5 T). The value of γ, which is 35.5 mJ/K^2 mol in zero field, decreases during the MT and

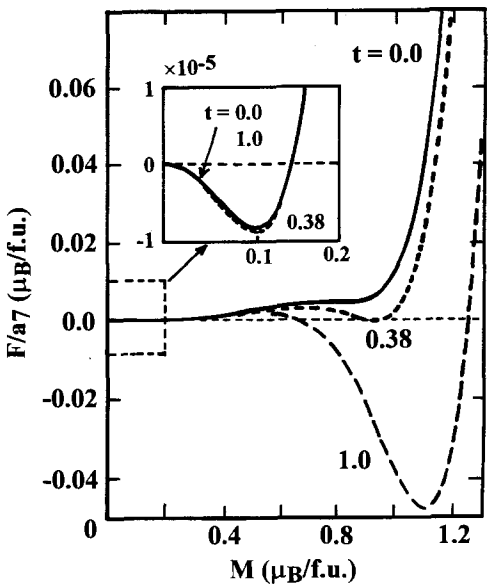

Fig. 30. The calculated $F(M)/a_7$ dependences for $t=0.0$, 0.38 and 1.0 for $(Y_{1-t}Lu_t)(Co_{0.88}Al_{0.12})_2$. The inset shows the enlarged curves of $F(M)/a_7$ at small M. (After Dubenko et al. 1994.)

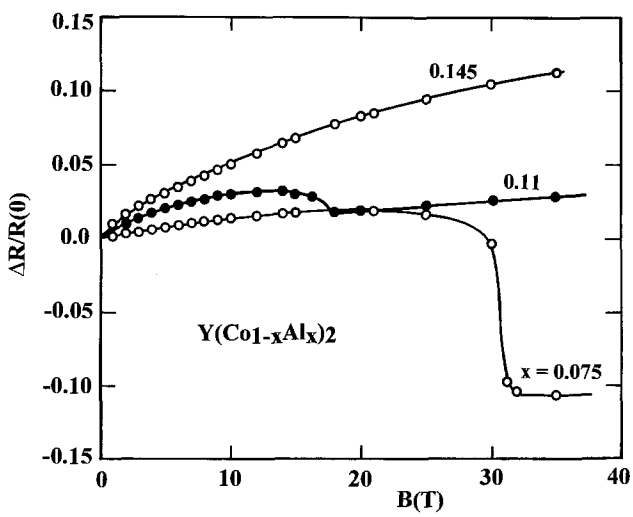

Fig. 31. Magnetoresistance as a function of the magnetic field for $Y(Co_{1-x}Al_x)_2$. (After Duc et al. 1995b.)

becomes 25 mJ/K^2 mol in the ferromagnetic state. The reduction of γ due to the transition is $\Delta\gamma = -10.5$ mJ/K^2 mole. It is consistent with that estimated from $B_c(T)$ of YCo_2.

3.1.1.3. *The Y(Lu)(Co,M)$_2$ compounds with an invariable crystal unit cell parameter.* The evolution of magnetic properties of RCo_2 is related to the increase of the DOS

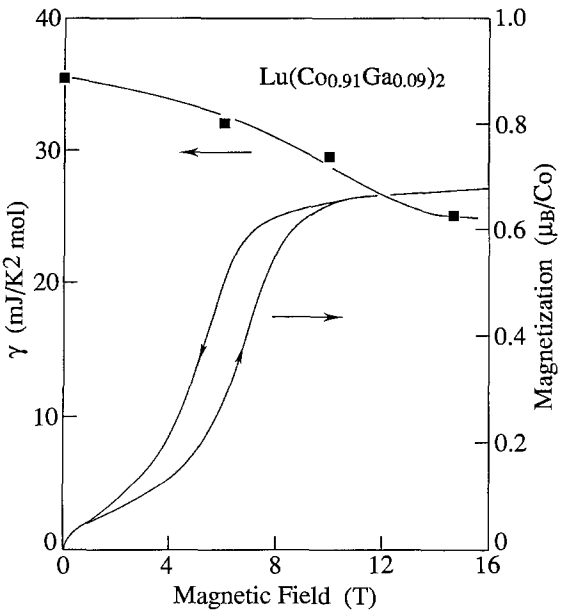

Fig. 32. The field dependence of the magnetization and the electronic specific heat constant for $Lu(Co_{0.91}Ga_{0.09})_2$. (After Murata et al. 1991.)

at the Fermi level $N(\varepsilon_F)$. Nevertheless, the nature of increasing $N(\varepsilon_F)$ in $R(Co_{1-x}Al_x)_2$ systems has various and quite different interpretations. Some authors (Yoshimura and Nakamura 1985, Sakakibara et al. 1986, 1987, Endo et al. 1988) supposed that the increase of $N(\varepsilon_F)$ as aluminum substitutes cobalt is caused by the narrowing of the d-band because of increasing crystal cell parameter (the metallic radius of Al, $r_{Al} = 1.432$ Å, is considerably larger than that of Co, $r_{Co} = 1.252$ Å). Aleksandryan et al. (1985), however, considered that the main reason for the transformation of magnetism in $Y(Co_{1-x}Al_x)_2$ is the decrease of the 3d-electron concentration at Co ($3d^7$ configuration) substitutions by Al ($3d^0$ configuration). To separate these two parameters, high pressure experiments are important. Moreover, special compositions have been invented in order to fix values of some of the variables and to study systematically involvement of the other parameters. Such studies were performed with the $(Y_{1-t}Lu_t)(Co_{1-x}Al_x)_2$ compounds with the invariable lattice-parameter (Gabelko et al. 1991). In this case, since the lattice parameter of YCo_2 ($a(YCo_2) = 7.221$ Å) is substantially greater than that of $LuCo_2$ ($a(LuCo_2) = 7.121$ Å) the condition $a((Y,Lu)(Co_{1-x}Al_x)_2) = \text{constant} = a(YCo_2)$ was fulfilled in a rather wide concentration range up to $x = 0.22$ in the $(Y_{1-t}Lu_t)(Co_{1-x}Al_x)_2$ systems. The magnetic investigations have shown that the obtained variation of the critical field of the MT with varying x is very close to that of two other systems, $Y(Co_{1-x}Al_x)_2$ and $Lu(Co_{1-x}Al_x)_2$: $dB_c/dx \approx 6$ T/%Al. Ferromagnetic ordering of these three systems arises at approximately the same concentration of Al, $x_c \approx 0.1$. These comparisons of experimental data for compounds with an invariable crystal cell parameter $(Y_{1-t}Lu_t)(Co_{1-x}Al_x)_2$ and compounds with a lattice parameter that increases with increasing x show that the change in the unit cell volume may not be the dominant factor affecting the magnetic properties

of RCo_2 compounds, and that the concentration of 3d electrons plays an important role. In this study, however, the different effects of the hybridization between the 3d and 4d states in $Y(Co_{1-x}Al_x)_2$ and those between the 3d and 5d states in $Lu(Co_{1-x}Al_x)_2$ has not yet been established. As already mentioned above, the distinction between characteristics of 4d electrons of Y and 5d electrons of Lu causes quite different magnetic behaviours in these systems (Dubenko et al. 1994, Duc and Brommer 1999).

There is also another way to obtain systems with a constant lattice parameter. That is the series of $R(Co_{1-x}Si_x)_2$ compounds. Since the atomic radius of Si atoms is smaller than that of Co atoms, the lattice constant is expected to be reduced in these systems. However, it was found that within experimental error the change in lattice parameter cannot be detected in the $R(Co_{1-x}Si_x)_2$ systems with R = Gd, Tb, Dy, Er, Y and Sc (Michels et al. 1990, Duc 1996, Cuong et al. 1998b). For the $Lu(Co_{1-x}Si_x)_2$ compounds, a linear decrease of lattice constant with a rate $da/dx = -0.4\times10^{-3}$ Å/%Si was shown (Murata et al. 1994b). This, however, is negligible compared to the 5.5×10^{-3} Å/%Al found in $Y(Co,Al)_2$. Thus one can consider these systems as having an invariable crystal unit cell. The magnetic investigations show that the substitution of Si for Co in the $R(Co_{1-x}Si_x)_2$ (R = Y and Lu) compounds leads to susceptibility enhancement and to reduction of the critical field of the MT, but does not trigger the itinerant ferromagnetic state as observed in $R(Co,Al)_2$ (Michels et al. 1990, Murata et al. 1994b). In the next section, we will show (Duc 1996, Duc and Oanh 1997) that for the compounds with magnetic rare earths, the variation of the 3d-magnetic moment in $R(Co_{1-x}Si_x)_2$ is still rather similar to that in the $R(Co_{1-x}Al_x)_2$ compounds, but the enhancement of T_c is much smaller. In a more detailed analysis, the magnetic behaviour of the $R(Co_{1-x}Si_x)_2$ compounds was governed by the effects of the 3d–p hybridization, which shows various effects on the magnetic behaviour and 4f–3d exchange interactions in the rare-earth intermetallics (Duc and Givord 1995, Duc 1996). Indeed, an NMR study of the magnetically ordered state of the weak itinerant ferromagnet $Y(Co,Al)_2$ (Yoshimura and Nakamura 1990) has also suggested that the stability of ferromagnetism in this system may relate to the existence of the hybridization between the 3d wave function of Co and the s- or p-like wave function. Band calculations performed for $Y(Co_{1-x}Al_x)_2$ and $Y(Co_{1-x}Si_x)_2$ (Aoki and Yamada 1992) have shown that the DOS for YCo_2 is characterized by double sharp peaks near the Fermi level ε_F. By partially substituting Al for Co the sharp peak at higher energy is reduced. However, when ε_F shifts towards lower energy and goes across this peak, the DOS is relatively increased and ferromagnetic state is formed in the $Y(Co,Al)_2$ system. In the case of Si substitution, the peak of d(Co) DOS at higher energy has already been destroyed at $x = 0.25$, whereas a broad peak at ε_F is established in the local p(Si) DOS. Additionally, it was found that the height of the p(Si) DOS is larger than the p(Al) ones and most of the occupied p(Si) states appear in the lower energy region. This difference in the degree of the 3d–p hybridization is due to the Si atom having an extra p-electron compared to Al and is the reason for the differences in the magnetic ordering phenomena observed in these two systems. At fixed volume, it is the hybridization between the 3d(Co) and p(Al and/or Si) states that plays an important role on 3d magnetism in the $R(Co_{1-x}Al_x)_2$ and $R(Co_{1-x}Si_x)_2$ systems.

Table 3
The concentration of Co (x), Al (y) and Cu (z), the estimated d-electron number (n_d), the lattice parameter (a) and the critical magnetic field (B_c) for the $Y(Co_xAl_yCu_z)_2$ system[a]

No.	x	y	z	n_d	a (Å)	B_c (T)
1	0.925	0.075	0.00	8.35	7.2660	30.3
2	0.890	0.080	0.03	8.31	7.2715	26.0
3	0.825	0.085	0.09	8.32	7.2800	22.5
4	0.800	0.088	0.112	8.35	7.2835	21.5

[a] After Duc and Tai (1993).

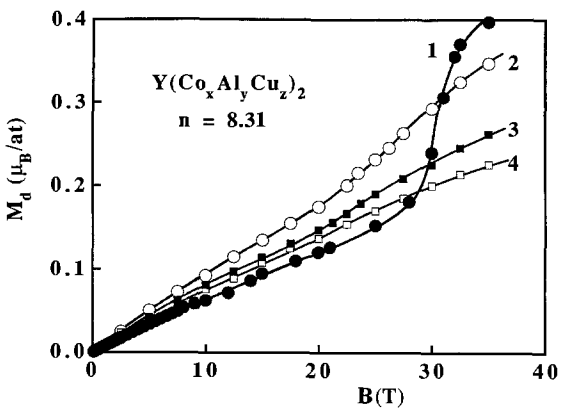

Fig. 33. $Y(Co_xAl_yCu_z)_2$, high-field magnetization. See text and table 3 for the alloy compositions of samples 1–4. (After Duc and Tai 1993.)

3.1.1.4. *The $Y(Co_xAl_yCu_z)_2$ compounds with invariable d-electron concentration.* The MT of the invariable d-electron concentration $Y(Co_xAl_yCu_z)_2$ compounds was studied by Duc and Tai (1993). In YCo_2 the average number of d-electrons [including 3d(Co) and 4d(Y)] is considered to be 9 (Voiron 1973, Bloch et al. 1975). The 3d configurations of Al and Cu are $3d^0$ and $3d^{10}$, respectively. By this way, the Al and Cu concentrations were chosen such as to keep the total number of d-electrons constant in all the considered alloys. The estimated number of d-electrons and lattice parameters of these samples are presented in table 3. The high-field magnetization data is shown in fig. 33. For the $Y(Co_{0.925}Al_{0.075})_2$ compound (sample 1), a clear MT takes place at $B_c = 30.3$ T. By substitution of Al and Cu for Co, the low field susceptibility is initially enhanced in sample 2, then it slightly decreases in samples 3 and 4. Moreover, it can also be seen from this investigation that the alloying has strongly affected the MT in these compounds: with increasing Cu(Al) concentration B_c decreases slightly, whereas the magnetization jump at the transition falls fast and the MT almost disappears in sample 4. As already introduced, the effect of the d-electron concentration can be isolated in this study. Thus, this decrease of B_c can be attributed to the volume effects caused by the lattice expansion. However, the smearing and disappearance of the MT in this system can also be related to the effect of Cu alloying. According to the new approach to IEM proposed by Duc et al. (1992b), see

also sect. 2.1.1.3, the elastic properties also play an important role. Since Cu is very stiff, the Cu-alloying effect can be attributed to the resulting increase in the elastic constant K and thus the system will stay in the paramagnetic state and MT disappears in the invariable d-electron concentration $Y(Co_xAl_yCu_z)_2$ compounds.

3.1.1.5. *The R(Co,M)$_2$ (M = Fe, Ni, Cu) compounds.* Studies to confirm the existence of the MT in other magnetically enhanced systems have been made by Yoshimura et al. (1987). In magnetic fields of 43 T, the metamagnetism inherent in YCo_2 has been observed in the $Y(Co_{1-x}Fe_x)_2$ compounds in the concentration range $0.04 \leqslant x \leqslant 0.09$ near the onset of ferromagnetism. Other exchange-enhanced paramagnets $Y(Co_{1-x}Cu_x)_2$ and $(Y_{1-x}La_x)Co_2$ do not exhibit the MT.

In order to get further information about the change of B_c by the shift of the Fermi level, the effects of Ni and Fe substitutions on the metamagnetic behaviour of the YCo_2 Laves-phase intermetallic compound were studied in pulsed magnetic fields up to 110 T by Goto et al. (1994). The concentration dependence of the metamagnetic critical field B_c for the substituted $Y(Co_{1-x}M_x)_2$ compounds is presented in fig. 34. A linear increase of B_c is observed for Ni substitution (with rate of $dB_c/dx \approx 7$ T/%Ni), whereas the Fe doping is found to lower B_c (with about 4.5 T/%Fe). The volume effect may not be responsible for the discrepancy since the lattice constant of YFe_2 is even larger than that of YCo_2. Moreover, the experimental results shown in fig. 34 seem to contradict the simple rigid band picture, in which symmetrical changes are expected at least for small doping of Ni and Fe. Indeed, an appreciable increase of 2 T is observed for $x = 2\%$ in a compound with simultaneous doping by equal amounts of Ni and Fe (see also fig. 34). This fact, however, can be entirely accounted for by the d-electron number: Fe substitution shifts ε_F to the lower-energy side, while Ni substitution shifts it to the higher-energy side. Consequently,

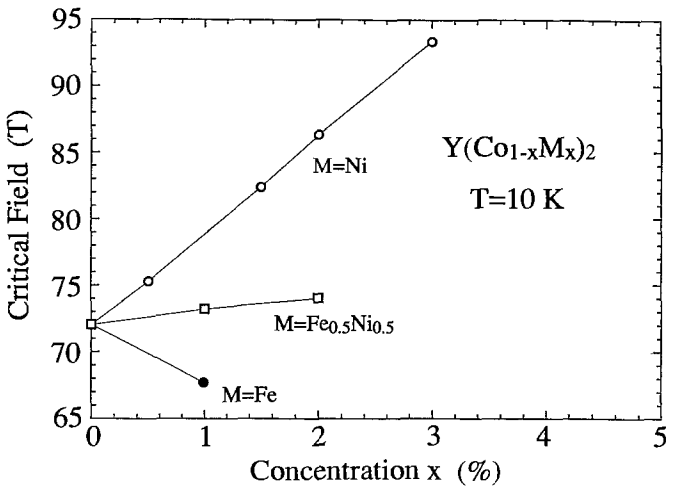

Fig. 34. Concentration dependence of B_c for the substituted compounds of $Y(Co_{1-x}M_x)_2$, M = Fe, Ni and $Fe_{0.5}Ni_{0.5}$. (After Goto et al. 1994.)

the condition for the IEM is satisfied at low and high magnetic fields for the $Y(Co,Fe)_2$ and $Y(Co,Ni)_2$ compounds, respectively.

Sakakibara et al. (1994) also suggest the existence of a critical concentration of Ni near $x = 0.03$ above which the FOT disappears in the $Y(Co_{1-x}Ni_x)_2$ system. This is not simply explained by the randomness or disorder of the Co sublattice introduced by the substitution, because a rather sharp MT (with $\Delta B \approx 2$ T) is still observed in the $Y(Co_{1-x}Al_x)_2$ system at an Al concentration of 10%. Further experimental and theoretical studies are needed to clarify this point.

3.1.2. *Magnetic rare-earth–Co_2 compounds*

3.1.2.1. *Ferrimagnetic spin ordering in RCo_2.* In the intermetallic compounds based on magnetic rare earths and transition metals, it is found in general (Campbell 1972, Buschow 1980, Franse and Radwanski 1993) that 4f–3d spin–spin coupling is antiparallel, which consequently leads to the parallel alignment of 3d (Fe, Co, Ni) and 4f moments in the light rare-earth compounds and to the antiparallel alignment in the heavy rare-earth compounds. This universal picture can be understood by a simple approach to the hybridization between 5d and 3d states (Brooks and Johansson 1993, Duc 1997). In this mechanism, the effective exchange interactions between the 4f and 3d spins are involved by the positive 4f–5d exchange (I_{4f-5d}) in the R atoms, the 3d exchange energy (proportional to I_{3d-3d}) and the 3d–5d hybridization. In the case where I_{3d-3d} is large enough to develop a magnetic moment at the T-sites, the hybridization, firstly, produces a negative 5d moment (in comparison to the direction of the 3d moment) and secondly, is responsible for the positive 4f–5d coupling which leads in turn to the antiparallel 4f–3d coupling. This is the case for almost all of the R–Fe and R–Co compounds. When I_{3d-3d} is small, i.e. in the case of the RCo_2 compounds under consideration, 3d–3d exchange by itself is not sufficient to stabilize a 3d-band splitting as observed in $Y(Lu)Co_2$ (see sect. 3.1.1). In this case, the 5d moment is induced by the exchange field from the localized 4f moments and then the 3d–5d hybridization produces an enhanced 3d moment aligned antiparallel to the 5d moment. The details of this mechanism for the appearance of 3d-magnetism in RCo_2 is presented as follows.

For most rare-earth compounds, the direct coupling can take place essentially within the rare-earth atom and mainly with 5d electrons because the 4f-wave function is limited and the density and overlap between 4f and 5d states are larger than those between 4f and 6p, 6s states. The 5d electrons on R atoms are polarized by the exchange field from localized 4f moments. This polarization of 5d electrons is in the same direction as that of the localized 4f moment. This is in accordance with the experimental observation that the 5d electrons do contribute a moment of $0.6\mu_B$ to the total value of $7.6\mu_B$/at. measured for Gd metal (Roeland et al. 1975) or of $0.1\mu_B$ in $GdNi_2$ (Farrell and Wallace 1966) and $GdAl_2$ (Swift and Wallace 1968). When the exchange field created by the (local) 4f moments is applied to the 5d electrons, the up-spin 5d-band shifts towards the lower energy side and the down-spin 5d-band to the higher energy side. Then, because of the difference in the relative position of the subbands, the mixing between 5d and 3d states

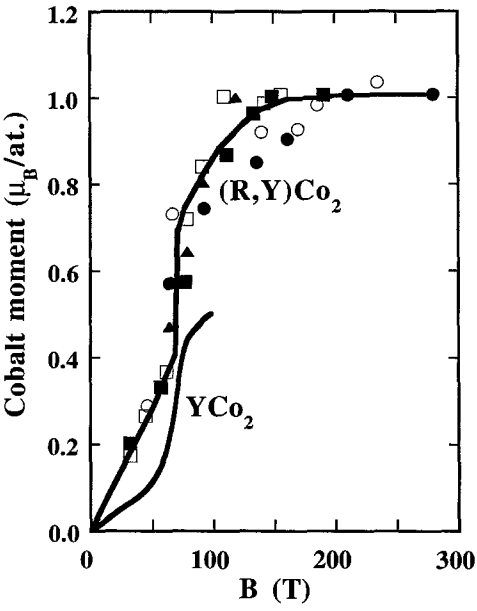

Fig. 35. Magnetic moment of Co in $R_xY_{1-x}Co_2$, with R = Gd (•), Tb (○), Dy (■), Ho (□) and Er (▲). (After Duc et al. 1992a.)

with up-spin becomes stronger than that between the states with down-spin. In the case where the Fermi level lies near the top of the 3d band, the number of 3d electrons with up-spin will be smaller than that with down-spin. In that case, a negative Co moment is induced. Furthermore, due to the molecular field of the developed Co-moment itself, the 3d subbands with spin-up and down-spin shift in the opposite direction to those of the 5d electrons. The negative 3d moment is thus stabilized and ferrimagnetic spin ordering is formed in RCo_2 compounds.

3.1.2.2. *Effect of molecular field on the induced Co metamagnetic behaviour.* Although there may not be a consensus on the exact mechanism of the 4f–3d exchange interaction, it is common usage to express this interaction as an effective exchange of the Heisenberg type. There, within a mean-field approach, the cobalt moment is described as being induced by the molecular field exerted by the localized 4f moments. Gignoux et al. (1975, 1977a,b), Steiner et al. (1978), Duc et al. (1988a, 1992a) have estimated the induced moments of Co in RCo_2 and $(R,Y)Co_2$ compounds. By changing concentration x, they can change the molecular field acting on the Co subsystem $B^{Co}_{mol,RCo}(=xn_{RCo}g_JJ)$. A complete collection of data for the spontaneous Co magnetic moment was reported by Goto et al. (1989) and Duc et al. (1992a), see fig. 35. They found that a metamagnetic behaviour of the Co-subsystem in $R_xY_{1-x}Co_2$ appears at a molecular field which is lower than that in $ErCo_2$. The critical R concentration x_c for the onset of 3d magnetism is equal to 0.75, 0.65, 0.55, 0.4 and 0.33 for RCo_2 with R = Er, Ho, Dy, Tb and Gd, respectively. Under the assumption that in the RCo_2 (R = heavy rare earth) compounds, the MT occurs at the same (molecular) field, i.e., B_c is equal to 70 T as observed for $Y(Lu)Co_2$, it turns out

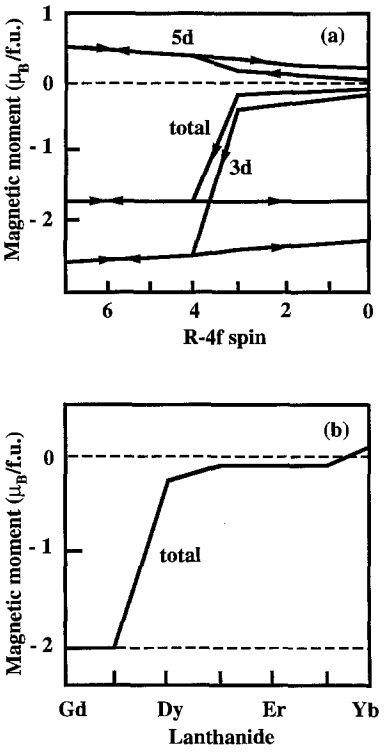

Fig. 36. (a) The calculated partial Co 3d, Gd 5d and total conduction electron moments of $GdCo_2$ as a function of 4f-spin moment. The arrows denote the direction in which the 4f spin is changed. (b) The calculated total conduction electron moments of RCo_2, where R = Gd–Yb. (After Nordström et al. 1992.)

that the value of the exchange coupling parameter A_{RCo} is about 11.5×10^{-23} J. This is in support of Bloch and Lemaire's values (Bloch and Lemaire 1970), however, is rather small compared with that deduced from other methods (Ballou et al. 1993, Duc et al. 1993c). Indeed, the smaller values of x_c have been determined from the specific heat and resistivity measurements (see: Hilscher et al. (1988), Pillmayr et al. 1988, Duc 1994). Using these values, one can reach the value of 20×10^{-23} J for A_{RCo} (Duc and Brommer 1999).

It is worthwhile to note that, in comparison, both the low field susceptibility (i.e., below critical field) and the magnitude of the Co-magnetic moment (of about $0.55\mu_B$/Co at. at $B = 100$ T) in YCo_2 is smaller than those in RCo_2 ($m_{Co} = 0.8$–$1.0\mu_B$/Co at.). In terms of the effect of the 3d–5d hybridization, this difference may relate to the detail of the way that the 3d state hybridizes the 5d states in the external and internal fields. In the calculations reported by Yamada and Shimizu (1985) for YCo_2 the external magnetic field of 150 T applied in the same direction on Y and Co atoms yields the values of $0.454\mu_B$/Co at. and $0.1\mu_B$/Y at. for Co and Y atoms, respectively. In order to get the values of the magnetic moments in RCo_2, the magnetic field B_Y at the Y site was applied in the opposite direction to B_{Co} at the Co site. In the case of $HoCo_2$, the exchange field acting on 5d electrons due to the local exchange interaction is evaluated as $B_{5d} = -2400$ T (Yamada and Shimizu 1985). On the other hand, the exchange field on Co from the localized 4f moments of

Ho is $B_{Co} = 156$ T (Gignoux and Givord 1979). For this case, they obtained the values of m_{Co} and M_Y equal to 0.61 and $-0.236\mu_B$/at., respectively. Subtracting the contribution of the orbital part ($0.14\mu_B$/at.), the spin part of the observed m_{Co} becomes $0.66\mu_B$. The agreement between the calculated and observed values of M_{Co} is satisfactory.

The influence of the 4f spin upon the magnetism of the transition metal in RCo_2 has been calculated by Nordström et al. (1992) using the self-consistent LMTO approximation. The resulting computed d-electron moment is shown in fig. 36a for $GdCo_2$ in which the 4f moment on Gd was changed from 0 to 7 and then back again to 0. For increasing 4f moment on the Gd from 0 to 3 (corresponding to Lu → Er) the moment induced on Co is small but at R = Ho the d-electron moment jumps to $1.75\mu_B$/f.u. Note that both R 5d and Co 3d moments increase as the 4f spin increases, but they are always antiparallel. The effect of the 3d–5d hybridization on the ferrimagnetic coupling between 3d and 5d spins (and then between 3d and 4f spins) is thus well demonstrated for this series of compounds. For the real system, i.e., with real lattice parameters, the results of the calculations show a transition at R = Tb, see fig. 36b. This finding suggests the influence of the volume effect on the 3d–5d hybridization.

3.1.2.3. *Anomalous magnetization process.* In most RCo_2, the molecular field acting on T moment due to the R–T intersublattice interactions, $B^{Co}_{mol,RCo}$, is larger than B_c and the Co magnetic moment is stabilized. For these HR–Co_2 ferrimagnets (HR = heavy lanthanide), the direction of $B^{Co}_{mol,RCo}$ is antiparallel to that of the HR-moment, and hence is antiparallel to the applied magnetic field B_0. This means that the effective field acting upon the Co subsystem, B^{Co}_{mol} ($= B^{Co}_{mol,RCo} - B_0$) decreases with increasing applied field. When B_0 is large enough to satisfy $B^{Co}_{mol,RCo} < B_c$, the Co moment abruptly collapses, which corresponds to a MT. In principle, this case of the inverse MT can be seen in the HR–Co_2 compounds. However, this kind of MT has not been observed since the magnetic field required for the collapse of the Co moment is too large for usual magnetic facilities. A study of the pseudobinary system, where the HR is diluted by a non-magnetic element is a useful method to observe the collapse of the Co moment. In practice, this MT was observed at a lower field for the $(Gd,Y)Co_2$ (Yamaguchi et al. 1992), $(Er,Y)Co_2$ (Levitin et al. 1984) and $(Er,Lu)Co_2$ (Wada et al. 1994). Anomalous magnetization is illustrated in fig. 37a for $Er_{0.75}Lu_{0.25}Co_2$. In order to confirm the origin of the collapse of the Co moment for this anomaly, the magnetostriction has also been measured (see fig. 37b). Both the longitudinal and transverse magnetostriction show an anomalous shrinkage around $B = 15$ T, where the magnetization anomaly occurred. The large and negative volume change ω is consistent with the model of the Co-moment collapse. Ballou et al. (1993) have also reported the induced MT for the $Y_{1-y}Gd_y(Co_{0.915}Al_{0.085})_2$ with $y < 0.04$. As can be seen in fig. 38, the original $Y(Co_{0.915}Al_{0.085})_2$ compound shows a MT at $B_c = 22.5$ T. The effect of the substituted Gd atom is simply to lower the applied magnetic field which is necessary to observe the MT and form a collinear ferrimagnet phase with two stable Gd and Co magnetic sublattices (fig. 38 for $y = 0.04$ and 0.1).

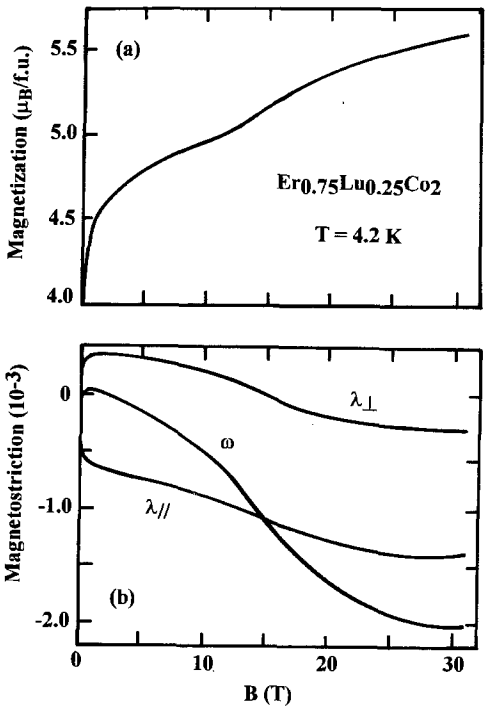

Fig. 37. (a) Magnetization and (b) magnetostriction curves at 4.2 K for $Er_{0.75}Lu_{0.25}Co_2$. (After Wada et al. 1994.)

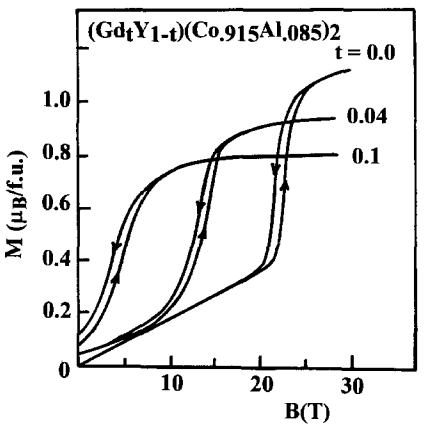

Fig. 38. Metamagnetic transitions in $Y_{1-t}Gd_t$-$(Co_{0.915}Al_{0.085})_2$. (After Ballou et al. 1993.)

For the light lanthanide LR–Co_2 compounds, $B^{Co}_{mol,RCo}$ is parallel to that of the LR-moment (and then parallel to the external field B_0). The applied field will strengthen the effective field acting on the Co subsystem and easily bring the pseudobinary compounds $LR_xY_{1-x}Co_2$ with $B^{Co}_{mol,RCo} < B_c$ to the MT. We present in figs. 39a,b the high-field magnetostriction data for the $Nd_xY_{1-x}Co_2$ compounds (Duc et al. 1992c, 1994). The volume magnetostriction ω in the compounds with $x \approx 0.2$–0.32 shows an positive contribution and non-linearly increases with increasing magnetic field. The MT, moreover, can be clearly seen in the $d\omega/dB$ vs. B curves. As regards the induced character of Co moment, the relation $\omega = \kappa C M^2_{Co}$ has been considered. It was also found that κC is slightly increased in the $Nd_xY_{1-x}Co_2$ compounds which are close to the critical concentration for the onset of Co magnetism. As will be presented below (sect. 3.1.2.4), this may relate to an anomaly of the elastic properties at the MT (Klimker and Rosen 1976). This may also be the reason why the MT is more clearly detected in magnetostriction measurements than in magnetization measurements. Nevertheless, it is clear that the MT in this kind of compound is rather broad. Wada et al. (1994) have claimed that this is a result of the anisotropy field. Due to this field some R moments cannot rotate to the applied field direction, resulting in a distribution of the metamagnetic transition fields. The magnetization curve measured in the powder samples, which is

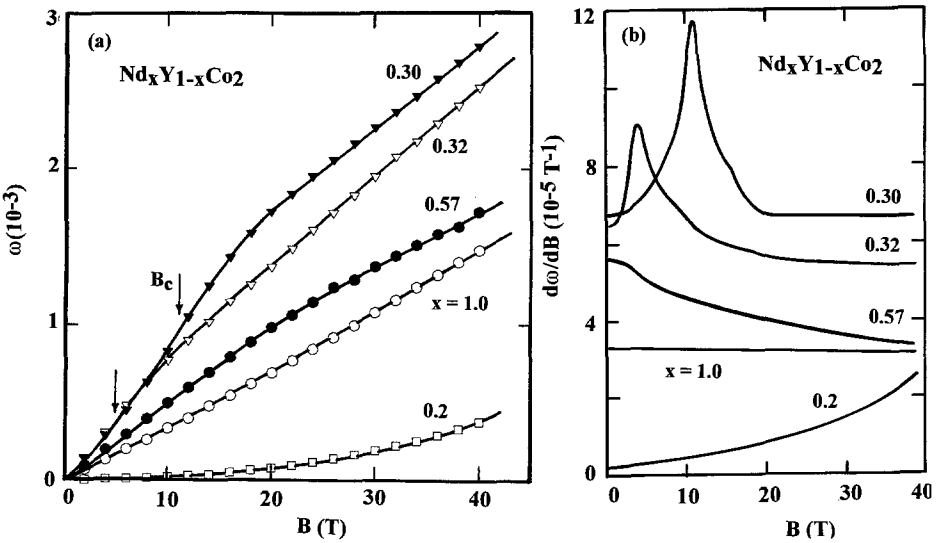

Fig. 39. Plots of (a) ω and (b) $d\omega/dB$ as a function of B at 4.2 K for the $Nd_xY_{1-x}Co_2$ compounds. (After Duc et al. 1994.)

able to rotate freely, however, shows a similar metamagnetic behaviour. The effect of the concentration inhomogeneity may be the origin.

In high magnetic fields, one can expect a transition from this collinear structure to a non-collinear one to be induced for the ferrimagnets. A multi field-induced magnetic phase transition, can thus occur in the RCo_2-based compounds. Practically, a sequence of phase transitions different in their nature has been examined in $Y_{0.75}Tm_{0.25}(Co_{0.88}Al_{0.12})_2$ (Brommer et al. 1994). The experimental magnetization curve at 4.2 K is presented in fig. 40a; this curve is characterized by two jump-like transitions at 6.5 T and 28 T and a region of a pronounced peculiarity (a bend) between them. The corresponding Y compound, $Y(Co_{0.88}Al_{0.12})_2$, is a very weak ferromagnet (moment $0.08\mu_B$/f.u.) with a MT (at 12 T, moment about $0.5\mu_B$/f.u.) to a strongly ferromagnetic state with a moment of more than $0.82\mu_B$/f.u. (see fig. 40b). This was also taken to be the moment of the Co subsystem in the corresponding $(Y,Tm)(Co_{0.88}Al_{0.12})_2$ powdered sample. From a fitting procedure, the molecular field parameter was found to be $-16.4\,T/\mu_B$f.u. The Tm-moment was taken to be equal to $4.3\mu_B$/Tm ion (Brommer et al. 1993). Thus, in the absence of the external field, the Co subsystem feels a molecular field $B^{Co}_{mol,TmCo} = |n_{TmCo}| \times M_{Tm} = 17.6\,T$, forcing it to be in the strongly ferromagnetic state. Upon application of a field, however, the effective field acting on the Co subsystem will decrease as long as the Co moment is pointing in the opposite direction. Consequently, the Co subsystem is driven, via the MT, to the weak ferromagnetic state. At still higher fields, the self-consistent solution mentioned above is attained, and a non-collinear structure is formed. After rotation to the ferromagnetic structure, further increase of the applied field forces the Co subsystem into the strongly ferromagnetic state again, via a second MT. The

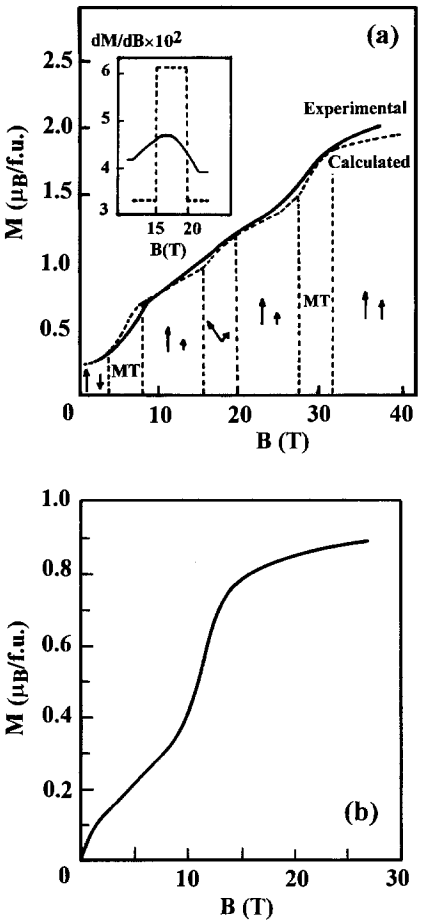

Fig. 40. Metamagnetic transitions in the compounds (a) $Y_{0.75}Tm_{0.25}(Co_{0.88}Co_{0.12})_2$ and (b) $Y(Co_{0.88}Co_{0.12})_2$. (After Brommer et al. 1994.)

magnetic phase diagrams of such multi field-induced magnetic transitions in the RCo_2-based compounds were recently completed by Dubenko et al. (1996).

3.1.2.4. *First-order transitions at T_c.* The transition from the paramagnetic to the magnetically ordered state in RCo_2 has attracted much attention for more than 25 years. The transition at T_c for the compounds with Dy (at 140 K), Ho (75 K) and Er (32 K) is found to be of first order. It is characterized by a sharp change of magnetization (Lemaire 1966, Duc et al. 1988a) (fig. 41), by a double peak of a.c. susceptibility χ_{ac} in the vicinity of T_c (Duc et al. 1988a,b, Duc 1996) (see fig. 42), by the resistivity (Gratz et al. 1981) (see fig. 43), by a large and sudden change of the volume (Minataka et al. 1976) (see fig. 44), by a large peak of specific heat (Voiron 1973, Duc et al. 1988a) (see fig. 45) and by a sharp anomaly of the elastic parameter (Klimker and Rosen 1976) (see fig. 46a,b). The transition in the compounds with a high T_c, i.e., in $GdCo_2$ (400 K) and $TbCo_2$ (230 K), however, is of

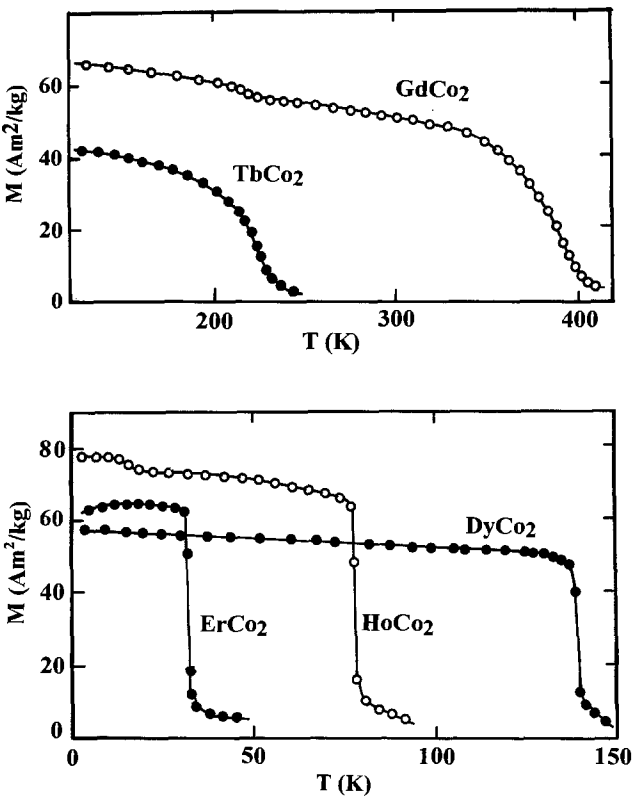

Fig. 41. Temperature dependence of the magnetization in RCo_2 compounds.

second order. This leads to the smooth change of the above mentioned physical parameters (see also figs. 41–46). A value of 200 K of T_c was regarded as the border temperature below which the transition is first order (Bloch et al. 1975). This argument was proposed on the basis of the consideration of the metamagnetic behaviour of the 3d subsystem (Cyrot and Lavagna 1979), in particular, on the connection of the change in sign of the coefficient a_3 (Bloch et al. 1975, see also sect. 3.1.1.1). Indeed, a change from SOT to FOT was observed in $Tb_xY_{1-x}Co_2$ (Franse et al. 1983), $Tb_xHo_{1-x}Co_2$ (Duc et al. 1989) (see figs. 47a,b) at about $x = 0.7$ ($T_c = 176$ K and 185 K, respectively). Such a change was not found in $(Gd_xY_{1-x})Co_2$ (Muraoka et al. 1977). Moreover, the FOT in $DyCo_2$, $HoCo_2$ and $ErCo_2$ changes to SOT in $(Dy_xY_{1-x})Co_2$ (Yoshimura et al. 1984, Duc et al. 1985, see fig. 48), $Ho_xY_{1-x}Co_2$ (Steiner et al. 1978, see fig. 49) and $Er_xY_{1-x}Co_2$ (Duc et al. 1988a, see fig. 50) at $x \approx 0.4$, 0.5 and 0.7, respectively. The origin of this phenomenon is as follows. For the $(Tb,Y)Co_2$ and $(Tb,Ho)Co_2$ compounds with a high T_c, the value of the effective field acting on Co is large enough to induce a moment on the Co sites but the sign of $a_3(T_c)$ is positive then the transition is of second order. With increasing Y (in $(Tb,Y)Co_2$) or Ho (in $(Tb,Ho)Co_2$) concentration, the value of T_c decreases and the sign

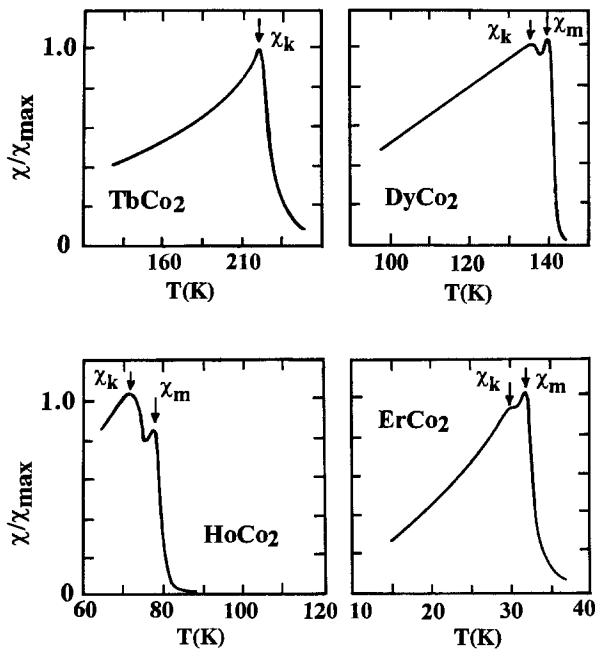

Fig. 42. AC susceptibility in the vicinity of T_c for RCo_2 compounds.

of a_3 at T_c becomes negative and the value of $B^{Co}_{mol,RCo}$ is still large enough to pass the MT of the Co subsystem. Then the transition becomes first order. With further increase of Y concentration the value of $B^{Co}_{mol,RCo}$ decreases, the system cannot reach the MT and the transition changes to second order once again. Franse et al. (1983) and Duc et al. (1989) have pointed out that the FOT in $(Tb,Y)Co_2$ observed at $x = 0.5$ and 0.3 is clearly evident in the magnetization measurements, but less clear in the resistivity and thermal expansion. Berthier et al. (1986) have also reported that the FOT cannot be observed by specific heat measurements for this system. This is attributed to inhomogeneities rather than to an indication that the FOT–SOT borderline is approached. However, as already mentioned, the above argument of the change from FOT to SOT due to the weakness of $B^{Co}_{mol,RCo}$ is clearly observed in the $(Dy,Y)Co_2$, $(Ho,Y)Co_2$ and $(Er,Y)Co_2$ systems.

Inoue and Shimizu (1982) estimated the value of $c_3(T_c)$ on the basis of eq. (56) for RCo_2 with $T_3 = 250$ K (see also eq. 76) and $\chi_d(T_c)$ independent of T, and were then able to explain the type of the phase transition. Using eqs. (56) and/or (73) and taking into account the temperature dependence of $\chi_d(T_c)$, Duc et al. (1988a, 1989, 1992a) explained the observed behaviour in RCo_2 and $(R,Y)Co_2$. The calculated $c_3(T_c)$ results are illustrated in tables 4 and 5 for $Tb_xY_{1-x}Co_2$ and $Tb_xHo_{1-x}Co_2$, respectively. Clearly, the sign of $c_3(T_c)$ is in accordance with the type of the transition. Here it was necessary to adopt a lower T_3 value (178 K). A reduced value (150 K) was also adopted by Inoue and Shimizu (1988). A magnetic diagram, i.e. the boundary between FOT and SOT in all $(R,Y)Co_2$ compounds, has been calculated with $T_3 = 178$ K and $a_3(0) = -15$ T(mol/Am^2)^3 and is

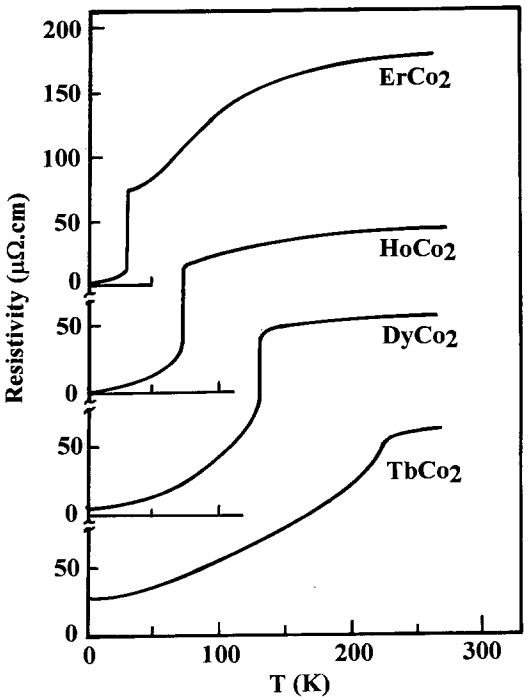

Fig. 43. Temperature dependence of the resistivity in RCo_2 compounds. (After Gratz et al. 1981.)

presented in fig. 51. We stress that the lower $T_c(x)$ values (as occurred in $(Er,Y)Co_2$) are strongly influenced by a change in $a_3(0)$, whereas the higher $T_c(x)$ values (e.g., $(Tb,Y)Co_2$) are intimately related to T_3, i.e., to the temperature at which a_3 changes sign. Moreover, the calculated values also depend on the other parameters. One might, for instance, wish to find a more realistic value for the coefficient b_1 by taking into account the crystal field effects. The magnetic behaviour of rare-earth moments may be influenced by the level splitting in the crystalline electric field (CEF), even to the extent that the CEF-effects are the cause of the occurrence of the SOT at relative low temperatures. The crystal field effect, which is larger in LR–Co_2 compounds than in HR–Co_2, may play an important role in the SOT of $NdCo_2$ and $PrCo_2$ (Bloch et al. 1975, Inoue and Shimizu 1988). The volume effects may also be important. It has been suggested that going from HR– to LR–compounds the Co subsystem is magnetically enhanced, with an optimum at lattice parameter $a = 7.272$ Å (Duc et al. 1992a). According to Cyrot and Lavagna (1979), the increase of 3d-magnetic susceptibility is also the cause of the destruction of the metamagnetic behaviour. From this discussion, the study of the magnetic properties in the compounds with mixing of both LR and HR atoms are interesting. Duc et al. (1993b) have reported an investigation of the magnetic transitions in $(Nd,Dy)Co_2$ and $(Pr,Dy)Co_2$. The substitution of Dy by Nd and Pr lowers the ordering temperature. However, the magnetic phase transition changes from FOT to SOT at a Dy concentration x between

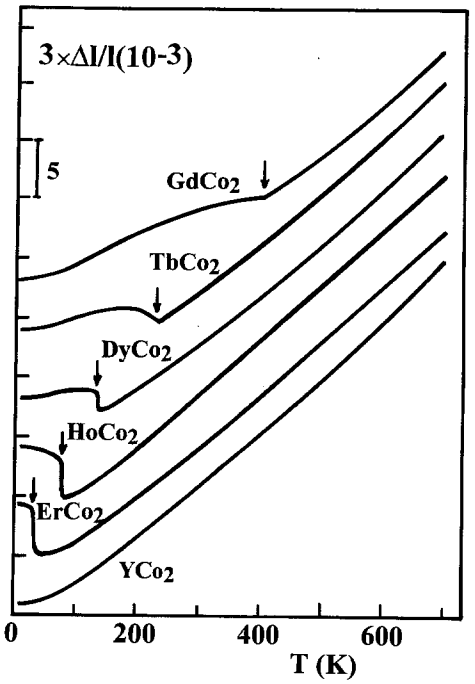

Fig. 44. Temperature dependence of $\Delta l/l$ in RCo_2 compounds. (After Minataka et al. 1976.)

20% and 40% for both series of compounds as indicated by magnetization and resistivity measurements.

Note that a gradual change from "light" to "heavy" rare earths brings along a corresponding lowering of the lattice parameter. Consequently, in the consideration of the type of the transition, CEF-effects were ignored and the volume dependence of the coefficient a_3 was introduced (Duc et al. 1993b). In fact, it was assumed that

$$a_3(T) = a_3(0) + |a_3(0)| \left(\frac{T}{178}\right)^2, \tag{78}$$

with $a_3(0)$ varying from $-15\,\mathrm{T(mol/Am^2)^3}$ for $ErCo_2$ up to $+3.1\,\mathrm{T(mol/Am^2)^3}$ for $PrCo_2$, in a linear dependence on the lattice parameter, chosen in such a way that $a_3(0)$ changes sign at a lattice parameter $a = 7.275$ Å (i.e., between $GdCo_2$ with $a = 7.256$ Å and $NdCo_2$ with $a = 7.300$ Å). For simplicity, T_3 was taken to be equal to 178 K for all compounds (lattice parameters), bearing in mind that the T_3 contribution in eq. (78) is small anyway, in the compounds with low Curie temperature. In accordance with the three-sublattice model, i.e., the generalization of the Inoue–Shimizu model, (Brommer 1989, Duc et al. 1993b, see also sect. 2.1.2.2), the coefficient c_3 was calculated. The calculated results, in which both R–T and R–R interactions were taken into account, are presented in tables 6 and 7 for the $(Nd,Dy)Co_2$ and $(Pr,Dy)Co_2$ systems, respectively. The model shows a change in sign of $c_3(T_c)$, which is in good agreement with the

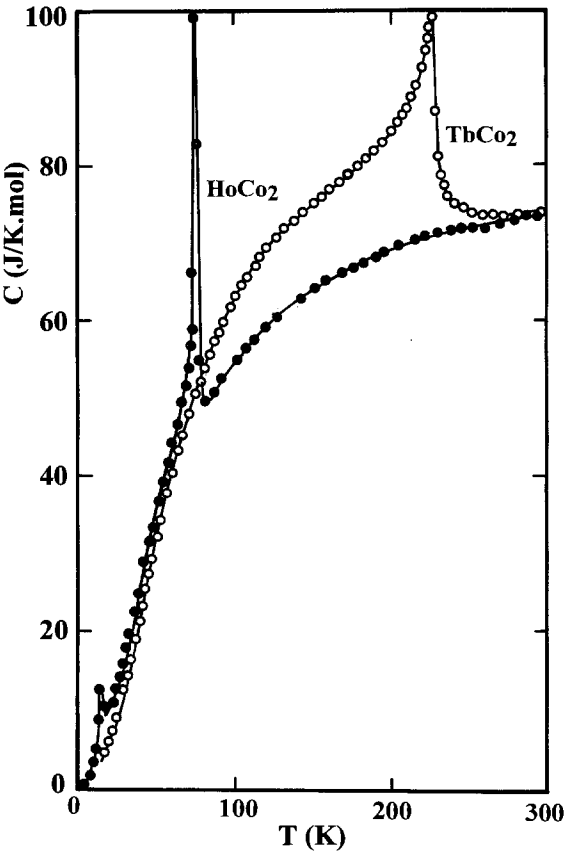

Fig. 45. Specific heat of the $TbCo_2$ and $HoCo_2$ compounds. (After Voiron 1973.)

experimentally observed change in type of magnetic transition from first order to second order in the compounds under consideration. Notice that there are many adjustable parameters. Here, we undoubtedly can find more sets of parameters for which such a change of sign occurs. This approach is only the possibility to conclude that the change of the type of the magnetic phase transition in the rather "complex" $(HR,LR)Co_2$ can also be explained in the generalized Inoue–Shimizu model.

The application of a magnetic field primarily causes an increase of the magnetic ordering temperature and a gradual change of the FOT towards a SOT (Gratz et al. 1993). In this case, the effect of the external field is to prolong the alignment of the 4f moment when heating through T_c. The onset of the Co magnetism is also shifted to higher temperatures. The influence of external pressure is not only to reduce T_c but also to change the magnetic transition if it is of FOT towards a SOT. The critical pressure of this change is of about 30 kbar (Voiron and Bloch 1971). The boundary between the FOT and SOT in RCo_2 with respect to the change in the volume was studied in a similar way to that used for $(R,Y)Co_2$ compounds (Inoue and Shimizu 1988), assuming that only $\chi_d(T)$ depends on

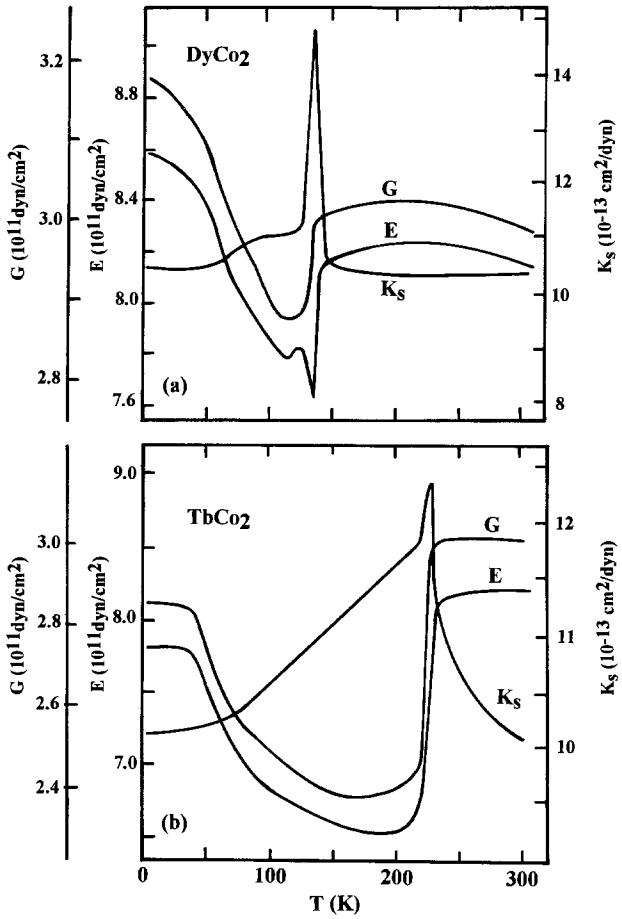

Fig. 46. Temperature dependence of the Young modulus (E), shear modulus (G) and adiabatic compressibility (K_s) for the compounds (a) $DyCo_2$ and (b) $TbCo_2$. (After Klimker and Rosen 1976.)

the volume. Physically, this may relate to the effect of volume on the magnetic behaviour of the Co subsystem: an increase of external pressure reduces the Co susceptibility and increases the critical field of the MT and even destroys the metamagnetic behaviour. Then the condition for the FOT in the RCo_2 compounds is more difficult to fulfill under higher pressure and the transition becomes SOT.

The effect of the substitution of Co by Al in the $R(Co_{1-x}Al_x)_2$, primarily is a giant increase of the Curie temperature. This increase is rather strong for R = Tm, Er, Ho and Dy (with a maximum at $x \approx 0.13$) (Gignoux et al. 1978, Aleksandryan et al. 1984a, Duc et al. 1992d) but only slight for Tb and Gd (maxima at $x = 0.09$ and 0.03, respectively). Inoue and Shimizu (1988) have calculated T_c for $R(Co,Al)_2$ by using the same value of the R–R and R–Co exchange interactions as those in RCo_2 and the temperature dependence

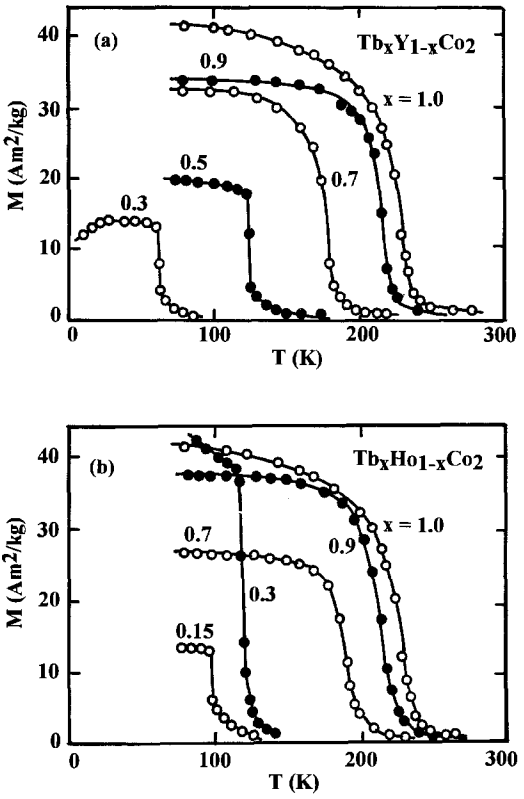

Fig. 47. Temperature dependence of the magnetization in the compounds (a) $(Tb,Y)Co_2$ and (b) $(Tb,Ho)Co_2$. (After Duc et al. 1989.)

of the susceptibility for the corresponding $Y(Co_{1-x}Al_x)_2$. The calculated results fit well the variation of T_c for the compounds with R = Gd, Tb, Dy but show a large scattering for R = Ho, Er and Tm. Duc et al. (1992a), however, plotted the ratio T_c/T_c^{max} as a function of lattice parameter. This figure strongly suggests a major influence of the volume, and the existence of a "critical" lattice parameter $a_c = 7.27$ Å above which T_c decreases with the lattice expansion. Notice that at roughly the same lattice parameter, $Y(Co,Al)_2$ becomes ferromagnetic.

Magnetic phase transitions of the $R(Co,Al)_2$ compounds were studied by means of the magnetization, thermal expansion and resistivity (Duc et al. 1992d). The thermal expansion data are illustrated in figs. 52 and 53 for $R(Co,Al)_2$ with R = Dy and Ho, respectively. In $Dy(Co_{1-x}Al_x)_2$, $Ho(Co_{1-x}Al_x)_2$ and $Er(Co_{1-x}Al_x)_2$, a change from FOT to SOT occurs at $x = 0.025$, 0.075 and 0.075, respectively. In a first approximation, one expects a FOT in case $T_c < T_3 < T_{max}$ and a SOT otherwise. Experimentally, one finds that T_{max} decreases with increasing Al content both in $Lu(Co,Al)_2$ and $Y(Co,Al)_2$, see e.g., fig. 20. Moreover, the critical field for the MT decreases at the same time (see sect. 3.1.1.2). Taking this behaviour as an indication that the influence of the peculiarities of the band structure is scales towards lower temperatures, Duc et al. (1992d) expect

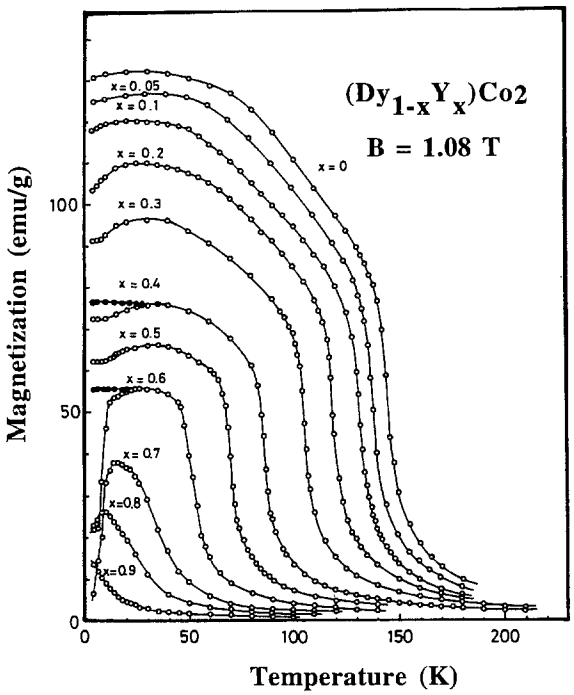

Fig. 48. Temperature dependence of the magnetization in $(Dy,Y)Co_2$ compounds. (After Yoshimura et al. 1984.)

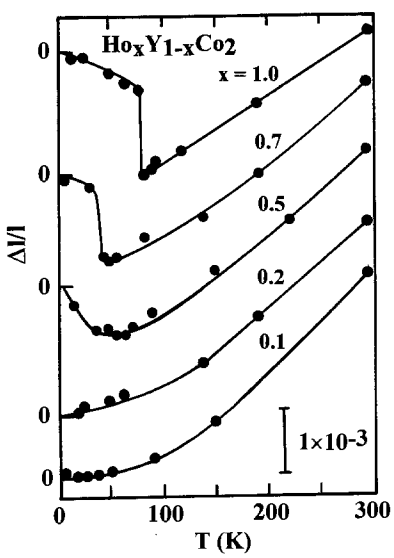

Fig. 49. Temperature dependence of $\Delta l/l$ in $(Ho,Y)Co_2$ compounds. (After Steiner et al. 1978.)

$T_3(x)$ to decrease with increasing Al content x, too. Moreover Yamada (1992, 1993) has shown that, in a simple model based on a dominant role of spin fluctuations, the

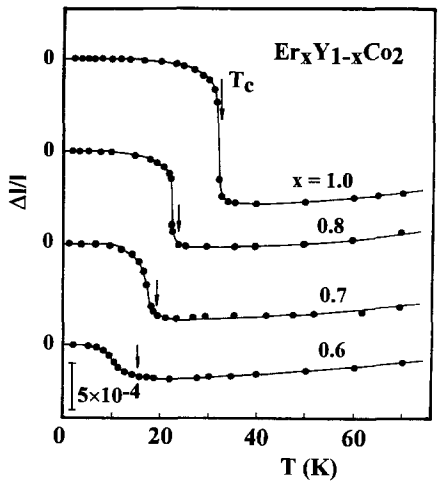

Fig. 50. Temperature dependence of $\Delta l/l$ in (Er,Y)Co_2 compounds. (After Duc et al. 1988a.)

Table 4
The $c_3(T_c)$ values for the $Tb_xY_{1-x}Co_2$ compounds calculated with $a_3(0) = -6.8\,T(mol/Am^2)^3$ and $T_3 = 178\,K$[a]

x	T_c (K)	$100a_3(T_c)$ (T(mol/Am^2)^3)	$100c_3(T_c)$ (T(mol/Am^2)^3)
0.2	38	−649	−3.02
0.3	67	−584	−6.26
0.4	98	−474	−8.35
0.5	128	−328	−7.35
0.6	154	−171	−3.84
0.7	176	−15	−0.23
0.8	197	153	2.87
0.9	217	303	4.66
1.0	227	426	5.11

[a] After Duc et al. (1989).

temperatures T_{max} and T_3 are closely related or even equal. Guided by this conclusion, $T_3(x)$ was determined by scaling with $T_{max}(x)$, taking the T_{max} values observed in corresponding Y(Lu) compounds. The c_3 values were calculated with T_3 taken from the $Y(Co_{1-x}Al_x)_2$ systems. The T_3 values and results of calculations are listed in table 8 for the $R(Co_{1-x}Al_x)_2$ system. The transition temperature increases with increasing Al content, whereas T_3 decreases. For both $Dy(Co,Al)_2$ and $Ho(Co,Al)_2$ the sign of $c_3(T_c)$, or the cross-over of $T_3(x)$ and $T_c(x)$, agrees with the observed change of the type of the transition, for either set of T_3 values. For the $Er(Co,Al)_2$ compounds, the change in sign of c_3, as calculated, agrees satisfactorily with the experimental observation of the change in type of the transition. If the c_3 are calculated on the basis of the T_3 values for $Lu(Co,Al)_2$, however, no agreement is found. This suggests that the magnetic properties

Table 5
The $c_3(T_c)$ values for the $Tb_xHo_{1-x}Co_2$ compounds calculated with $a_3(0) = -6.8\,T(mol/Am^2)^3$ and $T_3 = 178\,K$ [a]

x	T_c (K)	$100a_3(T_c)$ (T(mol/Am^2)^3)	$100c_3(T_c)$ (T(mol/Am^2)^3)
0.0	75	−559	−0.14
0.1	85	−525	−0.21
0.15	94	−490	−0.29
0.3	129	−323	−0.67
0.7	185	55	0.37
0.9	210	226	2.48
1.0	227	426	5.11

[a] After Duc et al. (1989).

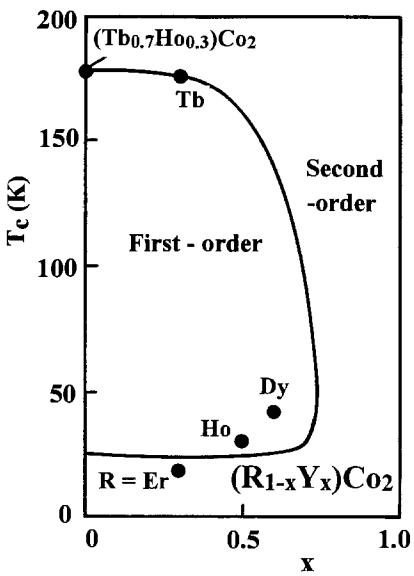

Fig. 51. The boundary between FOT and SOT for the $R_xY_{1-x}Co_2$ compounds. Experimental values are indicated for R = Tb, Dy, Ho and Er. At $x = 0$: boundary value for $(Tb,Ho)Co_2$. (After Duc et al. 1992a.)

of the 3d subsystem in $Er(Co,Al)_2$ can be approximated better by those of $Y(Co,Al)_2$ than those of $Lu(Co,Al)_2$. This may also be related to the so-called "lutetium paradox" (Dubenko et al. 1992).

The magnetic and electrical properties of the $R(Co,Si)_2$ compounds (R = Gd, Tb, Dy, Ho, Er) with invariable crystal unit cell parameters have been investigated by Duc (1996), Duc and Oanh (1997) and Cuong et al. (1997, 1998a,b). Under the condition of fixed volume, somewhat similar effects to those in $R(Co,Al)_2$ on the enhancement of the ordering temperature are still observed in the $R(Co,Si)_2$ compounds (with R = Er, Ho). The change from the FOT to SOT was also observed in the compounds $R(Co_{1-x}Si_x)_2$ with R = Dy, Ho and Er at $x = 0.05$, 0.075 and 0.1, respectively. In terms of the Inoue–

Table 6
The $c_3(T_c)$ values for the $Dy_xNd_{1-x}Co_2$ compounds calculated with the lattice parameter dependence of $a_3(0)$ (see text) and $T_3 = 178\,K$ [a]

x	T_c (K)	$a_3(T_c)$ (T(mol/Am^2)^3)	$100c_3(T_c)$ (T(mol/Am^2)^3)
0.0	95	3.98	2.7
0.2	100	0.39	66.08
0.4	105	–1.63	–17.30
0.5	110	–2.41	–3.48
0.6	115	–3.09	–1.29
0.8	125	–4.11	–0.36
1.0	140	–4.16	–0.20

[a] After Duc et al. (1993b).

Table 7
The $c_3(T_c)$ values for the $Dy_xPr_{1-x}Co_2$ compounds calculated with the lattice parameter dependence of $a_3(0)$ (see text) and $T_3 = 178\,K$ [a]

x	T_c (K)	$a_3(T_c)$ (T(mol/Am^2)^3)	$100c_3(T_c)$ (T(mol/Am^2)^3)
0.0	56	3.41	1.71
0.2	69	0.35	12290
0.4	78	–2.02	–0.13
0.6	95	–3.79	–0.28
0.8	115	–4.72	–0.22
1.0	140	–4.16	–0.20

[a] After Duc et al. (1993b)

Shimizu model, the character of these phase transitions can be explained in the same way as discussed for $R(Co,Al)_2$, if the fact that the temperatures T_{max} and T_3 decrease as Si content increases in the $Y(Lu)(Co,Si)_2$ compounds is considered (Duc 1996). The calculated results of $c_3(T_c)$ are listed in table 9 for the $R(Co_{1-x}Si_x)_2$ compounds (Duc and Oanh 1997).

The average 3d magnetic moment, the susceptibility and the specific heat of the $R(Co_{1-x}Cu_x)_2$ and $Y(Co_{1-x}Cu_x)_2$ compounds (Duc et al. 1985, 1988c, Hien et al. 1986) confirm the picture that has been developed for the density of states curve of the YT_2 compounds with T = Fe, Co, Ni (Cyrot and Lavagna, 1979). The additional d electrons supplied on substituting Co partly by Cu bring the Fermi level to a flat part in the DOS curve. As a consequence the magnetic phase transition changes from FOT to SOT in the $R(Co_{1-x}Cu_x)_2$ with R = Dy, Ho and Er. This change can be understood in terms of the Inoue–Shimizu model by taking into account the decrease of the 3d susceptibility with increasing Cu-content. Magnetic phase transitions in $Ho(Co_{1-x}Ni_x)_2$ were studied by Tari (1982). The FOT was indicated for $x \leqslant 0.1$ and the SOT for $x > 1$. The magnetic

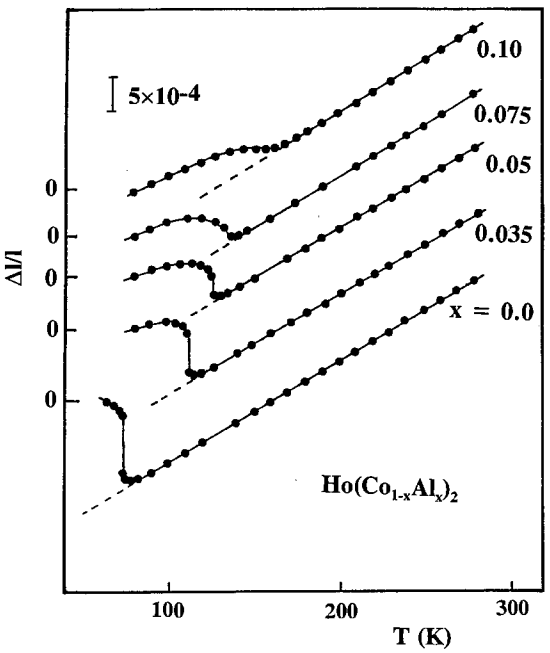

Fig. 52. Temperature dependence of $\Delta l/l$ in $Ho(Co,Al)_2$ compounds. (After Duc et al. 1992d.)

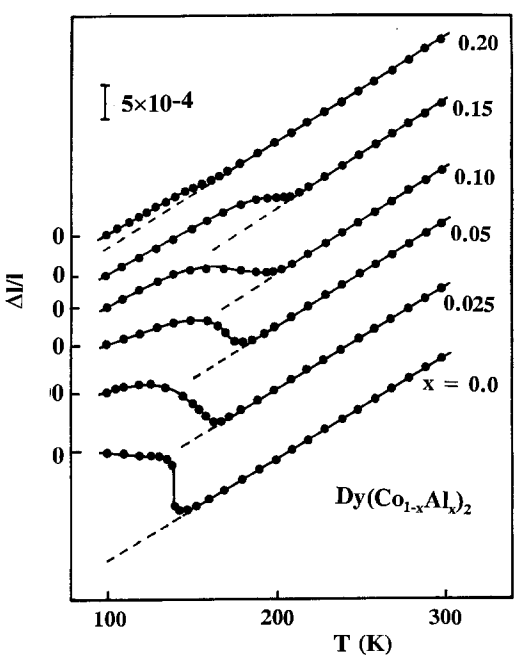

Fig. 53. Temperature dependence of $\Delta l/l$ in $Dy(Co,Al)_2$ compounds. (After Duc et al. 1992d.)

Table 8
T_3 (in K), the temperature at which $a_3(T)$ changes sign for $Lu(Co_{1-x}Al_x)_2$ (Lu) and $Y(Co_{1-x}Al_x)_2$ (Y), the observed transition temperature T_c and the calculated $c_3(T_c)$ (in T(mol/Am^2)^3) on the basis of T_3 values for $Y(Co,Al)_2$ [a]

x	T_3		$Dy(Co_{1-x}Al_x)_2$		$Ho(Co_{1-x}Al_x)_2$		$Er(Co_{1-x}Al_x)_2$	
	Lu	Y	T_c	$c_3(T_c)$	T_c	$c_3(T_c)$	T_c	$c_3(T_c)$
0.0	178	178	140	−12.0	75	−0.36	32.6	−0.018
0.025	160	145	162	45.8	90	−16.6		
0.050	145	125	180	575.3	120	−31.2	60	−56
0.065							70	−886
0.075	125	78	190	4406	140	35600	90	1570
0.1	100	35	200	72450	160	97710	120	532286

[a] After Duc et al. (1992d).

Table 9
T_3, the temperature at which $a_3(T)$ changes sign for $Y(Co_{1-x}Si_x)_2$ (Y), T_c, the observed transition temperature, and $c_3(T_c)$ (in 10^{-2} T(mol/Am^2)^3), calculated on the basis of the T_3 values for $Y(Co,Si)_2$

x	T_3 (K) Y	$Dy(Co_{1-x}Si_x)_2$		$Ho(Co_{1-x}Si_x)_2$		$Er(Co_{1-x}Si_x)_2$	
		T_c	$c_3(T_c)$	T_c	$c_3(T_c)$	T_c	$c_3(T_c)$
0.0	178	142	−0.850	78	−0.089	32.6	−0.039
0.025	145	142	−0.086	95	−0.41	44	−0.085
0.050	100	148	6.8	112	−0.64	54	−0.41
0.075	80	146	25.2	115	13.9	64	−0.57
0.100	80	146	46.5	112	15.6	68	−1.48

[a] After Duc and Oanh (1997).

behaviour can be simply understood within the band filling on the substitution Co by Ni. Since rhodium and cobalt are isoelectronic, the substitution of Rh for Co in $HoCo_2$ should provide a simpler system for the study of the magnetic phase transition. The FOT was observed in the $Ho(Co_{1-x}Rh_x)_2$ compounds with $x \leqslant 0.08$ (Tari 1987 and Henry et al. 1991). In this system, therefore a large decrease in the paramagnetic susceptibility is not anticipated. The change from FOT to SOT was suggested to be due to the reduction of the Ho–Co exchange interactions.

3.1.2.5. *Metamagnetic transitions above T_c.* The MT at temperatures above T_c is evident in the magnetization and magnetoresistance (Steiner et al. 1978, Aleksandryan et al. 1984b, Cuong et al. 1998b, Duc 1999; figs. 54–58). Magnetization isotherms are presented in figs. 54a–c for polycrystalline $ErCo_2$, $HoCo_2$ and $DyCo_2$ samples. Metamagnetism is characterized by (i) a large hysteresis of magnetization and (ii) an increase of the critical field B_c and the a decrease of the magnetization jump at the MT with increasing temperature. In addition, the MT exists only in a small range of temperature, with

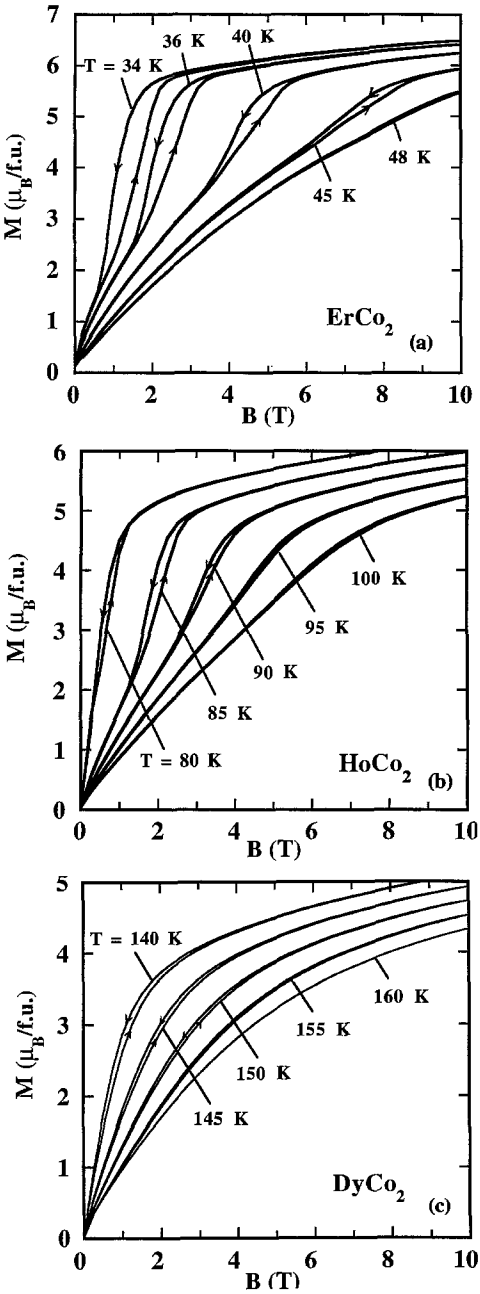

Fig. 54. Magnetization isotherms at $T > T_c$ for RCo_2, for R = Er (a), Ho (b) and Dy (c). (After Duc 1999.)

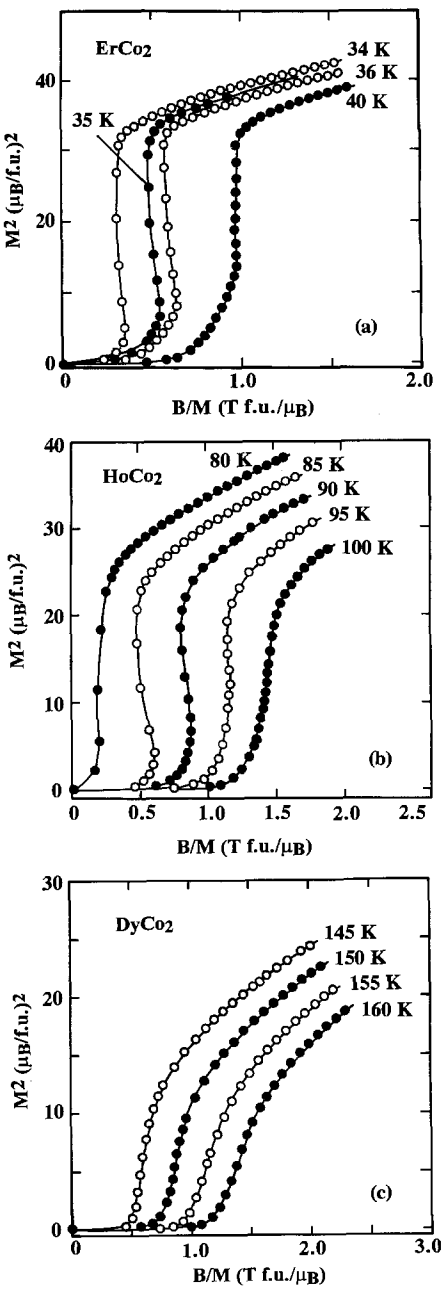

Fig. 55. The Arrott plots at $T > T_c$ for RCo_2, for R = Er (a), Ho (b) and Dy (c). (After Duc 1999.)

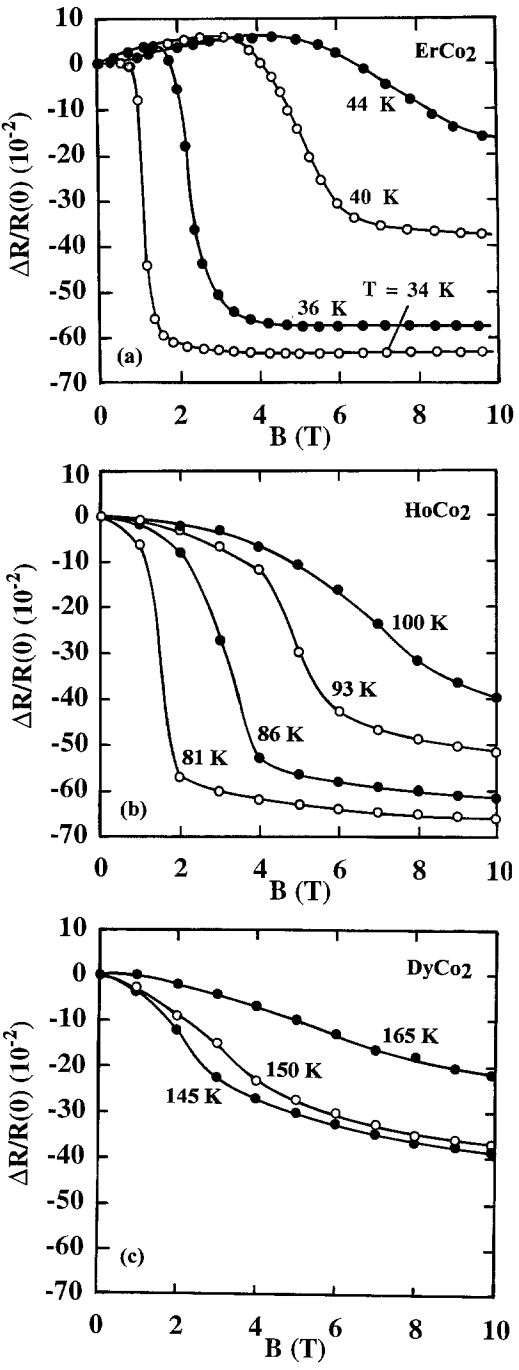

Fig. 56. Magnetoresistance at $T > T_c$ for RCo_2, for R = Er (a), Ho (b) and Dy (c). (After Duc 1999.)

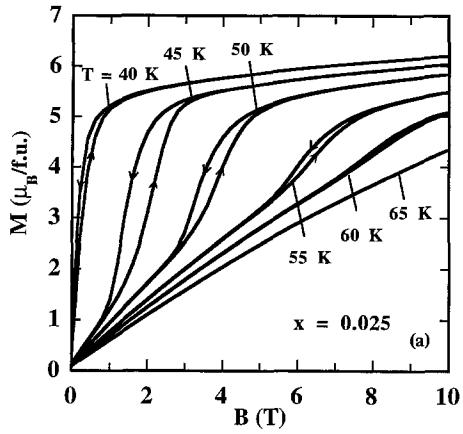

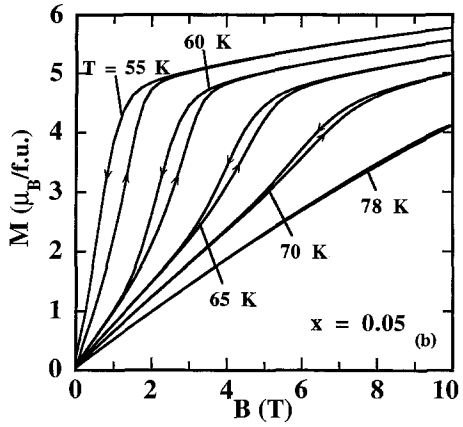

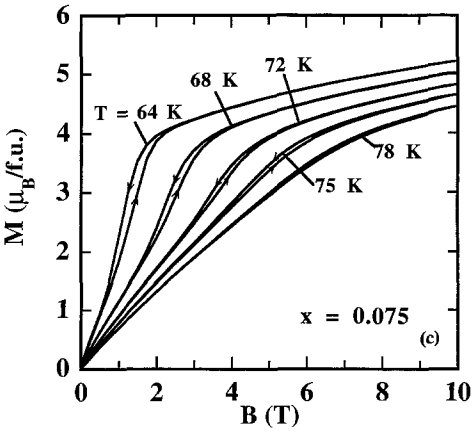

Fig. 57. Magnetization isotherms for $Er(Co_{1-x}Si_x)_2$ at $T > T_c$: (a) $x = 0.025$; (b) $x = 0.05$; (c) $x = 0.075$. (After Cuong et al. 1998b.)

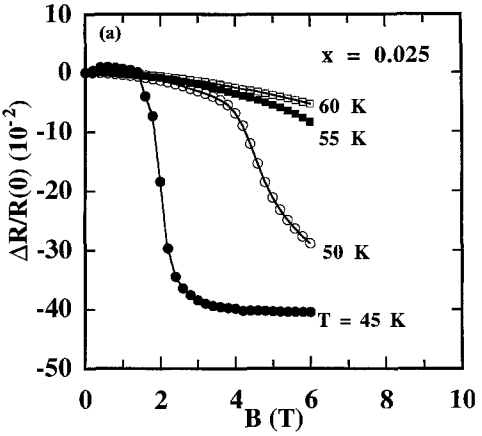

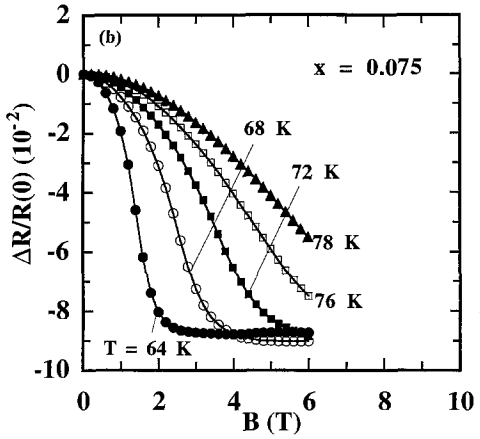

Fig. 58. Magnetoresistance for $Er(Co_{1-x}Si_x)_2$ at $T > T_c$: (a) $x = 0.025$; (b) $x = 0.075$. (After Cuong et al. 1998b.)

$\Delta T \approx 20$ K above the FOT. In this temperature range an almost linear relationship between B_c and T was found. The disappearance of the MT is characterized by the disappearance of not only the magnetization jump but also the hysteresis. For $DyCo_2$ the MT is weakly evident only in the hysteresis of the magnetization curves above T_c. The Arrott plots of the investigated compounds are presented in figs. 55a–c. They show an S shape with two linear parts characteristic of the paramagnetic and ferromagnetic states in low and high magnetic fields, respectively. This is a clear indication of the negative contribution of the coefficient c_3 to the equation of state.

Magnetoresistance data for $ErCo_2$ are presented in fig. 56a in a plot of $\Delta R/R(0)$ versus B. This figure indicates that a rise in B to B_c at $T > T_c$ initially causes an insignificant change in $\Delta R/R(0)$ even though the magnetization of the compounds, which is determined by the R-subsystem in these fields, reaches a rather large value (approximately more than one-third of the maximum value at several temperatures). The metamagnetic nature of the magnetization process at $T > T_c$, however, becomes more clearly manifested in magnetoresistance analyses. A sharp drop in the electrical resistance of $ErCo_2$ amounting to nearly a factor of three is observed for $B \approx B_c$ where there is a jump in the magnetization. A similar result is also observed for $HoCo_2$ and $DyCo_2$ (see also figs. 56b,c).

The MT above T_c was studied systematically for $Er(Co,Si)_2$ and $Ho(Co,Si)_2$ (Cuong et al. 1998b, Duc and Oanh 1997). The magnetization and magnetoresistance isotherms are illustrated in figs. 57a–c and 58a,b for the $Er(Co_{1-x}Si_x)_2$ system. Resistance suppression is observed in the compounds with $x \leqslant 0.075$, i.e. in the compounds showing the FOT only. The magnitude of this resistance suppression at B_c decreases with increasing Si content and magnetoresistance becomes positive in the compounds where the SOT at T_c occurs. The analysis has indicated that the suppression of the magnetoresistance at the MT can be considered as mainly due to the quenching of spin fluctuation scattering. The magnetoresistance at the MT, thus, can be considered as a useful way to measure the effects of spin fluctuations in the investigated compounds.

3.2. *The RCo_3-based compounds*

The RCo_3 compounds crystallize in the rhombohedral $PuNi_3$-type of structure, space R3m. This structure is obtained by systematic replacements of the Cu ions by R ions in every second basal plane of the $CaCu_5$ structure according to the formula

$$2RCo_5 + R - Co \rightarrow 3RCo_3.$$

In the rhombohedral structure, the R atoms are situated at two different crystallographic sites, 3c(I) and 6c(II), whereas the 3d atoms are distributed over three different sites 3d(I), 6c(II) and 18h(III), see fig. 59. In the first approximation, the local arrangement of the R_I site is that of the hexagonal RCo_5 structure whereas the local arrangement of the R_{II} site resembles that of the cubic RCo_2 Laves phase structure. Thus, different magnetic behaviour can be expected for R ions placed at different sites. The same holds for the

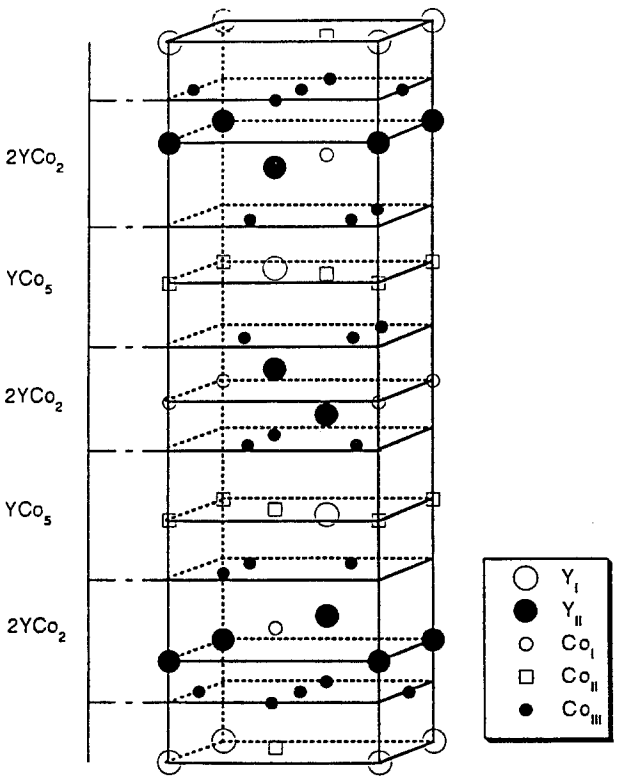

Fig. 59. Crystal structure of the RCo_3 compounds.

Co ions where one expects to find Co ions both in the paramagnetic state as in YCo_2 and in the magnetic state as in YCo_5 with the occupancy ratio 1 to 2. Indeed, instabilities of the Co magnetism in RCo_3 have experimentally been observed by applying ultra-high magnetic fields or by the effect of the 4f–3d exchange interactions.

3.2.1. *YCo_3-based compounds*

The YCo_3 compound is an itinerant ferromagnet. According to data given in different works, the Curie temperature of this compound ranges from 264 K to 320 K and the total magnetic moment ranges from $1.45\mu_B$/f.u. to $1.8\mu_B$/f.u. (Buschow 1980, Franse and Radwanski 1993). This large spread in data of the basic magnetic characteristics may be caused by stoichiometic differences between the samples studied in different experiments. Investigations of the magnetization of the pseudobinary compounds $Y(Fe,Co)_3$, $Y(Fe,Ni)_3$ and $Y(Co,Ni)_3$ at 4.2 K in pulsed high magnetic fields up to 36 T (Goto et al. 1991) indicated that these compounds are classified into weak, intermediately saturated and completely saturated ferromagnets. The magnetic moment as a function of 3d electron concentration can be explained qualitatively in terms of the rigid band model using

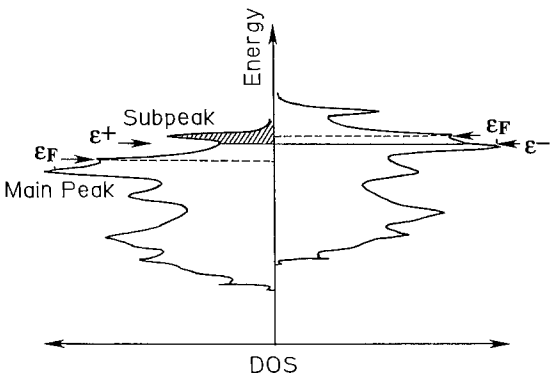

Fig. 60. The DOS for the 3d band in YCo_3. Dashed lines present the Fermi level determined by band filling in the paramagnetic state. ε^+ and ε^- are the Fermi levels of the majority- and minority-spin states, respectively. The location of ε^+ at the minimum of DOS implies the ISF state of YCo_3. The shaded area denotes the part of DOS corresponding to the CSF state, see text. (After Inoue and Shimizu 1985.)

the calculated DOS reported by Inoue and Shimizu (1985). Here, the DOS shows the existence of a sharp subpeak above a main peak and near the top of the 3d band, fig. 60. Then, their magnetic properties are rather sensitive to the variation of the position of the Fermi level relative to the 3d band. For YCo_3, the Fermi level of the major-spin states is located at the minimum of the DOS between the main peak and the subpeak. According to this study, YCo_3 is in the intermediate saturated ferromagnetic (ISF) state (or a weak ferromagnetic (WF) state). However, a MT from the ISF state to the complete saturated ferromagnetic (CSF) state has been predicted for this compound if one can move the Fermi level of the majority-spin state to the top of the 3d band, i.e. to the subpeak (fig. 60, shaded area). This is the case of the effect of the substitution of Co by Fe (Goto et al. 1991) or the case of the high-field effect as will be discussed below. In the hydrides, this subpeak still exists. However, the electron population in the 3d band is not affected by hydrogen absorption. The changes in magnetic properties are mainly governed by the modification in the exchange interaction (Yamaguchi et al. 1991).

Magnetization measurement of YCo_3 have been performed in super-strong magnetic fields up to 110 T at 10 K (Goto et al. 1992). Figure 61 shows the derivative signal of the magnetization with respect to time (dM/dt) and the magnetic field signal. Two peaks corresponding to the two transitions are clearly seen in increasing and decreasing fields. The observed magnetization curve of YCo_3 is presented in fig. 62 and reveal two successive metamagnetic transitions at 60 T and 82 T. The magnetization changes from $0.72\mu_B$/Co to $0.88\mu_B$/Co and from $0.88\mu_B$/Co to $1.23\mu_B$/Co at each transition, respectively. Thus, the variations in magnetization due to these two transitions are $0.16\mu_B$/Co and $0.35\mu_B$/Co, respectively. It is interesting to note that the ratio of the variation in the magnetization is about 1:2. Above 90 T, the magnetization is completely saturated with the spontaneous magnetization comparable to that of Y_2Co_7. The above mentioned rigid band model (Inoue and Shimizu 1985, Yamaguchi et al. 1991) predicts that YCo_3 is in the ISF state with the estimated magnetic moment of $0.8\mu_B$/Co and a transition from ISF state to CSF one with a magnetization jump of $0.4\mu_B$/Co. This is in good agreement with the experimental observation of magnetization. However, it cannot explain the two metamagnetic transitions observed in YCo_3.

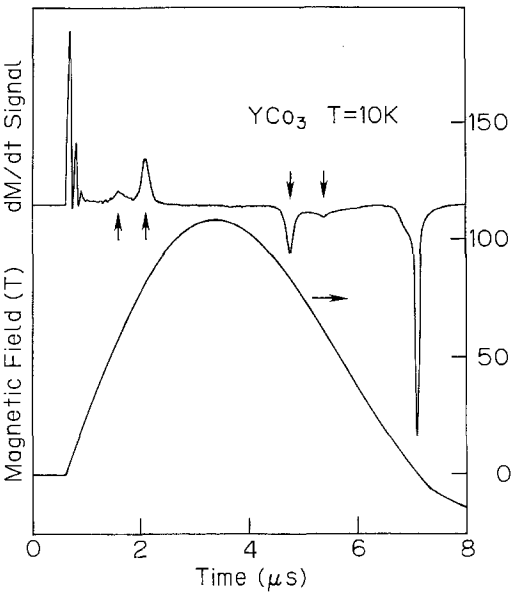

Fig. 61. The dM/dt and magnetic signals measured at 10 K in ultrahigh magnetic fields for YCo_3. (After Goto et al. 1992.)

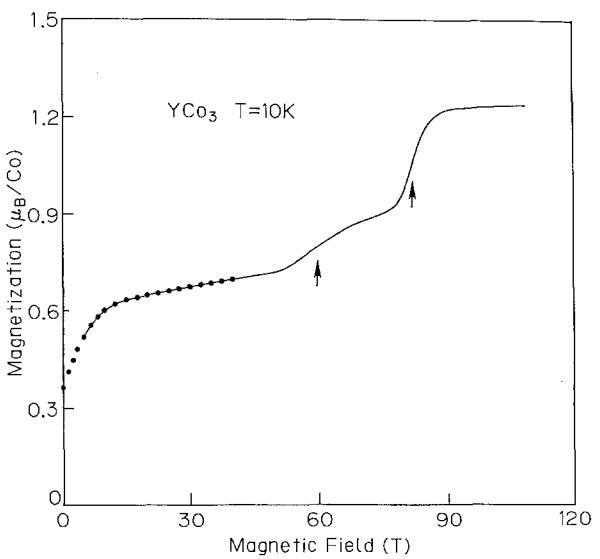

Fig. 62. Magnetization curve in ultrahigh magnetic field for YCo_3. (After Goto et al. 1992.)

In YCo_3, as mentioned above, Co atoms are on three different sites. All Co atoms are ferromagnetic, but the magnetic moment depends strongly on the sites: the order of the magnitudes of the magnetic moment is $m_{6c} > m_{3b} > m_{18h}$ (Kren et al. 1969). Since the molecular field and the local DOS of Co on each site are different from each other, it is likely that the two MT occur successively on the different sites. The fact that the increase

Table 10
Magnetic properties[a] of the system YCo_3H_x[b]

Compound	Phase	m_{Co} (μ_B/at)	m_{UHF} (μ_B/at)	B_c(IEM) (T)	B_c(s–f) (T)	T_c, T_N (K)
YCo_3	(Parent)	0.65	1.23	60, 82	–	$T_c = 301$
$YCo_3H_{1.0}$	β_1	0	0.87	–	(110)	$T_N = 273$
$YCo_3H_{1.8}$	β_2	0.65	1.16	5, 20	–	$T_c = 237$
$YCo_3H_{3.4}$	γ	0	1.0	–	14	$T_N = 222$
$YCo_3H_{4.0}$	γ	0	1.1	–	29	$T_N = 209$

[a] Quantities: m_{Co}, spontaneous magnetic moment at 4.2 K;
m_{UHF}, ultrahigh field magnetic moment at 110 T (130 T for $YCo_3H_{1.0}$);
B_c(IEM), critical field of IEM from ISF to CSF at 4.2 K;
B_c(s–f), critical field of the spin-flip transition from AF to F at 4.2 K;
T_c, T_N, Curie or Néel temperature.
[b] After Bartashevich et al. (1994a).

of magnetization at the transition at 60 T is about half of the magnetization increase at 82 T suggests that the Co moment on the 3b and 6c sites exhibits metamagnetic transition at 60 T and the Co_{18h} atoms at 82 T. A similar behaviour was reported for $ThCo_5$-based compounds (Givord et al. 1983, see sect. 3.3.1). A theoretical study of the mechanism of this successive MT in YCo_3, however, is still absent.

3.2.2. *The YCo_3H_x system*

The system YCo_3H_x forms two hydride phases: the β-phase ($1.0 \leqslant x \leqslant 1.9$) and the γ-phase ($3.4 \leqslant x \leqslant 4.0$) (Yamaguchi et al. 1985a). A neutron diffraction study indicated that in the β-phase hydrogen fills the interstitial sites in the YCo_2 blocks of the YCo_3 crystal structure (Benham et al. 1989). In the γ-phase, hydrogen begins to occupy interstitial sites in the YCo_5 blocks. Magnetic parameters for the YCo_3H_x system are given in table 10.

The magnetic properties of the YCo_3H_x system are quite sensitive to the concentration x of absorbed hydrogen (Yamaguchi et al. 1985a,b). The β-phase has two modifications: β_1 (or β_L) with $1.0 \leqslant x \leqslant 1.5$, and β_2 (or β_H) with $1.5 \leqslant x \leqslant 1.9$. The parent compound YCo_3 and the β_2-hydride are ferromagnetic with the ground state of ISF, whereas the spontaneous magnetization disappears in the β_1- and γ-hydrides. The magnetization curve of the β_2-hydride, $x = 1.8$, shows a small anomaly at 5 T and a sharp change at 20 T (Bartashevich et al. 1994a,b, see figs. 63 and 64a). These anomalies correspond to the first and the second itinerant MT in YCo_3. Note that the first transition (B_1) is rather difficult to see at low temperature. However, it is pronounced at elevated temperatures. This is due to the existence of uniaxial magnetocrystalline anisotropy which is close to the critical field at low temperature. The critical fields of these two itinerant MT are shown as a function of temperature in fig. 64b. The transitions disappear above about 150 K.

The γ-hydrides are antifferomagnetic (AF). In this phase, a spin-flip transition from AF to F state was observed at critical fields of 14 T and 29 T for $x = 3.4$ and 4.0, respectively

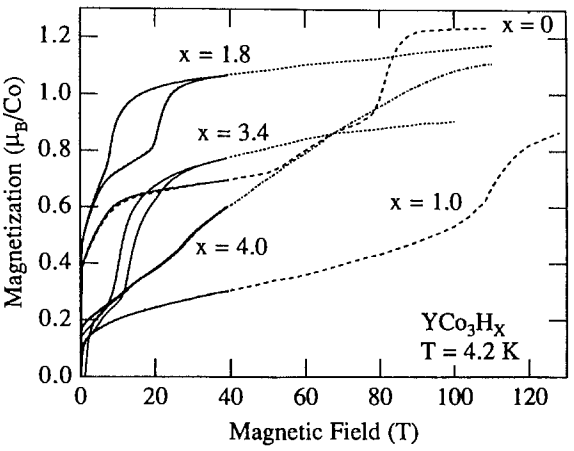

Fig. 63. Magnetization curve in ultrahigh magnetic field for YCo_3H_x at 4.2 K. (After Bartashevich et al. 1994b.)

(see fig. 63). The magnetization of the β_1-hydride ($x = 1.0$, fig. 63) increases linearly above 60 T with increasing field, then shows a pronounced MT at 110 T. The magnetic state is presumed to be AF at the ground state and F at the maximum field of 130 T. The nature of this transition is assumed to be related to an itinerant MT or a spin-flip transition. In the former explanation, the Co spins are considered to become almost parallel to each other owing to spin alignment to the applied field direction just below the critical field. They then undergo the itinerant MT from the lower ISF to the higher ISF states. In the latter explanation, a spin-flip transition probably occurs from the AF state to the ISF state at the critical field.

The additional electrons originating from hydrogen atoms are mostly contained in the metal–hydrogen bonding band. The rest of them occupy the 3d band and upwards to the Fermi level (Yamaguchi et al. 1995). Hydrogen, however, has two effects. Firstly, it is slightly modifies the DOS curve in the β-phase. The two magnetic groups of Co sites (i.e., the 3d, 6c and 18h sites) then still exist and the two itinerant metamagnetic transitions occur in this hydride as in YCo_3. Secondly, it strongly modifies the DOS in the γ-phase and destroys the itinerant MT in this phase. This difference in the modification of the DOS is related to the different site occupation of hydrogen: hydrogen atoms are located on interstitial sites in the YCo_2 blocks for β-phase, whereas they occupy interstitial sites of the YCo_5 blocks for the γ-phase.

3.2.3. *Effects of the 4f–3d exchange interactions*

Due to the effective 4f–3d exchange interactions, the Co atoms in most of the RCo_3 phases are in the strongly ferromagnetic states. The 4f moment is in antiparallel alignment to the Co moment in the heavy lanthanide compounds, whereas they are parallel coupled in the light lanthanide compounds. For the former system, besides the inverse MT of the Co sublattice from the CSF state to the ISF state, one expects also an induced-field transition from the ferrimagnetic collinear structure to noncollinear structure. These do not occur in $GdCo_3$ since the exchange field acting on Co is too large (about 285 T)

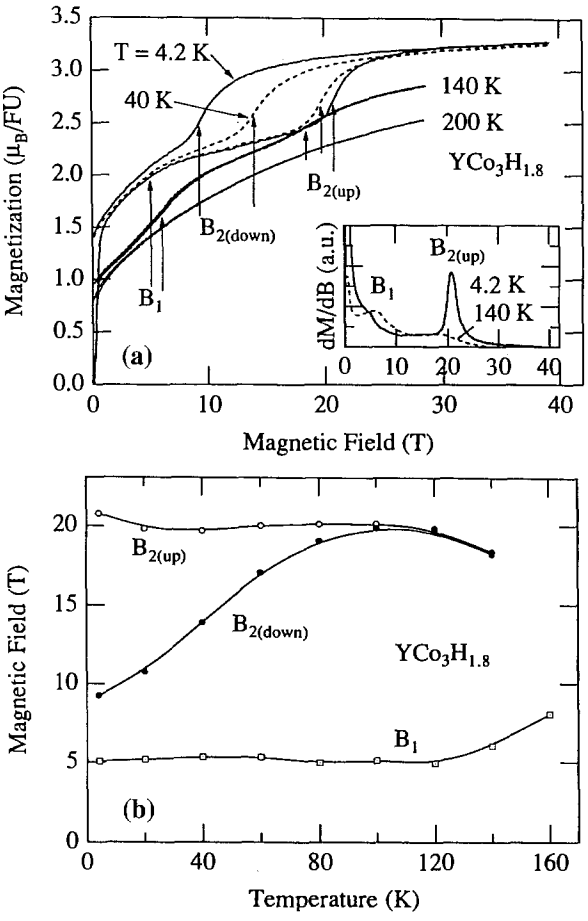

Fig. 64. (a) Magnetization curve in ultrahigh magnetic field for β_2 hydride at different temperatures. The inset shows the dM/dB signal with increasing field at 4.2 K and 140 K. (After Bartashevich et al. 1994a.) (b) Temperature dependence of the first and second MT fields.

(Katori et al. 1994a,b), however, they are observed in $ErCo_3$ and $HoCo_3$ (Goto et al. 1995), see figs. 65 and 66.

$ErCo_3$ is a collinear ferrimagnet with uniaxial anisotropy in the completely magnetically ordered region (Yakinthos and Rossat-Mignod 1972). The high spin moment of Co was estimated to be $1.3\mu_B$/Co. The magnetization along the c-axis exhibits two transitions at 29.5 T and 90 T. The first transition corresponds to the itinerant MT at 82 T in YCo_3: the Co moment in the high-spin state is reduced due to the decrease of the effective field (exchange and external fields) acting on the Co sublattice. No transition corresponding to the MT at 60 T in YCo_3 is clearly observed in $ErCo_3$ since the transition is rather broad. The transition at 90 T is a spin-flip transition of the Co moment towards the direction of the applied field (and the direction of the Er moment). In contrast, the magnetization perpendicular to the c-axis (i.e., along the b-axis), on the other hand, exhibits only a collinear–noncollinear transition at about 3 T and then increases gradually up to 110 T.

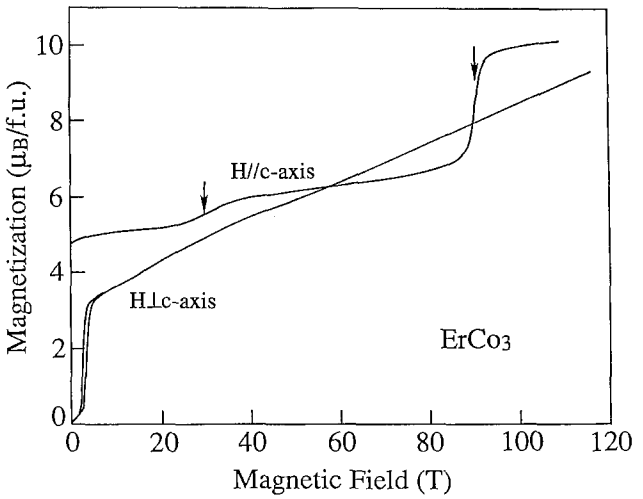

Fig. 65. Magnetization curves at 4.2 K for $ErCo_3$. (After Goto et al. 1995.)

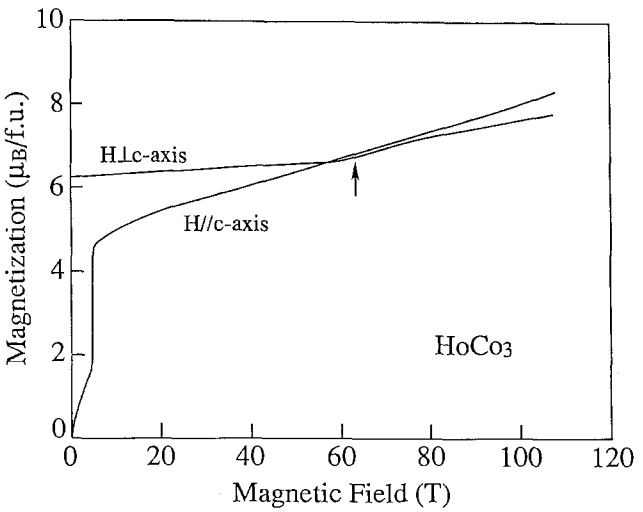

Fig. 66. Magnetization curves at 4.2 K for $HoCo_3$. (After Goto et al. 1995.)

$HoCo_3$ is a collinear ferrimagnet with easy-plane type of anisotropy below 55 K (Shcherbakova and Ermolenko 1982). The magnetization in the basal plane shows an itinerant MT of the Co sublattice at 66 T as in $ErCo_3$ (see fig. 66). Meanwhile, the magnetization along the *c*-axis exhibits a collinear–noncollinear transition at about 5 T.

$TmCo_3$ is considered to be a noncollinear ferromagnet with an easy-cone type of anisotropy below 30 K (Shcherbakova and Ermolenko 1982). The easy direction deviates from the *c*-axis by an angle of 13° at 4.2 K due to the local anisotropy energy of

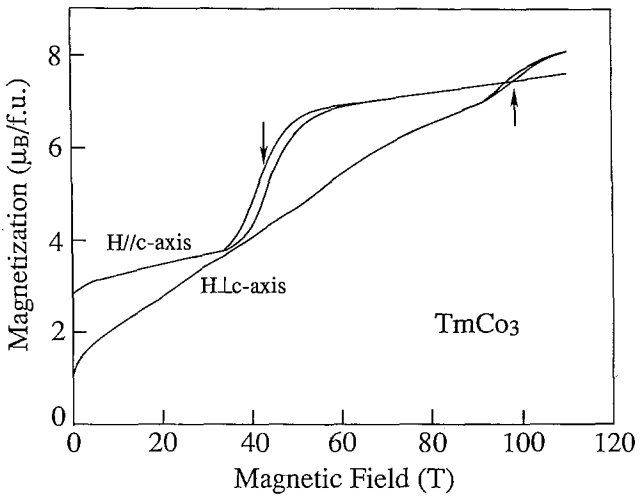

Fig. 67. Magnetization curves at 4.2 K for $TmCo_3$. (After Goto et al. 1995.)

the Tm_{II} ion. In zero field, Co is in the low-spin state with a magnetic moment of $0.76\mu_B$/Co (Ikonomon and Yakinthos 1976). Thus the sharp transition at 43 T observed in the magnetization along the *c*-axis, see fig. 67, cannot be associated with the itinerant MT, but is produced by a flip of the Co moment as in $ErCo_3$ and $HoCo_3$. In this case, however, the spin structure remains noncollinear. On the other hand, the magnetization perpendicular to the *c*-axis increases monotonically and exhibits a broad transition at 99 T. The corresponding magnetization jump is $1.1\mu_B$/f.u. It has been suggested that this transition may be an itinerant MT of the Co sublattice (Goto et al. 1995).

The dependence of the Co-sublattice magnetism on the rare-earth concentration in $Y_{1-t}Gd_tCo_3$ was studied by Katori et al. (1994a,b). Figure 68 presents the Gd-

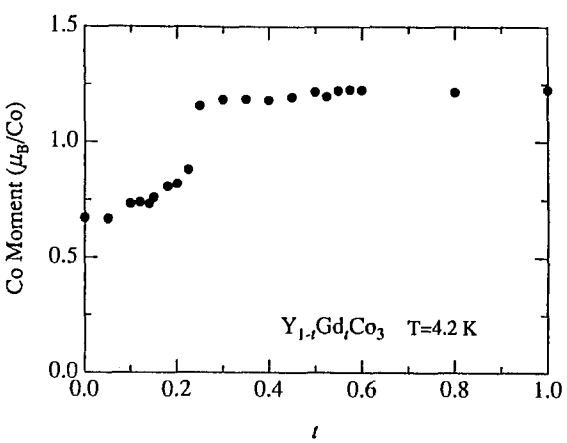

Fig. 68. Gd-concentration dependence of m_{Co} derived from saturation magnetization in $Y_{1-t}Gd_tCo_3$ compounds. (After Katori et al. 1994a.)

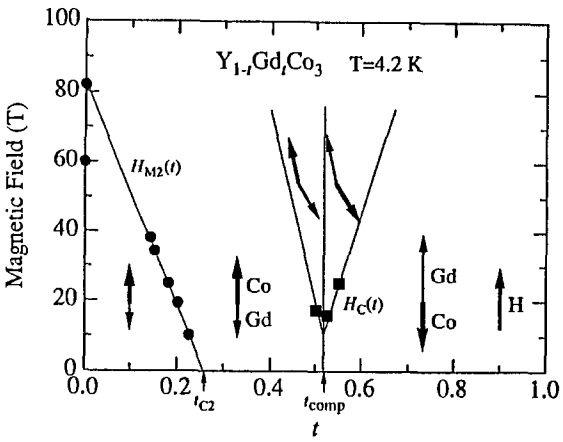

Fig. 69. Magnetic field versus Gd concentration phase diagram in $Y_{1-t}Gd_tCo_3$ compounds. (After Katori et al. 1994a.)

concentration dependence of the spontaneous Co moment. Clearly, the substitution of Gd for Y in YCo_3 leads to enhancement of the Co moment with a step of $0.27\mu_B$/Co at $t_{c2} \approx 0.25$. These results reveal that the second MT of the Co sublattice induced by the magnetic field owing to the molecular field from the Gd sublattice, is stabilized even without an external field for $t > t_{c2}$. The first MT of the Co sublattice, however, cannot be observed in fig. 68. This may be due to the inhomogenous molecular field.

A field versus Gd concentration phase diagram of the $Y_{1-t}Gd_tCo_3$ compounds is summarized in fig. 69. The second MT of the Co sublattice is observed below 40 T for $0.15 \leqslant t \leqslant 0.25$. In this concentration range, $B_{c2}(t)$ decreases linearly with increasing t. At $t > 0.25$, no MT appears. However, the transition from the collinear to the noncollinear structure may occur in these compounds. For the $Y_{1-t}Gd_tCo_3$ compounds, the compensation composition t_c where the total magnetization of the compound becomes zero, i.e., the Co sublattice magnetization equals that of the Gd sublattice, was estimated

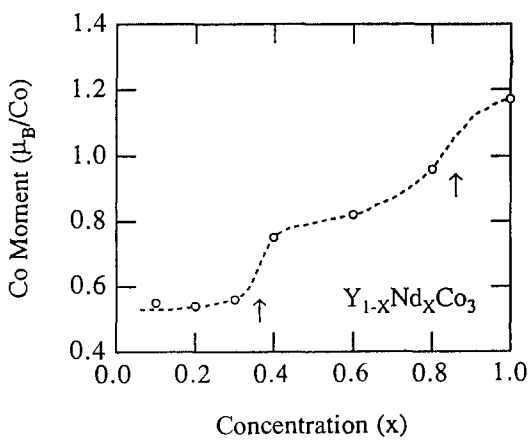

Fig. 70. Nd-concentration dependence of m_{Co} derived from saturation magnetization in $Y_{1-x}Nd_xCo_3$ compounds. (After Goto et al. 1993.)

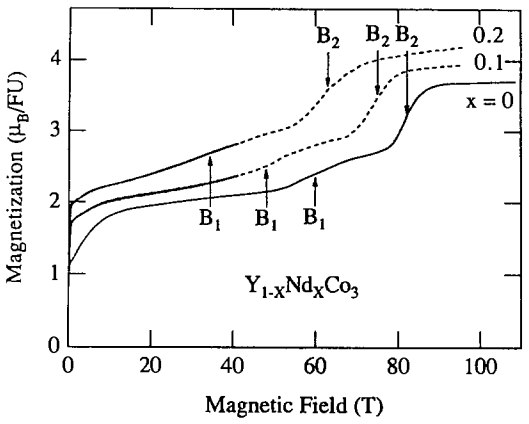

Fig. 71. Magnetization curves for $Y_{1-x}Nd_xCo_3$ compounds. (After Goto et al. 1993.)

to be 0.52. At this concentration the transition field should be zero; however, in practice, it appears at 10 T. In this case, the anisotropy effect of the Co sublattice may be important.

The analysis of the high-field magnetization data is easier in the case of the $Y_{1-x}Nd_xCo_3$ system. Substitution of Nd for Y in YCo_3 leads to enhancement of the spontaneous Co moment M_{Co} from $0.55\mu_B$/Co in YCo_3 to $1.17\mu_B$/Co in $NdCo_3$. The Co moment exhibits a double-step increase as shown in fig. 70 (Goto et al. 1993, Koui et al. 1994) at the critical concentrations $x = 0.35$ and 0.85. This behaviour reflects well the magnetic characteristics of the Co in YCo_3. In an applied magnetic field, the compound exhibits two MT of the Co sublattice to a higher magnetic moment. The magnetization process is illustrated in fig. 71 for $Y_{1-x}Nd_xCo_3$ with $x = 0.0$, 0.1 and 0.2. The critical fields of both transitions decrease linearly with increasing Nd concentration, see fig. 72. The values of these transition fields were used to estimate the strength of the 4f–3d exchange

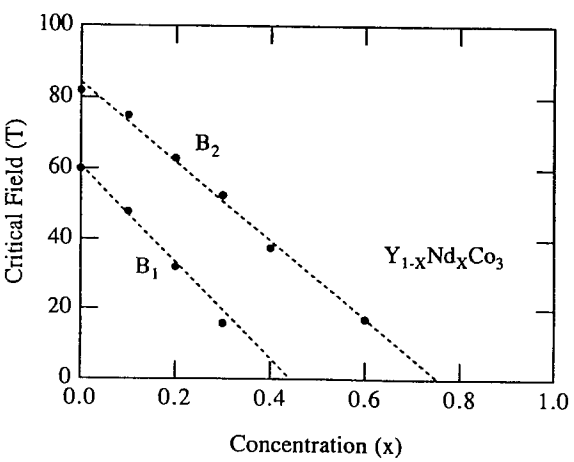

Fig. 72. The concentration dependence of the first and second MT fields for $Y_{1-x}Nd_xCo_3$ compounds. (After Goto et al. 1993.)

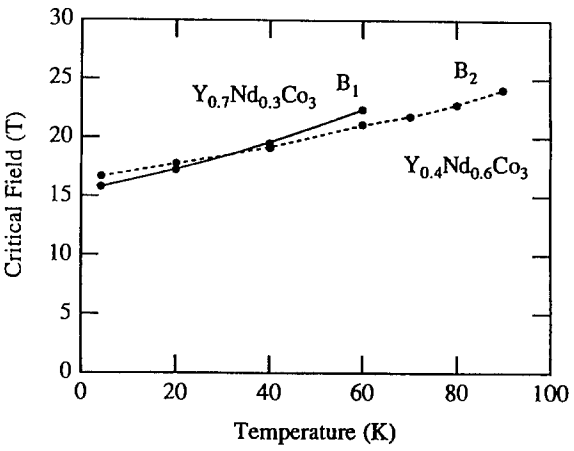

Fig. 73. Temperature dependence of the MT fields for $Y_{1-x}Nd_xCo_3$ compounds with $x=0.3$ (curve B_1) and $x=0.6$ (curve B_2). (After Goto et al. 1993.)

interactions. With increasing temperature, the critical MT fields increase. However, no T^2 dependence was observed (fig. 73).

3.3. *The RCo_5 compounds*

Due to the transfer of 5d electrons contributed by lanthanide to the unfilled 3d band, the 3d–5d hybridization is created for the R–T compounds. The degree of this hybridization increases with increasing R concentration. Beyond a critical concentration of the rare earth, the 3d atoms are no longer magnetic because the DOS at the Fermi level becomes too low. With Co and trivalent rare earths, as mentioned before, the critical concentration is achieved in the RCo_2 compounds. For the system with tetravalent rare-earth atoms, additional electrons shift the ε_F more quickly to the region of higher energy with low DOS. In this case, the critical concentration is close to RCo_5. In practice, whereas Y_2Co_7 and YCo_3 with trivalent yttrium are ferromagnets, no spontaneous magnetization is observed down to 4.2 K in Th_2Co_7, $CeCo_3$, Ce_2Co_7 and Ce_5Co_{17} with tetravalent thorium and cerium (Givord et al. 1983). The susceptibility of these compounds shows a maximum around 160 K, which does not correspond to any magnetic phase transition. Below this temperature, a transition towards a state of higher magnetic moment is induced by an applied field. In $ThCo_5$ and $CeCo_5$ however, the rare-earth concentration is lower, and they exhibit a spontaneous magnetization at room temperature. The onset of 3d magnetism in $ThCo_5$ and $CeCo_5$ occurs through the MT. These compounds crystallize in the hexagonal $CaCu_5$-type structure. Co atoms occupy two sites, Co_{2c} with uniaxial symmetry and Co_{3g} with orthorhombic symmetry. The peculiar behaviour of 3d magnetism in these compounds is associated with the difference of the magnetic properties on different sites. This is described below.

3.3.1. *$ThCo_5$-based compounds*

In the RCo_5 intermetallic compounds, there is an increasing tendency for the heavy lanthanide to form compounds richer in Co: RCo_{5+x}. The off-stoichiometric compounds have been reported for $GdCo_{5.14}$, $TbCo_{5.1}$, $DyCo_{5.2}$, $HoCo_{5.5}$ and $ErCo_6$. The additional Co atoms are located at the lanthanide sites in the form of dumbbell pairs (Schweizer and Tasset 1969). The same tendency occurs for $ThCo_5$ phase. The non-stoichiometric $Th_{1-\delta}Co_{5+2\delta}$ compounds exist within a homogeneity range running from $ThCo_5$ up to $Th_{0.92}Co_{5.16}$. Magnetic properties strongly depend on the substitution rate δ. The Curie temperature increases with increasing δ from 410 K for $ThCo_5$ up to 730 K for $Th_{0.92}Co_{5.16}$ (van der Goot and Buschow 1971). The magnetic behaviour of Co also depends on δ: whereas in the stoichiometic $ThCo_5$ compound the Co magnetism remains in the low magnetic state and the MT is not accessed experimentally, in $Th_{0.95}Co_{5.10}$ the Co magnetism is already in the high magnetic state at zero applied field (Givord et al. 1983, see fig. 74c). In the Co-poor compounds, the temperature dependence of the spontaneous magnetization and that of the superimposed susceptibility show a maximum near 200 K (Ganapathy et al. 1974). Below 100 K, a transition towards a state of higher magnetization is induced by a larger applied field (fig. 74a). Polarized neutron diffraction studies indicate that in the low-magnetic state the magnetization density is lower by about 20% on Co_{3g} atoms than on Co_{2c} ones, i.e. $m(Co_{2c}) = 1.21\mu_B/Co$ and $m(Co_{3g}) = 0.96\mu_B/Co$ for the $Th_{0.965}Co_{5.07}$ compound, whereas the magnetization densities on both Co sites are the same, $m(Co_{2c}) = m(Co_{3g}) = 1.58\mu_B/Co$, for the $Th_{0.95}Co_{5.10}$ compound (Givord et al. 1977, 1979). The magnetic behaviour at finite temperature also originates from the Co_{3g} atoms. These atoms exhibit metamagnetic behaviour analogous to those observed in Y(Lu)Co_2. The critical field in the present case, however, can be reached either by an applied magnetic field in the Co-poor compounds (figs. 74a,b) or by an increase of the exchange field on the Co_{3g} atoms in the Co-rich compounds caused by statistical substitution of Co dumbbells for Th atoms (fig. 74c). The effect of the decrease of the internal field can be observed in the temperature dependence of the spontaneous magnetization of the $Th_{1-\delta}Co_{5+2\delta}$ compounds. Since the magnetization of the 2c subsystem decreases as temperature increases, at some temperature in the compounds with $\delta = 0.04$ and 0.05, the Co_{2c}-exchange field acting on the 3g subsystem becomes less than B_c. This leads to a transition of the 3g subsystem into the paramagnetic state with a jump-like decrease in the magnetization. The discontinuity in the 3d-band splitting associated with metamagnetism in these compounds results also in an additional volume anomaly. At T_c, it reaches 7% and essentially affects the c-axis parameter which only depends on Co_{2c}–Co_{3g} distance.

The schematic field and temperature dependence of the spontaneous magnetization and of the superimposed susceptibility of Co_{2c} and Co_{3g} atoms in $ThCo_5$ compounds are presented in fig. 75 (Givord et al. 1983). The spontaneous magnetization is contributed by ferromagnetic Co_{2c} atoms. The Co_{3g} atoms are enhanced paramagnetic and are close to the conditions of the itinerant electron metamagnetism. Susceptibility shows a maximum around 200 K and the critical field of the MT is about 50 T. This field is almost the same

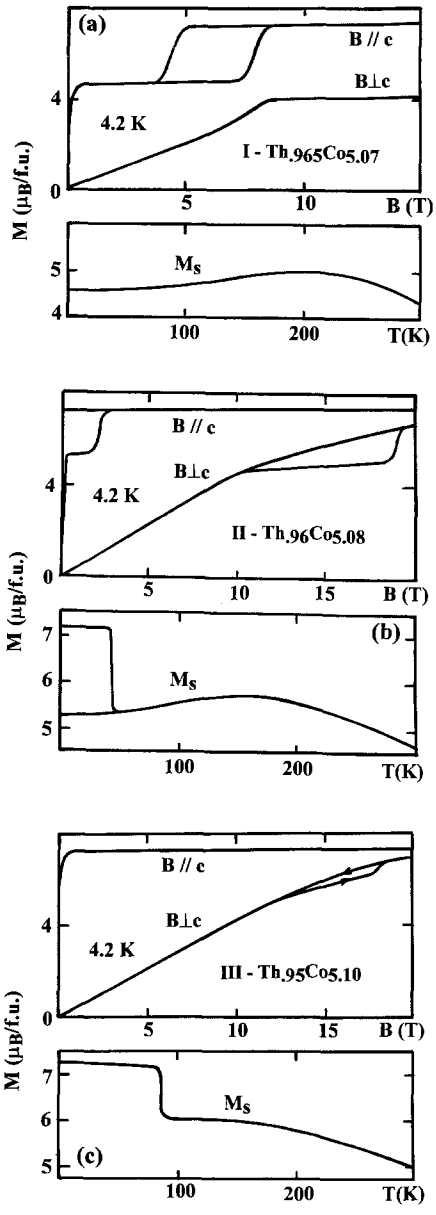

Fig. 74. Field variation of magnetization at 4.2 K and temperature dependence of the spontaneous magnetization up to 300 K for three $Th_{1-\delta}Co_{5+2\delta}$ compounds. (After Givord et al. 1983.)

order of magnitude as the Co_{2c}-exchange field in $Th_{0.96}Co_{5.08}$. For these compounds, the MT takes place in an applied field of 2 T with a rather large hysteresis. It should also be noted that there is a large anisotropy of the critical metamagnetic field along different

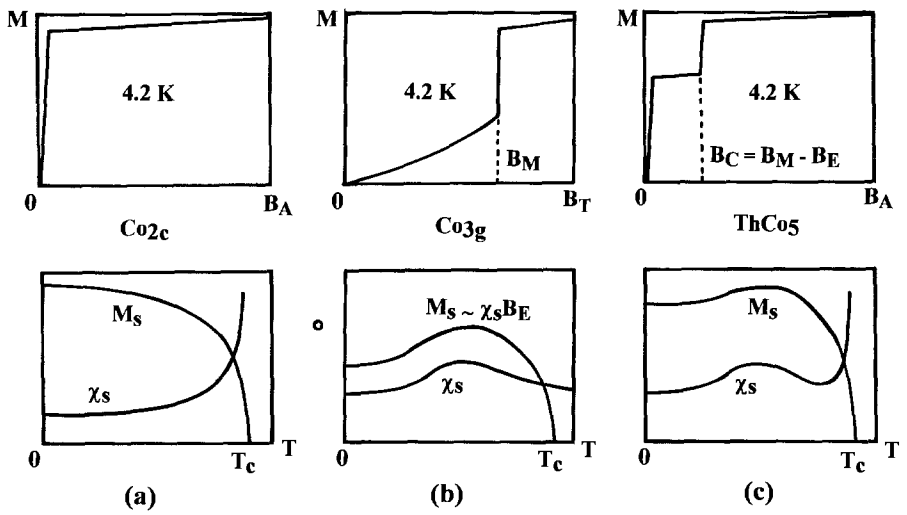

Fig. 75. Schematic field and temperature dependences of the spontaneous magnetization M_s and of the superimposed susceptibility χ_s of (a) Co_{2c} atoms and (b) Co_{3g} atoms in (c) $ThCo_5$. Abbreviations: B_A, applied magnetic field; B_E, exchange field on the Co_{3g} atoms due to the Co_{2c}; $B_T = B_A + B_E$, the total field acting on Co_{3g} atoms; B_M, critical field for metamagnetism for Co_{3g} atoms; B_C, experimental transition field in $ThCo_5$. (After Givord et al. 1983.)

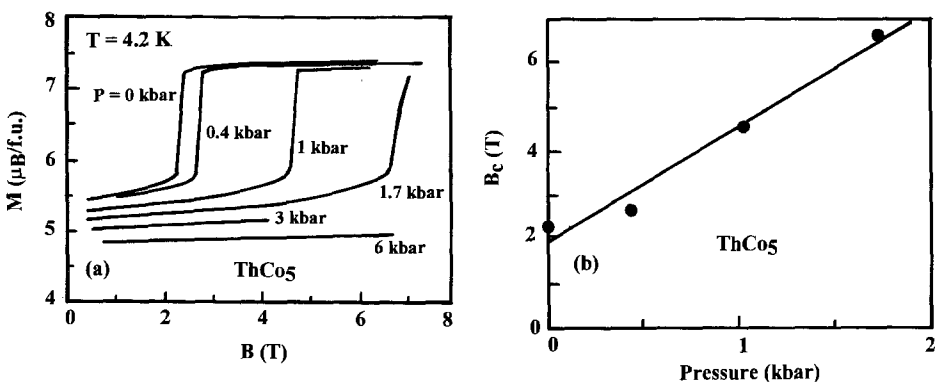

Fig. 76. (a) Magnetization curves measured at 4.2 K along the *c*-axis by increasing field at various pressures. (b) Pressure dependence of B_c at 4.2 K in $ThCo_5$. (After Ballou et al. 1990.)

directions (see fig. 74b). The strong increase of B_c in the direction of the difficult direction is linked with the significant magnetic anisotropy in the Co_{3g} sublattice.

The magnetization measurements under pressure have been carried out for single crystalline $ThCo_5$ by Ballou et al. (1990). The magnetization curves are presented in fig. 76a. Large effects of pressure on magnetization are obtained in the low magnetic state whereas relatively small effects are observed in the high magnetic state. Additionally, B_c is found to increase linearly with pressure at a rate of 2.8 T/kbar (see fig. 76b). Ballou

et al. described the obtained results by making use of a very simple model for the volume dependence of the DOS and the molecular field coefficient. It supports the itinerant electron metamagnetic character in $ThCo_5$.

3.3.2. *$CeCo_5$-based compounds*

$CeCo_5$ is a ferromagnet with large uniaxial anisotropy which belongs to a famous family of permanent magnet materials. Mixed-valence properties have been reported in this compound on the basis of NMR experiments by Yoshie and Nakamura (1988). The tetravalent ion does not carry a magnetic moment and does not contribute to anisotropy. A significant amount of Ce^{4+} ions in $CeCo_5$ has been observed by L_3 X-ray absorption spectroscopy (Croft et al. 1987). Recent electronic structure calculations for $CeCo_5$ suggest that the 4f state of Ce is itinerant (Nordström et al. 1990). However, the anisotropy energy of $10\,MJ\,m^{-3}$ reported by Ermolenko (1979) and Andreev et al. (1985) indicates that some Ce ions are in the trivalent state.

Within the homogeneity range, all the Co atoms in $CeCo_5$ are in the high moment state with a moment of $1.42\mu_B$/Co (Yermolenko and Shcherbakova 1980, Ermolenko et al. 1977, Bartashevich et al. 1994b). The substitution of Ni for Co supplies excess electrons in the d-band. This leads to the appearance of the low moment state due to the decrease in the density of states at the Fermi level and in the exchange field acting on the Co sublattice in the $Ce(Co_{1-x}Ni_x)_5$ with $x \geqslant 0.075$. A MT to the high magnetic moment state has been observed in the oriented powder $Ce(Co_{0.925}Ni_{0.0075})_5$ sample (Givord et al. 1983). High field magnetization studies on single-crystalline samples indicate also that a MT for $Ce(Co_{0.9}Ni_{0.1})_5$, see fig. 77 (Bartashevich et al. 1996), occurs at $B_c = 21$ T applied along the (easy) c-axis, whereas the critical field of the transition along the hard direction is estimated to be about 47 T. The spontaneous magnetization of this compound as a function of temperature exhibits a broad maximum around 200 K and the critical field of the transition increases monotonically with temperature (see figs. 78 and 79). This

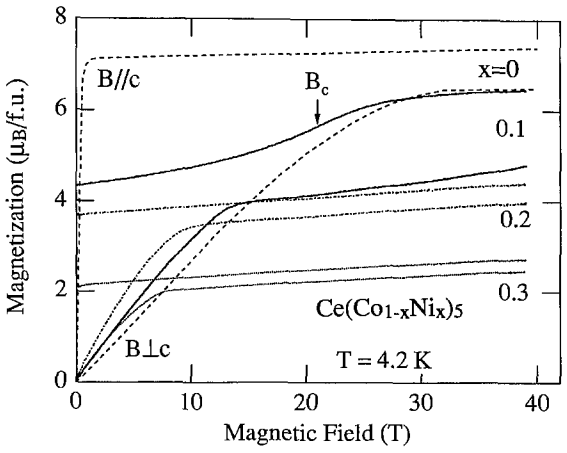

Fig. 77. Magnetization curves of single crystalline $Ce(Co_{1-x}Ni_x)_5$ along the c-axis and in the basal plane. The arrow indicates a MT point. (After Bartashevich et al. 1996.)

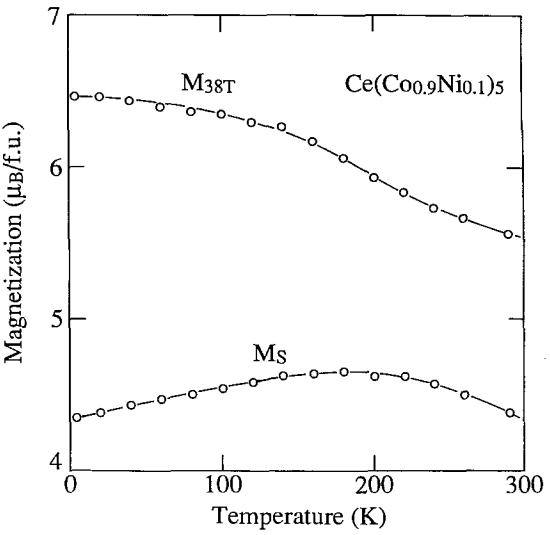

Fig. 78. Temperature dependence of the spontaneous magnetization M_s and the magnetization M_{38T} for $Ce(Co_{0.9}Ni_{0.1})_5$, at $B = 38$ T. (After Bartashevich et al. 1996.)

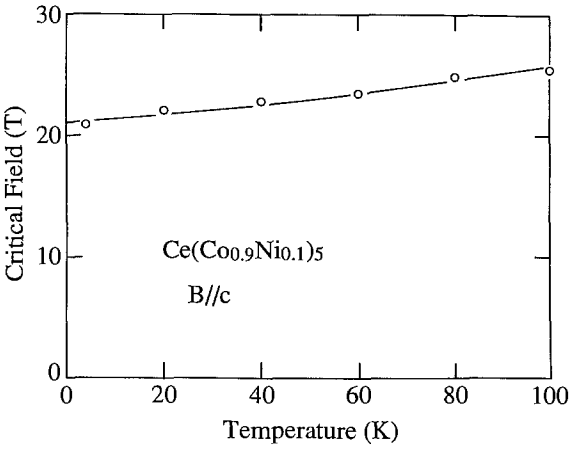

Fig. 79. Temperature dependence of B_c for the MT along the c-axis for $Ce(Co_{0.9}Ni_{0.1})_5$. (After Bartashevich et al. 1996.)

metamagnetic behaviour is similar to that of the $Th_{0.965}Co_{5.07}$ compound (see above). It was suggested that in the metamagnetic $Ce(Co,Ni)_5$ compounds, the Co atom on the 2c site behaves ferromagnetically. The application of a magnetic field changes the paramagnetic Co on the 3g site to ferromagnetic and the Co moments on both sites increase to the same value of $1.42\mu_B$/Co in the high-moment state. If the Ni atoms are randomly substituted for Co atoms on the 2c and 3g sites, one obtains for the magnetic moments in the low-moment state of the Co atom the values $m(Co_{2c}) = 1.10\mu_B$/Co at the 2c site and $m(Co_{3g}) = 0.88\mu_B$/Co at the 3g site. However, the Ni atoms are considered to occupy preferentially the 2c sites (Elemans and Buschow 1976). This corresponds to the

magnetic moment of $m(Co_{2c}) = 1.12\mu_B/Co$ and at the 3g site, $m(Co_{3g}) = 0.89\mu_B/Co$ in the state of low magnetization.

4. Summary and perspectives

The phenomenon of itinerant-electron metamagnetism – the subject of this chapter – has been studied intensively since the prediction by Wohlfarth and Rhodes 1962. Crucial advances, however, were obtained mainly in the last decade. Attention has been paid not only on the observations of the MT in many series of the RCo_2, RCo_3 and RCo_5-based compounds, but also on the general relationships between the characteristic parameters of the nearly ferromagnets. The current situation indicates that the jump-like change in the magnetic ground state due to the MT of an itinerant-electron system in an external field or pressure may be described by several approaches, however, a description of the thermal effects of itinerant-electron magnetism is complete only when the collective modes of spin fluctuations are taken into account. In order to confirm the mechanism, it is necessary to have the right information about the nature of the magnetic states. For this purpose, besides the magnetic measurements one needs other additional experiments. Among those, calorimetric and magnetoresistance measurements are useful because they allow one to detect the quenching of spin fluctuations. Such studies have been performed on the RCo_2-based compounds, and the MT in these compounds can be described as a transition from the "low-spin state" (or "spin fluctuation state") to the "high-spin state" (or "strongly ferromagnetic state"). For the compounds based on RCo_3 and RCo_5, unfortunately, these kinds of data are still lacking.

Important theoretical developments have also been obtained for metamagnetism in multisublattice magnets. However, these improvements have been performed for multisublattice materials with different localized spin subsystems and a single subsystem of the itinerant electrons. Again, this is only the case of the Laves phase compounds but is not the case of the Co-rich compounds. In order to solve this problem, the band calculations are needed which can describe separately the magnetic behaviour for each d subsystem.

Finally, the multisublattice magnets with one (or several) unstable magnetic sublattice can exhibit a field induced multi-magnetic phase transition with different natures. Such a magnetization process gives the possibility of obtaining a good knowledge not only of the IEM, but also of the exchange coupling constant and the crystalline-field parameters.

Acknowledgments

One of the authors (N.H.D) is grateful to Prof. Dr. T.D. Hien, Prof. Dr. J.J.M. Franse, Dr. P.E. Brommer and all colleagues at the Cryogenic Laboratory for collaboration and discussion over a number of years. The other author thanks Prof. T. Sakakibara, Prof. K. Fukamichi, Prof. M. Yamaguchi, Dr. M.I. Bartashevich and Dr. H. Aruga-Kotory for useful discussion and cooperation throughout this research.

References

Acker, F., Z. Fisk, J.L. Smith and C.Y. Huang, 1981, J. Magn. Magn. Mater. **22**, 250.

Aleksandryan, V.V., K.P. Belop, R.Z. Levitin, A.S. Markosyan and V.V. Snegirev, 1984a, JETP Lett. **40**, 815.

Aleksandryan, V.V., N.V. Baranov, A.I. Kozlop and A.S. Markosyan, 1984b, Fiz. Met. Metalloved. **66**, 714.

Aleksandryan, V.V., A.S. Lagutin, R.Z. Levitin, A.S. Markosyan and V.V. Snegirev, 1985, Zh. Eksp. Teor. Fiz. **89**, 271 [Sov. Phys. JETP **62**, 153].

Andreev, A.V., A.V. Deryagin, S.M. Zadvorkin and G.M. Kvashnin, 1985, Sov. Phys.-Solid State **27**(10), 1905.

Aoki, M., and H. Yamada, 1992, Physica B **177**, 259.

Armitage, J.G.M., I.R.G. Graham, P.C. Riedi and J.S. Abell, 1990, J. Phys.: Condens. Matter **2**, 8779.

Ballou, R., M. Shimizu and J. Voiron, 1990, J. Magn. Magn. Mater. **84**, 23.

Ballou, R., Z.M. Gamishidze, R. Lemaire, R.Z. Levitin, A.S. Markosyan and V.V. Snegirev, 1993, Sov. Phys. JETP **75**, 1041.

Bartashevich, M.I., H.A. Katori, T. Goto, I. Yamamoto and M. Yamaguchi, 1994a, Physica B **201**, 135.

Bartashevich, M.I., T. Goto, R.J. Radwanski and A.V. Korolyov, 1994b, J. Magn. Magn. Mater. **131**, 61.

Bartashevich, M.I., T. Goto, A.V. Korolyov and A.S. Ermolenko, 1996, J. Magn. Magn. Mater. **163**, 199.

Béal-Monod, M.T., 1982, Physica B **109–110**, 1837.

Béal-Monod, M.T., and J.M. Lawrence, 1980, Phys. Rev. B **21**, 5400.

Benham, M.J., S.M. Bennington, D.K. Ross, D. Noreus and M. Yamaguchi, 1989, Z. Phys. Chem. N.F. **163**, 283.

Berk, N., and J.R. Schrieffer, 1966, Phys. Rev. Lett. **17**, 433.

Berthier, Y., D. Gignoux, R. Kuentzler and A. Tari, 1986, J. Magn. Magn. Mater. **54–57**, 479.

Bloch, D., and R. Lemaire, 1970, Phys. Rev. B **2**, 2648.

Bloch, D., D.L. Camphausen, J. Voiron, J.B. Aasse, A. Berton and J. Chaussy, 1972, C.R. Acad. Sci. Paris **275**, 601.

Bloch, D., D.M. Edwards, M. Shimizu and J. Voiron, 1975, J. Phys. F **5**, 1217.

Brommer, P.E., 1989, Physica B **154**, 197.

Brommer, P.E., I.S. Dubenko, J.J.M. Franse, R.Z. Levitin, A.S. Markosyan, R.J. Radwanski, V.V. Snegirev and A.Yu. Solokov, 1993, Physica B **183**, 363.

Brommer, P.E., I.S. Dubenko, J.J.M. Franse, F. Kayzel, N.P. Kolmakova, R.Z. Levitin, A.S. Markosyan and A.Yu. Sokolov, 1994, Physica A **189**, 253.

Brooks, M.S.S., and B. Johansson, 1993, in: Ferromagnetic Materials, Vol. 7, ed. K.H.J. Buschow (North-Holland, Amsterdam) p. 139.

Burzo, E., and R. Lemaire, 1992, Solid State Commun. **84**, 1145.

Burzo, E., E. Gratz and V. Pop, 1994, J. Magn. Magn. Mater. **123**, 159.

Buschow, K.H.J., 1980, in: Ferromagnetic Materials, Vol. 1, ed. E.P. Wohlfarth (North-Holland, Amsterdam) p. 297.

Campbell, I.A., 1972, J. Phys. F **2**, L47.

Croft, M., R. Neifield, B. Qi, G. Liang, I. Perez, S. Gunapala, F. Lu, S.A. Shaheen, E.G. Spencer, N. Stoffel and M. den Boer, 1987, in: 5th Conf. on Valence Fluctuations, eds S.K. Malik and L.C. Gupta (Plenum Press, New York) p. 217.

Cuong, T.D., L. Havela, V. Sechovski, A.V. Andreev, Z. Arnol, J. Kamard and N.H. Duc, 1997, J. Alloys & Compounds **262**, 141.

Cuong, T.D., L. Havela, V. Sechovski, Z. Arnol, J. Kamard and N.H. Duc, 1998a, J. Magn. Magn. Mater. **179–181**, 597.

Cuong, T.D., N.H. Duc, P.E. Brommer, Z. Arnol, J. Kamard and V. Sechovski, 1998b, J. Magn. Magn. Mater. **182**, 143.

Cyrot, M., and M. Lavagna, 1979, J. Phys. (Paris) **40**, 763.

de Châtel, P.F., and F.R. de Boer, 1970, Physica B **48**, 331.

Doniach, S., 1967, Proc. Phys. Soc. **91**, 86.

Doniach, S., and S. Engelsberg, 1966, Phys. Rev. Lett. **17**, 750.

Dubenko, I.S., R.Z. Levitin and A.S. Markosyan, 1992, J. Magn. Magn. Mater. **111**, 146.

Dubenko, I.S., R.Z. Levitin, A.S. Markosyan, V.V. Snegirev and A.Yu. Sokolov, 1994, J. Magn. Magn. Mater. **135**, 326.

Dubenko, I.S., N.P. Kolmakova, R.Z. Levitin, A.S. Markosyan and A.K. Zvezdin, 1996, J. Magn. Magn. Mater. **153**, 207.

Duc, N.H., 1994, J. Magn. Magn. Mater. **131**, 224.

Duc, N.H., 1996, J. Magn. Magn. Mater. **152**, 219.

Duc, N.H., 1997, in: Handbook on the Physics and Chemistry of Rare Earths, Vol. 24, eds K.A. Gschneidner Jr and L. Eyring (North-Holland, Amsterdam) ch. 163, p. 339.

Duc, N.H., 1999, to be published.

Duc, N.H., and P.E. Brommer, 1999, in: Ferromagnetic Materials, ed. K.H.J. Buschow (North-Holland, Amsterdam) in press.

Duc, N.H., and D. Givord, 1995, J. Magn. Magn. Mater. **151**, L13.

Duc, N.H., and T.K. Oanh, 1997, J. Phys.: Condens. Matter **9**, 1585.

Duc, N.H., and L.T. Tai, 1993, Phys. Status Solidi (a) **141**, K103.

Duc, N.H., T.D. Hien and J.J.M. Franse, 1985, Acta Phys. Polon. A **68**, 127.

Duc, N.H., T.D. Hien, P.E. Brommer and J.J.M. Franse, 1988a, J. Phys. F **18**, 275.

Duc, N.H., T.D. Hien and N.H. Chau, 1988b, Acta Phys. Pol. A **74**, 51.

Duc, N.H., T.D. Hien, P.E. Brommer and J.J.M. Franse, 1988c, Physica B **149**, 352.

Duc, N.H., T.D. Hien, P.P. Mai, N.H.K. Ngan, N.H. Sinh, P.E. Brommer and J.J.M. Franse, 1989, Physica B **160**, 199.

Duc, N.H., T.D. Hien, P.P. Mai and P.E. Brommer, 1991, Physica B **172**, 339.

Duc, N.H., T.D. Hien, P.E. Brommer and J.J.M. Franse, 1992a, J. Magn. Magn. Mater. **104–107**, 1252.

Duc, N.H., D. Givord, C. Lacroix and C. Pinettes, 1992b, Europhys. Lett. **20**, 47.

Duc, N.H., L.T. Tai, X. Li, F.R. de Boer and T. Goto, 1992c, Proc. Int. Conf. on the Physics of Magnetic Materials, Beijing, p. 11.

Duc, N.H., T.D. Hien, R.Z. Levitin, A.S. Markosyan, P.E. Brommer and J.J.M. Franse, 1992d, Physica B **176**, 232.

Duc, N.H., J. Voiron, S. Holtmeier, P. Haen and X. Li, 1993a, J. Magn. Magn. Mater. **125**, 323.

Duc, N.H., P.E. Brommer and J.J.M. Franse, 1993b, Physica B **191**, 239.

Duc, N.H., T.D. Hien, D. Givord, J.J.M. Franse and F.R. de Boer, 1993c, J. Magn. Magn. Mater. **124**, 305.

Duc, N.H., T.D. Hien, M.I. Bartashevich and T. Goto, 1994, Proc. 1st Magneto-Electronics Int. Symp., Nagano, Japan (Shishu University Press, Japan) pp. 363–366.

Duc, N.H., P.E. Brommer, F.R. Kayzel, C.V. Thang and J.J.M. Franse, 1995a, in: Proc. Int. Workshop on Materials Science, Hanoi, eds F.F. Bekker, N.D. Chien, J.J.M. Franse and T.D. Hien, p. 137.

Duc, N.H., P.E. Brommer, X. Li, F.R. de Boer and J.J.M. Franse, 1995b, Physica B **212**, 83.

Edwards, D.M., and E.P. Wohlfarth, 1968, Proc. R. Soc. A **303**, 127.

Elemans, J.B.A.A., and K.H.J. Buschow, 1976, Phys. Status Solidi (a) **34**, 35.

Endo, K., M. Iijima, A. Shinogi, T. Goto and T. Sakakibara, 1988, J. Phys. Colloq. (Paris) **49**, 265.

Ermolenko, A.S., 1979, IEEE Trans. Mag. **MAG-15**, 1765.

Ermolenko, A.S., A.V. Korolyov and A.F. Rozda, 1977, IEEE Trans. Magn. **Mag-13**, 1339.

Farrell, J., and W.E. Wallace, 1966, Inorg. Chem. **5**, 105.

Franse, J.J.M., and R.J. Radwanski, 1993, in: Ferromagnetic Materials, Vol. 7, ed. K.H.J. Buschow (North-Holland, Amsterdam) p. 307.

Franse, J.J.M., T.D. Hien, N.H.K. Ngan and N.H. Duc, 1983, J. Magn. Magn. Mater. **39**, 275.

Gabelko, I.L., R.Z. Levitin, A.S. Markosyan and V.V. Snegirev, 1987, Pis'ma Zh. Eksp. Teor. Fiz. **45**, 360.

Gabelko, I.L., R.Z. Levitin, A.S. Markosyan, V.I. Silant'ev and V.V. Snegirev, 1991, J. Magn. Magn. Mater. **94**, 287.

Ganapathy, E.V., W.E. Wallace and R.S. Craig, 1974, in: Proc. 11th Rare-Earth Conf., eds J.M. Haschke and H.A. Eick (USAEC, Oak Ridge, TN) p. 430.

Gignoux, D., and F. Givord, 1979, J. Phys. F **9**, 1409.

Gignoux, D., F. Givord and R. Lemaire, 1975, Phys. Rev. B **12**, 3878.

Gignoux, D., F. Givord and W.C. Koehler, 1977a, Physica B **88–86**, 165.

Gignoux, D., F. Givord and J. Schweizer, 1977b, J. Phys. F **7**, 1823.

Gignoux, D., F. Givord, R. Lemaire and N.V. Tinh, 1978, Inst. Phys. Conf. Ser. **37**, 300.

Givord, D., J. Laforest and R. Lemaire, 1977, Physica B **86–88**, 204.

Givord, D., J. Laforest and R. Lemaire, 1979, J. Appl. Phys. **50**, 7489.

Givord, D., J. Laforest, R. Lemaire and Q. Lu, 1983, J. Magn. Magn. Mater. **31–34**, 191.

Givord, F., and R. Lemaire, 1971, Solid State Commun. **9**, 341.

Givord, F., and J.S. Shah, 1972, C.R. Acad. Sci. (Paris) B **274**, 923.

Goto, T., K. Fukamichi, T. Sakakibara and H. Komatsu, 1989, Solid State Commun. **12**, 945.

Goto, T., T. Sakakibara, K. Murata, K. Komatsu and K. Fukamichi, 1990, J. Magn. Magn. Mater. **90–91**, 700.

Goto, T., M. Yamaguchi, T. Kobayashi and I. Yamamoto, 1991, Solid State Phys. **77**, 867.

Goto, T., H.A. Katori, T. Sakakibara and M. Yamaguchi, 1992, Physica B **177**, 225.

Goto, T., K. Koui, M.I. Bartashevich, H.A. Katori, M. Yamaguchi, I. Yamoto and F. Sugaya, 1993, Physica B **193**, 10.

Goto, T., H.A. Katori, T. Sakakibara, H. Mitamura, K. Fukamichi and K. Murata, 1994, J. Appl. Phys. **76**, 6682.

Goto, T., M.I. Bartashevich, H.A. Katori, Ye.V. Shcherbakova and A.S. Yermolenko, 1995, Physica B **211**, 131.

Gratz, E., H. Sassik and H. Nowotny, 1981, J. Phys. F **11**, 429.

Gratz, E., E. Bauer, R. Hausen, M. Maikis, P. Haen and A.S. Markosysan, 1993, Int. J. Mod. Phys. **7**, 366.

Hathaway, K., and J. Cullen, 1991, J. Phys.: Condens. Matter **3**, 8911.

Henry, L.L., L.E. Wenger, G.D. Khattak and A. Tari, 1991, Phys. Rev. B **39**, 5972.

Hien, T.D., N.H. Duc and J.J.M. Franse, 1986, J. Magn. Magn. Mater. **54–57**, 471.

Hilscher, G., N. Pillmayr, C. Schmitzer and E. Gratz, 1988, Phys. Rev. B **37**, 3480.

Iijma, K., K. Endo and G. Kido, 1989, Physica B **155**, 203.

Ikeda, K., K.A. Gschneidner Jr, R.J. Steirman, T.W.E. Tsang and O.D. McMasters, 1984, Phys. Rev. B **29**, 5039.

Ikonomon, P.F., and J.K. Yakinthos, 1976, Z. Phys. B **24**, 77.

Inoue, J., and M. Shimizu, 1982, J. Phys. F **12**, 1811.

Inoue, J., and M. Shimizu, 1985, J. Phys. F **15**, 1511.

Inoue, J., and M. Shimizu, 1988, J. Phys. F **18**, 2487.

Ishiyama, K., K. Endo, T. Sakakibara, T. Goto, K. Sugiyama and M. Date, 1987, J. Phys. Soc. Japan **56**, 29.

Jarlborg, T., and A.J. Freeman, 1981, Phys. Rev. B **23**, 3577.

Katori, H.A., T. Goto, I.Yu. Gaidukova, R.Z. Levitin, A.S. Markosyan, I.S. Dubenko and A.Yu. Sokolov, 1994a, J. Phys.: Condens. Matter **6**, 11119.

Katori, H.A., T. Goto, I.Yu. Gaidukova, R.Z. Levitin, A.S. Markosyan, I.S. Dubenko and A.Yu. Sokolov, 1994b, JETP **79**, 805.

Klimker, H., and M. Rosen, 1976, J. Magn. Magn. Mater. **7**, 367.

Koui, K., M.I. Bartashevich, T. Goto, H.A. Katori and M. Yamaguchi, 1994, Physica B **201**, 143.

Kren, E., J. Schweizer and F. Tasset, 1969, Phys. Rev. B **186**, 479.

Lee, E.W., and F. Pourarian, 1976, Phys. Status Solidi (a) **33**, 483.

Lemaire, R., 1966, Cobalt **33**, 201.

Levitin, R.Z., and A.S. Markosyan, 1988, Sov. Phys. Usp. **31**, 730.

Levitin, R.Z., A.S. Markosyan and V.V. Snegirev, 1984, Phys. Met. Metall. **57**, 274.

Michels, D., J. Tiinlin and T. Mihhlisin, 1990, J. Appl. Phys. **67**, 5289.

Minataka, R., M. Shiga and Y. Nakamura, 1976, J. Phys. Soc. Japan **41**, 1435.

Misawa, S., 1988, Physica B **149**, 162.

Misawa, S., 1995, Physica B **211**, 158.

Moriya, T., 1979, J. Magn. Magn. Mater. **14**, 1.

Moriya, T., 1991, J. Magn. Magn. Mater. **100**, 261.

Moriya, Y., 1985, Spin Fluctuations in Itinerant Electron Magnetism (Springer, Berlin).

Muraoka, Y., M. Shiga and Y. Nakamura, 1977, J. Phys. Soc. Japan **42**, 2067.

Muraoka, Y., M. Shiga and Y. Nakamura, 1979, J. Phys. F **9**, 1889.

Murata, K., K. Fukamichi, H. Komatsu, T. Sakakibara and T. Goto, 1990, Tech. Rep. ISSP Ser. A, No. 2297.

Murata, K., K. Fukamichi, H. Komatsu and T. Goto, 1991, J. Phys.: Condens. Matter **3**, 2515.

Murata, K., K. Fukamichi, T. Sakakibara, T. Goto and H.A. Katori, 1993a, J. Phys.: Condens. Matter **5**, 2583.

Murata, K., K. Fukamichi, T. Sakakibara, T. Goto and K. Suzuki, 1993b, J. Phys.: Condens. Matter **5**, 1525.

Murata, K., K. Fukamichi, T. Goto, H.A. Katori, T. Sakakibara and K. Suzuki, 1994a, Physica B **201**, 147.

Murata, K., K. Fukamichi, T. Goto, K. Suzuki and T. Sakakibara, 1994b, J. Phys.: Condens. Matter **6**, 6659.

Nordström, L., O. Eriksson, M.S.S. Brooks and B. Johansson, 1990, Phys. Rev. B **41**, 9111.

Nordström, L., M.S.S. Brooks and B. Johansson, 1992, J. Magn. Magn. Mater. **104–107**, 1378.

Ohkawa, F.J., 1989, Solid State Commun. **11**, 1767.
Pillmayr, N., G. Hilscher and E. Gratz, 1988, J. Phys. Colloq. (Paris) **49**, 273.
Pillmayr, N., G. Hilscher, M. Forsthuber and K. Yoshimura, 1990, J. Magn. Magn. Mater. **90–91**, 694.
Roeland, L.W., G.J. Cock, F.A. Muller, C.A. Moleman, K.A. McEwen, R.C. Jordan and D.W. Jones, 1975, J. Phys. F **5**, L233.
Sakakibara, T., T. Goto, K. Yoshimura, M. Shiga and Y. Nakamura, 1986, Phys. Lett. A **117**, 243.
Sakakibara, T., T. Goto, Y. Yoshimura, M. Shiga, Y. Nakamura and K. Fukamichi, 1987, J. Magn. Magn. Mater. **70**, 126.
Sakakibara, T., T. Goto and Y. Nishihara, 1988, J. Phys. Colloq. (Paris) **C8**, 263.
Sakakibara, T., T. Goto, K. Yoshimura and K. Fukamichi, 1989, Tech. Rep. ISSP, Univ. Tokyo ser. A, No. 2208.
Sakakibara, T., H. Mitamura and T. Goto, 1992, Physica B **172**, 127.
Sakakibara, T., H. Mitamura and T. Goto, 1994, Physica B **201**, 127.
Schinkel, C.J., 1978, J. Phys. F **8**, L87.
Schinkel, C.J., F.R. de Boer and B. de Horn, 1973, J. Phys. F **3**, 1463.
Schwarz, K., and P. Mohn, 1984, J. Phys. F **14**, L129.
Schweizer, J., and F. Tasset, 1969, J. Less-Common Met. **18**, 245.
Shcherbakova, Y.V., and A.S. Ermolenko, 1982, Phys. Met. Metall. **54**, 53.
Shimizu, M., 1981, Rep. Prog. Phys. **44**, 329.
Shimizu, M., 1982, J. Phys. (Paris) **43**, 155.
Slater, J.C., and G. Koster, 1954, Phys. Rev. **94**, 1498.
Steiner, W., E. Gratz, H. Ortbauer and H.W. Cammen, 1978, J. Phys. F **8**, 1525.
Swift, W.N., and W.E. Wallace, 1968, J. Chem. Phys. **49**, 154.
Takahashi, T., and M. Shimizu, 1965, J. Phys. Soc. Japan **20**, 26.
Takahashi, T., and M. Shimizu, 1966, J. Phys. Soc. Japan **21**, 681.
Tari, A., 1982, J. Magn. Magn. Mater. **30**, 209.
Tari, A., 1987, J. Magn. Magn. Mater. **69**, 247.
van der Goot, A.S., and K.H.J. Buschow, 1971, Phys. Status Solidi (a) **5**, 665.
Voiron, J., 1973, Thesis (Grenoble).
Voiron, J., and D. Bloch, 1971, J. Phys. (Paris) **32**, 949.
Vonsovski, S., 1971, Magnetism (Nauka, Moscow).
Wada, H., K. Yoshimura, G. Kido, M. Shiga, M. Mekata and Y. Nakamura, 1988, Solid State Commun. **65**, 23.
Wada, H., M. Shiga and Y. Nakamura, 1990, J. Magn. Magn. Mater. **90–91**, 727.
Wada, H., T. Mori, M. Shiga, H.A. Katori, M.I. Bartashevich and T. Goto, 1994, Physica B **201**, 139.
Wohlfarth, E.P., and P. Rhodes, 1962, Philos. Mag. **7**, 1817.
Yakinthos, J.K., and J. Rossat-Mignod, 1972, Phys. Status Solidi (b) **50**, 747.
Yamada, H., 1991, J. Phys.: Condens. Matter **3**, 4115.
Yamada, H., 1992, Physica B **177**, 115.
Yamada, H., 1993, Phys. Rev. B **47**, 11211.
Yamada, H., and M. Shimizu, 1985, J. Phys. F **15**, L175.
Yamada, H., J. Inoue, K. Terao, S. Kanda and M. Shimizu, 1984, J. Phys. F **14**, 159.
Yamaguchi, M., H. Ikeda, T. Ohata, T. Katayama and T. Goto, 1985a, J. Less-Common. Met. **106**, 165.
Yamaguchi, M., D.K. Ross, T. Goto and T. Ohta, 1985b, Z. Phys. Chem. N.F. **145**, 101.
Yamaguchi, M., T. Kobayashi, I. Yamamoto and T. Goto, 1991, Solid State Commun. **77**, 871.
Yamaguchi, M., T. Futakata, I. Yamamoto and T. Goto, 1992, J. Magn. Magn. Mater. **104–107**, 731.
Yamaguchi, M., I. Yamamoto, M.I. Bartashevich, H.A. Katori and T. Goto, 1995, J. Alloys & Compounds **231**, 159.
Yermolenko, A.S., and Ye.V. Shcherbakova, 1980, Phys. Met. Metall. **48**, 39.
Yoshie, H., and Y. Nakamura, 1988, J. Phys. Soc. Japan **57**, 3649.
Yoshimura, K., and Y. Nakamura, 1985, Solid State Commun. **56**, 767.
Yoshimura, K., and Y. Nakamura, 1990, J. Magn. Magn. Mater. **90–91**, 697.
Yoshimura, K., S. Harosawa and Y. Nakamura, 1984, J. Phys. Soc. Japan **53**, 2120.
Yoshimura, Y., Y. Yoshimoto, M. Mekata, T. Sakakibara and T. Goto, 1987, J. Magn. Magn. Mater. **70**, 147.

Handbook on the Physics and Chemistry of Rare Earths
Vol. 26
edited by K.A. Gschneidner, Jr. and L. Eyring

Chapter 172

PHOTOELECTRON SPECTROSCOPY IN HEAVY FERMION SYSTEMS: Emphasis on Single Crystals

A.J. ARKO[1], P.S. RISEBOROUGH[2], A.B. ANDREWS[3], J.J. JOYCE[1], A.N. TAHVILDAR-ZADEH[4] and M. JARRELL[4]
[1]*Los Alamos National Laboratories, Los Alamos, NM, USA;*
[2]*Polytechnic University, Brooklyn, NY, USA;* [3]*Brookhaven National Laboratory, Upton, NY, USA;* [4]*University of Cincinnati, Cincinnati, OH, USA*

Contents

List of symbols

$d^{+}_{k,\alpha}$	d electron creation operator
$d_{k,\alpha}$	d electron destruction operator
D	width of the conduction band (also see W)
D_0	Drude weight
D_S	spatial dimension
E_0	energy of the non-interacting Fermi sea of conduction electrons
E_b	energy of a conduction electron state bound to the f hole
E_F	Fermi energy
E_f	bare f level binding energy
$E_{f,l}$	energy of the lower spin–orbit split f multiplet
$E_{f,u}$	energy of the upper spin–orbit split f multiplet
E_g	ground state energy
ΔE_g	hybridization induced binding energy
δE_g	binding energy of the Kondo ground state
δE_h	binding energy of the excited Kondo state
ΔE_{so}	spin–orbit splitting
δE_α	binding energy of the αth crystal field state
$\Delta E(\alpha)$	αth energy splitting of $J_{5/2}$ state due to crystal field
$e(k)$	dispersion relation for the conduction electrons
eV	electron-Volt
f^0	f level binding energy with no f occupancy
f^1	f level binding energy with one f electron occupancy
f^2	f level binding energy with double f electron occupancy
f^{+}_{α}	f electron creation operator
$f^{+}_{\alpha,l}$	electron creation operator for the lower spin–orbit f multiplet
$f^{+}_{\alpha,u}$	electron creation operator for the upper spin–orbit f multiplet
f_α	f electron destruction operator
$f_{\alpha,l}$	electron destruction operator for the lower spin–orbit f multiplet
$f_{\alpha,u}$	electron destruction operator for the upper spin–orbit f multiplet
$G^0(k,\omega)$	non-interacting f electron Green's function
$G^f_{\alpha,\beta}(z)$	f electron Green's function
$g_{m,n}(z)$	matrix elements of the resolvent between states $\langle m\vert$ and $\vert n\rangle$
H	total Hamiltonian
H_f	f-electron Hamiltonian
H_d	d-electron Hamiltonian
H_{fd}	f–d coupling Hamiltonian
h	Planck's constant
$I(\omega)$	calculated photoemission intensity at energy ω
J	antiferromagnetic exchange coupling
$\boldsymbol{k}$	electron momentum
L	Langmuir (exposure to 10^{-6} Torr for one second)
meV	milli-electron-Volts
$N_{\{\alpha\}}$	degeneracy of the $\{\alpha\}$ spin–orbit/crystal field split multiplet which has the single-particle energy, $E_f + \Delta E(\{\alpha\})$.
$N(E)$	density of states
$n(\varepsilon_k)$	electronic distribution function
N_{el}	number of conduction electrons
N_f	degeneracy of the f level
$N_{f,l}$	degeneracy of the lower spin–orbit f multiplet
$N_{f,u}$	degeneracy of the upper spin–orbit f multiplet
N_s	number of lattice sites
n_f	f electron (or hole) occupancy
n_d	filling of the conduction band
$\vert n\rangle$	an arbitrary state taken from a complete set
P	pressure
T^*	coherence scale

T_0	Wilson Kondo scale of the PAM
T_0^{SIM}	Wilson Kondo scale of the SIM
T	absolute temperature
T_{CF}	effective Kondo temperature of crystal field level
T_{F}	Fermi temperature
T_{m}	temperature of specimen during measurement
T_{K}	Kondo temperature
T_{SO}	effective Kondo temperature of spin orbit state
T_{W}	Wick's time
t^*	Gaussian width of the infinite dimensional band
U_{fd}	Coulomb interaction between an f electron and a conduction electron
U_{ff}	Coulomb interaction between a pair of f electrons
V	f–d hybridization (also V_{fd})
$V(\mathrm{k})$	hybridization matrix element
W	width of the conduction band
Z^{-1}	Fermi-liquid stability criterion
Z	quasiparticle weight
z	location of zeroes in the complex plane
α	spin index
$\{\alpha\}$	index of αth spin compensated state
β	spin index
Γ	hybridization width
Γ-point	Brillouin zone center
Δ	hybridization width
Δ_{CF}	energy of crystal field level
Δ_{SO}	spin–orbit splitting
$\Delta_{\mathrm{s,b}}$	surface core level shift
ϵ	energy of electron state (see also ω)
μ	Fermi energy
$\rho(\mu)$	conduction band density of states at the Fermi level
$\Delta\rho(\omega)$	change in the conduction band density of states due to the presence of an f hole
$\rho_{\mathrm{d}}(\omega)$	d-band density of states
$\rho^{\mathrm{f}}(\mu)$	f electron density of states
ρ_{Kondo}	spectral density due to Kondo effect
ρ_{f}	f-component on electron removal/addition spectrum
$\Sigma(k,\omega)$	electronic self energy
$\lvert\Phi_0\rangle$	wave function of the non-interacting Fermi sea of conduction electrons
χ	magnetic susceptibility
$\chi(q,\omega)$	RPA dynamical susceptibility
$\chi^0(q,\omega)$	non-interacting dynamical susceptibility
$\lvert\Psi_{\mathrm{g}}\rangle$	ground state wave function
$\lvert\Psi_\alpha\rangle$	αth crystal field state wave function
ω	energy of electron state
$\aleph$	wave function normalization

Acronyms

ARPES	angle-resolved photoelectron spectroscopy
BIS	bremsstrahlung isochromat spectroscopy (also BIS)
CMA	cylindrical mirror analyzer
dHvA	de Haas–van Alphen effect
DMF	dynamical mean field theory
DOS	density of states
FWHM	full width at half maximum
KR	Kondo resonance
LDA	local density approximation
LEED	low-energy electron diffraction
NCA	non-crossing approximation
NRG	numerical renormalization group
PAM	periodic Anderson model
PES	photoelectron spectroscopy
QMC	quantum Monte Carlo
SIAM	single-impurity Anderson model (same as SIM)
SIM	single-impurity model
SCLS	surface core level shift
UHV	ultra-high vacuum
UPS	ultraviolet photoelectron spectroscopy
XPS	X-ray photoelectron spectroscopy

1. Introduction

The unusual properties of heavy fermion (or heavy electron) materials have sparked an avalanche of research over the last few years in order to understand the basic phenomena responsible for these properties. The reader is referred to numerous review articles, such as Fisk et al. (1995), Grewe and Steglich (1991), Hess et al. (1993), Lawrence and Mills (1991), Ott and Fisk (1987), Stewart (1984), Malterre et al. (1996), Thompson and Lawrence (1994). The term heavy fermion refers to materials (thus far only compounds with elements having an unfilled 4f or 5f shell) whose electronic properties suggest that the conduction electrons have a very heavy effective mass. This is inferred from the linear term in the low-temperature specific heat ($C_p = \gamma T +$ higher-order terms) which often has an upturn at low temperatures and suggests[1] γ-values as large as 1500 mJ/mole K^2. De Haas–van Alphen measurements have confirmed the existence of heavy masses (Springford and Reinders 1988, Lonzarich 1988, Onuki 1993). The quadratic term in the resistivity and the Pauli susceptibility also indicate the existence of a mass enhancement. It is well established that indeed it is the f electrons that are responsible for the unusual properties (Grewe and Steglich 1991).

Magnetic susceptibility measurements, χ, generally yield a Curie–Weiss behavior at high temperatures with a well developed moment (see, for example, Thompson and Lawrence 1994), which would be consistent with a localized behavior of the f electrons. Indeed, the f electrons appear to behave as non-interacting single impurities at elevated temperature, while below some characteristic temperature, usually referred to as the Kondo temperature or T_K, the susceptibility levels off or even decreases. This phenomenon is interpreted as a compensation of the magnetic moment by the ligand conduction electrons that are believed to align anti-parallel to the f electrons to form a singlet state (see, for example, Grewe and Steglich 1991). At still lower temperatures a dramatic drop in the electrical resistivity, ρ, is associated with the formation of a coherent periodic lattice of these compensated f electrons so that the low temperature electronic structure can be consistently interpreted as being due to a band of very heavy mobile fermions. This is often referred to as the Kondo lattice or the Anderson lattice. The concept of a Kondo or Anderson lattice appears to date back to Lawrence et al. (1981), but the reader is referred also to an excellent review of theoretical approaches by Lee et al. (1986).

There is, however, another school of thought that claims that the f electrons form well-defined Bloch states and very narrow bands at all temperatures (Zwicknagl 1992, Liu 1993, Sheng and Cooper 1995). While there is little quarrel with this view at low temperatures, conventional band theory (using the Local Density Approximation, or LDA) is clearly unable to explain the high-temperature properties as well as the very heavy mass. Renormalized band theories (Strange and Newns 1986, Zwicknagl 1992) may yet prove useful, especially those that incorporate physics similar to the Kondo effect and

[1] Some of the first discoveries were by Andres et al. (1975), followed by Steglich et al. (1979), Stewart et al. (1984), and Ott et al. (1983).

its temperature dependence, perturbatively (Steiner et al. 1994, Norman 1985, Norman et al. 1985). However, the success of the Single-Impurity Model (SIM) in explaining macroscopic bulk phenomena suggests a correctness, at least at some level, of the model. The heart of the issue clearly then is the exact role of the f electrons in the formation of the heavy fermion state. In this respect the effect of the periodic lattice is non-negligible. The periodic Anderson model (PAM) has made headway in treating this problem and will be discussed in detail though other periodic models are not yet ruled out.

As stated, the localized approach utilizes the SIM as the starting point. The assumption here is that even in periodic systems (i.e., ordered compounds), where an f electron exists within each unit cell, the f–f overlap is so small that at high temperatures the f electrons can be treated as completely localized impurities in a sea of ligand conduction electrons having a density of states $N(E)$. It is the very slight residual hybridization with $N(E)$ which yields the low temperature behavior as the hybridization energy exceeds $k_B T$. The Gunnarsson–Schönhammer (1985, 1986) approximate solution (we will refer to it as GS) of SIM calculates the particle–hole excitation spectrum and has been hailed as a breakthrough in the understanding of heavy fermion systems. The non-crossing approximation, or NCA, has in addition been able to introduce (Bickers 1987, Bickers et al. 1985, 1987) the effects of temperature, and has recently included (Pruschke and Grewe 1989) the effect of finite f–f Coulomb repulsion, U_{ff}, thus including the possibility of double occupancy of f levels. Without a doubt the GS and NCA approximations are the most comprehensive, as well as the most widely accepted approximations of the particle–hole excitation spectrum in heavy fermions, in the Kondo limit. More recently numerical renormalization group (NRG, Wilson 1975) and Quantum Monte-Carlo (QMC, Hirsch and Fye 1986) approaches have been extended to treat dynamics (Oliveira and Wilkins 1981, Silver et al. 1990, Jarrell and Gubernatis 1996). A universal behavior for the f electron DOS comes out of these approximate solutions, the core of which is the prediction of scaling with T_K.

Photoelectron spectroscopy (often referred to as PES in the following sections), the most direct measurement of the electronic structure of a material, should in principle be able to shed considerable light on this matter. In general the distinction between a localized and a band-like state is trivially observed in band dispersion. However, in the case of heavy fermions such distinctions pose a serious problem since any dispersion of an f band within the coherent state is expected to be of the order of T_K which is generally far below the resolution of present day apparatus. Nonetheless, PES measurements on heavy fermions have been abundant (for a review of some of the early work on polycrystals see Allen et al. 1986, Allen 1992), owing to the very specific predictions of the GS and NCA approximations regarding the width, position, spectral weight, and temperature dependence of the f-electron DOS, which lends itself readily to a photoemission measurement.

Much of the past work was performed on polycrystalline samples, scraped in situ to expose a clean surface for PES. Further, despite the fact that the features studied were at least an order of magnitude narrower than the then-available experimental resolution (or perhaps because of it), good agreement with the GS approximation was often reported

(Patthey et al. 1985, 1986, 1987a,b, 1990, Malterre et al. 1992a,b, Tjeng et al. 1993, Kang et al. 1990b, Allen et al. 1986, Liu et al. 1992a, Weibel et al. 1993). There have since been considerable advances both in the quality of specimens as well as experimental resolution, which raise questions regarding these conclusions. Much of the past work on polycrystalline samples has been reported in several review articles, most notably by Allen et al. (1986) and Allen (1992), and it is not necessary here to review those efforts again, with the exception of subsequent work performed at high resolution. The primary focus of the present review will be on new measurements obtained on single crystals, cleaved or prepared in situ and measured at high resolution, which seem to suggest (Joyce et al. 1992a–c, 1993, 1994a,b, 1996, Joyce and Arko 1993, Arko et al. 1993, 1994, 1996, 1997a,b, 1998, Andrews et al. 1994, 1995a,b, 1996, Blyth et al. 1992, 1993) that agreement with the GS and NCA approximations is less than perfect, and that perhaps the starting models need to be modified, or that even an entirely new approach is called for. Of the promising new models the Periodic Anderson Model is most closely related to the SIM. Indeed, at high temperatures it reverts to the SIM. However, the charge polaron model of Liu (1997) as well as the two-electron band model of Sheng and Cooper (1995) cannot yet be ruled out.

Inasmuch as the bulk of the single-crystal work was performed by our own Los Alamos group (Andrews et al. 1995a,b, 1996, Joyce et al. 1996), this review will draw heavily on those results. Moreover, since the GS and NCA approximations represent the most comprehensive and widely accepted treatment of heavy-fermion PES, it is only natural that we primarily concern ourselves with analysis of PES data in terms of these models, in order to thoroughly test their validity in light of the new data. We also make qualitative comparisons with newly developed lattice model calculations though these are not yet available for real systems. Perhaps an advance apology is in order for any possible lapses in objectivity.

In the following sections we will first thoroughly review the theoretical aspects of SIM and its calculational approximations GS, NCA, as well as various screening models and new pairing approaches. This will be followed by a summary of NCA predictions for PES. We will then discuss recent calculations of the periodic Anderson model and its application to photoemission. Briefly we will look at the more recent published data on polycrystalline samples (with emphasis on high-resolution results) which suggests agreement with GS. We will then review the single-crystal data, both on Ce and Yb compounds, and test for the applicability of SIM in periodic systems. This is followed by a discussion of data that suggests that at least in Ce compounds the 4f states form very narrow, weakly temperature dependent bands, not inconsistent with the PAM. Finally we will also consider heavy fermions within the 5f series of elements (primarily U) and emphasize the similarities with and differences from the 4f series. We will see that there exists significant dispersion of the 5f bands in uranium compounds, and that the similarity to 4f systems strongly suggests a similar electronic structure in both types of materials. Also, please note that in most figures the x-axis is simply labeled "Binding Energy" although a more correct labeling would be "Energy Relative to the Fermi Energy".

2. Theoretical descriptions of Ce compounds

The evolution of theoretical models has been driven by experiment. To date, the f component of the one-electron addition/removal spectra of alloys containing Ce ions, as well as ordered Ce compounds, are qualitatively similar. Due to the difficulty of separating out the f component of the spectrum, the only concentration dependence that has been identified is the linear dependence of the overall intensity. This unsatisfactory state of affairs has caused theorists to focus their attention primarily on single-impurity models that have the same qualitative features as observed in experiments. Thereby, effects that are present in ordered compounds have been, hitherto, largely ignored. We shall categorize these theories into two classes, namely Kondo models and screening models.

2.1. *Kondo models*

Kondo models are based on the single-impurity Anderson (1961) model, which describes an f shell that is bathed in a Fermi sea of conduction electrons. The Hamiltonian, H, can be written as the sum of three terms,

$$H = H_{\mathrm{f}} + H_{\mathrm{d}} + H_{\mathrm{fd}}, \tag{1}$$

where H_{f} describes the f electron system, H_{d} describes the conduction electron systems and H_{fd} describes the coupling between these two systems. The Hamiltonian H_{f} can be written as

$$H_{\mathrm{f}} = \sum_{\alpha} E_{\mathrm{f}} f_{\alpha}^{+} f_{\alpha} + \sum_{\alpha,\beta} \tfrac{1}{2} U_{\mathrm{ff}} f_{\alpha}^{+} f_{\beta}^{+} f_{\beta} f_{\alpha}, \tag{2a}$$

where the operators f_{α}^{+} and f_{α}, respectively, create and annihilate an electron of spin α in the f shell. The first term, proportional to E_{f}, represents the binding energy of an electron in the f level, and the second term represents the Coulomb repulsion between pairs of electrons in the f shell. The Pauli exclusion principle makes this term, proportional to U_{ff}, inactive when $\alpha = \beta$. The conduction electron states are described by H_{d}, as non-interacting conduction electrons in band states,

$$H_{\mathrm{d}} = \sum_{\boldsymbol{k},\alpha} e(\boldsymbol{k})\, d_{\boldsymbol{k},\alpha}^{+} d_{\boldsymbol{k},\alpha}, \tag{2b}$$

where the operators $\mathrm{d}_{\boldsymbol{k},\alpha}^{+}$ and $\mathrm{d}_{\boldsymbol{k},\alpha}$, respectively, create and annihilate electrons of spin α in the conduction band state labeled by the Bloch wave-vector $\boldsymbol{k}$. The quantity $e(\boldsymbol{k})$ is the dispersion relation of the conduction band states. The f electron and d electron systems are coupled via the hybridization process, H_{fd}, which can be written as

$$H_{\mathrm{fd}} = \sum_{\boldsymbol{k},\alpha} (V(\boldsymbol{k})\, d_{\boldsymbol{k},\alpha}^{+} f_{\alpha} + V^{*}(\boldsymbol{k}) f_{\alpha}^{+} d_{\boldsymbol{k},\alpha}). \tag{2c}$$

The first term represents a process in which an electron of spin α is taken out of the f shell and placed in a conduction band state, the Hermitean conjugate represents the

reverse process. The hybridization term conserves the spin index α. This term, when treated in second-order perturbation theory yields a lifetime, or effective width of the f level given by $\Delta = \pi |V|^2 \rho(\mu)$, where $\rho(\mu)$ is the conduction band density of states at the Fermi level.

This model was first introduced by Anderson (1961) to describe the properties of magnetic impurities in a metal. Anderson treated the formation of the local moments by the Hartree–Fock approximation. For sufficiently large U_{ff}/Δ, the presence of an electron of spin α in the f level makes the addition of further f electron of spin β energetically unfavorable. As a result, the f component of the one electron density of states may split into α and β sub-bands, separated by an energy of the order U_{ff}. The split density of states, when occupied by electrons in accordance with the Pauli principle, may lead to the formation of a local f moment. For f electron systems, with a fractional number n_f of f electrons per f ion, where $n_f < 1$, the Hartree–Fock treatment requires that $|E_f - \mu| < \Delta$, which places the lower sub-band at the Fermi level and the upper band above the Fermi level. For an almost integer occupation of the f level, the lower sub-band will lie at even lower energies and may have very little weight at the Fermi energy μ. This latter regime is defined as the Kondo regime, in which the Hartree–Fock theory would predict well developed local moments, and as Schrieffer and Wolff (1966) have shown these moments are anti-ferromagnetically coupled, via an exchange interaction of strength $J = |V|^2/E_f$, to the spin polarization of the conduction electrons.

The most marked modifications to the Hartree–Fock picture are required in the Kondo regime, $\mu - E_f > 2\Delta$, as is suggested by renormalization group scaling arguments (Anderson 1976, Haldane 1978a,b). In these arguments one integrates out the degrees of freedom corresponding to the high energy excitations, at the expense of renormalizing parameters in a generalized Hamiltonian that describes the remaining low energy excitations. In the Kondo regime the antiferromagnetic coupling J scales to a strong coupling fixed point, as the energy cut-off is decreased to lower excitation energies. Physically, what happens is that J produces a bound state that, when occupied by an electron, produces a compensating spin polarization in the conduction electrons. At low temperatures the resulting complex yields a spin singlet, whereas at higher temperatures the bound state is ionized leading to the reappearance of the local moment. This low energy behavior leads to the appearance of a narrow, temperature dependent, resonance in the single-electron spectrum at the Fermi level. Nozières (1974) has shown that the low temperature properties can be described quite adequately by a Fermi liquid, in which the impurity produces a phase shift for the conduction electrons, which reaches $\delta_0(\boldsymbol{k}_f) = \pi/2$ at the Fermi energy. Confidence in the above picture has resulted from exact numerical renormalization group (Krishnamurthy et al. 1980a,b) and Bethe Ansatz solutions (Andrei et al. 1983, Tsvelick and Wiegmann 1983, Schlottmann 1989), although these primarily focus on thermodynamic properties.

The picture of a low energy, low temperature, Fermi liquid can also be obtained by several projection methods for minimizing the Coulomb interaction energy (Gutzwiller 1965, Coleman 1984, Grewe and Keiter 1981). The first of these methods was developed by Gutzwiller (1965). These methods basically renormalize the hybridization width Δ by

a factor of $(1-n_f)$ corresponding to the elimination of processes in which an electron may hop into an f shell that is already occupied. The impurity Abrikosov–Suhl or Kondo resonance is located near the Fermi energy μ, in accordance with arguments based on Luttinger's theorem that loosely speaking require that the zero temperature value of the f density of states at the Fermi energy is independent of the strength of U_{ff}. Furthermore, if in addition to the requirement $\mathrm{Im}\,\Sigma(\omega)|_{\omega=\mu}=0$, the above arguments may be extended by using the criterion of stability of a Fermi liquid $Z^{-1}=1-\partial/\partial\omega\Sigma(\omega)|_{\omega=\mu}>1$, one can show that the f density of states in the vicinity of the Fermi energy is given by $\rho_f(\omega)=\rho_{f0}((\omega-\mu)/Z+\mu)$, where $\rho_{f0}(\omega)$ is the f density of states evaluated with $U_{ff}=0$. For systems such as Ce, in which the f band is less than half filled, the energy of the maximum intensity in any Kondo peak would have to be above the Fermi energy. Therefore, the resulting picture of the one electron spectra, in this Kondo regime, is that of a filled lower sub-band below the Fermi energy, separated by an energy U_{ff} from an unfilled upper sub-band, and a temperature dependent Kondo resonance located at the Fermi energy. The width of the Kondo resonance is related to the Kondo temperature T_k, where $k_B T_k \approx \Delta(1-n_f)$ and its peak height is $\sim 1/(\pi\Delta)$.

A quantitative formulation, of the above picture, for the photoemission spectrum of Ce has been developed by Gunnarsson and Schönhammer (1983a,b). In Ce systems, U_{ff} is estimated to be of the order of 6 to 7 eV (Herbst and Wilkins 1987), whereas the f level width Δ is expected to be of the order less than 0.1 eV, so the local moment picture may apply. The limit $U_{ff}\to\infty$ is taken, in order to prohibit the f level being occupied by two or more electrons. Spin–orbit interactions usually cause the 14-fold degeneracy to split these states into two multiplets with degeneracy 6 and 8, respectively. The crystalline electric field may cause further splittings (Bickers et al. 1985, 1987) (cf. appendix A). The degeneracy of the lowest level is usually denoted by N_f. The quantitative formulation is based on the recognition (Grewe and Keiter 1981) that the contributions to the Green's Function can be expressed in terms of the number m of electron hole pairs, and each term with m electron hole pairs contributes a factor of order $(\Delta\rho)^m$. By rescaling $\Gamma=N_f\Delta$, the expansion can be ordered in powers of $1/N_f$, and the approximation obtained by retaining only the first non-trivial term in the above expansion becomes exact in the limit $N_f\to\infty$, if Γ is kept constant. However, for finite N_f, processes involving an arbitrary number of low energy electron–hole pairs do contribute to the wave functions and can lead to an orthogonality catastrophe, in which the physical properties do not have simple relationships to those of the bare states.

The one-electron addition or removal spectrum can be obtained from the imaginary part of the Fourier-transformed, zero-temperature, time ordered one-electron Green's function defined by

$$G^f_{\alpha,\beta}(t)=-\frac{i}{\hbar}\left\langle \Psi_g \left| T_W f_\alpha(t) f^+_\beta(0) \right| \Psi_g \right\rangle, \tag{3a}$$

where T_W is Wick's time ordering operator, $|\Psi_g\rangle$ is the ground state, the f creation and annihilation operators are in the Heisenberg representation, and α indexes the degeneracy

of the f shell. The Fourier Transform $G^{\mathrm{f}}(\omega)$ can be expressed as the limit, $\delta \to 0+$, of the sum

$$G^{\mathrm{f}}_{\alpha,\beta}(\omega) = \langle \Psi_{\mathrm{g}} | f_\alpha (h\omega + \mu + \mathrm{i}\delta - E_{\mathrm{g}} + H)^{-1} f^+_\beta | \Psi_{\mathrm{g}} \rangle + \langle \Psi_{\mathrm{g}} | f^+_\beta (h\omega + \mu - \mathrm{i}\delta - E_{\mathrm{g}} + H)^{-1} f_\alpha | \Psi_{\mathrm{g}} \rangle . \tag{3b}$$

The first term represents processes in which an electron is added to an f orbital, when the system is in the ground state, and the second term corresponds to the removal of an f electron from the systems ground state. Hence, the second term is related to the f component of the zero temperature photoemission spectrum, whereas the first term is related to the f component of the zero temperature limit inverse photoemission spectrum.

The lowest non-trivial approximation (Gunnarsson and Schönhammer 1983a,b) for the compensated spin singlet ground state (Yosida and Yoshimori 1963) $|\Psi_{\mathrm{g}}\rangle$ is obtained by a variational procedure, by using the ansatz

$$|\Psi_{\mathrm{g}}\rangle = \aleph^{-1} \left(|\Phi_0\rangle + \frac{1}{N_{\mathrm{s}}} \sum_{\boldsymbol{k},\alpha} c_{\boldsymbol{k}} f^+_\alpha d^+_{\boldsymbol{k},\alpha} |\Phi_0\rangle \right), \tag{4}$$

in which $|\Phi_0\rangle$ is the filled Fermi sea and $c_{\boldsymbol{k}}$ is a variational coefficient and $\aleph$ is the normalization. [The singlet nature of this state is most apparent in SU(2), where $(f^+_{+\sigma} d_{\boldsymbol{k},+\sigma} + f^+_{-\sigma} d_{\boldsymbol{k},-\sigma})(d^+_{\boldsymbol{k},+\sigma} d^+_{\boldsymbol{k},-\sigma}) |0\rangle = (f^+_{+\sigma} d^+_{\boldsymbol{k},-\sigma} - f^+_{-\sigma} d^+_{\boldsymbol{k},+\sigma}) |0\rangle$.] The above ansatz is motivated by the assumption that the compensated spin singlet ground state can be analytically continued to a filled Fermi sea, in the limit $V(\boldsymbol{k}) \equiv 0$. With this assumption, the constant $\aleph^{-2}$ may be identified with the wave function renormalization. The second term corresponds to f electron conduction hole pairs, and thus the f occupancy is related to the $c_{\boldsymbol{k}}$'s and is given by $n_{\mathrm{f}} = (1 - \aleph^{-2})$. The absence of other terms is due to the assumption of $U_{\mathrm{ff}} \to \infty$, and by the desire to minimize the number of electron hole pairs. The variational coefficients $c_{\boldsymbol{k}}$ and the energy of the ground state E_{g} are found from the equations

$$c_{\boldsymbol{k}} = \frac{V(\boldsymbol{k})}{E_{\mathrm{g}} + e(\boldsymbol{k}) - E_0 - E_{\mathrm{f}}}, \tag{5a}$$

and

$$E_{\mathrm{g}} - E_0 = \sum_{\boldsymbol{k}} V(\boldsymbol{k}) c_{\boldsymbol{k}}, \tag{5b}$$

where E_0 is the energy of the filled Fermi sea $|\Phi_0\rangle$. The pair of equations has a solution given by the lowest energy solution of

$$E_{\mathrm{g}} - E_0 = N_{\mathrm{f}} \int \mathrm{d}\omega \, \rho(\omega) \frac{|V(\omega)|^2}{(E_{\mathrm{g}} - E_0 + \omega - E_{\mathrm{f}})}, \tag{6}$$

which, because of the logarithmic singularity, is in turn given by $E_g = E_0 + E_f - \mu - \delta E_b$ for the Kondo regime where $\mu - E_f > N_f \Delta$. The binding energy δE_b is a low energy scale related to the Kondo temperature and is given by

$$\delta E_b = k_B T = (W + \mu) \exp\left(\frac{\pi (E_f - \mu)}{N_f \Delta} \right), \tag{7}$$

where W is half the conduction band width. The ground state (4) can be shown to have a lower energy than the corresponding local moment states comprised from $(f_\alpha^+ + \sum b_k d_{k\alpha}^+) |\Phi_0\rangle$, wherever $N_f \geqslant 2$.

The Green's function (3b) is evaluated by first inserting complete sets of states on both sides of the resolvent, between the f operators, and then by truncating these complete sets so that they lay within the variational basis set. Thus, the imaginary part of the Green's function can be written as

$$\begin{aligned} \operatorname{Im} G_{\alpha,\beta}^f(\omega) = \aleph^{-2} \sum_{k,k';m,n} & c_k c_{k'}^* \langle \Phi_0 | d_{k,\beta}^+ | m \rangle \operatorname{Im} \{ g_{m,n}(h\omega) \} \langle n | d_{k',\alpha} | \Phi_0 \rangle \\ & - \aleph^{-2} \sum_{m,n} \langle \Phi_0 | f_\alpha | m \rangle \operatorname{Im} \{ g_{m,n}(h\omega) \} \langle n | f_\beta^+ | \Phi_0 \rangle , \end{aligned} \tag{8a}$$

where the resolvent is to be evaluated in the space of states with one extra hole or electron, from

$$g_{m,n}(z) = \langle m | \left(z + \mu - E_g + H \right)^{-1} | n \rangle . \tag{8b}$$

The first term of eq. (8a) corresponds to the photoemission spectrum, whereas the second term corresponds to the BIS spectrum. If the photoemission part of the resolvent (8b) is evaluated in the sub-space described by $d_{k,\beta} |\Phi_0\rangle$, one obtains the expression

$$\frac{1}{\pi} \sum_\alpha \operatorname{Im} G_{\alpha,\alpha}^f(\omega) = \aleph^{-2} \frac{1}{\pi} \sum_\alpha \frac{\Delta}{(h\omega + \mu - E_f)^2}, \tag{9}$$

which represents an approximate evaluation of the expected spectral weight function,

$$\aleph^{-2} \frac{1}{\pi} \frac{N_f \Delta}{(h\omega + \mu - E_f)^2 + N_f^2 \Delta^2}. \tag{10}$$

The width of this peak is expected to be $N_f \Delta$ as there are N_f channels available for filling a completely unoccupied f level. Including higher-order electron–hole pairs in the variational ansatz for $|\Psi_g\rangle$, is expected to introduce the expected factors of Δ into the denominators of the c_k's and hence yield the expected result (10). Similarly, on including

terms of higher order in the number of electron–hole pairs, such as $f_\beta^+ d_{k,\beta} d_{k',\alpha} \mid \Phi_0\rangle$, in the evaluation of the resolvent one obtains

$$g_{k,k}(z) = \left[z + \mu + E_0 - E_g - e(k) - N_f \int d\omega \, \rho(\omega) \frac{|V(\omega)|^2}{(z + \mu + E_0 + E_f - E_g - e(k) - \omega)} \right]^{-1}. \tag{11}$$

This expression, due to the cut-off of the integral at the Fermi surface, has a pole at $z + \mu = e(k)$. The residue at this pole is small, given by the approximate expression

$$\frac{\pi \delta E_b}{N_f \Delta} \left[\frac{1 + \pi \delta E_b}{N_f \Delta} \right]^{-1} = 1 - n_f. \tag{12}$$

Close to the Fermi energy, this leads to a peak in the spectral density of the approximate form

$$\rho_{\text{Kondo}}(\omega) = \frac{1}{\pi} (1 - n_f)^2 \frac{N_f \Delta}{(h\omega - \delta E_b)^2}. \tag{13}$$

The above approximate expression is valid for $\omega < 0$, but has the form of a pole above the Fermi energy. The maximum intensity within its region of validity is at the Fermi level $\omega = 0$, where

$$\rho_f(0) = \left(n_f - \frac{(1 - n_f) \frac{N_f \Delta}{\pi}}{|\epsilon_f - \Delta E + B|} \right)^2. \tag{14}$$

This should be contrasted with the asymptotic large N_f limit of the exact result, $\rho_f(0) = \pi n_f^2 / N_f \Delta$, which indicates that the validity of the method is restricted to $n_f \approx 1$ (Zhang and Lee 1983, 1984). Equation (13) represents the lowest-order term in the expansion of an asymmetric Lorentzian located δE_b above the Fermi energy, of width $(1 - n_f)\Delta = \pi \delta E_b / N_f$. This estimate of the width is based on the decay rate of an f electron Δ divided by the bound state wave function renormalization (12). The total integrated intensity of the peak should be $N_f(1 - n_f)$, as it corresponds to the number of ways of adding one f electron to the f^0 component of the ground state $\mid \Psi_g\rangle$. However, the integrated intensity of the occupied portion of this peak is only $n_f(1 - n_f)$. Thus, at zero temperature, the Kondo resonance has a small integrated intensity, of the order $k_B T_k / \Delta$, and for Ce compounds and alloys most of this weight should occur in the inverse photoemission spectrum. For Yb alloys, particle–hole symmetry would suggest that the weight in the Kondo resonance should occur in the photoemission side of the spectrum.

If one allows for a finite value of U_{ff} (cf. appendix B), then an f^2 component will occur in the spectrum, and a generalization of the above method yields a peak in the unoccupied portion of the spectrum at an energy

$$h\omega + \mu \approx E_f + U_{ff} + \delta E_b. \tag{15}$$

The width of this f^2 peak is expected to be $\sim 2\Delta$ as the f^2 configuration has two decay channels for losing an electron. Thus, an approximate expression for the total, $T=0$, f component of the one-electron removal/addition spectrum is given by

$$\rho_f(\omega) = \frac{1}{\pi} n_f \frac{N_f \Delta}{\left\{(h\omega + \mu - E_f)^2 + N_f^2 \Delta^2\right\}} + \rho_{\text{Kondo}}(\omega) + \frac{1}{\pi} n_f \frac{(N_f - 1)2\Delta}{\left\{(h\omega + \mu - E_f - U_{ff})^2 + 4\Delta^2\right\}}. \tag{16}$$

Gunnarsson and Schönhammer (1983a,b) have considered the effect that structure in the conduction band densities of states produces in the photoemission spectrum. They show that for a conduction band density of states near the lower band edge $e(\boldsymbol{k}) = -W$, and with a large value of $V/(W + E_f)$ the spectrum may exhibit a sharp f-derived peak below the band edge. They also consider the changes in the spectrum due to splitting the N_f fold degeneracy, by either spin–orbit or crystalline electric field effects. Their results show that the spin–orbit coupling produces a lower energy edge to the Kondo peak in the photoemission spectrum.

One of the limitations of this approach is the restriction to the case of nearly integer f occupancy, i.e. $n_f \approx 1$. In the mixed valent regime of the Anderson model, where $\mu - E_f < N_f \Delta$, the ground state energy E_g approaches E_0 and the above expansion in powers of the number of electron–hole pairs no longer converges (Zhang and Lee 1983, 1984). It is expected that in this mixed valent regime the Kondo peak will broaden and completely merge with the bare 4f peak in the photoemission spectrum. When the bare f level is positioned above the Fermi level $E_f > \mu$, then there is only a single f peak with a width which just becomes Δ, corresponding to the rate for an electron to tunnel out of the f orbital.

As pointed out by Bickers et al. (1985, 1987), the effects of spin–orbit coupling in the Kondo model are important in the interpretation of experiments. The effect of spin–orbit coupling and crystalline electric fields is to split the degeneracy of the Ce f orbitals N_f into two or more multiplets. For spin orbit coupling, this usually splits the 14 fold degenerate f level into two groups, the lower group corresponds to a $j = \frac{5}{2}$ multiplet, with energy $E_{f,l}$ and degeneracy $N_{f,l} = 6$. The remaining states are at a higher energy $E_{f,u}$ and corresponds to the $j = \frac{7}{2}$ multiplet with degeneracy $N_{f,u} = 8$. The spin–orbit splitting is defined by $\Delta E_{s\text{-}o} = E_{f,u} - E_{f,l}$.

The breaking of the full degeneracy of the f orbital has two consequences. The first consequence is that the spin compensated ground state $|\Psi_g\rangle$ no longer has the same weighting factors for states of the lower and upper multiplets, i.e.,

$$|\Psi_g\rangle = \aleph^{-1}\left\{1 + \sum c_{l,k} f_\alpha^+ d_{\alpha,k} + \sum c_{u,k} f_\alpha^+ d_{\alpha,k}\right\}|\Phi_0\rangle . \tag{17}$$

One expects $c_{l,k}$ to be larger than $c_{l,k}$, as $|\Psi_g\rangle$ has its energy minimized if it contains more of the lower energy multiplet. The second consequence, is the existence of a higher energy spin compensated state $|\Psi_h\rangle$, in which the relative magnitudes of c_l and c_u are reversed. The binding energies of these two compensated states are denoted as

$$\delta E_g = E_{f,l} + E_0 - \mu - E_g, \tag{18a}$$

and

$$\delta E_h = E_{f,u} + E_0 - \mu - E_h. \tag{18b}$$

Thus, for sufficiently small $\Delta E_{s\text{-}o}$, the binding energies can be found from the two solutions of the equation

$$\begin{aligned} E_{g,h} - E_0 = {} & N_{f,l}\int d\omega\,\rho(\omega)\frac{|V(\omega)|^2}{(E_{g,h} - E_0 + \omega - E_{f,l})} \\ & + N_{f,u}\int d\omega\,\rho(\omega)\frac{|V(\omega)|^2}{(E_{g,h} - E_0 + \omega - E_{f,u})}. \end{aligned} \tag{19}$$

The solutions may be approximated as

$$\delta E_g = (W + \mu)\exp\left(\frac{\pi\,(E_{f,l} - \mu)}{N_{f,l}\Delta}\right)\left\{\frac{(W + \mu)}{\Delta E_{s\text{-}o}}\right\}^{(N_{f,u}/N_{f,l})}, \tag{20a}$$

and

$$\delta E_h = (W + \mu)\exp\left(\frac{\pi(E_{f,u} - \mu)}{N_{f,u}\Delta}\right)\left\{\frac{(W + \mu)}{\Delta E_{s\text{-}o}}\right\}^{(N_{f,l}/N_{f,u})}, \tag{20b}$$

respectively.

A similar analysis to that given above yields the photoemission spectrum to be given by

$$\rho_{\mathrm{f}}(\omega) = \sum \left\{ N_{\mathrm{f,l}} |c_{\mathrm{l},\boldsymbol{k}}|^2 + N_{\mathrm{f,u}} |c_{\mathrm{u},\boldsymbol{k}}|^2 \right\} \mathrm{Im}\, g_{\boldsymbol{k},\boldsymbol{k}}(h\omega), \tag{21}$$

where $g_{\boldsymbol{k},\boldsymbol{k}}(h\omega)$ has the form

$$g_{\boldsymbol{k},\boldsymbol{k}}(z) = \Bigg[z + \mu + E_0 - E_{\mathrm{g}} - e(\boldsymbol{k}) - N_{\mathrm{f,l}} \int \mathrm{d}\omega\, \rho(\omega) \frac{|V(\omega)|^2}{z + \mu + E_0 + E_{\mathrm{f,l}} - E_{\mathrm{g}} - e(\boldsymbol{k}) - \omega} - N_{\mathrm{f,u}} \int \mathrm{d}\omega\, \rho(\omega) \frac{|V(\omega)|^2}{z + \mu + E_0 + E_{\mathrm{f,u}} - E_{\mathrm{g}} - e(\boldsymbol{k}) - \omega} \Bigg]^{-1}. \tag{22}$$

The imaginary part of $g_{\boldsymbol{k},\boldsymbol{k}}(z)$ has a pole at $z + \mu = e(\boldsymbol{k})$, by virtue of the singularity of the self-energy like factor, at $e(\boldsymbol{k}) + E_{\mathrm{g}} = z + E_0 + E_{\mathrm{f,l}}$. That the denominator vanishes exactly at this energy can be confirmed by using the definition of the ground state energy, and the residue at this pole is $(1 - n_{\mathrm{f}})$. A second feature occurs near $z + \mu \approx e(\boldsymbol{k}) - \Delta E_{\mathrm{s\text{-}o}} - \delta E_{\mathrm{g}} + \delta E_{\mathrm{h}}$, by virtue of the second singularity of the self-energy like factor at $e(\boldsymbol{k}) + E_{\mathrm{g}} = z + E_0 + E_{\mathrm{f,u}}$. This second singularity is connected with the excited spin compensated multiplet $|\Psi_{\mathrm{h}}\rangle$.

Using only the first narrow delta function contribution from $\mathrm{Im}\, g_{\boldsymbol{k},\boldsymbol{k}}(z)$ at $z + \mu = e(\boldsymbol{k})$, one finds the photoemission spectrum contains the tails of two narrow Kondo resonances, located at δE_{g} and $\Delta E_{\mathrm{s\text{-}o}} + \delta E_{\mathrm{g}}$ above the Fermi level. These tails merely correspond to the spectrum of hole states which screened the lower and upper f multiplet configurations in the ground state, i.e., $|c_{\mathrm{l},\boldsymbol{k}}|^2$ and $|c_{\mathrm{u},\boldsymbol{k}}|^2$. Roughly speaking, the photoemission process takes an f electron from the ground state, leaving the f level empty together with a hole in the conduction band which formed part of the compensating screening cloud. The f shell is then refilled by the hybridization process leading to another compensated singlet like $|\Psi_{\mathrm{g}}\rangle$, but with the conduction band hole near the Fermi level. The two tails correspond to the two distributions of screening holes, for the lower and upper multiplets in $|\Psi_{\mathrm{g}}\rangle$. These tails, are of course, not resolvable in the photoemission spectrum, but should lead to a resolvable splitting of the Kondo peak in the inverse photoemission spectrum. The interpretation of the Kondo peaks in the BIS is much more straightforward, since they merely correspond to the ways of adding an f electron to the f^0 component of the ground state $|\Psi_{\mathrm{g}}\rangle$. This leaves the system in either of the uncompensated final states, $f^+_{\alpha,\mathrm{l}} |\Phi_0\rangle$ or $f^+_{\alpha,\mathrm{u}} |\Phi_0\rangle$, which correspond to excitation energies of δE_{g}, and $\Delta E_{\mathrm{s\text{-}o}} + \delta E_{\mathrm{g}}$ above the Fermi level. From this argument, the integrated intensities of these peaks should be given by $(1 - n_{\mathrm{f}}) N_{\mathrm{f,l}}$ and $(1 - n_{\mathrm{f}}) N_{\mathrm{f,u}}$, respectively. These intensities and peak energies are consistent with the calculations of the two spin–orbit split Kondo tails expected in the photoemission spectra.

A Kondo side band, should appear below the Fermi energy as a result of the second singularity in the denominator of $g(z)$. This corresponds to a photoemission process in which the higher compensated singlet $|\Psi_h\rangle$ appears in the final state. This implies, that an intermediate state, containing only the spin compensating conduction band hole but no f electron, is filled by the hybridization process leading to the final state. The excitation energy of this process is estimated to be $h\omega = -\Delta E_{s\text{-}o} + \delta E_h$. For reasonably large values of $\Delta E_{s\text{-}o}/\delta E_h$, the integrated intensity of this Kondo side band is estimated to be of the order $(\delta E_h/\delta E_g)(1-n_f)$, and has a width $\sim\pi(N_{f,l}/N_{f,u})\delta E_h$. The additional factor of $N_{f,l}$ in the expression for the width, occurs as the process involves an intermediate state which decays by filling of an f hole. In addition to this broadened peak, we find a similarly broad peak above the Fermi level. The existence of this broad Kondo side-band has been previously discussed by Bickers et al. (1985, 1987). The effects of further splittings, such as from the crystalline electric field are discussed in appendix A.

The effect of temperature on the above picture is non-trivial, as there exists a low temperature or energy scale given by T_K. For temperatures significantly below T_K, the local moment states are not expected to have an appreciable weight in the thermal averages, so the excited states of the system described by eq. (1) may be put into a one to one correspondence with the excited states of the non-interacting Fermi liquid $|\Phi_0\rangle$ (Nozières 1974). Thus, below T_K one may expect the system to be described by a Fermi liquid theory, albeit with an unusual temperature dependence. Physically, the Kondo resonance is formed from conduction band states within δE_b of the Fermi energy, so thermal smearing due to Fermi function broadening is expected to have a considerable effect when $k_B T \approx \delta E_b$. In particular, the strength of the singularity near $z+\mu = e(\boldsymbol{k})$ in $g_{k,k}(z)$ is expected to be weakened and the presence of electrons above the Fermi surface will broaden the pole into a resonance. This might be expected to broaden the Kondo resonance and reduce its binding energy. A concomitant expectation based on eq. (13), is that the integrated intensity of the Kondo resonance, $\sim N_f(1-n_f)$, ought to decrease with increasing temperature. However, due to the nature of the variational approach, the method cannot be easily generalized to include a thermal average over a large manifold of excited states, including the local moment states.

In addition to the effects of spin–orbit splitting, the temperature dependence of the Kondo resonance has been investigated by Bickers et al. (1985, 1987) using a self-consistent perturbation approach. The method resums a selected set of diagrams to infinite order. The characteristic form of this set has led to the above approximation being named the non-crossing approximation (NCA) (Bickers 1987, Rasul and Hewson 1984, Müller-Hartmann 1984, Read and Newns 1983a,b). This approximation has been shown to lead to a correct self-consistent description of the thermodynamic properties (Rasul and Hewson 1984). However, the method does not yield spectral densities that satisfy the zero-temperature, low-frequency, self-consistency relations expected from Fermi-liquid descriptions (Müller-Hartmann 1984). Nevertheless, the above approximation does exhibit a Kondo resonance which has a total integrated intensity that decreases rapidly with increasing temperature. Most of the spectral weight of this feature has vanished at T_k, but the small remaining contribution does have significant effects on the thermodynamic

properties at temperatures above T_k. Studies of the spin–orbit split Kondo effect show that the intensity of the Kondo side band, below the Fermi energy, has a weaker temperature dependence than the intensity of the Kondo peak. Since in most cerium-based systems the combined effect of spin–orbit and crystalline electric fields is to produce an f-level scheme comprised of three low-lying doublets and a higher-energy octet, it is questionable whether the $1/N_f$ expansion represents a reasonable approximation.

Slave boson theories (Read and Newns 1983a,b, Newns and Read 1987, Coleman 1987, Read 1985, Doniach 1987, Houghton et al. 1988) are, in a sense, complementary to the NCA in that they do yield a good Fermi-liquid description of the zero-temperature state, but become inadequate at temperatures of the order of T_k. In these slave boson theories, the temperature dependence of the integrated intensity of the Kondo resonance is most apparent, where $1-n_f$ rapidly decreases with increasing temperature and finally vanishes for temperatures above a critical temperature of the order of T_k. At the critical temperature $T_c \approx T_k/\ln(N_f-1)$ a continuous phase transition occurs from a low-temperature Bose condensate to a high-temperature normal state (Read 1985, Doniach 1987, Houghton et al. 1988). In contrast to the NCA, above the critical temperature the local moment is completely decoupled from the system of conduction electrons. It has been argued that, for finite N_f, the effects of fluctuations will restore the broken symmetry at all finite temperatures, yet the vestiges of the $T=0$ phase will remain apparent in the physical properties (Read 1985).

Recently, QMC methods have been combined with maximum entropy methods (MEM) to treat the dynamics of strongly correlated systems. Hirsch and Fye (1986) developed a technique, derived with fermion path-integral formalism, to simulate impurities embedded in a non-interacting metallic host. The host is integrated out of the path integral and a Hubbard–Stratonovich (HS) transformation is introduced to reduce the interaction to integrable form at the expense of the introduction of time-dependent auxiliary HS fields. The remaining electronic degrees of freedom are integrated out, leaving an f-electron Green's function of two time-variables and the HS fields. Quantum Monte Carlo is then used to integrate over the HS field configurations. The technique may be used to estimate all one- and two-particle Green's functions of imaginary time. Various methods have been used to analytically continue these to real time. Padé approximants generally overfit the QMC data (they fit to the statistical noise) and produce unreliable results. The problem is that infinitely many spectral functions $A_f(\omega)$ will reproduce the QMC data within the statistical error. MEM recasts the problem in statistical language so that Bayesian statistics may be used to define the conditional probability of the real-frequency spectrum A given the QMC data $G, P(A|G)$. We choose the A which maximizes $P(A|G)$ (Jarrell and Gubernatis 1996). Entropy is invoked to define a prior probability of A, $P(A)$. $P(A)$ enforces the prior knowledge that A is positive definite and normalizable. Together QMC plus MEM is a very accurate technique; for example, the calculated Kondo resistivity agrees with that of $La_{1-x}Ce_xB_6$ for about three decades in temperature.

The applicability of the single-impurity Anderson model description to concentrated compounds and alloys does remain the subject of much debate. It is apparent that as the temperature is lowered, the f moments start to induce a compensating polarization cloud

around the f ion. It has been speculated that at a characteristic temperature, the coherence temperature T_c, the compensating spin polarizations interact and become coherent. This has motivated the study of the two-impurity Anderson model, in which the possibility of at least two regimes becomes apparent (Jayaprakash et al. 1981). One regime corresponds to the case when the exchange interaction between the two impurity moments, mediated by the polarization of the conduction band, is weaker than the Kondo energy. In this case, one may expect that the local moments will be independently screened. In the other regime, where the exchange interaction is larger than the Kondo energy, one expects that the moments may be correlated and the resulting spin complex be subsequently screened by the formation of a compensating polarization cloud. Real space renormalization group analyses (Jones and Varma 1987, Jones et al. 1988, Rasul and Hewson 1985) of the two-impurity model show that these competing phenomena may both have to be treated by strong coupling techniques. Nozières (1985) has also pointed out that the formation of the polarization clouds may be expected to only involve the conduction electrons within $k_B T_k$ of the Fermi energy. Thus the number of electrons forming the compensating polarization cloud may be expected to be of the order of $k_B T_k \rho(\mu)$, where $\rho(\mu)$ is the conduction band density of states evaluated at the Fermi level. Since $k_B T_k$ is much less than the depth of the occupied portion of the conduction band density of states, this yields an estimate of much less than one conduction electron per f ion. Thus, the estimated number of electrons in the polarization cloud is less than the number of f moments to be screened, so an alternative description, other than the single-impurity description, may have to be utilized for concentrated compounds.

As outlined above, the physics associated with the Kondo model can be ascribed to the local moment inducing a compensating spin polarization cloud in the gas of conduction electrons, at low temperatures. The models considered in the next section are categorized as screening models, in which considerations of electrical charge neutrality in the unit cell are brought into play.

3. Screening models

The physics behind the two screening channel picture of the photoemission spectrum can be understood by consideration of the simplified model Hamiltonian (Mahan 1967, Nozières and DeDominicis 1969, Hewson and Riseborough 1977, Combescot and Nozières 1971, Liu and Ho 1982, 1983, Riseborough 1986),

$$H = H_f + H_d + H'_{fd}, \tag{23}$$

where H_f and H_d are the Hamiltonians describing the f shell and the conduction band at the f site, and have been previously described in eqs. (2a) and (2b) respectively. The coupling term H'_{fd}, is not given by eq. (2c), but instead is given as

$$H'_{fd} = \frac{1}{N_s} \sum_{k,k'} U_{fd}\, d^+_{k,\beta}\, d_{k',\beta} \left(\sum_{\alpha} f^+_{\alpha} f_{\alpha} - n_f \right), \tag{24}$$

which represents the Coulomb interaction between the electrons in the conduction band and the excess charge in the f shell. The Coulomb interaction is assumed to be screened so that it is highly local. This is consistent with the estimates of Norman et al. (1984, 1985) and Freeman et al. (1987), who show that the full relaxation shifts associated with the conduction band screening are of the order of 7 eV. More realistic descriptions of the cerium pnictides have been provided by cluster super cell electronic structure calculations (Norman et al. 1984, 1985, Freeman et al. 1987).

The f electron number operators f_α^+ and f_α commute with the above Hamiltonian, and therefore correspond to good quantum numbers. As shown by Hewson and Riseborough (1977), the above Hamiltonian can be exactly diagonalized in the sub-spaces corresponding to the different f quantum numbers. For the ground state of Ce, where it is assumed that $n_f \approx 1$, the conduction band density of states per atom is simply given by $\rho(\omega)$. However, in the presence of an f hole, the local conduction band density of states becomes distorted to $\rho(\omega)+\Delta\rho(\omega)$, where

$$\Delta\rho(\omega) = \frac{\partial}{\partial\omega}\log_e[1 - U_{fd}F(\omega)], \qquad F(\omega) = \int d\omega' \frac{\rho(\omega')}{(\omega - \omega')}. \tag{25a,b}$$

This expression represents the shift in the conduction electron states, so as to screen the f hole. It is important to note that, for sufficiently large values of U_{fd}, a bound state may split off from the bottom of the conduction band, $\omega = -W$. This occurs whenever

$$U_{fd} \geqslant \left.\frac{1}{F(\omega)}\right|_{\omega=-W}, \tag{26}$$

which strongly depends on the variation of the conduction band density of states $\rho(\omega)$ at the lower band edge, $\omega = -W$. The value of U_{fd} can be fixed by requiring that, in the presence of an f hole, the distortion of the density of states satisfies the Friedel sum rule. If the above criterion on U_{fd} is satisfied, the resulting bound state has an energy E_B that is given by

$$1 - U_{fd}F(E_B) = 0. \tag{27}$$

Similar physics applies for the addition of an f electron, as may occur in BIS experiments, however, in that case the bound state represents an anti-screening channel, which splits off from the top of the conduction band. The presence of the bound state depends on the variation of the density of states $\rho(\omega)$ at the upper band edge. Since, in general, one does not expect that the conduction band density of states will have particle hole symmetry, the existence of two peaks in the photoemission spectrum does not ensure the existence of the two peaks in the unoccupied portion of the spectrum at excitation energies of the order of $E_f + U_{ff}$.

The f component of the photoemission spectrum is given by the occupied portion of the f one electron density of states. This can be expressed, directly, in terms of the above eigenvalues and eigenstates as

$$\frac{1}{\pi}\mathrm{Im}\, G_{\mathrm{ff}}(\omega) = \sum \delta(\omega + E_{\mathrm{g}} - E_{\mathrm{exc}}) \left|\langle \Psi_{\mathrm{g}} | \Psi_{\mathrm{exc}} \rangle\right|^2, \tag{27}$$

where Ψ_{g} and Ψ_{exc} are the anti-symmetrized wave functions of the conduction electrons in the ground state and the excited final states, respectively. The energy of the ground state is given by the usual expression for non-interacting electrons,

$$E_{\mathrm{g}} = E_{\mathrm{f}} + N_{\mathrm{s}} \int \mathrm{d}\omega\, \omega \rho(\omega) f(\omega); \quad n_{\mathrm{f}} = 1, \tag{28a}$$

where $f(\omega)$ is the Fermi function. The energies of the excited states are given by the expression

$$E_{\mathrm{exc}} = N_{\mathrm{s}} \int \mathrm{d}\omega\, [\rho(\omega) + \Delta\rho(\omega)]\, \omega\, n(\omega); \quad n_{\mathrm{f}} = 0, \tag{28b}$$

where $n(\omega)$ represents a non-equilibrium distribution function for the electrons. The distribution function is subject to the usual restriction

$$\int \mathrm{d}\omega\, [\rho(\omega) + \Delta\rho(\omega)]\, n(\omega) = \frac{N_{\mathrm{el}}}{N_{\mathrm{s}}}. \tag{28c}$$

In general, the spectrum cannot be evaluated analytically, and has to be evaluated numerically. However, certain features of the spectrum may be obtained analytically (Liu and Ho 1982, 1983, Riseborough 1986).

Two distinct features in the photoemission spectra may occur, when U_{fd} is sufficiently large to produce a bound state. The well screened channel corresponds to processes in which the bound state is occupied in the final state, and the less well screened peak occurs when the bound state remains unoccupied. It is assumed that the Coulomb interaction between the d electrons, U_{dd}, is sufficiently large that it will prevent more than one electron from occupying the bound state in the final excited states. The threshold energy corresponds to final excited states in which the lowest electronic states within the conduction band continuum are completely occupied, in accordance with the Pauli-exclusion principle. Above the threshold energies, the spectrum corresponds to excited states with arbitrary number of electron–hole pairs in the continuum. The characteristic energy dependence of the intensity, near threshold, has been studied by Combescot and Nozières (1971). The separation ΔE of the two threshold energies is simply given by the energy required to take an electron in the bound state and place it at the Fermi level, i.e.

$$\Delta E = \mu - E_{\mathrm{B}}. \tag{29}$$

The relative integrated intensity of the two features is simply given by the ratio of the probability that an electron present in the initial state occupies the bound state, to the

probability that the bound state is unoccupied in the final state. The relative integrated intensity of the well screened channel is simply controlled by the ratio $I_1/(I_1+I_2)$, where

$$I_1 = \frac{\partial}{\partial E_B}\int d\omega\, f(\omega)\frac{\rho(\omega)}{E_B-\omega}, \qquad I_1+I_2 = \frac{\partial}{\partial E_B}\int d\omega\,\frac{\rho(\omega)}{E_B-\omega}. \tag{30}$$

The essential parameters of the model are U_{fd}/W and the occupied width of the f band, $\mu+W$. The latter can be estimated directly from the off-resonance valence band photoemission spectra, which have been measured by Lang et al. (1981). This yields a rough estimate of the energy separation of the two peaks to be 2 to 3 eV.

In the above simplified picture, the position of the bare f level relative to the Fermi level is not subject to any restrictions. For Ce compounds and alloys, E_f may be fixed by consideration of the observed valence, so that the f density of states is expected to cut across the Fermi energy. This does indicate that the effects of the hybridization with the conduction band should also be included, in any more realistic model of Ce systems. However, the model should be equally applicable to other light rare earths as both experiment and band structure calculations show that the width and filling of the rare earth conduction band is roughly similar all across the lanthanide row. Also, from considerations of charge neutrality, the value of U_{fd} is expected to be only slowly varying across the row. Hence the observation of similar satellite structures in Pr and Nd compounds may be taken to be an affirmation of the above pictures.

These model calculations do ignore or simplify many of the features crucial to a complete understanding of the process, including the range of the Coulomb screening interaction, the spatial and angular momentum character of the resulting bound state. Presumably, complete screening would also involve balancing the higher-order Coulomb multi-pole moments of the f hole by equal and opposite multi-pole moments in the conduction band, as is suggested by the work of Rusic et al. (1983). These questions may be resolved by examination of ab-initio electronic structure calculations.

Norman et al. (1984, 1985) and Freeman et al. (1987) have performed super cell cluster calculations of the excited states of ordered Ce compounds, using the local density functional method. This technique is used to calculate the energy of meta-stable excitations, using the method developed by Kohn and Sham to yield the ground state electronic density and energy. These electronic structure calculations are performed by restricting the f occupation on all sites to be integer-valent with atomic wave functions, and to contain one less f electron on one site, representing the final state of the photoemission process. The conduction band electron density is calculated self-consistently, but excluding any $l=3$ components at that site, and the results indicate the existence of an excited state of Ce pnictides at an energy 2.5 eV below the Fermi energy, in agreement with the expectations based on the simple model calculations. The peak at the Fermi energy is attributed to the screening process in which an $l=3$ component in the conduction band states is filled. Clearly, this interpretation does imply that the many features seen in the calculated f band structures should also show up in the photoemission spectrum.

The above calculations neither have explicit spin correlations between the local f moment and the conduction band polarization, nor do they exhibit unusual temperature

dependencies, in contrast to the Kondo model. However, the Kondo effect does play a crucial role in the description of the thermodynamic properties of dilute Ce alloys. This curious state of affairs may be reconciled, if one notes that both the hybridization and screening terms should be included in the description of Ce (Nunez-Regueiro and Avignon 1985, Liu 1988). Renormalization group calculations (Alascio et al. 1986) on this generalized Hamiltonian have shown that the low-energy and low-temperature thermodynamic properties are governed by a fixed point described by an effective Anderson impurity model. This still requires the existence of a Kondo peak in the one-electron spectrum, but the integrated intensity associated with the Kondo peak is at most of the order of $k_B T_k/\Delta$, and may be unobservable in comparison with the higher-energy features. Although the effects of a crystalline array of f ions has not been calculated, one may expect that the periodicity will almost certainly have some effect on the low-energy spectrum which should be most apparent in angle resolved spectra.

4. Theoretical descriptions of uranium systems

Whereas most cerium systems show joint photoemission/inverse photoemission spectra with distinct separated structures that can be identified with the upper and lower split Hubbard bands, the same is not true for most uranium compounds. The uranium systems, with the exceptions of the uranium oxides and UPd_3, all show a single f peak that cuts right across the Fermi level. This may be interpreted as indicating that the strength of the effective Coulomb interaction U_{ff} is smaller than the f band width Δ, and in the spirit of the Hartree–Fock approximation can be considered as a band of non-interacting f electrons. The f bands are found to be quite comparable to those derived from LDA electronic structure calculations (Boring et al. 1985a,b, Albers et al. 1985, Koelling et al. 1985). In these calculations, the f band widths are found to be dominated by indirect hybridization process, although in the materials with small inter-uranium spacings the direct 5f–5f overlap is found to be quite considerable.

Despite the qualitative agreement, there appear to be discrepancies and additional structures that do not seem to be attributable to contaminants or surface shifts. These anomalous features become more prominent for the systems that are expected to have the narrowest f bands and are most extreme for the heavy fermion class of uranium systems. In view of the large value of the underlying non-interacting f band width Δ, it therefore seems reasonable to assume that the effect of Coulomb interactions may be introduced via perturbation theory. Thus, within the formalism of the Anderson impurity model, or even the Hubbard model, the spectra bear resemblance to a Lorentzian band of width $\Delta \approx 2$ eV, and since the 14-fold degenerate f band is expected to contain only 2 or 3 electrons, most of the spectral weight is located above the Fermi level μ.

Encouraged by the correct description of the thermodynamic properties, of the electron–hole symmetric Anderson impurity model (Horvatic and Zlatic 1985, Okada et al. 1987), by straightforward perturbation theory in U_{ff}, several groups have examined the spectral density of the Anderson lattice model using second-order perturbation theory

(Czycholl 1986). For the electron–hole symmetric case, which occurs when $\mu - E_f = \frac{1}{2}U_{ff}$, the spectrum starts to show peaked structures at both the upper and lower band edges for sufficiently large values of U_{ff}. This may be regarded as being a precursor of the Hubbard band splitting. Furthermore, the remaining peak in the f spectral density at the Fermi level shows a temperature dependent suppression reminiscent of that discussed in the Kondo models of cerium. However, it should be stressed that this temperature dependence is not a signature of the Kondo effect but it is a more general feature expected of correlated electronic systems, which have a Fermi-liquid description at low energies and temperatures.

Within second-order perturbation theory, the structures at $h\omega = \pm\frac{1}{2}U_{ff}$ can be related to the large energy limiting form of the second-order result for the self-energy $\Sigma(\boldsymbol{k},\omega)$,

$$\Sigma(\boldsymbol{k},\omega) = U_{ff}^2 N_s^{-1} \sum \int d\omega'\, G^0(\boldsymbol{k}-\boldsymbol{q}, \omega-\omega') N_s^{-1} \times \sum \int d\omega''\, G^0(\boldsymbol{k}'+\boldsymbol{q}, \omega'+\omega'') G^0(\boldsymbol{k}', \omega''), \tag{31}$$

where $G^0(\boldsymbol{k},\omega)$ is the unperturbed f component of the one-electron Green's function. This has a large ω limiting form, represented by the approximate expression

$$\Sigma(\boldsymbol{k},\omega) \approx (N_f - 1)U_{ff}^2 \frac{n_f(1-n_f)}{h\omega - E_f}, \tag{32}$$

which for $N_f = 2$ and large U_{ff} yields two poles in the Green's function, representing the upper and lower Hubbard peaks split U_{ff} apart. However, the peak positions do not agree with those expected from simple considerations when $N_f > 2$. Furthermore, both the discrepancy with exact Bethe Ansatz results for the thermodynamics and with the form of the experimental spectra are heightened when the bare f level is positioned above the Fermi energy.

Steiner et al. (1991) have gone beyond this by performing second-order perturbation theory using a Hartree–Fock band structure calculation to provide the set of basis states. That is, the unperturbed Green's function $G^0(\boldsymbol{k},\omega)$ in eq. (24) is replaced by the expression for the Green's function evaluated in the Hartree–Fock approximation, $G^{HF}(\boldsymbol{k},\omega)$. For the Anderson impurity model, the Hartree–Fock approximation not only leads to a shift in the Fermi energy, as in the paramagnetic phase of the Hubbard model, but also has a relative shift between the energy of the f level and the centroid of the conduction band. Similar types of calculations have been performed by Sarma et al. (1986), in which the electronic structure calculated within LDA was used as the set of basis states instead of the states given by the Hartree–Fock approximation. However, Sarma et al. also used a simplifying assumption in order to calculate the summations over $\boldsymbol{k}$, which appear in the expression for the self energy. This assumption amounts to assuming that the electronic self energy only involves scattering processes that occur on a single ion. This approximation was first introduced by Friedel and Sayers (1977) and has been applied to

the description of nickel compounds by Treglia et al. (1980, 1982). Recently, this local approximation has been found to be exact (Metzner and Wohlhardt 1989) in the limit of large spatial dimensionality d. Furthermore, expansion in powers of $1/d$ shows that the local approximation gives reasonable results for $d=3$.

For large values of $U_{\rm ff}/\Delta$ it seems desirable to have a fully self-consistent theory. Schweitzer and Czycholl (1989a,b) have performed such a self-consistent second-order perturbation theory calculation. That is, the propagators $G^0(\boldsymbol{k},\omega)$ in the expression for $\Sigma(\boldsymbol{k},\omega)$ are replaced by the expressions $G(\boldsymbol{k},\omega)$ which contain the approximate expression for the self-energy $\Sigma(\boldsymbol{k},\omega)$. This self-consistency process has the effect of altering the spectra by pulling the Hubbard split peaks to energies closer to the Fermi level. Thus, for single–particle properties, these results seem to be less accurate than those produced by site-excluded approaches (Horvatic and Zlatic 1985).

An alternate scheme of resumming perturbation theory in $U_{\rm ff}$ is given by calculating the self-energy in the Random Phase Approximation (Rivier et al. 1974, Kim and Riseborough 1990, Zlatic et al. 1986). Here it is recognized that the expression

$$\chi^{(0)}(\boldsymbol{q},\omega) = N_{\rm s}^{-1} \sum \int {\rm d}\omega'\, G(\boldsymbol{k}+\boldsymbol{q},\omega+\omega')\, G(\boldsymbol{k},\omega') \tag{33}$$

is recognized as being the Hartree–Fock expression for the frequency dependent susceptibility of the f electrons. For a separable interaction, the Random Phase Approximation for the longitudinal susceptibility results in the expression

$$\chi(\boldsymbol{q},\omega) = \frac{\chi^{(0)}(\boldsymbol{q},\omega)}{[1-U_{\rm ff}\chi^{(0)}(\boldsymbol{q},\omega)][1+(N_{\rm f}-1)\chi^{(0)}(\boldsymbol{q},\omega)]}, \tag{34}$$

which shows an enhancement at low frequencies, due to the presence of the factor $[1-U_{\rm ff}\,\chi^{(0)}(\boldsymbol{q},\omega)]$ in the denominator. The low-frequency, $\boldsymbol{q}\to 0$, limit of $\chi^{(0)}(\boldsymbol{q},\omega)$ yields the f electron density of states per 5f ion, $\rho_{\rm f}(\mu)$. In the Hartree–Fock approximation, the system is stable against the formation of a magnetic state with periodicity $\boldsymbol{q}$, whenever the Stoner–Wohlfarth criterion, $1 > U_{\rm ff}\,\chi^{(0)}(\boldsymbol{q},0)$, is satisfied. The large value of the dynamic susceptibility at low frequencies can be interpreted as indicating the presence of long lived, large-amplitude collective spin fluctuation modes. The second factor represents the coupling of spin and charge fluctuations due to the Pauli-exclusion principle. The second factor in the denominator leads to the existence of damped high-frequency plasmon excitations, due to the vanishing of the real part of $[1+U_{\rm ff}\,\chi^{(0)}(\boldsymbol{q},\omega)]$. The characteristic energy scale for these excitations, $\hbar\omega$, has a lower bound placed on it by Δ, since the response $\chi^{(0)}(\boldsymbol{q},\omega)$ only changes sign for energies of the order of the f band width. The damping of these plasmon-like charge fluctuation modes is caused by the non-vanishing of the imaginary part. Due to the coupling of these boson modes, the self-energy can show a rapid energy variation at low frequencies, which leads to a narrow quasi-particle peak near the Fermi energy. The satellites at the upper and lower f band edges can be interpreted as being due to the emission or absorption of the damped plasmon excitations

(Zlatic et al. 1986). Clearly, the peak at the Fermi level sharpens as the ground state of the system approaches a magnetic instability. To date, there has been little work directed at performing RPA in a self-consistent manner, for the Anderson lattice.

The above physical picture does offer the hope that a consistent physical picture of the uranium systems may be found, starting from the point of view that the electronic structure is that of a relatively narrow f band pressing up close to the Fermi energy, and that the presence of satellite structures are the precursors of the Hubbard band splitting, due to considerations of screening of the f electron charge.

Other groups have started with the other extreme, and have generalized the infinite U_{ff} approach to the uranium systems. In these approaches, one projects out all the configurations except f^2 and f^3, using a variation on the slave boson methods (Nunes et al. 1985, 1986, Rasul and Harrington 1987, Evans et al. 1989). It is found that these methods are able to account for large enhancements in certain thermodynamic properties, however the spectra still retain marked separations between features in the unoccupied and occupied 5f density of states.

5. Pairing model

Sheng and Cooper (1995) took an alternative approach to the heavy fermion materials. The model which they use is based on the Anderson lattice, however, the on-site couplings play a crucial role. The most novel aspect of their model is the detailed recognition of how the non-spherical crystalline environment causes hybridization between the on site f electrons and ligand electrons centered off site. Their approach to the model is to first diagonalize the local parts of the Hamiltonian. For Ce based heavy fermion systems this is done in the space of local two particle states, supplemented with the trivial vacuum state $|0\rangle$. The periodic nature of the lattice is then re-introduced by treating the localized two electron states as forming composite particles.

The two particle basis states that are used to diagonalize the local parts of the interaction, are composed of the non-degenerate two ligand (s i.e., the $l=0$ tail of the conduction electron wavefunctions on the neighboring sites) electron states $|\varepsilon\rangle$:

$$|\varepsilon\rangle = s_{\downarrow}^{+} s_{\uparrow}^{+} |\varepsilon\rangle \tag{35}$$

and the highly degenerate set of states composed from one spin orbit coupled $j=\frac{5}{2}$ f electron and one ligand electron. These states are specified as eigenstates of the total angular momentum $|j,\mu\rangle$:

$$|3,\mu\rangle = 6^{-1/2}[(3-\mu)^{1/2} f_{\mu+1/2}^{+} s_{\downarrow}^{+} + (3+\mu)^{1/2} f_{\mu-1/2}^{+} s_{\uparrow}^{+}]\,|0\rangle\,, \tag{36}$$

$$|2,\mu\rangle = 6^{-1/2}[(3-\mu)^{1/2} f_{\mu+1/2}^{+} s_{\downarrow}^{+} - (3-\mu)^{1/2} f_{\mu-1/2}^{+} s_{\uparrow}^{+}]\,|0\rangle\,, \tag{37}$$

where the $j=\frac{5}{2}$ states of the spin–orbit coupled f electrons are created by the operators

$$f_{\upsilon}^{+} = 7^{-1/2}\left[\left(\tfrac{7}{2}+\upsilon\right)^{1/2} f_{\upsilon+1/2,\downarrow}^{+} - \left(\tfrac{7}{2}-\upsilon\right)^{1/2} f_{\upsilon-1/2,\uparrow}^{+}\right]. \tag{38}$$

The on-site Coulomb interaction between the f electrons U_{ff} is assumed to be infinite, so the manifold of multiply occupied f states can be neglected.

These basis states are mixed by the non-spherical hybridization potential V_μ^*, and the 12-fold degeneracy due to the angular momentum of the electrons is partially lifted by an on-site Coulomb exchange, J, between the f electron and the ligand electron. The net result of the diagonalization of the local interactions is one singlet state and a set of magnetic states. The singlet state, $|\Phi_0\rangle$, can be interpreted as resulting from the hybridization with two ligand electron singlet. Using this starting point, the hybridization process serves to select a singlet state out of the degenerate manifold of states containing both f and ligand electrons:

$$|\Phi_0\rangle = \aleph^{-1}\left[\sqrt{\tfrac{6}{7}}\, V_\mu^* |3,\mu\rangle + \Delta E\, |\varepsilon\rangle\right]. \tag{39}$$

This strong hybridization results in an energy lowering of the singlet state, by an amount proportional to ΔE, where

$$\Delta E \approx \frac{6|V|^2}{E_f - \varepsilon_s}. \tag{40}$$

The hybridization does not lift the degeneracy of the manifold of magnetic states. Depending on the relative strength of ΔE to J, either the localized singlet state or the magnetic states can be stabilized.

The effect of inter-site hopping is then introduced into the system. The manifold of basis states are limited to those in which the local correlations have been diagonalized. The wave functions for the composite particles then obey Bloch's theorem, which results in the formation of a dispersion relation consisting of two bands for the quasi-bosons: the first band describes spinless quasi-boson excitations, the second band describes the magnetic quasi-bosons. Although these composite particles are bosons in that they commute on different sites, they nevertheless have local occupation numbers which are Fermi–Dirac like.

This approach does at first sight seem limited to cerium systems, because the two body correlations coincide with the dominance of the $n_f = 0$ and $n_f = 1$ configurations which involve precisely two electrons. However, this can be extended to uranium as indicated by preliminary calculations by Cooper, Lin and Sheng (unpublished). These calculations show that the essential features of the above description are preserved if the mixing occurs between the $n_f = 1$ and $n_f = 2$ configurations which involve three electrons.

6. GS and NCA predictions for PES

6.1. *The predicted spectrum*

A graphic representation of the predictions of GS and NCA is perhaps most useful to the reader even though the theory is fully discussed in sect. 2.1. An unbroadened calculated

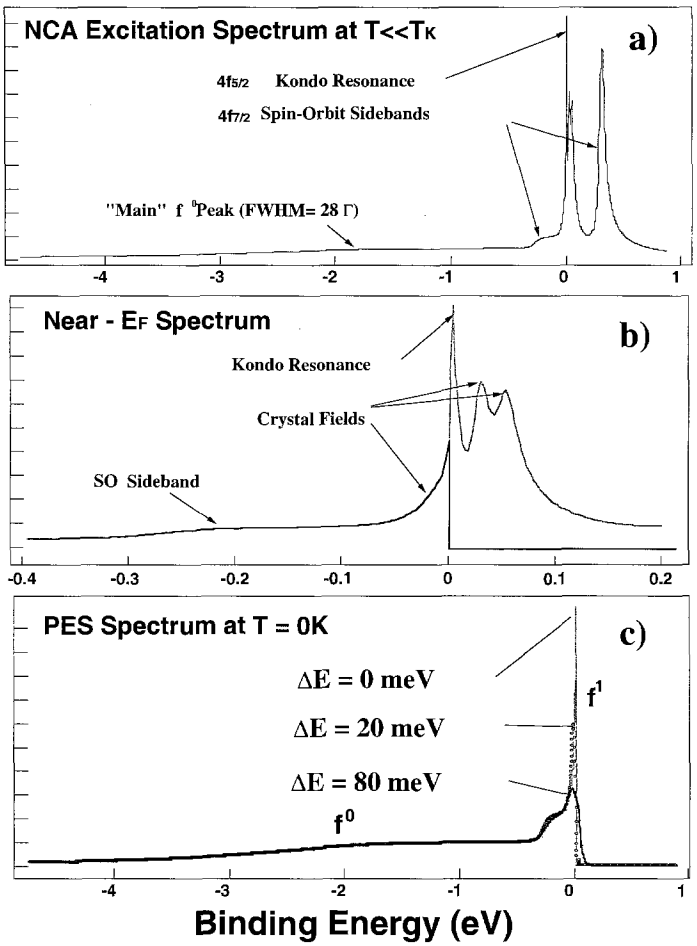

Fig. 1. (a) Particle–hole excitation spectrum calculated for $T = 11$ K using NCA code provided by D.L. Cox. Parameters approximately correspond to those expected for $CeSi_2$, namely: $T_K = 37$ K; $W = 5$ eV (Lorentzian); $\Gamma = 0.1439$; $\Delta_{SO} = 280$ meV; $\varepsilon_f = -2.4$ eV; $\Delta_{CF1} = -25$ meV; $\Delta_{CF2} = -48$ eV; $U_{ff} = 7$ eV. (b) Blow-up of near-E_F region. Dark line corresponds to convolution of spectrum with a $T = 0$ K Fermi function. (c) Calculated PES spectrum at $T = 0$ K using three different instrument resolutions.

spectrum is shown in fig. 1a (code provided by D.L. Cox) for a typical heavy fermion material having a T_K of 35 K, a model (flat) conduction band 5 eV wide, crystal field levels at −25 and −48 meV, U_{ff} of 7 eV, and a bare f level positioned at $\varepsilon_f \approx -2.3$ eV. These parameters approximately correspond to those of the heavy fermion compound $CeSi_2$ which has been heavily reported in the literature (Patthey et al. 1986, Joyce et al. 1992c, Takahashi et al. 1994, Malterre et al. 1992a,b). It should be stressed that within the SIM the 4f DOS in fig. 1a is obtained by averaging the hybridization over all conduction electron states, so that dispersion is precluded. To be more precise, we are not actually

dealing with a 4f DOS at the Fermi energy but rather only the response of the system to a core hole. We will nevertheless refer to the intensity at the Fermi energy as the 4f DOS. This was nicely explained for the experimentalist by Hüfner (1986) and Hüfner and Schlapbach (1986). In any case it is argued that NCA yields an excellent representation of the 4f DOS at high temperatures, while at low temperatures (far below T_K where a Kondo lattice model is more appropriate) any dispersion in the coherent state is in any case smaller than $k_B T_K$ and thus negligible. The essential predictions of SIM (i.e., the scaling of 4f spectral features with T_K) are of necessity retained at all temperatures.

Although Ce contains only one f electron, the GS theory (Gunnarsson and Schönhammer 1985, 1986) as well as NCA (Bickers et al. 1985, 1987) predict at least three features in a PES spectrum (occupied states) and at least two features in a BIS spectrum (remaining 13 empty states). In fig. 1a the occupied features are labeled as the f^0 or "main" peak which represents the primary f^1 to f^0 excitation, while the f^1 portion of the spectrum consists of the narrow $4f_{5/2}$ feature (called the Kondo resonance, KR) located at $k_B T_K$ above E_F with only a small occupied tail extending below E_F (see fig. 1b), as well as a spin–orbit split sideband (the $4f_{7/2}$ feature) located at $\Delta_{SO} - k_B T_{SO}$ below the KR. (Here Δ_{SO} is the spin–orbit splitting while T_{SO} is an effective Kondo temperature for the sideband, usually about an order of magnitude larger than T_K). Above the Fermi energy we have the bulk of the KR at $\sim k_B T_K$, an equally intense spin–orbit sideband at $+\Delta_{SO}$, as well as a broad f^2 feature (not shown) corresponding to double f occupancy at finite U_{ff}, and situated at U_{ff} above the occupied f^0 peak. The KR may additionally be split into crystal field levels situated at Δ_{CF} relative to T_K, which have their own effective Kondo temperature, T_{CF}, and which may actually carry more spectral weight than the KR. These are shown in the expanded view in fig. 1b.

Because of particle–hole symmetry, the PES spectrum for Yb heavy fermions, where one has only one f hole (f^{13} vs f^{14}) rather than one f electron, can be obtained from fig. 1a simply by applying mirror symmetry about the Fermi energy (Bickers et al. 1987). Thus in Yb heavy fermions the bulk of the KR is predicted to be occupied, which makes them ideal candidates for studying spectral weights, widths, and temperature dependencies.

From Bickers et al. (1987) we note several important points regarding fig. 1a: (1) The width of the f^0 peak varies with the hybridization Γ (width = 28Δ when using a model DOS; but see below), and has a spectral weight of about one electron (i.e., $\sim n_f$). (2) The width of the KR is $\sim k_B T_K$, while its total spectral weight (including the unoccupied portion) scales with T_K approximately as $\pi T_K/\Gamma$. (3) The position of the SO sideband varies as $\Delta_{SO} - k_B T_{SO}$ so that for increasing T_K it shifts closer to E_F as T_{SO} also increases along with T_K. Thus most of the spectral features at E_F increase with T_K (the sidebands, of course, scale directly with T_{SO} and T_{CF}) and readily lend themselves to measurement in PES.

The existence of crystal field levels yields additional features near the Fermi energy. For the spectrum of fig. 1a two crystal field levels have been introduced (at –24 meV and –48 meV) to approximately correspond to those reported for $CeSi_2$ in neutron diffraction measurements (Galera et al. 1989). A blowup of the near-E_F region is shown in fig. 1b with the crystal field levels delineated. Note that on the occupied portion of the spectrum

these levels are relatively weak and in fact do not account for the bulk of the occupied spectral weight. Although crystal field levels have never been unambiguously observed in a PES measurement, their theoretical spectral weight cannot always be assumed to be small (it depends on the parameters), particularly in Yb compounds.

In an actual PES measurement the spectrum in fig. 1a would be convoluted with a Fermi function to yield only the occupied states, as well as broadened by instrument resolution. The dark lined spectrum in fig. 1b corresponds to a convolution with a T=0 K Fermi function. In fig. 1c this $T=0$ K spectrum has been further broadened with a 20 meV Gaussian to match the stated resolution of Patthey et al. (1987a) as well as with an 80 meV Gaussian to match the best resolution of a measurement at resonance ($h\nu=120$ eV). This then is the expected shape of a typical Ce heavy fermion PES spectrum, while a typical Yb spectrum would mimic the unoccupied states of fig. 1a broadened by instrument resolution.

6.2. *Temperature dependence*

Besides the scaling with T_K, a major prediction of SIM and its extensions (in particular, NCA) is the temperature dependence of the KR. Figure 2 is taken from Bickers et al. (1987) and shows a typical temperature dependence of the KR in terms of the Kondo temperature, denoted as T_0 in the figure. The quantity D refers to the conduction bandwidth. Note that substantial temperature dependence already exists at $0.23T_K$, while at $29T_K$ all the f^1 spectral features have been renormalized to nearly zero. A real spectrum at temperatures comparable to T_K may be complicated somewhat by the existence of possible crystal field (or CF) levels where $T_K < T_{CF} < T_{SO}$. Nonetheless, at $29T_K$ it

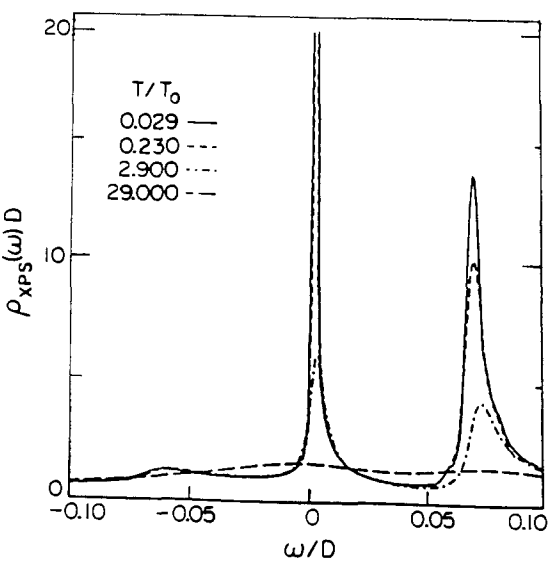

Fig. 2. Universal expected temperature dependence of the KR and its sidebands (crystal fields not included) from Bickers et al. (1987).

is clear that all f^1 states should renormalize to near zero. This will be of particular importance when later considering the $T = 80$ K spectrum of $YbAuCu_4$, a material which has been considered as the quintessential trivalent compound (Kang et al. 1990a).

6.3. *Crystal fields and finite U_{ff}*

Effects of CF levels and finite U_{ff} have been singled out as complicating the PES spectra of heavy fermions (Allen et al. 1986, Allen 1992). In particular, because of their larger effective Kondo temperature, CF levels may result in a lack of scaling with T_K. Hüfner (1992) views these as single particle states, although that argument cannot not hold for large-T_K materials such as $CeBe_{13}$ where the width of the KR is broader than any CF states. Likewise, it is possible that spectral weight from the very broad f^2 states at finite U_{ff} may spill over into the occupied portion of the spectrum and strongly affect the scaling. Joyce and Arko (1993) have shown however that while CF states indeed add extra weight (though not much, as shown in fig. 1b), the scaling with T_K remains dominant within GS theory, as shown in fig. 3b. Here the CF states were positioned at −60 and −80 meV, somewhat higher than usually observed in order to more clearly demonstrate the residual scaling effect of both the CF states and the KR. The calculated spectra have been convoluted with a 20 K Fermi function as well as a 20 meV Gaussian instrument broadening. *Clearly the GS model predicts the f^1 intensity to scale with T_K even in the presence of CF states.* The intensity of the CF states themselves scales with T_{CF} which in turn is dependent on T_K.

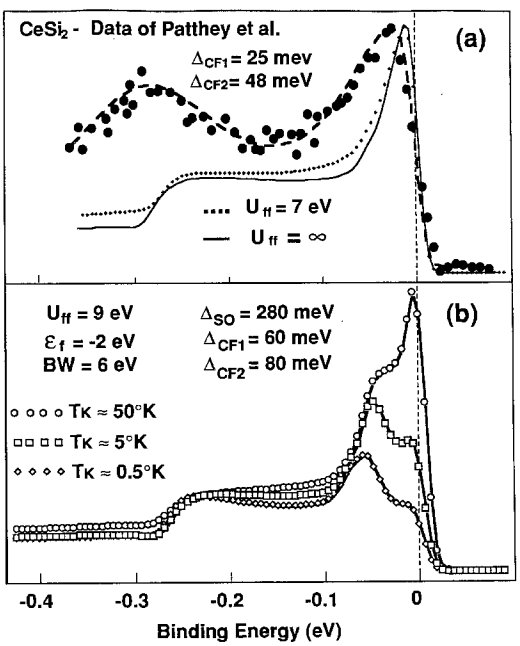

Fig. 3. GS calculations to show lack of effect due to finite U_{ff} and crystal field levels, from Joyce and Arko (1993). (a) Near-E_F spectrum calculated using $U_{ff} = 7$ eV, $T_K = 37$ K, $\Delta_{SO} = 280$ meV, $\varepsilon_F = -2.0$ eV, $W = 5.0$ eV (flat), $\Gamma = 0.0877$ eV, CF's as labeled in the figure. For $U_{ff} = \infty$, it was necessary to use $\Gamma = 0.12$ eV and $e_f = -2.4$ eV in order to maintain T_K at 37 K. Calculated spectra were broadened by 20 meV to match the stated resolution of Patthey et al. (1987a), superimposed on the calculated spectra. (b) GS calculated spectra with CF's as labeled in the figure, artificially placed for better viewing. Parameters as shown. Γ was adjusted to obtain the T_K's shown. Note that scaling with T_K is maintained in the presence of CF's.

The effect (or lack thereof) of the finite U_{ff} is demonstrated in fig. 3a. Here Joyce and Arko (1993) have shown that while indeed a finite U_{ff} will draw spectral weight from the f^2 levels into the occupied portion of the spectrum, its net effect is merely to increase all intensities without changing the overall shape of the spectra, thus keeping all relative weights unaffected. In this figure the T_K was kept constant for the two values of U_{ff} by varying the hybridization Γ, while the spectra were normalized at the f^0 maximum. Keeping T_K constant is important, otherwise a comparison of intensities is meaningless. The lack of an effect is not surprising since spillover of the very broad f^2 states into the occupied portion of the spectrum should resemble the extreme end of the tail of a Gaussian which cannot affect the f^1 features much more than the f^0 peak. *The important result is that within GS the finite U_{ff} will again not affect the scaling with T_K.* In the figure the data of Patthey et al. (1987a) are superimposed on the calculated spectra and will be discussed later in connection with the width of the KR which experimentally is found always to be about an order of magnitude broader than calculation.

6.4. *Lineshape of f^0 peak*

The lineshape of the f^0 peak is in principle dependent on the exact shape of the conduction electron DOS as well as an energy dependent hybridization. Patthey et al. (1990) have extensively discussed this problem in their excellent paper. They demonstrated the differences in f^0 lineshape and linewidth obtained when using an elliptical DOS with a sharp cut-off vs a smoother Lorentzian lineshape. This is summarized in fig. 4 for the two model DOS at different hybridization strengths. The peaking of f^0 occurs at the bottom of the elliptical conduction band. Kang et al. (1990b) calculated the GS spectrum for $CeCu_2Si_2$ using a full LDA-derived conduction band DOS and hybridization and obtained reasonably good fits to the experimental spectra of Parks et al. (1984). However, a model

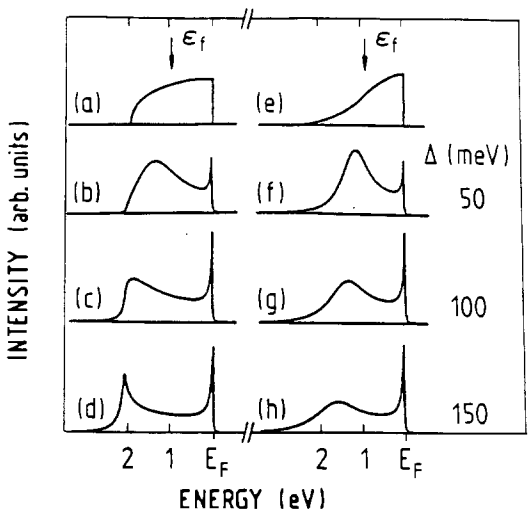

Fig. 4. Influence of the conduction band shape [(a) semi-elliptical, (b) Lorentzian] on the excitation spectra for various values of hybridization strength Δ (or Γ in our notation). Figure is from Patthey et al. (1990). Note that the f^0 peak appears near the bottom of the band.

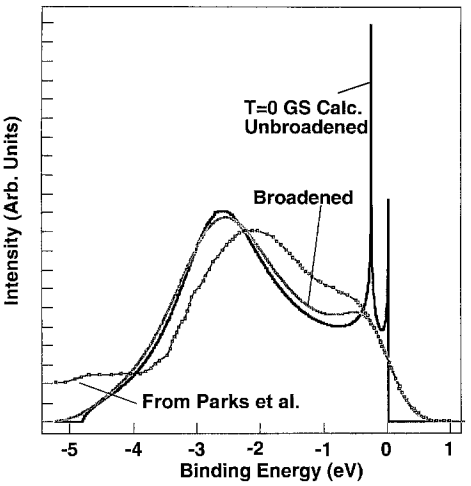

Fig. 5. $CeCu_2Si_2$ data of Parks et al. (1984) (data points) and used by Kang et al. (1990b) to compare to their GS calculations using a real DOS. The GS spectrum in the figure uses the parameters of Kang et al. but with a flat DOS. The broadened spectrum nearly reproduces the data.

DOS consisting of a flat band having the same width as the exact DOS, and using the same average values for the hybridization and U_{ff}, produced a 4f spectrum very similar to that of Kang et al. (1990b). This is demonstrated in fig. 5 where the two calculated spectra are overlaid. There are small differences that could undoubtedly be overcome with minor adjustments of parameters. An unbroadened spectrum for $T = 0$ K is also shown for comparison. Whether this result will hold universally remains to be seen. But what it does show is that the integration over all conduction DOS greatly averages out the hybridization effects and that it is the width W of the conduction band which is likely the more relevant parameter. A sharpening of the f^0 peak occurs at the lower band edge even when using a flat DOS whenever the two are degenerate in energy. W must be sufficiently large so that the final position of the f^0 peak lies within the band.

The important conclusions of this section then are that the major predictions of GS and NCA are those of scaling of 4f features with hybridization (and hence T_K) together with a strong temperature dependence of these features as the hybridization decreases with increasing temperature. The scaling is complicated somewhat by the exact choice of parameters, but the increase in spectral weight with T_K is at the very least monotonic.

7. Quasiparticle formation and Kondo screening in the periodic Anderson model

7.1. *Introduction*

Heavy fermion materials are usually modeled by the single impurity Anderson model or the periodic Anderson model depending on the concentration of the correlated f orbitals. Although at high temperatures the SIM captures the same physics as the lattice model, it cannot account for the electronic coherence at low temperatures. The periodic Anderson model (PAM) is believed to describe the strong correlation of f electrons as well as their

coherence at low temperatures and the interaction between the screened moments. The PAM is the simplest model of a periodic Kondo system with a conduction band composed of strongly hybridizing d orbitals, and a localized band composed of weakly hybridizing correlated f orbitals. The Coulomb correlation on the f orbitals suppresses the formation of local spin singlets, so moments form. At low temperatures, these moments are screened by the conduction band, suppressing spin-flip scattering so that quasiparticle formation may occur. However, as pointed out by Nozières (1985), the f-electron moments must compete for a limited number of conduction electronic states available for screening. Thus the low-temperature physics of the SIM and the PAM may be quite different.

In this section we discuss the Kondo screening and quasiparticle formation in the PAM. The PAM predicts a much weaker temperature dependence for the quasiparticle or Kondo peak than the SIM. We also show that the Kondo peak is dispersive in the PAM, giving rise to heavy quasiparticle bands near the Fermi energy. Nozières' idea of the effective Hubbard model for the screening clouds (Nozières 1985) is used to interpret this "band formation" and the slow evolution of the Kondo peak. This also gives insight into the emergence of multiple low-energy energy scales in the PAM.

7.2. *Formalism*

The PAM is studied in the high-dimensional limit mentioned in sect. 4. Since the Kondo effect is independent of lattice dimensionality, working in this limit will not inhibit the study of screening in the lattice. The PAM Hamiltonian on a D_S-dimensional hypercubic lattice is

$$H = -\frac{t^*}{2\sqrt{D_S}} \sum_{\langle ij\rangle\sigma} (d^\dagger_{i\sigma} d_{j\sigma} + \text{h.c.}) + \sum_{i\sigma} (\varepsilon_d d^\dagger_{i\sigma} d_{i\sigma} + \varepsilon_f f^\dagger_{i\sigma} f_{i\sigma}) + V \sum_{i\sigma} (d^\dagger_{i\sigma} f_{i\sigma} + \text{h.c.}) + \sum_i U_{ff} \left(n_{fi\uparrow} - \tfrac{1}{2}\right)\left(n_{fi\downarrow} - \tfrac{1}{2}\right). \tag{41}$$

In eq. (41), $d(f)^{(\dagger)}_{i\sigma}$ destroys (creates) a $d(f)$ electron with spin σ on site i. The hopping is restricted to the nearest neighbors and scaled as $t = t^*/2\sqrt{D_S}$. U_{ff} is the screened on-site Coulomb repulsion for the localized f states and V is the hybridization between d and f states. This model retains the features of the impurity problem, including moment formation and screening, but is further complicated by the lattice effects.

Metzner and Wohlhardt (1989) observed that the irreducible self-energy and vertex-functions become purely local as the coordination number of the lattice increases. As a consequence, the solution of an interacting lattice model in $D_S = \infty$ may be mapped onto the solution of a local correlated impurity coupled to a self-consistently determined host (for reviews, see Georges et al. 1996 and Pruschke, Jarrell and Freericks 1995). The quantum Monte Carlo (QMC) algorithm of Hirsch and Fye (1986) is employed to solve the remaining impurity problem and the imaginary time local Green's functions are calculated. Finally the maximum entropy method (Jarrell and Gubernatis 1996) is used to find the f and d density of states and the self-energy.

7.3. *Results*

The PAM was simulated for a wide variety of fillings and parameters. Results are presented here for $U_{ff} = 1.5$, $V = 0.6$, and $U_{ff} = 2.0$, $V = 0.5$ (measured in units of t^* which is considered to be a few electronvolts, the typical bandwidth of conduction electrons in metals). In order to model the Ce-based Kondo lattice materials, the correlated f-band is placed below the Fermi level (so $n_f \approx 1$) and the conduction band filling is adjusted by varying the Fermi level. Since the model is particle–hole symmetric when $n_f = n_d = 1$ it is only necessary to study $n_d < 1.0$. The properties of the model for $n_d > 1$ may be inferred from these results. Thus, beginning at $\beta = 1/k_B T = 10$, we choose ε_f and ε_d so that $n_f = 1$ and n_d assumes a chosen value less than unity. When the temperature is changed, $\varepsilon_f - \varepsilon_d$ is kept fixed and the chemical potential varied to conserve the *total* number of electrons. For the results presented here, the variation of n_f from one is less than a few percent. Results from simulations of the SIM are presented for comparison.

7.3.1. *Thermodynamics*

The thermodynamics of the system, especially the local susceptibility, allows the study of the Kondo screening and identifies the relevant energy scales. The Kondo scales are obtained by extrapolating $\chi_{imp}(T \to 0) = 1/T_0$, where $\chi_{imp}(T)$ is the additional local susceptibility due to the introduction of the effective impurity into a host of d electrons. As shown in fig. 6, at the symmetric limit ($n_f = n_d = 1$) the Kondo scale for the PAM T_0 is strongly enhanced compared to T_0^{SIM}, the Kondo scale for a SIM with the same model parameters. This behavior has been observed before (Rice and Ueda 1986, Jarrell

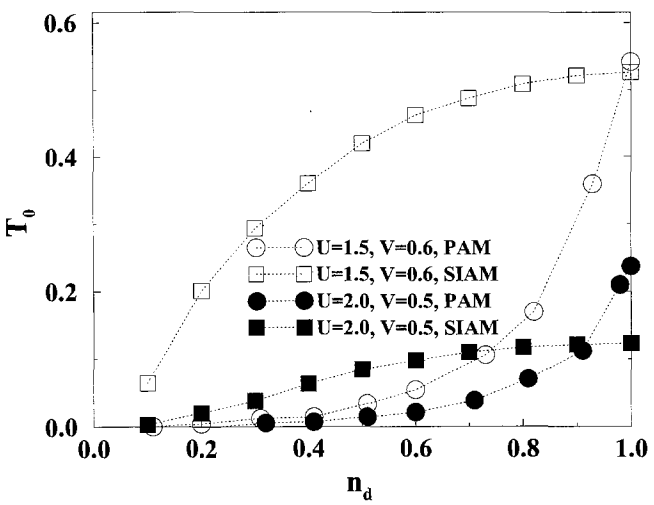

Fig. 6. Kondo temperature vs. d-band filling for the PAM and SIAM (or SIM) when $n_f \approx 1$ and for two different sets of model parameters.

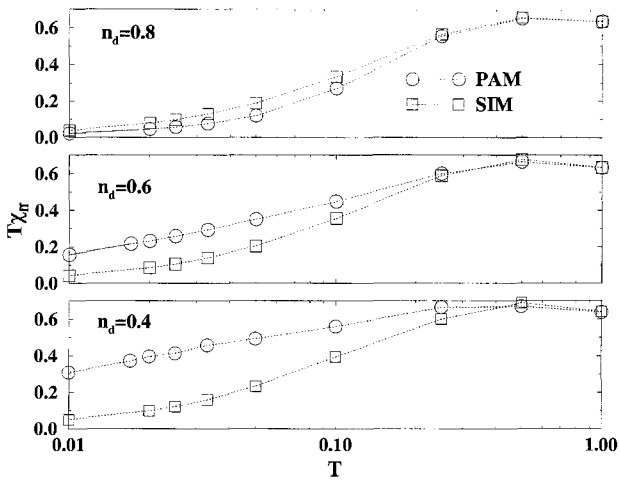

Fig. 7. The f-band magnetic moments for the PAM and the SIM vs. temperature for three different values of d-band filling when $U_{ff} = 1.5$ and $V = 0.6$.

1995). However, far from the symmetric limit the Kondo scale for the PAM is strongly *suppressed.*

The main consequence of this suppression is that the temperature dependence of the screening in the PAM is quite different from that of the SIM. The high-temperature ($T > T_0^{SIM}$) properties of the two models are similar, so that T_0^{SIM} is the relevant scale for the onset of screening in *both* models. This is shown in fig. 7 where the screened local f moments $T\chi_{ff}$ for both models are plotted versus temperature. As expected from the impurity problem $T\chi_{ff}$ displays a log-linear T dependence in some temperature interval. However, concomitant with the differences in the Kondo scales, the screening of the PAM and the SIM local moments are quite different: for most values of n_d these two curves *cannot be made to overlap by rescaling their temperature dependencies* (nor is it possible, in the PAM case, to make the curves for different d fillings overlap by rescaling the temperature). Thus, unlike the SIM, the screened local moment in the PAM is not a universal function of temperature. At high temperatures, the screened local moments are identical for the PAM and the SIM, and as the temperature is lowered below T_0^{SIM} the screening begins; however, if $n_d \lesssim 0.8$ and $n_f \approx 1$ ($n_d \approx n_f = 1$), the screening is significantly protracted (contracted) in temperature for the PAM compared to that in the SIM.

7.3.2. *Dynamics*

Drude weight and quasiparticle fraction. The physical relevance of T_0 in the PAM is revealed by the dynamical properties of the system. For example, the Drude weight D_0, calculated by extrapolation of the current–current correlation function (Scalapino, White and Zhang 1993), is shown in the inset to fig. 8. For all of the data shown in fig. 8, D_0 is quite small and the effective electron mass (not shown) is large, $m^*/m = 1/Z \geqslant 15$,

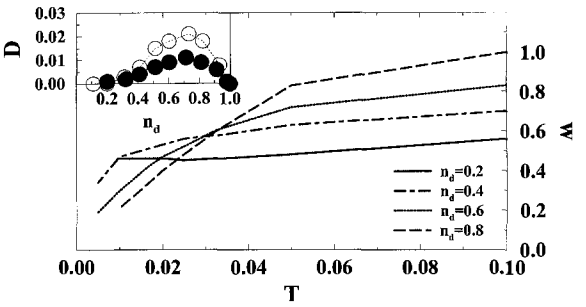

Fig. 8. Half-width of the derivative of the total occupation number, $dn(\varepsilon_k)/d\varepsilon_k$ at low temperatures when $U_{ff} = 1.5$ and $V = 0.6$. In a Fermi liquid this quantity should be proportional to ZT. Any residual value represents the scattering rate at the Fermi surface. The flat slope of $w(T)$ at low temperatures for the low-filling case suggests that the Fermi liquid does not begin to form before the ferromagnetic transition. The inset shows the Drude weight when $U_{ff} = 1.5$, $V = 0.6$ (open symbols) and $U_{ff} = 2.0$, $V = 0.5$ (solid symbols).

where Z is the quasiparticle renormalization factor. In the symmetric limit, where a gap opens in the single-particle density of states, we have $D_0 = Z = 0$. However, consistent with what is seen in the Kondo scale for the PAM, D_0 and Z also become small when n_d is reduced. That is, T_0 falls quickly as the d band is doped away from half filling, mirroring the behavior of the Drude weight and quasiparticle fraction. Thus, in the metallic regime, $n_d \lesssim 0.8$, T_0 is also identified as the coherence scale of the PAM: the temperature below which a Fermi liquid begins to form.

It is clear from the Drude weight shown in the inset to fig. 8, that the unscreened moments have a dramatic effect on the Fermi-liquid properties of the system. This may also be seen by examining the electronic distribution function

$$n(\varepsilon_k) = T \sum_n \left(G^{dd}(\varepsilon_k, i\omega_n) + G^{ff}(\varepsilon_k, i\omega_n) \right),$$

where $G^{dd}(\varepsilon_k, i\omega_n)$ and $G^{ff}(\varepsilon_k, i\omega_n)$ are the fully dressed d- and f-band Green's functions calculated with the QMC. $dn(\varepsilon_k)/d\varepsilon_k$ is calculated by numerically evaluating the derivative of the above sum. This has a peak located at the Fermi energy. The width of this peak at low temperatures (shown in fig. 8) gives an estimate of the single-particle scattering rate, which must go to zero if a Fermi-liquid is to form. This appears to happen when $n_d = 0.8$, 0.6 and 0.4; however, for $n_d = 0.2$ it is not clear whether a Fermi-liquid forms. When $n_d \lesssim 0.4$, there is a protracted region in temperature of strong spin-flip scattering, beginning at $T \gtrsim T_0^{SIM}$, and extending down to low temperatures. However, due to magnetic ordering for $n_d \lesssim 0.6$, no compelling evidence for a non-Fermi-liquid (paramagnetic) ground state was found (Tahvildar-Zadeh et al. 1997).

7.3.3. *Density of states*

The densities of states (DOS) of the PAM have been calculated for a wide variety of fillings and parameters. Here the f-band DOS is presented for $U_{ff} = 1.5$, $V = 0.6$ (measured

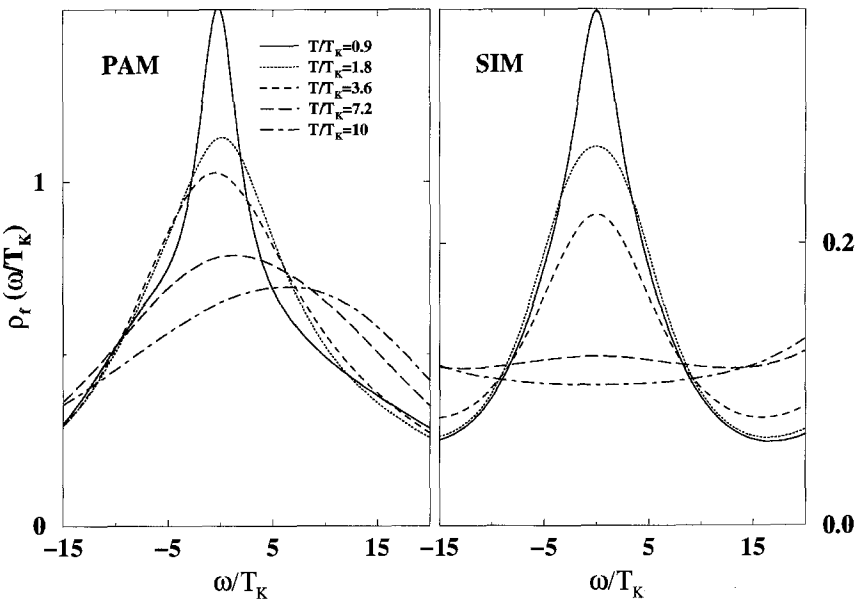

Fig. 9. Near-Fermi-energy structure of the f density of states for the asymmetric PAM (left) and the symmetric SIM (right). The model parameters are $U_{ff}=1.5$, $V=0.6$, $n_d=0.4$ for the PAM and $U_{ff}=2.75$, $V=0.5$, $n_d=1$ for the SIM. The temperature dependence of the peak is universal for the SIM and hence independent of the band fillings. Note that T_K refers to the two different Kondo scales; T_0 for the PAM (left) and T_0^{SIM} for the SIM (right).

in units of t^* which is considered to be a few electronvolts, the typical bandwidth of conduction electrons in metals), $n_f \approx 1$ with $n_d=0.4$ and $T_0=0.014$. The symmetric limit of the SIM is used for the comparison since the results for the SIM are universal and hence independent of the filling. The choice of $U_{ff}=2.75$, $V=0.5$ is made for the SIM, which corresponds to $T_0^{SIM}=0.05$.

Figure 9 shows the f-density of states for the PAM and SIM near the Fermi energy $E_F=0$. Both models show temperature-dependent Kondo peaks of similar width $\sim 10T_K$, where T_K is the corresponding Kondo scale. However, the rate of change of the peak intensity with temperature is much smaller and the Kondo peak persists up to much higher temperatures in the PAM than in the SIM. This is consistent with the protracted behavior of screened moments in the PAM described above (Tahvildar-Zadeh et al. 1997) when $n_d \lesssim 0.8$ and $n_f \approx 1$. There is a difference in the vertical scales of the two parts of this figure: both the intensity and the spectral weight of the Kondo peak are larger in the PAM than in the SIM although the hybridization parameter V is larger for the PAM in this case. This shows (and we generally find) that the height of the Kondo peak in the PAM does not scale like $1/V^2$ as it does in the impurity models.

The evolution of the near-Fermi surface features in the f DOS is not universal as a function of T/T_0 since there is a strong dependence on n_d. For example, the evolution of

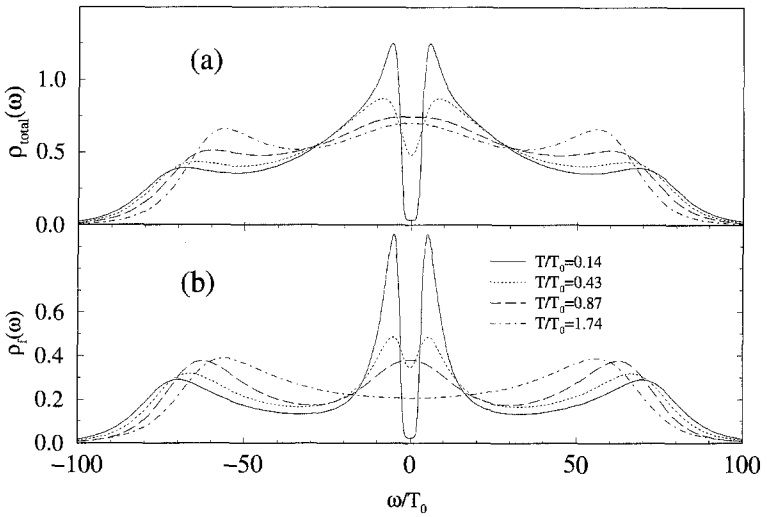

Fig. 10. Temperature dependence of (a) the total density of states $\rho_{tot}(\omega)$ and (b) the f-electron density of states $\rho_f(\omega)$ when $U_{ff}=2.0$, $V=0.5$, $\varepsilon_f=\varepsilon_d=0$, and $T_0=0.23$.

both the f and total DOS of the symmetric model are shown in fig. 10. As T is lowered below T_0 a gap of full width $\sim 5T_0$ develops at the Fermi surface indicating the formation of an insulating state (consistent with the vanishing of D and Z discussed previously). Note that the near-Fermi surface features in the f DOS evolve *very quickly* as T is lowered. In fact, the gap almost completely develops as the temperature falls from $T/T_0=0.43$ to $T/T_0=0.22$. In other words, the evolution of the near-Fermi surface features is much faster in the symmetric model than in the metallic regime ($n_d \lesssim 0.8$ and $n_f \approx 1$). Indeed it is generally found that the near-Fermi surface features in the f DOS develop more quickly as a function of T/T_0 as n_d increases towards unity. In addition, in the symmetric regime, many of the features show scaling with T/T_0, including the screened local moment, the f DOS, and the electronic specific heat (Jarrell 1995).

7.3.4. *Band dispersion*

Figure 11 shows the momentum dependence of the f and d spectral functions for the PAM along the diagonal direction of the Brillouin zone (the main conclusions do not depend on the chosen direction) when $U_{ff}=1.5$, $V=0.6$, $n_f \approx 1$ and $n_d=0.6$. In the large-D_S hypercubic lattice, the zone center (corner) corresponds to a very large negative (positive) ε_k. Near the zone center (lowest part of the figure) there are two apparent maxima, the lower one having mostly d character, the upper one mostly f character. The latter has a narrow Kondo-like feature but would not be seen in a photoemission experiment since it is located above the Fermi energy. The quasiparticle peak (Kondo peak) slightly below the Fermi surface starts to develop only as $\boldsymbol{k}$ moves well away from the zone center. Note that there is a gradual transformation of this peak from a mixed

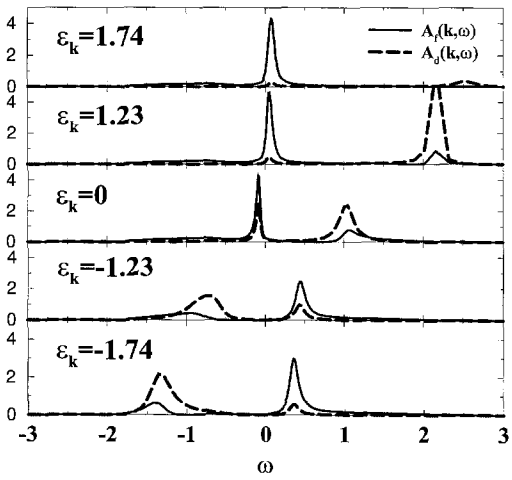

Fig. 11. The PAM f and d-spectral functions for different values of the momentum vector $\boldsymbol{k}$ for $U_{ff}=1.5$, $V=0.6$, $n_v=1$, $n_d=0.6$ and $T/T_0=0.46$. ε_k is the unrenormalized band energy. The Fermi energy is located at $\omega=0$.

f–d character at $\varepsilon_k=0$ to an almost entirely f character at and above $\varepsilon_k=1.23$. In addition to these narrow peaks the data show a small and broad non-dispersive peak near $\omega=-0.8$ which has mostly f character. This is a remnant of the lower unhybridized f level, though the peak corresponding to the upper f level for these model parameters has not been resolved (this peak can be resolved if a larger value for U_{ff}/V^2 is used).

This situation is clarified in fig. 12. The symbols in this figure show the positions of the maxima of the f and d spectral functions versus ε_k, and the solid line shows the

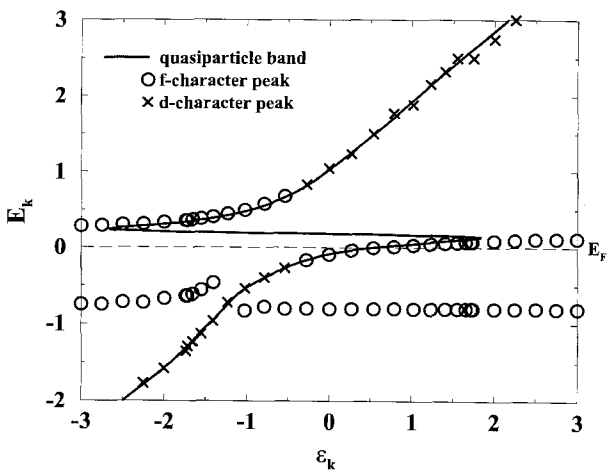

Fig. 12. Band structure for the PAM. The model parameters are the same as in fig. 11. However the features persist up to $T/T_0 \gtrsim 10$. The solid line shows the real part of the Green's functions poles vs. ε_k the unrenormalized band energy. The symbols show the positions of the maxima in the f and d spectral functions. We characterize these peaks to be of f character whenever $A_f(\varepsilon_k,E_k) > A_d(\varepsilon_k,E_k)$ or d character whenever $A_f(\varepsilon_k,E_k) < A_d(\varepsilon_k,E_k)$.

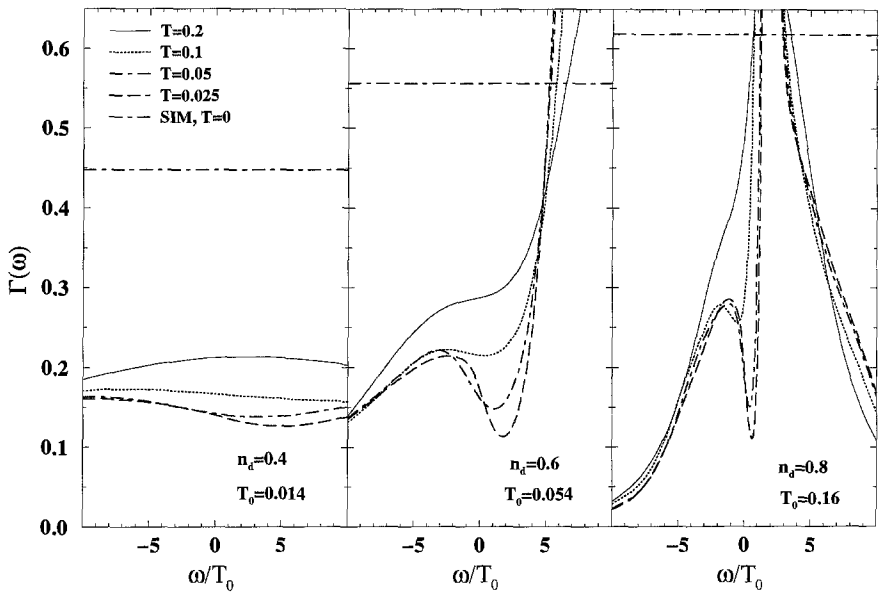

Fig. 13. Near-Fermi-energy structure of the hybridization function for the asymmetric PAM. The model parameters are $U_{\rm ff} = 1.5$, $V = 0.6$ and $n_{\rm v} = 1$. The dip at the Fermi energy denotes a decrease in the number of states available for screening, leading to a suppressed "coherence" Kondo scale T_0. The zero temperature hybridization for the single-impurity Anderson model is shown for comparison.

quasiparticle energy, calculated from the real part of the pole of the Green's functions. In the narrow region above the Fermi surface an almost dispersionless band is obtained. The imaginary parts of these poles are very large, so they correspond to very broad peaks in the spectral functions which are difficult to resolve. The bands above and below this region correspond to well defined peaks in the spectral functions. The general features of this band structure for the PAM persist up to very high temperatures ($T/T_0 \gtrsim 10$).

Perhaps the most unusual feature of the band dispersion shown in fig. 12 is the presence of a weakly-dispersive f quasiparticle band as much as $0.3t^*$ above the Fermi energy. The quasiparticle bands which form due to Kondo screening are expected to lie within about T_0 of the Fermi surface (Martin and Allen 1979). The presence of a screening band this far from the Fermi surface would seem to correspond to a significantly larger f–d hybridization than that which is required to form a small Kondo scale T_0. To study this apparent inconsistency one introduces an effective hybridization strength $\Gamma(\omega)$,

$$\Gamma(\omega) = \mathrm{Im}\left(\Sigma(\omega) + \frac{1}{G(\omega)} \right),$$

where $G(\omega)$ is the local f Green's function and $\Sigma(\omega)$ is the local f-electron self-energy. $\Gamma(\omega)$ is a measure of the hybridization between the effective impurity in the DMF problem and its medium. (For example, in the SIM $\Gamma(\omega) = \pi V^2 \rho_{\rm d}(\omega)$, where $\rho_{\rm d}$ is the d-band

density of states. In finite dimensions, $\Gamma(\omega)$, as defined, will contain parts of the self energy of order $1/D_0$.) Figure 13 shows the effective hybridization for the PAM near the Fermi surface. In this figure the model parameters are chosen to be $U_{\rm ff} = 1.5$, $V = 0.6$, $n_{\rm f} \approx 1$ and three different d-band fillings: $n_{\rm d} = 0.4$ ($T_0 = 0.014$), $n_{\rm d} = 0.6$ ($T_0 = 0.054$), and $n_{\rm d} = 0.8$ ($T_0 = 0.16$). A relatively small value of $U_{\rm ff}/V^2$ was chosen for presentation purposes; however, the features shown are also present for larger values of $U_{\rm ff}/V^2$.

The feature we want to emphasize in $\Gamma(\omega)$ is the dip at the Fermi energy which develops as the temperature is lowered. Since only the electronic states within about T_0 of the Fermi surface participate in the screening (Nozières 1985) this indicates a reduced number of states available for screening at the Fermi energy, and since the dip becomes narrower as $n_{\rm d} \to 1$, the effect is more dramatic for small $n_{\rm d}$. Thus, as the temperature is lowered and $n_{\rm d} \lesssim 0.8$, the Kondo scale of the DMF effective impurity problem is self-consistently suppressed and hence the "coherence" Kondo scale T_0 is also suppressed. However, for the model parameters chosen in figs. 11 and 12, and for the same d-band filling, the effective hybridization increases dramatically at frequencies $\omega \gg k_{\rm B} T_0$, and thus could support quasi-particle bands with significant f character at higher energies, as found in fig. 12.

7.4. *Interpretation*

7.4.1. *Band formation*

Some of these results are consistent with a simple band-formation picture. When $V = 0$ the available electronic states consist of a d band and two (doubly degenerate) local f levels separated by $U_{\rm ff}$. When V is turned on, a new resonant state forms slightly above the Fermi surface when $n_{\rm d} < 1$ and slightly below when $n_{\rm d} > 1$. Furthermore, the original d band mixes with the local f levels and the resonant level, giving rise to a renormalized band which has f character near the renormalized f-level energies and has d character far from them as can be seen in fig. 12. The Kondo states slightly below the Fermi level are only present for $\boldsymbol{k}$ near the zone center when $n_{\rm d} < 1$ and near the zone corner when $n_{\rm d} > 1$. They have mostly f character, indicating that the f electrons themselves are involved in screening the local moments through hybridization with the d band. This is like the situation in a single-band Hubbard model, where the electrons within the band are responsible for screening the "local moments" in that band.

7.4.2. *Nozières exhaustion principle and energy scales*

The emergence of the two energy scales ($T_0^{\rm SIM}$ and T_0) and the protracted screening of the moments in the metallic regime, $n_{\rm d} \lesssim 0.8$, can be understood using the arguments of Nozières. He argued that since the screening cloud of a local magnetic moment involves conduction electrons within $T_0^{\rm SIM}/T_{\rm F}$ of the Fermi surface, only a fraction of the moments $n_{\rm eff} \approx \rho_{\rm d}(0)\, T_0^{\rm SIM}$ may be screened by the conventional Kondo effect. We consider the f moment together with its conduction-band screening cloud to form a spin polaron. Nozières then proposed that the spin polaron and unscreened sites may be mapped onto

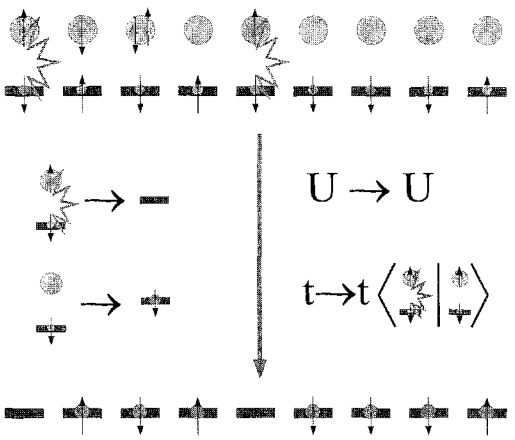

Fig. 14. Mapping to Nozières' single-band Hubbard state. In the PAM (top) f-orbitals are represented by shaded rectangles, d-orbitals by shaded circles, electrons by small shaded circles pierced by up and down pointing arrows, and the Kondo singlet is represented by a thick wavy line. Only the conduction electrons with energies within $k_B T_0^{SIM}$ of the Fermi surface can participate in Kondo screening of the moments. Thus, only a fraction of the moments $n_{eff} \approx \rho_d(0) k_B T_0^{SIM}$ may be screened by the conventional Kondo effect. The screened and unscreened sites may be mapped onto holes and particles (left) of a single-band Hubbard model (bottom). The local Hubbard repulsion U_{ff} is unchanged by this mapping, but the hopping constant of this effective model is strongly suppressed by the overlap of the screened and unscreened states (right).

particles and holes of a single-band Hubbard model with local Coulomb repulsion U_{ff}. The polarons hop from site to site and effectively screen all the moments in a dynamical fashion. Thus it is proposed that the hopping constant of this effective single-band model is strongly suppressed relative to t^* by the overlap of the screened and unscreened states. Hence the Kondo scale of the effective model becomes much less than T_0^{SIM}. This mapping is sketched in fig. 14. The protracted screening behavior is a crossover between the two regimes of Kondo screening at the higher scale T_0^{SIM} and dynamical screening at the lower scale T_0. The two energy scales have well defined meaning: T_0^{SIM} is the scale for the onset of screening, and T_0 is the scale where screening is almost complete and a Fermi liquid begins to form. In this argument the relation between the two scales depends on n_{eff} and hence there can be no universal relation between them. Rather, the rate and extent of the protracted screening depend upon both the ratio and difference of T_0 and T_0^{SIM}.

It is believed that Nozières' argument pertains in the limit of large orbital degeneracy N even though the Kondo scales of the SIM and PAM are the same here. The limit is taken so that the ratio of the f and d occupancies as well as NV^2 remain constant (Read and Newns 1983a,b). Thus, there are still far too many f-electron moments to be completely screened by the conduction band degrees of freedom alone. However, the effective Hubbard model to which the system is mapped will also have an orbital degeneracy of N. Gunnarsson et al. (1996) have argued that the critical correlation needed to open a Mott gap in such a model diverges as N diverges (this due to the enhanced hybridization between multiple

channels). Thus the effective one-band model is largely uncorrelated and the degeneracy temperature of this effective model will be larger than T_0^{SIM}, and hence irrelevant.

In the symmetric limit ($n_{\mathrm{d}} = n_{\mathrm{f}} = 1$), the argument of Nozières fails, since the gap forces all of the electrons into singlet pairs. Tightly bound local singlets form between the f and d orbitals on each site where the antiferromagnetic exchange is strongest. Since each site is fully screened by conduction band spins, Nozières' exhaustion should no longer be prevalent. However, T_0 is not simply equal to the SIM scale here, since the hopping is between tightly bound singlets on each site which hybridize with an effective matrix element $t/2$. Since the bare conduction band density of states changes inversely with the hybridization matrix element, the reduced hopping of singlets will increase the effective conduction band DOS, so that the Kondo scale in the symmetric PAM is resonantly enhanced; i.e., in the symmetric limit

$$T_0 \propto \exp\left(\frac{1}{2\rho_{\mathrm{d}}(0)J}\right), \quad \text{whereas} \quad T_0^{\mathrm{SIM}} \propto \exp\left(\frac{1}{\rho_{\mathrm{d}}(0)J}\right).$$

The formation of the gap at low T, $T \lesssim T_0$, enhances the screening! This positive feedback causes the gap to open very quickly as the temperature is lowered. Only the energy scale T_0, which characterizes the onset of screening, is then relevant, and many of the physical properties of the system show scaling with T/T_0.

In the near-insulating regime $0.9 \lesssim n_{\mathrm{d}} < 1.0$, T_0^{SIM} and T_0 cannot have the same interpretation as they do in the metallic regime $n_{\mathrm{c}} \lesssim 0.8$. As $n_{\mathrm{d}} \to 1$, T_0 increases dramatically while D_0 decreases. That is, near the insulating state, T_0 is the scale for the onset of screening, and T_0^{SIM} appears to be irrelevant. Concomitant with the disappearance of D_0 and Z as $n_{\mathrm{d}} \to 1$, another scale, T^*, is proposed which goes to zero as $n_{\mathrm{d}} \to 1$, which is the scale for the onset of Fermi liquid behavior. Roughly, $k_{\mathrm{B}}T^*$ should be the difference in energy between the chemical potential and the bottom of the gap. Again, since T^* depends upon n_{d}, there would appear to be no universal relationship between T^* and T_0, and no single-parameter scaling of the physical properties of the system. These scales are sketched in fig. 15 (overleaf).

7.5. *Conclusions*

In the Kondo limit, $n_{\mathrm{f}} \approx 1$ and for sufficiently large U_{ff}, the behavior of the PAM may be characterized by three different regimes, depending upon d-band filling n_{d}:
In the *metallic regime* where $n_{\mathrm{d}} \lesssim 0.8$,

(i) The PAM predicts a Kondo peak which has a weaker temperature dependence and persists up to much higher temperatures (in units of the Kondo scale) compared to the predictions of the SIM.
(ii) Both the intensity and the spectral weight of the Kondo peak are larger in the PAM than in the SIM.
(iii) The Kondo peak intensity does not scale like $1/V^2$ in the PAM.

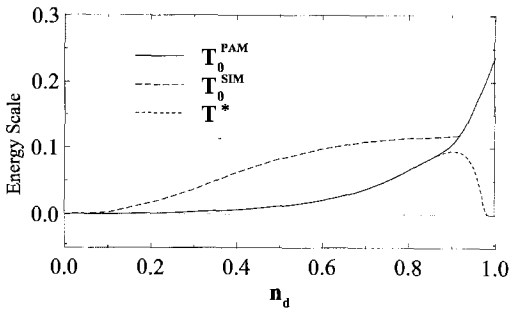

Fig. 15. A sketch of the relevant energy scales for the PAM. In the metallic regime $n_d \lesssim 0.8$, T_0^{SIM} is the scale for the onset of screening, and T_0 is the scale where screening is almost complete and a Fermi liquid begins to form. In the near-insulating regime, $0.9 \lesssim n_d < 1$, T_0 becomes the scale for the onset of screening, and we propose that there must be another scale T^*, which goes to zero as $n_d \to 1$, which is the scale for the onset of Fermi liquid behavior. Roughly, $k_B T^*$ should be the difference in energy between the chemical potential and the bottom of the gap. In the symmetric regime $n_d = n_f = 1$, there is only energy scale T_0 below which the screening begins and a gap quickly opens.

(iv) The Kondo peak is dispersive in the PAM making a heavy quasi-particle band with strong f-electron character which crosses the Fermi surface and persists up to energies $\gg T_0$ due to a strongly frequency-dependent hybridization function $\Gamma(\omega)$.
(v) When $n_d < 1$ ($n_d > 1$) the Kondo peak below the Fermi energy starts to develop only as $\boldsymbol{k}$ deviates from the zone center (corner).
(vi) There are two relevant energy scales for the PAM: the onset of screening scale T_0^{SIM}, and the onset of coherence scale T_0 which is strongly suppressed compared to the latter.
(vii) The arguments of Nozières (1985) may be extended to provide a consistent interpretation of (i)–(vi).

In the *near-insulating regime*, $0.9 \lesssim n_d < 1$ and $n_f \approx 1$:

(i) The PAM predicts that the near-Fermi-energy structure of the f density of states has a much stronger temperature dependence than is predicted for the near-Fermi-energy structure in the f DOS of the SIM. The temperature dependence of these features generally increase as $n_d \to 1$.
(ii) There are again two relevant energy scales in this regime: the onset of screening scale T_0, and the onset of coherence scale T^*.
(iii) T^*, D and Z vanish as $n_d \to 1$.

In the *symmetric limit*, $n_d = n_f = 1$:

(i) As T is lowered, $T \lesssim T_0$, a gap of width $5T_0$ develops very quickly at the Fermi surface and the system has an insulating ground state.
(ii) There is only one relevant energy scale for the low-temperature properties of the system, T_0, that describes the onset of screening. Many of the physical properties of the system, including the f-electron DOS, show universal scaling as a function of T/T_0.

(iii) T^* is strongly enhanced relative to the T_0^{SIM} for the same model parameters. Finally, we note that the extent of the metallic and near-insulating regimes depends strongly upon the model parameters, and that there is generally a region between these two regimes that displays some combination of the near-insulating and metallic behaviors.

8. Single-crystal vs polycrystal PES

As indicated in the introduction, the emphasis in this chapter will be primarily on single-crystal photoemission spectra and their comparison to the various models. It may be useful to show from the start that indeed major differences exist between single-crystal and polycrystal heavy fermion PES spectra, in order to demonstrate the need for this review. Additionally, most of the spectra presented are taken at the 4d absorption edge so that the 4f (and to some extent the 5d) spectral features are resonantly enhanced. The reader is referred to the excellent review by Allen (1992) on the merits of resonant photoemission. It was also shown by Arko et al. (1988a) that spectra at resonance adequately reflect the spectra away from resonance. Suffice it here to say that in general the 4f spectra at resonance reproduce quite accurately the 4f spectra away from resonance in angle-integrated measurements. Angle-resolved spectra at resonance, however, do not have the same momentum resolution as at lower photon energies, thus yielding less information in the way of dispersion. With this in mind we begin to analyze data by first comparing single-crystal and polycrystal spectra.

8.1. *Ce heavy fermions*

In fig. 16 a comparison is made between a single-crystal spectrum (Arko et al., unpublished) of $CeCu_2Si_2$ and the polycrystal spectrum taken from Parks et al. (1984). Both 4f spectra have been obtained by subtracting the spectrum at anti-resonance ($h\nu = 112$ eV) from a spectrum at resonance ($h\nu = 120$ eV) where the 4f features are dramatically enhanced. This is needed in order to eliminate the strong contribution from the Cu 3d states. We will later show that such subtracted spectra still contains substantial Ce 5d-derived intensity which also resonates at the 4d threshold, but for now we simply call it the 4f spectrum. In order to preclude questions about differences in resolution, the single-crystal spectrum has also been smoothed by a 750 meV Gaussian in order to match the resolution of the polycrystalline data. Note that the bulk of the f^1 4f DOS is totally missing in the data from the scraped polycrystalline surface. By contrast the single-crystal result not only yields an intense feature near E_F, but at high resolution this feature is split into both the $4f_{5/2}$ (i.e., the so-called KR) and $4f_{7/2}$ (i.e., the SO) peaks, just as has been observed in nearly every Ce heavy fermion compound. It is true that the two spectra were taken at different temperatures (20 K vs 300 K) but, as will be shown in sect. 12, the temperature dependence of all Ce heavy fermions is in any case minimal. Moreover, the 20 K temperature already exceeds T_K by at least a factor of 2 so that temperature is

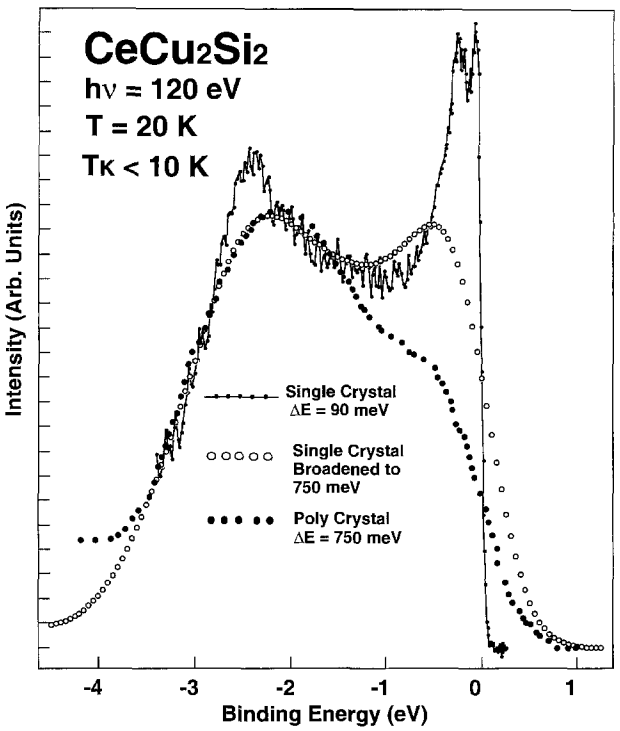

Fig. 16. $CeCu_2Si_2$ data of Parks et al. (1984) at 750 meV resolution and room temperature superimposed on single crystal data taken with 90 meV resolution and $T = 20$ K. Open circles are single crystal data broadened to 750 meV. Note the missing intensity in the f^1 region. The temperature effect is minimal and does not account for the difference.

not a serious consideration except for resolution. In sect. 13 we show that the effect could come from surface contamination, but as we see below, the effect is widespread even in clean samples.

It is natural to suspect poor sample quality for the above result, and this is certainly expected to be a contribution, given the great strides made in sample preparation since the time the data were taken. However, although the quenching of the $4f_{5/2}$ feature in polycrystals is not totally universal, it occurs often enough that an effect other than poor sample stoichiometry must be suspected. Even when the specimen is not scraped to prepare a clean surface, as in the case of the cleaved polycrystal of $CePt_3$ from Andrews et al. (1995a) shown in fig. 17, the $4f_{5/2}$ feature is often missing in the polycrystalline spectrum. The single crystal of $CePt_{2+x}$ ($0 < x < 1$) in fig. 17 was prepared by evaporating Ce onto a single crystal of Pt (111) and annealing *in situ*. It was checked via a PES study of Pt 4f core levels for correct stoichiometry, and via LEED for correct crystal structure (Tang et al. 1993). Most of the differences in the spectra can be attributed to angle-resolved effects in the single crystal. However, within SIM and its extensions, GS and NCA, the 4f features are purely localized at the measurement temperature of

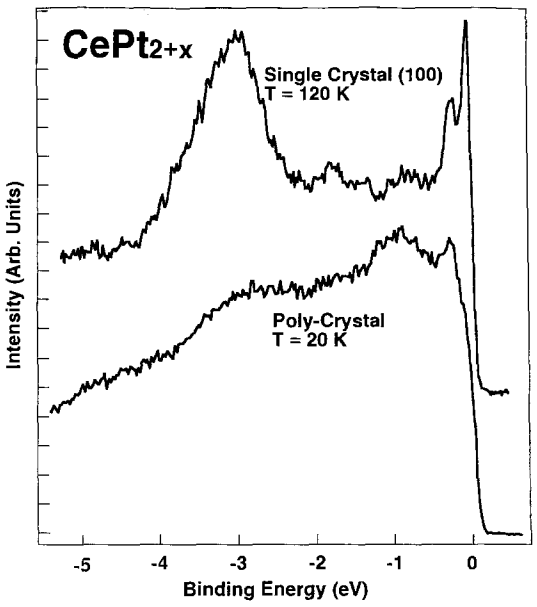

Fig. 17. Comparison of single crystal and polycrystal data of $CePt_{2+x}$ taken from Andrews et al. (1995a). Note that the $4f_{5/2}$ peak is missing in the polycrystal data even though the sample was cleaved and not scraped.

120 K and hence independent of angle. Indeed, at this temperature the near-E_F features should be absent. At the very least they should be independent of crystalline orientation since momentum dependence of the hybridization is eliminated via equal coupling to all momentum states. Nevertheless, the single crystal shows an intense $4f_{5/2}$ feature, vs none in the polycrystal, where the T_K for this material cannot be more than 10 to 20 K (verified with a susceptibility measurement on an arc-melted sample). While the single crystal was measured at a temperature of 120 K which is at least 6 to 12 times T_K and possibly even more, so that within NCA all f^1 features should have been renormalized to near zero (Bickers et al. 1987), the polycrystalline spectrum was measured at $T = 20$ K and still lacks the $4f_{5/2}$ feature. Momentum-dependent hybridization can account for these effects, but this already requires a periodic lattice and use of the PAM to the exclusion of the SIM.

Inasmuch as single-crystal data, as we will see, are more out of line with bulk properties than polycrystal data, it is occasionally suggested that this could be due to a surface effect. Unfortunately this runs counter to conventional wisdom which states that best coupling to the bulk is obtained in single crystals at normal emission. Indeed, polycrystals, especially scraped polycrystals, are far more likely to exhibit strong surface effects.

8.2. *Yb heavy fermions*

Similar results are also obtained in Yb heavy fermion compounds in which the KR is now identified with the $4f_{7/2}$ state and is fully occupied. In fig. 18 a comparison is made between single- and polycrystalline $YbCu_2Si_2$, both specimens (Arko et al., unpublished)

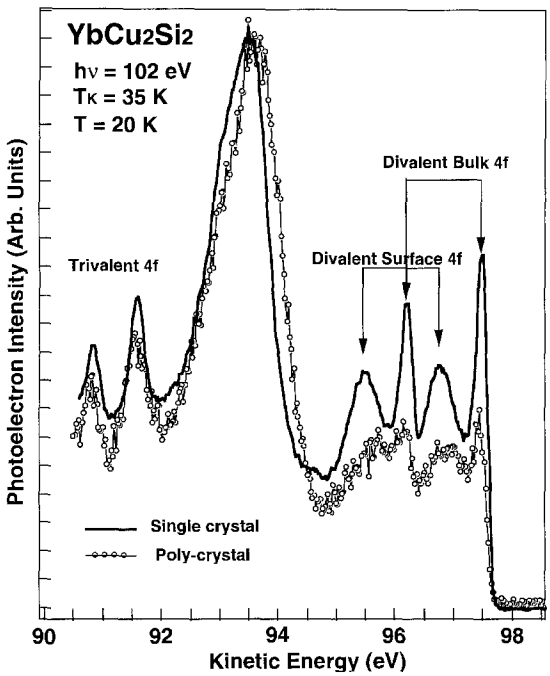

Fig. 18. Single crystal and polycrystal $YbCu_2Si_2$ spectra taken under identical conditions (CMA analyzer, 150 meV resolution, data of C.G. Olson at SRC). Note the large reduction in polycrystal divalent intensity even though the trivalent intensities are equal.

cleaved (not scraped) *in situ* at 20 K, and measured at 20 K. The T_K for this material is approximately 35 K. The spectra have been normalized so that the trivalent portion of the spectrum (presumed to be entirely due to the bulk) has equal intensities in both curves when measured peak to valley. While the Cu 3d feature at $h\nu = -4$ eV normalizes in this way to equal intensity in both materials (the slight shifts are due to angle-resolved effects), the divalent portion of the Yb 4f spectrum within 2 eV of the Fermi energy is dramatically reduced in the polycrystalline specimen relative to the trivalent portion, both for surface and bulk features. In terms of the 4f hole occupancy discussed in sect. 10, the n_f is apparently increased from 0.65 to about 0.8 in the polycrystal. Stoichiometry does not seem to be the problem since the Cu 3d peak has the correct intensity. If the SIM truly applies in Yb heavy fermions, then all the $4f_{7/2}$ intensity at E_F is of necessity due to the Kondo interaction. The SIM by definition implies that the 4f element is an impurity with no interaction with its neighbors at high temperatures. Why the existence of long-range atomic order (or lack thereof) then so dramatically affects the 4f spectrum is at this point a mystery. Some suggestions will be presented later in sect. 13 where we consider the possibility that these are band states even at high temperatures.

To sum up this section, then, it is apparently crucial for a correct measurement of the near-E_F intensities in heavy fermions that the surface is a single crystal. Scraping of the surface should be particularly avoided since it was found that in $YbAgCu_4$, a material having a T_K of about 35 K, the scraping of a coarse-grained surface totally eliminated all divalent 4f features (Arko et al., unpublished), much more consistent with thermodynamic

data. Perhaps it is so that the destruction of long-range order via scraping indeed puts us into the single-impurity regime, while a good single-crystal surface with long-range order requires a treatment within the PAM.

9. Lack of scaling with T_K of the near-E_F features

Perhaps the single most important prediction of the GS and NCA models is that of scaling of the various spectral properties with T_K or the universal parameter. In particular, the spectral weight, position, and width of the KR is predicted to increase with T_K. While instrument resolution has been insufficient in the past to deal properly with the position and width of the $4f_{5/2}$ feature, researchers have concentrated on the spectral weight. Allen et al. (1986) were first to find a relationship between T_K and spectral weight of the near-E_F features, although the limited resolution of the early research did not allow a quantitative comparison to theory.

Patthey et al. (1990) published a monumental paper on the application of the SIM to spectral properties of Ce and Yb heavy fermions. For the first time they performed high-resolution ($\Delta E \approx 20$ meV) systematic experiments on a number of materials with T_K's (in their nomenclature they use the energy equivalent, δ(meV)) ranging from less than 10 K for $CeCu_6$ to about 200 K for α-Ce, observing the trends in the near-E_F spectral weight (see fig. 19). They obtained their data using HeI and HeII radiation, using the difference curves obtained by subtracting the spectra obtained at two different photon energies. More importantly, they also performed model calculations using NCA at the appropriate temperatures to compare to the results.

While at first glance there appears to be excellent agreement between theory and experiment in fig. 19, there are a number of issues to consider. In the first place, nearly all of these measurements were performed on scraped polycrystals so that in view of the discussion above it is not certain whether the $4f_{5/2}$ intensity properly represents the material. It is important to keep stressing this point since, as will be discussed later, there is a strong possibility that the $4f_{5/2}$ feature is actually a very narrow band dispersing above E_F. In a scraped polycrystal one would measure at best a spectral weight averaged over the Brillouin zone, and at worst a meaningless spectral weight due to the introduction of defects via scraping and consequent loss of phase coherence of the narrow bands in the surface region.

There are other questions. One revolves around the normalization which is done in such a way as to eliminate as much as possible the non-f symmetries, and which, away from resonance is difficult indeed. While the shape of the 4f spectrum can be reproduced, it may cause problems with intensities so that comparing intensities between samples is difficult. Another obvious problem, evident in fig. 19, is one of the widths of the $4f_{5/2}$ features that appear nearly constant irrespective of T_K. Even for their highest T_K material, α-Ce, there is at least a factor of 2 discrepancy between theory and experiment; i.e., experiment is too broad. [Incidentally, Liu et al. (1992a) would place the T_K for α-Ce as high as 800 K, but even this is insufficient to bring theory and experiment into line.] The discussion on

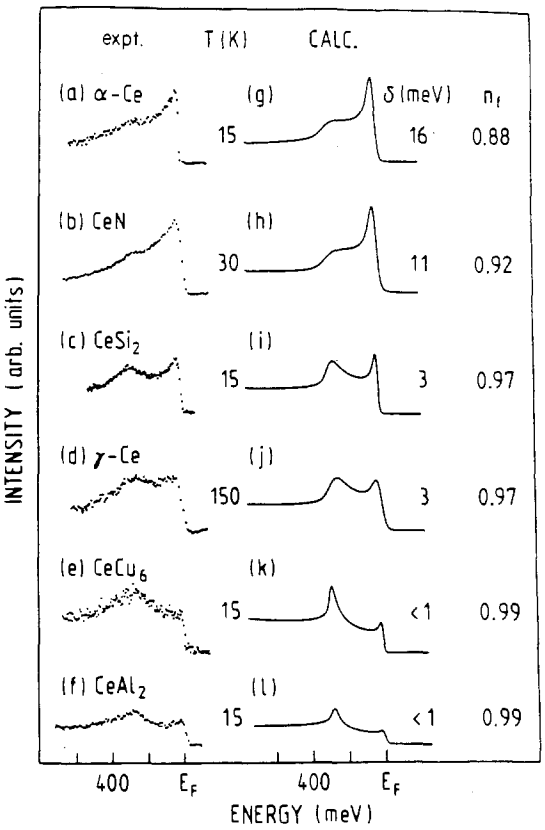

Fig. 19. Near-E_F spectra of Patthey et al. (1990) for several materials with varying T_K's [displayed as δ(meV)]. The calculated spectra (solid lines) have been broadened by instrument resolution. Note that in each case the measured spectra are much broader than calculations.

the width of the $4f_{5/2}$ feature will be more extensive below, but it is useful to point out that to a first approximation all the widths in fig. 19 appear about the same magnitude and far broader than their 20 meV instrument resolution. We have seen in the previous section that crystal field states cannot account for the nearly constant width. Finally, the authors admit that when they calculate the specific heat γ-values for these materials from the Rajan formula, namely

$$\gamma(T \to 0) = \frac{N_A \pi k_B (N_f - 1)}{6T_0},$$

where $T_K = T_0/1.29$, and N_f is the orbital degeneracy of the occupied f level, the values obtained are in general more than an order of magnitude too large. Reducing N_f to a value of 2 by introducing crystal field levels may help some, but not enough.

Scaling behavior with T_K was again reported in the $CeSi_x$ series by Malterre et al. (1994), Baer et al. (1994), and Malterre et al. (1993). Here the intensity of the near-E_F feature was correlated with the Curie–Weiss temperature as the Si concentration was decreased. Needless to say, this was done on scraped polycrystalline materials with severe

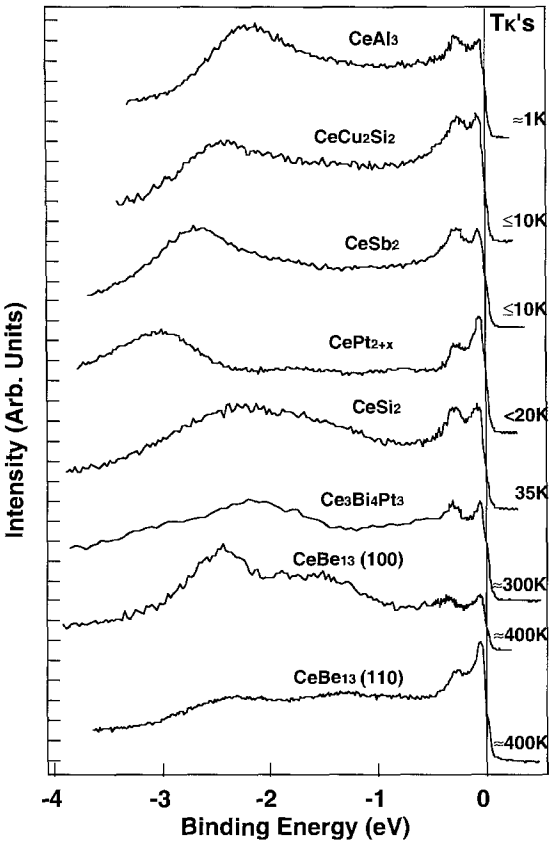

Fig. 20. Wide scan single crystal spectra (except $CeAl_3$ and $CeSi_2$) for several Ce heavy fermions with T_K's ranging fron ~1 K to ~400 K. Data taken at 20 K, 120 eV, and 90 meV resolution. Note the lack of scaling of the $4f_{5/2}$ peak with T_K. Two different directions are shown for $CeBe_{13}$ with vastly different spectra.

defect concentrations. Since the maximum T_K in that system is only 35 K in $CeSi_2$, and decreases gradually with x from there, it does not compare with the orders of magnitude change in T_K presented in fig. 20 where no scaling is observed (see below). The relatively small decrease in the KR intensity could easily result from the introduction of defects in the $CeSi_x$ system and the associated change in electronic structure.

Joyce et al. (1992c), by contrast, pointed out that by using high quality single crystals there obtains an amazing similarity between all Ce heavy fermion spectra, regardless of T_K. This can be seen in fig. 20 (Arko et al. 1997a) where spectra for 7 Ce heavy fermions (including two directions for $CeBe_{13}$) are plotted. Indeed, one observes the interesting effect that spectral differences with momentum within the same crystal ($CeBe_{13}$) are in fact larger than differences between materials whose T_K's differ by as much as 2 orders of magnitude (more on that later). All the spectra in fig. 20 were taken at a photon energy of 120 eV which roughly corresponds to the 4d absorption edge and thus resonantly enhances the 4f emission. The energy resolution in each case is about 90 meV. All spectra represent raw data except in the case of $CeCu_2Si_2$ where the spectrum at

anti-resonance ($h\nu = 112$ eV) has been subtracted from the resonance spectrum in order to eliminate the very strong Cu 3d emission. In fig. 20 one should further note that $CeAl_3$ and $CeSi_2$ are cleaved polycrystal specimens so that the polycrystal effect discussed above is not universal (but common). The normalization of the spectra in fig. 20 is to the f^0 peak maxima at −2 to −3 eV, except for $CeBe_{13}$ (110) where the f^0 peak is clearly much smaller than that for $CeBe_{13}$ (100), and it just is not obvious which maximum is the true bulk f^0 (this is further discussed below). While nearly all the spectra in fig. 20 represent 4f and 5d Ce emission only (due to the nearly negligible ligand emission), in the case of $CePt_{2+x}$ (111) and $Ce_3Pt_4Sb_4$ there is also substantial Pt 5d emission so that the f^0 peak intensities should be ignored for these. To the list of spectra in fig. 20 one should also add α-Ce ($T_K \approx 800$ K, Weschke et al. 1991) and CeB_6 ($T_K \approx 10$ K, Kakizaki et al. 1995) which likewise exhibit spectra nearly identical to those in fig. 20.

Irrespective of the precise normalization of the data in fig. 20, the interesting fact emerges that the spectral weights of the $4f_{5/2}$ features are more or less constant for all materials, or at least do not monotonically increase with T_K. While the 90 meV resolution precludes any firm conclusions about the widths and positions of the $4f_{5/2}$ peaks, it has little effect on the broad $4f_{7/2}$ peaks so that their peak amplitudes relative to f^0 need no deconvolution. One is forced to the conclusion that there is no apparent scaling of the $4f_{5/2}$ spectral weights with T_K relative to the f^0 peak. This lack of scaling cannot be blamed, as has been discussed above (Joyce and Arko 1993), on inclusion of f^2 intensity originating from finite U_{ff} effects, since the f^2 DOS, if present, is broad and featureless and hence cannot change the relative amplitudes. Nor can one resort to a lowering of the $4f_{5/2}$ degeneracy to $N_f = 2$ by the introduction of two additional crystal field levels, since, as again shown by Joyce and Arko (1993), even in the presence of these CF states the GS and NCA models predict a scaling of the $4f_{5/2}$ spectral weight with T_K. The nearly constant and much too broad (relative to GS) width of the $4f_{5/2}$ has been attributed by Patthey et al. (1993) to lifetime broadening. Even if this were the case, such broadening will not affect the spectral weight so that the inevitable conclusion of a lack of scaling with T_K remains a reality.

To underscore the lack of scaling still further we point out the amazing similarity in fig. 20 between $CeBe_{13}$ (110) ($T_K \approx 400$ K) and the spectrum for $CePt_{2+x}$ (111) ($T_K \approx 10$ K). In fig. 20 the comparison is somewhat less striking than actuality because of the strong Pt 5d emission in the region of the f^0 peak. For a better comparison one must first subtract out the non-Ce portion of the $CePt_{2+x}$ (111) spectrum by subtracting the $h\nu = 112$ eV spectrum (anti-resonance) from the $h\nu = 120$ eV spectrum (resonance). For $CeBe_{13}$ the intensity at 112 eV is negligible. The two curves are overlaid in fig. 21 (normalized at the $4f_{5/2}$ peak), with the secondary backgrounds also removed. With the exception of the shift in the f^0 peak the two curves overlay almost exactly. The region of the Ce 5d emission (between −0.5 eV and −2 eV) also overlays if the f^0 peaks are removed. This type of agreement is astounding when one considers that there is a factor of 40 difference in T_K's. Moreover, the $CePt_{2+x}$ (111) spectrum was taken at 120 K. On the basis of the single-crystal data, then, it would be difficult to reach a conclusion other than one of a total lack of scaling of the spectral weight with T_K.

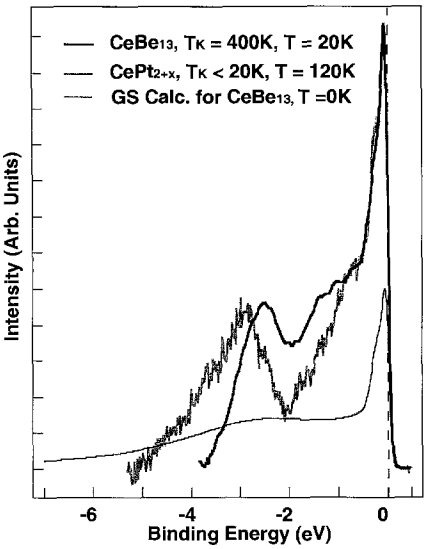

Fig. 21. Overlay of $CeBe_{13}$(110) spectrum with $CePt_{2+x}$ (001) spectrum after subtracting backgrounds (from Andrews et al. 1995a). Except for a slight shift of the f^0 peak the spectra are nearly identical in spite of a factor of 40 difference in T_K's. The calculated GS spectrum approximates the parameters for $CeBe_{13}$; i.e., $T_K = 400$ K, $\Gamma = 0.116$, $W = 10$ eV, $\Delta_{SO} = 280$ meV, no CF's, $\varepsilon_f = -2.5$ eV, $U_{ff} = 14$ eV. It was normalized to the data by using equal areas of the f^0 peaks. Note the large discrepancy in the f^0 peak width between experiment and calculation.

The thin lined spectrum in fig. 21 is a GS calculation with parameters approximately matching $CeBe_{13}$ (i.e., $W = 10$ eV, $U_{ff} = 14$ eV, $T_K = 400$ K), smoothed to match the instrument resolution, and normalized in such a way that the total area of the calculated Lorentzian f^0 peak matches the total area of the measured Gaussian f^0 peak in $CeBe_{13}$. The mismatch is obvious. While better fits can be obtained with different parameters such as a smaller W, these are not justified. The width of the conduction band used above (10 eV) may in fact be even conservative since experimentally it peaks at about −8 eV. Also, there are no Ce nearest neighbors in $CeBe_{13}$ so that the 4f electron can only hybridize with the Be conduction band.

One may argue that the comparison to GS in fig. 21 is flawed since a model conduction band DOS of width 10 eV was used for UBe_{13} rather than an actual calculated DOS. To this it can be countered that a model DOS has been used in nearly all investigations (e.g., fig. 19), so that if the comparison in fig. 21 is to be discounted, all comparisons utilizing a model DOS should likewise suffer the same fate. In only two instances was an actual calculated DOS used to produce the GS spectrum – α-Ce (Liu et al. 1992a) and $CeCu_2Si_2$ (Kang et al. 1990b). In the first case the width of the d conduction band is in fact only about 2 eV, a value typically used in model DOS calculations. Interestingly enough, simply using a flat model DOS 2eV wide effectively reproduces the more elaborately calculated spectrum. This would suggest that the DOS cut-off energy is an important parameter. In the second case a good fit was obtained to the then available PES valence band spectrum as well as to the core level spectra, but subsequent spectra from single crystals (fig. 16, Arko et al., unpublished) appear fundamentally different.

A quantitative comparison to GS and NCA is further complicated by a lack of knowledge of crystal field levels. In fig. 21 the comparison is made to $CeBe_{13}$ with a T_K of about 400 K so that crystal field levels should be absent (none have been reported)

or at least should be split off the main peak by more than 40 meV (i.e., they should be deeper than $k_B T_K$). If the latter were the case they would have been observable in a photoemission experiment having 56 meV resolution. None were observed. Thus the comparison of $CeBe_{13}$ to GS is perhaps the most clean cut of all comparisons, and it fails as seen above. Most other comparisons suffer from the above stated problems and will not be considered further in this article. Only qualitative predictions of GS, i.e. predicted trends, will be compared to experiment in the remainder of this chapter. While it is possible, by adjusting parameters, to reproduce reasonably well a particular spectrum, it is the systematics with T_K (or lack thereof) which is the real determinant of the applicability of the SIM.

10. The f-level occupancy, n_f

It can already be seen in fig. 21 that the spectral weight ratio $W_r = f^1/f^0$ in $CeBe_{13}$ is too large relative to a calculation; indeed, about a factor of 2.5 too large. This indicates that the calculated f occupancy n_f of the bare f level at ~–2.5 eV is much larger than measured. One can, of course, vary the parameters (primarily increase the hybridization) until calculation matches experiment, but this will increase T_K to values incommensurate with the thermodynamic quantities. Basically, the lack of scaling seen in fig. 21 implies that the n_f in Ce compounds does not change very dramatically with T_K. This is totally at odds with expectations.

The f-level occupancy is best studied in Yb compounds where it becomes the hole occupancy rather than electron occupancy, and where GS theory places the KR centroid on the occupied side of the Fermi energy, unlike the case for Ce compounds. Here the integrated intensities of the f^{13} (trivalent) and f^{14} (divalent) portions of the photoemission spectrum are expected to be directly related to the f-hole occupancy, n_f, by the relation

$$n_f = \frac{I(f^{13})}{I(f^{13}) + \frac{13}{14} I(f^{14})},$$

where $I(f^n)$ represents an integral spectral weight of the f^n feature. One of the best compounds for this study is $YbAl_3$ where the Al states yield almost no photocurrent, thus making it relatively easy to subtract the background and to delineate the trivalent and divalent (bulk) intensities. An early study for this material (Oh 1993) was an XPS study where direct integration yielded $n_f = 0.65$ which is far lower than expected for a material having $T_K \approx 400$ K. Indeed this places it well into the mixed valent regime, outside the range of the validity of NCA. Tjeng et al. (1993) later utilized the temperature dependence of the $4f_{7/2}$ level and obtained an n_f value of 0.85 which is in exact agreement with NCA predictions (Bickers et al. 1987). However, using the temperature dependence is difficult at best. The assumption is made that all of the temperature dependence of the $4f_{7/2}$ level is due to the Kondo effect. With no effort made to delineate the effects of a 300 K Fermi function this assumption seems tenuous at best. Additionally the choice of backgrounds in

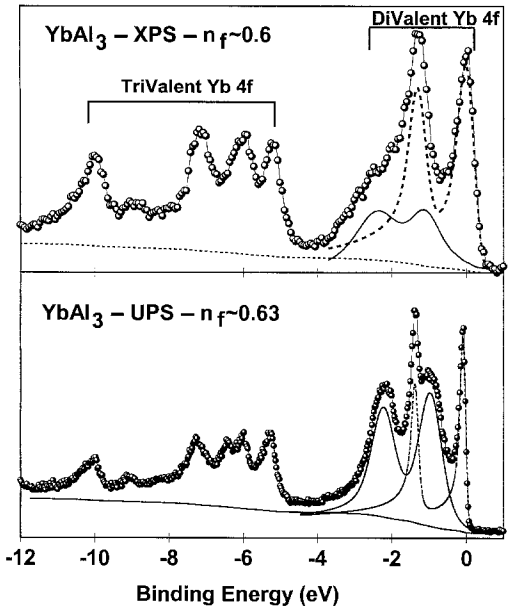

Fig. 22. XPS and UPS ($h\nu = 120$ eV) spectra for $YbAl_3$ taken at $T = 20$ K to determine any differences in signal due to escape depth. Values of n_f were obtained by direct integration after separating out the background and surface features as shown. Nearly identical values were obtained thus confirming the bulk nature of the divalent peaks in UPS.

that study is somewhat questionable. Since the non-$4f_{7/2}$ (bulk) background in the polycrystalline samples was assumed to comprise more than 80% of the signal, one can see how even in the case of correct assumptions regarding temperature dependence, small errors in the choice of background can yield huge errors in the temperature dependence.

The most reliable method for determining n_f would seem to be direct integration of the divalent and trivalent features in a material where the background is relatively small. Toward this end Joyce et al. (1996) and Andrews et al. (1994) analyzed $YbAl_3$ spectra both from XPS as well as UPS and came up with values basically agreeing with the first investigation of Oh (1993). This is shown in fig. 22 where the delineation into background and surface components is also illustrated. Similar analyses for $YbCu_2Si_2$ (Andrews et al. 1994, Joyce et al. 1996) yielded nearly the identical values despite the fact that $YbCu_2Si_2$ has a T_K of only 35 K, an order of magnitude lower than $YbAl_3$. All of these values are totally out of the range of NCA validity and clearly belong to the mixed valence regime. While there remains some question as to whether the photoelectron cross sections for the f^{13} and f^{14} states are identical (a necessary condition in order to compare intensities), the fact that identical n_f values are obtained at both XPS energies as well as near $h\nu = 120$ eV would suggest that the photoelectron cross sections of the f^{13} and f^{14} states are at least very similar if not identical. Thus direct integration of the spectra to obtain n_f would seem preferable to the method of Tjeng et al. (1993).

An even more pronounced disagreement with NCA occurs in the compound $YbAuCu_4$ (Andrews et al. 1994) which in the past has been proposed (Kang et al. 1990a) as a nearly trivalent material. Here T_K is assumed to be $\ll 35$ K (i.e., much less than the value for $YbAgCu_4$) so that n_f would be perhaps of the order 0.99. Instead Andrews et al. (1994)

find it to be closer to 0.85 based on direct integration – a serious discrepancy when one also considers that the PES measurements were done at $T = 80\,\mathrm{K} \gg T_K$. From all this it would appear that the concept of f-hole occupancy, and by analogy also the f-electron occupancy, is not directly related to T_K in a fashion described by NCA or GS.

From sect. 7 (dealing with the PAM) one can see that the ratio of the f^1 to f^0 (or, the divalent to trivalent in Yb compounds) spectral weights is substantially larger when calculated within the PAM than when calculated within the SIM. It would seem that the trends predicted by the PAM are much more consistent with the experimental spectra obtained from single crystals.

There is no question about the fact that the n_f values obtained from PES are dramatically in disagreement with those obtained from bulk properties as well as those obtained from X-ray absorption L_{III} edge studies (Lawrence et al. 1994). While it is our contention that we must resort to a different model, such as the PAM, to resolve this discrepancy, a useful question to ask is whether photoemission measures the same material as is measured in L_{III} studies. In particular, is it possible that owing to its surface sensitivity a PES study does not probe the bulk but rather only a surface or a sub-surface layer whose n_f is dramatically different from the bulk? Such a scenario would render PES useless and would breathe new life into the SIM. It is also fair to ask whether the L_{III} results are to be taken at face value.

But let us look at all possibilities. The existence of a surface layer is not in question. Moreover it is clear that in Ce compounds the surface tends to be trivalent while in Yb compounds it is divalent. But while it is easy to delineate a surface feature and separate it from bulk electronic structure, it would require a thick sub-surface, different from the bulk, to mistake it for bulk. However, a thick sub-surface has never yet been reported in any system known to us. If it were to exist in one system, the likelihood of its existence in other systems is high, making PES useless as a bulk probe. Fortunately, excellent agreement between calculated and PES-derived electronic structure is often reported. Indeed, most calculations suggest that only about 3 atomic layers below the surface are sufficient to obtain the bulk electronic structure.

But let us say for the sake of argument that a thick sub-surface layer may exist only in strongly correlated f-electron systems. Immediately we can rule it out in Ce compounds since studies at photon energies as high as 3 keV show only bulk and surface states with no third layer. Such a sandwich would in any case be preposterous for Ce heavy fermion compounds since it would require a trivalent surface, a strongly mixed-valent sub-surface, and again a nearly trivalent bulk. We can also rule it out in purely trivalent as well as purely divalent Yb compounds since PES measurements yield the required purely trivalent ($YbBe_{13}$) or purely divalent ($YbSn_3$) spectra. It would be pathological that a sub-surface would exist only in mixed-valent Yb compounds, but that is all that we are left with.

But let us go further and assume that nature is indeed that pathological. Since the n_f values obtained at XPS energies are the same as those obtained at lower photon energies, this suggests that the desired sub-surface must be at least of the order of 100 Å thick, otherwise the larger escape depth at XPS energies would begin to probe the supposed true bulk and yield different n_f values. On the other hand it must not be so

thick as to constitute a significant percentage of the probing depth in L_{III} edge studies where a sub-surface has never been observed (again pathological). But the real question to be asked is the following: If a single-crystal compound is cleaved *in situ* at about 20 K, what is the driving force which causes this ~100 Å thick layer to form instantly, and why is the LEED pattern representative of the bulk structure? Certainly there are no dangling bonds as on the surface. The answer remains elusive.

One is forced to the conclusion that there exists no sub-surface and that the measured n_f values are real. The disagreement with L_{III} studies remains unresolved.

11. Linewidth and lineshape of the near-E_F feature

From GS and NCA one obtains that the linewidth of the near-E_F feature associated with the KR should follow the relationship FWHW $= 3\pi k_B T_K$ (Bickers et al. 1987) which can be easily tested with high resolution PES. To be sure, this is again a property best investigated in Yb compounds since in Ce compounds presumably only the tail of the otherwise empty KR is occupied, thus making it difficult to reach solid conclusions about the FWHM. Still, in order to yield the observed bulk properties, one would expect that even the tail of the KR should be no wider than $k_B T_K$. To keep things simple, however, we will only consider Yb materials.

11.1. *Linewidth*

Prior to the single-crystal work of Joyce et al. (1992c) and Lawrence et al. (1993) and their subsequent publications, very few investigators concerned themselves with the KR lineshape and linewidth since in general the resolution was insufficient to reveal the intrinsic lineshape. Subsequently, several papers dealt with lineshape; α-Ce (Liu et al. 1992a), $YbAl_3$ (Tjeng et al. 1993) and $YbAgCu_4$ (Weibel et al. 1993). Liu et al. and Tjeng et al. reported exact agreement between theory and experiment while Weibel et al. reported a FWHM larger than GS predictions. PES measurements on single crystals, however, reveal that the $Yb_{7/2}$ intrinsic linewidth is generally of the order of 70 to 100 meV, irrespective of material (Joyce et al. 1996). With this in mind the near agreement with GS in α-Ce ($T_K \approx 800$ K) can be construed as inconclusive since the GS prediction for α-Ce coincides with the 70–100 meV range. Both Joyce et al. (1994a) and Weibel et al. (1993) studied $YbAgCu_4$ and agreed that the intrinsic FWHM for the $4f_{7/2}$ feature was about 70 meV. Since the T_K for this material is about 100 K, the intrinsic width should have been of the order of 10 meV, thus yielding a discrepancy of nearly an order of magnitude. A value of 70 meV (Joyce et al. 1996, Arko et al., unpublished) for the FWHM of the KR is also obtained in $YbCu_2Si_2$ ($T_K = 35$ K) where based on GS and NCA it should have been closer to 4 meV. While Weibel et al. (1993) and Patthey et al. (1993) dismiss these discrepancies as due to lifetime broadening, Joyce et al. felt that the nearly constant value of 70 to 100 meV obtained in all Yb compounds [and for that matter, Ce compounds as well, as reported by Andrews et al. (1996) and Joyce et al. (1992c)] must have some significance, particularly in view of the large values of n_f discussed in sect. 10.

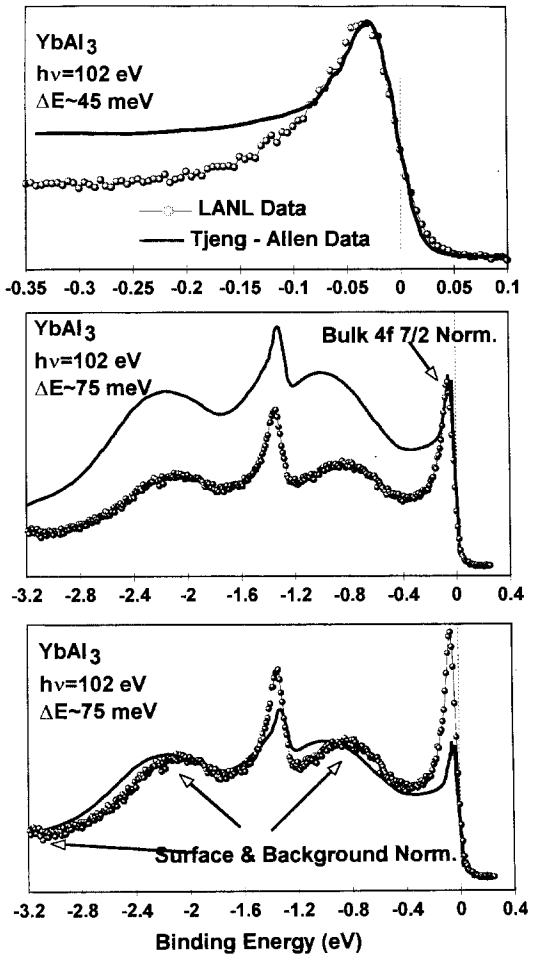

Fig. 23. Comparison of single crystal $YbAl_3$ divalent spectra to polycrystal spectra of Tjeng et al. (1993), and first discussed by Joyce et al. (1994a). Two different normalizations are presented which both clearly show that the polycrystal data misses at least half of the $4f^{7/2}$ intensity. Since Tjeng et al. placed their background at the valley at −0.4 eV their FWHM was half of true value. The top frame shows that in the peak region both spectra coincide as expected for similar resolutions.

The compound $YbAl_3$ was studied in great detail since this was the only material where there was apparent exact agreement between GS theory and experiment. Indeed, the polycrystalline data of Tjeng et al. (1993) obtained an intrinsic FWHM of about 45 meV for the $4f_{7/2}$ peak which makes it, within experimental error, exactly what one would expect for a material having a $T_K \approx 400$ K. The single-crystal work of Joyce et al. (1994a,b, 1996), by contrast, obtains the usual 70 meV value. Figure 23 shows how such a discrepancy comes about when using polycrystalline materials. In this figure the solid lines represent the spectra of Tjeng et al. (1993) while the data points are the single-crystal spectra of Joyce et al. (1994a). In the upper frame the data are normalized on the peak of the KR and in the peak region they overlay each other quite well. However, while Tjeng et al. assumed a constant background equivalent to the PES intensity below −0.15 eV, the single-crystal data clearly show that the actual background is substantially smaller

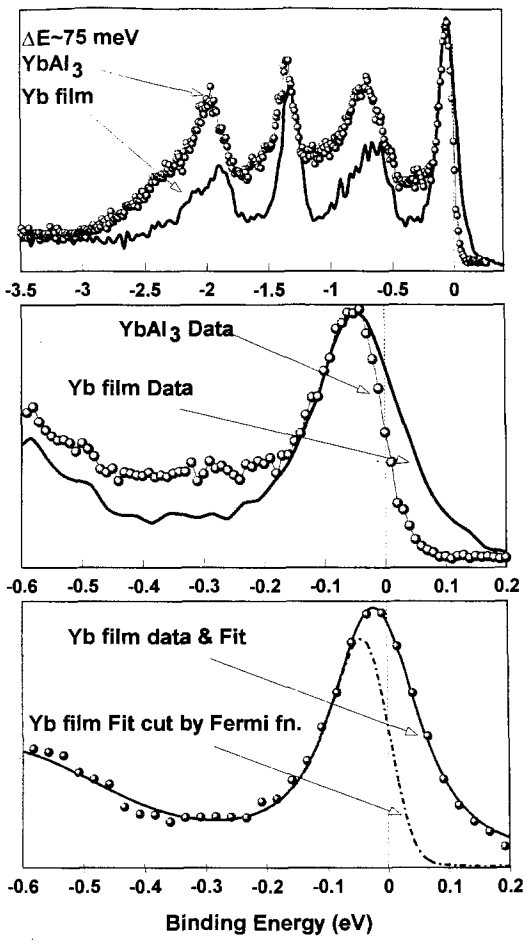

Fig. 24. Comparison of $YbAl_3$ divalent portion of spectrum (upper frame) to that of pure Yb film data appropriately shifted to coincide with $YbAl_3$. The similarity is striking. Middle frame: blow-up of the $4f_{7/2}$ peaks to show that the high binding energy side of the peaks coincides while the low binding energy side of $YbAl_3$ appears to have been cut by a Fermi function. Lower frame: Yb film data cut by Fermi function. Note similarity to $YbAl_3$. (From Joyce et al. 1996.)

near E_F. Thus Tjeng et al. eliminated the bottom 50% of the $4f_{7/2}$ peak from consideration. The middle frame of fig. 23 shows the entire divalent region of $YbAl_3$ and points to the obvious increase in surface emission in polycrystalline samples vs single crystals, so that the true background should have been approximately a Gaussian centered at about –0.8 eV on the surface $4f_{7/2}$ peak. With this adjustment there is then no difference between the two sets of data, and the intrinsic FWHM is about 70 meV. The bottom frame merely shows that by normalizing on the surface features the bulk components in single crystals are dramatically more intense.

Having thus established that indeed nearly all Yb compounds display a 70 to 100 meV linewidth, Joyce et al. (1996) further noticed the similarity of Yb heavy fermion 4f spectra to those of pure divalent Yb metal where the $4f_{7/2}$ feature is found at ~–1 eV and thus is surely an ordinary core level. This is shown in fig. 24 where in the upper frame the

Yb metal data (obtained by evaporating a film onto a substrate) have been shifted by ~1 eV so that the bulk $4f_{5/2}$ and $4f_{7/2}$ peaks overlay. The similarity is striking, although the surface peaks in the pure metal are smaller relative to the compound. This is easily explained by the fact that Yb metal is strictly divalent and thus the intensity of the bulk 4f peaks represents 14 f electrons, while in the $YbAl_3$ compound more than half of the bulk 4f intensity is found in the trivalent portion of the spectrum.

In any case, the middle frame shows an expanded view of this overlay in the $4f_{7/2}$ region to demonstrate that the Yb metal data coincides with the $YbAl_3$ data on the high-binding-energy side of the $4f_{7/2}$ feature, but not on the low-binding-energy side (i.e., at E_F). The latter discrepancy, of course, may simply be due to the fact that in Yb metal the $4f_{7/2}$ peak is not convoluted with a Fermi function owing to its position at -1 eV. If the Yb metal data is artificially convoluted with a 20 K Fermi function and broadened to the same resolution as the $YbAl_3$ data, one sees in the bottom frame of fig. 24 that the result (dashed line) is nearly identical to the $4f_{7/2}$ peak in $YbAl_3$. To a first approximation, then, the PES data from Yb heavy fermions appears as if it were a localized state pinned at the Fermi energy. While this presents some obvious problems in the theoretical understanding, the similarity of the two sets of data cannot be denied. The significance of this, if any, remains to be determined.

11.2. *Surface states*

Occasionally the FWHM of the KR measured on single crystals (Arko et al. 1993) appears broader than 70 meV (sometimes as much as 150 meV) in spite of the very clean appearance of the overall spectra. Indeed, the cleanest spectra tend to show the broadest KR when measured at photon energies of 60 eV or lower. In all likelihood, surface features similar to those reported by Bodenbach et al. (1994) in metallic Yb may also be present in Yb compounds. Indeed, very recent high-resolution data (Arko et al., unpublished) on $YbCu_2Si_2$ indicate that these extremely sharp states are primarily seen at low photon energies ($h\nu < 60$ eV) and are strongest near the Γ-point in the Brillouin zone, occurring at approximately 100 meV binding energy. This is entirely similar to the states reported by Bodenbach et al. Their orbital symmetry is d-like based on the photon energy dependence. These features are to be distinguished from the usual surface shifted divalent components found at ~-0.8 eV. It has not been entirely ruled out, however, that these new features are possibly 4f band states and that even Yb heavy fermions may show some of the same dispersive effects which are clearly evident in Ce compounds and will be discussed in sect. 14. Tjeng et al. (1994) pointed out the extra width of single-crystal data (taken at $h\nu = 60$ eV) vs their polycrystalline data. However, their conclusion that single-crystal data are thus inferior should be considered in light of the apparent surface states which are only present in the most perfect samples. Moreover, there is no discrepancy at $h\nu = 120$ eV where these surface features are absent.

11.3. *Lack of crystal field levels*

The observation of crystal field states in neutron diffraction experiments (Currat et al. 1989, Yashima and Satoh 1982, Galera et al. 1989) has often been cited as the reason why

most PES 4f lineshapes appear similar in spite of large differences in T_K's. Aside from the fact that Joyce and Arko (1993) have shown that the presence of crystal field states does not alter the scaling behavior, these states have not been observed in photoemission. Indeed, a search for these (Arko et al. 1993, Joyce et al. 1992b) in $YbCu_2Si_2$, where a prominent crystal field state should have been observable at 80 meV below the main $4f_{7/2}$ peak, proved fruitless. Very recent unpublished data of Arko et al., taken with 40 meV resolution at 40 meV photon energy on $YbCu_2Si_2$ also yield no evidence for crystal field states, but do yield evidence for an angle-dependent (apparent) surface state as described above. The typical Doniach–Sunjic (1970) lineshape appears common to all Yb heavy fermions.

In Ce heavy fermions crystal field levels likewise remain elusive although it was initially claimed (Patthey et al. 1987a) that these were observed in $CeSi_2$. While that claim has not been repeated, a more recent investigation of CeB_6 has again claimed to show evidence for the first observation of crystal field levels (Takahashi et al. 1995). Inasmuch as the intensity of the level seen by Takahashi et al. was barely above their noise level, it would seem prudent to reserve judgment until further confirmation. Kakizaki et al. (1995), working at the 4d–4f resonance, do not report a crystal field state in CeB_6 in spite of their substantially stronger signal.

12. Temperature dependence

12.1. *General considerations*

The determination of the temperature dependence of the near-E_F feature in heavy fermion compounds is perhaps the most difficult experiment to accomplish correctly. Every material (even Cu, Matzdorf et al. 1993) displays a temperature dependence to some degree in its electronic structure, and it is difficult to determine whether the behavior observed is due to conventional effects of lattice contraction and phonon broadening, or whether it is due to the unconventional behavior predicted by the NCA.

The difficulty of the experiment has precluded much investigation in this arena outside the single-crystal work of Joyce et al. Indeed, in polycrystalline materials the only PES studies are on $CeSi_2$ (Patthey et al. 1987a,b), $YbAl_3$ (Tjeng et al. 1993) and $YbAgCu_4$ (Weibel et al. 1993), while some BIS data exist for $CeSi_2$ (Malterre et al. 1992a, Grioni et al. 1993) and $CePd_3$ (Malterre et al. 1992b). In each of the above studies it was determined that the temperature dependence of the near-E_F feature follows the single-impurity model exactly. However, they all have in common the fact that the surfaces are those of scraped polycrystals. Moreover, there is the ever present problem of the choice of a background which, as we see in fig. 23 for the PES study of $YbAl_3$, can be varied by more than a factor of two thus leading to nearly any desired result. In none of the experiments above was the background determined from measurements of related La or Lu compounds to properly delineate first the non-f contribution, and second, the contribution due to the ever present surface components. In general, the background

is grossly overestimated with the assumption that all the spectral intensity at the valley immediately below the near-E_F peak (i.e., all spectral weight at ~–0.2 eV in fig. 23) is due to background. By drawing a horizontal line between this valley and the Fermi energy and calling it background at least half of the $4f_{7/2}$ peak intensity in fig. 23 is eliminated. Clearly this will exaggerate any temperature dependence.

12.2. *Single crystals vs polycrystals*

In general, single-crystal data tend to show much less temperature dependence than polycrystal data (Arko et al. 1993). Also, the intensities of the near-E_F features, as clearly evidenced in fig. 23, are far stronger in single crystals than in scraped polycrystals. As pointed out earlier, the reason for this is not yet totally understood, but, at least in Ce compounds, the suspicion exists that the $4f_{5/2}$ state is actually a band state so that scraping can destroy the delicate phase coherence of the very narrow band. If scraping can have such a strong effect on this band, then surely temperature and phonons can also play a role.

The existence of some temperature dependence in heavy fermion PES spectra has been the main driving force in pursuing the validity of the single-impurity model. Thus it clearly requires more substantial treatment than given in some of the previous sections. Additionally, in view of the superiority of single-crystal data (cleaved rather than scraped) the latter will be given more weight than polycrystalline results. The focus will be on three materials (again Yb compounds where all agree that the $4f_{7/2}$ level is filled), namely $YbAgCu_4$, $YbCu_2Si_2$, and $YbAl_3$.

12.3. *BIS temperature effects*

The approximate solutions of SIM also predict the behavior of empty states in correlated compounds. These can be studied with bremsstrahlung isochromat spectroscopy, or BIS. But in regard to BIS data, a number of problems need to be addressed before it can be accepted as validating the single-impurity model. In the first place, the resolution is insufficient to determine whether 4f states just above E_F are actually consistent with a Kondo resonance (i.e., correct width, weight, position, consisting of the KR and the sideband, etc.), or are just a manifold of the 13 empty 4f states (in the case of Ce). Secondly, it has not been satisfactorily demonstrated that the weight lost in the near-E_F peak exactly equals the weight gained by the f^2 peak (a necessary condition). Thirdly, there is no reason to assume that the balance between the f^1 and f^2 peaks cannot change simply as a result of lattice expansion with temperature if we have single-particle states. Fourthly, surface effects are common in Ce compounds and no delineation of these has been done in BIS. Finally, if the empty states are near the Fermi energy the simple convolution with a 300 K Fermi function will yield some temperature dependence, particularly in the presence of phonon broadening. Also, in the end it will still be necessary to explain the single-crystal PES data which clearly fail to conform with the single-impurity model. For all these reasons it is best to study temperature dependence

via PES in Yb compounds where the full power of high-resolution PES can be applied to fully occupied 4f states.

12.4. *Yb compounds – comparison to NCA*

The NCA predictions (code provided by D. Cox) for the temperature behavior of these materials are shown in fig. 25 (from Joyce et al. 1996). Here the $4f_{7/2}$ and $4f_{5/2}$ features are shown without the omni-present surface states which cannot be modeled by NCA.

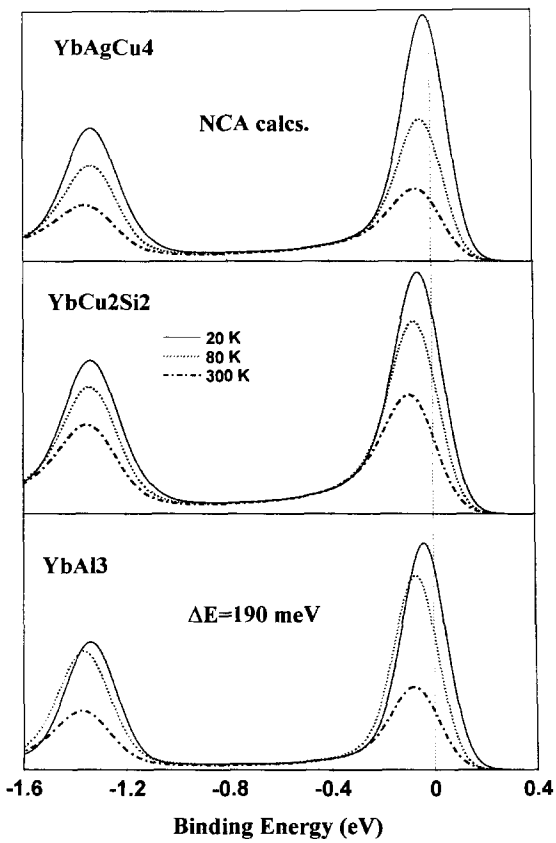

Fig. 25. NCA calculations (code provided by D.L. Cox) at three different temperatures for three materials discussed here. Surface states are not modeled by NCA. Note the large temperature dependence expected for $YbAgCu_4$. The parameters used are:
Upper frame, $YbAgCu_4$: $T_K = 100\,K$, $U_{ff} = \infty$, $W = 6.0\,eV$ (Lorentzian), $\Delta_{SO} = 1.29\,eV$, $\varepsilon_f = 1.0\,eV$, CF states – none, $\Gamma = 0.05462\,eV$.
Middle frame, $YbCu_2Si_2$: $T_K = 40\,K$, $U_{ff} = 8\,eV$, $W = 6.0\,eV$ (Lorentzian), $\Delta_{SO} = 1.29\,eV$, $\varepsilon_f = 1.0\,eV$, $\Delta_{CF1} = 12\,meV$, $\Delta_{CF2} = 30\,meV$, $\Delta_{CF3} = 80\,meV$, $\Gamma = 0.0606\,eV$.
Lower frame, $YbAl_3$: $T_K = 400\,K$, $U_{ff} = 8\,eV$, $W = 10.0\,eV$ (Lorentzian), $\Delta_{SO} = 1.29\,eV$, $\varepsilon_f = 1.0\,eV$, CF states – none, $\Gamma = 0.05856\,eV$. (From Joyce et al. 1996.)

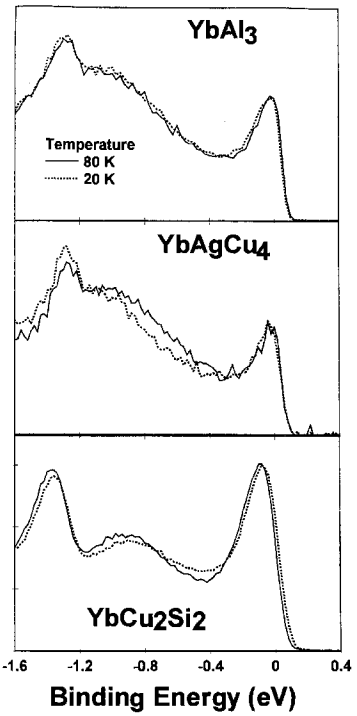

Fig. 26. Experimentally measured temperature dependence between 20 K and 80 K for the three materials calculated in fig. 25. Essentially none. (From Blyth et al. 1993.)

The three temperatures for which calculations exist are those most easily accessible experimentally. The parameters are given in the figure caption, but are chosen so as to approximate the three materials and their respective T_K's. The data have also been smoothed with a 190 meV Gaussian to match the resolution of the $YbCu_2Si_2$ data shown in the bottom frame of fig. 26. In all cases a large temperature dependence is predicted. In particular, note the large decrease in intensity between 20 K and 80 K for $YbAgCu_4$, a material having a T_K in the vicinity of 100 K.

By contrast, fig. 26 shows that the measured temperature dependence between 20 K and 80 K in all three materials (Blyth et al. 1993) is almost nil, with the surface states usually showing larger effects than the bulk states. Here the $YbAgCu_4$ specimen was a coarse-grained polycrystal cleaved *in situ*. The results contrast sharply with the measurements of Malterre et al. (1992a) who reported a large temperature effect in $YbAgCu_4$ between 20 K and 80 K. Again, however, in view of the superiority of single-crystal data (or at least cleaved vs scraped surfaces) more weight is given to results from cleaved surfaces, the scraped polycrystal data having too many uncertainties. Indeed, Arko et al. (unpublished) observed that scraping their $YbAgCu_4$ surface totally destroys the $4f_{7/2}$ and $4f_{5/2}$ bulk peaks which were present on the same specimen when the surface was prepared by cleaving. The intensities slowly recover with time and a large temperature dependence

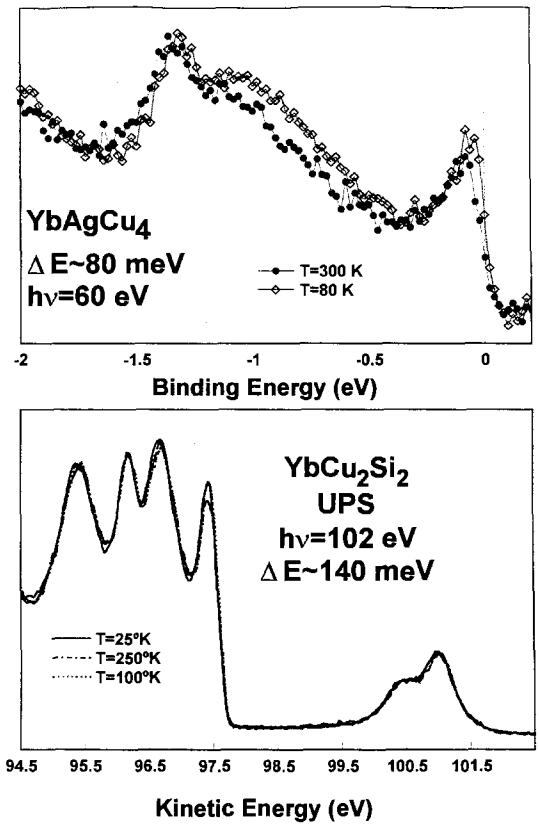

Fig. 27. Experimentally determined temperature dependence for 2 materials calculated in fig. 25. Only the $4f_{7/2}$ peak shows some temperature dependence due to Fermi function effects. The $YbCu_2Si_2$ data are those of C.G. Olson using a CMA analyzer with the sample mounted on a cryostat horizontal to beam to avoid sample movement during warm-up. Data were normalized on the Si 2p levels above E_F (kinetic energy = 101 eV) due to second-order light. (From Joyce et al. 1996.)

can now be observed below 80 K, but the surface composition prepared in this fashion surely is no longer representative of the starting material.

Above 80 K a substantial temperature dependence is usually observed even in single-crystal Yb heavy fermions, albeit not always. The lack of exact reproducibility may in fact be the smoking gun which points to the fact that these effects are probably more related to the quality of the surface. First we show in fig. 27 cases where the features, both bulk and surface, are nearly temperature independent, except for the effect of the Fermi function. The $YbCu_2Si_2$ spectra in the lower frame are unpublished data of C.G. Olson at SRC. Although $YbCu_2Si_2$ generally yields smaller effects than other materials in spite of its $T_K = 35$ K, these moderate-resolution spectra are particularly important because of the method in which they were taken. For these data (measured with a CMA analyzer) the sample was mounted at the bottom of a cryostat which itself was mounted in a horizontal position parallel to the beam direction. This is important because as the cryostat temperature decreases, the contraction of the cryostat is parallel to the direction of the light so that the sample position with respect to the light source does not change. Indeed, one possible source of temperature dependence is simply the change in sample position.

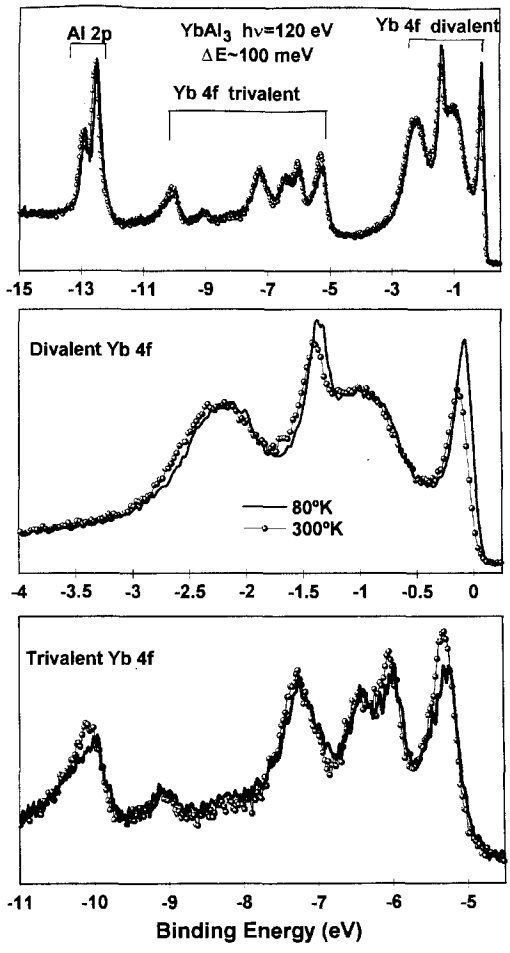

Fig. 28. Typical temperature dependence for single crystal $YbAl_3$ between 80 K and 300 K. Spectral weight loss for the $4f_{7/2}$ peak is rarely more than 10% vs the predicted 60% in fig. 15. This is easily accounted for by Fermi function effects. There is little spectral weight loss in the $4f_{5/2}$ peak nor gain in the trivalent portion of the spectrum. Data are normalized on the Al 2p levels at −13 eV due to third-order light. (From Joyce et al. 1996.)

It was found by Olson that simply illuminating a different part of the surface results in spectral changes which can exceed any temperature effect. This is due to the fact that at different parts of the crystal surface different crystal planes are exposed, which have wildly differing $4f_{7/2}$ intensities. Indeed a cleave was found in $YbCu_2Si_2$ which showed almost no bulk $4f_{7/2}$ intensity, with nearly all intensity in the surface $4f_{7/2}$. Another important aspect of the bottom frame of fig. 27 is that the data were normalized on the Si 2p states occurring just above E_F due to second-order light. By normalizing to the integrated spectral weight of these Si 2p states which are presumably temperature independent, the minimal temperature dependence of fig. 27 was obtained.

More common in Yb heavy fermions, however, are spectral weight changes ranging from 0% to about 15%. A more typical temperature dependence between 80 K and 300 K is shown in fig. 28 for $YbAl_3$ (Joyce et al. 1996, Andrews et al. 1994). Here again the data

are normalized to the Al 2p core levels which this time are obtained in third order, while the spectrum itself is obtained in second-order light for better resolution. For the set of data in fig. 28 the spectral weight loss of the $4f_{7/2}$ is about 7%, assuming a Doniach–Sunjic (1970) lineshape, and about 10% assuming a symmetric Lorentzian lineshape. While the fit to the data is noticeably worse with a symmetric lineshape, the spectral weight loss is still only about 10%, a value substantially less than the 60% predicted in fig. 25. In addition to the deterioration of fit quality, the symmetric Lorentzian lineshape requires a FWHM of about 140 meV which is in gross contrast to the GS and NCA predictions of ~45 meV. In the bottom frame of fig. 28 an expanded view of the trivalent portion of the spectrum at first shows what appears to be an increase in trivalent signal with increasing temperature, just as one would expect from SIM. However, direct integration of this signal yields almost no change in the total spectral weight. In all likelihood the small spectral weight loss in the divalent signal is not detectable as a weight gain above noise level in the trivalent portion in this mixed valent material. From all this one would have to conclude that the small temperature dependence observed in Yb heavy fermions does not fit the NCA predictions despite claims to the contrary (Tjeng et al. 1993, Weibel et al. 1993). On the other hand, the PAM predicts a much slower temperature evolution of the KR relative to the SIM. Although calculations for real systems are not yet possible with PAM, the trend is in the right direction and offers hope for a resolution of the dilema.

Joyce et al. (1992c) suggested already in connection with $CeSi_2$ data of Patthey et al. (1987a) that one should consider phonon broadening as a source of temperature dependence. In reply it was pointed out (Patthey et al. 1993) that while core level phonon broadening can be understood within the Franck–Condon model, the near-E_F features in heavy fermions should not couple to the phonons owing to the well-screened condition of these states. Nevertheless, phonon broadening is observed in the valence bands of many materials, even in excellent metals like Cu (Matzdorf et al. 1993), where the screening is expected to be good. Thus, while not entirely understood, phonon broadening is an existing fact and must be considered. In $CeSi_2$ Joyce et al. (1992c) estimated the magnitude of the broadening (about 100 meV) from the broadening of the Si 2p core levels. While this is certainly not expected to be identical to the Ce states, it should serve as a first-order approximation.

In Yb compounds the phonon broadening was estimated from a measurement of pure Yb metal, which, as we have already seen in fig. 24, displays 4f spectra similar to those of the heavy fermion compounds despite the position of the $4f_{7/2}$ peak at ~−1 eV below E_F. The temperature dependence of these levels, now due entirely to phonon broadening, is shown in fig. 29. The data were fitted at each temperature with Gaussian broadened Doniach–Sunjic (1970) lineshapes and separated into bulk and surface components. The fits are overlaid in the upper frame, normalized to equal integrated intensities. A substantial apparent temperature dependence is observed even in the absence of the Fermi function cut-off, and in the absence of any spectral weight loss. The 300 K spectra are broadened by 130 meV over the 25 K spectra (added as root mean square).

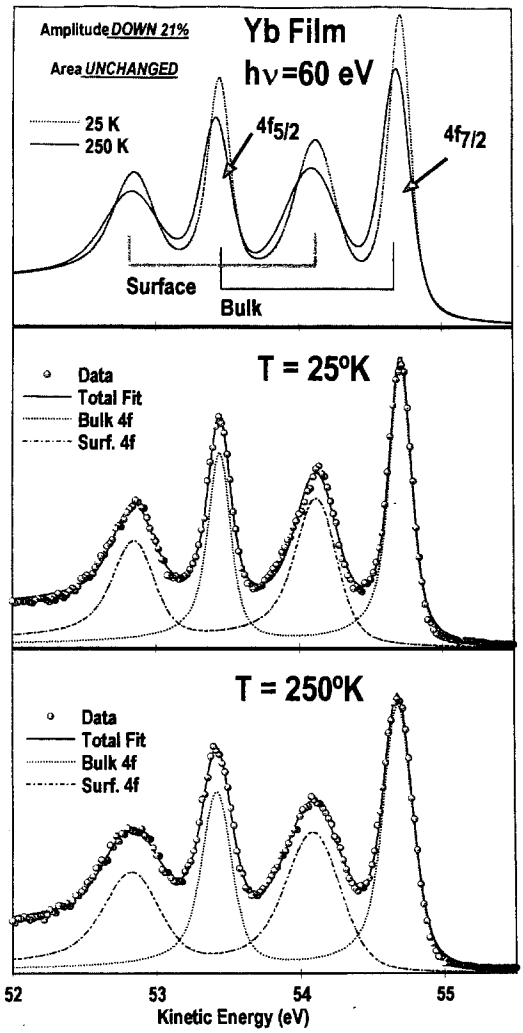

Fig. 29. Yb metal film data at 25 K (middle frame) and 250 K (lower frame) to show that a temperature dependence is observed even in the absence of any Kondo phenomena. Spectra were normalized to equal areas by fitting to the bulk and surface peaks as shown. Upper frame shows an overlay of these equal area fitted curves. 130 meV of broadening in quadrature over the 25 K spectrum was needed to fit the 300 K spectrum. (From Joyce et al. 1996.)

12.5. *Phonon broadening and Fermi function*

Assuming that a similar 130 meV broadening occurs in heavy fermion compounds where the $4f_{7/2}$ is within 20 to 30 meV of the Fermi energy, one can then simulate the effect of the Fermi function on the $4f_{7/2}$ intensity (Joyce et al. 1996). This is done in fig. 30 where fits to the bulk divalent 4f peaks of fig. 28 (i.e., the bulk $4f_{7/2}$ and $4f_{5/2}$) measured at 20 K are broadened by 130 meV in quadrature and convoluted with a 300 K Fermi function. The middle frame shows the effect near the Fermi energy using a 45 meV experimental resolution, while the bottom frame gives the same result with 100 meV experimental

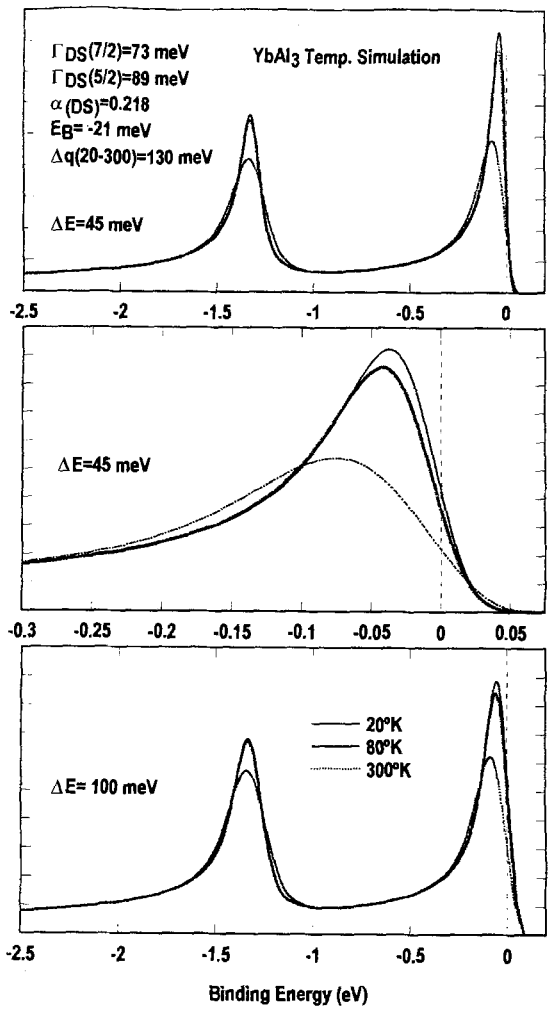

Fig. 30. Simulated temperature dependence of the fitted $YbAl_3$ spectrum of fig. 18 with the surface states removed. The 300 K spectrum was broadened in quadrature by the 130 meV found for Yb metal and subsequently cut with a 300 K Fermi function. A 12.5% spectral weight loss is obtained for the $4f_{7/2}$ peak and none for the $4f_{5/2}$ peak although the latter appears to have lost spectral weight. This is more than is actually observed. Minor scatter in the data can easily account for a mistaken temperature dependence. (From Joyce et al. 1996.)

resolution. The calculated spectral weight loss of the Yb $4f_{7/2}$ peak is about 15% which is actually larger than the measured result. Thus the broadening in compounds is perhaps somewhat less than 130 meV, indeed most likely closer to 100 meV as found (Joyce et al. 1992c) in $CeSi_2$. It is important to note from the bottom frame of fig. 30 that given some degree of data scatter one could never unambiguously distinguish between peak broadening and spectral weight loss, although a careful subtraction of the backgrounds often yields a zero weight loss for the Yb $4f_{5/2}$ even in the presence of a 10% weight loss for the Yb $4f_{7/2}$. In fig. 27 no data analysis is needed to see this effect.

The lack of temperature dependence of the Yb $4f_{5/2}$ is significant, since the SIM predicts it to be large (e.g., fig. 25). It almost certainly points to a failure of the SIM

in favor of other models, perhaps the PAM. At this writing, however, the PAM cannot be solved for Yb compounds.

12.6. *Ce compounds*

The concept of phonon broadening works especially well for Ce compounds. This was already shown in the re-analysis (Joyce et al. 1992c) of the $CeSi_2$ data of Patthey et al. (1987a), but it is always more convincing when the signal is strong, as in $CeBe_{13}$. In this material (Andrews et al. 1996) there is the added advantage in that the large T_K (≈ 400 K) precludes the existence of any crystal field levels (indeed, none have been reported), so that from SIM all of the Ce $4f_{5/2}$ intensity is in the Kondo resonance which should then follow the temperature dependence of fig. 2. Since at $T = 300$ K we obtain to first order that $T/T_K \approx 1$, about 50% of the KR spectral weight should be lost between 20 K and 300 K based on fig. 2.

In fig. 31 the spectra at resonance for $CeBe_{13}$ (110) are shown with 90 meV resolution at 20 K and 300 K (Andrews et al. 1996). In this figure the spectra are analyzed assuming that the 4f states at this location in the Brillouin zone are fully occupied below E_F and are not a consequence of a mere tail from an intense KR feature above E_F. In other words the spectrum at 20 K was fit with a symmetric Lorentzian centered at –20 meV for the $4f_{5/2}$ state and a Gaussian peak at –280 meV to simulate the $4f_{7/2}$ feature. A background

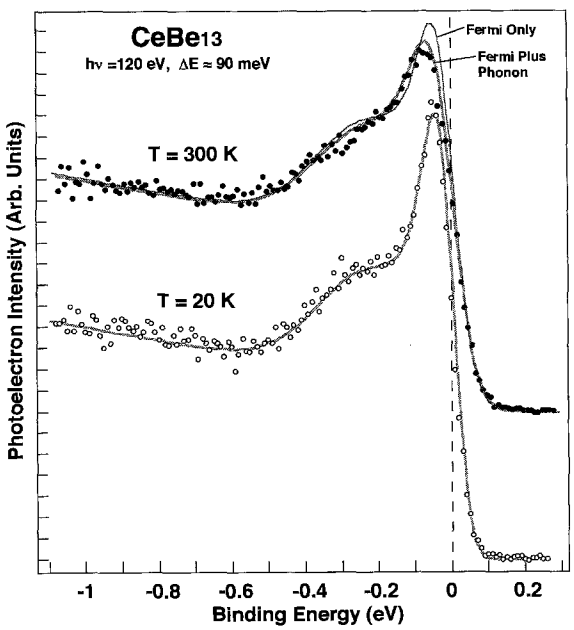

Fig. 31. Spectra for $CeBe_{13}$(110) at 20 K and 300 K to determine temperature dependence. The 20 K spectrum was fitted with a 90 meV wide (FWHM) Lorentzian (gray line through data) at –20 meV for $4f_{5/2}$, plus a Gaussian at –250 meV for $4f_{7/2}$, as well as a featureless background (see Andrews et al. 1996). This fitted curve was then just cut with a 300 K Fermi function to produce the "Fermi Only" fit in the upper curve. However, by first broadening the entire 20 K fitted curve by 100 meV and then cutting with a 300 K Fermi function an exact fit to the 300 K data is obtained (thick gray line).

was also included and the total fit is shown as the gray line through the data points. If this

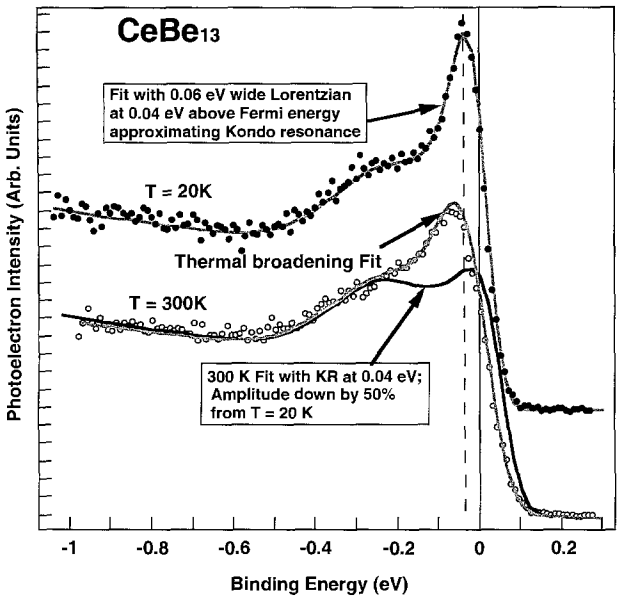

Fig. 32. Here the 20 K data of fig. 31 are fit with a 0.06 eV wide (FWHM) Lorentzian centered at 0.04 eV above E_F so that only the tail is occupied, thus simulating a KR. Crystal field levels are absent in this material. All other parameters are identical to those of fig. 31. The temperature dependence is then simulated by decreasing the KR intensity to 50% of its 20 K value and cutting with a 300 K Fermi function to produce the dark line curve superimposed on the 300 K data. Note the peak shift toward E_F vs the observed shift away from E_F.

entire fitted lineshape is now convoluted with a Gaussian (FWHM = 100 MeV) to simulate 100 meV of phonon broadening, and then convoluted with a 300 K Fermi function, the resulting lineshape fits the 300 K data exactly as shown by the gray line in the 300 K spectrum. The thin black line in the 300 K spectrum represents convolution with a Fermi function only. While it yields nearly all the temperature dependence, it is clearly insufficient to fit the 300 K spectrum exactly.

The fits in fig. 31 show that 100 meV of phonon broadening combined with Fermi function convolution are entirely sufficient to explain all temperature effects, provided that the peak of the narrow DOS feature is below the Fermi energy as assumed in the fits. It is however fair to ask whether a similar fit can be obtained with the assumption that the peak of the narrow feature is above the Fermi energy and only the tail of this feature is occupied, as would be the case for a KR. It is straightforward to simulate this using Lorentzians since within GS the KR has nearly a Lorentzian lineshape. The 20 K spectrum of fig. 31 can indeed be fit quite well by assuming a symmetric Lorentzian centered at 0.04 eV (above E_F) and having a FWHM of 0.06 eV. This new fit is shown in fig. 32 as the gray line through the $T = 20$ K spectrum. The parameters for this Lorentzian are surprisingly close to what one would expect for a Kondo resonance in a material having a T_K of ~400 K so that at first glance it would seem to confirm the existence of a KR. (Recall from fig. 21, however, that the actual calculation misses badly on the f^0 peak.

In fig. 32 is shown a simulation of the KR only.) If the temperature is now increased to 300 K, the spectral weight of the Lorentzian representing the KR at 0.04 eV above E_F must be decreased to about half of its intensity (based on fig. 2) and the entire spectrum convoluted with a 300 K Fermi function in order to simulate the 300 K spectrum. The result is shown as the dark line spectrum superimposed on the 300 K data. Immediately we see that far too much temperature dependence is predicted, and it would take a severe renormalization of the theory to bring the temperature dependence in line. More importantly, however, the centroid of the simulated peak shows a positive energy shift while experimentally the peak actually shifts away from the Fermi energy with increasing temperature.

The positive energy shift of the Ce $4f_{5/2}$ peak with increasing temperature was in fact first calculated by Gunnarsson and Schönhammer (1987). In that paper they also show that because of the intense and narrow KR just above E_F one may actually obtain an increase in measured $4f_{7/2}$ intensity at elevated temperatures despite the fact that the KR intensity is decreasing. This amplitude effect is purely a consequence of the occupation of only a small tail of a much more intense narrow feature above E_F. It is easy to understand this amplitude effect if the KR (or any sharp feature above E_F) is positioned within k_BT of the 300 K Fermi function (i.e., within about 20 meV of E_F) and its width is no more than about 20 meV. Outside of these approximate parameters one will always get a decrease, but more importantly, in all cases there will be a shift toward the Fermi energy with the broader Fermi function.

The experimental shift away from the Fermi energy, by contrast, is a direct consequence of the broadening of the $4f_{5/2}$ feature. A peak shift cannot be obtained if only the Fermi function convolution is used with no phonon broadening. Thus, the observed shift of the peak toward higher binding energies, observed almost universally in Ce heavy fermions, is a smoking gun in favor of phonon broadening.

Because of the positive energy shift inherent in the GS calculation (vs. the experimentally observed negative shift in most Ce heavy fermions with the possible exception of the Kondo insulators) one can never obtain a fit to the 300 K data using GS without changing the position and the FWHM of the Kondo resonance, as well as shift the position of the spin–orbit peak, no matter how much spectral weight is assumed lost in the KR. By contrast, we see that an exact fit is trivially obtained by assuming a feature fully occupied below the Fermi energy and broadened with temperature. To restate, the shift toward the Fermi energy is a direct consequence of a convolution of a broader Fermi function with a sharp intense DOS feature immediately above E_F, while a shift away from the Fermi energy can only occur if the peak in the DOS is fully below E_F and broadened.

All these effects were observed in single crystals in angle-resolved spectra. For the directions measured, the observed temperature effect would suggest a $4f_{5/2}$ quasiparticle peak fully occupied below E_F and no intense DOS features within k_BT above E_F. This is consistent with a narrow band which could cross E_F, but for the directions measured it is situated below E_F. Clearly an experiment still to be performed is one where the band has just crossed E_F (i.e., the $\theta = 10°$ spectrum in fig. 41b, below). Here one would expect a peak shift in the opposite direction (toward E_F) as the temperature increases.

It appears, then, that in Ce compounds there is no temperature dependence of the DOS over and above conventional effects. The same appears to be true in Yb compounds at least where single-crystal data are concerned. Data from scraped polycrystalline surfaces clearly display stronger temperature effects and it remains to be determined whether disruption of the narrow bands by scraping changes the 4f electronic structure sufficiently that the single-impurity case is actually realized.

While we have been calling the broadening effect as phonon broadening, it must be pointed out that the PAM likewise predicts a broadening of PES features with temperature, but not associated with phonons. Experimentally there is no way to distinguish between phonons and the magnetic polaron interactions inherent in the PAM. Suffice it to say that the temperature effects observed in PES measurements are not inconsistent with the PAM predictions.

13. Surface-related effects

For the photon energies employed in high-resolution spectroscopy of lanthanide materials ($h\nu = 40$–120 eV; $\Delta E = 40$–70 meV), the escape depth of the photoelectrons is typically ~10 Å at the 4d resonance, so that the top one or two layers of the material may contribute as much as 50% to the PES signal. At the higher energy 3d resonance, $h\nu \approx 900$ eV, the surface contribution is reduced to only ~10% of the total signal, but the concomitant lower energy resolution achieved at this photon energy ($\Delta E = 300$ meV) is insufficient to test the accuracy of the lineshapes, so it is the more surface sensitive 4d resonance which is most often used to test the theoretical models.

It has been suggested that the lack of agreement between GS calculations and photoemission experiments might be attributed to the fact that PES does not sample the bulk electronic structure, due to its intrinsic surface sensitivity. While relatively little is known about the surface behavior of actinide materials, limited progress has been made on understanding lanthanides. Here we must content ourselves with a brief summary of those findings which bear relevance to the spectroscopy of heavy fermions. In this section the chief focus will be on Ce compounds rather than Yb, because it is Ce which presents the greater challenge to identify the surface 4f contribution.

In their atomic form, all rare earths except Ce, Gd and Lu are divalent $4f^n(5d6s)^2$. The cohesive energy gain upon solidification favors the trivalent state in the solid $4f^{n-1}(5d6s)^3$ in all metals except Eu and Yb. At the surface however, the electronic structure of the bulk is strongly perturbed, and the charge rearrangement can produce a surface atom core-level shift (SCLS) which results in an energy splitting of the surface and bulk core levels $\Delta_{s,b}$ typically on the order of ± 0.1–1.0 eV. The magnitude and direction of the SCLS will depend on the net sign of the sum of five separate contributions:

$$\Delta_{\mathrm{SCLS}} = \Delta_{\mathrm{environment}} + \Delta_{\mathrm{hybridization}} + \Delta_{\mathrm{configuration}} + \Delta_{\mathrm{relaxation}} + \Delta_{\mathrm{charge\ transfer}}$$

(the fifth term should be included when adsorbates are present). For pure metals, the SCLS leads to stabilization of the divalent state at the surface in Sm and Tm. In compounds,

the difference in energy between the trivalent and divalent configurations is modified, and many intermetallics formed of either Sm, Tm, Eu or Yb (such as $YbAl_3$ already discussed) also exhibit surface valence transitions.

The existence of surface valence transitions in the rare earths and their compounds is well established, however it was not until quite recently that 'analogous' effects were discovered for Ce and Ce intermetallics (Laubschat et al. 1990, Weschke et al. 1991, 1992). In the context of Ce the term 'valence transition' will refer to the difference in hybridization strength that occurs between the α and γ phases, rather than 4f population changes which can occur for the pure metals as noted above. The discovery of this behavior in Ce has important consequences for the spectroscopy of heavy fermion compounds inasmuch as it may help explain some of the discrepancies between model calculations and experiment noted above.

13.1. *Studies at high hν*

The first evidence that the electronic structure of the surface layer of Ce differed substantially from the bulk came from the XPS study by Laubschat et al. (1990) in which 3d core level spectra of $CeIr_2$, $CePd_3$ and $CeRh_3$ were analyzed using a simplified version of the GS model (Imer and Wuilloud 1987). They found 20% larger f occupancies for the surface layer indicating a reduced hybridization relative to the bulk. High-resolution UPS of the Ce 4f core levels by Weschke et al. (1991) used *in situ* growth to achieve a clean Ce surface. The sample temperature was varied across the α–γ phase transition from 20 K to 150 K while photoemission spectra were recorded at the 4d ($h\nu = 120$ eV, fig. 33) and 3d ($h\nu = 884$ eV, fig. 34) resonance thresholds. For Ce in the γ phase, spectra

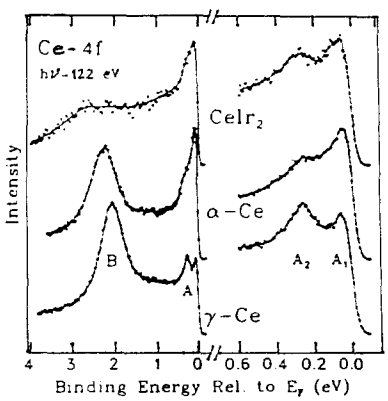

Fig. 33. 3d and 4d resonant spectra for α- and γ-Ce and $CeIr_2$ from Laubschat et al. (1992), fig. 2.

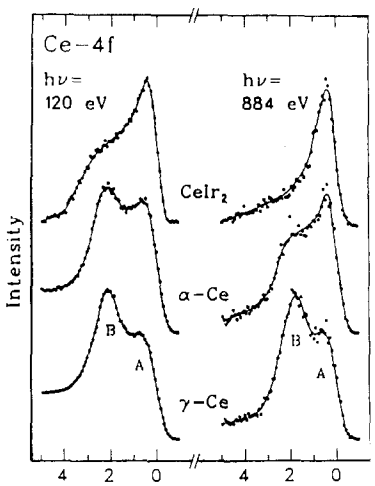

Fig. 34. Surface and bulk components of α-Ce and $CeIr_2$ from Laubschat et al. (1992), fig. 3.

at the 3d and 4d edges appear identical. In marked contrast, for the α phase Ce we see that the spectra taken at the more surface sensitive 4d energy exhibit a larger f^0/f^1 ratio than the corresponding 3d spectra, giving it an appearance similar to the γ phase of the material. Furthermore, when the surface and bulk signals were extracted for the α phase (using estimated surface–bulk intensity ratios based on the photoelectron escape depth), the f^0 peak was found to contain a much larger surface component than the f^1 (fig. 34 bottom spectra). In subsequent studies, Weschke et al. (1992) and Laubschat et al. (1992) went on to discover that in the 'bandlike' materials $CeIr_2$ and $CeRh_3$ the f^0 peak originates almost entirely from surface layer.

These findings partially invalidated much of the earlier XPS work on deriving GS model parameters and 4f occupancies which did not take account of the surface contribution. However, since the authors employed a simplified version of the GS model in their analysis, the larger issue of the appropriateness of the GS model for describing Ce PES cannot be answered by their work. Nevertheless, these findings represent one of the more important contributions to the understanding of Ce photoemission spectra.

The presence of a sizable surface contribution with a smaller hybridization strength than the bulk complicates analysis of the photoemission spectra, because it doubles the number of parameters which must be employed in the fit. Since the number of adjustable parameters is already large this would seem to be a highly undesirable situation. The implications of this for the spectroscopy of heavy fermion systems appear to have been largely overlooked: to date we know of only one study, Liu et al. (1992a), which attempts to account for the surface contribution using the full-blown GS model. In this work the authors argue that the large discrepancy between the magnetic susceptibility values derived from photoemission and those obtained directly from bulk measurements, is entirely due to failure to include the surface contribution in the analysis. It is, however, a pure assumption that the surface can be treated as a separate Kondo material with a much lower Kondo temperature since there is no evidence that there is a surface contribution to the f^1 features.

13.2. *Dosing studies*

Without exception, the surface layers of all the compounds discussed in this review are highly sensitive to the presence of contaminants. This is true for both valence states and core levels. In a limited number of cases, it is actually possible to quench the surface components by dosing them with light impurities such as oxygen or hydrogen. We have conducted dosing studies over the past two years on almost all of the materials mentioned in this review, chiefly in order to identify the surface contribution, but also in order to help us understand the reasons why the photoemission spectra from single crystals differ so dramatically from older data from polycrystalline samples, which we suspect may have suffered from the presence of contaminants. We have confined our studies to the low coverage regime, $\leqslant 1.0$ Langmuir, and have not tried to determine oxidation rates or precursor states which depend on the crystallographic plane of the surface, which was not always possible to uniquely identify. Higher concentrations of O_2 will eventually result

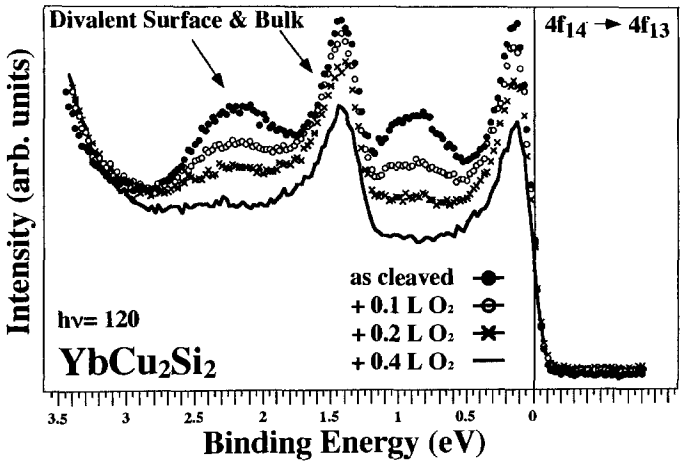

Fig. 35. $YbCu_2Si_2$: solid circles, as cleaved; open circles, +0.1 L O_2; crosses, +0.2 L O_2; solid lines, +0.4 L O_2.

in the formation of an oxide layer, but prior to this, oxygen may penetrate into the bulk lattice and change the surface morphology.

Figure 35 shows the response of a freshly cleaved $YbCu_2Si_2$ surface to the addition of small quantities of oxygen via a gas dosing valve (1 Langmuir = 1×10^{-6} torr for 1 s.). The solid line shows the familiar divalent surface and bulk peaks ($\Delta_{s,b} \approx 0.9$ eV) as discussed in sections 8–10 above. The dotted/dashed lines and markers show the gradual reduction in the magnitude of the surface component with dosage. The emission from the surface components clearly decreases more rapidly than the bulk ones. The small amount of apparent decrease in the bulk peaks is due in part to the loss of the underlying surface signal, as well as an increase in the depth traversed by the bulk electrons due to the oxygen adlayer. The surface component is completely quenched by only ~0.4 Langmuirs of O_2.

Ce is much more reactive than Yb, so that samples remain clean for shorter time periods under standard UHV conditions ($P < 10^{-10}$ torr). While there have been a number of earlier studies on the oxidation of polycrystalline Ce metal [see Lynch and Weaver (1987) and references therein] we know of no published investigations pertaining to the oxidation of Ce heavy fermion compounds. The two most stable oxides of Ce are trivalent Ce_2O_3 and tetravalent CeO_2. The signature (in a PES spectrum) of the trivalent form of the oxide will be the presence of a 4f peak at ~2 eV with the 4f weight at the Fermi level much reduced or altogether absent (except for the remaining 5d's), while for the tetravalent oxide the spectrum will appear similar to that of La metal, indicating the complete absence of 4f electrons. The results of dosing studies on many other Ce compounds have been reported by Blyth et al. (1994).

For Ce the surface–bulk splitting is too small to be resolved, however small amounts of O_2 can dramatically change the spectral weights of the f^0 and f^1. In fig. 36 [$CeBe_{13}$] the solid circles show the as-cleaved surface of $CeBe_{13}$ while the open circles, diamonds, crosses, open triangles and solid line correspond to increasing O_2 concentrations. Between

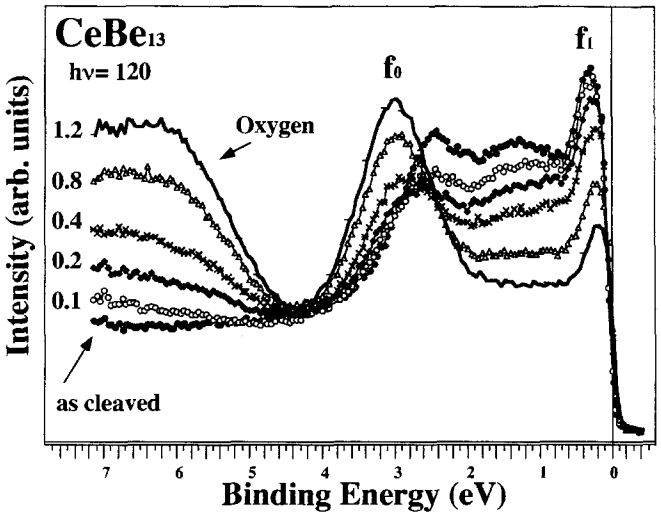

Fig. 36. $CeBe_{13}$: solid circles, as cleaved; open circles, +0.1 La O_2; diamonds, +0.2 L O_2; crosses, +0.4 L O_2; triangles, +0.8 L O_2; solid lines, +1.2 L O_2.

0.1 and 0.2d Langmuirs, the apparently greater loss in intensity of the f^0 (~20%) relative to the f^1 (~10%) may indicate a larger surface contribution, which agrees with the findings cited earlier (Laubschat et al. 1990, 1992, Weschke et al. 1991, 1992), i.e., that the f^0 has a larger surface component than the f^1 due to the γ-like surface layer. Between a coverage of 0.1 and 0.2 L, the f^0 peak begins to shift toward higher binding energy, then from 0.2 to 1.2 L it gains intensity, while the f^1 peak progressively looses weight. The direction of the peak shifts, the f^1 toward E_F and the f^0 to higher binding energy, are in accord with the presence of a γ-like surface layer, however the covalent bonding with the oxygen adds spectral weight to the resonance at ~2 eV so that the comparison is obscured, making it difficult to draw conclusions about the precise extent of the surface contribution. It is tempting, albeit speculative, to suppose that the spectra displayed listing a coverage of 0.2 L of O_2 may more closely approximate the true bulk spectra of this material. Above this coverage oxide formation has begun to occur, as signaled by the steadily increasing intensity of the f^0 peak.

Figure 37 [$CeCu_2Si_2$] illustrates how even a small amount of contamination (<0.5 L O_2) can lead one to the erroneous conclusion that there is no f^1 weight at the Fermi level. By 0.4 L any sign of the f^0 peak which was prominent on the freshly cleaved surface has vanished and all that remains is a flat DOS which is attributed to the 5d bands. There is far less noticeable effect on the Cu 3d bands at 4 eV binding energy. It is particularly worrisome that the O_2 peak at 6 eV appears as only a weak shoulder of the main Cu d band since this too could lead one to incorrect assessment of the surface cleanliness. The loss of weight at the Fermi level, together with the growth of the ~2 eV 'covalent' resonance, indicates the formation of the trivalent oxide Ce_2O_3. If the 0.4 L spectrum is broadened by the appropriate amount, it strongly resembles PES spectra from polycrystalline samples

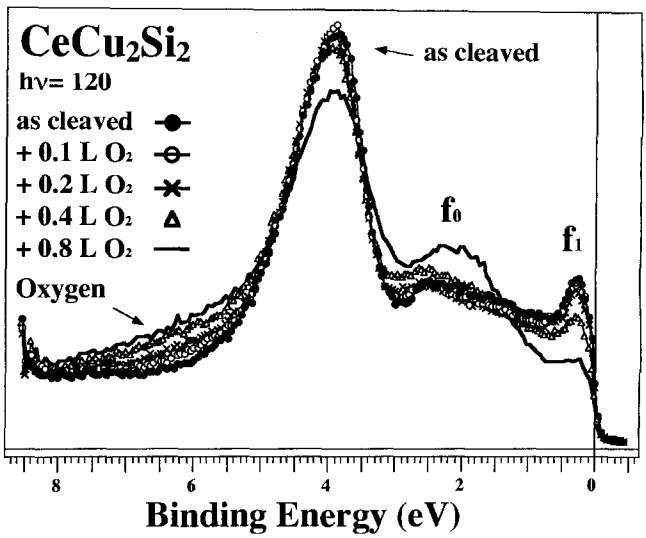

Fig. 37. $CeCu_2Si_2$: solid circles, as cleaved; open circles, +0.1 L O_2; crosses, +0.2 L O_2; triangles, +0.4 L O_2; solid lines, +0.8 L O_2.

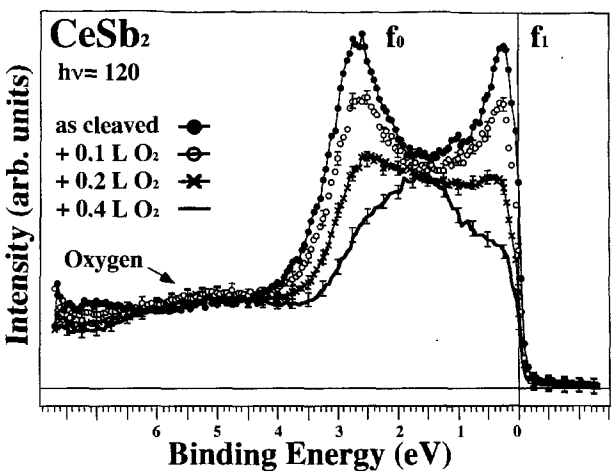

Fig. 38. $CeSb_2$: solid circles, as cleaved; open circles, +0.1 L O_2; crosses, +0.2 L O_2; solid lines, +0.4 L O_2.

presented by Kang et al. (1990b) in their fig. 2, suggesting the need for a re-evaluation of this material with respect to the GS model.

Figure 38 [$CeSb_2$] shows that of all the Ce compounds we have studied, $CeSb_2$ is the only one which exhibits a concurrent loss of 4f weight in both the f^0 and f^1 peaks, indicating a rapid transition to tetravalence caused by ionic bonding with the oxygen

adatoms. The remaining spectral intensity bears a close resemblance to the 5d spectrum of La metal.

Similar dosing studies have been performed on uranium compounds but their presentation is reserved for sect. 15 on uranium.

To sum up, then, we have found that the relative weights of the f^0 and f^1 can be dramatically altered by small amounts of contaminants ($\ll$0.5 Langmuir). Since the relative spectral weight of the f^0 and f^1 peaks is an important parameter in the GS model because it is correlated with the Kondo temperature, this means that it is of paramount importance to maintain stringent UHV conditions. Furthermore, since emission from the surface layer will always be part of the total intensity in any photoemission experiment and it is doubtful that the bulk electronic structure of Ce can be reliably discerned without adequate characterization of the surface component, it follows that if further progress is to be made, the surface contribution must be experimentally identified and then either subtracted from the data to give the true bulk signal, or alternatively, the theoretical models must include the surface contribution in their calculations.

14. Momentum-dependent effects

Perhaps the strongest argument in favor of a model which includes the periodic lattice is the observation of momentum-dependent effects at temperatures far above the Kondo temperature. The PAM allows for such an electronic structure. By contrast, within GS and NCA the KR and its sidebands are a dispersionless feature (Bickers et al. 1987), indeed a thermodynamic quantity of a material, whose properties (i.e., the width, position in energy, spectral weight, etc.) are essentially determined by the value of T_K. True enough, at low temperatures it is agreed that there is band formation once coherence sets in [after all, the de Haas–van Alphen effect has been observed by Lonzarich (1988), Springford and Reinders (1988) and more recently by Aoki et al. (1992) and others too numerous to list], but the dispersion must be of the order of T_K, and then only at $T \ll T_K$, or below the so-called coherence temperature. The manifestation of angle-dependent effects, particularly if these exist at $T \gg T_K$ then, would represent a serious disagreement with NCA.

14.1. *$CePt_{2+x}$ amplitude modulations*

Just such angle dependent effects have been reported by Andrews et al. first in $CePt_{2+x}$ ($0 < x < 1$) (Andrews et al. 1995a), and later in $CeSb_2$ (Andrews et al. 1995b) and $CeBe_{13}$ (Andrews et al. 1996). The data for $CePt_{2+x}$ are shown in fig. 39 where the amplitude of the near-E_F feature is seen to undergo periodic amplitude modulation, the period of which coincides exactly with the inverse lattice. The insets indicate the positions in the lattice (surface projection of the Brillouin zone) where the various spectra were taken, while the angles are measured with respect to the surface normal (i.e., the Γ-point). Very large effects are observed, which bring into question the thermodynamic nature of the near-E_F feature. The data were taken at resonance (photon

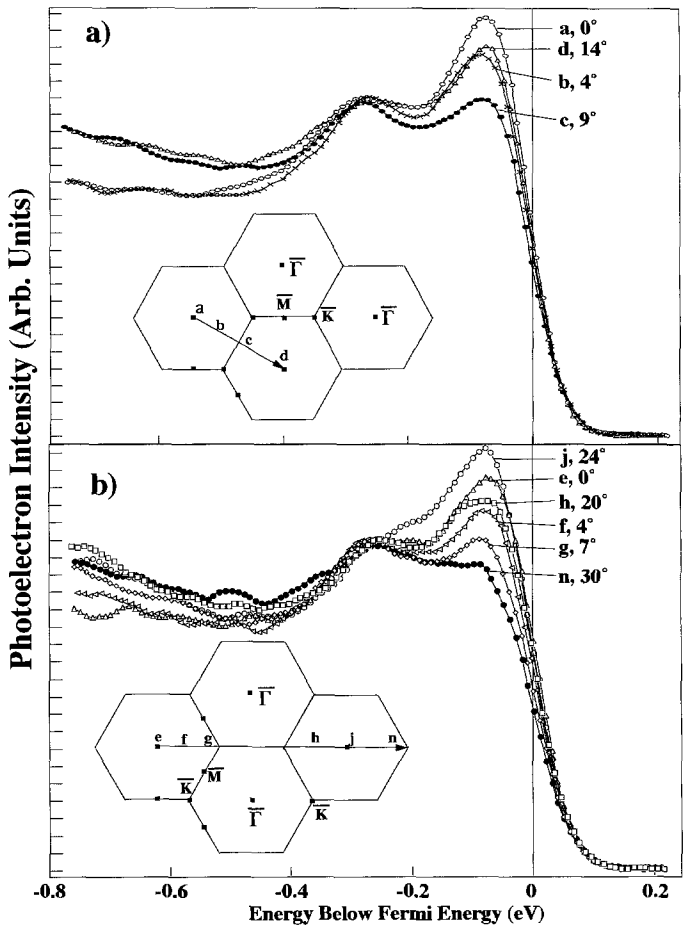

Fig. 39. $CePt_{2+x}$ ARPES spectra at the indicated point in the Brillouin zone. Note that the $4f_{5/2}$ amplitude shows amplitude variations exactly periodic with the Brillouin zone, suggestive of band states (from Andrews et al. 1995a).

energy = 120 eV) at a temperature of 120 K using a VSW HA50 angle-resolved analyzer with a 2° acceptance cone and about 90 meV energy resolution. The data are highly reproducible.

The $CePt_{2+x}$ sample was prepared *in situ* by evaporating Ce onto a Pt (111) single crystal. Analysis with LEED and XPS (Tang et al. 1993) as well as comparison of Pt 4d intensities of the *in-situ* grown specimen to arc-melted polycrystals, determined the composition to be most likely $CePt_{2.2}$, with the value of x determined to within $0 < x < 1$. Bulk property measurements on arc-melted specimens with compositions between $CePt_2$ and $CePt_3$ indicated very similar properties throughout the composition range so that the inexact determination of x is irrelevant to the physics. The Kondo temperatures were found

to be less than 20 K for all compositions, with the magnetic susceptibility showing Curie–Weiss behavior down to 20 K. From bulk property measurements one would conclude that the materials are nearly trivalent so that it is all the more surprising that such an intense KR is observed at $T = 120$ K.

It is significant that the amplitude modulation effects are seen primarily in the KR. Indeed, in the figure the data have been normalized to the peak value of the spin–orbit peak, the Ce $4f_{7/2}$. Because the amplitude modulation is seen primarily in the KR it rules out photoelectron diffraction as the source of the amplitude effect, since the orbital symmetry and the atomic point of origin of both features is identical, while the kinetic energies of the photoemitted electrons from the two features are likewise nearly identical. From photoelectron diffraction both peaks would be expected to undergo similar amplitude modulation. Moreover, photoelectron diffraction effects are not necessarily periodic with the inverse lattice, but are rather a geometric effect (Fadley 1987) which yields maximum amplitude from forward scattering around masking atoms near the surface (the forward flashlight). The observation of dispersion in some systems in any case points to Bloch states.

In their first paper on the subject Andrews et al. (1995a) interpreted the amplitude effect as resulting from the dispersion of an extremely narrow band above E_F. They showed that the effect can easily be accounted for if a Lorentzian feature, derived from a very flat band about 20 meV below E_F, disperses to just above E_F. The dispersion itself was not observable owing as much to the large natural linewidth (~100 meV) as to instrument resolution. In subsequent materials studied there appears to be actual evidence for dispersion (see below) but surprisingly in a direction opposite to that assumed by Andrews et al. (1995a).

The temperature at which the measurements were taken ($T_m = 120$ K) is a most important factor in solving the heavy fermion puzzle. For $CePt_{2+x}$ we see that the measuring temperature is very high, $6T_K < T_m < 10T_K$. Based on NCA, the KR and any possible sidebands should not even exist at $10T_K$, much less be exhibiting Bloch-state behavior which should have been observable only at $T_m \ll T_K$.

Superb confirmation of the above results was reported in a recent publication (Garnier et al. 1997) in which the reported resolution was 5 meV and the data were taken at 40.8 eV photon energy. While the authors reported that no dispersion was evident, a replotting of the data in fig. 40 suggests that one could reach different conclusions. Indeed, if the feature at ~100 meV in the $\theta = 6°$ spectrum can be considered as 4f-derived, then there exists about 100 meV of dispersion. The double arrow on this feature at $\theta = 6°$ signifies the uncertainty of the exact peak position, but irrespective of the exact position it is hard to avoid the conclusion that the peak disperses. Indeed, not only the $4f_{5/2}$ but also the $4f_{7/2}$ is seen to strongly disperse in the left panel of fig. 40. A blowup of the $4f_{5/2}$ dispersion is shown in the right panel. The observed dispersion is surprisingly close to the predictions of the PAM which suggest that the 4f band crosses E_F away from a symmetry direction and loses f character as it disperses below E_F. In fig. 40 the most intense 4f peak is obtained at $\theta = 2°$ [away from (111)] and is nearly totally attenuated at $\theta = 6°$ where it is found below E_F. At normal emission the $4f_{5/2}$ intensity is consistent with a peak just above E_F.

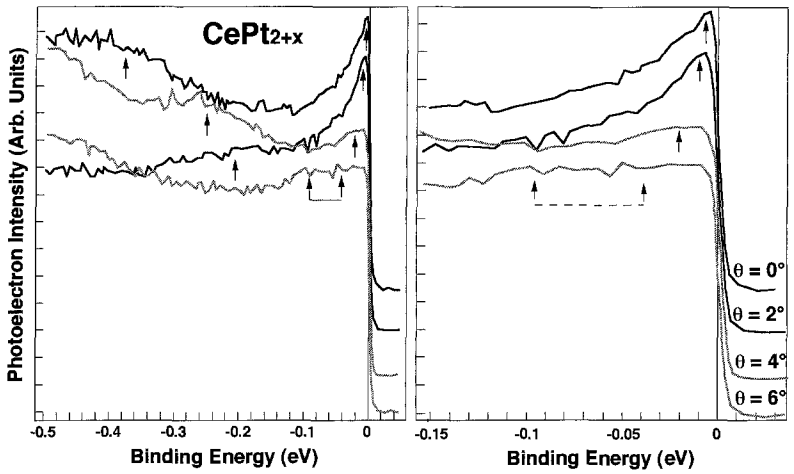

Fig. 40. Digitized and replotted data of Garnier et al. (1997) which strongly suggest (left panel) dispersion of both the $4f_{5/2}$ and $4f_{7/2}$ features. Arrows indicate apparent peak positions. The double arrow for $\theta = 6°$ derives from the uncertainty of the peak position. The right panel is a blowup of the near-E_F region for better viewing of dispersion.

All these observations are entirely consistent with the PAM predictions in which 4f-band dispersion is much larger than T_K, persists to very high temperatures, and crosses E_F away from symmetry points in a cubic lattice.

14.2. *$CeSb_2$*

Amplitude modulation of the Ce $4f_{5/2}$ is seen to some degree in nearly every single-crystal Ce heavy fermion investigated, but direct evidence for dispersion requires better energy and momentum resolution. The intensity of the Ce $4f_{5/2}$ as well as the strength of the amplitude modulations correlates more strongly with crystalline perfection and surface flatness than with T_K, with the most perfect single crystals yielding the most intense KR's. Indeed, an intense Ce $4f_{5/2}$ peak is observed in $CeSb_2$, a layered material with a ferromagnetic transition at 10 K which implies that $T_K < 10$ K. Amplitude modulation was first reported by Andrews et al. (1994). Subsequently (Arko et al. 1997a), data at lower energies and $T = 20$ K revealed about 25 meV of dispersion, with behavior amazingly similar to that found in fig. 40. The left panel of fig. 41 shows ARPES data at 45 eV photon energy, and we see that as the peak disperses away from E_F it rapidly loses intensity as the f character is diminished and replaced by d character (according to the PAM). On the other hand, if the dispersion is toward E_F (fig. 41b), the $4f_{5/2}$ intensity is only slightly diminished as the 4f band disperses just above E_F and presumably flattens out, leaving the tail on the occupied side. This flattened region can be identified with the KR as in the SIM, though it persists far above T_K.

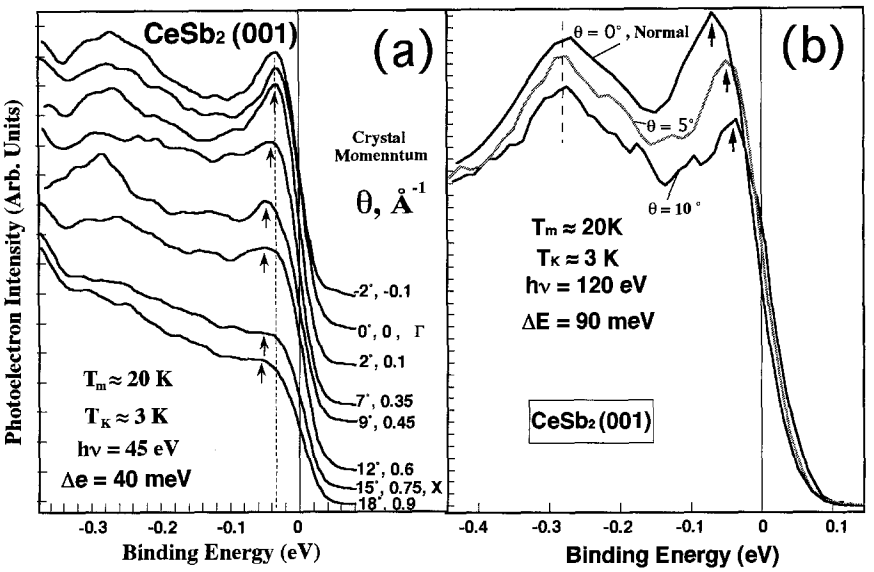

Fig. 41. $CeSb_2$ data along two directions in the Brillouin zone. Note the amplitude effect and dispersion. (Arko et al. 1998.)

14.3. *$CeBe_{13}$*

Andrews et al. (1996) also studied the compound $CeBe_{13}$, a material having a $T_K \approx 400$ K. This material is significant in that the large T_K precludes any complications from crystal field levels which are often cited as responsible for the nearly constant spectral weight of the KR, despite the fact that Joyce and Arko (1993) have definitively shown (sect. 6) that inclusion of crystal field states in the GS code does not alter the predicted scaling with T_K. The temperature dependence of this material has already been discussed in sect. 12 and shown to be conventional, while the dosing experiments in sect. 13 clearly point to the Ce $4f_{5/2}$ as being bulk-like.

Dispersion of all 4f-related features is observed in this material as shown in figs. 42–44, although, as discussed below, dispersion of the $4f_{5/2}$ again required measurements at low photon energies where the momentum resolution is better. Data at $h\nu = 120$ eV (i.e., at resonance) and about 90 meV resolution are shown in fig. 42. Here are shown two spectra from a (100) surface as well as a spectrum from a (110) surface. The gray lines are fits through the data points using Lorentzians for the $4f_{5/2}$ and Gaussians for the $4f_{7/2}$. Arrows point to the centroids of the Gaussians which are shifted by nearly 0.1 eV between the 10° and 15° spectra. While the Γ-point in this experiment was well determined, the direction in which the data was taken was not known precisely owing to an inadequate LEED pattern. It was, however, assumed to be in the (100) plane. The actual direction, however, is irrelevant if dispersion is observed. It is the fact of dispersion which is of relevance, not its details. In fig. 42 one does not observe dispersion of the near-E_F peak despite an

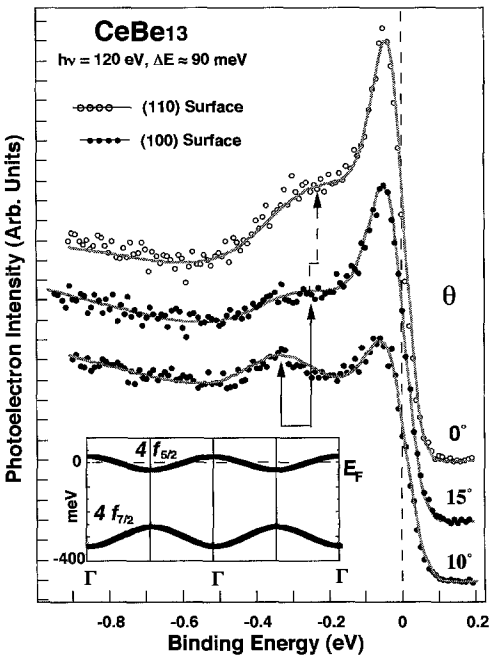

Fig. 42. ARPES data for $CeBe_{13}$(100) and $CeBe_{13}$(110). Two angles are shown for $CeBe_{13}$ (100) with the $4f_{7/2}$ peak showing about 100 meV of dispersion, while the $4f_{5/2}$ peak shows a large amplitude modulation. The inset shows the imagined band structure which could produce such an effect (from Andrews et al. 1996).

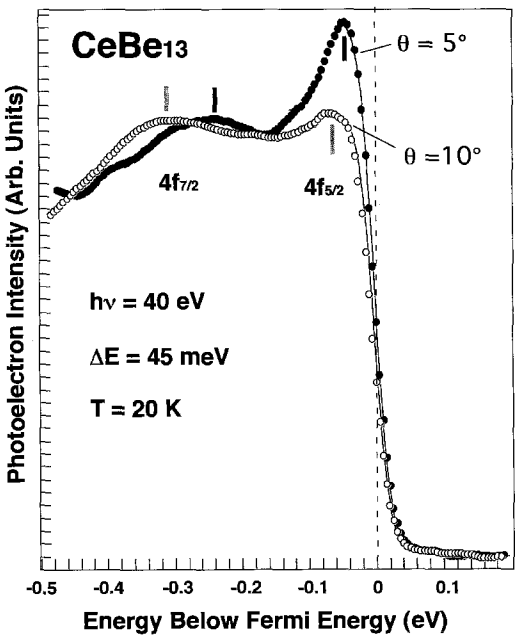

Fig. 43. $CeBe_{13}$(100) ARPES spectra taken at 40 eV photon energy to improve both the energy and momentum resolution. The $4f_{7/2}$ peak dispersed by about 65 meV while a clear 20 meV of dispersion is seen for the $4f_{5/2}$ peak, made possible by sampling a smaller portion of the Brillouin zone. The FWHM of the $4f_{5/2}$ is about 80 meV, smaller than in the resonance data (from Arko et al., unpublished).

energy resolution and experimental accuracy sufficient to see even 5 meV shifts in peak positions. The large amplitude effect was attributed by Andrews et al. (1996) to dispersion of the $4f_{5/2}$ above E_F. Indeed, their simulation of the bands based on their initial data is shown as the inset in fig. 42, but experiments with improved momentum resolution would now alter these simulated bands.

The difficulty with ARPES measurements at 120 eV is that the 2° acceptance cone of the analyzer results in a momentum resolution $\Delta k \approx 0.2\,\text{Å}^{-1}$. The large lattice parameter ($a \approx 10.5$ Å) for $CeBe_{13}$ further complicates matters in that $2\pi/a \approx 0.61\,\text{Å}^{-1}$ and $\pi/a \approx 0.3\,\text{Å}^{-1}$. Thus the 5° separation between the ARPES spectra in fig. 42 already represents a momentum difference larger than π/a for $CeBe_{13}$. Clearly at 120 eV one samples a large percentage of the Brillouin zone in any measurement so that even if dispersion exists it is being averaged out. However, the momentum resolution can be vastly improved at 30 to 40 eV photon energy with Δk now in the 0.1 Å^{-1} range. At 40 eV we sample half as much momentum direction in an ARPES measurement as we do at 120 eV and only one fourth as much momentum space (in two directions). Moreover, the energy resolution is improved to $\Delta E \approx 45$ meV. The price is paid in photocurrent intensity since the photoemission cross-section is down by more than an order of magnitude. Nevertheless the experiment is possible and the results are shown in fig. 43.

Shown in fig. 43 are two spectra taken at $h\nu = 40$ eV with analyzer settings again separated by 5° in angle. At this lower photon energy a 5° separation much more closely approximates the Γ–X momentum distance. The improved momentum resolution now allows for an unambiguous measurement of 20 meV of dispersion in the Ce $4f_{5/2}$ peak as indicated in the figure, as well as ~60 meV of dispersion in the Ce $4f_{7/2}$ peak (the spin–orbit sideband). The dispersion, as stated, is in a direction opposite to that assumed by Andrews et al. (1996). However, the decrease in $4f_{5/2}$ intensity is now understood within PAM as a loss of 4f character as the band disperses below E_F.

14.4. *Dispersion of the f^0 peak*

Dispersion and amplitude modulation is evident even in the f^0 or "main peak". In fig. 44 are shown two spectra corresponding to normal emission from the (100) and (110) surfaces. Not only is there a large difference in the intensities of the f^0 peaks between the two directions, but one obtains about 0.1 eV of dispersion as well, as indicated by the vertical lines. In the figure the dark lines correspond to fresh cleaves while the gray lines correspond to spectra taken at the indicated time after a cleave. As discussed in sect. 13 dealing with surface effects, the time dependence of the spectra suggests a surface component to f^0 as the adsorption of the residual chamber gasses suppresses the surface components. The spectrum for $h\nu = 112$ eV (anti-resonance) merely confirms the negligible non-f intensity. The Ce d bands between –0.5 and –2 eV likewise disperse with direction. Indeed, two d-band peaks are seen from the (110) surface while only one is measured from the (100) surface. These likewise appear to be weakly contamination dependent.

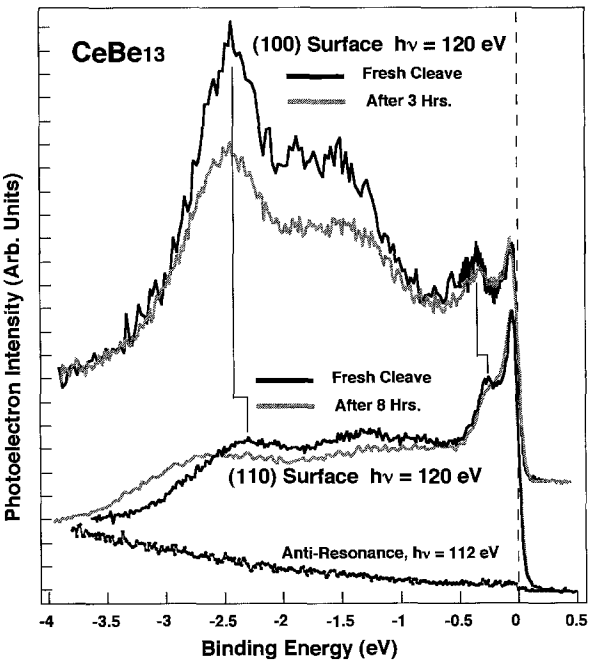

Fig. 44. Wide scan ARPES spectra for $CeBe_{13}(100)$ and $CeBe_{13}(110)$ to show the dispersion of the f^0 peak as well (about 100 meV). The time dependence of the spectra is attributed to residual gas adsorption which suppresses some of the surface-related features. The f^0 peak for $CeBe_{13}(110)$ may be entirely surface-related (from Andrews et al. 1996).

All indications, then, are that in the case of Ce heavy fermions we are dealing with very narrow, nearly temperature independent (or only weakly so) 4f bands. It is true that $CeBe_{13}$ is not particularly heavy so that a measuring temperature $T_m = 20$ K already is much less than T_K for this material and perhaps even lower than the poorly defined coherence temperature below which one would expect band formation even in a Kondo system. However, the 100 meV of dispersion in the $CeBe_{13}$ $4f_{7/2}$ peak is much larger than one would expect from a Kondo lattice with $T_K = 400$ K. What is confusing is that the dispersion of the $4f_{5/2}$ peak appears no larger than that seen in the two other materials with much lower T_K's.

15. Uranium compounds

15.1. *Early results*

Although the bulk properties of 5f-electron heavy fermions are entirely similar to those of 4f-electron heavy fermions (see, for example, Stewart 1984), the respective photoelectron spectra appear substantially different (an excellent review of the early work is given by Allen 1992). Unlike the triple-peaked 4f spectra in Ce compounds (the f^0 and f^1 states within the SIM interpretation), measurements at the 6d absorption edge where the 5f signal is enhanced, generally yield a rather broad, triangular shaped spectrum

which in polycrystalline materials is almost featureless and pinned at the Fermi energy (Arko et al. 1984, 1987a,b, 1988a,b, Allen et al. 1985, Landgren et al. 1984, Zolnierek et al. 1986). There were some early indications of narrow features at E_F even in uranium compounds (Arko et al. 1984), but these were not followed up. The only single-crystal work was that of Arko et al. (1983, 1986) on UIr_3 and UO_2 respectively, but these were not heavy fermions. It became common lore that the width of a typical 5f heavy fermion spectrum, obtained by subtracting the spectrum at the anti-resonance ($h\nu = 92$ eV) from a spectrum at resonance ($h\nu = 99$ eV or $h\nu = 108$ eV), is often far broader (FWHM ≈ 1.5 eV) than is predicted even by a typical LDA calculation (Albers 1985, Albers et al. 1985, 1986, Boring et al. 1985a,b, 1987) for uranium heavy fermions (FWHM ≈ 0.5 eV). The interpretation of this broad spectrum as being entirely due to 5f DOS has led to speculation by some that uranium compounds cannot be treated within the single-impurity model, while others tend to view the unusually large width as the indicator of correlation effects similar to those in Ce compounds (Allen et al. 1985). The most common assessment of the situation, however, appears to be that uranium is simply different from Ce and no attempt is made to reconcile the spectroscopic differences. This is an unsatisfactory state of affairs.

To date the spectral behavior of 5f systems remains unresolved with different groups giving different opinions. Some sampling of the variety of views may be of interest. The prevailing opinion, primarily based on work of Kang et al. (1987) with dilute alloys, is that the U-5f DOS exhibits single-impurity signatures since the shape of the extracted 5f DOS does not vary significantly with U concentration. Perhaps based on this as well, recent high-resolution photoemission measurements (Imer et al. 1991a,b) at 40.8 eV in polycrystalline URh_3, which yielded a narrow 5f feature at the Fermi energy, have been interpreted entirely within SIM despite the fact that this material has a specific heat γ-value of only about 20, with measured dHvA masses in agreement with band masses (Arko et al. 1975, 1976) and never exceeding values of 5 to 10, and periods showing excellent agreement with band calculations. In a different approach, recent high-resolution spectra on the heavy fermion UPd_2Al_3 have been interpreted (Takahashi et al. 1996) as showing a dual role of 5f electrons (i.e., simultaneously itinerant and localized) with the features near the Fermi energy presumed to result from band states while a peak at about -0.5 eV is interpreted as arising from the localized nature of 5f electrons. Recent de Haas–van Alphen data from UPd_2Al_3 (Inada et al. 1994, 1995), however, show nearly exact agreement with the band calculations of Sandratskii et al. (1994) and Knopfle et al. (1996). In a still different approach, resonant PES studies on URh_3B_x (Zolnierek et al. 1986) suggested that as the band narrows with x, a satellite at about -1 eV builds up, similar to the -6 eV two-hole satellite in Ni. A subsequent work (Imer et al. 1991a) at $h\nu = 40.8$ eV found no evidence for the satellite, which may provide a hint as to the nature of the intensity at -1 eV. Quite likely this "satellite" is the manifold of d bands which become prominent as the 5f intensity decreases upon alloying. Clearly there is a great deal of confusion and room for understanding, and clearly there is a need for high-resolution work on single crystals.

15.2. *Results in single crystals*

Inasmuch as this chapter is devoted primarily to studies of single-crystal surfaces, the work on dilute alloys which gave impetus to the single-impurity ideas will not be considered in detail. In the same vein the substantial efforts devoted to the understanding of non-Fermi liquid behavior and Fermi level tuning in $Y_{1-x}U_xPd_3$ (Kang et al. 1989, Seaman et al. 1991, Liu et al. 1992b) will be touched on only very lightly. An understanding of the electronic structure of well-characterized single crystals is useful before one proceeds to more complex systems.

Measurements on highly correlated single-crystal uranium compounds again seem to point to a band nature of 5f electrons. Indications of this were already evident in early publications of Arko et al. (1983) in an angle-resolved PES study of UIr_3 where evidence for slight dispersion of 5f states was presented for the first time. In that paper dispersion was not considered unusual however, since, just as in URh_3, dHvA measurements (Arko et al. 1976, Arko 1976) indicated a rather normal, transition-metal-like material with effective masses again no larger than 5 to 10. More intriguing were the indications of periodic ARPES structure (Arko et al. 1990) in the 5f features of the heavy fermion material UPt_3 measured at 300 K. Although in UPt_3 the near-E_F 5f feature never showed measurable dispersion, its width was resolution-limited (~200 meV) while its intensity vanished near the M-point in the hexagonal lattice. Thus knowledge of the existence of sharp 5f features having intensities periodic with the inverse lattice in uranium compounds

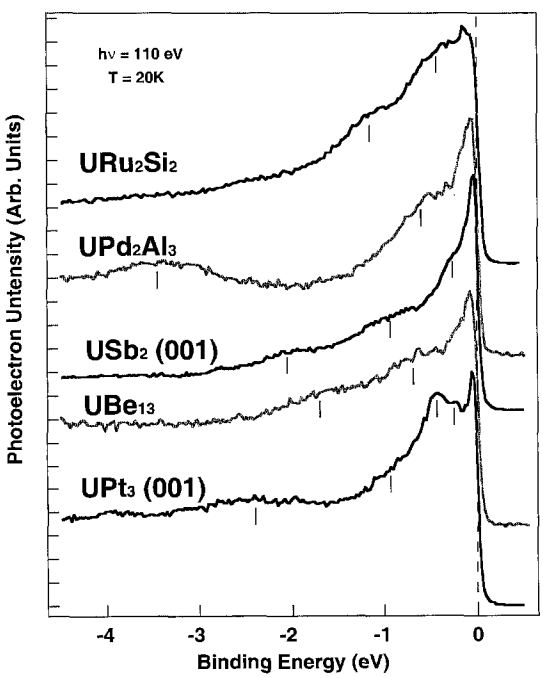

Fig. 45. Wide scan ARPES spectra for several uranium heavy fermions taken at 110 eV photon energy and $T = 20$ K. The crystallographic directions are known for USb_2 and UPt_3, but not for others. Note the persistent sharp features at E_F. Additional features are indicated with tic marks and are probably 6d-related, except for features near −0.5 eV (Arko et al., unpublished).

even at 300 K, which corresponds to a temperature as high as $20T_K$, was available some time ago, but this information was mostly overlooked.

Recently single-crystal uranium compounds have been investigated (Arko et al., unpublished) both at the resonant photon energy and at much lower photon energies where momentum and energy resolution is substantially better. Resonance spectra of some of these compounds are shown in fig. 45, taken at a photon energy $h\nu = 110$ eV. In all cases these are ARPES spectra using a $\pm 1°$ aperture in the analyzer, with the crystalline direction of electron emission corresponding to the c-axis for UPt_3 and USb_2, while the precise direction is unknown for the others. All spectra were taken at temperatures of either 20 K or 80 K. A wealth of structure is revealed within the first 1 eV below the Fermi energy including a pervasive sharp feature at E_F. This feature is much narrower in UPt_3 than in, e.g., UBe_{13}, whose T_K is on the order of 1 K vs about 15 K for UPt_3. The tic marks indicate the position of additional broad features that also resonate along with the sharp 5f feature at E_F. In most cases there are two or more additional broad features, which makes it difficult to interpret them in term of the equivalent of the f^0 peak in Ce compounds.

15.3. *The 5f spectrum*

If one performs the usual operation of subtracting a spectrum at anti-resonance (92 eV) from that at resonance (≈ 98 eV for the $5d_{3/2}$ edge) to obtain the 5f DOS, one in fact obtains the usual broad triangular shape for the subtracted DOS even for a single-crystal compound such as USb_2 (Arko et al. 1996) which in general shows much narrower structure than the other compounds in fig. 45. This is illustrated in fig. 46 where the difference curve is the result of the subtraction. Here the spectra were normalized at −5.5 eV after first subtracting off the secondary background. Although

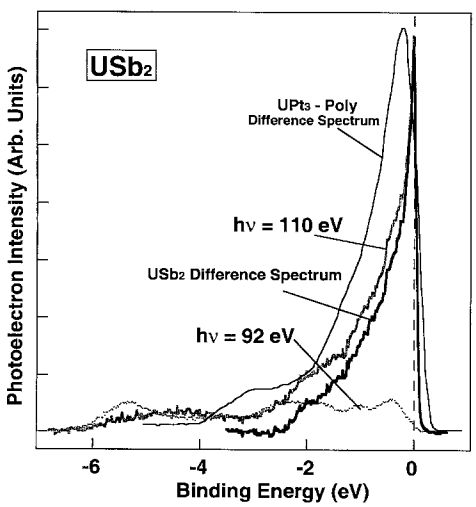

Fig. 46. Resonance, anti-resonance, and difference spectra for $USb_2(001)$, taken at 20 K in the ARPES mode. The nearly complete absence of a DOS in the 92 eV spectrum suggests that almost all intensity within 0.5 eV of E_F is 5f-related. A difference spectrum of scraped UPt_3 polycrystal is also included for comparison.

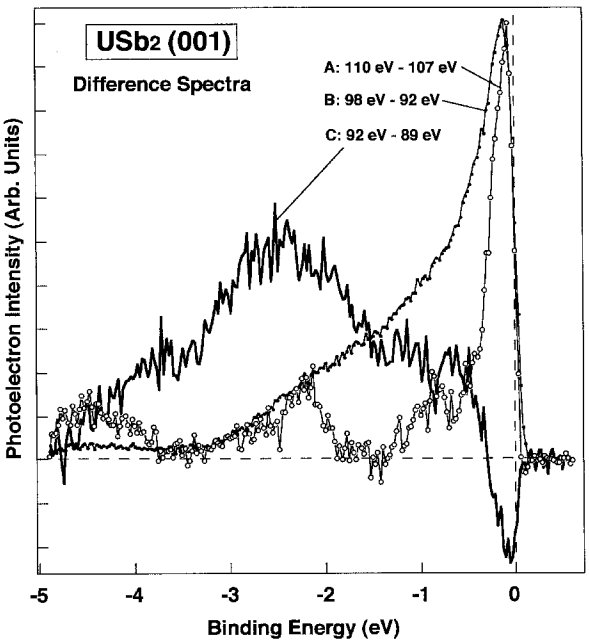

Fig. 47. The figure illustrates how different parts of the spectrum resonate at different photon energies. The 92 eV spectrum is common to all subtractions, including fig. 46. The negative-going DOS in curve C is similar to the sharp peak in curve A and is probably of 5f character. The remaining features are probably 6d-related.

determining the correct normalization is problematic, different normalizations result in only minor changes in the subtracted spectrum. In fig. 46 a 5f spectrum of UPt_3, obtained in polycrystalline samples at room temperature and much poorer resolution, is also superimposed for comparison. The width of the polycrystalline spectrum is broader than can be accounted for by the poorer resolution, but the overall shape is qualitatively similar.

What is the likely explanation for the broad nature of the 5f spectrum? The most probable explanation seems to be that the intensity below about –0.5 eV is primarily U-6d-related, together with possible surface-related 5f intensity. Most LDA calculations (Albers 1985, Albers et al. 1985, 1986, Boring et al. 1985a,b, 1987) indicate that the 5f DOS is no more than about 0.5 eV wide in heavy fermions, and perhaps somewhat wider in well-hybridized materials like URh_3. Support for this view comes from intensity changes in the vicinity of the resonant photon energy. In all likelihood the 6d states resonate at photon energies somewhat lower than 5f states. Thus when one looks at intensity variations between, say, 107 and 110 eV, the difference spectrum looks entirely different from that obtained between 98 and 92 eV.

It is even more informative to look at intensity variations between 89 and 92 eV. While the 5f anti-resonance (i.e., minimum 5f intensity) is well known to occur at 92 eV it turns out that the spectrum at binding energies below –0.5 eV actually increases in intensity as the photon energy is raised from 89 eV to 92 eV, while within 0.5 eV of E_F the spectral intensity decreases. This can be seen in spectrum B in fig. 47 where difference spectra are plotted for 110 – 107 eV (A), 98 – 92 eV (B) and 92 – 89 eV (C) for the material USb_2

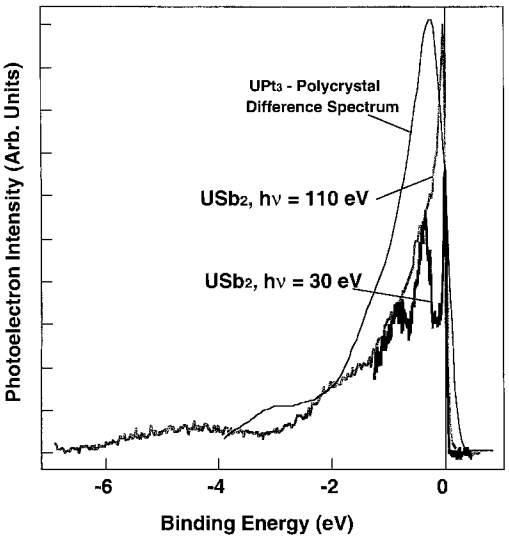

Fig. 48. Comparison of an angle-resolved spectrum at resonance (110 eV) with a spectrum at $h\nu = 30$ eV in single-crystal USb_2. Note the improved momentum and energy resolution. The sharp near-E_F spike at $h\nu = 30$ eV is no more than 30 meV FWHM, thus making it the sharpest f-electron feature ever observed. A difference spectrum of scraped polycrystal UPt_3 is included to illustrate previous measurements of 5f-DOS width.

at normal emission and along the c-axis. The most logical explanation for this is that the anti-resonance for the 6d states occurs below 92 eV. One may then suppose that the resonance energies for the 6d states (i.e., maximum 6d intensity) may likewise be slightly lower than 98 eV or 108 eV. Thus the negative going feature in difference curve B is most likely due to 5f DOS while the positive intensities are most likely related to U 6d DOS. Further, based on these assumptions, spectrum A in fig. 47 may be primarily 5f-like since at 107 eV the U 6d's may have already peaked and only the 5f's continue to increase. The intense feature in curve A within 0.5 eV of E_F corresponds exactly to the negative going feature in curve B and it seems eminently reasonable to assign this feature to the 5f-related DOS. Some of the smaller peaks in curve A at higher binding energies are again due to highly dispersive U 6d bands and result from the fact that this is an ARPES experiment where dispersion with photon energy is a factor. Thus it appears that the 5f DOS is pinned at E_F and is most likely no more than about 0.5 eV wide in USb_2.

It becomes even more informative to look at USb_2 at lower photon energies with ARPES. This material is an antiferromagnet below 200 K and exhibits a layered tetragonal structure which is ideal for ARPES since the two-dimensional nature allows for band mapping without the complication from the third dimension. In fig. 48 a spectrum of USb_2 taken at $h\nu = 30$ eV, $T = 20$ K, resolution of 40 meV, and within 4° of the c-axis, is superimposed on a spectrum taken at 110 eV and nominally along the c-axis. The natural linewidth of the near-E_F peak is now about 30 meV which makes it the sharpest feature ever observed in f-electron systems. The two additional peaks in the 30 eV spectrum correspond closely to the features in the 110 eV spectrum and are probably 6d-derived (but not entirely, as we will see below). A difference spectrum for polycrystalline UPt_3 is again superimposed for comparison in order to emphasize the astounding narrowness of the 5f features relative to earlier observations in polycrystalline materials. It is evident

that the spectrum obtained at resonance via subtraction must contain numerous features not related to 5f structure – primarily 6d electrons.

15.4. *5f dispersion in USb_2*

ARPES data at $h\nu = 30$ eV and $T = 20$ K are shown as a function of angle (Arko et al. 1997b) along the Γ–X direction in fig. 49. Two dispersive peaks labeled A and B are evident. Both peaks are unambiguously 5f derived based on the photon energy dependence of the intensity, but peaks B appear to have substantial 6d admixture, particularly as the binding energy increases. The dispersion of peak B is obvious and clearly 5f in nature, apparently as large as 600 meV. This represents the first clear and unambiguous evidence of 5f dispersion.

The dispersion of peak A is smaller, but nevertheless definite, as shown in fig. 50 where the dispersion becomes more evident as the spectra near Γ are expanded. The data shown here were taken at a photon energy of 35 eV and have been smoothed with a 30 meV FWHM Gaussian (i.e., smaller width than instrument resolution). The peak normalization is arbitrary, chosen primarily to emphasize dispersion. In actual fact, peak A is nearly absent near Γ. Interestingly, band A disperses below E_F as its intensity decreases, which is similar to the effect seen in Ce heavy fermions above.

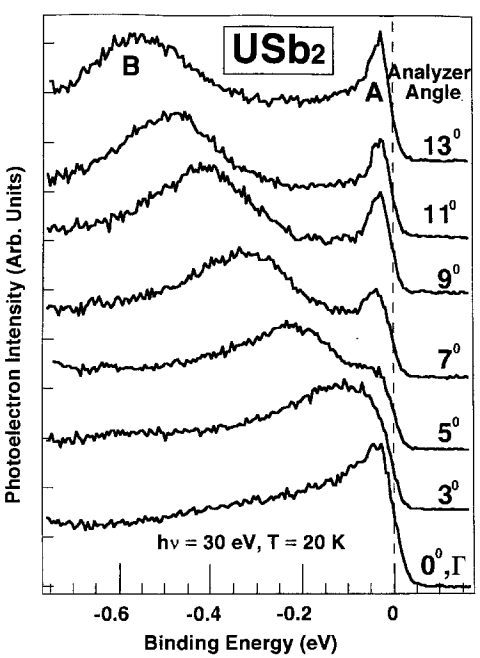

Fig. 49. ARPES spectra of USb_2(001) for analyzer settings within 13° of the Γ-point (001). Feature B contains substantial 5f character based on photon energy dependence and shows 600 meV of dispersion, while feature A is almost of purely 5f character. Note the amplitude effect of feature A similar to that observed in Ce systems (Arko et al. 1997b).

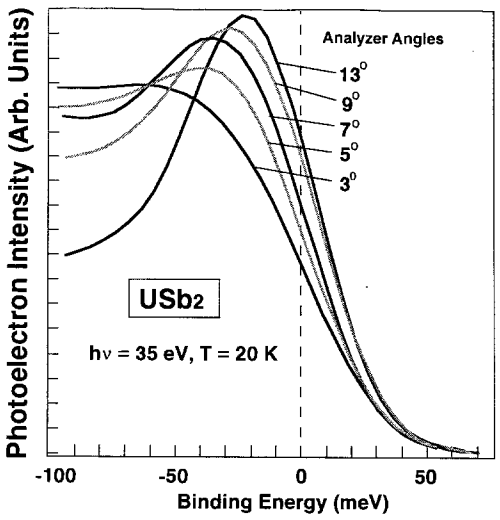

Fig. 50. A near-E_F blowup of feature A in USb_2 ARPES spectra of fig. 49 to emphasize dispersion of about 30 meV. Normalization is arbitrary to enable viewing of dispersion (Arko et al. 1997b).

15.5. *Temperature dependence*

There can be no doubt that in USb_2 the 5f states are band states, albeit quite narrow. The sharp feature at E_F is not related to a Kondo resonance as can again be seen from the temperature dependence shown in fig. 51 where spectra at $h\nu = 110$ eV and $T = 20$ K and $T = 300$ K are shown. Although a good simulation of the data is difficult owing to the numerous features, the small reduction in the peak amplitude is totally accountable

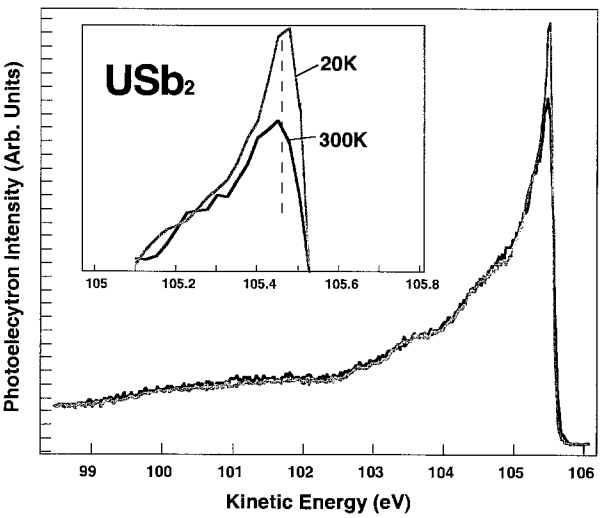

Fig. 51. Temperature dependence of $USb_2(001)$ at $h\nu = 110$ eV. The inset shows that just as in Ce compounds there is an apparent peak shift away from E_F indicating a broadening of the features by about 100 meV. The temperature dependence is thus explained by conventional effects.

from the effects of a 300 K Fermi function combined with 100 meV of phonon broadening of the narrow 5f peak (at $h\nu = 110$ eV the natural linewidth may be as large as 60 meV owing to the poorer momentum resolution). The shift of the 300 K spectrum toward higher binding energies, as shown in the inset, is again a clear indication of broadening effects as well as an absence of a very intense peak just above E_F, just as was shown for the case of $CeBe_{13}$. It would seem that a strong case can be made for the band nature of f-electron features. Although at 20 K we are well below $T_N = 200$ K, this is not the case at 300 K. Still the peak shifts to higher binding energy.

15.6. *5f dispersion in other compounds*

Since USb_2 is an antiferromagnet below 200 K it leaves some room for argument regarding the band nature of heavy fermions despite the fact that one normally expects a magnetic state to exhibit greater localization. The next logical step is to look for evidence of dispersion and 5f band states in uranium compounds which, unlike antiferromagnetic USb_2, are unambiguously heavy fermions – e.g., UPt_3.

We begin by looking at the near-E_F region, in fig. 52, for all the single-crystal uranium heavy fermions thus far investigated. In fig. 52 the spectra for UPt_3 and USb_2 are taken with $h\nu = 30$ eV (along the c-axis) and have been broadened with a 60 meV FWHM Gaussian in order to approximate the 90 meV resolution of the remaining spectra taken at $h\nu \approx 110$ eV. The precise directions of electron emission for UBe_{13}, UPd_2Al_3 and URu_2Si_2 are not known. These crystals were small and unoriented, and a cleave was effected as the geometry allowed. At this stage of understanding it is in any case not as important to nail down the details of the band structure as it is to determine the existence of dispersion and its approximate magnitude. A more thorough investigation with oriented

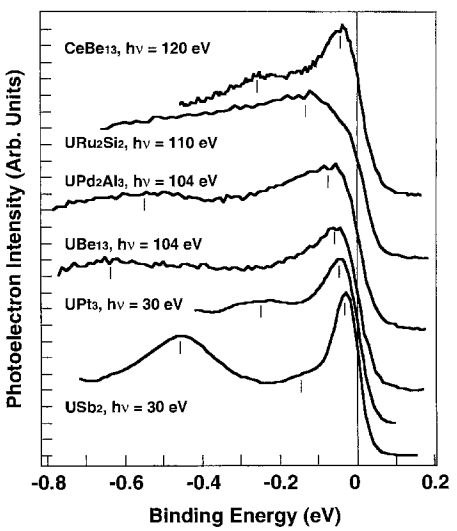

Fig. 52. Expanded view of the near-E_F region for several uranium heavy fermions. All spectra have been appropriately broadened to equal the 90 meV resolution of $CeBe_{13}$. In many instances, uranium near-E_F features tend to be sharper than those for Ce heavy fermions.

single crystals and low photon energies is pending. A spectrum of $CeBe_{13}$ (110) is also shown in fig. 52 for purposes of comparison.

An obvious fact emerges from fig. 52, namely that uranium heavy fermions display sharp structure at E_F just as is found in Ce heavy fermions. Indeed, for UPt_3 and USb_2 this structure is far narrower than in a typical Ce heavy fermion. It is estimated that the natural linewidth of the USb_2 feature is of the order of 30 meV vs. about 100 meV for $CeBe_{13}$, the latter determined with 56 meV resolution. Thus the myth of 5f DOS being much broader than the 4f DOS is dispelled. What does emerge different from 4f, however, is that there is more structure associated with 5f spectra, which seems reasonable in view of the additional 5f electrons (perhaps as many as three). We have already discussed the highly dispersive 5f band in USb_2 which in fig. 52 is situated at –0.45 eV. A second 5f peak is also clearly evident in UPt_3 at –0.25 eV but is less obvious in the remaining spectra. However, it will be noticed that the remaining uranium heavy fermion spectra are indeed broader than the near-E_F feature in UPt_3. In all likelihood both 5f features are contained under one broad peak and are not resolved. This assumption is strengthened by the observation that in URu_2Si_2 the maximum of the broad peak occurs at –0.15 eV, far below the Fermi energy. It is highly unlikely that a feature this far below E_F can be responsible for the heavy-fermion behavior. One possible explanation for the broadness is disorder. Another plausible explanation is that in URu_2Si_2 the second band just happens to have more intensity than the near-E_F band, thus yielding a peak below E_F, while the band nearer E_F merely contributes a shoulder. Clearly there is extra intensity at E_F, but the possible observation of a second peak will have to await work at lower photon energies, higher resolution and lower temperatures (URu_2Si_2 was measured at 80 K). Obviously, then, the position of the second band varies dramatically from material to material, unlike the position of the spin–orbit sideband in Ce compounds. We will see below that this position can vary within the same material as a function of direction.

The assumption of a second band yielding intensity below E_F is suggested in UBe_{13} where several cleaves of crystals yielded different results along different directions. In fig. 53 spectra are shown from two different cleaves and different photon energies. The near-E_F peak shows apparent dispersion (about 0.1 eV) as well as a change in width, entirely consistent with band effects. The $h\nu = 115$ spectrum was actually obtained with better resolution (about 65 meV) than the $h\nu = 104$ spectrum (about 90 meV). It shows a clear shoulder at E_F indicative of additional unresolved 5f intensity (i.e., an unresolved peak), while in the $h\nu = 104$ spectrum the lower band may have dispersed toward E_F totally overshadowing the near-E_F feature. These spectra will require further work and reproducibility. To date dispersion has not been observed on the same cleaved surface.

However, consistent with the above interpretation are the data in fig. 54 where UBe_{13} was measured along the same direction (unknown) and at the same photon energy, the same sample, but with two different acceptance cones of the emitted electrons. Indeed the spectrum with the $\pm 1°$ aperture is the very same one as the 104 eV spectrum in fig. 53, but now extended to higher binding energies. By increasing the analyzer acceptance cone to $\pm 4°$ and keeping everything else constant one obtains the spectrum shown as the gray line. It must be emphasized that this is not a result of a change in instrument resolution which

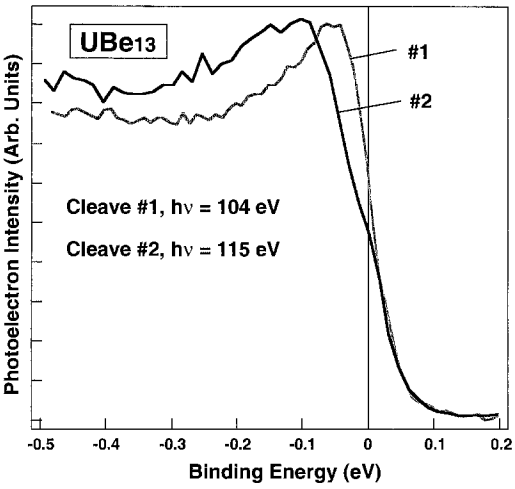

Fig. 53. Preliminary data for UBe_{13}, suggesting dispersion in two different cleaves of crystals. The resolution for cleave 2 is better than for cleave 1 (about 80 meV vs. about 90 meV).

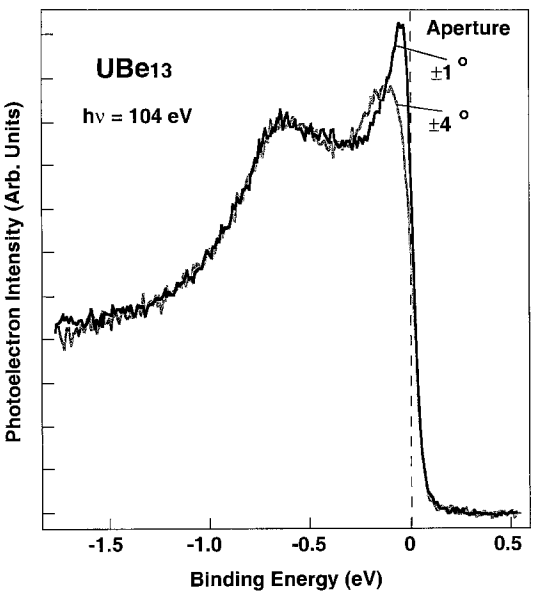

Fig. 54. UBe_{13} spectra taken for the same cleave and direction but with different acceptance angles (apertures). The ±4° acceptance angle results in a broadened near-E_F peak suggestive of dispersive states, though there could be other interpretations of this effect. The larger acceptance cone worsens the resolution by no more than about 10%.

changes by no more than 3%. The new lineshape results from a much larger sampling of the Brillouin zone. This too would suggest dispersion although it has not yet been observed by varying the analyzer angle. Perhaps light polarization effects above and below the measurement plane need to be considered with the ±4° aperture.

The intense peak at –0.65 eV in UBe_{13} is as yet not totally understood, but it may be related to a surface state of 5f–6d nature. It reaches a maximum intensity at $h\nu = 104$ eV, or 3 eV lower than the remaining 5f structure, consistent with our previous assumptions.

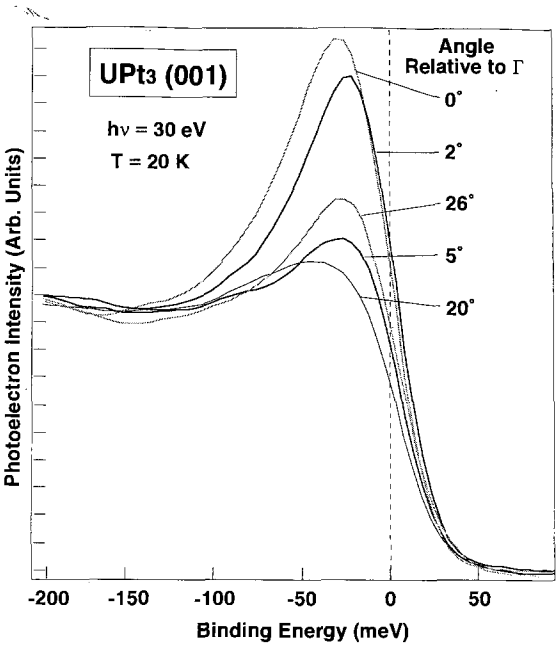

Fig. 55. Near-E_F ARPES spectra for UPt_3 showing clear evidence of dispersion. The intense peaks may not derive from the same band as the weak peaks, as predicted by band calculations. Similar data are obtained at a measuring temeperature of 80 K, thus indicating a lack of a temperature effect.

A similar peak is observed in UPd_2Al_3 at about −0.5 eV and has been attributed (Takahashi et al. 1996) to a signature of the localized nature of the 5f's, similar to the f^0 peak in Ce heavy fermions. While this feature has not been studied in detail in UPd_2Al_3, a similar feature at −0.5 eV in UPt_3 appears to be surface-related, as we will see below. But first we continue with possible dispersion of the near-E_F peaks.

UPt_3 (001) was studied at lower photon energies, at temperatures of 20 K and 80 K, and the results are highly suggestive of dispersion of the near-E_F peak as seen in fig. 55. Here the data were taken at 20 K, $h\nu = 30$ eV, resolution $\Delta E = 40$ meV, and different angles relative to Γ, i.e., the surface normal in the Brillouin zone. They were also smoothed with a 30 meV FWHM Gaussian to allow a clear overlay of data. There is an obvious amplitude effect just as in Ce compounds. Note the extremely large intensity reduction in the spectrum separated by a mere 5° in analyzer angle. The drop in intensity corresponds reasonably well with band calculations which show a narrow band, located precisely at E_F at the Γ-point, dispersing above E_F at about 0.3 $Å^{-1}$, or, just about 5° from Γ. The peak at 2° from Γ is dispersing toward the Fermi energy. The peaks at 5° and 20° are then due to different bands at slightly higher binding energies. It is not certain that improved resolution will be able to separate out the additional bands since the natural linewidths may be larger than the band separations, but it is nevertheless an experiment worth doing. Data taken at 80 K essentially reproduce the 20 K data.

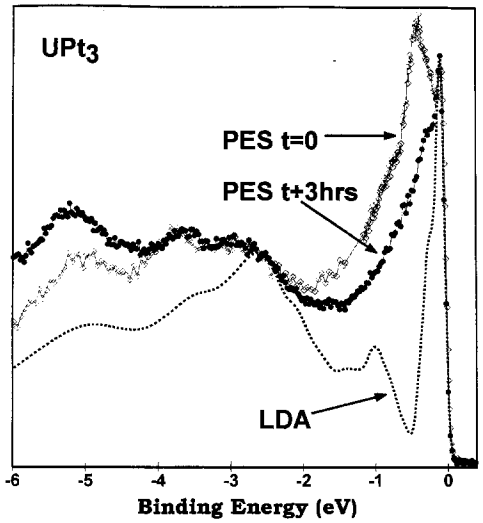

Fig. 56. Wide scan ARPES spectra of $UPt_3(001)$ at $h\nu = 110$ eV and $T = 20$ K. The fresh cleave ($t = 0$) indicates a strong peak at −0.5 eV which is nearly of negligible intensity at $t = 3$ h. This is strongly suggestive of a surface-related feature. An LDA calculated spectrum (Albers et al.) is superimposed for comparison and shows a valley in the −0.5 eV region, while the two features near E_F, both of 5f character, are reproduced by LDA.

15.7. *Surface effects*

Finally, in fig. 56 we consider the very intense, clearly 5f-related (based on intensity at resonance) feature at −0.5 eV in UPt_3. It was first reported by Grassman (1990) and assumed to be the equivalent of the −2 eV peak in Ce heavy fermions. A similar interpretation is given by Takahashi et al. (1996) in UPd_2Al_3. Although band calculations predict Pt-derived d bands at this energy and momentum in the Brillouin zone, no 5f bands are predicted. Indeed, a highly dispersive, most likely 6d-derived, feature exists at a binding energy of −0.5 eV using $h\nu = 30$ eV light, but it is unlikely to be related to the peak seen at resonance based on its intensity. The maximum intensity at resonance is reached slightly below the resonance energy of the near-E_F peak (104 vs 108 eV) which would suggest a different origin for this feature. A likely scenario is that this feature is surface-related but it has not been determined whether this is a true surface state which exists in a gap in the density of states, or is related to the lower coordination number of uranium at the surface which would decrease its valence. A large gap in the DOS exists at H and L in the Brillouin zone which could accommodate a surface state.

A standard test for surface sensitivity of a feature is a slight dosing of the surface with an impurity gas. Indeed, the residual gas in the chamber can serve as the dosing gas as a function of time. In fig. 56 spectra of UPt_3 along (001) are shown immediately after a cleave as well as three hours after a cleave, at a photon energy of 108 eV. Also shown is a density of states calculated for the (001) direction. Note that every calculated peak is accounted for in the data except for the −0.5 eV peak. Moreover, note that the calculation predicts a deep minimum at this binding energy. Three hours after the sample was cleaved, the (001) spectrum was re-measured and the −0.5 eV peak was vastly diminished, a typical phenomenon for surface-related features as the sample adsorbs residual chamber gas. The remaining structure is much more consistent with the calculated DOS. Further dosing

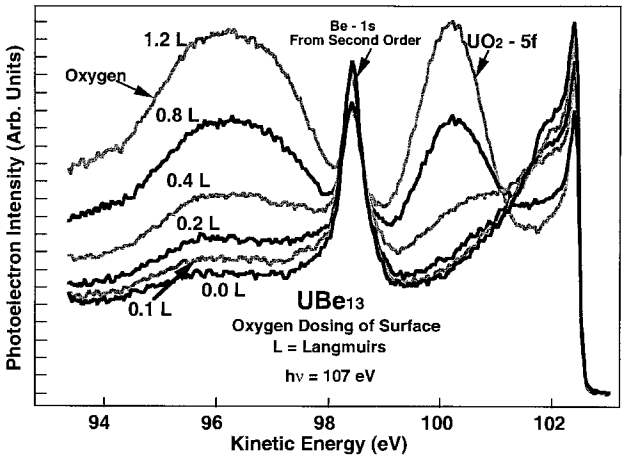

Fig. 57. Oxygen dosing studies on a surface of UBe_{13}. The fresh cleave again shows a strong feature near –0.5 eV which diminishes with dosing. The 5f-derived near-E_F feature is maintained with dosing and is thus likely to be bulk-related. The Be 1s peak in the center of the figure is due to second-order light and serves as a calibration of the bulk intensity. Note the build-up of the UO_2 intensity with dosing.

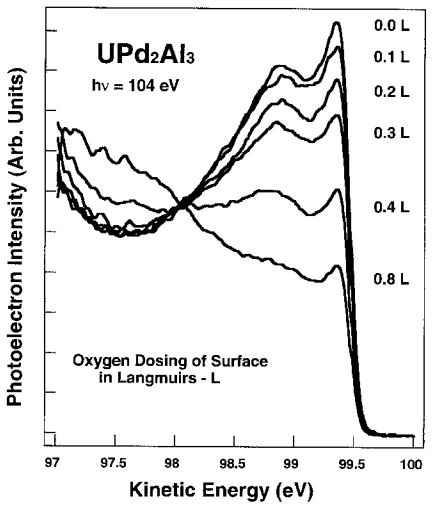

Fig. 58. Oxygen dosing studies of UPd_2Al_3. In this material the –0.5 eV peak is less sensitive to dosing. However, by analogy to other uranium heavy fermions it is not unreasonable to assign it to a surface feature.

(intentional) with up to 1 L of oxygen does not alter the lineshape, but only diminishes all bulk-related intensities. Thus all characteristics of the –0.5 eV peak are consistent with this being a surface-related feature.

There is then a strong suspicion that features at ~–0.5 eV in other materials are likewise surface-related. Although the proof is not as complete as it is for UPt_3, figs. 57 and 58 show oxygen dosing dependence of the valence bands of UBe_{13} and UPd_2Al_3 respectively which again suggests surface states. In UBe_{13} a surface dose of 0.8 L of O_2 is sufficient

to completely eliminate the –0.5 eV feature while the near-E_F peak remains strong. In fig. 57 the sharp peak at –4 eV results from the Be 1s core level from second-order light and is not to be confused with valence bands. It is seen that the surface-related peak loses intensity long before there is any evidence of a build-up of UO_2 with its typical 5f state at –2 eV relative to E_F.

For UPd_2Al_3 the situation is not so clear. Although in fig. 58 the –0.5 eV peak loses intensity faster than the near-E_F peak, there remains some residual intensity even after a build-up of UO_2. However, when viewed in the context of other materials it seems unreasonable to make an exception for UPd_2Al_3 when other materials so clearly show surface effects. Moreover, the –0.5 eV peak in UPd_2Al_3 exhibits about 0.1 eV of dispersion near the resonant photon energies which makes it at odds with the concept of a localized state.

To summarize this section, then, a number of observations are to be emphasized:

(1) The broad triangular shape of the typical difference spectrum in uranium heavy fermions is not entirely due to 5f DOS only, but includes substantial 6d admixture.
(2) The 5f portion of the DOS appears in all cases to be no more than about 0.5 eV wide, very much in keeping with LDA predictions.
(3) There is strong evidence for dispersion of the (typically) two 5f bands near the Fermi energy. The near-E_F peak displays an amplitude effect very similar to that seen in Ce compounds.
(4) A feature at about –0.5 eV is often found in uranium heavy fermions which is most likely surface-related, but additional confirmation is needed.
(5) The 5f features near the Fermi energy are every bit as narrow as those found in 4f heavy fermions, and occasionally even narrower.
(6) There is no evidence for a spin–orbit sideband.
(7) The temperature dependence in USb_2 is consistent with a fully occupied state being broadened and cut by a wider Fermi function with increasing temperature inconsistent with a KR above 200 K.

From all the above it would follow that 5f states are not qualitatively different from 4f states, the primary difference being the lack of a clear f^0 peak and the existence of at least two closely spaced bands near the Fermi energy, and possibly more. To be sure, the dispersion is larger and more readily observable, but this is a quantitative and not a qualitative difference. It is even possible that the –0.5 eV peak in 5f systems may be the equivalent of the –2 eV peak in 4f systems (Grassman 1990). However, inasmuch as there is ample evidence that in 5f systems it is surface-related, the suspicion is raised that the –2 eV peak in Ce systems is likewise mostly due to the surface.

16. Conclusions

Nearly every recent measurement performed on Ce- or U-based single-crystal heavy fermion compounds seems to point to the existence of very narrow f-electron bands for a wide range of temperatures. Yb compounds are less clear but are not totally

inconsistent with this idea. The clearest evidence for bands is in uranium systems where actual dispersive bands have been observed in USb_2 and UPt_3, as well as suggestions of dispersion in UBe_{13}. In Ce compounds dispersion has been observed in $CePt_{2+x}$, $CeSb_2$, nad $CeBe_{13}$, at temperatures far above T_K. The least obvious are Yb compounds where the 4f PES features for all intents and purposes are indistinguishable from core levels pinned at the Fermi energy, but with complications of surface states at lower photon energies. Some very recent data on $YbCdCu_4$, not included in this chapter, do actually provide the first hint of dispersion even in Yb compounds so that it appears that all systems may yet show some universal behavior. In all cases the n_f is far too low relative to SIM predictions.

By contrast, few systems unambiguously exhibit the behavior predicted by the single-impurity model. While it is possible to fit a particular spectrum within NCA by adjusting parameters, the lack of systematics with T_K is glaring. In particular, there is no clear systematic scaling of the near-E_F spectral weight with T_K, the width of the f^0 peak is approximately constant with T_K, there is no temperature dependence which cannot be explained by conventional effects of phonon broadening and Fermi function effects (here, perhaps, the broadening may be attributed to the PAM), the spin–orbit feature does not shift toward E_F as T_K increases, and no clear-cut observation of a crystal field state has been reported despite sufficient resolution. Indeed, the temperature dependence in Ce compounds does not provide evidence for the existence of an intense 4f DOS feature just above E_F, otherwise one would observe a shift of the near-E_F peak toward the Fermi energy (vs the observed shift in the opposite direction) as was first predicted by Gunnarsson and Schönhammer (1986). In Yb compounds the spectral weight of the near-E_F peaks (i.e., the n_f) is so totally inconsistent with SIM predictions as to be sufficient by itself to seriously question the model. The theory is only valid down to n_f values of about 0.75, while typical n_f's in Yb compounds are measured at 0.65 even for T_K's of 35 K. If the existence of the Kondo resonance with the stated properties is a necessary consequence of the SIM, as appears to be the case, then we must look beyond SIM to understand heavy-electron behavior.

One the other hand, thermodynamic data are in agreement with the predictions of SIM. There is a consistent relationship between T_K and, say, the peak in the magnetic susceptibility, the specific heat γ, and inelastic neutron scattering results. Actually, the only important parameter is in fact T_K from which all other parameters follow within SIM. This has presented a dilemma prior to the emergence of new theories, many of which build on the SIM. Any successful theory must simultaneously be able to correctly predict the microscopic as well as the macroscopic properties. SIM and its extensions appear primarily successful with the latter. Nevertheless, this fact suggests that at some level NCA is correct. Electron–electron correlations are indeed important, and formation of the singlet state with conduction electrons is not in dispute [except in the model of Liu (1993, 1997)]. Somehow this must be reconciled with the existence of bands far above T_K which are suggested by ARPES measurements.

Various renormalized band approaches (Zwicknagl 1992, Strange and Newns 1986] have succeeded in effectively reproducing the large electron masses in heavy fermions,

but they are not in general able to accommodate the numerous magnetic states as well as superconductivity within the same model. A very interesting model that has been recently proposed is the two-electron band approach of Sheng and Cooper (1995), in which correlations are first included explicitly between the f electrons and ligand conduction band states (f–l correlations) while f–f correlations are treated within an infinite–U approximation. While this is quite similar to the SIM approach, it differs in that a collective response of the ligand electrons which yields the Kondo resonance is not included. Instead, the singlet (or triplet) state is formed as an f–l pair of electrons which then form paired band states.

The nascent studies of the periodic Anderson lattice model (PAM) do contain some of the ingredients crucial to the description of the photoemission spectrum, such as substantially more intensity in the f^1 peaks vs the f^0 peak thus yielding much smaller n_f values, the formation of dispersive quasiparticle bands, a much slower temperature dependence than found in the SIM, broadening wich was initially attributed to phonons, and the weak hybridization at E_F yielding flat bands at E_F while strong hybridization away from E_F allows f spectral weight to disperse to energies far larger than $k_B T_K$ (as observed).

It is, of course, a long road from the first inception of any model to the final detailed proof of its applicability. In its early stages it appears to qualitatively fit the ARPES data, including the mild temperature dependence. Final proof – or discarding – of this theory, however, will occur only after successful – or unsuccessful – attempts to fit real spectra.

Note added in proof

Lawrence and Booth (private communication) now find inconsistencies even between bulk properties and the SIM.

Acknowledgements

We would like to acknowledge useful conversations with J. Allen, J. Bonca, Barry Cooper, A. Chattopadhyay, D.L. Cox, P. van Dongen, J.K. Freericks, B. Goodman, M. Grioni, D.W. Hess, M. Hettler, H.R. Krishnamurthy, Jon Lawrence, D. McLaughlin, Th. Pruschke, R.N. Silver, Joe Thompson and F.C. Zhang. Jarrell and Tahvildar-Zadeh acknowledge the support of NSF grants DMR-9704021 and DMR-9357199. Computer support was provided by the Ohio Supercomputer Center. Jarrell acknowledges the hospitality of the Los Alamos Center for Nonlinear Studies and the Los Alamos branch of the National High Magnetic Field Laboratory. Riseborough acknowledges the support from the US Department of Energy, Office of Basic Energy Sciences (DE-FG-84-ER45127), and wishes to thank Los Alamos National Laboratory, MST-10 for its hospitality. Much of the experimental work (i.e., Arko et al.) was performed under the auspices of the US Department of Energy, Office of Basic Energy Sciences, Division of

Materials Science. Measurements done by Arko et al. were performed at the Los Alamos U3C beamline at the NSLS and at the Synchrotron Radiation Center of the University of Wisconsin.

Appendix 1. Spin–orbit and crystal field split Kondo peaks

We shall assume that the spin–orbit coupling splits the 14-fold degeneracy of the f level into two multiplets; the lowest energy level being the $j=\frac{5}{2}$ multiplet, and the $j=\frac{7}{2}$ multiplet at an energy $E_f+\Delta E_{s\text{-}o}$. We also assume that the effect of crystalline electric field is to produce a splitting of the six-fold degenerate $j=\frac{5}{2}$ level into three doublets, with energies denoted by E_f, $E_f+\Delta E(b)$ and $E_f+\Delta E(c)$, respectively.

An analysis similar to that discussed in the text yields a set of four spin-compensated Kondo states $|\Psi_a\rangle$, $|\Psi_b\rangle$, $|\Psi_c\rangle$, and the spin–orbit split state $|\Psi_{s\text{-}o}\rangle$, with binding energies δE_a, δE_b, δE_c and $\delta E_{s\text{-}o}$, respectively. These binding energies are given by the expressions

$$\delta E_a = \left|1+\frac{W+\mu}{\Delta E(b)}\right|\left|1+\frac{W+\mu}{\Delta E(c)}\right|\left|1+\frac{W+\mu}{\Delta E_{s\text{-}o}}\right|^4 (W+\mu)\exp\left(\frac{\pi E_f-\mu}{2\Delta}\right), \tag{42a}$$

$$\delta E_b = \left|1-\frac{W+\mu}{\Delta E(b)}\right|\left|1+\frac{W+\mu}{\Delta E(c)-\Delta E(b)}\right|\left|1+\frac{W+\mu}{\Delta E_{s\text{-}o}}\right|^4 \times (W+\mu)\exp\left(\frac{\pi(E_f+\Delta E(b)-\mu)}{2\Delta}\right), \tag{42b}$$

$$\delta E_c = \left|1-\frac{W+\mu}{\Delta E(c)}\right|\left|1+\frac{W+\mu}{\Delta E(b)-\Delta E(c)}\right|\left|1+\frac{W+\mu}{\Delta E_{s\text{-}o}}\right|^4 \times (W+\mu)\exp\left(\frac{\pi(E_f+\Delta E(c)-\mu)}{2\Delta}\right), \tag{42c}$$

and finally,

$$\delta E_{s\text{-}o} = \left|1-\frac{W+\mu}{\Delta E_{s\text{-}o}}\right|^{3/4} (W+\mu)\exp\left(\frac{\pi(E_f+\Delta E_{s\text{-}o}-\mu)}{8\Delta}\right). \tag{42d}$$

It has been assumed that the energy scales obey the chain of inequalities

$$\Delta \gg \Delta E_{s\text{-}o} \gg \Delta E(\alpha) \gg \delta E_\alpha.$$

This analysis yields the spectrum shown in fig. 1, which has a peak at the Fermi level, which is in fact a tail of the Kondo peak, and several broad features located below the

Fermi energy. The latter set of peaks can be categorized as a set of crystal field Kondo side bands with excitation energies of

$$-\Delta E(\mathrm{b}) + \delta E_{\mathrm{b}}, \quad -\Delta E(\mathrm{c}) + \delta E_{\mathrm{c}}, \quad -\Delta E(\mathrm{c}) + \Delta E(\mathrm{b}) + \delta E_{\mathrm{c}}, \tag{43a,b,c}$$

measured from the Fermi level. The widths of these peaks are given by $\pi\delta E_{\mathrm{b}}$, $2\pi\delta E_{\mathrm{c}}$, and $2\pi\delta E_{\mathrm{c}}$ respectively. Note these widths are larger than those associated with the Kondo peaks above the Fermi level by factors of at least 2, i.e. the degeneracy. In addition to these there are three higher-energy spin–orbit Kondo side bands with excitation energies of

$$-\Delta E_{\mathrm{s\text{-}o}} + \delta E_{\mathrm{s\text{-}o}}, \quad -\Delta E_{\mathrm{s\text{-}o}} + \Delta E(\mathrm{b}) + \delta E_{\mathrm{s\text{-}o}}, \quad -\Delta E_{\mathrm{s\text{-}o}} + \Delta E(\mathrm{c}) + \delta E_{\mathrm{s\text{-}o}}, \tag{44a,b,c}$$

measured from the Fermi energy. These last three peaks are the broadest and have their widths given by $\frac{6}{8}\pi\delta E_{\mathrm{s\text{-}o}}$. The estimates of the widths are found by considering the available decay channels times Δ divided by the wave function renormalization for the three excited spin-compensated bound states, $|\Psi_{\mathrm{b}}\rangle$, $|\Psi_{\mathrm{c}}\rangle$ and $|\Psi_{\mathrm{s\text{-}o}}\rangle$.

Since all of these f photo-emission peaks are side bands of the basic Kondo peak, they are all proportional to the weight of the f^0 component in the ground state $|\Psi_{\mathrm{a}}\rangle$. That is, the Kondo peaks represent processes whereby a single electron is added to the f level (for $U_{\mathrm{ff}} \to \infty$ this requires the presence of an unoccupied f orbital in the initial state), the intensities of the side bands are all proportional to $(1 - n_{\mathrm{f}})$. As the peaks do not have simple Lorentzian forms, they are asymmetric: the total intensities are not straightforward to estimate. However, by assuming a Lorentzian shape, we have the estimates of the integrated intensities of the crystal field split Kondo side bands given by the expressions

$$\frac{1-n_{\mathrm{f}}}{2}\left[\frac{\delta E_{\mathrm{b}}}{\delta E_{\mathrm{a}}} - \frac{1}{2} + \frac{1}{\pi}\tan^{-1}\left(\frac{\delta E_{\mathrm{a}}}{\pi\delta E_{\mathrm{b}}}\right)\right], \tag{45a}$$

$$\frac{1-n_{\mathrm{f}}}{2}\left[\frac{\delta E_{\mathrm{c}}}{\delta E_{\mathrm{a}}} - \frac{1}{4} + \frac{1}{2\pi}\tan^{-1}\left(\frac{\delta E_{\mathrm{a}}}{2\pi\delta E_{\mathrm{c}}}\right)\right], \tag{45b}$$

$$\frac{1-n_{\mathrm{f}}}{2}\left[\frac{\delta E_{\mathrm{c}}}{\Delta E(\mathrm{b})} - \frac{1}{4} + \frac{1}{2\pi}\tan^{-1}\left(\frac{\Delta E(\mathrm{b})}{2\pi\delta E_{\mathrm{c}}}\right)\right]. \tag{45c}$$

The last intensity is considerably smaller than the first two intensities as it has a value

$$\approx \frac{1}{12\pi}(1-n_{\mathrm{f}})\left(\frac{2\pi\delta E_{\mathrm{c}}}{\Delta E(\mathrm{b})}\right)^3, \tag{46}$$

which is much smaller than the background terms that are neglected by our analysis.

The three spin–orbit split Kondo side bands have intensities that are estimated to be

$$\frac{1-n_f}{8}\left[\frac{\delta E_{s\text{-}o}}{\delta E_a}-\frac{2}{3}+\frac{4}{3\pi}\tan^{-1}\left(\frac{4\delta E_a}{3\pi\delta E_{s\text{-}o}}\right)\right], \tag{47a}$$

$$\frac{1-n_f}{8}\left[\frac{\delta E_{s\text{-}o}}{\Delta E(b)}-\frac{2}{3}+\frac{4}{3\pi}\tan^{-1}\left(\frac{4\Delta E(b)}{3\pi\delta E_{s\text{-}o}}\right)\right], \tag{47b}$$

$$\frac{1-n_f}{8}\left[\frac{\delta E_{s\text{-}o}}{\Delta E(c)}-\frac{2}{3}+\frac{4}{3\pi}\tan^{-1}\left(\frac{4\Delta E(c)}{3\pi\delta E_{s\text{-}o}}\right)\right]. \tag{47c}$$

The last two intensities are negligible, for reasons similar to those for the intensity given in eq. (46).

The approximate spectrum, based on the assumed Lorentzian forms with the expressions given above, and the more accurate numerical results are shown in fig. 2.

Appendix 2. Effects of finite Coulomb interaction strengths, U_{ff}

When the Coulomb interaction between the f electrons is still considered to be a large but finite value, then higher-order configurations such as $(4f)^2$ and $(4f)^3$ should also be taken into consideration. The effect of including the $(4f)^2$ configuration in the variational basis has been evaluated in the infinite-degeneracy limit, $N_f \to \infty$, however, the effects of the $(4f)^n$ configurations which should be comparable have been excluded. To the extent that finite U_{ff} corrections turn out to be sizeable, then the assumption that the $(4f)^3$ and higher configurations may be neglected should be critically re-examined. Crystal field and spin–orbit splittings can be incorporated into the analysis via trivial modifications if the effect of the scattering due to inter-particle spin–orbit interactions, within the manifold of $(4f)^2$ configurations, is neglected.

A2.1. *The ground state*

The ground state is assumed to lay in the space spanned by the normalized basis states,

$$|\Phi_0\rangle = \prod_{\alpha,\boldsymbol{k};\ e(\boldsymbol{k})<\mu} d^+_{\alpha,\boldsymbol{k}}\,|0\rangle\,, \tag{48a}$$

$$|\{\alpha\}\,\boldsymbol{k}\rangle = [N_{\{\alpha\}}]^{-1/2}\sum_{\alpha} f^+_\alpha\, d_{\alpha,\boldsymbol{k}}\,|\Phi_0\rangle\,;\quad \alpha\varepsilon\,\{\alpha\}\,, \tag{48b}$$

$$|\{\alpha\}\,\boldsymbol{k},\{\beta\}\,\boldsymbol{k}'\rangle = [N_{\{\alpha\}}N_{\{\beta\}}]^{-1/2}\sum_{\alpha,\beta} f^+_\alpha d_{\alpha,\boldsymbol{k}} f^+_\beta\, d_{\beta,\boldsymbol{k}'}\,|\Phi_0\rangle\,;\quad \alpha\varepsilon\,\{\alpha\}\,,\ \beta\varepsilon\,\{\beta\}\,, \tag{48c}$$

where $N_{\{\alpha\}}$ is the degeneracy of the $\{\alpha\}$ spin–orbit/crystal field split multiplet which has the single particle energy, $E_f + \Delta E(\{\alpha\})$.

In the extended basis set, the ground state $|\Psi_g\rangle$ is written in the form

$$|\Psi_g\rangle = \aleph^{-1}\left(|\Phi_0\rangle + \sum_{\{\alpha\}\boldsymbol{k}} a_{\{\alpha\}\boldsymbol{k}}\,|\{\alpha\}\,\boldsymbol{k}\rangle + \sum_{\{\alpha\}\boldsymbol{k},\{\beta\}\boldsymbol{k}'} b_{\{\alpha\}\boldsymbol{k},\{\beta\}\boldsymbol{k}'}\,|\{\alpha\}\,\boldsymbol{k},\{\beta\}\,\boldsymbol{k}'\rangle\right), \tag{49}$$

in which the last summation is restricted such that it does not count the contribution from any one state twice, by requiring that $e(\boldsymbol{k}) > e(\boldsymbol{k}')$. The wave function renormalization is denoted by $\aleph$, and is given by

$$\aleph^2 = 1 + \sum_{\{\alpha\}\boldsymbol{k}} |a_{\{\alpha\}\boldsymbol{k}}|^2 + \sum_{\{\alpha\}\boldsymbol{k},\{\beta\}\boldsymbol{k}'} |b_{\{\alpha\}\boldsymbol{k},\{\beta\}\boldsymbol{k}'}|^2. \tag{50}$$

The variational equations for the non-zero ground state amplitudes [with $e(\boldsymbol{k})$ and $e(\boldsymbol{k}')$ $<\mu$] are given by

$$\begin{aligned}&\left(E_f + \Delta E(\{\alpha\}) - e(\boldsymbol{k}) - \Delta E_g\right) a_{\{\alpha\}\boldsymbol{k}} \\ &\quad = -\sqrt{N_{\{\alpha\}}}\,V(\boldsymbol{k}) - \sum_{\{\beta\},\boldsymbol{k}'} \sqrt{N_{\{\beta\}}}\,V^*(\boldsymbol{k}')\,b_{\{\alpha\}\boldsymbol{k},\{\beta\}\boldsymbol{k}'},\end{aligned} \tag{51a}$$

$$\begin{aligned}&\left(2E_f + U_{ff} + \Delta E(\{\alpha\}) + \Delta E(\{\beta\}) - e(\boldsymbol{k}) - e(\boldsymbol{k}') - \Delta E_g\right) b_{\{\alpha\}\boldsymbol{k},\{\beta\}\boldsymbol{k}'} \\ &\quad = -\sqrt{N_{\{\beta\}}}\,V(\boldsymbol{k}')\,a_{\{\alpha\}\boldsymbol{k}} - \sqrt{N_{\{\alpha\}}}\,V(\boldsymbol{k})\,a_{\{\beta\}\boldsymbol{k}'},\end{aligned} \tag{51b}$$

where the ground state energy is defined as $E_g = E_0 + \Delta E_g$, in which the last term represents the effects of the hybridization. We have also used the limit $N_{\{\alpha\}} \to \infty$, for the degeneracies of all the manifolds. The above equations can be combined to yield the integral equation for the amplitude $a_{\{\alpha\}\boldsymbol{k}}$ of the $(4f)^1$ configuration in the ground state,

$$\begin{aligned}&\left(E_f + \Delta E(\{\alpha\}) - e(\boldsymbol{k}) - \Delta E_g - \Gamma_{\{\alpha\}\boldsymbol{k}}\right) a_{\{\alpha\}\boldsymbol{k}} \\ &\quad = -\sqrt{N_{\{\alpha\}}}\,V(\boldsymbol{k}) \\ &\qquad \times \left[1 - \sum_{\{\beta\},\boldsymbol{k}';\ e(\boldsymbol{k}')<\mu} \frac{\sqrt{N_{\{\beta\}}}\,V^*(\boldsymbol{k}')\,a_{\{\beta\}\boldsymbol{k}'}}{U_{ff} + 2E_f + \Delta E(\{\alpha\}) + \Delta E(\{\beta\}) - e(\boldsymbol{k}) - e(\boldsymbol{k}') - \Delta E_g}\right],\end{aligned} \tag{52a}$$

where

$$\Gamma_{\{\alpha\}\boldsymbol{k}} = \sum_{\{\beta\},\boldsymbol{k}';\ e(\boldsymbol{k}')<\mu} \frac{N_{\{\beta\}}\,|V(\boldsymbol{k}')|^2}{U_{ff} + 2E_f + \Delta E(\{\alpha\}) + \Delta E(\{\beta\}) - e(\boldsymbol{k}) - e(\boldsymbol{k}') - \Delta E_g}. \tag{52b}$$

The hybridization-induced binding energy ΔE_g is to be evaluated self-consistently from the equation

$$\Delta E_g = \sum_{\{\alpha\},k} \sqrt{N_{\{\alpha\}}}\, V^*(\boldsymbol{k})\, a_{\{\alpha\},k}. \tag{53}$$

Since the integral equation (52) is not separable, it ought to be solved numerically. An approximate solution is found by a decoupling procedure, valid whenever the Coulomb interaction strength is greater than the occupied conduction band width,

$$U_{ff} + 2E_f - \Delta E_g - e(\boldsymbol{k}') - \mu \gg (W + \mu).$$

This approximation is completely inappropriate for systems such as $CeAl_3$, where the occupied portion of the Al conduction band which hybridizes with the f orbitals is expected to have a width of the order of 10 eV, and U_{ff} is at most 6 or 7 eV. The approximation is best for Ce transition metal alloys, where the occupied portion of the transition metal d band is expected to be 2 or 3 eV, leading to an expansion parameter in the range of $\frac{2}{7}$ to $\frac{1}{2}$.

In the limit $U_{ff} + E_f - e(\boldsymbol{k}') - \mu \gg (W + \mu)$, the denominator of the second term in the square brackets of eq. (52a) can be approximated by a value independent of $\Delta E(\{\alpha\}) - e(\boldsymbol{k})$ according to

$$\begin{aligned} &\sum_{\{\beta\},\boldsymbol{k}';\ e(\boldsymbol{k}')<\mu} \frac{\sqrt{N_{\{\beta\}}}\, V^*(\boldsymbol{k}')\, a_{\{\beta\}\boldsymbol{k}'}}{U_{ff} + 2E_f + \Delta E(\{\alpha\}) + \Delta E(\{\beta\}) - e(\boldsymbol{k}) - e(\boldsymbol{k}') - \Delta E_g} \\ &\approx \sum_{\{\beta\},\boldsymbol{k}';\ e(\boldsymbol{k}')<\mu} \frac{\sqrt{N_{\{\beta\}}}\, V^*(\boldsymbol{k}')\, a_{\{\beta\}\boldsymbol{k}'}}{U_{ff} + 2E_f + \Delta E(\{\beta\}) - \mu - e(\boldsymbol{k}') - \Delta E_g}. \end{aligned} \tag{54}$$

The resulting approximate equation is separable, and has a solution given by the expression

$$a_{\{\alpha\}\boldsymbol{k}} = -\frac{\sqrt{N_{\{\alpha\}}}\, V(\boldsymbol{k})\, C}{E_f + \Delta E(\{\alpha\}) - e(\boldsymbol{k}) - \Delta E_g - \Gamma_{\{\alpha\}\boldsymbol{k}}}, \tag{55a}$$

where the constant C is given by

$$C = 1 - \sum_{\{\beta\},\boldsymbol{k}';\ e(\boldsymbol{k}')<\mu} \frac{\sqrt{N_{\{\beta\}}}\, V^*(\boldsymbol{k}')\, a_{\{\beta\}\boldsymbol{k}'}}{U_{ff} + 2E_f + \Delta E(\{\beta\}) - \mu - e(\boldsymbol{k}') - \Delta E_g}. \tag{55b}$$

Without further loss of accuracy, the same approximation made above can be used to together with eq. (53) to simplify the above expression to

$$\begin{aligned} a_{\{\alpha\}\boldsymbol{k}} = &-\sqrt{N_{\{\alpha\}}}\, V(\boldsymbol{k}) \frac{U_{ff} + E_f + \Gamma - \mu - \Delta E_g}{U_{ff} + E_f + 2\Gamma - \mu} \\ &\times \frac{1}{E_f + \Delta E(\{\alpha\}) - e(\boldsymbol{k}) - \Delta E_g - \Gamma_{\{\alpha\}\boldsymbol{k}}}. \end{aligned} \tag{56a}$$

Likewise in neglecting the $\boldsymbol{k}$ and $\{\alpha\}$ dependence of $\Gamma_{\{\alpha\},\boldsymbol{k}}$, one finds the binding energy ΔE_g from the transcendental equation

$$-\Delta E_g = \frac{U_{ff} + E_f + \Gamma - \mu - \Delta E_g}{U_{ff} + E_f + 2\Gamma - \mu} \times \sum_{\{\alpha\},\boldsymbol{k};\ e(\boldsymbol{k}) < \mu} \frac{N_{\{\alpha\}} |V(\boldsymbol{k})|^2}{\left[E_f + \Delta E(\{\alpha\}) - e(\boldsymbol{k}) - \Delta E_g - \Gamma\right]^{-1}}. \tag{56b}$$

Due to the Fermi energy cut-off, the right-hand side of the above equation diverges logarithmically at the points where

$$E_f + \Delta E(\{\alpha\}) - \mu - \Delta E_g - \Gamma = 0.$$

Hence in the Kondo limit, when E_f lies far below the Fermi energy, there is at least one solution of the above equation with

$$\Delta E_g = \Delta E_{\{\alpha\}} = E_f + \Delta E(\{\alpha\}) - \mu - \Gamma - \delta_{\{\alpha\}}.$$

Whenever

$$\delta_{\{\alpha\}} = E_f + \Delta E(\{\alpha\}) - \mu - \Delta E_{\{\alpha\}} \ll \Delta E(\{\alpha\}),$$

the binding energy of the spin-compensated state $\delta_{\{\alpha\}}$ can be written as

$$\delta_{\{\alpha\}} \approx (W + \mu) \prod_{\{\beta\} \neq \{\alpha\}} \left| 1 + \frac{W + \mu}{\Delta E(\{\beta\}) - \Delta E(\{\alpha\})} \right|^{N_{\{\beta\}}/N_{\{\alpha\}}} \times \exp\left(\frac{\pi(U_{ff} + E_f + 2\Gamma - \mu)(E_f + \Delta E(\{\alpha\}) - \mu - \Gamma)}{(U_{ff} - \Delta E(\{\alpha\}) + 2\Gamma) N_{\{\alpha\}} \Delta} \right), \tag{57}$$

where $\Delta = \pi \sum_{\boldsymbol{k}} |V(\boldsymbol{k})|^2 \delta(\mu - e(\boldsymbol{k}))$ is the hybridization times the conduction band density of states at the Fermi level. The binding energies $\delta_{\{\alpha\}}$ are closely related to the Kondo temperatures of the $\{\alpha\}$ spin-compensated states. Taking into consideration the approximation made in decoupling the integral equation, one finds $\Delta \gg \Gamma$, and the exponent in $\delta_{\{\alpha\}}$ can be recognized to be the inverse product of the Schrieffer–Wolf exchange interaction between the local moment and the conduction electrons, and the conduction band density of states.

A2.2. *The resolvent*

The photoemission spectrum is given by the expression

$$I(\omega) = \frac{1}{\pi} \sum_{\alpha,\alpha'} \sum_{m,n} \mathrm{Im}\left(\langle \Psi_g | f^+_{\alpha'} | m \rangle \langle m | g(\hbar\omega) | n \rangle \langle n | f_\alpha | \Psi_g \rangle \right), \tag{58}$$

where $g(z) = (z - E_g + H)^{-1}$. The matrix elements of the resolvent or Green's function $\langle m | g(z) | n \rangle$ are evaluated in the sub-space spanned by the states

$$|m\rangle \in \left\{ \left| \boldsymbol{k} \{\alpha\}^* \right\rangle, \left| \boldsymbol{k} \{\alpha\}^*, \{\beta_1\} \boldsymbol{k}_1 \right\rangle, \left| \boldsymbol{k} \{\alpha\}^*, \{\beta_1\} \boldsymbol{k}_1, \{\beta_2\} \boldsymbol{k}_2 \right\rangle \right\}, \tag{59a}$$

where

$$\left| \boldsymbol{k} \{\alpha\}^* \right\rangle \equiv \left[N_{\{\alpha\}} \right]^{-1/2} \sum_{\alpha \in \{\alpha\}} d_{\alpha \boldsymbol{k}} | \Phi_0 \rangle, \tag{59b}$$

$$\left| \boldsymbol{k} \{\alpha\}^*, \{\beta_1\} \boldsymbol{k}_1 \right\rangle \equiv \left[N_{\{\alpha\}} \right]^{-1/2} \sum_{\alpha \in \{\alpha\}} d_{\alpha \boldsymbol{k}} | \{\beta_1\} \boldsymbol{k}_1 \rangle, \tag{59c}$$

$$\left| \boldsymbol{k} \{\alpha\}^*, \{\beta_1\} \boldsymbol{k}_1, \{\beta_2\} \boldsymbol{k}_2 \right\rangle \equiv \left[N_{\{\alpha\}} \right]^{-1/2} \sum_{\alpha \in \{\alpha\}} d_{\alpha \boldsymbol{k}} | \{\beta_1\} \boldsymbol{k}_1, \{\beta_2\} \boldsymbol{k}_2 \rangle. \tag{59d}$$

The matrix elements of $g(z)$ satisfy the equations

$$\sum_n \langle m | (z - \mathrm{H} + E_g) | n \rangle \langle n | g(z) | m' \rangle = \delta_{m,m'}, \tag{60}$$

which can be reduced to a closed set of coupled integral equations, such as

$$\begin{aligned} &\left[z - \Delta E_g - e(\boldsymbol{k}) \right] \left\langle \boldsymbol{k} \{\alpha\}^* | g(z) | \boldsymbol{k}' \{\alpha'\}^* \right\rangle \\ &+ \sum_{\{\beta\}, \boldsymbol{k}} \sqrt{N_{\{\beta\}}}\, V^*(\boldsymbol{k}_1) \left\langle \boldsymbol{k} \{\alpha\}^*, \{\beta_1\} \boldsymbol{k}_1 | g(z) | \boldsymbol{k}' \{\alpha'\}^* \right\rangle \\ &\quad = \delta_{\{\alpha\},\{\alpha'\}}\, \delta(\boldsymbol{k} - \boldsymbol{k}'), \end{aligned} \tag{61a}$$

$$\begin{aligned} &\left[z - \Delta E_g - e(\boldsymbol{k}) - \mathrm{e}(\boldsymbol{k}_1) + E_f + \Delta E(\{\beta_1\}) \right] \left\langle \boldsymbol{k} \{\alpha\}^*, \{\beta_1\} \boldsymbol{k}_1 | g(z) | \boldsymbol{k}' \{\alpha'\}^* \right\rangle \\ &+ \sqrt{N_{\{\beta\}}}\, V(\boldsymbol{k}_1) \left\langle \boldsymbol{k} \{\alpha\}^* | g(z) | \boldsymbol{k}' \{\alpha'\}^* \right\rangle \\ &+ \sum_{\{\beta\}, \boldsymbol{k}} \sqrt{N_{\{\beta\}}}\, V^*(\boldsymbol{k}_2) \left\langle \boldsymbol{k} \{\alpha\}^*, \{\beta_1\} \boldsymbol{k}_1, \{\beta_2\} \boldsymbol{k}_2 | g(z) | \boldsymbol{k}' \{\alpha'\}^* \right\rangle \\ &\quad = 0, \end{aligned} \tag{61b}$$

$$
\begin{aligned}
&\left[z-\Delta E_{\mathrm{g}}-e(\boldsymbol{k})-\mathrm{e}(\boldsymbol{k}_1)-\mathrm{e}(\boldsymbol{k}_2)+U_{\mathrm{ff}}+2E_{\mathrm{f}}+\Delta E(\{\beta_1\})+\Delta E(\{\beta_2\})\right]\\
&\quad\times\left\langle \boldsymbol{k}\,\{\alpha\}^*,\{\beta_1\}\,\boldsymbol{k}_1,\{\beta_2\}\,\boldsymbol{k}_2\,|g(z)|\,\boldsymbol{k}'\,\{\alpha'\}^*\right\rangle\\
&+\sqrt{N_{\{\beta\}}}\,V(\boldsymbol{k}_2)\left\langle \boldsymbol{k}\,\{\alpha\}^*,\{\beta_1\}\,\boldsymbol{k}_1\,|g(z)|\,\boldsymbol{k}'\,\{\alpha'\}^*\right\rangle\\
&+\sqrt{N_{\{\beta\}}}\,V(\boldsymbol{k}_1)\left\langle \boldsymbol{k}\,\{\alpha\}^*,\{\beta_2\}\,\boldsymbol{k}_2\,|g(z)|\,\boldsymbol{k}'\,\{\alpha'\}^*\right\rangle\\
&\quad=0.
\end{aligned}
\tag{61c}
$$

The other matrix elements needed for the calculation of the spectra,

$$
\left\langle m\,|g(z)|\,\boldsymbol{k}'\,\{\alpha'\}^*,\{\beta_1'\}\,\boldsymbol{k}_1'\right\rangle,
$$

satisfy similar equations. Equations (61b) and (61c) can be combined to yield an integral equation,

$$
\begin{aligned}
&\left[z-\Delta E_{\mathrm{g}}-\mathrm{e}(\boldsymbol{k})-\mathrm{e}(\boldsymbol{k}_1)+E_{\mathrm{f}}+\Delta E(\{\beta_1\})-\Gamma_{\{\beta\}\boldsymbol{k}}(z-e(\boldsymbol{k}))\right]\\
&\quad\times\left\langle \boldsymbol{k}\,\{\alpha\}^*,\{\beta_1\}\,\boldsymbol{k}_1\,|g(z)|\,\boldsymbol{k}'\,\{\alpha'\}^*\right\rangle\\
&+\sqrt{N_{\{\beta\}}}\,V(\boldsymbol{k}_1)\left\langle \boldsymbol{k}\,\{\alpha\}^*\,|g(z)|\,\boldsymbol{k}'\,\{\alpha'\}^*\right\rangle\\
&-\sqrt{N_{\{\beta\}}}\,V(\boldsymbol{k}_1)\sum_{\{\beta\},\boldsymbol{k}}\frac{\sqrt{N_{\{\beta\}}}\,V^*(\boldsymbol{k}_2)\left\langle \boldsymbol{k}\,\{\alpha\}^*,\{\beta_2\}\,\boldsymbol{k}_2\,|g(z)|\,\boldsymbol{k}'\,\{\alpha'\}^*\right\rangle}{z-\Delta E_{\mathrm{g}}-\mathrm{e}(\boldsymbol{k})-\mathrm{e}(\boldsymbol{k}_1)-\mathrm{e}(\boldsymbol{k}_2)+U_{\mathrm{ff}}+2E_{\mathrm{f}}+\Delta E(\{\beta_1\})+\Delta E(\{\beta_2\})}\\
&\quad=0,
\end{aligned}
\tag{62a}
$$

in which $\Gamma_{\{\beta\}\boldsymbol{k}}(z-e(\boldsymbol{k}))$ is the obvious generalization of the definition of $\Gamma_{\{\beta\}\boldsymbol{k}}$, given by

$$
\begin{aligned}
&\Gamma_{\{\beta\}\boldsymbol{k}}(z-e(\boldsymbol{k}))\\
&\quad\equiv\sum_{\{\beta\},\boldsymbol{k};\ e(\boldsymbol{k})<\mu}\frac{N_{\{\beta\}}\,|V(\boldsymbol{k}_2)|^2}{z-e(\boldsymbol{k})-\Delta E_{\mathrm{g}}+U_{\mathrm{ff}}+2E_{\mathrm{f}}+\Delta E(\{\beta_1\})+\Delta E(\{\beta_2\})-e(\boldsymbol{k}_1)-e(\boldsymbol{k}_2)}.
\end{aligned}
\tag{62b}
$$

The resulting set of equations, (61a, 62a,b), is not separable, but exactly like the integral equation for $a_{\{\alpha\}\boldsymbol{k}}$, they can be reduced to separable equations if the third term of eq. (62a) is decoupled according to the approximation

$$
\begin{aligned}
&\sqrt{N_{\{\beta\}}}\,V(\boldsymbol{k}_1)\sum_{\{\beta\},\boldsymbol{k}}\frac{\sqrt{N_{\{\beta\}}}\,V^*(\boldsymbol{k}_2)\left\langle \boldsymbol{k}\,\{\alpha\}^*,\{\beta_2\}\,\boldsymbol{k}_2\,|g(z)|\,\boldsymbol{k}'\,\{\alpha'\}^*\right\rangle}{z-\Delta E_{\mathrm{g}}-e(\boldsymbol{k})-e(\boldsymbol{k}_1)-e(\boldsymbol{k}_2)+U_{\mathrm{ff}}+2E_{\mathrm{f}}+\Delta E(\{\beta_1\})+\Delta E(\{\beta_2\})}\\
&\quad\approx\sqrt{N_{\{\beta\}}}\,V(\boldsymbol{k}_1)\sum_{\{\beta\},\boldsymbol{k}}\frac{\sqrt{N_{\{\beta\}}}\,V^*(\boldsymbol{k}_2)\left\langle \boldsymbol{k}\,\{\alpha\}^*,\{\beta_2\}\,\boldsymbol{k}_2\,|g(z)|\,\boldsymbol{k}'\,\{\alpha'\}^*\right\rangle}{z-\Delta E_{\mathrm{g}}-e(\boldsymbol{k})-\mu-e(\boldsymbol{k}_2)+U_{\mathrm{ff}}+2E_{\mathrm{f}}+\Delta E(\{\beta_2\})}.
\end{aligned}
\tag{63}
$$

As previously mentioned, this approximation is expected to be reasonable if

$$(W+\mu) \ll U_{\mathrm{ff}} + 2E_{\mathrm{f}} + z - \Delta E_{\mathrm{g}} - \mathrm{e}(\boldsymbol{k}) - 2\mu.$$

The approximate solution for the matrix elements of $\langle \boldsymbol{k}\,\{\alpha\}^* \,|g(z)|\, \boldsymbol{k}'\,\{\alpha'\}^* \rangle$ are given by the expressions

$$\left[z - \Delta E_{\mathrm{g}} - e(\boldsymbol{k}) - \Lambda\{z - e(\boldsymbol{k}) - \Gamma(z - e(\boldsymbol{k}))\}\, C(z - e(\boldsymbol{k}))\right] \langle \boldsymbol{k}\,\{\alpha\}^* \,|g(z)|\, \boldsymbol{k}'\,\{\alpha'\}^* \rangle = \delta_{\{\alpha\},\{\alpha'\}}\, \delta(\boldsymbol{k} - \boldsymbol{k}'), \tag{64a}$$

where

$$\Lambda\{z - e(\boldsymbol{k})\} = \sum_{\{\beta\}\boldsymbol{k}'} \frac{N_{\{\beta\}}\, |V(\boldsymbol{k}')|^2}{z - \Delta E_{\mathrm{g}} - e(\boldsymbol{k}) - e(\boldsymbol{k}') + E_{\mathrm{f}} + \Delta E(\{\beta\})} \tag{64b}$$

and

$$C(x) = \frac{U_{\mathrm{ff}} + E_{\mathrm{f}} + \Gamma(x) - \mu}{U_{\mathrm{ff}} + E_{\mathrm{f}} + 2\Gamma(x) - \Lambda(x) - \mu}. \tag{64c}$$

The real part of the denominator of the resolvent $\langle \boldsymbol{k}\,\{\alpha\}^* \,|g(z)|\, \boldsymbol{k}\,\{\alpha\}^* \rangle$ has zeroes at the energies related to the solutions of eq. (56b), such as $z = e(\boldsymbol{k}) + \Delta E_{\mathrm{g}} - \Delta E_{\{\alpha\}}$. The derivatives of the real part of the denominator at these zeros are given by

$$Z_{\{\alpha\}} = 1 - \frac{\Lambda'(x)(1 - \Gamma'(x))(U_{\mathrm{ff}} + E_{\mathrm{f}} + \Gamma(x) - \Delta E_{\{\alpha\}} - \mu)^2 + \Gamma'(x)\Delta E_{\{\alpha\}}(U_{\mathrm{ff}} + E_{\mathrm{f}} - 2\Delta E_{\{\alpha\}})}{(U_{\mathrm{ff}} + E_{\mathrm{f}} + 2\Gamma(x))(U_{\mathrm{ff}} + E_{\mathrm{f}} + 2\Gamma(x))}, \tag{65}$$

where the prime indicates a derivative, and the functions $\Lambda(x)$ and $\Gamma(x)$ are evaluated at $x = \Delta E_{\mathrm{g}} - \Delta E_{\{\alpha\}}$. These are the wave-function renormalizations $\aleph^2$ of the approximate eigenstates $|\Psi_{\{\alpha\}}\rangle$, given by eq. (50). The magnitude of the derivative Λ' is large, as it is greater than $N_{\{\alpha\}}\Delta/\pi\delta_{\{\alpha\}}$. As expected, these are simply related to the amplitudes of the vacuum, $|\Phi_0\rangle$, in the states $|\Psi_{\{\alpha\}}\rangle$. The imaginary part of the denominator has discontinuous steps of $N_{\{\alpha\}}\Delta$ located at

$$z = e(\boldsymbol{k}) + \Delta E_{\mathrm{g}} - E_{\mathrm{f}} - \Delta E(\{\alpha\}) + \Gamma + \mu. \tag{66}$$

Thus, only the first zero, located at $z = e(\boldsymbol{k})$, within $-\delta_{\mathrm{g}}$ of the Fermi level represents a bound state or simple pole of $\langle \boldsymbol{k}\,\{\alpha\}^* \,|g(z)|\, \boldsymbol{k}\,\{\alpha\}^* \rangle$, within this infinite-$N_{\mathrm{f}}$ approximation. The other zeroes merely represent resonances, although the large value of the wave-function renormalization near the zeroes of the real part does have the effect of dramatically reducing the width of the resonances.

The Green's function $\langle \boldsymbol{k}\{\alpha\}^*, \{\beta_1\}\boldsymbol{k}_1 | g(z) | \boldsymbol{k}'\{\alpha'\}^*, \{\beta_1'\}\boldsymbol{k}_1' \rangle$ is given by the expression

$$\begin{aligned}
&\left[z - \Delta E_g - e(\boldsymbol{k}) - e(\boldsymbol{k}_1) + E_f + \Delta E(\{\beta_1\}) - \Gamma\right] \langle \boldsymbol{k}\{\alpha\}^*, \{\beta_1\}\boldsymbol{k}_1 | g(z) | \boldsymbol{k}'\{\alpha'\}^*, \{\beta_1'\}\boldsymbol{k}_1' \rangle \\
&\quad = \delta_{\{\alpha\},\{\alpha'\}}\,\delta(\boldsymbol{k}-\boldsymbol{k}') \\
&\qquad \times \Bigg(\delta_{\{\beta\},\{\beta'\}}\,\delta(\boldsymbol{k}_1 - \boldsymbol{k}_1') \\
&\qquad\quad + \left| N_{\{\beta\}} V^*(\boldsymbol{k}_1) T(z - e(\boldsymbol{k})) \right| \frac{N_{\{\beta'\}} V(\boldsymbol{k}_1')}{z - \Delta E_g - e(\boldsymbol{k}) - e(\boldsymbol{k}_1') + E_f + \Delta E(\{\beta_1'\}) - \Gamma} \Bigg),
\end{aligned} \tag{67a}$$

where the T matrix is given by

$$\begin{aligned}
T(x) = &\left(1 + \frac{x - \Delta E_g}{x + U_{ff} + 2E_f - 2\mu - \Delta E_g}\right) \\
&\times \frac{U_{ff} + E_f + \Gamma(x) - \mu}{(x - \Delta E_g)(U_{ff} + E_f + 2\Gamma(x) - \Lambda(x) - \mu) - \Lambda(x)(U_{ff} + E_f + \Gamma(x) - \mu)}.
\end{aligned} \tag{67b}$$

In addition to the simple pole at $z = e(\boldsymbol{k})$ stemming from the analytic structure of $\langle \boldsymbol{k}\{\alpha\}^* | g(z) | \boldsymbol{k}\{\alpha\}^* \rangle$, the T matrix has another isolated pole located at

$$z - e(\boldsymbol{k}) - \mu + U_{ff} + 2E_f - \Delta E_g = 0,$$

which will be discussed below.

A2.3. *The spectrum*

In the energy range $\mu - h\omega < \delta_g$, the imaginary part of the denominator of

$$\langle \boldsymbol{k}\{\alpha\}^* | g(z) | \boldsymbol{k}\{\alpha\}^* \rangle$$

vanishes and $g(h\omega)$ only has a simple pole at $h\omega = e(\boldsymbol{k})$, with residue $\aleph^{-2}$. This leads to the photoemission spectrum, within the energy range δ_g below μ, being given by the expression

$$\begin{aligned}
I(\omega) = \aleph^{-2} \sum_{\{\alpha\},\boldsymbol{k}} &Z_g^{-1} \delta(h\omega - e(\boldsymbol{k})) \\
&\times \left| a_{\{\alpha\}\boldsymbol{k}} - a_{\{\alpha\}\boldsymbol{k}} \sum_{\{\beta\}\boldsymbol{k}'} \frac{\sqrt{N_{\{\beta\}}}\, V^*(\boldsymbol{k}') a_{\{\beta\}\boldsymbol{k}'}}{U_{ff} + 2E_f - \Delta E_g - e(\boldsymbol{k}') - \mu} \right. \\
&\qquad \left. - \sqrt{N_{\{\alpha\}}}\, V(\boldsymbol{k}) \sum_{\{\beta\}\boldsymbol{k}'} \frac{|a_{\{\beta\}\boldsymbol{k}'}|^2}{U_{ff} + 2E_f - \Delta E_g - e(\boldsymbol{k}') - e(\boldsymbol{k})} \right|^2.
\end{aligned} \tag{68}$$

in accord with the expression given by Gunnarsson and Schönhammer. This expression can be further simplified, by using the same approximation used in decoupling the integral equations for both the ground state and the resolvent $g(z)$, leading to

$$I(\omega) = \aleph^{-4} \sum_{\{\alpha\}} \left(\frac{U_{\mathrm{ff}}}{U_{\mathrm{ff}} + E_{\mathrm{f}}} \right)^2 \times \left[a_{\{\alpha\}k} - \sqrt{\frac{N_{\{\alpha\}}\Delta}{\pi}} \frac{U_{\mathrm{ff}}}{(U_{\mathrm{ff}} + E_{\mathrm{f}})^2} \sum_{\{\beta\}} \frac{N_{\{\beta\}}\Delta}{\pi} \left(\frac{1}{\Delta E(\{\beta\}) + \delta_{\mathrm{g}}} - \frac{1}{(W + \mu)} \right) \right]^2, \tag{69}$$

where $h\omega = e(\boldsymbol{k})$. Thus, within this restricted energy range, the effect of including the large Coulomb interaction U_{ff} is to renormalize the intensity by a constant multiplicative factor, and also to add a constant value to the energy-dependent $(4f)^1$ amplitude. This can be further reduced to

$$I(\omega) = \aleph^{-4} \left(\frac{U_{\mathrm{ff}}}{U_{\mathrm{ff}} + E_{\mathrm{f}}} \right)^4 \sum_{\{\alpha\}} \frac{N_{\{\alpha\}}\Delta}{\pi} \left[\frac{1}{\Delta E(\{\alpha\}) + \delta_{\mathrm{g}} + \mu - h\omega} + \frac{1}{U_{\mathrm{ff}} + E_{\mathrm{f}}} \sum_{\{\beta\}} \frac{N_{\{\beta\}}\Delta}{\pi} \left(\frac{1}{\Delta E(\{\beta\}) + \delta_{\mathrm{g}}} - \frac{1}{(W + \mu)} \right) \right]^2. \tag{70}$$

An estimate of the size of the finite U_{ff} corrections can be found, for systems with small δ_{g} as compared to $\Delta E(\{\alpha\})$ and $W + \mu$, by considering the point of maximum intensity $h\omega = \mu$. At the Fermi energy, the second term in the amplitude with $\{\alpha\} = g$ can be recognized as being smaller than the first term by a factor with magnitude less than $14\Delta/\pi(U_{\mathrm{ff}} + \mathrm{E_f} - \mu)$. Since, as has been emphasized previously, the approximations made in the above theory require that $U_{\mathrm{ff}} + E_{\mathrm{f}} - \mu \gg (W + \mu)$, these corrections are only reasonable when they are small. A rough analysis of the effects of including the $(4f)^n$ configurations shows that they are needed if the $(4f)^2$ corrections are sizeable, as they appear to be of order $(\Delta/\pi(U_{\mathrm{ff}} + E_{\mathrm{f}}))^{n-1} N!/(N - n + 1)!(n - 1)!$. Furthermore, the finite U_{ff} $(4f)^2$ corrections are smaller than the estimate of the size by which the $U_{\mathrm{ff}} \to \infty$ limit of the above theory violates Luttinger's theorem, since these corrections can be shown to be of order $14\Delta/\pi(W + \mu)$.

The resolvent has another isolated pole at $z - e(\boldsymbol{k}) - \mu - \Delta E_{\mathrm{g}} + U_{\mathrm{ff}} + 2E_{\mathrm{f}} = 0$, which has a finite residue, when $2E_{\mathrm{f}} - 2\mu + U_{\mathrm{ff}} \neq 0$. This may lead to structure in the spectrum at energies $h\omega \approx -(U_{\mathrm{ff}} + E_{\mathrm{f}} - \mu)$. However, since the theory does require that $U_{\mathrm{ff}} + E_{\mathrm{f}} - \mu \gg (W + \mu)$, this occurs far from the energies where the theory is applicable. The other significant contribution to the spectrum comes from the finite, continuous imaginary part of the resolvent in the energy range $-\delta_{\mathrm{g}} > z - e(\boldsymbol{k}) > -(W + \mu)$. The integration in the spectral density stemming from this continuous contribution is evaluated numerically. The resonances due to the Kondo side bands appear at energies given by $h\omega \approx -\Delta E(\{\alpha\}) + \delta_{\{\alpha\}}$. Most of the intensity in the spectrum occurs in the main peak, of halfwidth $N_{\mathrm{f}}\Delta$, which is located at energies near $h\omega = E_{\mathrm{f}} - \mu$.

References

Alascio, B., R. Allub and C.A. Balseiro, 1986, Phys. Rev. B **34**, 4786.

Albers, R.C., 1985, Phys. Rev. B **32**, 7646.

Albers, R.C., A.M. Boring, P. Weinberger and N.E. Christensen, 1985, Phys. Rev. B **32**, 7571.

Albers, R.C., A.M. Boring and N.E. Christensen, 1986, Phys. Rev. B **33**, 8116.

Allen, J.W., 1992, in: Synchrotron Radiation Research: Advances in Surface and Interface Science, Vol. I: Techniques, ed. R.Z. Bachrach (Plenum Press, New York) pp. 253–323.

Allen, J.W., S.-J. Oh, L.E. Cox, W.P. Ellis, M.S. Wire, Z. Fisk, J.L. Smith, B.B. Pate, I. Lindau and A.J. Arko, 1985, Phys. Rev. Lett. **54**, 2635.

Allen, J.W., S.-J. Oh, O. Gunnarsson, K. Schönhammer, M.B. Maple, M.S. Torikachvili and I. Lindau, 1986, Adv. Phys. **35**, 275.

Anderson, P.W., 1961, Phys. Rev. **124**, 41.

Anderson, P.W., 1976, J. Phys. C **3**, 2346.

Andrei, N., K. Furuya and J.H. Lowenstein, 1983, Rev. Mod. Phys. **55**, 331.

Andres, K., J.E. Graebner and H.R. Ott, 1975, Phys. Rev. Lett. **35**, 1779.

Andrews, A.B., R.I.R. Blyth, A.J. Arko, J.J. Joyce, Z. Fisk, J.D. Thompson, R.J. Bartlett, P.C. Canfield, C.G. Olson, P. Benning and P.S. Riseborough, 1994, Physica B **199&200**, 15.

Andrews, A.B., J.J. Joyce, A.J. Arko, J.D. Thompson, J. Tang, J.M. Lawrence and J.C. Hemminger, 1995a, Phys. Rev. B **51**, Rapid Commun., 3277.

Andrews, A.B., J.J. Joyce, A.J. Arko, J.D. Thompson, Z. Fisk, J. Tang, J.M. Lawrence, P.S. Riseborough and P.C. Canfield, 1995b, Physica B **206&207**, 83.

Andrews, A.B., J.J. Joyce, A.J. Arko, Z. Fisk and P.S. Riseborough, 1996, Phys. Rev. B **53**, 3317.

Aoki, H., S. Uji, A.K. Albessard and Y. Onuki, 1992, J. Phys. Soc. Japan **61**, 3457.

Arko, A.J., 1976, in: Proc. 2nd Int. Conf. on Electronic Structure of Actinides, Vol. 2, Wroclaw, Poland, p. 309.

Arko, A.J., M.B. Brodsky, G.W. Crabtree, D. Karim, D.D. Koelling, L.R. Windmiller and J.B. Ketterson, 1975, Phys. Rev. B **12**, 4102.

Arko, A.J., M.B. Brodsky, G.W. Crabtree, D. Karim, L.R. Windmiller and J.B. Ketterson, 1976, in: Plutonium 1975 and other Actinides, eds H. Blank and R. Linder (North-Holland, Amsterdam) p. 325.

Arko, A.J., D.D. Koelling and B. Reihl, 1983, Phys. Rev. B **27**, 3955.

Arko, A.J., C.G. Olson, D.M. Wieliczka, Z. Fisk and J.L. Smith, 1984, Phys. Rev. Lett. **53**, 2050.

Arko, A.J., D.D. Koelling, A.M. Boring, W.P. Ellis and L.E. Cox, 1986, J. Less-Common Met. **122**, 95.

Arko, A.J., B.W. Yates, B.D. Dunlap, D.D. Koelling, A.W. Mitchell, D.J. Lam, C.G. Olson, M. del Giudice, Z. Fisk and J.L. Smith, 1987a, in: Theoretical and Experimental Aspects of Valence Fluctuations and Heavy Fermions, eds L.C. Gupta and S.K. Malik (Plenum Press, New York) pp. 39–46.

Arko, A.J., B.W. Yates, B.D. Dunlap, D.D. Koelling, A.W. Mitchell, D.J. Lam, Z. Zolnierek, C.G. Olson, Z. Fisk, J.L. Smith and M. del Giudice, 1987b, J. Less-Common Met. **133**, 87.

Arko, A.J., D.D. Koelling, C. Capasso, M. del Giudice and C.G. Olson, 1988a, Phys. Rev. B **38**, 1627.

Arko, A.J., D.D. Koelling, B.D. Dunlap, A.W. Mitchell, C. Capasso and M. del Giudice, 1988b, J. Appl. Phys. **63**, 3680.

Arko, A.J., P. Armstrong and M. Wire, 1990, Physica B **163**, 167.

Arko, A.J., J.J. Joyce, P.C. Canfield, J.D. Thompson, R.J. Bartlett, Z. Fisk, J. Lawrence, J. Tang and P. Riseborough, 1993, in: Vacuum Ultraviolet Radiation Physics, eds F.J. Wuilleumier, Y. Petroff and I. Nenner (World Scientific, Singapore), p. 291.

Arko, A.J., J.J. Joyce, A.B. Andrews, R.I.R. Blyth, C.G. Olson, P.C. Canfield, P.J. Benning, D.M. Poirier, J.H. Weaver and P.S. Riseborough, 1994, in: Strongly Correlated Electronic Materials, eds K. Bedell, S.-Y. Huang, A. Balatsky, D.E. Meltzer and E. Abrahams (Addison-Wesley, Reading, MA), p. 101.

Arko, A.J., J.J. Joyce, A.B. Andrews, J.D. Thompson, J.L. Smith, D. Mandrus, M.F. Hundley, A.L. Cornelius, E. Moshopoulou, Z. Fisk, P.C. Canfield and A. Menovsky, 1996, Phys. Rev. B **56**, Rapid Commun., R7041.

Arko, A.J., J.J. Joyce, A.B. Andrews, J.L. Smith, J.D. Thompson, Z. Fisk, E. Moshopoulou, A. Menovsky and P.C. Canfield, 1997a, Physica B **230–232**, 16.

Arko, A.J., J.J. Joyce, A.B. Andrews, D. Mandrus, E. Moshopoulou, Z. Fisk and P.C. Canfield, 1997b, Philos. Mag. B **75**, 603.

Arko, A.J., J.J. Joyce, L.E. Cox, L. Morales, J. Sarrao, J.L. Smith, Z. Fisk, A. Menovsky, A. Tahvildar-Zadeh and M. Jarrell, 1998, J. Alloys and Compounds **271–273**, 826.

Baer, Y., D. Malterre, M. Grioni, P. Weibel and B. Dardel, 1994, J. Electron Spectrosc. Rel. Phenom. **68**, 121.

Bickers, N.E., 1987, Rev. Mod. Phys. **59**, 845.

Bickers, N.E., D.L. Cox and J.W. Wilkins, 1985, Phys. Rev. Lett. **54**, 230.

Bickers, N.E., D.L. Cox and J.W. Wilkins, 1987, Phys. Rev. B **36**, 2036.

Blyth, R.I.R., J.J. Joyce, A.J. Arko, J. Tang and J.M. Lawrence, 1992, Phys. Rev. Lett. **69**, 3418.

Blyth, R.I.R., J.J. Joyce, A.J. Arko, P.C. Canfield, Z. Fisk, J.D. Thompson, R.J. Bartlett, J. Tang and J.M. Lawrence, 1993, Phys. Rev. B **48**, 9497.

Blyth, R.I.R., A.B. Andrews, A.J. Arko, J.J. Joyce, P.C. Canfield, Z. Fisk, U. Lahiase and L. DeLong, 1994, Surf. Rev. Lett. **1**, 1.

Bodenbach, M., A. Hohr, C. Laubschat, G. Kaindl and M. Methfessel, 1994, Phys. Rev B **50**, 14446.

Boring, A.M., R.C. Albers, G. Stewart and D.D. Koelling, 1985a, Phys. Rev. B **31**, 3251.

Boring, A.M., R.C. Albers, F. Mueller and D.D. Koelling, 1985b, Physica B **130**, 1711.

Boring, A.M., R.C. Albers, G. Schadler, P. Marksteiner and P. Weinberger, 1987, Phys. Rev. B **35**, 2447.

Coleman, P., 1984, Phys. Rev. B **29**, 3035.

Coleman, P., 1987, Phys. Rev. B **35**, 5072.

Combescot, M., and P. Nozières, 1971, J. Phys. (Paris) **32**, 913.

Currat, R., R.G. Lloyd, P.W. Mitchell, A.P. Murani and J.W. Ross, 1989, Physica B **156&157**, 812.

Czycholl, G., 1986, Phys. Rep. **143**, 277.

Doniach, S., 1987, Phys. Rev. B **35**, 1814.

Doniach, S., and M. Sunjic, 1970, J. Phys. C **3**, 285.

Evans, S.M., T. Chung and G.A. Gehring, 1989, J. Phys. C **1**, 437.

Fadley, C.F., 1987, Phys. Scripta T **17**, 39.

Fisk, Z., J.L. Sarrao, J.L. Smith and J.D. Thompson, 1995, Proc. Natl. Acad. Sci. USA **92**, 6663.

Freeman, A.J., B.I. Min and M.R. Norman, 1987, in: Handbook on the Physics and Chemistry of Rare Earths, Vol. 10, eds K.A. Gschneidner Jr, L. Eyring and S. Hüfner (North-Holland, Amsterdam) ch. 65, p. 165.

Friedel, J., and C.M. Sayers, 1977, J. Phys. (Paris) **38**, 697.

Galera, R.M., A.P. Murani and J. Pierre, 1989, Physica B **156&157**, 801.

Garnier, M., D. Purdie, K. Breuer, M. Hengsberger and Y. Baer, 1997, Phys. Rev. B **36**, R11399.

Georges, A., G. Kotliar, W. Krauth and M. Rozenberg, 1996, Rev. Mod. Phys. **68**, 13.

Grassman, A., 1990, Physica B **163**, 547.

Grewe, N., and H. Keiter, 1981, Phys. Rev. B **24**, 4420.

Grewe, N., and F. Steglich, 1991, in: Handbook on the Physics and Chemistry of Rare Earths, Vol. 14, eds K.A. Gschneidner Jr and L. Eyring (North-Holland, Amsterdam) ch. 97, pp. 343–474.

Grioni, M., D. Malterre, P. Weibel, B. Dardel and Y. Baer, 1993, Physica B **188**, 38.

Gunnarsson, O., and K. Schönhammer, 1983a, Phys. Rev. Lett. **50**, 604.

Gunnarsson, O., and K. Schönhammer, 1983b, Phys. Rev. B **28**, 4315.

Gunnarsson, O., and K. Schönhammer, 1985, Phys. Rev. B **31**, 4815.

Gunnarsson, O., and K. Schönhammer, 1986, in: Theory of Heavy Fermions and Valence Fluctuations, eds T. Kasuya and T. Saso (Springer, Berlin) p. 110.

Gunnarsson, O., and K. Schönhammer, 1987, in: Handbook on the Physics and Chemistry of Rare Earths, Vol. 10, eds K.A. Gschneidner Jr, L. Eyring and S. Hüfner (North-Holland, Amsterdam) ch. 64, p. 103.

Gunnarsson, O., E. Koch and R. Martin, 1996, Phys. Rev. B **54**, 11026.

Gutzwiller, M.C., 1965, Phys. Rev. A **137**, 1726.

Haldane, F.D.M., 1978a, Phys. Rev. Lett. **40**, 416.

Haldane, F.D.M., 1978b, Phys. Rev. Lett. **40**, 911.

Herbst, J.F., and J.W. Wilkins, 1987, in: Handbook on the Physics and Chemistry of Rare Earths, Vol. 10, eds K.A. Gschneidner Jr, L. Eyring and S. Hüfner (North-Holland, Amsterdam) ch. 68, p. 321.

Hess, D.W., P.S. Riseborough and J.L. Smith, 1993, in: Encyclopedia of Applied Physics, Vol. 7, ed. George L. Trigg (VCH Publishers, New York) pp. 435–463.

Hewson, A.C., and P.S. Riseborough, 1977, Solid State Commun. **22**, 379.

Hirsch, J.E., and R.M. Fye, 1986, Phys. Rev. Lett. **56**, 2521.

Horvatic, B., and V. Zlatic, 1985, Solid State Commun. **54**, 957.

Houghton, A., N. Read and H. Won, 1988, Phys. Rev. B **37**, 3782.

Hüfner, S., 1986, J. Phys. F **16**, L31.

Hüfner, S., 1992, Z. Phys. B **86**, 241.

Hüfner, S., and L. Schlapbach, 1986, Z. Phys. B **64**, 417.

Imer, J.M., and E. Wuilloud, 1987, Z. Phys. B **66**, 153.

Imer, J.M., D. Malterre, M. Grioni, P. Weibel, B. Dardel, Y. Baer and B. Delley, 1991a, Phys. Rev. B **43**, 1338.

Imer, J.M., D. Malterre, M. Grioni, P. Weibel, B. Dardel and Y. Baer, 1991b, Phys. Rev. B **44**, 10455.

Inada, Y., H. Aono, A. Ishigura, J. Kimura, N. Sto, N. Sawada and T. Komatsubara, 1994, Physica B **199&200**, 119.

Inada, Y., A. Ishigura, J. Kimura, N. Sato, A. Sawada, T. Komatsubara and H. Yamagami, 1995, Physica B **206–207**, 33.

Jarrell, M., 1995, Phys. Rev. B, **51**, 7429.

Jarrell, M., and J.E. Gubernatis, 1996, Phys. Rep. **269**, 133.

Jayaprakash, C., H.R. Krishnamurthy and J.W. Wilkins, 1981, Phys. Rev. Lett. **47**, 737.

Jones, B.A., and C.M. Varma, 1987, Phys. Rev. Lett. **58**, 843.

Jones, B.A., C.M. Varma and J.W. Wilkins, 1988, Phys. Rev. Lett. **61**, 125.

Joyce, J.J., and A.J. Arko, 1993, Phys. Rev. Lett. **70**, 1181.

Joyce, J.J., A.J. Arko, J.M. Lawrence, P.C. Canfield, Z. Fisk, R.J. Bartlett, J.D. Thompson and J.L. Smith, 1992a, J. Less-Common Met. **181**, 161.

Joyce, J.J., A.J. Arko, J.M. Lawrence, P.C. Canfield, R.J. Bartlett, Z. Fisk, J.D. Thompson and J. Tang, 1992b, Solid State Commun. **83**, 551.

Joyce, J.J., A.J. Arko, J.M. Lawrence, P.C. Canfield, Z. Fisk, R.J. Bartlett and J.D. Thompson, 1992c, Phys. Rev. Lett. **68**, 236.

Joyce, J.J., A.J. Arko, P.S. Riseborough, P.C. Canfield, J.M. Lawrence, R.I.R. Blyth, R.J. Bartlett, J.D. Thompson and Z. Fisk, 1993, Physica B **186–188**, 31.

Joyce, J.J., A.J. Arko, A.B. Andrews and R.I.R. Blyth, 1994a, Phys. Rev. Lett. **72**, 1774.

Joyce, J.J., A.J. Arko, A.B. Andrews, R.I.R. Blyth, R.J. Bartlett, J.D. Thompson, Z. Fisk, P.S. Riseborough, P.C. Canfield, C.G. Olson and P.J. Benning, 1994b, Physica B **205**, 365.

Joyce, J.J., A.B. Andrews, A.J. Arko, R.I.R. Blyth, R.J. Bartlett, C.G. Olson, D.M. Poirier, P.C. Canfield and P.J. Benning, 1996, Phys. Rev. B **54**, 17515.

Kakizaki, A., A. Harasawa, T. Ishii, T. Kashiwakura, A. Kamata and S. Kunii, 1995, J. Phys. Soc. Japan **64**, 302.

Kang, J.S., J.W. Allen, M.B. Maple, M.S. Torikachvili, B. Pate, W.P. Ellis and I. Lindau, 1987, Phys. Rev. Lett. **59**, 493.

Kang, J.S., J.W. Allen, M.B. Maple, M.S. Torikachvili, W.P. Ellis, B.B. Pate, Z.-X. Shen, J.J. Yeh and I. Lindau, 1989, Phys. Rev. B **39**, 13529.

Kang, J.S., J.W. Allen, C. Rossel, C.L. Seaman and M.B. Maple, 1990a, Phys. Rev. B **41**, 4087.

Kang, J.S., J.W. Allen, O. Gunnarsson, N.E. Christensen, O.K. Anderson, Y. Lassailly, M.B. Maple and M.S. Torikachvili, 1990b, Phys. Rev. B **41**, 6610.

Kim, Hayoung, and P.S. Riseborough, 1990, Phys. Rev. B **42**, 7975.

Knopfle, K., A. Mavromaras, L.M. Sandratskii and J. Kubler, 1996, J. Phys. : Cond. Matter **8**, 901.

Koelling, D.D., B.D. Dunlap and G.W. Crabtree, 1985, Phys. Rev. B **31**, 4966.

Krishnamurthy, H.R., J.W. Wilkins and K.G. Wilson, 1980a, Phys. Rev. B **21**, 1003.

Krishnamurthy, H.R., J.W. Wilkins and K.G. Wilson, 1980b, Phys. Rev. B **21**, 1044.

Landgren, G., Y. Jugnet, J.F. Morar, A.J. Arko, Z. Fisk, J.L. Smith, H.R. Ott and B. Reihl, 1984, Phys. Rev. B **29**, Rapid Commun., 493.

Lang, J.K., Y. Baer and P.A. Cox, 1981, J. Phys. F **11**, 121.

Laubschat, C., E. Weschke, C. Holtz, M. Domke, O. Strebel and G. Kaindl, 1990, Phys. Rev. Lett. **65**, 1639.

Laubschat, C., E. Weschke, M. Domke, C.T. Simmons and G. Kaindl, 1992, Surf. Sci. **269**, 605.

Lawrence, J.M., and D.M. Mills, 1991, Comm. Condens. Matter Phys. **15**, 163.

Lawrence, J.M., P.S. Riseborough and R.D. Parks, 1981, Rep. Prog. Phys. **44**, 1.

Lawrence, J.M., J.J. Joyce, A.J. Arko, R.J. Bartlett, P.C. Canfield and Z. Fisk, 1993, Phys. Rev. B **47**, 1546.

Lawrence, J.M., G.H. Kwei, P.C. Canfield, J.G. De Witt and A.C. Lawson, 1994, Phys. Rev. B **49**, 1627.

Lee, P.A., T.M. Rice, J.W. Serene, L.J. Sham and J.W. Wilkins, 1986, Comm. Condens. Matter Phys. **12**, 99.

Liu, L.-Z., J.W. Allen, C.L. Seaman, M.B. Maple, Y. Dalichaouch, J.-S. Kang, M.S. Torikachvili and M.L. Lopez de la Torre, 1992b, Phys. Rev. Lett. **68**, 1034.

Liu, L.Z., J.W. Allen, O. Gunnarsson, N.E. Christensen and O.K. Anderson, 1992a, Phys. Rev. B **45**, 8934.

Liu, S.H., 1988, Phys. Rev. B **37**, 3542.

Liu, S.H., 1993, in: Handbook on the Physics and Chemistry of Rare Earths, Vol. 17 (North-Holland, Amsterdam), ch. 111, pp. 87–148.

Liu, S.H., 1997, Physica B **240**, 49.
Liu, S.H., and K.M. Ho, 1982, Phys. Rev. B **26**, 7052.
Liu, S.H., and K.M. Ho, 1983, Phys. Rev. B **28**, 4220.
Lonzarich, G.G., 1988, J. Magn. Magn. Mater. **76–77**, 1.
Lynch, D.W., and J.H. Weaver, 1987, in: Handbook on the Physics and Chemistry of Rare Earths, Vol. 10, eds K.A. Gschneidner Jr, L. Eyring and S. Hüfner (Norht-Holland, Amsterdam) ch. 66, p. 231 and references therein.
Mahan, G.D., 1967, Phys. Rev. **163**, 612.
Malterre, D., M. Grioni, P. Weibel, B. Dardel and Y. Baer, 1992a, Phys. Rev. Lett. **68**, 2656.
Malterre, D., M. Grioni, P. Weibel, B. Dardel and Y. Baer, 1992b, Europhys. Lett. **20**, 445.
Malterre, D., M. Grioni, P. Weibel, B. Dardel and Y. Baer, 1993, Phys. Rev. B **48**, 10599.
Malterre, D., M. Grioni, P. Weibel, B. Dardel and Y. Baer, 1994, Physica B **199**, 76.
Malterre, D., M. Grioni and Y. Baer, 1996, Adv. Phys. **45**, 299.
Martin, R.M., and J.W. Allen, 1979, J. Appl. Phys. **50**, 7651.
Matzdorf, R., G. Meister and A. Goldmann, 1993, Surf. Sci. **286**, 56.
Metzner, W., and D. Wohlhardt, 1989, Phys. Rev. Lett. **62**, 341.
Müller-Hartmann, E., 1984, Z. Phys. B **57**, 281.
Newns, D.M., and N. Read, 1987, Adv. Phys. **36**, 799.
Norman, M.R., 1985, Phys. Rev. B **31**, 6261.
Norman, M.R., D.D. Koelling, A.J. Freeman, H.J.F. Hansen, B.I. Min, T. Oguchi and Ling Ye, 1984, Phys. Rev. Lett. **53**, 1673.
Norman, M.R., D.D. Koelling and A.J. Freeman, 1985, Phys. Rev. B **31**, 6251.
Nozières, P., 1974, J. Low. Temp. Phys. **17**, 31.
Nozières, P., 1985, Ann. Physique **10**, 19.
Nozières, P., and C. DeDominicis, 1969, Phys. Rev. **178**, 1097.
Nunes, A.C., J.W. Rasul and G.A. Gehring, 1985, J. Phys. C **18**, L873.
Nunes, A.C., J.W. Rasul and G.A. Gehring, 1986, J. Phys. C **19**, 1017.
Nunez-Regueiro, M.D., and M. Avignon, 1985, Phys. Rev. Lett. **55**, 615.
Oh, S.J., 1993, Physica B **186–188**, 637.
Okada, K., K. Yamada and K. Yosida, 1987, Prog. Theor. Phys. **77**, 1297.
Oliveira, L.N., and J. Wilkins, 1981, Phys. Rev. Lett. **47**, 1553.
Onuki, Y., 1993, Physica B **186–188**, 92.
Ott, H.R., and Z. Fisk, 1987, in: Handbook on the Physics and Chemistry of the Actinides, Vol. 5, eds A.J. Freeman and G.H. Lander (North-Holland, Amsterdam) pp. 85–225.
Ott, H.R., H. Rudigier, Z. Fisk and J.L. Smith, 1983, Phys. Rev. Lett. **50**, 1595.
Parks, R.D., S. Raaen, M.L. den Boer, Y.-S. Chang and G.P. Williams, 1984, Phys. Rev. Lett. **52**, 2176.
Patthey, F., B. Delley, W.D. Schneider and Y. Baer, 1985, Phys. Rev. Lett. **55**, 1518.
Patthey, F., W.D. Schneider, Y. Baer and B. Delley, 1986, Phys. Rev. B **34**, 2967.
Patthey, F., W.-D. Schneider, Y. Baer and B. Delley, 1987a, Phys. Rev. Lett. **58**, 2810.
Patthey, F., W.D. Schneider, Y. Baer and B. Delley, 1987b, Phys. Rev. B **35**, 5903.
Patthey, F., J.-M. Imer, W.-D. Schneider, H. Beck and Y. Baer, 1990, Phys. Rev. B **42**, 8864.
Patthey, F., W.D. Schneider, M. Grioni, D. Malterre and Y. Baer, 1993, Phys. Rev. Lett. **70**, 1179.
Pruschke, Th., and N. Grewe, 1989, Z. Phys. B **74**, 439.
Pruschke, Th., M. Jarrell and J.K. Freericks, 1995, Adv. Phys. **42**, 187.
Rasul, J.W., and A.P. Harrington, 1987, J. Phys. C **20**, 4783.
Rasul, J.W., and A.C. Hewson, 1984, J.Phys. C **17**, 3337.
Rasul, J.W., and A.C. Hewson, 1985, Solid State Commun. **52**, 267.
Read, N., 1985, J. Phys. C **18**, 2651.
Read, N., and D.M. Newns, 1983a, J. Phys. C **16**, 3273.
Read, N., and D.M. Newns, 1983b, J. Phys. C **16**, L1055.
Rice, T.M., and K. Ueda, 1986, Phys. Rev. B, **34**, 6420.
Riseborough, P.S., 1986, Solid State Commun. **57**, 721.
Rivier, N., V. Zlatic and G. Gruner, 1974, Solid State. Commun. **14**, 639.
Rusic, B., G.L. Goodman and J. Berkowitz, 1983, J. Chem. Phys. **78**, 5443.
Sandratskii, L.M., J. Kubler, P. Zahn and I. Mertig, 1994, Phys. Rev. B **50**, 15834.
Sarma, D.D., F.U. Hillebrecht, W. Speier, N. Martensson and D.D. Koelling, 1986, Phys. Rev. Lett. **57**, 2215.
Scalapino, D.J., S. White and S. Zhang, 1993, Phys. Rev. B **47**, 7995.
Schlottmann, P., 1989, Phys. Rep. **181**, 1.

Schrieffer, J.R., and P.A. Wolff, 1966, Phys. Rev. **149**, 491.

Schweitzer, H., and G. Czycholl, 1989a, Z. Phys. B **74**, 303.

Schweitzer, H., and G. Czycholl, 1989b, Solid State Commun. **69**, 171.

Seaman, C.L., M.B. Maple, B.W. Lee, S. Shamaty, M. Torikachvili, J.-S. Kang, L.-Z. Liu, J.W. Allen and D.L. Cox, 1991, Phys. Rev. Lett. **67**, 2882.

Sheng, Q.G., and B.R. Cooper, 1995, Philos. Mag. Lett. **72**, 123.

Silver, R.N., J.E. Gubernatis, D.S. Sivia and M. Jarrell, 1990, Phys. Rev. Lett. **65**, 496.

Springford, M., and P.H.P. Reinders, 1988, J. Magn. Magn. Mater. **76–77**, 11.

Steglich, F., J. Aarts, C.D. Bredl, W. Lieke, D. Meschede, W. Franz and H. Schafer, 1979, Phys. Rev. Lett. **43**, 1892.

Steiner, M.M., R.C. Albers, D.J. Scalapino and L.J. Sham, 1991, Phys. Rev. B **43**, 1637.

Steiner, M.M., R.C. Albers and L.J. Sham, 1994, Phys. Rev. Lett. **72**, 2923.

Stewart, G.R., 1984, Rev. Mod. Phys. **56**, 755.

Stewart, G.R., Z. Fisk, J.O. Willis and J.L. Smith, 1984, Phys. Rev. Lett. **52**, 679.

Strange, P., and D.M. Newns, 1986, J. Phys. F **16**, 335.

Tahvildar-Zadeh, A.N., M. Jarrell and J.K. Freericks, 1997, Phys. Rev. B **55**, R3332.

Takahashi, T., T. Morimoto, T. Yokoya, M. Kohgi and T. Satoh, 1994, Phys. Rev. B **49**, 15688.

Takahashi, T., T. Morimoto, T. Yokoya, S. Kunii, T. Komatsubara and O. Sakai, 1995, Phys. Rev. B **52**, 9140.

Takahashi, T., N. Sato, T. Yokoya, A. Chainani, T. Morimoto and T. Komatsubara, 1996, J. Phys. Soc. Japan **65**, 156.

Tang, J., J.M. Lawrence and J.C. Hemminger, 1993, Phys. Rev. B **48**, 15342.

Thompson, J.D., and J.M. Lawrence, 1994, in: Handbook on the Physics and Chemistry of Rare Earths, Vol. 19, eds K.A. Gschneidner Jr and L. Eyring (North-Holland, Amsterdam) ch. 133, pp. 383–478.

Tjeng, L.H., S.-J. Oh, E.-J. Cho, H.-J. Lin, C.T. Chen, G.-W. Gweon, J.-H. Park, J.W. Allen, T. Suzuki, M.S. Makivic and D.L. Cox, 1993, Phys. Rev. Lett. **71**, 1419.

Tjeng, L.H., S.-J. Oh, C.T. Chen, J.W. Allen and D.L. Cox, 1994, Phys. Rev. Lett. **72**, 1775.

Treglia, G., F. Ducastelle and D. Spanjaard, 1980, Phys. Rev. B **21**, 3729.

Treglia, G., F. Ducastelle and D. Spanjaard, 1982, J. Phys. (Paris) **43**, 341.

Tsvelick, A.M., and P.B. Wiegmann, 1983, Adv. Phys. **32**, 453.

Weibel, P., M. Grioni, D. Malterre, B. Dardel, Y. Baer and M. Besnus, 1993, Z. Phys. B **91**, 337.

Weschke, E., C. Laubschat, T. Simmons, M. Domke, O. Strebel and G. Kaindl, 1991, Phys. Rev. B **44**, 8304.

Weschke, E., C. Laubschat, R. Ecker, A. Hohr, M. Domke, G. Kaindl, L. Severin and B. Johansson, 1992, Phys. Rev. Lett. **69**, 1792.

Wilson, K.G., 1975, Rev. Mod. Phys. **47**, 733.

Yashima, H., and T. Satoh, 1982, Solid State Commun. **41**, 723.

Yosida, K., and A. Yoshimori, 1963, in: Magnetism, Vol. 5, ed. H. Suhl (Academic Press, New York) p. 253.

Zhang, F.C., and T.K. Lee, 1983, Phys. Rev. B **28**, 33.

Zhang, F.C., and T.K. Lee, 1984, Phys. Rev. B **30**, 1556.

Zlatic, V., S.K. Ghatak and K.H. Bennemann, 1986, Phys. Rev. Lett. **57**, 1263.

Zolnierek, Z., A.J. Arko and D.D. Koelling, 1986, J. Less-Common Met. **122**, 89.

Zwicknagl, G., 1992, Adv. Phys. **41**, 203.

AUTHOR INDEX

SUBJECT INDEX